Dynamics in Small
Confining Systems III

Dynamics in Small Confining Systems III

Symposium held December 2–5, 1996, Boston, Massachusetts, U.S.A.

EDITORS:

J.M. Drake
*Exxon Research and Engineering Company
Annandale, New Jersey, U.S.A.*

J. Klafter
*Tel Aviv University
Tel Aviv, Israel*

R. Kopelman
*University of Michigan
Ann Arbor, Michigan, U.S.A.*

CONTENTS

*Invited Paper

v

*Invited Paper

vii

*Invited Paper

PREFACE

The fourth symposium on "Dynamics in Small Confining Systems," held as part of the 1996 MRS Fall Meeting, covered a broad range of topics related to static and dynamic properties of confining systems: probing of confined systems, structure and dynamics of liquids at interfaces, nanorheology and tribology, adsorption, diffusion in pores, and reactions. Participants from various disciplines shared different points of view on the questions of how ultrasmall geometries can force a system to behave in ways significantly different from its behavior in the bulk, how this difference affects molecular properties, and how it is probed.

There appears to be a continuing interest in the dynamics and thermo-dynamics of confined molecular systems. The symposium was an effective way to bring together different disciplines interested in common problems. We are planning to organize the fifth symposium in the fall of 1998.

The contributions in the book reflect the broad range of topics discussed at the meeting, all related to dynamics in small confining systems. We hope that the interdisciplinary nature of the book and the meeting will help to bridge the gap among the different approaches and methods presented. The papers appear in the book in the order of their presentation during the symposium.

We would like to thank everyone who helped in the organization and execution of the 1996 MRS Fall Meeting, especially the authors and the presenters whose work has made this book possible and the symposium successful.

Special thanks are due to the ONR which sponsored this and previous symposia.

J.M. Drake
J. Klafter
R. Kopelman

February 1997

MATERIALS RESEARCH SOCIETY SYMPOSIUM PROCEEDINGS

MATERIALS RESEARCH SOCIETY SYMPOSIUM PROCEEDINGS

Prior Materials Research Society Symposium Proceedings available by contacting Materials Research Society

Dynamics in Small Confining Systems III

COMPUTER STUDIES ON FREE AND CONFINED AMORPHOUS POLYMER FILMS

G. PÄTZOLD, D.W. HEERMANN, A. LINKE, AND T. HAPKE
Institut für Theoretische Physik, Universität Heidelberg,
Philosophenweg 19, 69120 Heidelberg, Deutschland
und Interdisziplinäres Zentrum für wissenschaftliches Rechnen der Universität Heidelberg
E-mail: heermann@tphys.uni-heidelberg.de, URL: http://wwwcp.tphys.uni-heidelberg.de/

ABSTRACT

We study surface effects in amorphous polymer systems by means of computer simulation. In the framework of molecular dynamics, we present two different methods to prepare such surfaces. *Free* surfaces are stabilized solely by van-der-Waals interactions, whereas *confined* surfaces emerge in the presence of repelling plates. The buildup of density and pressure profiles from zero to their bulk values depends on the surface preparation method. In the case of confined surfaces, we find density and pressure oscillations next to the repelling plates. For free surfaces, we attest chain-end enrichment and present a comparison between density profile and particle coordination number.

INTRODUCTION

The technological applicability of polymeric materials depends in a number of important cases on the polymer's surface properties: the surface roughness determines the friction coefficient, cracks emerging from the surface influence the material's durability, and surface defects reduce the transparency of polymeric panes. At the same time, the experimental and manufacturing techniques advance to smaller and smaller scales. Nowadays one can pursue mechanical effects on the nano-scale. This opens new, challenging, and exciting roads for academic research and promising prospects for industrial applications. Nanomechanics influences the design of computer chips and is fundamental for new developments like miniaturized optical devices and nanoengines. A related topic is the mechanics of very thin films with thicknesses in the nano-range. Again, it is not just the bulk behavior that decides about the nano-technological applicability of a certain material but its surface properties. The nano-scale processes that lead to macroscopically relevant surface-related phenomena like friction, wear, hardness, and certain types of material failure like surface degradation are scarcely understood from the theoretical point of view. In some cases, phenomenological theories exist [1] which attempt to systematize the various experimental observations. A fundamental understanding, however, tentatively based on fundamental nano-scale processes, is lacking.

POLYMER AND SURFACE MODELING

For the polymer chains, we use a united atom model in conjunction with Newtonian dynamics. In addition to harmonic chain forces which keep the bond lengths next to the equilibrium value, we model the fluctuation of bond angles, again by a quadratic potential. Between monomers which do not participate in mutual bond length or bond angle interactions, Lennard-Jones forces are acting, both to model an excluded volume effect and to hold the polymer system together. The Lennard-Jones interaction is implemented with a

3
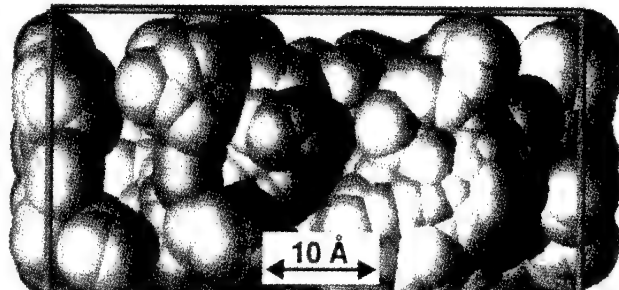
Figure 1: The *confined* polymer surface (at the top of the bulk). The horizontal line of the frame represents the repelling plate. The monomers are drawn with their Lennard-Jones radius σ=3.8 Å. In the lateral directions, periodic boundary conditions apply.

cutoff of $2.5\,\sigma$ and appropriate potential and force shifts are used to retain continuity. We use molecular dynamics methods to compute the motion of the monomers. Models of this kind are described at numerous places in the literature [2].

We employ two alternative methods to prepare amorphous polymer surfaces. The *confined polymer surface*, Fig. 1, is realized by plates that repel the monomeric units and thereby restrict the polymer to a certain region in space. This gives rise to a surface model which is mainly characterized by its smoothness. In the simulations, we set up the united atom model with periodic boundary conditions in the x- and y-direction. In the z-direction, we put two repelling plates at a distance chosen such that the resulting bulk density of the polymer system settles to the desired value. The other alternative, Fig. 2, is the *free polymer surface*. Here the polymer bulk is held together solely by the overall attracting intermolecular van-der-Waals interactions. Individual chains may evaporate or condense. The emerging surfaces are rougher than in the confined case.

RESULTS FROM THE COMPUTER SIMULATIONS

In the case of the polymer system with confined surfaces, the plates are rapidly brought from infinity to a distance such that the monomer number density in the resulting box is $\rho_{\text{bulk}} = 2.0$. The shock results in a distribution of the density in the z-direction (system height) as shown in Fig. 3. These typical periodic changes of the density distribution close to the surface [3] are due to the external pressure produced by the plates, which leads to a local partial crystallization. The same behavior has been found in simulations analyzing surface phenomena [4] and was studied in the context of one long chain between two parallel plates [5]. The chains experience strong packing constraints as well as a loss in entropy that must show up also in the surface properties that can be observed during indentation. Shown with the density profile is the relative frequency of end-monomers. This is computed by defining slices of height d in the z-direction and dividing the number of chain ends by the total number of monomers within each slice. The resulting relative frequency is fairly independent of the slice height d. We conclude from the figure that there is *no* appreciable chain-end enrichment at confined surfaces. This is in accordance with the fact that there are no energetic or entropic reasons for the end-monomers to gather in the vicinity of the plates.
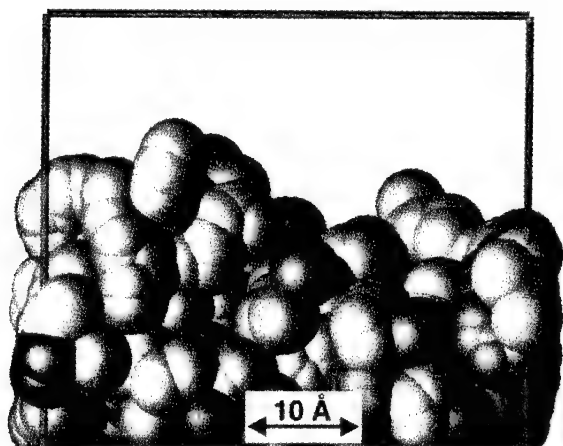
Figure 2: The *free* polymer surface (at the top of the bulk). The upper horizontal line of the frame is out of the interaction range. The monomers are drawn with their Lennard-Jones radius $\sigma=3.8$ Å. In the lateral directions, periodic boundary conditions apply.
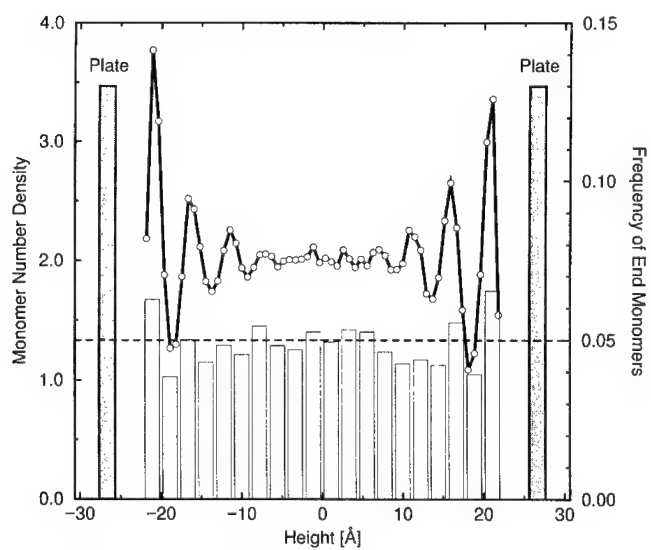
Figure 3: Distribution of density and end-monomers for the *confined* surface.
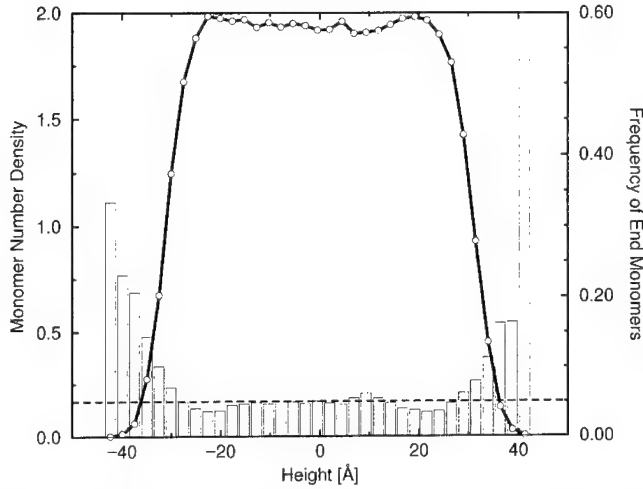
Figure 4: Density distribution and chain-end enrichment for the the *free* surface.

To study the effects of a rougher and presumably more realistic surface, we set up a free system with periodic boundary conditions in x- and y-direction and free boundary conditions in z-direction. At the beginning, this system can be prepared like a confined one with two repelling plates in the z-direction. This is mainly done to bring the polymer bulk initially into a regular shape. By previous experience, the density during the constrained phase is chosen close to the bulk density of a free system. After a time, the plates are removed and the system is free to relax into the surrounding vacuum.

In Fig. 4, the distribution of the monomer number density vs. the height direction (the direction normal to the surfaces) is plotted. As opposed to confined surfaces, no partial crystallization can be observed at free surfaces. Also shown in this figure is the chain-end enrichment. Again in contrast to confined surfaces, we observe the clear tendency for the chain-ends to escape from the bulk. Chain-end monomers require a greater static volume than mid-chain monomers. To reach close packing, they stick to the surface. This is also favored by reasons of entropy, since the end-monomers possess a higher mobility (they are only constrained by one chemical bond). The presence of end-monomers of high mobility and the local brush-like structure caused by the chain ends will certainly affect the mechanics of surface disturbances like in an indentation process.

In connection with amorphous materials, the coordination number of a given particle is the number of all its partners involved in van-der-Waals (Lennard-Jones) interactions. From the simulations, this number can simply be determined by counting all the monomers in the interaction range (a sphere of radius 2.5 Lennard-Jones σ) of a given monomer. We assume homogeneity in the lateral directions, associate with every coordination number the coordinates of its monomer, and set up the distribution of the average coordination number vs. the height direction. The result is shown in Fig. 5. A theoretical estimate for the coordination number distribution $c(z)$ must be based on the monomer number density
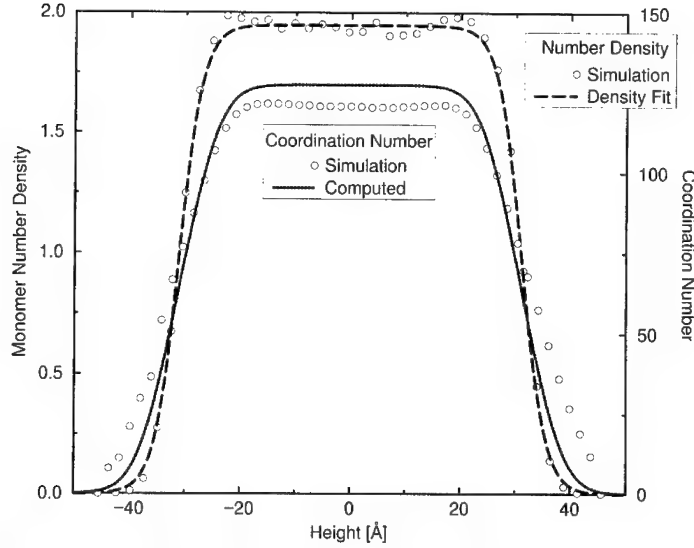
Figure 5: Comparison between density profile and coordination number for *free* surfaces.

profile $\rho(z)$. Geometric relations then yield the convolution type integral

$$c(z) = \int_{z-\sigma}^{z+\sigma} \rho(\zeta) \pi \left(\sigma^2 - (z-\zeta)^2 \right) d\zeta,$$

where σ is the Lennard-Jones radius. The monomer density profile over the entire film, $\rho(z)$, has two flanks ("left" and "right" in Fig. 5); accordingly we may use the ansatz

$$\rho(z) = \rho_{\text{bulk}} \left[\Theta(-z) \left(1 + \tanh\left(\frac{z + z_{\text{tL}}}{\xi_{\text{tL}}} \right) \right) + \Theta(z) \left(1 - \tanh\left(\frac{z - z_{\text{tR}}}{\xi_{\text{tL}}} \right) \right) \right]$$

with the parameters $\sigma = 9.8\,\text{Å}$, $\rho_{\text{bulk}} = 1.947$, $z_{\text{tL}} = 31.16\,\text{Å}$, $z_{\text{tR}} = 31.16\,\text{Å}$, $\xi_{\text{tL}} = 4.32\,\text{Å}$, and $\xi_{\text{tR}} = 4.32\,\text{Å}$. This results in the computed curve for the coordination number in Fig. 5. As expected, the flanks of the coordination number distribution are broader than the flanks of the density profile. This means that in the interaction picture, the surface region is further extended than according to the local density criterion.

CONCLUSION AND OUTLOOK

We have presented two methods to prepare amorphous polymer surfaces in molecular dynamics simulations with united atom models for the polymer chains. The ideas involved can easily be transfered to both more detailed models (which, as one extreme, explicitly treat each atom in a monomer, or, like the ellipsoidal model [6] for BPA-PC, extend the united atom model by considering the geometric shape of a monomer) and more coarse-grained polymer models. The use of classical molecular dynamics algorithms is not mandatory. Monte-Carlo and Hybrid Monte-Carlo techniques can be employed as well and the inclusion of stochastic Langevin forces (Brownian motion) is straightforward. The present work is

also a further step in extending the versatility of *The Materials Explorer*, a continuously growing, integrated software tool for the simulation, visualization, and quantitative analysis of engineering materials [7]. The work presented here will allow us to analyze our simulations on nano-mechanical surface indentation processes [8], in which we prepare a surface using one of the methods discussed above. After that, the impact of the indentation tool causes local disturbances and the deviation of the certain observables from their equilibrium values gives us information about the surface resistance and friction properties. Related to the indentation processes are also simulations on thin film bending [8]. Here a tool, which is more carefully driven than in the indentation experiment, causes non-local, large-scale deformations in the polymer film.

ACKNOWLEDGMENTS

REFERENCES

[1] R.T. Spurr, Wear **79**, 301 (1982); T.A. Stolarski, *Tribology in Machine Design* (Heinemann Newnes, 1990); I.M. Hutchings, *Tribology* (Edward Arnold, London, 1992); J.R. Cooper, D. Dowson, and J. Fisher, Wear **162**, 378 (1993).

[2] M.P. Allen and D.J. Tildesley, *Computer Simulation of Liquids* (Clarendon Press, Oxford, 1987); D. Rigby and R.J. Roe, J. Chem. Phys. **87**, 7285 (1987); T. Hapke, *Simulation mikromechanischer Eigenschaften von amorphen makromolekularen Gläsern am Beispiel von Polyethylen*, Diplomarbeit am Institut für Theoretische Physik der Universität Heidelberg, 1995.

[3] P.K. Brazhnik, K.F. Freed and H. Tang, J. Chem. Phys. **101**, 9143 (1994).

[4] Y. Rouault, B. Dünweg, J. Baschnagel, and K. Binder, Polymer **37**, 297 (1996).

[5] J.H.J. Van Opheusden, J.M.M. De Nijs, and F.W. Wiegel, Physica A **134**, 59 (1985).

[6] K.M. Zimmer and D.W. Heermann, J. Computer-Aided Materials Design **2**, 1 (1995).

[7] A. Linke, D.W. Heermann, and Ch. Münkel, in *Proceedings of the HPCN 1995* (Lect. Notes in Comp. Science, Springer-Verlag, Heidelberg, 1995), p. 928; *A tool for materials exploration*, contribution **JJ5.8** to the MRS 1996 fall meeting.

[8] G. Pätzold, T. Hapke, A. Linke, and D.W. Heermann, Thin Solid Films (to be published); Surface Science (to be published); *Deformation of polymer films by bending forces*, contribution **Ca9.14** to the MRS 1996 fall meeting.

SURFACE ROTATIONAL DYNAMICS OF LIQUIDS CONFINED IN NANOPORES

J.-P. KORB*, L. MALIER*, F. CROS*, SHU XU**, J. JONAS**
*Laboratoire de Physique de la Matière Condensée, CNRS, Ecole Polytechnique, 91128 Palaiseau, France
**Department of Chemistry, University of Illinois, Urbana, Illinois 61801, U.S.A.

ABSTRACT

^{2}H NMR relaxation times of selectively deuterated polar molecules confined to a set of calibrated nanoporous silica glasses are reported. These experiments, combined with the consideration of different time scales in the theory of surface relaxation, show how confinement effects can provide detailed information on the rotational dynamics of temporarily adsorbed liquid layers in presence of biphasic fast exchange.

INTRODUCTION

We aim at studying the structure and dynamics of a liquid layer near a solid boundary surface. This study is of fundamental importance for porous media, liquid crystals and membranes. This is all the more important as a liquid confined to a region that approaches molecular dimensions has dynamic [1-3] and thermodynamic [4] properties strongly changed relatively to the bulk. This study is also of technological significance for heterogeneous catalysis, membrane separation, lubrication and oil recovery. So far, the dynamics of such a wetting layer has not been fully determined because of its small fraction and its chemical exchange with the rest of the liquid. A surface partial ordering has been evidenced in confined liquid crystals where ^{2}H quadrupolar splitting persists [5]. However, such spectroscopic features cannot be observed for simple liquids because of motional averaging, therefore, another approach must be developped.

We propose a method to obtain information on the structure and rotational dynamics of polar liquids at the surface of nanopores. Our method is based on a clear separation of surface ($1/T_{1s}$) and bulk ($1/T_{1b}$) contributions of the overall ^{2}H nuclear relaxation rate ($1/T_1$) of a polar liquid confined to a set of calibrated nanoporous silica glasses. The temperature dependences of $1/T_{1s}$ and the selective deuterium labelling have allowed us to isolate and quantify, for the first time, anisotropic activated and non-activated molecular motions at the pore surface. This is a new result different from the isotropic and activated molecular motions observed in bulk. An original model of anisotropic rotational dynamics of polar molecules linked by hydrogen bonds on the pore surface has been proposed. It is based on fast and slow (activated and non-activated) rotational motions. These different time scales in the theory of surface relaxation allows us to estimate the orientational order parameter as well as the complete rotational dynamics at the liquid-solid interface even in presence of a biphasic fast exchange with the bulk liquid.

9

EXPERIMENTAL

When the liquid interacts strongly with the surface, as for a polar liquid in contact with a solid surface, there are two distinct phases in fast exchange : a surface-affected liquid phase of thickness ε and a bulk liquid phase. Our earlier NMR studies [6] proved the applicability of the biphasic fast exchange model for the analysis of the observed exponential relaxation ($1/T_1$) for polar liquid in cylindrical pores of radius R :

$$\frac{1}{T_1} = \frac{1}{T_{1b}} + \frac{2\varepsilon}{R}\left(\frac{1}{T_{1s}} - \frac{1}{T_{1b}}\right).$$

(1)

The calibrated porous samples are silica glasses, prepared as previously described [6]. EPR measurements have revealed no paramagnetic impurities which would have made the relaxation analysis quite difficult. The surface of these porous glasses exhibits approximately two to three SiOH groups per nm^2. The samples were filled with pyridine using a bulb to bulb method [6]. The experiment and surface dynamics analysis we describe here are general and not limited to pyridine, but this liquid offers several advantages which make it a good model case. First, being strongly polar, it ensures to be in the wetting limit; second, its molecular rigidity prevents internal motions to contribute to the nuclear relaxation; last, it allows selective labelling. For the spin probe, we chose deuterium (^2H) because its relaxation proceeds through molecular reorientations. In the extreme narrowing limit, the relaxation rate $1/T_1$ is thus simply proportionnal to the reorientationnal correlation time [7]. Selectively deuterated pyridines were prepared from corresponding bromopyridines following literature procedures [8]. Deuterium relaxation times, T_1, was measured by the inversion-recovery technique at a Larmor frequency of 27.6 MHz on a home-built spectrometer. In Eq. (1), ε=0.5 nm corresponds to the hard sphere diameter of the pyridine molecule. The dynamical properties have been studied for temperature varying from -9°C to 37°C.

The benefit of selective labelling clearly appears in Fig. 1 which presents the pore radius dependencies of the ^2H relaxation rates at different temperatures, both for ortho or para deuterium substitution. The net difference between these two rates is the experimental evidence of the anisotropy of the molecular reorientations. The linear dependence of $1/T_1$ upon $1/R$ is clearly verified. This validates the Eq. (1) to calculate the surface relaxation rates $1/T_{1s}$.

The temperature dependences of $1/T_{1s}$ for both deuterium substitutions are displayed in the top of Fig. 2. For the sake of comparison, the bulk relaxation rates $1/T_{1b}$ have also been plotted. Inspection of Fig. 2 leads to the following conclusions. First, the surface relaxation rates are more than tenfold larger than the bulk rates, providing evidence of a much slower dynamics at surface. Second, the ratio between ortho and para substituted pyridines relaxation times is very different between both cases. It reveals a near isotropy in the bulk dynamics as well as large temperature dependent anisotropy at surface. Moreover, the apparent activation energy associated with $1/T_{1s}$(para), estimated at 2.1 kJ.mol^{-1}, is of the order of the thermal energy (kT), thus ruling out any activated reorientationnal process. This is important as it shows unambiguously that the chemical exchange between the surface layer and the bulk is not responsible for the

surface relaxation. Therefore, T_{1s} is only sensitive to the dynamics within the wetting layer. This temperature dependence cannot be explained by the usual theory of nuclear relaxation which does not take into account any restriction in the motion [9].
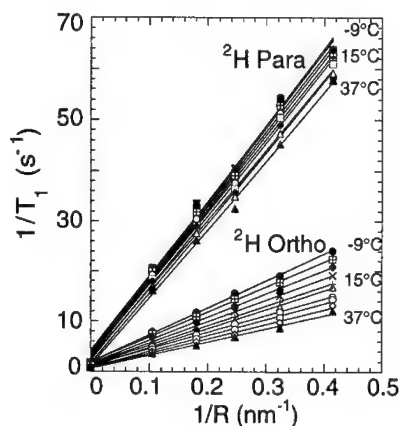
Fig. 1 : The ^2H spin-lattice relaxation rates $1/T_1$ of liquid pyridine selectively deuterated at ortho and para positions as function of pore radius (1/R) in porous sol-gel glasses with $R \in \{\infty(bulk), 9.5, 5.6, 4.1, 3.1,$ and 2.4 nm\} at temperatures -9, 5, 0, 5, 10, 15, 20, 25, 30 and 37°C downwards. The different lines correspond to the best fits obtained according to Eq. (1) with ε=0.5 nm.
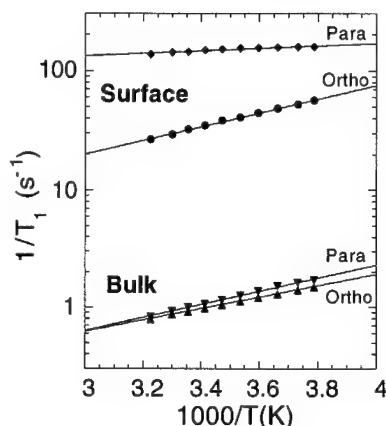
Fig. 2 : Semilogarithmic plot of the surface ^2H spin-lattice relaxation rates $1/T_{1s}$ (ortho) and $1/T_{1s}$ (para) of liquid pyridine-d_1 as function of the inverse of temperature in porous sol-gel silica glasses (top). The corresponding bulk rates are also given (bottom). The experimental points are obtained from the slopes and intercepts of Fig. 1 according to Eq. (1). The continuous lines are the best fits obtained with Eqs. (3).

DISCUSSION

We propose a theoretical model which considers the effects of the interaction with the pore solid surface on the local anisotropic reorientational molecular motions. This will allow us to account quantitatively for the experimental results shown in Fig. 2.

The liquid-surface interactions of the pyridine molecules proceed through hydrogen bonding between the SiOH groups on the surface and the nitrogen atom (Fig. 3). This allows definition of the molecular symmetry axis (C_2),from the nitrogen atom to the para carbon. Relatively to the OH axis, the molecular rotational dynamics is described by a dynamical tensor whose three principal values of diffusion coefficients are $D_{//}{}^s$, corresponding to rotations around the C_2 axis of the molecule, and $D_{\perp 1s}$ and $D_{\perp 2s}$, related to swinging motions of this C_2 axis, respectively in and out of the molecular plane. The OH dipole is an instantaneous director $n(t)$ making an angle $\zeta \sim 70°$ relative to the local normal director n_0 defined by the Si-O bond of the silicon oxide surface. This director $n(t)$ can freely rotate around n_0, but due to the large momentum of inertia, this motion is slow as compared to the rotation of C_2 around $n(t)$ and will further be referred as

the "slow motion". The hydrogen bond is characterized by an electrostatic dipole-dipole interaction U which depends only on the angle $\beta(t)$ between $\mathbf{n}(t)$ and the molecular dipole along C_2. Then $U = -E_H \cos\beta$, where E_H is the bonding energy in alignment of the two dipoles. The angular distribution of the ensemble of surface molecules is described by a Boltzmann distribution $P_{eq}(\beta) \propto \exp[E_H \cos\beta/RT]$ at a given temperature T.
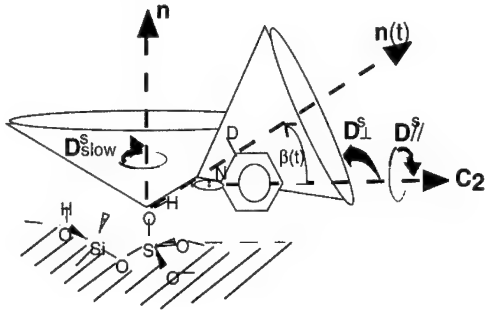
Fig. 3 : Schematic diagram of the anisotropic motions of the pyridine molecules adsorbed by hydrogen bond between the SiOH groups on the pore surface and the nitrogen atom.

As it is well known, the deuterium nuclear spin relaxes through the fluctuations of the quadrupolar Hamiltonian $H_Q(t)$ due to molecular reorientation [7]. As the dynamics within the adsorbed layer is restricted, $H_Q(t)$ tends to a non zero time-averaged value $\langle H_Q(t)\rangle$ at long times [10]. For instance, the fast (f) rotational diffusion of the C_2 axis around $\mathbf{n}$ leads to $\langle H_Q(t)\rangle_f$ on time scales of the order of $1/D_{//s}$, $1/D_{\perp 1s}$ or $1/D_{\perp 2s}$. Similarly, the slow motion of $\mathbf{n}(t)$ around $\mathbf{n}_0$ leads to $\langle H_Q\rangle_s \equiv \langle\langle H_Q(t)\rangle_f\rangle_s$ on time scale longer than the various $1/D^s$. In the calculation of $1/T_{1s}$, the squared modulus of the fluctuating part of $H_Q(t)$ must then be reduced from $\langle |H_Q(t)|^2\rangle$ either to $(\langle |H_Q(t)|^2\rangle - |\langle H_Q(t)\rangle_f|^2)$ or $(\langle |\langle H_Q(t)\rangle_f|^2\rangle_s - |\langle H_Q\rangle_s|^2)$ for fast and slow motions, respectively. Owing to the axial symmetry about the $\mathbf{n}$ and C_2 axes, only a single Euler angle $\beta(t)$ is needed in the calculation of $\langle H_Q(t)\rangle_f$. Of course, we average orientationally over the angle between $\mathbf{n}_0$ and the constant magnetic field $\mathbf{B}_0$. Assuming no correlation between fast and slow fluctuations, $1/T_{1s}$ is the superposition of the fast and slow relaxation rates: $(\langle 1/T_{1s}\rangle_f + \langle 1/T_{1s}\rangle_s)$. Calculations similar to those used for liquid crystals [10] lead to the following expressions for $\langle 1/T_{1s}\rangle_f$ and $\langle 1/T_{1s}\rangle_s$, valid for both ortho and para substitutions:

$$\left\langle\frac{1}{T_1^s}\right\rangle_f = \frac{3}{8}\left(\frac{e^2qQ}{\hbar}\right)^2\left\{\frac{\frac{1}{4}(3\cos^2\theta-1)^2\left[1-S_f^2(x)\right]}{6D_\perp^s} + \frac{3\cos^2\theta\,\sin^2\theta}{5D_\perp^s+D_{//}^s} + \frac{\frac{3}{4}\sin^4\theta}{2D_\perp^s+4D_{//}^s}\right\}, \qquad (2\ a)$$

$$\left\langle\frac{1}{T_1^s}\right\rangle_s = \frac{3}{8}\left(\frac{e^2qQ}{\hbar}\right)^2\left\{\frac{\frac{1}{4}(3\cos^2\theta-1)^2 S_f^2(x)\left(1-S_s^2\right)}{6D_{slow}^s}\right\}. \qquad (2\ b)$$

Here $(e^2qQ/\hbar)$ is 2π times the nuclear quadrupole coupling constant which is 178 kHz for ^2H in pyridine (assuming the same value for ortho and para positions). θ is the angle between C_2 and the electric field gradient (*efg*) symmetry axis (along the C-^{2}H bond). D^s_{slow} represents the

isotropic diffusion coefficient for the slow motion of the SiOH around $\mathbf{n}_0$. In Eq. (2a) we assumed that $D_{\perp 1s}$ and $D_{\perp 2s}$ were much smaller than $D_{//}{}^s$, thus producing axial degeneracy in the dynamical tensor and leaving $D_{//}{}^s$ and $D_{\perp s}$ as principal values. This hypothesis will be justified later, when we show that only this assumption can account for the experimental values of T_{1s} and their respective ratio $T_{1s}(ortho)/T_{1s}(para)$. $S_f(x) = <(3\cos^2\beta(t)-1)/2>_f$ is the residual time-averaged orientational term calculated over the fast motion. It represents an order parameter S_f with values between -1/2 and 1 and only depends on $x=E_H/RT$. It can be calculated over $P_{eq}(\beta)$ with $0\leq\beta\leq\pi/2$, as : $S_f(x) = \left[e^x\left(2x^2 - 6x + 6\right) + x^2 - 6\right]/\left[2x^2\left(e^x - 1\right)\right]$. This order parameter S_f is higher as the ordering energy E_H gets higher. Similarly, Eq.(2b) exhibits an order parameter for the slow motion : $S_s=<(3\cos^2\zeta - 1)/2>_s$. Its value is imposed by the angle of the (Si-O-H) bond ($\zeta\sim70°$) (Fig. 3) and gives a negligible contribution $S_s^2 \sim 0.1$ to Eq. (2b).

Eqs. (2 and 3) give the relaxation rates in ortho and para substituted positions ($\theta=0$ and $\theta=2\pi/3$). These equations clearly show the importance of selective deuteration for characterization of complex motions of adsorbed molecules. On the one hand, the surface relaxation rate of pyridine-d-para is sensitive to the rotation of C_2 around $\mathbf{n}(t)$ as well as to the slow wobbling around $\mathbf{n}_0$ (through $D_{\perp s}$ and D^s_{slow}). On the other hand, a linear combination of pyridine ortho and para deuterium relaxation rates is only dependent on the fast axial and swinging rotations ($D_{//}{}^s$ and $D_{\perp}{}^s$) :

$$\frac{1}{T_1^s(para)} = \frac{3}{8}\left(\frac{e^2qQ}{\hbar}\right)^2\left(\frac{1-S_f^2}{6D_{\perp}^s} + \frac{S_f^2}{6D_{slow}^s}\right),$$

$$\frac{1}{T_1^s(ortho)} = \frac{1}{64T_1^s(para)} + \frac{27}{128}\left(\frac{e^2qQ}{\hbar}\right)^2\left(\frac{1}{5D_{\perp}^s + D_{//}^s} + \frac{3/4}{2D_{\perp}^s + 4D_{//}^s}\right).$$

(3a, b)

At that point, one has to remember that $D_{\perp}{}^s$ quantifies the restricted diffusion inside a potential well defined by the hydrogen bond energy and D^s_{slow} is related to free diffusion. The numerical simulations we performed show that the characteristic time (1/D) of such diffusions varies very little with the temperature and can be considered as constant over the explored temperature range. Hence, the thermal variation of $T_{1s}(para)$ is determined by the orientational order parameter $S_f(x)$, which decreases when the temperature raises.

The experimental increase of $T_{1s}(para)$ with temperature then proves that the overall molecular motion around $\mathbf{n}_0$ determines this relaxation rate, thus confirming the assumption that D^s_{slow} is lower than $D_{\perp}{}^s$. Similarly, the experimental Arrhenius behavior of the term $[1/T_{1s}(ortho)-1/(64\ T_{1s}(para))]$ indicates that the activated rotation around the molecular symetry axis C_2 determines the left term of Eq. (3b). This shows that $D_{//}{}^s$ is much larger than $D_{\perp}{}^s$.

In view of these observations, the experimental $T_{1s}(para)$ gives the diffusion coefficient D^s_{slow} as well as the hydroxyl-pyridine hydrogen bond energy E_H which determines the amplitude of S_f. Similarly, $T_{1s}(ortho)$ gives the value of $D_{//}{}^s$ together with the activation energy $E_{//}{}^s$ of the rotation around C_2. The figure 2 shows the quality of the fits which give a hydrogen bond energy E_H of 15.1 kJ.mol^{-1} and D^s_{slow} = 2 10^8 rad^{2}s^{-1}. Let us point out that this value of E_H is in agreement with the value for normal hydrogen bonds. As it is E_H which restricts the wobbling of C_2 around $\mathbf{n}(t)$, it determines the order parameter $S_f(x)$ which ranges from 0.55 to

0.64 . This S_f implies that C_2 wobbles within a cone whose semi-apperture varies from $2\pi/9$ at low temperature to $\pi/4$ at 37°C.

The rotation around C_2 is characterized by an activation energy $E_{//}^s$ of 14.6 kJ.mol^{-1} and $D_{//}^s$ ranges from 4.10^9 to 16.10^9 rad^{2}s^{-1}. Last, $D_\perp^s$ can only be defined within an interval : [5.1, 9.1 rad^{2}s^{-1}]. It is interesting to compare these values with the bulk values obtained from Eqs. (3) with $S_f = 0$ (unrestricted motions) and with activated diffusion for $D_{//}^b$ and $D_\perp^b$. This gives $D_{//}^b$ ranging from $5\ 10^{10}$ to $12.5\ 10^{10}$ rad^{2}s^{-1} and $D_\perp^b$ from $4\ 10^{10}$ to $12\ 10^{10}$ rad^{2}s^{-1}, with their respective activation energies being 7.1 and 10.9 kJ.mol^{-1}. The values found for the surface motions illustrate the slowing down of the dynamics caused by solid-liquid interactions and how the activation energies increase with the steric hindrance due to adsorbed neighbour molecules. Finally, one notes that recent ^{13}C NMR relaxation measurements of pyridine in confinement support the presented theoretical model [11].

CONCLUSIONS

This experiment shows how confinement effects can provide detailed information on the dynamics of temporarily adsorbed layers. Even when the two populations (adsorbed and bulk) are in fast exchange and prevent spectroscopic resolution, the confinement allows one to study the surface layer dynamical parameters. By selective labelling, NMR relaxation allows one to determine the anisotropy of the motions at the surface. In the case of pyridine on a wetting surface, we have shown how rotation about the molecular axis is hindered by neighbouring molecules restricting the motion of this molecular axis to a narrow cone which opens slightly as the temperature increases. This molecular ensemble is also in slow rotational motion around the local normal to the surface. The various diffusion coefficients have been determined. The proposed method can easily be generalized to other polar molecules.

[1] J.-P. Korb, L. Malier, F. Cros, Shu Xu, J. Jonas, Phys. Rev. Lett. **77**, 2312 (1996).

[2] J.-P. Korb, Shu Xu, J. Jonas, J. Chem. Phys. **98**, 2411 (1993); J.-P. Korb, A. Delville, Shu Xu, G. Demeulenaere, G. Costa, J. Jonas, ibid. **101**, 7074 (1994).

[3] S. Stapf, R. Kimmich, R.O. Seitter, Phys. Rev. Lett. **75**, 2855 (1995).

[4] R. Mu and V. M. Malhotra, Phys. Rev. B **46**, 532 (1992); J.H. Strange, M. Rahman, E.G. Smith, Phys.Rev. Lett. **71**, 3589 (1993).

[5] G.P. Crawford, D.K. Yang, S. Zumer, J.W. Doane, Phys. Rev. Lett. **66**, 723 (1991).

[6] G. Liu, Y. Li , J. Jonas, J. Chem. Phys. **95**, 6892 (1991).

[7] A. Abragam, "The Principles of Nuclear Magnetism", The Clarendon Press, Oxford, 1961.

[8] B. Bak; J. Org. Chem. 21, 797 (1956); J.P. Kintzinger, Mol. Phys. **30**, 673 (1975).

[9] W.T. Huntress, J. Chem. Phys. **48**, 3524 (1968).

[10] M. Brown, J. Chem. Phys. **77**, 1576 (1982).

[11] Shu Xu and J. Jonas, J. Phys. Chem. **100**, 16242 (1996).

ADSORPTION MONOLAYER FORMATION IN CONFINED GEOMETRY: APPARENT FRACTAL DIMENSION

A.G. OKUNEV, YU.I. ARISTOV
Boreskov Institute of Catalysis, Novosibirsk 630090, Russia
fax: 007-383-235-4573
e-mail: okunev@catalysis.nsk.su

ABSTRACT:

Here we present experimental results on adsorption of fatty acids, aliphatic alcohols, and acetone on the mesoporous silica gels with various porosity. Conclusion has been drawn that fractal resolution analysis of the silica surface may lead to apparent values of the surface dimension. These data are suggested to be analyzed by a simple model taking into account adsorbed layer thickness and steric difficulties of monolayer formation in narrow pores.

KEYWORDS: adsorption, fractal dimension, monolayer thickness, silica gels.

INTRODUCTION

A number of adsorption experiments made this century have shown a simple scaling relationship between the measured specific surface S_{sp} of an adsorbent and cross sectional area σ of a test molecule

$$S_{sp} \propto \sigma^{\alpha}, \qquad (1)$$

where α is a constant [1]. The exponent α was found to be negative and commonly lie between $-1/2$ and 0 for many particular solids of different nature. Simple physical interpretation of α has been done by fractal geometry. It was proved that a rough surface for large test-molecules is somewhat smoothed. It results in a decrease of the measured surface according to relation (1). Moreover, this approach allows to express α in terms of surface fractal dimension D [2, 3]

$$\alpha = 1 - D/2. \qquad (2)$$

Fractal dimension D of the surface characterizes its roughness and varies from 2 for smooth surface (it gives integer α equal to 0) to 3 for completely rough and irregular surface.

The essential point of this approach is an assumption that the surface tested is self-similar and rough at the atomic scale. The surface possesses a number of atomic size defects. Such strong irregularity seems doubtful from thermodynamic point of view for solids with high interatomic energy such as silica gels, aluminas, etc. SAXS and SANS measurements [4,5] typically indicate rather small surface roughness ($D \approx 2.0 \div 2.2$) and it contradicts to the adsorption experiments. The adsorption from solution method yields higher D values, including those having no physical meaning (the values of $D > 3$ were obtained for porous silica gels when aliphatic alcohols were used as test molecules [6,7]).

15

If real oxide surface has a few defects of atomic size, then there is a question - why is relation (1) with noninteger α a common case for many meso- and microporous solids? The aim of this paper is to clear up and describe forming of monolayer of organic molecules on mesoporous silica gels. This work is a further development of a concept of steric difficulties for monolayer adsorption in narrow pores. It was shown in ref. [8] that in such pores an apparent value of surface dimension D > 2 may be obtained by a standard fractal approach even for pores with a smooth surface, and the ratio <monolayer thickness>/<average pore radius> determines a scale of the effect.

Here we present experimental results on adsorption of fatty acids, aliphatic alcohols, and acetone on the mesoporous silica gels with various porosity and describe these data by a simple model that takes into account adsorbed layer thickness and steric difficulties of monolayer formation in narrow pores.

EXPERIMENTAL

Commercial mesoporous silica gels of the KCC-3, KCK-2 (both former USSR), Davisil 60 and Davisil 150 (both Aldrich) types were used as sorbent materials. Their specific areas and average pore diameters measured by nitrogen adsorption at 77 K are given in Table I. Before the experiments all the samples were carefully dried at 180°C for 5 hours *in vacuo*.

Table I. Some geometric characteristics of the silica gels used.

Adsorbent	S_{sp}^{*}, m^2/g	Average pore diameter, nm	S_{sp}^{**}, m^2/g	K, nm$^{-1} \times 10^{-1}$
Davisil 150	272	15	270±10	0
KCK-2	380	13	330±25	0
Davisil 60	494	7	440±45	-6±6
KCC-3	525	5.5	500±30	-16±4

* N$_2$ BET value
** calculated from (7)

n-Aliphatic alcohols (C$_3$H$_7$OH, C$_6$H$_{13}$OH, C$_{10}$H$_{21}$OH), pentanoic acid and acetone were adsorbed from their solutions in CCl$_4$. The amount of adsorbed compound was determined from the decrease in the intensity of the C-H vibration (v = 2975 cm^{-1}, 2920 cm^{-1}, 3005 cm^{-1} for alcohols, pentanoic acid and acetone, respectively).

RESULTS AND DISCUSSION

Typical excess adsorption isotherms $\Gamma_\sigma(x_\sigma)$ of aliphatic alcohols, pentanoic acid and acetone at 18°C are presented in Figure 1. All the isotherms have shapes predicted by equation

$$\Gamma_\sigma = n_\sigma \frac{(K-1) \cdot x_l \cdot (1-x_l)}{1+(K-1) \cdot x_l} \qquad (3)$$

where Γ_σ is the adsorbate surface excess, n_σ is the total number of moles at the interface (per mass unit of adsorbent), x_l is the adsorbate molar fraction in the solution and K is the adsorption equilibrium constant [9].

16
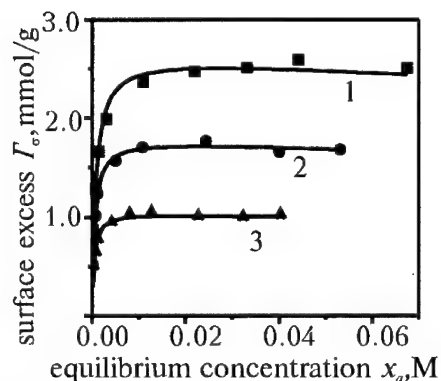
Figure 1. The excess adsorption isotherms of n-propanol (1), n-hexanol (2) and pentanoic acid (3) on KCC-3. Solid lines fit the equation (3) to the experimental data.

Figure 2. Determination of the KCC-3 surface dimension: solid line – all available data are taken into consideration, dotted line – for the aliphatic alcohols only.

The isotherms reach the plateaus at concentrations lower than 0.02 M. At very low equilibrium concentrations the slopes of the isotherms are usually above the value calculated for the whole isotherm. This effect is likely to be due to the strong adsorption mode discussed elsewhere [7, 10].

The monolayer capacities and specific surface areas obtained from the isotherms are collected in Table II. This table depicts a certain tendency for a decrease in S_{sp} - value as the size of test molecule increases, however there is no simple monotonous correlation between these two values.

Table II. Results of the adsorption isotherm measurements.

Adsorbent	Adsorbate	Monolayer capacity n_σ, mmol/g	Specific surface, S_{sp}, m^2/g	Monolayer volume, V_m, μl/g
Davisil 150	acetone	1.18	254	91
	pentanoic acid	0.9	265	100
	propanol	1.85	200	140
	hexanol	1.37	197	167
	decanol	1.1	228	204
KCK-2	acetone	1.36	297	106
	pentanoic acid	1.12	345	130
	decanol	1.27	283	252
Davisil 60	acetone	1.98	423	151
	pentanoic acid	1.35	409	154
	decanol	1.63	360	320
KCC-3	acetone	2.07	425	152
	pentanoic acid	1.37	403	152
	propanol	2.8	423	209
	hexanol	1.77	332	227
	decanol	1.41	311	276

Adsorption data for the adsorbates from the different homological sets (including N_2) are presented in Figure 2 in the double logarithmic coordinates $\ln(S_{sp})$ - $\ln(\sigma)$ as it is usually done in the frame of a fractal "surface resolution analysis" [2]. The data can be fitted to a straight line with the low correlation coefficient (for instance, 0.63 for KCC-3 and 0.52 for Davisil 150) giving surface dimensions equal to 2.4 ± 0.3, 2.7 ± 0.4, 2.24 ± 0.2, 2.5 ± 0.2 for the KCK-2, KCC-3, Davisil 150 and Davisil 60, respectively. Since the only alcohols data are approximated, the linear fitting becomes very good (the correlation coefficients are about 0.99 for all the samples tested), however, the D-values calculated from the line slopes (4.0 ± 0.3 for KCC-3 and 3.2 ± 0.12 for Davisil 150) have no physical meaning.

Thus, the results obtained (see Table II and Figure 2) clearly show that the silica gels monolayer capacity is not uniquely determined by the cross-sectional area of adsorbate. Among the other factors which may influence the monolayer capacity the most important ones are the chemical adsorbate-adsorbent interaction [6, 7] and geometrical restrictions resulted from confined pore geometry [8, 11]. As the silica gels studied differ mainly by porous structure we have focused our attention here on the steric peculiarities of monolayer adsorption.

Figure 3. V/V_{st} as a function of the adsorbed layer thickness.

Table III. Cross-sectional area of the adsorbates and adsorbed volume thickness.

Adsorbate	Cross-sectional area, σ, nm^2	Cross-sectional area[***], σ, nm^2	Adsorbed layer thickness, d, nm
Acetone	0.338[*]	0.386	0.34 ± 0.02
Pentanoic acid	0.478[*]	0.502	0.37 ± 0.02
Propanol	0.25[*]	0.24	0.52 ± 0.025
Hexanol	0.305[**]	0.34	0.61 ± 0.03
Decanol	0.356[**]	0.424	0.75 ± 0.035

[*] from ref. [12]
[**] from ref. [13]
[***] calculated from adsorption on Davisil 150 (see text).

The ratio <monolayer thickness>/ <average pore radius> has been previously specified as a factor which may strongly influence monolayer formation [8]. For further analysis of this influence, we have studied the adsorbed volume V dependence on the monolayer thickness (Figure 3). The monolayer thickness d for the adsorbates involved (Table III) was calculated from the adsorption data on Davisil 150 considering its surface to be flat and making use of evident formula

$$d = \frac{V_{D150}}{S_{D150}} \, ,$$

(4)

where S_{D150} and V_{D150} are the BET(N_2) specific surface area and the monolayer volume for Davisil 150. The monolayer volume V was calculated from the monolayer capacity n_σ

$$V = \frac{n_\sigma \cdot \mu}{\rho} \, , \tag{5}$$

where ρ is the adsorbate liquid density and μ is its molecular mass.

To avoid the influence of the chemical factors mentioned above, the monolayer volumes V in Figure 3 are related to the monolayer volume V_{st} of the standard sample (Davisil 150). V vs d dependencies obtained are nearly linear and may be understood from a simple geometrical consideration.

Let us consider two surfaces of the same area one of which is flat and another is turned into a spherical pore of radius R. At the same layer thickness, the relation of the volumes adsorbed on the spherical V_{sp} and flat V_f surfaces is given by

$$\frac{V_{sp}}{V_{fl}} = 1 - \frac{d}{R} + \frac{d^2}{3R^2} \, . \tag{6}$$

This expression shows that the volume adsorbed on the surface of the positive curvature is always less than that for a flat surface of the same area. Neglecting the term proportional to d^2, the volume ratio for a small enough arbitrary twisted piece of surface may be written as

$$\frac{V}{V_{fl}} \approx \frac{S}{S_{fl}} \left(1 - \frac{K}{2} \frac{V_f}{S_{fl}} \right) = \frac{S}{S_{fl}} \left(1 - \frac{K \cdot d}{2} \right) \tag{7}$$

where K is the average curvature of the twisted surface. Equation (7) demonstrates that the volume gets lower as the adsorbed layer thickness goes up, that is in line with our results. For common mesoporous solids the scale of the effect may reach some tens of percents.

If the consideration is valid, the slopes of the straight lines in Figure 3 allow to find accordingly to (7) the specific surface area S_{sp} and average sample surface curvature for each sample (see Table I). For the calculations we suppose the specific surface of Davisil 150 to be equal to 272 m^2/g (N$_2$ BET value) and its curvature to be conditionally equal to zero. So determined specific surface areas S_{sp} appears to coincide with the areas determined for the samples by a common BET technique within $10 \div 15\%$ accuracy that is typical for S_{sp} measuring by different methods (Table I). There is also a good correlation between the average pore diameter and the average surface curvature K (see Table I).

It is of interest that the model developed allows to account for abnormally high surface dimensions which were observed for n-aliphatic alcohols adsorption on silica gels [6, 7]. This effect appears due to the strongly elongated elliptical (rodlike) adsorption conformation of these alcohols [13 , 14]. In the adsorbed state they are linked to the surface by hydrogen bonds and are oriented perpendicularly to the surface. Hence, the adsorbed molecule occupies a large volume in the near-wall region, thus, creating steric difficulties for adsorption of the other molecules. The effect is especially pronounced for adsorption of higher alcohols in narrow pores. Thus, the measured surface area quickly decreases with the increase of alcohol size. It results in the sharp slope of a straight line fitting to the data in the $\ln(N)$ - $\ln(\sigma)$

coordinates and leads to abnormally high apparent D values which may have no physical meaning.

CONCLUSIONS

Our experimental results on adsorption of fatty acids, aliphatic alcohols, and acetone on the mesoporous silica gels with various porosity have shown that fractal resolution analysis may lead to apparent values of the surface dimension. To analyze these data we suggest a simple model taking into account steric difficulties of monolayer formation in narrow pores. The model allows to determine the silica gel specific area and average pore curvature directly from the data on the organic molecules adsorption from solution.

REFERENCES

1 S.J.Gregg, K.S.W.Sing Adsorption, Surface area and Porosity, (Academic Press, New York, 1982).
2 D.Avnir, P.Pfeifer, Nouv.J.Chim. **7**, 71 (1983).
3 B.B.Mandelbrot, The Fractal Geometry of Nature, (Freeman, San Francisco, 1982).
4 P.Shmidt, A.Hohr, H.-B.Neumann, H.Kaiser, D.Avnir, J.S.Lin, J.Chem.Phys. **90**, 5016 (1989).
5 A.J.Hurd, D.W.Schaefer, D.M.Smith, S.B.Ross, A.Mehaute, S.Spooner, Phys.Rev.B **39**, 9742 (1989).
6 J.M.Drake, P.Levitz, J.Klafter, Isr. J. Chem. **31**, 135 (1991).
7 Ya.E.Kutsovskii, E.A.Paukshtis, Yu.I.Aristov, React.Kin.Catal.Lett. **46**, 57 (1992).
8 K.B.Gavrilov, A.G.Okunev, Yu.I.Aristov, Monolayer adsorption in narrow pores: apparent surface dimension, React.Kinet.Catal.Lett. **58**, N.1, 39 (1996).
9 D.H.Everett, Trans.Farad.Soc. **61**, 2478 (1965).
10 K.Gavrilov, Ya.Kutsovskii, E.Paukshtis, A.Okunev, Yu.Aristov, Mol.Cryst.Liq.Cryst. **248**, 159 (1994).
11 H.Van Damme, P.Levitz, F.Bergaya, J.F.Alcover, L.Gatineau, J.J.Fripiat, J.Chem. Phys. **85**, 616 (1986).
12 A.L.McClellan, H.F.Harnsberger, Journal of Colloid and Interface Science **23**, 577 (1967).
13 D.Farin, A.Volpert, D.Avnir, J.Am.Chem.Soc. **107**, 3368 (1985).
14 J.J.Kipling, Adsorption from Solution of Non-Electrolytes, (Academic Press, New York, 1965).

RELAXATION PHENOMENA AND THERMODYNAMICS
OF LIQUIDS AT VERY HIGH PRESSURES

W. F. Oliver III
Department of Physics, University of Arkansas, Fayetteville, AR 72701,
woliver@comp.uark.edu

ABSTRACT

Complex liquid glass-forming systems ranging from those composed of simple molecules to polymer melts and amorphous polymers have been studied extensively as a function of temperature resulting in a basic understanding of liquid-state dynamics and glass transition phenomenology as these systems are supercooled to the vitreous state. An important aspect of this problem that remains largely unexplored, and that is relevant to the topic of this symposium, involves liquid-state dynamics and vitrification (as well as crystallization) in the regime of high pressure and high density. We describe work on "fragile" to "intermediate strength" simple organic glass-forming liquids where both temperature (T) and pressure (P) are varied. Diamond anvil cells are used to achieve pressures exceeding 10 GPa. Several optical and light scattering techniques are used to explore both static and dynamic properties of these systems. High-pressure Brillouin scattering enables us to model the longitudinal relaxation time in these systems as well as their equations of state. These can now be refined by direct measurements of the pressure dependence of the glass transition, $T_g(P)$. Finally, we summarize depolarized light scattering studies which allow us to compare both the isobaric and isothermal evolution of structural (α) and fast (β) relaxation processes.

INTRODUCTION

An increasing effort has been directed in recent years at understanding the physical and chemical properties of materials under extreme conditions of very high pressure. This effort has many driving forces including basic curiosity, the dearth of pressure-dependent data relative to other variables such as temperature or composition, the fact that many material phases naturally exist or are formed under extreme pressures, and technological need. For the case of liquids, an example of the last of these is elastohydrodynamic lubrication, a lubrication regime where both hydrodynamic action and deformations of the contact surfaces must be considered. Lubricant pressures can reach values as high as several tens of kilobars at Hertzian contact points (or lines) in various types of gears, cams, or bearings.[1] In this paper we describe our work aimed at exploring both thermodynamic and dynamical properties of several organic liquids in the regime of very high pressures and hence very high density.

Given the relative ease of conducting temperature-dependent experiments, i.e., of achieving and controlling a specific temperature, it is generally true that temperature-dependent properties of most condensed matter systems are understood much better than pressure-dependent properties are. During the past two decades this situation has begun to change as high-pressure technology has evolved significantly, due largely to the development of diamond anvil cells (DACs)[2] and the ruby fluorescence manometer.[3] This has opened the way for the exploration of vastly greater regions of

the pressure-volume-temperature (PVT) parameter space. Volume effects are present in temperature-dependent experiments due to thermal expansion. Isothermal high-pressure studies now enable us to separate these effects from purely temperature-dependent effects. Furthermore, the high pressures attainable with DACs enable us to reach extreme compression states where PV is comparable to or greater than inter-molecular attractive potentials allowing for a fundamentally deeper understanding of material behavior into the regime of strong repulsive interactions.

Sample volumes in the DAC are on the order of nanoliters at atmospheric pressure and they become significantly smaller as the pressure increases. These volumes are still macroscopic and certainly large relative to those of many of the other studies presented in these proceedings. Nevertheless, an understanding of the thermodynamic and dynamic properties of dense liquids are important for sorting out pressure effects from confinement and geometry effects.

The primary experimental techniques involved in this work are ruby fluorescence and Brillouin scattering, both of which are optical techniques for which DACs are particularly well suited. Ruby fluorescence provides for a way to determine the pressure within the DAC sample chamber[3] as well as pressure gradients, and hence, the onset (or disappearance) of nonhydrostatic conditions, which in turn enables us to determine the static glass transition, $P_g(T)$ or $T_g(P)$. Brillouin scattering is the scattering of laser light by acoustic modes. Energy and momentum conservation dictate that light will couple with hypersonic acoustic modes, i.e., those with frequencies of one to several GHz. This technique therefore allows the direct probing of fairly fast liquid dynamics such as structural relaxation times of several picoseconds, which for many systems correspond to the metastable supercooled (or superpressed) liquid state. For this reason, we will present data on moderate to good glass-forming systems, and while problems related to the competition between crystallization and vitrification at high pressure are also interesting,[4] they will not be discussed here.

With careful high-pressure Brillouin scattering measurements one determines the acoustic velocity, v, as a function of pressure. Typically these data are then integrated using basic thermodynamic relations in order to calculate the equation of state (EOS) of the material under study.[5] Equations of state determined in this way almost always require estimations of the pressure dependencies of certain physical quantities such as the thermal expansion coefficient, α, or the ratio of the isobaric to isochoric heat capacities, $\gamma = c_p/c_v$.[6] A more important, and often overlooked, problem arises when equations of state are calculated from high-pressure Brillouin data for glass-forming liquids since as pressure increases these systems fall out of equilibrium on the picosecond time scales of the Brillouin experiment and simple thermodynamic relations no longer provide a valid description. This is due to the strong increase in the structural relaxation time, τ, of the liquid with pressure. By accurately measuring both hypersonic sound velocities and attenuations and by incorporating relaxation equations into our EOS calculations we have been able to model the pressure dependence of τ and improve EOS calculations for a simple alkane glass former over a strain range of $\Delta V/V_0$ = 0 to 0.5 corresponding to a pressure range of 1 bar to 12 GPa (120 kbar).[7] Modeling of τ can be further improved by measuring the P dependence of the glass transition temperature, $T_g(P)$, and an example of such data will be presented below.

By analyzing the depolarized light scattering spectra in glass-forming liquids as a function of T one obtains information on the temperature dependence of the slow (α or

structural) relaxation already discussed and fast (β) relaxation processes.[8] Fairly recent mode coupling theories of the glass transition[9] provide specific predictions for the behavior of these relaxation modes and have achieved success in explaining both the light scattering and neutron scattering data for more than one "fragile,"[10] and very recently an intermediate,[11] liquid glass-forming system. For completeness, we will summarize our recent work in this area.[12]

Finally, a brief and by no means exhaustive review of some of the earlier important work on liquid state dynamics at high pressure is given. P. W. Bridgman determined some of the earliest relaxation rates at high pressure by measuring viscosity in several liquids up to 30 kbar (3 GPa).[13] Viscosity measurements were later extended to higher pressures using multianvil presses and DACs.[14] Other moderate (and in some cases high) pressure studies of liquids have been conducted over the years including ultrasonic velocity and attenuation measurements,[15,16] NMR studies of translational and reorientational motions in liquids, some of which were viscous,[17,18,19] dielectric measurements,[20,21,22,23] Brillouin scattering,[24,25] and impulsive stimulated light scattering.[26] With the exception of a few recent studies, almost all of this work involved studies along the room-T isotherm at P < 2.0 GPa. As a result, little is known concerning the static and dynamic properties of viscoelastic liquids at very high pressures.

EXPERIMENTAL

Diamond Anvil Cell

Diamond anvil cells (DACs) with single crystal anvils now enable us to attain multi-megabar pressures. Briefly, a sample is confined by a small hole in a metal gasket and then squeezed between two opposing diamond anvils, typically of 1/4 to 1/3 carat size. Round cut single crystal diamonds are used in which small faces, called culets, are cut parallel to the diamond tables and used to form the top and bottom walls of the sample chamber. Several different mechanical devices have been developed for holding the diamond anvils and applying opposing forces.[2] One of the simplest is the Merrill-Bassett cell which was used in all of the work presented here.

Homemade heaters that enclose the DAC enable us to perform high pressure measurements at temperatures up to about 200 °C. Thermocouples, thermistors, and RTDs have been used for controlling and measuring the temperature of the sample. A LakeShore Crytronics Model 330 temperature controller allows for temperature control to better than 0.01 °C and the ability to ramp the temperature at a controlled rate.

Ruby Fluorescence Manometer

Initially, the DAC had little impact on high pressure research due to tiny sample sizes (nl or less) and the difficulty of determining pressures within the sample chamber. This changed dramatically with the development of the ruby fluorescence manometer.[3] Tiny chips (5-10 μm in size) of ruby are placed with the liquid sample into the chamber. When illuminated with blue or green laser light the ruby chips fluoresce in the red with two prominent peaks between 694.2 nm and 692.9 nm at 1 bar and room T. The frequencies and widths of these ruby peaks shift with P and T and have been calibrated accurately allowing for *in situ* pressure measurement in the DAC. Since the ruby

fluorescence peaks also shift with T, a ruby chip is placed on the diamond table where it remains at P = 1 bar but has the same T as the sample chamber. This enables us to measure directly the contribution of the peak shift due to temperature.

The ruby fluorescence manometer in our lab consists of a customized Olympus microscope through which Ar-ion laser light at 514.5 nm is directed via a red/green dichroic filter and focused onto a ruby chip within the DAC. The DAC sits on a x-y microscope translation stage. Red fluorescent light is collected by the objective, passed through the dichroic filter, and coupled into a single fiber optic. Filtered neon and argon lamps can also be slid into or out of the beam path. The fiber optic directs emission from the different sources into a Scientific Instruments 0.5 m monochrometer which operates in eighth order using a 316 groove/mm Echelle grating. Spectra are collected and analyzed very quickly (<1 s per spectrum) with our manometer due to the use of a micro-computer controlled red sensitive photodiode array detector. Measurement of the neon lines at 692.95 nm and 703.24 nm and an argon line at 696.54 nm provide an absolute frequency calibration. We typically use the center frequency of the higher wavelength peak (the ruby R_1 line) which is determined by nonlinear least squares fitting of the entire ruby fluorescence spectrum as described by Munro *et al.*[27]

The pressure dependence of the glass transition, $T_g(P)$, can also be mapped out using ruby fluorescence and we report here preliminary results from an ongoing study of glycerol. Ruby chips are placed in many regions of the sample chamber and the fluorescence from several of these chips is analyzed at each P and T. The onset (or disappearance) of pressure gradients across the liquid sample, i.e., nonhydrostatic conditions, indicate the glass transition.

In particular, samples are pressurized at room T until nonhydrostatic conditions are first observed (see the ♦ data point in Fig. 1). A slight increase in P further into the glassy region produces larger pressure gradients. The sample is then heated at a rate of 0.2 °C/minute until it is near the glass transition at which point the ramp is slowed to 0.1 °C/minute, which is slow enough that we can monitor the pressure at four to five different positions in the sample while maintaining changes in T of no more than 0.1–0.2 °C. Once the sample melts to a highly viscous liquid it is then slowly cooled to an annealed glass. A small increase in P again produces significant pressure gradients and the process is repeated to obtain a new $T_g(P)$ point in the PT phase diagram (see Fig. 1). These temperature ramps are actually only pseudo-isobaric as the average pressure does increase with T due to differential thermal expansion of the sample and chamber. Over small temperature ranges (~ 20 °C), dP/dT ~ 0.05 kbar/°C.

Brillouin Scattering

Brillouin scattering is the scattering of photons by thermally generated acoustic excitations within the sample. A Brillouin spectrum consists of an elastically scattered central line at the laser frequency and symmetrically displaced Stokes and anti-Stokes sidebands due to longitudinal acoustic (LA) and transverse acoustic (TA) modes. If ω and $\mathbf{q}$ are the acoustic frequency and momentum transfer in the scattering process and if ω_I, ω_S, $\mathbf{k}_I$ and $\mathbf{k}_S$ are the incident (I) and scattered (S) frequencies and wavevectors, respectively, then energy and momentum conservation for the Stokes (+) and Anti-Stokes (-) scattering process: $\omega = \pm(\omega_I - \omega_S)$ and $\mathbf{q} = \pm(\mathbf{k}_I - \mathbf{k}_S)$ dictate that only long wavelength (q~0) acoustic modes will couple to photons. These acoustic modes lie in
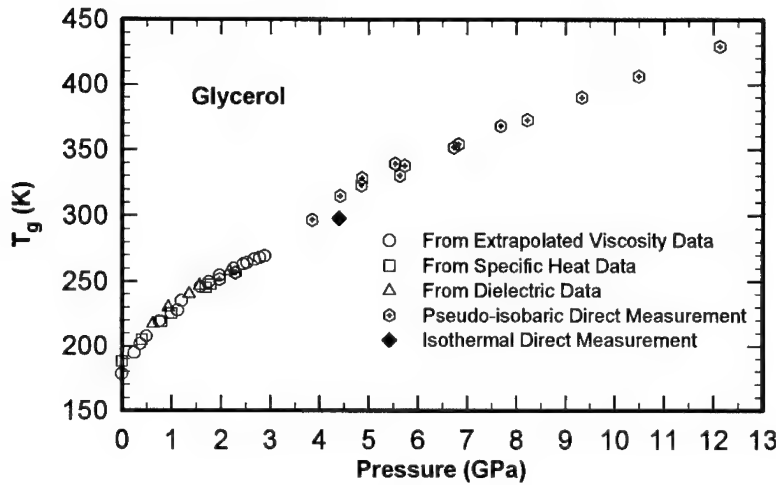
Figure 1. The pressure dependence of the glass transition temperature, $T_g(P)$, for glycerol obtained by ruby fluorescence techniques [pseudo-isobaric data (hexagons) and isothermal datum (diamond)]. Also shown are lower pressure values determined from heat capacity data[28] (squares), dielectric data[20] (triangles), and viscosity data[29] (circles).

the hypersonic (~1 to several GHz) regime. For isotropic materials with refractive index, n, the acoustic mode wavenumber, q, and sound velocity, v, are given by:

$$q = 2nk_0 \sin\left(\frac{\phi}{2}\right) \quad \text{and} \quad v = \frac{2nv}{\lambda_0} \sin\left(\frac{\phi}{2}\right), \tag{1}$$

where k_0 is the wavenumber of the incident light in vacuum, $\lambda_0 = 2\pi/k_0$, v is the measured acoustic mode frequency, and ϕ is the scattering angle internal to the sample. Together sound speed and density measurements yield the incompressibility of a liquid: $\beta^{-1} = \rho v^2$.

Brillouin scattering in the DAC often takes advantage of an equal-angle forward scattering geometry in which case $n \sin(\phi/2) = \sin(\theta/2)$, where θ is the scattering angle external to the DAC, and $v(P)$ can be determined from $v(P)$ without knowing $n(P)$:

$$q = 2k_0 \sin\left(\frac{\theta}{2}\right) \quad \text{and} \quad v = \frac{2v}{\lambda_0} \sin\left(\frac{\theta}{2}\right). \tag{2}$$

Finally, the LA (and TA) linewidths, Γ (HWHM), yield the acoustic mode attenuations. Γ, is related to v, the acoustic wavelength λ_a, and spatial amplitude absorption coefficient α as $\Gamma = \alpha\lambda_s v/2\pi$. Care must be exercised to account for instrumental and finite-size aperture effects in calculating true acoustic-mode linewidths.[30]

The Brillouin scattering results presented in this paper were obtained using more than one instrument, the newest being a state-of-the-art six-pass Sandercock tandem

Fabry-Perot interferometer mounted on a dynamic vibration isolation system. Laser radiation at 514.5 nm is provided by a Coherent Model 306 argon ion laser operating in a single longitudinal mode via a temperature and software controlled intracavity etalon. All Brillouin data presented here were obtained using an external scattering angle of 60° $0'$ $\pm$ 0° $5'$ in an equal-angle forward scattering geometry. After passing through the scanning Fabry-Perot interferometer the scattered light is focused onto the photocathode of a Hamamatsu R585 photomultiplier tube which converts the signal to an electrical signal that is then passed through an amplifier/discriminator circuit. Finally, the signal is recorded with an EG&G multichannel scaler (MCS) board in an Intel 486-based micro-computer used to collect, store, and preprocess the Brillouin data.

Depolarized Light Scattering

Depolarized low-frequency Raman scattering in viscous liquids, combined with depolarized Brillouin spectra of different free spectral ranges, enables one to probe the α- and β-relaxation regimes over about four orders of magnitude in frequency.[8] In the next section we summarize our recent P- and T-dependent depolarized light scattering, as well as viscosity, experiments on the glass-forming liquid cumene.[12] A near backscattering ($\theta = 173^\circ$) geometry was used in these experiments. Vertically polarized light was incident on the sample and only the depolarized (horizontal) component of the scattered light was selected using a Glan-Thompson polarizer with an extinction ratio of greater than 10^{-5}. Raw spectra, spanning four orders of magnitude in frequency, are converted to susceptibility spectra, $\chi(\omega)$, by dividing the intensity, $I(\omega)$, by the Bose factor, $n(\omega)$. For details see ref. 12.

RESULTS

To begin with, we discuss ways in which Brillouin scattering data enables us to model the pressure dependence of the structural relaxation time in a liquid by summarizing earlier work on the pentane isomeric system.[7] This will be followed with results from work that is in progress on alcohols that supplement and extend the earlier work. Finally, we summarize our depolarized light scattering study in which fast and slow relaxation processes in a dense liquid are compared with those in the same liquid at atmospheric pressure.

Figure 2 shows our results from a room temperature Brillouin scattering study of a 1:1 mixture of n-pentane and isopentane between pressures of 1 bar and 12 GPa (120 kbar). Figure 2(a) shows our LA velocity and linewidth results as well as lower pressure ultrasonic velocities taken by Houck.[31] Note that $\Gamma(P)$ exhibits a clear maximum at a pressure of $P_\alpha = 2.25$ GPa. The relaxation time associated with the dominant relaxation process of the liquid at P_α can be determined from $\omega(P_\alpha)\tau(P_\alpha) = 1$ and is found to be $\tau(P_\alpha) = 20 \times 10^{-12}$ s. This can be compared to 2.0×10^{-12} s at 1 bar (0.1 MPa)[32] and a typical value of 10^2–10^3 s at P_g(T=25 °C). Note the static glass transition pressure, P_g(25 °C), in this system is determined by ruby fluorescence to be ~7.4 GPa.

Brillouin scattering probes sound velocities associated with adiabatic moduli and while in principal both LA and TA or shear acoustic modes can couple to light, it is found in most cases that this coupling is extremely weak or nonexistent for TA modes in the case of liquids.[33] Only experimentally measured LA modes will be presented in
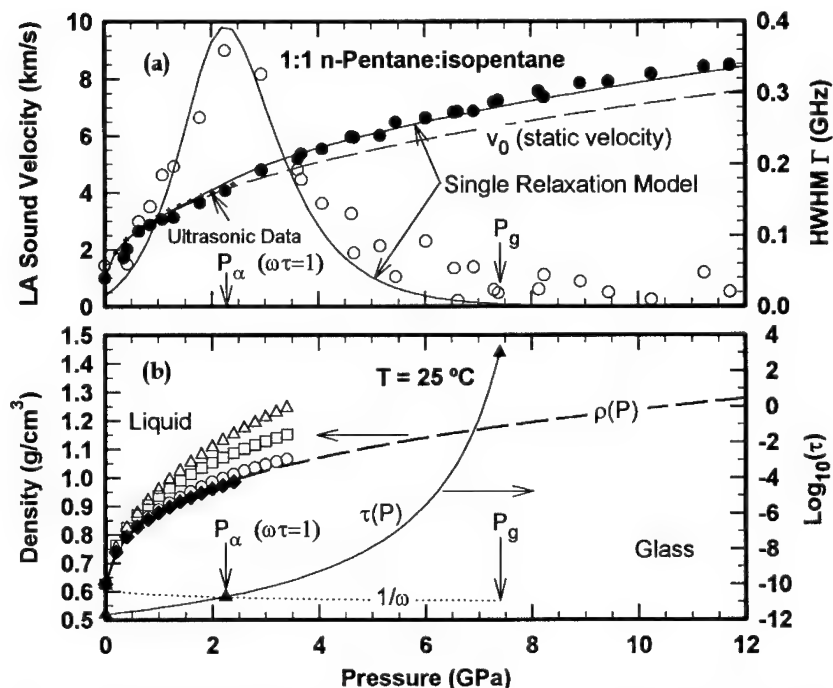
Figure 2. High-pressure Brillouin scattering results for 1:1 n-pentane:isopentane at 25 °C. (a) Sound velocity (•) and HWHM (o) data. Also shown are sound velocities below 2.5 GPa determined ultrasonically (+).[31] The solid lines represent fits using a single relaxation time model and the dashed line is the "relaxed" velocity calculated from the fits. (b) Relaxation time (solid line) determined from a modified VTF fit to the measured points (▲). Also shown are direct density measurements due to Houck (♦),[31] our calculated EOS (dashed line) which accounts for relaxation effects, EOS calculations from our Brillouin data which do not consider relaxation and where C_P (o), γ (□), and α (△), respectively, are assumed constant as in several early studies.

this paper. To incorporate relaxation into an analysis of these data we consider the frequency-dependent adiabatic longitudinal modulus, $M(\omega) = K(\omega) + 4/3\ G(\omega)$, where K and G are the adiabatic bulk compressional and shear moduli, respectively. $M(\omega)$ can be written as[34]

$$M(\omega) = \gamma K_T + M_r \int_0^\infty g(\tau)\frac{i\omega\tau}{1+i\omega\tau}d\tau,\qquad(3)$$

where $\gamma = c_p/c_v$, K_T is the static isothermal bulk modulus, $M_r = (K_\infty - K_0) + 4/3\ G_\infty$ is the "relaxing" part of the modulus (K_∞ and G_∞ being the infinite-frequency moduli and K_0 the static modulus), τ is the longitudinal relaxation time, and $g(\tau)$ is its distribution. The LA velocity is related to the real part of $M(\omega)$ as $\mathrm{Re}\{M(\omega)\} = \rho v^2$, where ρ is the mass density, and the linewidth is proportional to the $\mathrm{Im}\{M(\omega)\}$ as we show below.

We assumed a single relaxation time in analyzing our data on the pentane isomeric system resulting in the following expression for the LA frequency:

$$\omega^2(P) = \frac{\gamma(P)K_T(P)q^2}{\rho(P)} + \frac{M_r(P)q^2}{\rho(P)}\frac{\omega^2(P)\tau^2(P)}{1+\omega^2(P)\tau^2(P)},\qquad(4)$$

where pressure dependencies are now shown explicitly. Similarly, $\Gamma(P)$ is:

$$\Gamma(P) = \frac{M_r(P)q^2}{4\pi\rho(P)\omega(P)}\frac{\omega(P)\tau(P)}{1+\omega^2(P)\tau^2(P)}.\qquad(5)$$

To fit these dynamical Brillouin scattering equations to our LA frequency and linewidth data required modeling $\rho(P)$, as well as $M_r(P)$, $\gamma(P)$, and $\tau(P)$. We used the highly successful Vinet EOS for $\rho(P)$,[35] a linear expansion in P for the relaxing part of the adiabatic modulus: $M_r(P) = M_{r0} + M_{r0}'P$, and published results for $\gamma(P)$.[31] For details see reference 7. Finally, the structural relaxation time, $\tau(P)$, was modeled by assuming a linear pressure dependence for the zero-mobility temperature, T_0, in the Vogel-Tammann-Fulcher equation, commonly used to describe $\tau(T)$ at P = 1 bar:[36]

$$\tau(P) = A\exp\left\{\frac{C}{P_0 - P}\right\}.\qquad(6)$$

Fitting the values of $\tau(P)$ at 1 bar, P_α, and P_g, given above, gives reasonable values of 2.1 × 10⁻¹⁵ s, 61.1 GPa, and 8.90 GPa for the parameters A, C, and P_0, respectively. This fit is shown in Fig. 2(b) (right ordinate) as are density data and calculations (left ordinate). Note the importance of accounting for relaxation in EOS calculations for liquids.

Knowledge of the pressure dependence of T_g could in principle improve on this modeling of $\tau(P)$. Although these measurements have not yet been done for the pentane isomeric system, the preliminary results for glycerol up to 12 GPa and 453 K (Figure 1) show clearly that $T_g(P)$ is not linear for that system at pressures below the room temperature glass transition pressure. Furthermore, these data agree nicely with $T_g(P)$ values calculated from extrapolated high-pressure viscosity data by assuming, based on several earlier studies, that $T_g(P) = T_0(P) + 55$ K.[29] To the extent that such an assumption is reasonable, it would be interesting to combine direct $T_g(P)$ data with Brillouin data to provide new models of $\tau(P)$. We are currently exploring these ideas with new experiments. Note that the $T_g(P)$ results for glycerol also provide the most stringent test to date of predictions for the pressure dependence of the glass transition.[37] This will be explored further in a forthcoming paper.

Figure 3 shows room-T Brillouin data for glycerol up to pressures of 7.43 GPa. Note that only the high-pressure side of the peak at P_α is visible since P_α is at negative pressure at 25 °C for glycerol. The DAC heaters that were constructed for the $T_g(P)$ work are being modified for T-dependent high-pressure Brillouin scattering so that the full peak can be explored and the ideas discussed above can be tested.

Figure 4 also shows preliminary room-T Brillouin data for both methanol and a 4:1 methanol:ethanol mixture. These systems have a $P_g(T=25 °C) \sim 10.4$ GPa as determined
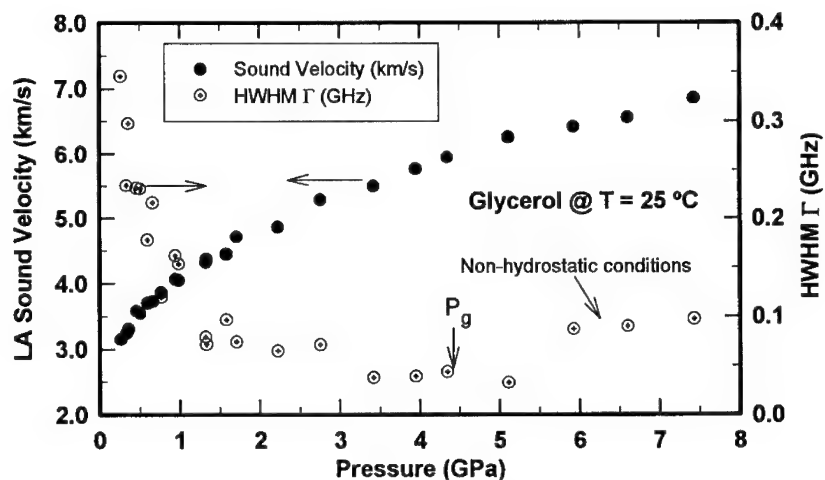
Figure 3. High-pressure Brillouin scattering results for glycerol at 25 °C.

by ruby fluorescence. Note that the maxima in Γ (at ~3.7 GPa) are much broader than that observed in the alkane system and indicates of a broader distribution of relaxation times, which might be related to a distribution in cluster sizes due to hydrogen bonding in the alcohols. Indeed, single relaxation time approximations do not describe these data well and we are trying models using various distributions of relaxation times. Our data are consistent with the impulsive stimulated light scattering data of Brown *et al.*[26] whose analysis also required more than one relaxation time.

Finally, for completeness, another important recent experiment involving the first high-pressure depolarized light scattering study of a fragile glass former, cumene
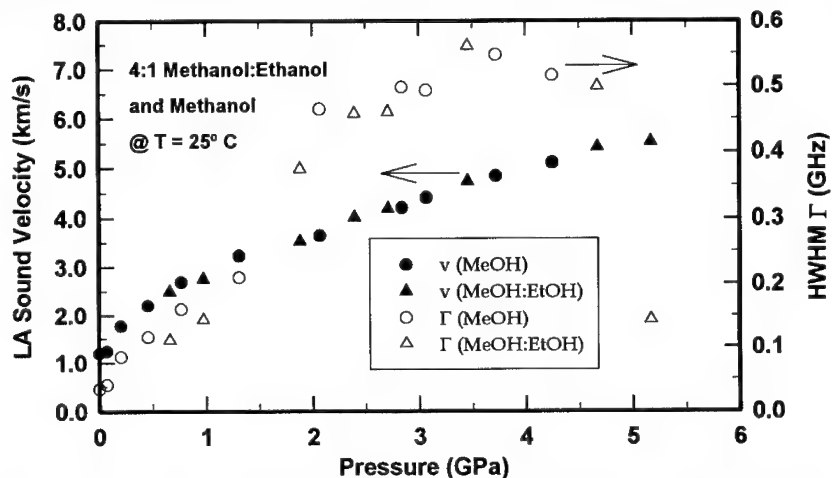
Figure 4. High-pressure Brillouin scattering results for both methanol and a 4:1 mixture of methanol and ethanol at 25 °C. Note the broad peaks in the HWHM.

[C6H5CH(CH3)2], will be discussed.[12]   This work is significant in that both a T-dependent study at 1 bar and a P-dependent study at 293 K were performed so that effects due to both T and V on liquid-state dynamics could be compared.

King *et al.* also performed both T- and P-dependent viscosity measurements on cumene up to 14 kbar.[38] Extrapolation of the viscosity data to $\eta(P) \sim 10^{15}$ cP using both a Tait EOS fit to Bridgman's P-dependent density data[13] and a free-volume fit[39] to $\eta(P)$ resulted in a value of $P_g \sim 25$ kbar and $\rho_g \sim 1.224$ g/cm^3 at T = 293 K.

Variable-T and variable-P susceptibility spectra show both a maximum (due to structural relaxation) that moves to lower frequency as the liquid is cooled or pressurized and a higher-frequency minimum. These data were analyzed in terms of the mode coupling theory (MCT) of the glass transition[9] which describes the susceptibility minimum as being due to the fast β-relaxation process.

Figure 5(a), shows two isochoric susceptibility spectra, one taken at high P and room T and the other at low T and 1 bar. From these spectra it is clear that density is not the only parameter controlling the liquid-glass transition β-relaxation dynamics. Two spectra having the same viscosity but different T and P are shown in Fig. 5(b). These indicate that the α-relaxation process (peaks in the spectra) is probably controlled
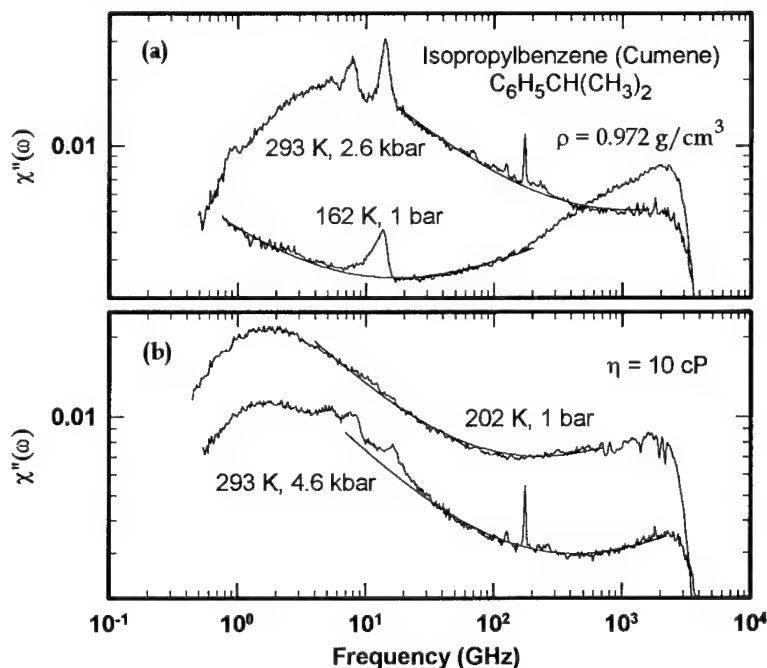
Figure 5. Depolarized susceptibility spectra of isopropylbenzene. (a) Comparison of two susceptibility spectra at the same density $\rho = 0.972$ g/cm^3: the upper one taken at T = 293 K and P = 2.6 kbar, and the lower one taken at T = 162 K and P = 1 bar. (b) Comparison of two susceptibility spectra at the same viscosity $\eta = 10$ cP: the upper one taken at T = 202 K and P = 1 bar, and the lower one taken at T = 293 K and P = 4.6 kbar.

by combinations of P and T in the same way that viscosity is. These results pique our curiosity and indicate clearly the importance of this type of data for illuminating liquid-state dynamics at both high and low densities.

CONCLUSIONS

In summary, a combination of several powerful high-pressure light scattering techniques have been brought to bear on the problem of understanding both thermodynamic and dynamical aspects of liquids at very high densities. These experiments are yielding new and important information on both structural and fast relaxation processes in liquids under extreme conditions, which in turn is improving our understanding of other fundamental aspects of these systems such as their equations of state. This research is fairly new and much still needs to be done. In particular, it is clear from the work presented here that only with the combination of several techniques can we fully understand liquid state dynamics and provide stringent tests of theory. It is also clear that the effect of temperature on the liquid-glass transition goes beyond just changing the density through thermal expansion. Finally, it should be stated that a crucial "missing link" in this work is the behavior of slower dynamical processes at high pressure, i.e., those near $T_g(P)$ [or $P_g(T)$]. It is our hope that dynamic light scattering in the DAC can yield new insights into this problem.

ACKNOWLEDGMENTS

REFERENCES

[1] *Elastohydrodynamic Lubrication* by H. S. Cheng, in the CRC Handbook of Lubrication 2, ed. by E. R. Booser (CRC Press, Boca Raton, 1983), p. 139; see also the chapter entitled *Liquid Lubricants* by E. E. Klaus and E. J. Tewksbury, *ibid*, p. 229.

[2] A. Jayaraman, Rev. Mod. Phys. **55**, 65 (1983).

[3] G. J. Piermarini, S. Block, J. D. Barnett, R. A. Forman, J. Appl. Phys. **46**, 2774 (1975); G. J. Piermarini, S. Block, J. D. Barnett, J. Appl. Phys.**44**, 5377 (1973).

[4] M. J. P. Brugmans and W. L. Vos, J.Chem.Phys. **103**, 2661 (1995).

[5] H. Shimuzu, E. M. Brody, H. K. Mao, and P. M. Bell, in Advances in Earth and Planetary Sciences, vol. 12, edited by S. Akimoto and M. H. Manghnani, (1989), p. 135.

[6] W. F. Oliver, C. A. Herbst, and G. H. Wolf, J. Non-Cryst. Solids **131-133**, 84 (1991).

[7] W. F. Oliver, C. A. Herbst, S. M. Lindsay, and G. H. Wolf, Phys. Rev. Lett. **67**, 2795 (1991).

[8] H. Z. Cummins, W. M. Du, M. Fuchs, W. Götze, S. Hildebrand, A. Latz, G. Li, and N. J. Tao, Phys. Rev. E **47**, 4223 (1993); see also refs. within.

[9] W. Götze and L. Sjögren, Rep. Prog. Phys. **55**, 241 (1992).

[10] We use the term "fragile" in the sense of: C. A. Angell, J. Non-Cryst. Solids **102**, 205 (1988).

[11] W. Götze, see Symposium Proceedings from this Meeting entitled: *Glasses and Glass Formers – Current Issues*, ed. by C. A. Angell, T. Egami, J. Kieffer, U. Nienhaus, and K. L. Ngai.

[12] G. Li, H. E. King, Jr., W. F. Oliver, C. A. Herbst, and H. Z. Cummins, Phys. Rev. Lett. **74**, 2280 (1995).

[13] P. W. Bridgman, Collected Experimental Papers, (Harvard Univ. Press, Cambridge, 1964).

[14] J. D.Barnett and C. D. Bosco, J. Appl. Phys. **40**, 3144 (1969); G. J. Piermarini, R. A. Forman, and S. Block, Rev. Sci. Instrum. **49**, 1061 (1978); R. L. Cook, C. A. Herbst, and H. E. King Jr., J. Phys. Chem. **97**, 2355 (1993).; H. E. King, Jr, see the article in this proceedings.

[15] W. M. Slie and W. M. Madigosky, J. Chem. Phys. **48**, 2810 (1968).

[16] S. Hawley, J. Allegra, and G. Holton, J. Acoust. Soc. Am. **47**, 137 (1970); J. Allegra, S. Hawley, and G. Holton, J. Acous. Soc. Am. **47**, 144 (1970).

[17] J. Jonas, D. Hasha, and S. A. Huang, J. Chem. Phys. **71**, 3996 (1989).

[18] S. H. Lee, M. S. Conradi, and R. E. Norberg, Phys. Rev. B **40**, 12492 (1989).

[19] J. L. Yarger, R. A. Nieman, G. H. Wolf, and R. F. Marzke, J. Mag. Res., Ser. A **114**, 255 (1995).

[20] G. P. Johari and E. Whalley, Faraday Symp. Chem. Soc. **6**, 23 (1972).

[21] D. L. Questad, K. D. Pae, B. A. Newman, and J. I. Scheinbeim, J. Appl. Phys. **51**, 5100 (1980).

[22] O. Mishima and E.Whalley, J. Chem. Phys. **84**, 2795 (1986).

[23] H. Forsman, Molecular Phys. **63**, 65 (1988).

[24] J. R. Stevens, R. W. Coakley, K. W. Chau, and J. L. Hunt, J. Chem. Phys. **84**, 1006 (1986).

[25] D. Miles, N. Lee, and D. Kivelson, J. Chem. Phys. **90**, 5327 (1989).

[26] J. M. Zaug, L. J. Slutsky, and J. M. Brown, J. Phys. Chem. **98**, 6008 (1994).

[27] R. G. Munro, F. J. Piermarini, S. Block, and W. B. Holzapfel, J. Appl. Phys. **57**, 165 (1985).

[28] O. Sandberg, P. Andersson, and G. Backström, *Proc. 7th Symp. Thermophys. Prop.*, 181 (1977).

[29] C. A. Herbst, R. L. Cook, and H. E. King, Jr., Nature **361**, 518 (1993).

[30] W. F. Oliver, C. A. Herbst, S. M. Lindsay, and G. H. Wolf, Rev. Sci. Instrum. **63**, 1884 (1992).

[31] J. Houck, J. Res. Nat. Bur. Stand. Sect. A **78**, 617 (1974).

[32] M. G. Sceats and J. M. Dawes, J. Chem. Phys. **83**, 1298 (1985).

[33] For examples where hypersonic shear modes are observed in liquids see refs. 6 and 7 and M. Grimsditch, R. Bhadra, and L. M. Torell, Phys. Rev. Lett. **62**, 2616 (1989).

[34] P. J. Carroll and G. D. Patterson, J. Chem. Phys. **81**, 1666 (1984).

[35] P. Vinet, J. Ferrante, J. H. Rose, and J. R. Smith, J. Geophys. Res. **92**, 9319 (1987).

[36] C. A. Angell, L. J. Pollard, and W. Strauss, J. Solution Chem. **1**, 517 (1972).

[37] Edmund A. DiMarzio, Julian H. Gibbs, Paul D. Fleming III, and Isaac C. Sanchez, Macromolecules, **9**, 763 (1976).

[38] R. L. Cook, H. E. King, Jr., C. A. Herbst, and D. R. Herschbach, J. Chem. Phys. **100**, 5178 (1994). See also the paper in this symposium by H. E. King, Jr.

[39] C. A. Herbst, R. L. Cook, and H. E. King, Jr., J. Non-Cryst. Solids **172-174**, 265 (1994).

GLASS-FORMING LIQUIDS IN MESOPORES PROBED BY SOLVATION DYNAMIC

AND DIELECTRIC TECHNIQUES

X. YAN, C. STRECK, R. RICHERT
Max-Planck-Institut für Polymerforschung, Ackermannweg 10, D-55128 Mainz, Germany

ABSTRACT

The orientational dynamics of organic supercooled liquids of low molecular weight confined to the geometry of porous glasses are studied by two highly related techniques, the optical method of probing the dynamics of solvation regarding a chromophoric host molecule and dielectric relaxation spectroscopy. The dielectric results display marked effects of the confinement to mesopores in terms of altered structural dynamics which appear to separate into a faster and slower responses relative to the bulk liquid. We also demonstrate that there is no trivial relation between the $\varepsilon^*(\omega)$ data and the liquid dynamics in these heterogeneous samples. These effects are partially paralleled by the solvation dynamics results, but with the spatial range inherent in the optical technique being inconsistent with associating the fast and slow dynamical components to spatially distinct regimes. We conclude on the slow component being a signature of non-ergodicity which arises from the competition between the length scale of cooperativity and the pore size.

INTRODUCTION

The impact of mesoscopical and microscopical geometrical confinement on the structure and dynamics of condensed matter is an active field of research [1]. Although a plethora of marked features are experimentally observed in studies comparing the bulk and confined behaviour of liquids [2], there is no satisfactory overlap between theoretical approaches and experimental findings to date. The setup of two parallel atomically smooth plates as used in the surface force apparatus is certainly the most defined geometry possible, especially when the plate distance can be controlled on a molecular scale [3]. However, systematic dynamic measurements like dielelctric relaxation as a function of temperature in such a configuration have not been achieved. For this kind of experiment it is more practical to exploit the tremendous surface to volume ratio offered by porous materials, so that also techniques which are not specifically sensitive to a surface or to a liquid-solid interface are capable of resolving confinement effects.

Dielectric relaxation of organic liquids and supercooled liquids has been measured in different porous glasses with average pore diameters ranging between 2.5 nm and 10 nm [4-7]. The qualitative similar results in all cases are that the structural or α-process of the liquid displays an altered mean relaxation time and a more pronounced relaxation time dispersion relative to the dynamics of the corresponding bulk material. Secondly, one or more further relaxation peaks appear at lower frequencies, i.e. associated with longer relaxation time scales [4-7]. Bearing in mind that the liquid under study usually exhibits dc-conductivity due to the presence of ionic impurities and that the confined liquid is surrounded by an insulating solid, one should expect the appearance of a Maxwell-Wagner-Sillars (MWS) type relaxation process [8,9]. This process, which is not seen in the pure liquid filler or solid matrix material, originates from the charge carriers in the filler material whose motion is in part restricted to the pore size, so that their contribution to the dielectric signal becomes equivalent to that of a dipole with orientational freedom. Because of the dielectric enhancement in heterogeneously mixed materials the resulting

Maxwell-Wagner (MW) peak is often too large to comply with the molecular dipole-moments in the liquid. Therefore, one of the slower peaks appearing in dielectric data on porous samples is assigned to this more trivial effect of geometrical confinement, which is absent in other relaxation techniques. Partially stimulated by the observation of a solid like interfacial layer in surface force experiments, the remaining non-trivial slow relaxation component has been attributed to a surface layer of the liquid where the long relaxation times are believed to be a consequence of physical and/or chemical interactions with the pore walls. Qualitatively, these features have been observed in porous glasses prepared by sol-gel technologies as well as in those made by spinodal decomposition methods [4,6,7].

A conceptually very different method of probing the orientational relaxation phenomena in polar liquids is the optical method of measuring the dynamics of the solvation regarding a chromophoric probe molecule dissolved at very low concentration in the material under study [10]. In such an experiment the probe molecule experiences at time $t = 0$ an electronic excitation from its ground state S_0 to one of the metastable excited states, S_1 or T_1, which is usually accompanied by a change $\Delta\mu = \mu_E - \mu_G$ in the permanent dipole moment. The bulk of the molecules constituting the liquid is transparent at the excitation wavelength, i.e. they are not subject to electronic excitation. Assuming that the surrounding polar liquid has been in equilibrium with the ground state μ_G at times $t < 0$, the effect of the $\mu_G \rightarrow \mu_E$ transition is to initiate a relaxation process of the neighboring liquid towards the equilibrium with respect to the excited state dipole moment μ_E [11]. The quantity of interest observed by optical spectroscopy is the emission spectrum as a function of time, i.e. the energy differences $v(S_1) - v(S_0)$ for fluorescent or $v(T_1) - v(S_0)$ for phosphorescent molecules. Due to the electrostatic interactions between the permanent dipole moment of the chromophore and the polar medium, the polarization of the liquid in the electric field created by $\Delta\mu$ lowers the energy level of the excited state and increases that of the ground state. Therefore, the emission energy $v = v(t)$ becomes a function of time if orientational polarization is active within the excited state lifetime of the chromophore. The gradual change of the electronic energy levels along the time or solvation coordinate axis as depicted in Fig. 1 is the observed quantity in this experiment.
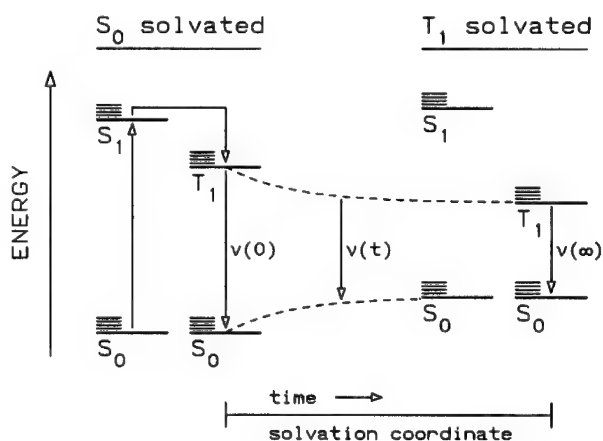
Fig. 1. Schematic outline of the energy levels of a solute molecule with the dipole moments $\mu_G \neq \mu_E$ interacting with a polar solvent. The population of the excited state T_1 is assumed fast relative to the solvation time scale. Note that the solvation of the excited triplet state is accompanied by increasing the energy levels of the other electronic states. An ensemble of chromophores would display gaussian distributions of energies.

As outlined above, the temporal progress of the Stokes shift $\Delta v(t) = v(t) - v(0)$ towards lower energies is highly linked to the orientational polarizability of the solvent, whereas the gas-to-solvent shift $v(0) - v_{gas}$ reflects the electronic polarizability of the material [11]. In cases where one is less interested in the absolute energy scales, it is convenient to normalize $v(t)$ to obtain the so called Stokes shift correlation function

$$C(t) = [v(t) - v(\infty)] / [v(0) - v(\infty)] , \tag{1}$$

with $C(0) = 1$ and $C(\infty) = 0$. In order to establish a quantitative relation between solvation dynamics $\Delta v(t)$ and time dependent dielectric properties $\varepsilon(t)$ one has to regard two differences regarding the experimental situation. First, the solvation process is due to the relaxation in the field of a molecular dipole, instead of a macroscopically homogeneous field in a usual dielectric experiment. Second, the charge distribution responsible for μ_E is independent of the progress of relaxation, whereas $\varepsilon(t)$ refers to the polarizability under the condition of a polarization invariant electric field and thus actually reflects a retardation phenomenon [12]. The concomitant relaxation process is described by the dielectric modulus $M(t)$ which is linked to the dielectric function via $M^*(\omega) = 1 / \varepsilon^*(\omega)$, where $M(t)$ reflects the time dependent polarization under the condition of a constant charge or constant dielectric displacement. Accounting for the different field geometries is less straightforward and involves sophisticated theoretical work even for approximate solutions for the $C(t) - \varepsilon(t)$ relation if the solvent is not simply treated as a continuum dielectric [13]. For the present purpose it suffices to regard the solvation dynamics results $C(t)$ as the equivalent to the dielectric modulus $M(t)$.

Based on the different field geometries the characteristic length scales inherent in the optical and dielectric methods are quite different. A dielectric experiment is bound to measure the macroscopic average over the entire sample between the electrodes of the capacitor. In contrast, the chromophores are electrostatically coupled only to the solvent in their immediate vicinity. An estimate on the spatial coupling range of a dipole within a polar equilibrium fluid can be derived from simple electrostatical arguments [14]. The radial components of the electric field created by a dipole decay as $E(r) \propto r^{-3}$. The average number density of dipoles on the surface of a sphere increases with r as $N(r) \propto r^2$. For an orientationally disordered system one has to replace the energy $w = -\mu \cdot E \cdot \cos\theta$ by the ensemble average $\langle w \rangle = -\mu \cdot E \cdot N \cdot \langle \cos\theta \rangle$ with $\langle \cos\theta \rangle = \mu E / 3kT$ for a fluid in thermodynamic equilibrium. For the distance dependence of $\langle w \rangle$ we thus have

$$\langle w \rangle(r) = -\mu \cdot E \cdot N \cdot \langle \cos\theta \rangle = -N(r) \cdot \mu^2 \cdot E^2(r) / 3kT \propto r^{-4} . \tag{2}$$

For the cumulative energy $\langle W \rangle = \int \langle w \rangle(r) \, dr$ arising from the contribution of all (non-interacting) dipoles within the sphere of radius r the result is $\langle W \rangle \propto r^{-3}$. Assuming similar diameters for solute and solvent molecules, the bulk of the solvation free energy is thus governed by the polarization of the first solvent shell, as confirmed by more detailed calculations [14] as well as by computer simulation [15]. The interesting consequence of this limited electrostatic coupling range for solvation dynamic experiments in porous media is the absence of a signature of dc-conductivity as well as of a MW polarization arising from the conductivity mismatch between the liquid filler material and the glass matrix. This relaxes the residual ambiguity in deciding which of the observed peaks is not associated with the structural relaxation of the liquid under study.

The aim of the present work is to compile the interpretations based on solvation dynamic data obtained for a glass-forming liquid confined to porous glasses of different nominal pore diameters. The dielectric data measured for equivalent samples is compared to the solvation dynamic results

and critically investigated with respect to evaluating the dielectric properties of the liquid filler inside the porous glass matrix on the basis of the data reflecting the dielectric behaviour of the composite liquid/glass sample.

EXPERIMENTS

The measurements under the condition of geometrically confined liquids have been carried out in Gelsil (GelTech) porous glasses with the different nominal diameters $\phi = 2.5$ nm, 5.0 nm, and 7.5 nm. For the optical method the cylindrical samples of 10 mm diameter and 5 mm thickness have been used as purchased. Dielectric measurements employed slices of 200 μm to 300 μm thickness of these original pieces. According to a BET analysis supplied by GelTech, the actual data in the order of increasing pore size are: average pore diameters 2.6, 4.6, and 8.4 nm; pore volume fractions $\varphi = 0.39$, 0.68, and 0.72; and surface areas 609, 594, and 342 m^2/g. In order to obtain clean pore surfaces, all glasses were heated in vacuum to 400°C for 24 hours prior to embibing the liquids under study.

Solvation Dynamics

The glass-forming liquid 2-methyltetrahydrofuran (MTHF) was distilled and passed through Al_2O_3 filters to remove polar contaminations directly before filling the the pores. Quinoxaline (QX) was distilled and sublimated and then dissolved in MTHF at a concentration of $\approx 10^{-4}$ mol/mol resulting in a practically vanishing probability for finding two QX molecules in one pore.The glasses were filled with QX/MTHF under dry N_2 atmosphere and placed into a vacuum sealed sample holder, where it is gently pressed in contact to a sapphire window. The remaining volume within the sample holder was also filled with the liquid to ensure complete liquid content in the pores for the entire experiment and to improve thermal contact to the brass walls. This sample housing was mounted to the cold stage of a closed cycle He refrigerator (Leybold, RDK 10-320, RW 2) and temperature stability within $\pm$ 50 mK was achieved by a temperature controller (Lake Shore, LS 330) equipped with calibrated diode sensors. Samples were allowed to equilibrate for at least one hour prior to each measurement.

As excitation source we used an excimer laser (Radiant Dyes, RD-EXC-100) operated at 308 nm with pulse width $\approx$ 25 ns, pulse energy 120 mJ, and at a repetition rate of 1 Hz. The aperture was limited such that excitation outside the porous glass cylinder is avoided. The phosphorescent emission from QX was coupled via fibre optics to a triple grating monochromator (EG&G, 1235) and registered by a MCP intensified diode array camera (EG&G, 1455B-700-HQ) with controller (EG&G, 1471A), gating options (EG&G, 1304), and synchronization facilities (EG&G, 9650). The spectra consisted of 730 channels with a resolution of 0.04 nm/channel and were wavelength calibrated with Xe and Kr lamps. The time resolution is defined either by gating the camera with gate widths between 100 ns and 10 ms or by successive readouts of the camera at a speed of up to 50 spectra per second. For the probe molecule QX the usable time range is lifetime limited (τ_{ph} ≈ 0.33 s) to 1 ms $\leq$ t $\leq$ 1s for experiments using porous glasses. The spectra obtained in the above manner were subject to a gaussian fit regarding the electronic $S_0 \leftarrow T_1$ (0-0) transition of QX which reduces the data to the relevant values of the mean emission energy $\nu(t,T)$ and gaussian width σ. Typical such spectra of QX/MTHF have been reported elsewhere [11].

Dielectric Relaxation

The glass former N-methyl-ε-caprolactam (NMEC) has been filtered with Al_2O_3. The porous glasses are carefully exposed to the liquid under dry N_2 atmosphere until no further liquid uptake

is observed. The disc shaped sample is placed between two gold plated brass electrodes. The top electrode is pressed onto the sample with a spring in order to accomodate slightly tilted surfaces and to ensure a good contact over the entire temperature range. This sample capacitor is placed inside a gas stream cryostat with the gas being thermally controlled (Novocontrol, Quatro) by heating the N_2-gas emerging from a liquid N_2 reservoir. The admittance $Y^*(\omega)$ of the capacitor and thus the dielectric properties $\varepsilon^*(\omega)$ of the samples are measured using a gain-phase analyser (Solartron, SI-1260) equipped with a transimpedance amplifier (Mestec, DM-1360). The frequency range used is between 10^{-2} Hz and $5 \cdot 10^6$ Hz. The geometric capacity C_{geo} needed to perform the calculation $\varepsilon^*(\omega) = Y^*(\omega) / i \omega C_{geo}$ is subject to the uncertaincy of the sample thickness including deviations from a perfectly parallel cut porous glass disc.

RESULTS

The emission spectra of the electronic $S_0 \leftarrow T_1$ (0-0) transition of QX were analysed in terms of gaussian profiles in order to obtain the mean emission energy $\nu(t,T,\phi)$ and the according gaussian widths $\sigma(t,T,\phi)$. Normalization of $\nu(t)$ to the cases $t = 0$ and $t = \infty$ according to equation (1) leads to the Stokes shift correlation function $C(t)$. A representative set of $C(t)$ decays is portrayed in Fig. 2 for QX/MTHF in pores at the temperature $T = 92.5$ K with the curves being parametric in the pore size ϕ. For the decay analysis the tendency of the geometrically confined cases to attain a quasi-stationary level well above zero is accounted for by an additional offset C_0 to a Kohlrausch-Williams-Watts [16] (KWW) like structural process, so that the curves can be represented by

$$C(t) = C_0 + (1 - C_0) \cdot \exp [- (t/\tau)^\beta] . \qquad (3)$$
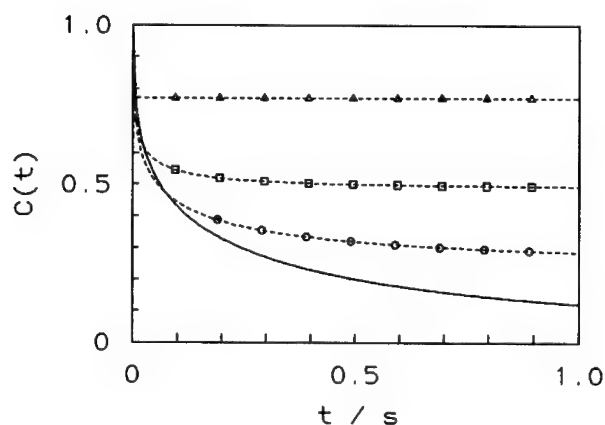
Fig. 2. Experimental data for the Stokes shift correlation function C(t) for MTHF probed by QX at $T = 92.5$ K $\approx T_g + 2$ K. The solid curve refers to the bulk liquid. The dashed curves are the results obtained in mesopores for the three different nominal pore diameters $\phi = 7.5$ nm (--O--), 5.0 nm (--□--), and 2.5 nm (--Δ--). The symbols are for curve identification purposes only.

Thereby the data reduces to $C_0(\phi,T)$, $\tau(\phi,T)$, and $\beta(\phi)$, where the bulk liquid is designated $\phi = \infty$. The qualitative features are that i) C_0 increases with decreasing pore size and temperature, ii) τ decreases with decreasing pore size, and iii) β in pores in smaller than $\beta(\infty)$. Taken the present

experimental time range limitation of $t \leq 1$ s, the offset C_0 should be understood as a contribution to $C(t)$ for which the relaxation time scale is well above 1 s so that its decay pattern remains unresolved. It should be noted that the entire Stokes shift $\Delta\nu = \nu(0) - \nu(\infty)$ is a measure for the dielectric relaxation strength $\Delta\varepsilon = \varepsilon_s - \varepsilon_\infty$. In contrast to evaluating $\Delta\varepsilon$ from dielectric data, the observed $\Delta\nu$ does not depend on the probed volume or number of chromophores contributing to the optical signals. Details regarding experimental procedure and data analysis have been reported elsewhere [17].

Dieletric relaxation data have been recorded for porous Gelsil samples filled with NMEC and for temperatures above the glass transition temperature $T_g \approx 170$ K. The pure silica glass has been shown to display no relaxation process in the present experimental frequency and temperature range, so that its dielectric behaviour is represented entirely by a dielectric constant $\varepsilon_m \approx n^2 \approx 3$, where n is the index of refraction. The loss spectra $\varepsilon''(\omega)$ obtained for the samples are subject to a fit procedure which accounts for the dc-conductivity of the sample and for the individual relaxation peaks in terms of the empirical dielectric function proposed by Havriliak-Negami [8] (HN). The total fit function thus reads

$$\varepsilon^*(\omega) = \varepsilon_\infty + \sum_\kappa \frac{\Delta\varepsilon_\kappa}{[\, 1 + (i\omega\tau_\kappa)^{\alpha_\kappa}\,]^{\gamma_\kappa}} + \frac{\sigma_{dc}}{i\,\omega\,\varepsilon_0} \,, \tag{4}$$

where ε_∞ is the dielectric constant in the limit $\omega \to \infty$, $\Delta\varepsilon = \varepsilon_s - \varepsilon_\infty$ is the relaxation strength, τ is a characteristic time constant, σ_{dc} measures the extent of dc-conductivity, and ε_0 denotes the absolute permittivity. The exponents α and γ in the range $0 < \alpha, \alpha\gamma \leq 1$ reflect the symmetric and asymmetric broadening of the loss profile relative to the simple Debye case with $\alpha = \gamma = 1$. The usual deviations from Debye type behaviour in real systems can equally be accounted for in terms of a relaxation time distribution. The fact that only a certain volume fraction φ given by the porosity of the glass is occupied by the liquid under study would be accounted for by substituting the observed $\Delta\varepsilon_i$ by $\Delta\varepsilon_i/\varphi$, where φ in the range 0.4 ... 0.7 varies with the nominal pore size. Fig. 3 displays typical loss spectra for the NMEC bulk liquid and for NMEC in the porous glasses.
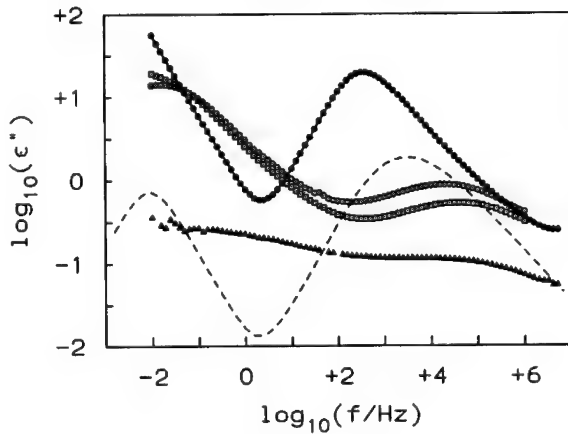
Fig. 3. Experimental data for the dielectric loss profiles of NMEC at T = 192 K. The filled circles represent the bulk liquid case. The other symbols refer to the results for NMEC in mesopores for the three different nominal pore diameters ϕ = 7.5 nm (O), 5.0 nm (□), and 2.5 nm (△). The dashed line is a MWS calculation with n = 1/3, ε_m = 3 and φ = 0.5 as described in the text.

The common features of the porous samples relative to the bulk material observed for NMEC at other temperatures and also for other glass-forming liquids are as follows. The α-process is situated at higher frequencies and relates to a broader and more symmetric relaxation time distribution. The relaxation strength of the α-like peak is smaller than in the bulk, even after correcting for the pore volume fraction φ. Further relaxation peaks occur at lower frequencies which are absent in the bulk case, where one of these peaks is expected to arise from MW polarisation.

DISCUSSION

The qualitative occurrence of a slow and fast relaxation component in the solvation dynamics $C(t)$ data operating on strongly separated time scales in confined liquids is confirmed by dielectric relaxation results by displaying a slower relaxation peak in addition to a process which is similar to the bulk α-relaxation but active on shorter time scales. On the basis of the dielectric loss spectra it seems straightforward to conclude on an acceleration of the structural or α-process and the additional appearence of slow relaxation components, where the former feature might reflect confinement effects and the latter one can be understood as an interfacial layer of the liquid whose dynamics are strongly frustrated by the interactions with the glass wall. Such an interpretation becomes less obvious when observing that the $C(t)$ curves for the confined cases actually contain no faster components on the absolute $C(t)$ scale and only the artificial decomposition into distinct processes is responsible for concluding on an accelerated structural relaxation for the confined liquids relative to the bulk behaviour [17]. Following the idea put forward by Donati and Jäckle [18] an alternative to the distinct processes is assuming spatially uniform dynamics instead of a spatial discrimination of the distinct relaxation times.

The experimental evidence for spatially uniform dynamics stems from observing that the emission spectra of QX in the porous samples at longer times ($0.5 \text{ s} \leq t \leq 1 \text{ s}$) show gaussian widths which vary no more than $\approx 5\%$ as a function of temperature and pore size relative to the bulk case. Spatially distinct relaxation components with considerably different time scales should result in an intermediate value for $v(t)$ because mobile sites emit from the equlibrated state at their $v(\infty)$ while immobile liquid parts emit at the unrelaxed energy at their $v(0)$. However, such a situation would lead to a width of the phosphorescence spectra which would display at least twice the value observed for the bulk MTHF. Therefore, the observation of a practically constant width at long times complies only with dynamics which are spatially uniform on the length scale of the solute-solvent coupling, which is 1 - 2 molecular diameters only. Assuming spatially uniform dynamics the pore size dependent relaxations as plotted in Fig. 2 are to be compared on the absolute $C(t)$ scale, which immediately indicates that the confined liquid displays at no time a decay pattern which is faster than the bulk curve. More specifically, the data of Fig. 2 reveals a bulk like decay at short times $t \leq \tau'$ for all pore sizes. Note that a comparison of the α-peaks in Fig. 3 suggest an acceleration of the α-process by a factor of ten or more. It should be emphasized that the qualitative features of Fig. 2 discussed here are paralleled by the results obtained at the other experimental temperatures [17]. The effect of the pore diameter or extent of geometrical confinement is thus to alter the time $\tau'(\phi)$ at which a transition from a bulk like behaviour to a freezing in of the remaining relaxation occurs at the amplitude $C(t \gg \tau') = C_0$. Therefore, at short times $t < \tau'$ the structural relaxation does not sense the geometrical

confinement, wheras it depends strongly on ϕ after which time τ' or after which relaxation extent $1 - C_0$ the systems appears to become non-ergodic on the experimental time scale $t \leq 1$ s.

A molecular scenario which supports the above mentioned transition from a bulk like decay to a non-ergodic appearence is schematically visualized in Fig. 4. The model underlying this scheme is that the ensemble averaged initial short time motion of a relaxing site involves only the cooperative motion of a few neighboring molecules. Further steps towards the equilibrium situation require more and more molecules to act cooperatively, so that the number of dynamically coupled relaxors increases during the progress of equilibration. In other words, the length scale $\xi(t)$ of cooperativity is an increasing function of time, an idea which is conceptually similar to Ngai's coupling scheme [19]. If subject to geometrical confinement such a relaxation mechanism proceeds initially as in the bulk material but is expected to differ from the bulk behaviour as soon as the spatial extent of cooperativity has reached the pore size. In this latter situation, the rigid pore wall is likely to block any further approach to equilibrium conditions in the entire pore because now all molecules are dynamically coupled to the interface. The transition time τ' at which this blocking of the dynamics takes effect will thus depend on pore size and on temperature. Eventually, the final equilibrium case is restored but on a much longer time scale dictated by the effectivity by which the pore boundary frustrates the molecules which reside in immediate contact with the pore wall.
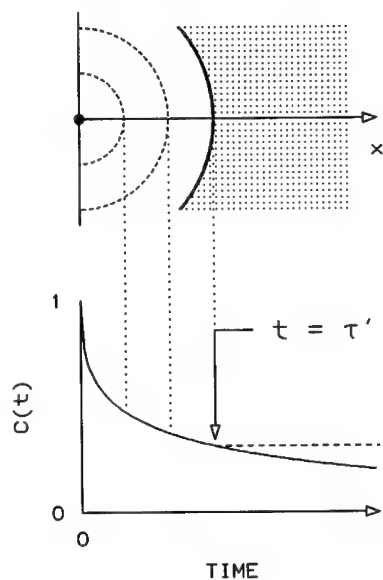
Fig. 4. Illustration of the interrelation between decay pattern and temporal progress of the length scale of cooperativity. The bold solid arc represents the pore wall and the SiO_2 glass surrounding the pore is indicated by the shaded area. The temporal increase of the cooperativity length (dashed semicircles) is understood to have no effect relative to the bulk decay (solid decay curve) until it matches the pore size and thus induces non-ergodicity on longer time scales. The axes are not ment to be scaled.

One could conclude one the same scenario without regarding the ensemble average only. Consider a statistical distribution of the number of adjacent molecules needed to move cooperatively for a certain site to relax. Those sites coupled dynamically to only a few molecules will dominate the short time response, while sites demanding a large number of cooperatively rearranging units will equilibrate on longer time scales. In the case of geometrical confinement, all sites associated with a few cooperative neighbors will relax as in the infinitely extenting liquid

while those which are dynamically coupled to the boundary will remain blocked for times well above the average bulk relaxation time. Within the scope of the present discussion, this idea is identical to an ensemble average length scale of cooperativity $\xi(t)$ which increases with time.

In Fig. 4 the transition of the decay into the quasi-stationary situation is oversimplified by assuming a sharp break at τ', which in reality should be smeared out on the time scale. In order to gain access to the transition time τ' as a function of pore size ϕ and temperature T, all C(t) fits following equation (2) are analysed by evaluating the time τ' which satisfies the condition $C_0(\phi, T) = C(t = \tau', \phi = \infty, T)$. According to Fig. 4, this is the time at which C(t) for the bulk case has decayed to the offset value $C_0 = C_0(\phi, T)$. From the resulting values $\tau' = \tau'(\phi, T)$, normalized to the average bulk relaxation time $\langle\tau\rangle(T)$, one can derive information on the ensemble averaged length scale of cooperativity as a function of time and temperature. Also of interest here is the extent of relaxation, $1 - C_0 = 1 - C_{bulk}(t=\tau')$, which is covered in the time range $0 \leq t \leq \tau'$. From these results it is seen that for a certain ϕ the time τ' (in units of the average relaxation time $\langle\tau\rangle$) needed for the cooperativity to spread over the entire pore size is a strongly increasing function of temperature, in accord with the idea of the characteristic length scale ξ of cooperativity increasing significantly as the temperature is lowered towards T_g. At a certain temperature slightly above T_g it is in turn a matter of the pore size after which time the blocking of the dynamics takes effect. At sufficiently high temperatures the spatial extent of cooperativity is low such that the crossover time τ' attains values above $\langle\tau\rangle$, i.e. the confinement has practically no effect on the dynamics of the liquid. The equivalent statement can be inferred from the $1 - C_0$ data which approaches $C_0 = 0$ only in the range $T \gg T_g$. The more quantitative results inferred from the $\tau'(\phi, T)$ data are as follows: If a specific characteristic length scale ξ_c of cooperativity is (arbitrarily) identified with its length $\xi(t_c)$ at the time $t_c = 0.1 \cdot \langle\tau\rangle$, then the condition $\tau' = t_c$ or $\log_{10}(\tau'/\langle\tau\rangle) = -1$ marks where the value of ξ_c is on average equal to the pore radius $\phi/2$. Reading this condition for $\xi_c = \phi/2$ from the $\log_{10}(\tau'/\langle\tau\rangle)$ data indicates that $\xi_c(T)$ varies approximately linearly with temperature and also that $\xi_c(T_g) \approx 3$ nm. At the glass transition temperature $T_g = 91$ K the temporal evolution of the cooperativity length $\xi(t)$ is found to increase as $\xi(t) \propto \log(t)$. Within the above concept the competition of cooperativity lengths and mesoscopic geometrical confinement thus leads to a characterization of cooperativity scales ξ summarized by:

$$\xi_c(T) \propto -T \ , \quad \xi_c(T_g) \approx 3 \text{ nm} \ , \quad \text{and} \quad \xi(t) \propto \log(t) \ , \tag{5}$$

where $\xi_c \equiv \xi(t_c)$ can be viewed as the length scale of cooperativity which leads to blocking almost the entire dynamics in the case of a geometrical confinement associated with this spatial scale ξ_c. The result for $\xi_c(T_g)$ is in good agreement with previous reasonings [20].

A comparison of the present results with a Monte-Carlo simulation conducted by Donati and Jäckle [18] on a geometrically confined system with inherent cooperativity appears in order. The simulated system is a lattice gas model with two-vacancy-assisted hopping where the relaxing units are associated with an orientation. It was therefore possible to calculate the orientation autocorrelation function $\phi_p(t)$ under the geometrical confinement to strips of different widths. In a case where the spatial confinement competes with the length scale of cooperativity in this system, the initial decay of $\phi_p(t)$ is only spuriously affected while $\phi_p(t)$ attains quasi-stationary behaviour at longer times. Qualitatively, these features are paralleled by the solvation dynamic data shown in Fig. 2. Both, the $\phi_p(t)$ simulation result and the C(t) experimental evidence, can be regarded as orientational dynamics in a supercooled liquid near the glass transition and subject to geometrical

constraints, so that the theoretical and experimental results are believed to reflect comparable quantities.

It should be possible to arrive at the above conclusions regarding confinement effects also on the basis of the dielectric relaxation results. Actually, the dielectric technique has the advantages of covering much broader frequency and temperature ranges combined with a dynamic resolution which is superior over that achievable in a solvation dynamics experiment. The obvious drawbacks of the dielectric results is the appearence of dc-conductivity and the MW polarization which interfere with a straightforward interpretation of the low-frequency data. Actually, the MW effect is much more general than transposing the conductivity of a filler material embedded in an insulating matrix into a relaxation like peak of the composite sample. The result of the Maxwell-Wagner-Sillars [9] (MWS) theory reads

$$\varepsilon^*_c(\omega) = \varepsilon^*_m(\omega) \cdot \frac{[n \cdot \varepsilon^*_f(\omega) + (1\text{-}n) \cdot \varepsilon^*_m(\omega)] + (1\text{-}n) \cdot [\varepsilon^*_f(\omega) - \varepsilon^*_m(\omega)] \cdot \varphi}{[n \cdot \varepsilon^*_f(\omega) + (1\text{-}n) \cdot \varepsilon^*_m(\omega)] - n \cdot [\varepsilon^*_f(\omega) - \varepsilon^*_m(\omega)] \cdot \varphi}, \quad (6)$$

where the dielectric functions $\varepsilon^*_f(\omega)$, $\varepsilon^*_m(\omega)$, and $\varepsilon^*_c(\omega)$ refer to the filler, matrix, and composite material, respectively. φ is the volume fraction of the filler and n is the depolarization factor which depends on the geometry of the filler particles. The value n = 1/3 holds for spheres and isotropically disordered shapes while other values refer to oblate or prolate structures which are oriented with respect to the field. The MWS result states for the range $0 < \varphi < 0.2$ that $\varepsilon^*_c(\omega)$ for any heterogeneous dielectric is not an additive function of $\varepsilon^*_f(\omega)$ and $\varepsilon^*_m(\omega)$ for all cases except the trivial one $\varepsilon^*_f(\omega) = \varepsilon^*_m(\omega)$. We restrict the further discussion to the case n = 1/3 and $\varepsilon^*_m(\omega)$ $\equiv \varepsilon_m$, i.e. to the case of an insulating matrix without dielectric relaxation activity as realsitic for silica glass in the present temperature range. Within these limitations no dc-conductivity will be predicted for the composite $\varepsilon^*_c(\omega)$ because there is no percolating path among the filler particles within this model. For the special case of a simple Debye type insulating filler dielectric of the form $\varepsilon^*_f(\omega) = \varepsilon_\infty + (\varepsilon_s - \varepsilon_\infty)/(1 - i\omega\tau)$ the composite property is also described by a Debye function but with a different relaxation time τ_c which is given by [21]

$$\frac{\tau_c}{\tau} = \frac{\varepsilon_\infty \cdot n \cdot (1\text{-}\varphi) + \varepsilon_m \cdot [1 - n \cdot (1 - \varphi)]}{\varepsilon_s \cdot n \cdot (1\text{-}\varphi) + \varepsilon_m \cdot [1 - n \cdot (1 - \varphi)]} \ . \quad (7)$$

Therefore, since $\varepsilon_\infty < \varepsilon_s$, we have $\tau_c < \tau$, i.e. the loss peak of the composite is allways positioned at higher frequencies relative to that of the filler in case of simple Debye systems.

We now turn to the more realistic cases where the parameters are adjusted to match our experimental situation and which have to be evaluated numerically. The dielectric relaxation of the bulk NMEC liquid at T = 192 K is well described by the HN type equation (4) with $\kappa = 1$ and the parameters $\tau = 6.46 \cdot 10^{-4}$ s, $\alpha = 0.986$, $\beta = 0.634$, $\varepsilon_\infty = 3.3$, $\Delta\varepsilon = 50.0$, $\sigma_{dc} = 3.12 \cdot 10^{-13}$ S/cm. Using this fit as $\varepsilon^*_f(\omega)$ together with $\varepsilon_m = 3$ and $\varphi = 0.5$ leads to the $\varepsilon^*_c(\omega)$ curve included in Fig. 3, which outlines the expected dielectric behaviour of NMEC in a porous glass in the *absence* of any confinement or surface effects. The result demonstrates that the dielectric heterogeneity already leads to shifting the average relaxation time to higher frequencies, to an increased and more symmetric broadening of the loss peak, and to substantial depression of the apparent relaxation strength by more than a factor φ. It is obvious that the MWS calculation is far from accounting for the entire differences between the bulk and confined case measurements. On the other hand, it also becomes evident that only parts of these differences can be assigned to geometrical confinement or interfacial features.

With the above importance of the dielectric heterogeneity in mind, it should be the goal of a data analysis to reconstruct the filler properties $\varepsilon^*_f(\omega)$ from the measured $\varepsilon^*_c(\omega)$ and to compare that result to the bulk properties in order to extract the impact of mesopores on the dynamics of the liquid. The applicability of such a method is inspected by calculating $\varepsilon^*_c(\omega)$ for a given set of parameters for $\varepsilon^*_f(\omega)$, ε_m, and φ and then reconstruct the function $\varepsilon^*_f(\omega)$ from the $\varepsilon^*_c(\omega)$ data but for experimentally realistic uncertainties as regards the values of ε_m, and φ. $\varepsilon^*_f(\omega)$ is determined by $\varepsilon_m = 3$, $\varphi = 0.5$ and a HN type $\varepsilon^*_c(\omega)$ with the parameter set given above for the bulk NMEC liquid at T = 192 K. For the reconstruction of the filler property $\varepsilon^*_f(\omega)$ the experimental uncertainty is modelled by variations of $2.75 \leq \varepsilon_m \leq 3.25$ and $0.47 \leq \varphi \leq 0.53$. The extremes of these calculations as regards the deviations from the case $\varepsilon_m = 3$ and $\varphi = 0.5$ are shown in Fig. 5. The real uncertainties are considered to be larger because of the problems of independently determining the geometrical capacitance and the possibility of a fraction of unfilled pores. The small variations of ε_m and φ considered here already lead to an uncertainty of approximately one order of magnitude with respect to both the amplitude and the peak frequency of the reconstructed loss profile. The additional systematic error emrging from the application of the MWS equation at volume fractions well above the upper limit at $\varphi \approx 0.2$ can not be quantified presently. More appropriate theories like the local porosity formalism proposed by Hilfer [22] should be applicable for these systems, but the required detailed input information concerning the geometry is currently not available for our samples.
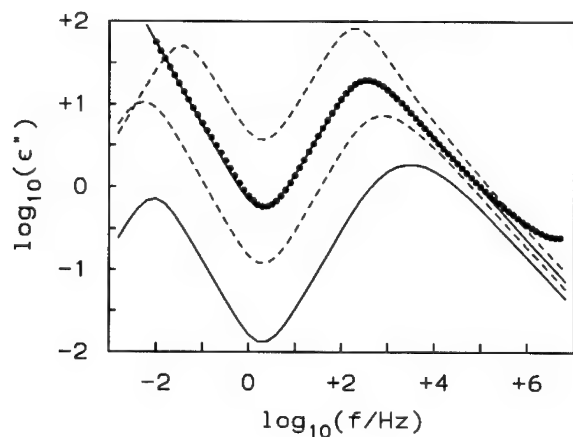
Fig. 5. Experimental data (filled circles) for the dielectric loss profile of bulk NMEC at T = 192 K togher with a HN fit (upper solid line) used as $\varepsilon^*_f(\omega)$. The lower solid line is the MWS result for $\varepsilon^*_c(\omega)$ for $\varepsilon_m = 3$ and $\varphi = 0.5$. The dashed lines are $\varepsilon^*_f(\omega)$ reconstructions based on the $\varepsilon^*_c(\omega)$ curve for $\varepsilon_m = 2.75$ and $\varphi = 0.47$ (upper) and for $\varepsilon_m = 3.25$ and $\varphi = 0.53$ (lower).

From the above MWS calculations we conclude that the previous method of correcting for the glass matrix only by regarding the volume fraction in terms of $\varepsilon^*_f(\omega) \approx \varepsilon^*_c(\omega) / \varphi$ leads to severe deviations relative to the actual dielectric properties of the filler material. It seems that the ambiguities involved in retrieving $\varepsilon^*_f(\omega)$ exceed the differences between the dielectric relaxation behaviours of the bulk and confined liquid. At present there seems to be no straightforward and reliable method of quantitatively extracting the confinement effects from dielectric relaxation data obtained for liquids in porous matrices.

CONCLUSIONS

It has been shown that the technique of solvation dynamics measurements is capable of accessing the molecular dynamics of liquids under mesoscopical geometrical confinement with the result that the competition between length scale of cooperativity and pore size is the main cause for the deviations from bulk like behaviour, which is consitent with a theoretical approach. Due to the Maxwell-Wagner effect present in dielectrically heterogeneous samples, the corresponding available dielectric relaxation data can not be interpreted in a reliable fashion.

ACKNOWLEGMENTS

REFERENCES

1. Dynamics in Small Confining Systems II, edited by J.M. Drake, J. Klafter, R. Kopelman and S.M. Troian (Mater. Res. Soc. Proc. 366, Pittsburgh, PA, 1995).
2. Molecular Dynamics in Restricted Geometries, edited by J. Klafter and J.M. Drake (John Wiley, New York, 1989).
3. J.N. Israelachvili and S.J. Kott, J. Chem. Phys. **88**, 7162 (1988).
4. M. Arndt, R. Stannarius, W. Gorbatschow and F. Kremer, Phys. Rev. E **54**, 5377 (1996).
5. J. Schüller, Y. Mel'nichenko, R. Richert and E.W. Fischer, Phys. Rev. Lett. **73**, 2224 (1994).
6. J. Schüller, R. Richert and E.W. Fischer, Phys. Rev. B **52**, 15232 (1995-I).
7. X. Yan, C. Streck and R. Richert, Ber. Bunsenges. Phys. Chem. **100**, 1392 (1996).
8. C.J.F. Böttcher and P. Bordewijk, Theory of Electric Polarization, Vol. 2 (Elsevier, Amsterdam, 1978).
9. R.W. Sillars, J. Inst. Electr. Eng. **80**, 378 (1937).
10. M. Maroncelli, J. Mol. Liquids **57**, 1 (1993).
11. R. Richert in Disorder Effects on Relaxational Processes, edited by R. Richert and A. Blumen (Springer-Verlag, Berlin, 1994).
12. R. Richert and H. Wagner, J. Phys. Chem. **99**, 10948 (1995).
13. H.-X. Zhou, B. Bagchi, A. Papazyan and M. Maroncelli, J. Chem. Phys. **97**, 9311 (1992).
14. R. Richert, J. Phys.: Condens. Matter **8**, 6185 (1996).
15. A. Papazyan and M. Maroncelli, J. Chem. Phys. **102**, 2888 (1995).
16. G. Williams and D.C. Watts, Trans. Faraday Soc. **66**, 80 (1970).
17. C. Streck, Y. Mel'nichenko and R. Richert, Phys. Rev. B **53**, 5341 (1996-I); R. Richert, Phys.Rev.B <u>54</u> (1996-II) 0000.
18. C. Donati and J. Jäckle, J. Phys.: Condens. Matter **8**, 2733 (1996).
19. K.L. Ngai in Disorder Effects on Relaxational Processes, edited by R. Richert and A. Blumen (Springer-Verlag, Berlin, 1994).
20. E. Donth, Relaxation and Thermodynamics in Polymers (Akademie Verlag, Berlin, 1992).
21. J. Jäckle, private communication.
22. R. Hilfer, Phys. Rev. B **44**, 60 (1991-I).

Notes on the Interpretation
of Nanorheology Experiments

ALI DHINOJWALA, LENORE CAI, AND STEVE GRANICK
Department of Materials Science and Engineering, University of Illinois, Urbana, IL 61801

ABSTRACT

We discuss the resolution of shear force measurement in determining the effective shear viscosity of molecularly-thin films. Recent findings for the shear of confined OMCTS (octamethylcyclotetrasiloxane) are presented.

INTRODUCTION

Properties of fluids confined within small pores and thin films are of interest in the areas of tribology, adhesion and wear, wetting and dewetting of surfaces, microfluidity of biological membranes, and flow behavior of granular materials. The surface forces apparatus modified for measurement of shear is now employed by various laboratories to study the dynamic behavior of a variety of confined systems. These systems include not only confined simple liquids, but also confined surfactants, polymer melts, solutions, and brushes. The reader is referred to the original literature for instrumental descriptions. The general conclusion so far has been that although fluids retain their bulk shear flow properties when the film is sufficiently thick, thicker than roughly 10 molecular dimensions (the exact number depends on the system), confined fluids display sluggish relaxation to the point of seeming solid-like over experimentally-accessible time scales. But recently discrepancies have appeared between measurements in different laboratories concerning the transition between the extremes of "liquid-like" and "solid-like" response.

Studies from this research group have shown that this transformation, from a simple liquid to a solid, is a continuous transition reminiscent of a glass transition process. This view, initially based on simple hydrocarbon liquids [1] and later on studies with a globular-shaped liquid [2,3], was further supported by the fact that even polymeric liquids that do not crystallize showed similar solid-like behavior upon extreme confinement [4]. However a recent study has argued,

based on experiments with a simple prototypical globular liquid (OMCTS, octamethylcyclotetrasiloxane), that the liquid undergoes a phase transition from a liquid, with viscosity close to the bulk, to a solid [5]. It was argued that the transition is abrupt, with a change of effective viscosity of at least 7 orders of magnitude when the film thickness is reduced by the spacing of one molecular diameter [5]. These two contrasting conclusions have far-reaching implications for seeking to understand properties of confined liquids from kinetic as well as thermodynamic perspectives.

This has motivated us to reevaluate whether the current instrumentation and interpretive analysis available in various laboratories can provide researchers with tools to decide these questions. Setting aside the conceptual problem of extrapolating notions of viscosity, shear rate, strain, and so forth to systems that have discrete molecular layers, we consider what range of effective viscosity is experimentally measurable by a surface forces apparatus in shear geometry. We note parenthetically that the use of the surface forces apparatus in drainage experiments, in the presence of static forces, is discussed elsewhere [6].

ISSUE OF EXPERIMENTAL GEOMETRY

The surface forces apparatus confines liquids between two crossed cylinders; the geometry is approximated as a sphere against a flat plate. The measured quantity is the force required to translate this sphere parallel to the flat plate. For this case the continuum hydrodynamics was worked out long ago and is given by

$$F_F = (16\pi/5)(vR\eta) \ln(R/b_o) \tag{1}$$

where v is the velocity, R is the sphere radius, η is the viscosity and b_o is the closest separation between the sphere and the plate. Clearly, with a curved geometry, any shear measurement probes the state of the liquid over a range of film thickness. Therefore it is ambiguous to draw conclusions regarding thickness-dependent viscosity unless the contribution from the zone of closest approach is much larger than that of the remaining zone of contact. The contribution to the total force from the point of closest approach will dominate only if the viscosity in this region

exceeds that farther away. In the context of drainage experiments, this point has also been considered elsewhere [7].

When a sphere is flattened at the apex, this is approximated as a parallel shear geometry and the shear force can be written as

$$F_F = \eta v A / \eta_o \qquad (2)$$

Here A denotes area and h_o denotes film thickness. Again by arguments in the same spirit as already made regarding Eq. (1) and its implications referred to above, this is useful to use only provided that the viscosity of the confined liquid is enhanced by at least one to two orders of magnitude beyond that of the liquid outside the zone of closest approach.

The effective contact area, from which viscosity is calculated, obviously is very different when dealing with Eqs. (1) and (2). The resulting danger of comparing experiments performed with curved and flattened surface geometry is evident. If one compares Eq. (1) and Eq. (2) for a lateral radius of only 7 μm away from the center-point of approach (the lateral distance over which the thickness of a confined film changes by typically 2-4 molecular diameters), one obtains $F_S/F_F = 24$. Therefore, simply the choice of Eq. (1) or Eq. (2) results in more than an order of magnitude difference of imputed viscosity from the same force measurement. In comparing viscosity calculations in a modified surface forces apparatus, it is useful to be consistent in the use of Eq. (1) or Eq. (2).

RESOLUTION IN MEASURING VISCOSITY

What is the sensitivity in measuring shear viscosity with a modified surface forces apparatus? What would be required to measure the viscosity of water, honey, or gelatin? Here we consider the two different approaches to measure shear forces. The first approach is to infer measure force by measuring the displacement of a spring that is translated at a steady velocity (or alternatively the held constant after having been translated at a steady velocity). The second approach is to apply a small sinusoidal displacement force and to measure the resulting phase and amplitude of motion [8]. The ratio of force to displacement, in the presence of confined liquid to that in free oscillation, v_f/v_c, has elastic and viscous contributions [8]. The elastic contribution (k)

47

is in phase with the displacement. The viscous contribution (ωb) is 90° out of phase. These quantities are determined by the relations:

$$k = k_s[(v_f/v_c)\cos\phi - 1] \qquad (3)$$

$$\omega b = k\omega[(v_f/v_c)\sin\phi]$$

Here k_s denotes spring constant of the apparatus force-measuring spring and ϕ denotes phase of output relative to input.

The viscous contribution in Eq. (3) can be quantified (omitting the elastic terms) as the effective viscosity,

$$\eta = \omega b h_o/A \qquad (4)$$

where the symbols have the same meanings as in the above equations. This model also allows one to accurately account for device compliance, since this also contributes to shear forces [4]. The sensitivity of this technique is limited by the absolute phase change that can be detected. Using lock-in amplifiers the resolution is typically 0.1° with oscillation amplitude of a few tenths of a nanometer. Better resolution is possible with larger amplitude.

As a concrete example, consider the viscosity that can be measured by these two methods. For forces measured by spring displacement, the resolution of ±0.5 μN has been reported [5]. Thus for a shear rate of 20 nm/sec [5] the minimum viscosity detectable is ~10^3 Pa-s, which is already 6 orders of magnitude higher than the bulk. The maximum measurable viscosity is also an issue, since the properties of a test sample cannot be measured if its resistance to an applied force exceeds that of the apparatus itself. But, since apparatus compliance has not been reported in measurements made with this approach, it is not possible at present to put an upper bound.

In the case of forces measured by dynamic oscillatory motion [1-4], a minimum change of phase by 0.1° corresponds to a viscosity of 0.5 Pa-s when using drive at 100 Hz. Similarly, since the device compliance is ~10^5 N/m, a typical upper bound is 10^7 to 10^8 Pa-s.

In both approaches the additional issue of apparatus resonance frequency also enters through the choice of the spring constant, k. Currently 300 N/m [5] or ~100,000 N/m [1-4] are used. These different spring constants result in considerably different resonance frequency.

ISSUES OF LINEARITY AND NONLINEARITY OF RESPONSE

Why should one be concerned about the shear rate or the amplitude of shear motion? For a simple liquid the shear force is proportional to shear rate, so it is tempting for an experimentalist to improve the sensitivity of force measurements by increasing the shear rate. Rheologists familiar with viscoelastic materials are well aware that viscosity depends on shear rate, however. To a bulk rheologist, deformations of tens of nanometers may seem negligibly small. But when considering the effective shear rate, the relevant quantity is the velocity normalized by film thickness. The effective viscosity is known to decrease markedly with increasing shear rate over a wide range of effective shear rate [1]. Whenever the shear rate is so large as to give a highly nonlinear response, the effective viscosity of the unperturbed film is surely underestimated.

IS THERE A LIQUID-TO-SOLID PHASE TRANSITION IN ULTRATHIN CONFINED LIQUIDS?

Now having a fair understanding of the limitations and advantages of the modified surface forces apparatus used in various laboratories, let us consider the argument of a first-order phase transition in confined liquids. The prototypical system for such studies concerns octamethylcyclotetrasiloxane (OMCTS), a globular-shaped molecule that is frequently used in studies of liquid microstructure. A recent study reported a transition to solidity, with diminishing film thickness, so abrupt as to seem first-order [5]. Dynamic oscillatory experiments came to the opposite conclusion [2,3], but the chemical purity of the samples used in that study has been questioned [9].

Reflection shows that the claim of an abrupt phase transition is actually consistent with the opposite interpretation. First, one notices that elastic and viscous forces in oscillatory deformation were not discriminated in the original study [5]. Second, the experimental uncertainty of ± 5 μN potentially amounted to a considerable effective viscosity, potentially orders of magnitude larger than for the bulk liquid. Third, the difference in effective viscosity calculated

from Eq. (1) and Eq. (2) was not distinguished. But rather than dwell on these problems of analysis, it seemed worthwhile to repeat dynamic oscillatory measurements with the same preparation procedure as in ref. [5].

We have repeated experiments similar to those in ref. [2] but with OMCTS samples prepared by the same distillation procedures as in ref. [5]. Fig. 1 shows measurements that confirm the previous conclusion from this laboratory [2,3], that the transition from "fluidity" to "solidity" is continuous.
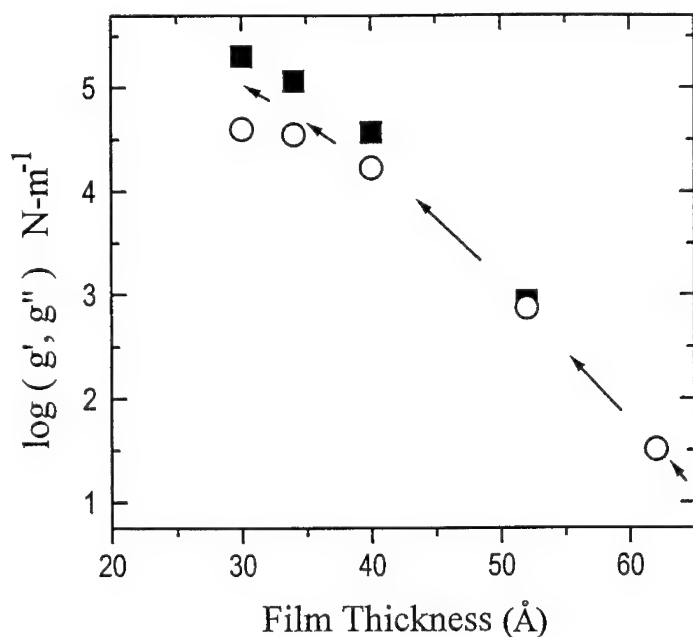
Figure 1. Shear experiments using the same distillation procedure as in ref. [5]. Arrows indicate increasing compression. The elastic spring constant at 1 Hz (g'; squares) and dissipative spring constant at 1 Hz (g"; circles) are plotted logarithmically against film thickness. Here g' is the in-phase force and g" is the out-of-phase force, both of them normalized by shear displacement. With increasing normal pressure, one notices the gradual transition from predominantly dissipative response, with elastic response too small to be resolved, to more-and-more prominent relative elasticity. The frequency-dependence at fixed film thickness is analyzed elsewhere [2,3].

In searching for possible alternative explanations, at first we reasoned that the transition to solidity might have been sharper if the surfaces had been brought together rapidly (rather than gently as in Fig.1). Rapid compression was then performed. But for this case we found that the film thickness spontaneously decreased rapidly from a thickness of 7 molecular dimensions (small compression time) to 4 molecular dimensions -- the zone of intermediate film thickness, evident in Fig. 2 when the applied pressure was increased slowly, was not stable.
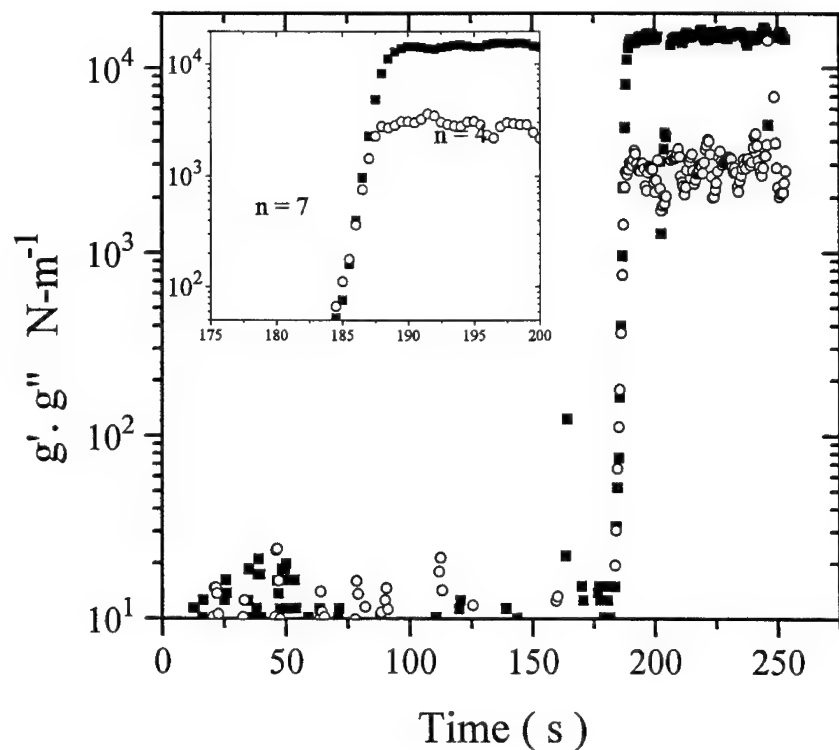
Figure 2. Shear responses while compressing mica surfaces separated by OMCTS more quickly than for the experiment shown in Fig. 1. The Insert shows an expanded time scale. The elastic spring constant at 1 Hz (g'; squares) and dissipative spring constant at 1 Hz (g"; circles) are plotted logarithmically against elapsed time. The zero of elapsed time is arbitrary. Data were taken in real time without signal averaging.

In summary, the available shear experiments show that the transition towards progressively more slugggish relaxation, with increasing confinement, is more reminiscent of a glass transition than a first-order process. With increasing pressure, time, or increase in confinement, a viscous state evolves to a solid-like state in which the elastic forces exceed the viscous forces at a given frequency or rate of deformation. This is reminiscent of a glass-forming liquids, in which a very sharp enhancement of viscosity is observed above the glass transition, eventually appearing as a glass over the time scale of the experiment.

For bulk fluids, an extremely small change of density leads to these large changes of viscosity. While it is true that the behavior of confined fluids is reminiscent of this as concerns sensitivity to film thickness and pressure, the clear reason for the observed slowing down of dynamics under extreme confinement is not yet fully understood.

ACKNOWLEDGEMENTS

REFERENCES

1. S. Granick, Science 253, 1374 (1991).

2. A. Levent Demirel and S. Granick, Phys. Rev. Lett. 77, 2261 (1996).

3. L. Cai and S. Granick, In B. Bhushan, Ed., Micro/Nanotribology and its Applications, NATO ASI Series, Kluwer Academic Publishers, Boston, in press.

4. S. Granick and H.-W. Hu, Langmuir 10, 3857 (1994).

5. J. Klein and E. Kumacheva, Science 269, 816 (1995).

6. A. Dhinojwala and S. Granick, Macromolecules, in press.

7. J. Van Alsten, S. Granick, and J. N. Israelachvili, J. Coll. Interface Sci. 125, 739 (1988).

8. J. Peachey, J. Van Alsten, and S. Granick, Rev. Sci. Inst. 62, 463 (1991).

9. J. Klein and E. Kumacheva, submitted.

CHAOS AND FORCE FLUCTUATIONS IN FRICTIONAL DYNAMICS

M. G. ROZMAN*, J. KLAFTER**, M. URBAKH**
*Institute of Physics, Riia 142, EE2400 Tartu, Estonia
**School of Chemistry, Tel Aviv University, Tel Aviv, Israel

ABSTRACT

A model is presented of a particle that interacts with two periodic potentials, representing two confining plates, one of which is externally driven. The model leads to various behaviors in the motion of the top driven plate: stick-slip, intermittent regime, characterized by force fluctuations, and two types of sliding above a critical driving velocity v_c. Similar behaviors are typical of a broad range of systems including thin sheared liquids. A detailed analysis of the different regimes displays a transition between the stick-slip and the kinetic regimes, ω^{-2} power spectra of the force over a wide range of velocities below v_c, and a decrease of the force fluctuations that follows $(v_c - v)^{1/2}$ for $v < v_c$. The velocity dependent Liapunov exponents demonstrate that the stick-slip motion is characterized by a chaotic behavior of the top plate and the embedded particle. An extension of the model to an embedded chain is introduced and preliminary results are presented and confronted with the single particle case. The role of the internal excitations of the chain in frictional dynamics is discussed.

INTRODUCTION

Sheared liquids confined between two atomically smooth parallel solid surfaces display a spectrum of behaviors which include stick-slip motion followed, as the relative velocity of the plates increases, by intermittent and smooth motion [1-5]. Different models have been proposed to account for these types of motion in confined liquids including spring-block models [6] and chain or layer motion on a substrate [7, 8]. The origin of stick-slip motion and the related phenomena is still unclear and under some debate. For example, in the case of molecularly thin liquid films, molecular-dynamics simulations [3-5] suggest that a first-order phase transition between solidlike and liquidlike phases is responsible for the stick-slip behavior. A phenomenological model describing shear-induced melting during the transition from stick to slip has been considered recently [9, 10]. In another example, of dry friction measurements [11], erratic stick-slip motion is claimed to be a manifestation of self-organized criticality [12, 13].

We have recently introduced a model of a single particle that interacts with two corrugated plates, one of which is externally driven [14]. This simple minimalistic model leads to most of the observed phenomena in thin liquids. Within this model we investigate the origin of stick-slip motion and the transition to intermittent and smooth behaviors. We study the chaotic properties of the system and propose an analysis of frictional force fluctuations.

THE MODEL: ONE PARTICLE

Consider a one-dimensional system of two rigid plates and a single particle of mass m embedded between them. The interaction between the particle and each of the plates is described by a periodic potential $U(x) = -U_0 \cos(2\pi x/b)$. There is no direct interaction between the plates. The top plate of mass M is pulled by a linear spring with a force constant K connected to a stage which moves with a velocity $\mathcal{V}$ (see Fig. 1).
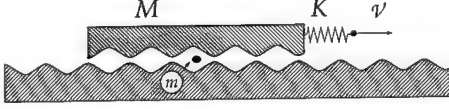
Figure 1: Schematic sketch of the model geometry.

The coupled equations of motion for the top plate and the particle are

$$M\ddot{X} + \eta(\dot{X} - \dot{x}) + K(X - \mathcal{V}t) + \frac{\partial U(x - X)}{\partial X} = 0, \qquad (1)$$

$$m\ddot{x} + \eta\dot{x} + \eta(\dot{x} - \dot{X}) + \frac{\partial U(x)}{\partial x} + \frac{\partial U(x - X)}{\partial x} = 0, \qquad (2)$$

where x and X are the coordinates of the particle and the top plate respectively. The second term in Eq. (1) and the second and the third terms in Eq. (2) describe the dissipative forces between the particle and the plates which are proportional to their relative velocities [7, 3-5, 14]. These terms account for dissipation which arises from interaction with phonons and/or other excitations. The third term in Eq. (1) is the driving force due to the stage motion. The remaining terms originate from the spatially periodic potential interaction between the particle and the plates.

Within our model the frictional force acting on the top plate is determined by the particle-plate interaction and is equal to

$$F = -\frac{\partial U(x - X)}{\partial X} - \eta(\dot{X} - \dot{x}) \qquad (3)$$

The first term is the potential component of the frictional force and the second one describes the dissipative contribution. When the top plate moves infinitely slowly, the particle follows adiabatically the motion of the plate. In this case the resistance force is $F = (2\pi U_0/b) \sin(2\pi f/b)$, where f is the relative displacement of the periodic potentials which correspond to the top and bottom plates. The maximum value of this force can be interpreted as the static frictional force,

$$F_s = 2\pi \frac{U_0}{b}. \qquad (4)$$

This force is the smallest driving force for which no stationary states exist.

It is convenient to introduce dimensionless space and time coordinates $y = x/b$, $Y = X/b$, and $\tau = t\omega$, where b is the period of the corrugation, represented by the potential $U(x)$, and $\omega = \frac{2\pi}{b}\sqrt{\frac{U_0}{m}}$ is the frequency of the small oscillations of the particle in the minima of potential. The solution of Eqs. (1) and (2) depends on the following dimensionless parameters: $\gamma = \eta/(m\omega)$ which represents a dimensionless friction constant, $\epsilon = m/M$ the ratio of particle and plate masses, $\alpha = \Omega/\omega$ the ratio of frequencies of the free oscillations of the top plate, and the particle, and $v = \mathcal{V}/(\omega b)$ the dimensionless stage velocity.

RESULTS OF SIMULATIONS

We concentrated on the dynamics of the system under the condition $\alpha = \Omega/\omega \ll 1$. In the calculations reported below we use parameter values that belong to the underdamped case: $\alpha = 0.02$, $\gamma = 0.1$, $\epsilon = 0.125$.

Our simulations demonstrate that already this model of a single particle in a driven two-wave potential is rich in transitions among different dynamical behaviors. We have observed four different dynamical regimes [14]: (a) at low velocities we observe a stick-slip motion of the top plate, (b) as the stage velocity increases, the motion of the top plate is characterized by irregular stop events with time intervals between them that increase rapidly with v, and the stick-slip motion becomes more erratic and intermittent, (c) kinetic regime, where the top plate never stops and the spring executes chaotic oscillations, and (d) smooth sliding which occurs when the stage velocity is above the critical velocity v_c. Fig. 2 illustrates the time dependence of the spring force, $-K(X - vt)$, in these typical regimes.

Regimes of motion

(a). Stick-slip motion. The motion of the top plate in the first regime [see Fig. 2(a)] is typical of relaxation oscillations. The top plate is initially at rest and the spring connecting it to the stage stretches linearly in time. When the force on the plate exceeds the static frictional force F_s, Eq. (4), the top plate begins to slide. Since the frictional force in this kinetic state is less than F_s, the plate accelerates. Owing to the inertia, the velocity of the plate $\dot{Y}$ is initially lower than the driving velocity v, and the spring will continue to extend until finally $\dot{Y} > v$. The maximum spring force will therefore be greater than F_s. When the plate velocity is $\dot{Y} > v$ the spring force decreases until it reaches some value where the motion stops and then the process repeats. Stopping of the top plate during every period of the spring force oscillations is the characteristic feature of the first regime. As a result, the plate motion is determined by the interplay between static and kinetic friction. It should be noted that the stick-slip motion is periodic only for very low stage velocities $v < v_0$, where $v_0 = 0.03$ for the above values of the parameters α, γ, ϵ. For higher velocities, still within regime (a), weak fluctuations of the amplitude and of the period of the spring force oscillations have been observed. For $v > v_0$ the trajectories of the top plate and the particle are sensitive to initial conditions, which is a manifestation of the chaotic nature of the system. The transition from periodic to chaotic stick-slip motion occurs through a sequence of period-doubling bifurcations and chaotic windows and depends on the mass of the top plate and on the spring constant.

In order to provide a quantitative measure of the degree of stochasticity of the motion we have calculated the velocity dependence of the largest Liapunov exponent of the trajectories (see Fig. 4). In regime (a) this exponent is negative only for $v < v_0$, supporting the periodicity of the motion. In this range of velocities the system (the particle and the top plate) has time to relax to the ground state after sliding. For higher velocities the largest Liapunov exponent becomes positive and increases slowly with the driving velocity. This points towards a rise in the dynamical chaos with the increase of v. It should be mentioned that Liapunov exponents can be extracted from experimental data of the time dependence of the spring force or the velocity of the top plate.

We have also noticed that at low stage velocities the amplitude of the spring force depends only slightly on v and the period of oscillations decreases with the increase of v. In
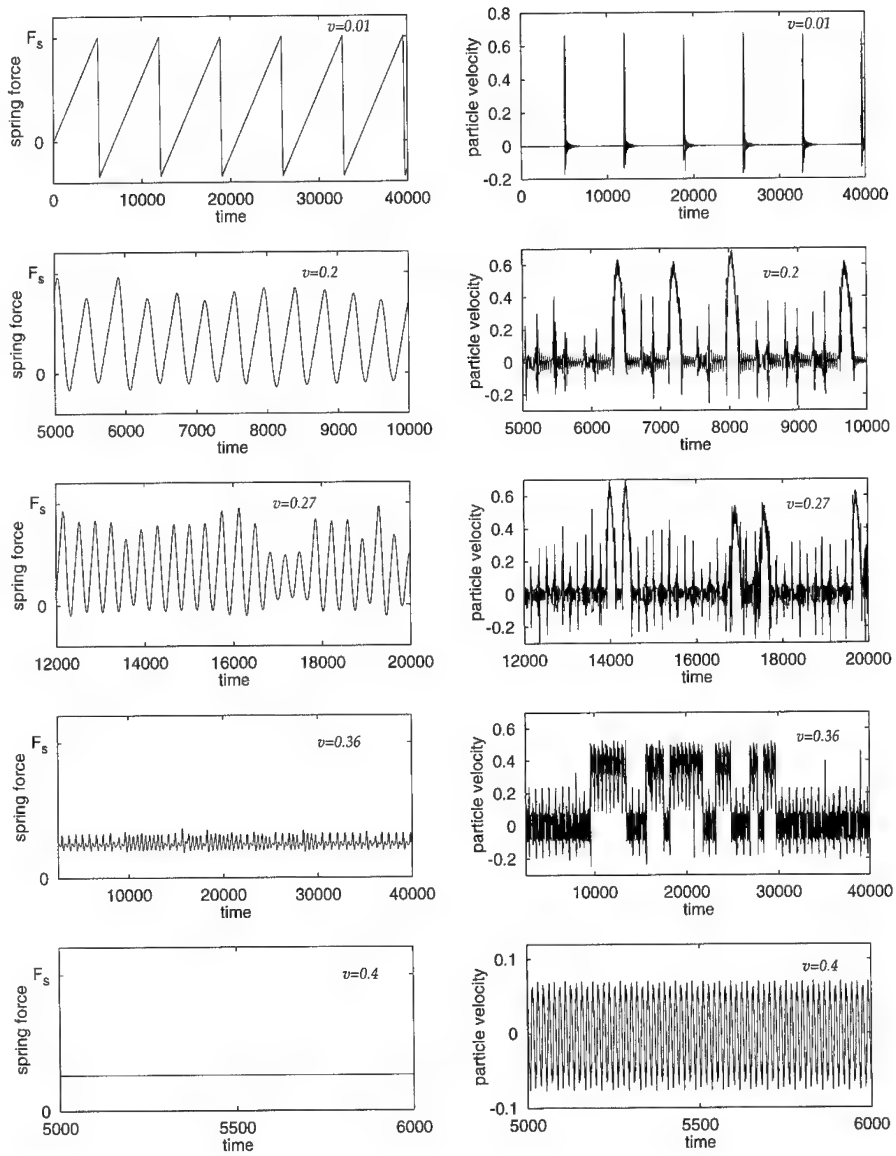
Figure 2: Different regimes of the particle and the plate motion. Left column - the spring force versus time, right column - the particle velocities versus time. Stage velocities are denoted on the graphs.
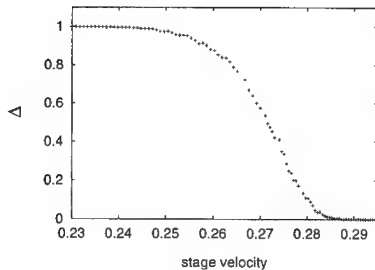
Figure 3: Δ versus stage velocity in the intermittent regime.
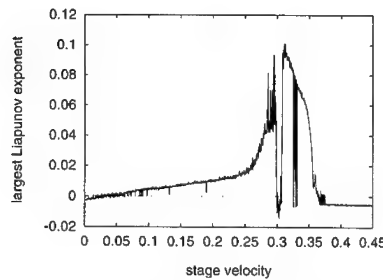
Figure 4: Velocity dependence of the largest Liapunov exponent

this range of velocities the time-averaged velocity and the displacement of the particle are much smaller than the average velocity and the displacement of the top plate.

(b). Intermittent stick-slip. For higher stage velocity the top plate does not necessarily stop during the spring oscillations and the motion becomes more erratic (see Fig. 2, $v = 0.27$). These higher velocities correspond therefore to a transition regime between the stick-slip and kinetic regimes. In order to define this transition quantitatively we introduce the parameter Δ, which measures how much time the plate spends in stick-slip motion relative to the total time, which includes kinetic segments. Fig. 3 presents Δ as a function of the stage velocity. The parameter Δ changes from $\Delta = 1$ (complete stick-slip) to $\Delta = 0$ (kinetic motion) within a narrow velocity interval which separates the stick-slip and kinetic regimes. This velocity interval, where $0 < \Delta < 1$, can be naturally defined as an intermittent regime. The calculation of the parameter Δ allows us to introduce a well defined boundary between the intermittent and kinetic regimes.

The trajectories of the top plate and the particle in this regime are sensitive to initial conditions, which is a manifestation of the chaotic nature of the system. In order to provide a quantitative measure of the degree of stochasticity of the motion we have calculated the velocity dependence of the largest Liapunov exponent of the trajectories (see Fig. 4). The Liapunov exponent is positive and grows rapidly in this intermittent regime, indicating an increase of the dynamical chaos in the system.

(c). Kinetic regime. In the kinetic regime, where the top plate never stops (Fig. 2, $v = 0.36$) the amplitude of the spring force strongly depends on the stage velocity. Here the frictional force is less than the static friction for all times and the time averaged velocity and displacement of the particle are close to half of those of the top plate. Within this regime the trajectories of the particle show that the particle jumps between the two plates. It clings to each of them for times much longer than the characteristic modulation time induced by the stage motion, $1/v$.

(d). Sliding regime. A sharp boundary at $v = v_c$ is observed between the kinetic and sliding regimes. When the velocity approaches the critical velocity v_c from below, the root mean square of the time oscillations of the spring force decreases as $\sqrt{v_c - v}$ and sliding sets in. In the sliding regime the spring force performs "microscopic" oscillations with a period

of the order $1/v$ and with amplitudes much smaller than in regimes (a)–(c). The time-averaged frictional force is proportional to the stage velocity (the single particle "analogue" of a liquid phase between two plates).

The velocity dependence of the Liapunov exponent gives a clear manifestation of the transition to sliding. As the stage velocity increases and approaches v_c, the largest Liapunov exponent decreases steeply and becomes negative at $v = v_c$, suggesting the disappearance of chaos at the transition. This concurs with the reduction in the amplitude of the spring force oscillations.

Under the condition $\Omega \ll \omega$ assumed in this paper, we have found a very weak dependence of v_c on the mass of the top plate M and on the spring constant K.

For $v_c < v < v_{\text{th}}$, where $v_{\text{th}} = 1.3$ for our choice of parameters, the particle does not jump between the two plates but rather clings to one of them and oscillates within one spatial period of the corrugated potential $U(x)$. At higher stage velocities $v > v_{\text{th}}$, the character of sliding changes. The particle ceases to feel the corrugation of the plates and moves with velocity $v/2$. The frictional force becomes the same as for flat plates. This change of the sliding state is accompanied by a drop of the frictional force and can be interpreted as analogous to the shear thinning effect [15, 16].
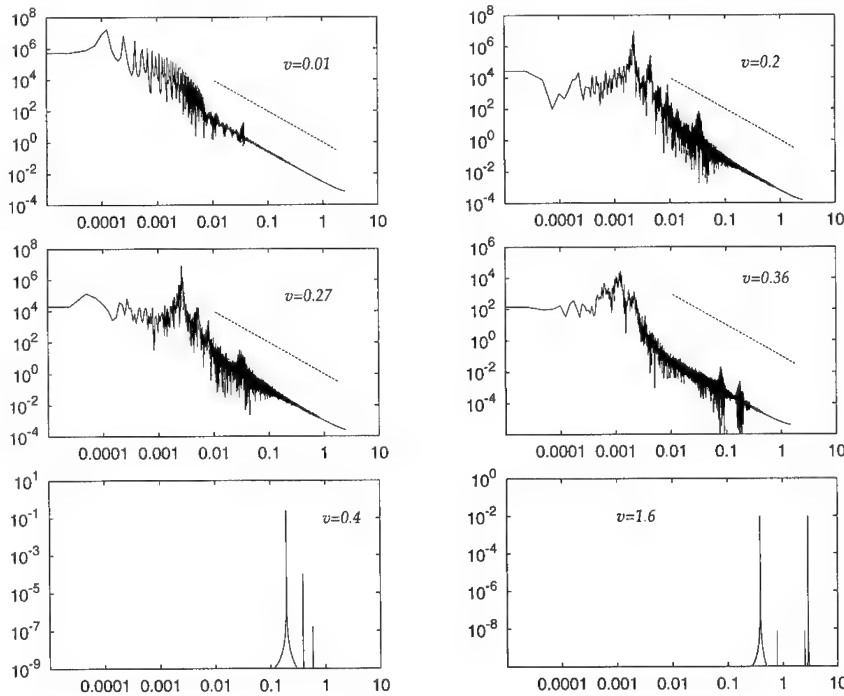
Figure 5: The power spectra of spring force fluctuations (in log-log scale) for different regimes of motion. The dotted line of slope -2 is provided for reference.

Power spectra

We have also calculated the power spectra, $S(\omega)$, of the spring force, and of the velocities of the top plate and the particle for the whole range of stage velocities. For $v < v_c$ a power law behavior $S(\omega) \sim \omega^{-2}$ for frequencies ω above some cutoff is observed (Fig. 5). At low stage velocities the origin of ω^{-2} frequency dependence is abrupt drops of the spring force typical of relaxation oscillations. Power spectra with the ω^{-2} tails were observed in real systems which demonstrate stick-slip motion [17, 18]. As discussed earlier, the time dependent spring force evolves from a periodic to an erratic behavior as the stage velocity v increases. This leaves the power law unchanged but introduces large fluctuations as we move from low velocities towards v_c. The noisy ω^{-2} behavior extends over a few orders of magnitude in $S(\omega)$ and ω. When sliding prevails the power spectra exhibit well defined dominating frequencies which originate from the motion of the periodic potential with velocity v (inset to Fig. 5).

Hysteresis

Another interesting property, amenable to experimental tests, is the hysteretic behavior of the spring force as the stage velocity changes. In order to investigate this phenomenon we have carried out calculations for the case where the stage moves with a small constant acceleration. Figure 6 shows the time dependence of the spring force for positive and negative accelerations a. For convenience, the x-axis shows the velocity of the stage at time t. The hysteresis shown in Fig. 6 reflects the coexistence of two dynamical states in the vicinity of v_c: one corresponds to a kinetic stick-slip motion and another corresponds to smooth sliding. The figure shows also the envelope of the time dependence of the spring force found within an analytical theory [19]. The envelope has a square root behavior near v_c. It should be mentioned that the transient time required to reach the stationary state diverges at $v = v_c$. The approximate analytical solution [19] predicts that the transient time diverges as $1/|v - v_c|$. The divergence of the transient time at $v = v_c$ leads to the deviation of the envelope from the square root law in the immediate vicinity of v_c, emphasizing that caution has to be taken when numerical calculations are carried out in this region.
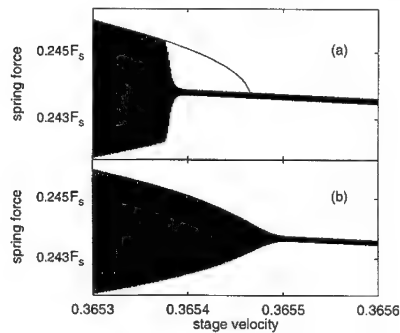
Figure 6: Hysteretic behavior of the spring force near v_c. The top figure corresponds to the motion of the driving stage with a small negative acceleration $a < 0$, the bottom figure corresponds to a positive acceleration $a > 0$.

A CHAIN IN A DRIVEN TWO-WAVE POTENTIAL

While already the single particle model has many of the characteristics of thin sheared liquids, a detailed investigation of a chain of particles can shed light on the energetic interplay between the chain and the two-wave potential. We therefore introduce a model of a chain in a driven two wave potential (Fig. 7).
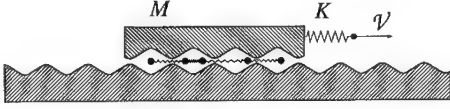
Figure 7: Schematic sketch of the model geometry.

The equations of motion for the top plate and chain molecules are:

$$M\ddot{X} + \sum_{i=1}^{N} \eta(\dot{X} - \dot{x}_i) = -K(X - \mathcal{V}t) - \sum_{i=1}^{N} \frac{\partial U(x_i - X)}{\partial X}, \tag{5}$$

$$m\ddot{x}_i + \eta\dot{x}_i + \eta(\dot{x}_i - \dot{X}) = k(x_{i+1} + x_{i-1} - 2x_i) \\ - \frac{\partial U(x_i)}{\partial x_i} - \frac{\partial U(x_i - X)}{\partial x_i}, \quad i = 2, \ldots, N-1 \tag{6}$$

$$m\ddot{x}_1 + \eta\dot{x}_1 + \eta(\dot{x}_1 - \dot{X}) = k(x_2 - x_1 - a) - \frac{\partial U(x_1)}{\partial x_1} - \frac{\partial U(x_1 - X)}{\partial x_1}, \tag{7}$$

$$m\ddot{x}_N + \eta\dot{x}_N + \eta(\dot{x}_N - \dot{X}) = k(x_{N-1} - x_N + a) - \frac{\partial U(x_N)}{\partial x_N} - \frac{\partial U(x_N - X)}{\partial x_N}. \tag{8}$$

The notations in Eqs. (5)–(8) are similar to those in Eqs. (1), (2) with addition of the chain properties: N is the number of molecules in the chain, x_i $(i = 1, \ldots, N)$ are the coordinates of chain molecules, k is the elastic spring constant, and a is the equilibrium spacing between molecules in a free chain.

This extension of the single particle model introduces two parameters: δ and ν, where

$$\delta = \frac{b - a}{b} \tag{9}$$

is the misfit of the substrate and chain periods and ν is given by

$$\nu = \left(\frac{\omega_{ch}}{\omega}\right)^2, \tag{10}$$

where $\omega_{ch} = \sqrt{\frac{k}{m}}$ is the characteristic frequency of the chain. The parameter δ describes the competition between the chain and potential periodicities and ν is the measure of the relative strength of the particle-particle and particle-potential interaction.

In the limits $\delta = 0$ and $\nu \ll 1$ or $\nu \gg 1$ the problem reduces to the single particle picture, where the case $\nu \ll 1$ corresponds to N independent particles and the case $\nu \gg 1$ to a rigid chain which acts as a single particle.

Our preliminary results demonstrate the possibility of exciting intra-chain vibrations. We note that for zero misfit such vibrations are observed only at high driving velocities which correspond to the sliding regime. For nonzero misfit the vibrations are excited already at the stick-slip regime (Fig. 8).
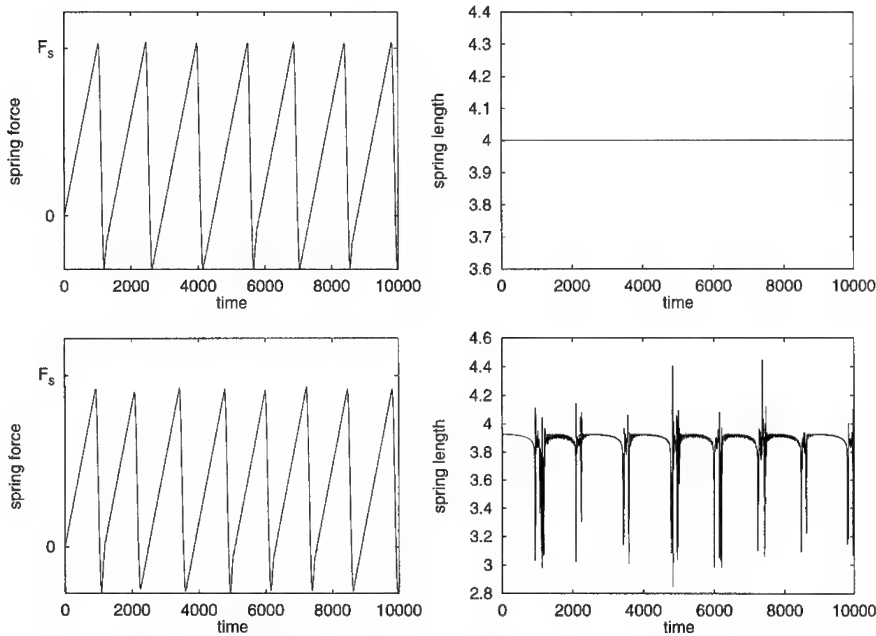
Figure 8: Stick-slip motion of the top plate. Left column — the spring force versus time, right column — the spring length versus time. $v = 0.05$, $\nu = 1.$; $\delta = 0.$ for the top graphs and $\delta = 0.1$ for the bottom ones.

In order to demonstrate the effect of intra-chain vibrations we present in Fig. 8 the time dependence of the chain length. It should be emphasized that at low velocities these excitations only slightly modify the motion of the top plate which is basically the experimental observable.

An interesting property of the embedded chain is the existence of two sliding phases at velocities higher than a critical velocity v_c which depends on δ and ν. Similar conclusions have been reached using linear stability analysis[20]. The same sliding phases occur, as mentioned above, in the single particle case. Here, however, we notice vibrational fluctuations superimposed on the corresponding single particle behavior (Fig. 9). Fig. 9 demonstrates the possibility that the change in the sliding phase can be accompanied by changes in the chain length, for example, motion in a stretched state in one phase and in a free state in the other phase.

DISCUSSION

To summarize, a single-particle model has been proposed which displays dynamical features resembling experimental and simulation results obtained for nanoscale molecular films under shear. For a wide range of system parameters we find that the motion is chaotic, as supported by calculated Liapunov exponents. Our calculations suggest that the information obtained by following the macroscopic motion of a plate does not allow one to draw
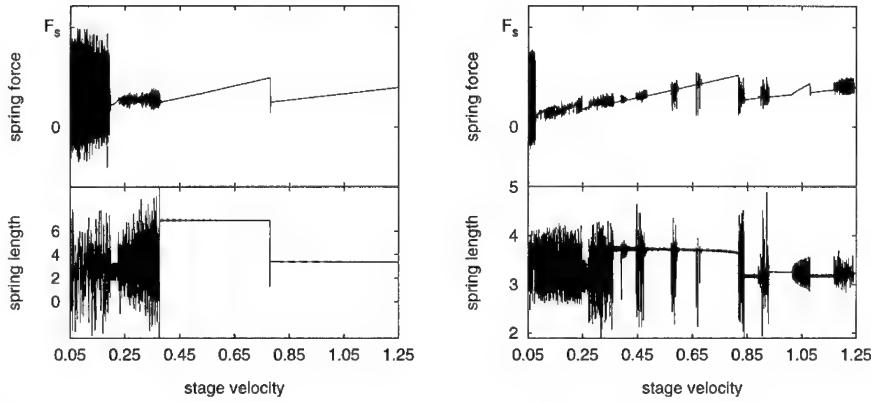
Figure 9: Time variations of the spring force and the chain length for the driving stage moving with a small constant acceleration. $\delta = 0.2$, $\nu = 0.1$ (left figure) and $\nu = 1.0$ (right figure).

unambiguous conclusions on the dynamical structure of a molecular system embedded between the plates. Our preliminary results suggest that the main features found in the single particle model survive when the particle is replaced by a chain, apart from superimposed intra-chain excitations and energy exchanges between the chain and the moving plate.

ACKNOWLEDGMENTS

References

1. H. Yoshizawa, P. McGuiggan, and J. Israelachvili, Science **259**, 1305 (1993).

2. G. Reiter, L. Demirel, and S. Granick, Science **263**, 1741 (1994).

3. P. A. Thompson and M. O. Robbins, Science **250**, 792 (1990).

4. P. A. Thompson, M. O. Robbins, and G. S. Grest, Isr. J. of Chem. **35**, 93 (1995).

5. M. O. Robbins, P. A. Thompson, and G. S. Grest, MRS Bull. **18**, 45 (1993).

6. J. M. Carlson, J. S. Langer, and B. E. Shaw, Rev. Mod. Phys. **66**, 657 (1994).

7. B. N. J. Persson, Phys. Rev. B **50**, 4771 (1994).

8. Y. Braiman, F. Family, and G. Hentschel, Phys. Rev. E **53**, R3005 (1996).

9. J. M. Carlson and A. A. Batista, Phys. Rev. E **53**, 4153 (1996).

10. B. N. J. Persson, Chem. Phys. Lett. **254**, 114 (1996).

11. H. J. S. Feder and J. Feder, Phys. Rev. Lett. **66**, 2669 (1991), **67**, 283E (1991).

12. P. Bak, C. Tang, and K. Wiesenfeld, Phys. Rev. Lett. **59**, 381 (1987).

13. F. J. Elmer in Physics of Sliding Friction, edited by B. N. J. Persson and E. Tosatti, Kluwer, Dordrecht, 1996, pp. 433–447.

14. M. G. Rozman, M. Urbakh, and J. Klafter, Phys. Rev. Lett. **77**, 683 (1996).

15. H.-W. Hu, G. A. Carson, and S. Granick, Phys. Rev. Lett. **66**, 2758 (1991).

16. M. Urbakh, L. Daikhin, and J. Klafter, J. Chem. Phys. **103**, 10707 (1995).

17. A. Johansen *et al.*, Phys. Rev. E **48**, 4779 (1993).

18. A. L. Demirel and S. Granick, 1996, to appear in Phys. Rev. Lett.

19. M. G. Rozman, M. Urbakh, and J. Klafter, Phys. Rev. E **54**, No. 6 (December 1996).

20. F. J. Elmer, private communication.

SIMULATIONS OF LUBRICANTS IN CONFINED GEOMETRIES

MARK J. STEVENS,* MAURIZIO MONDELLO,** GARY S. GREST**
*P.O. Box 5800, MS 1111, Sandia National Laboratory, Albuquerque, NM 87185-1111
**Corporate Research Science Laboratories, Exxon Research and Engineering Company, Annandale, NJ 08801

ABSTRACT

We examine the shear flow of hexadecane and squalane confined between plates with nm separation using molecular dynamics simulations. For both molecules substantial slip occurs at the walls and the density profile exhibits strong oscillations. In contrast to surface force apparatus measurements, our calculated effective viscosities are not much greater than bulk viscosities, but the simulations shear rates are much larger than the experimental ones. The actual viscosity calculated using the shear rate measured from the observed velocity profile is almost equal to the bulk viscosity within uncertainty.

INTRODUCTION

Over the past few years, our understanding of the properties of fluids in confined geometries has progressed considerably due to new experimental techniques. Measurements by the surface force apparatus (SFA) [1–9] and the quartz crystal resonator [10] have revealed much about boundary lubrication phenomena. The properties of fluids confined to the nanometer scale are found experimentally to be dramatically different from the bulk properties [6,8]. In the SFA experiments [6] an effective viscosity η_{eff} is obtained from measurements of the shear stress σ and the applied shear rate $\dot{\gamma}_{\text{app}} \equiv v_{\text{w}}/h$, where h is the plate separation and v_{w} is the velocity of the moving (top) wall. For h less than about 7 atomic diameters, the Newtonian viscosity is about 5 orders of magnitude larger than in the bulk [4,11]. At a critical shear rate $\dot{\gamma}_c$, there is a transition to a non-Newtonian regime where

$$\eta_{\text{eff}} \sim \dot{\gamma}_{\text{app}}^{-\alpha}. \tag{1}$$

Experiments [5,6] find that α varies with the fluid. For hexadecane α depends on the load and is between 0.4 and 0.5 [11,12]. For squalane (2,6,10,15,19,23 hexamethyl-tetracosane) [13], α varies between 0.6 and 0.9. Simulations on model molecular systems at constant load find $\alpha \simeq 2/3$ for a variety of applied loads and plate separations [14,15], while for constant plate separation, $\alpha \simeq 1/2$ [15]. Both model simulation and experiment find that as the load is increased at a fixed number of layers, η_{eff} increases.

Some aspects of the SFA experiments depend on whether the fluid molecule is linear or highly branched. An important example is the variation of the plate separation with applied load, $P_\perp$. For linear or nearly linear hydrocarbon chains, h is quantized when it is less than about 7 atomic diameters, while for branched alkanes, there is apparently only a single, wide minimum [1,16,17].

As already indicated, an understanding of some of the phenomena has come from simulations on simplified models of atomic or molecular fluids [14,15,18–22]. Here we present results of 'realistic' molecular dynamics simulations of linear (hexadecane) and branched (squalane) hydrocarbons. By using realistic molecular potentials, the effect of chain stiffness and architecture on the flow of confined fluids can be studied. In addition, we examine the effect of wall-fluid interaction strength on lubricant flow behavior.

SIMULATION METHOD

The model is similar to the one used in the earlier treatment of alkanes in the bulk [23–25]. We used a united atom (UA) model in which each carbon atom with its attached hydrogens is grouped to form a single 'united' atom. The linear alkane Lennard-Jones (LJ) parameters are taken from Siepmann *et al.* [26]. The LJ diameter $\sigma = 3.93$Å for all particles. The LJ energy ϵ for CH (squalane) is 0.080 kcal/mol, for CH_2 is 0.093 kcal/mol and for CH_3 is 0.227 kcal/mol. The LJ potentials were cutoff at 2.5σ. We extend the LJ parameters for hexadecane to squalane, but squalane has distinct LJ parameters and torsional potential at the branch points, where an ad hoc umbrella type potential is also applied. We use a harmonic bending potential and the torsional potentials are those used by Jorgensen *et al.* [27]. For details of our model implementation see Mondello and Grest [24]. Most of the simulations were performed using a fixed bond length (1.54Å) with constraint dynamics and a 5 fs timestep [24, 28]. We now prefer to use rRESPA multi-timestep dynamics [29] with a harmonic bond potential. The results are independent of the method. In rRESPA, a 1 fs timestep was used for all the intramolecular bonded interactions, and a 5 fs timestep was used for the LJ interactions. Most hexadecane simulations were performed for 1 ns, although at the lower shear rates runs were extended to several ns. Squalane simulations were usually run for at least 4 ns.

Temperature was controlled using a Langevin thermostat [30,31] with a damping constant of 1 ps^{-1}. For each atom, only the velocity component in the vorticity direction was coupled to heat bath. In this manner, the velocity profile is not disturbed by the thermostat. Since we are simulating systems confined to the nm scale, it is not necessary to thermostat the walls to prevent a thermal gradient.

The simulation setup, described in detail in ref. [32], is basically the same as in earlier simulations of Thompson *et al.* [14, 15]. The fluid is confined between two walls composed of LJ atoms which form a rigid fcc (111) lattice with nearest neighbor distance of 7 Å. The top wall is pulled at a velocity v_w in the x-direction with the bottom wall stationary. Simultaneously, a load $P_\perp$ is applied perpendicular to the top wall (z-direction). The wall motion in the z-direction is determined by the net force of the fluid particles on the wall particles and the load. The mass of a wall atom is equal to twice the mass of a CH_2 united atom as in Thompson *et al.* The stress on the wall is determined from the x-component of the force of the fluid on the wall. The height of the cell is naturally determined by the number of layers, m_ℓ. When the oscillations in $\rho(z)$ span the width of the cell, m_ℓ is easily determined as shown in Fig. 1.

The wall-fluid interaction is described in terms of the Lennard-Jones potential parameters $\sigma_w = 2.5$ Å and ϵ_w. We vary ϵ_w from 0.1 kcal/mol to 0.7 kcal/mol for hexadecane and used the maximum value for squalane. The minimum value of this range corresponds to ϵ_{CH_2} and the maximum to $3\epsilon_{CH_3}$. This range of values is similar to that used in the earlier model fluid simulations [14, 15]. The lower range corresponds to a hydrocarbon fluid interacting with a hydrocarbon surface, such as a self-assembled monolayer of alkanes on mica. For direct interaction with mica, the wall-atom parameter ϵ_w should be 0.7 to 1.0 kcal/mol [33].

It is important to note that the shear velocities, or, equivalently, the shear rates in our simulations are not in the same regime as the SFA experiments. The range we can study is about 1-400 m/s. These rates are encountered in many devices such as MicroElectroMechanical systems which have very narrow (μm) channels. However, the shear velocity range for the SFA is $v_w \sim 1$ nm/s - 100 μm/s [4,11]. A discussion of this issue as it applies to the earlier coarse-grained simulations is contained in ref. [32].
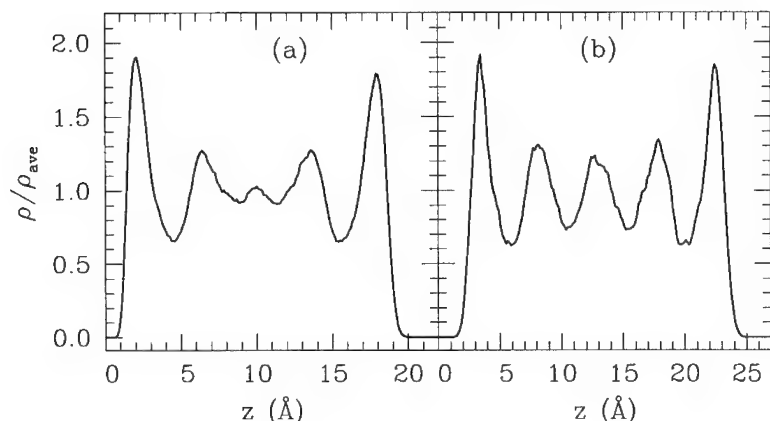
Figure 1: Density profiles for (a) hexadecane (ϵ_w =0.1 kcal/mol) and (b) squalane (ϵ_w =0.7 kcal/mol).

RESULTS AND DISCUSSION

The squalane simulations were performed at 300 K under a load of 1 MPa. We performed the hexadecane simulations at $T = 323$ K, because a tendency for partial crystallization of the system was observed at 300 K which is close to the bulk crystallization temperature. We varied the load for hexadecane, but here we mainly discuss the data at $P_\perp = 70$ MPa.

In Fig. 1 we show density profiles for hexadecane and squalane. Both molecules show 5 layers between the walls. For hexadecane $h = 22.8$ Å and for squalane $h = 26.8$ Å. The peak width for squalane is larger than for hexadecane which is expected due to the branches of squalane. The density oscillations for squalane occur even though the measured force profile [17] has apparently only a single minimum. Similar density oscillations for squalane have been seen in other simulations [34]. These simulation results suggest that an absence of oscillations in the measured force may not imply an absence of oscillations in the atomic density profile. Thus, one should not interpret the SFA force measurements as direct measurements of the density profile, even though the potential of mean force is often assumed to be proportional to $\ln \rho(z)$. The reason for this is that the experiments are carried out in an open system in which the fluid in the gap is in thermal equilibrium with a reservoir at fixed chemical potential. As the plates are brought closer together, the number of fluid molecules changes in such a way as to remain in equilibrium with the surrounding fluid. For linear and nearly linear molecules, the separation between plates is stable only at well defined layer spacing. This leads to well defined density oscillations across the gap. However for branched chains, the presence of density oscillations does not preclude a force profile with only a single minimum. Other possibilities also exist; for example, rough walls can result in a single minimum for the force profile, but still have multiple oscillations in the density profile [35]. While the SFA does not have rough walls, this example shows that various sources for the observed data must be considered carefully.

Substantial slip is found in the flow profiles for both molecules. Figure 2 shows some profiles. The velocity is almost the same for every layer for hexadecane with $\epsilon_w = 0.1$kcal/mol and for squalane with $\epsilon_w = 0.7$kcal/mol. Increasing ϵ_w to 0.7 kcal/mol for hexadecane yields more flow in the fluid, but still large slip. The substantial slip occurs because the cohesion
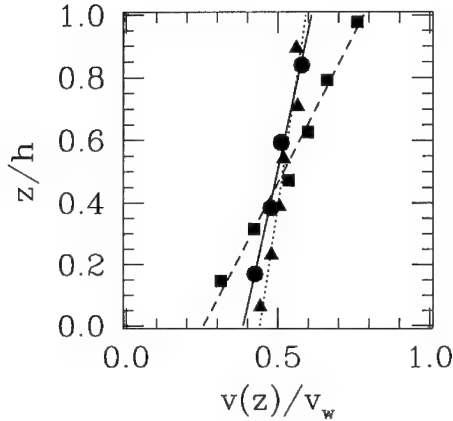
Figure 2: Velocity profiles at $v_w = 200$ m/s for hexadecane: at $\epsilon_w = 0.1$kcal/mol ($\blacktriangle$) and $\epsilon_w = 0.7$kcal/mol ($\blacksquare$) and for squalane: $\epsilon_w = 0.7$kcal/mol ($\bullet$).

within the fluid is stronger than the adhesion of the fluid to the wall. Squalane apparently adheres to the wall more weakly than hexadecane does, although we should note that the applied loads are not the same in the two cases. This raises an interesting point about the squalane simulations. We determine what load to apply by performing simulations at constant plate separation that yield the desired number of layers and an average density equal to the bulk density. For squalane, the value of the load determined in this way is actually negative implying we would need to pull the plates apart. We have instead applied a minimal load. An overestimate of the CH_3 LJ parameters is the most likely source of the negative pressure. Better potentials have been developed since this work was done and they change the pressure values [36]. However, the geometry of the squalane molecule may be the dominant factor. More refined simulations are needed to resolve these issues.

Since we have the velocity profiles, we calculated the actual shear rate by fitting a least squares line to the data (cf. Fig. 2). Fig. 3(a) shows shear thinning at shear rates comparable to bulk simulations [32]. The squalane data shows no sign of a crossover to Newtonian behavior. The hexadecane has some indication of a crossover, but the data is inconclusive since the uncertainty in the data becomes large at low shear rates. Previous confined simulations of bead-spring chains found $\alpha = 2/3$ independent of m_ℓ and $P_\perp$ [14,15], though more recent simulations find a dependence of α on the wall-fluid interaction [37]. The experimental value of α for hexadecane determined from effective viscosities is about 0.5 [11,12], though α is smaller for low loads. Using actual viscosities (Fig. 3(a)), the straight line for hexadecane has $\alpha = 0.40$, and for squalane, $\alpha = 0.70$.

To compare directly with experiment, we examine η_{eff} (Fig. 3(b)). For hexadecane at $\epsilon_w = 0.1$ kcal/mol the data is rather flat and appears almost Newtonian; the range of α is from 0.05 to 0.17. There is no indication of the crossover between Newtonian and non-Newtonian behavior. At larger ϵ_w, η_{eff} and α increase. In contrast to the results of experiments [4,6,11] and earlier simulations [14,15], η_{eff} *increases* with increasing plate separation. This observed dependence of η_{eff} on m_ℓ is a consequence of the large slip in the flow. In this case, there is only a weak dependence of the shear stress σ on h which implies $\eta_{\text{eff}} \sim h$. The squalane data is qualitatively different. Using η_w (Fig. 2(b)), we find a value $\alpha = 0.70$ quite similar
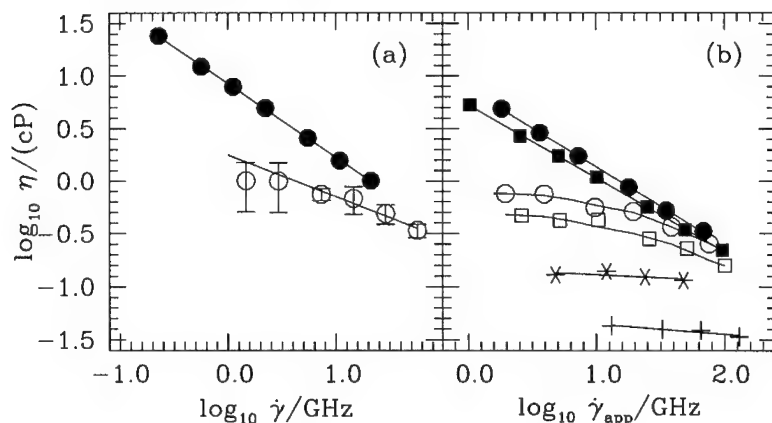
Figure 3: (a) The actual viscosities with shear rate determined from the flow profiles for hexadecane (○) at 6 layers and squalane (●) at 4 layers. Both have $\epsilon_w = 0.7$ kcal/mol. (b) The effective viscosities for hexadecane and squalane for various number of layers. For hexadecane symbols are at $\epsilon_w = 0.7$ kcal/mol, (○) 12 layers and (□) 4 layers; at $\epsilon_w = 0.1$ kcal/mol, (*) 9 layers and (+) 4 layers. For squalane the symbols are for $\epsilon_w = 0.7$ kcal/mol at (■) 4 layers and (●) 6 layers.

to experiment [13] and bead-spring simulations [14, 15]. There is almost no dependence of η_{eff} on the number of layers, although it again tends to increase with increasing h.

We performed some sequences of simulations at $T = 300$ K for hexadecane. We found it rather easy to partially crystallize the system. Since the bulk melting temperature is only 292 K, this is not surprising. Even with no load, $P_\perp = 0$, we find partial crystallization at $T = 300$ K for a 3 layer system at shear velocity $v_w = 20$ m/s [32]. The shear helps orient the chains and promotes crystallization. That the crystallization is induced by confinement is confirmed by the system remaining fluid in corresponding bulk simulations.

CONCLUSION

We have performed molecular dynamics simulations of hexadecane and squalane between shearing plates with nanometer scale separations. The calculated effective viscosities depend strongly on the nature of the walls. In general, we find large slip at the fluid-wall interface. For hexadecane between hydrocarbon walls and for squalane between mica-like walls, the slip is practically complete and plug flow occurs. A consequence of this interfacial flow is that the effective viscosity increases with increasing plate separation in contrast to experiment [4,6,11] and bead-spring simulations for short chains [14, 15]. Large slip occurs because the fluid cohesion is relatively stronger than fluid adhesion to the wall. Consequently, shearing occurs preferentially at the wall-fluid interface. As the wall is coupled more strongly to the fluid, more shearing is forced to occur in the bulk and the slip decreases. For strong wall coupling, the confined hexadecane and squalane simulations yield values of the viscosity exponent α in the range observed in experiments.

ACKNOWLEDGEMENT

REFERENCES

1. J. N. Israelachvili, *Intermolecular and Surface Forces*, 2nd ed. (Academic Press, San Diego, 1992).
2. J. N. Israelachvili, P. M. McGuiggan, and A. M. Homola, Science **240**, 189 (1988).
3. J. N. Israelachvili and P. M. McGuiggan, Science **241**, 795 (1988).
4. J. V. Alsten and S. Granick, Phys. Rev. Lett. **61**, 2570 (1988).
5. H.-W. Hu, G. A. Carson, and S. Granick, Phys. Rev. Lett. **66**, 2758 (1991).
6. S. Granick, Science **253**, 1374 (1991).
7. J. Klein, D. Perahia, and S. Warburg, Nature **352**, 143 (1991).
8. J. Klein and E. Kumacheva, Science **269**, 5225 (1995).
9. A. L. Demirel and S. Granick, Phys. Rev. Lett. **77**, 2261 (1996).
10. J. Krim, D. Solina, and R. Chiarello, Phys. Rev. Lett. **66**, 181 (1991).
11. G. A. Carson, H.-W. Hu, and S. Granick, Tribology Transactions **35**, 405 (1992).
12. G. A. Carson, Ph.D. thesis, U. Illinois, 1992.
13. S. Granick, private communication.
14. P. A. Thompson, G. S. Grest, and M. O. Robbins, Phys. Rev. Lett. **68**, 3448 (1992).
15. P. A. Thompson, M. O. Robbins, and G. S. Grest, Israel J. of Chem. **35**, 93 (1995).
16. M. L. Gee, P. M. McGuiggan, J. N. Israelachvili, and A. M. Homola, J. Chem. Phys. **93**, 1895 (1990).
17. S. Granick, A. L. Demirel, L. L. Cai, and J. Peanasky, Israel J. of Chem. **35**, 75 (1995).
18. F. F. Abraham, J. Chem. Phys. **68**, 3713 (1978).
19. S. Toxvaerd, J. Chem. Phys. **74**, 1998 (1981).
20. M. Schöen, J. H. Cushman, D. Diestler, and C. L. Rhykerd, J. Chem. Phys. **88**, 1394 (1988).
21. P. Padilla and S. Toxvaerd, J. Chem. Phys. **101**, 1490 (1994).
22. E. Manias, G. Hadziioannou, I. Bitsanis, and G. ten Brinke, Europhys. Lett. **24**, 99 (1993).
23. C. Mundy, J. Siepmann, and M. L. Klein, J. Chem. Phys. **102**, 3375 (1995).
24. M. Mondello and G. S. Grest, J. Chem. Phys. **103**, 7156 (1995); M. Mondello, G. S. Grest, A. R. Garcia, and B. G. Silbernagel, J. Chem. Phys. **105**, 5208 (1996).
25. S. T. Cui, P. T. Cummings, and H. D. Cochran, J. Chem. Phys. **104**, 255 (1996); S. T. Cui, S. A. Gupta, P. T. Cummings, and H. D. Cochran, J. Chem. Phys. **105**, 1214 (1996).
26. J. I. Siepmann, S. Karaborni, and B. Smit, Nature **365**, 330 (1993).
27. W. L. Jorgensen, J. D. Madura, and C. Swenson, J. Am. Chem. Soc. **106**, 6638 (1984).
28. M. Allen and D. Tildesley, *Computer Simulation of Liquids* (Clarendon Press, Oxford, 1987).
29. M. Tuckerman, B. Berne, and G. Martyna, J. Chem. Phys. **97**, 1990 (1992).
30. G. S. Grest and K. Kremer, Phys. Rev. **A33**, 3628 (1986).
31. W. F. van Gunsteren and H. Berendsen, Mol. Phys. **45**, 637 (1982).
32. M. S. Stevens *et al.*, submitted to J. Chem. Phys (1996).
33. C. Kessel and S. Granick, Langmuir **7**, 532 (1991).
34. S. Balasubramanian, M. L. Klein, and J. I. Siepmann, J. Phys. Chem. **100**, 11960 (1996).
35. L. Frink and F. van Swol, preprint (1996).
36. J. I. Siepmann, C. Mundy, and M. L. Klein, preprint (1996).
37. E. Manias, I. Bitsanis, G. Hadziioannou, and G. ten Brinke, Europhys. Lett. **33**, 371 (1996).

POLYMER BRUSHES IN STRONG SHEAR FLOW

GARY S. GREST
Corporate Research Science Laboratories, Exxon Research & Engineering Company, Annandale, New Jersey 08801

ABSTRACT

Polymers end-grafted to a surface in the presence of a shear flow are studied by molecular dynamics simulations. The solvent velocity field is observed to penetrate only a short distance into the brush consistent with predictions based on self-consistent field theory. The deformation of the brush is small except when the shear rate $\dot{\gamma}$ is very large. In this limit, while some of the polymer chains are stretched in the direction of flow, the brush height actually decreases slightly, in contrast to several theoretical predictions. When two surfaces bearing end-grafted chains are brought into contact, the normal force increases rapidly with decreasing plate separation, while the shear force is significantly smaller. For low relative velocity v_w of the two walls, the surfaces slide pass each other with almost no change in the chain's radius of gyration or the amount of interpenetration, while for very large v_w, there is significant stretching and some disentanglement of the chains. The results are in qualitatively good agreement with recent experiments using the surface force apparatus.

INTRODUCTION

Surfaces bearing polymers either end-grafted or adsorbed have important technological applications in many areas, including colloidal stabilization and lubrication. Chain confinement near a surface leads to configurations which are qualitatively different from those of free chains. For example, polymer chains which are end-grafted to a surface and then swollen in a good solvent are strongly stretched. For coverages above an overlap coverage, the end-to-end distance of end-grafted polymer chains scales with the chain length N as N^1 compared to $N^{0.59}$ for a free chain. When surfaces coated with end-grafted chains, commonly referred to as polymer brushes, are brought into contact, long ranged repulsive forces, of entropic origin, act to keep the surfaces apart while maintaining a relatively fluid layer at the interface between them. The normal forces between polymer brushes have been well studied experimentally using the surface force apparatus (SFA) [1,2]. However only recently has the lateral forces between sliding surfaces been investigated [3–5]. Klein et $al.$ [3] found that in a good solvent, the effective friction coefficient μ_b -defined by the shear-to-normal ratio of forces- between polymer brushes is very small, often below the detection limit of their apparatus ($\mu_b < 0.001$) for a wide range of sliding velocities and separations between the surfaces. Granick et $al.$ [5] found that in solvents near Θ conditions, the shear forces were predominantly viscous for weak compression while predominantly elastic for strong compression. In both cases, the surfaces had to be highly compressed before the shear force was even large enough to be measured [3,5].

The mechanism for the very low friction observed for surfaces bearing end-grafted chains in a good solvent [3] must be different from the standard picture of interfacial sliding [6], in which the friction arises from the forces required to shear an adhesive junction. In this case, as the surfaces are brought closer together, the solvent molecules are squeezed out until the surfaces are only a few atomic layers apart. The resulting shear motion is characterized by stick-slip behavior [7]. Under a steady shear force, the relative motion of the two surfaces is discontinuous for small shear forces and only becomes continuous above a critical shear force [8–10]. Polymer brushes, on the other hand, are strongly stretched in a good solvent and the interface between them contains a large amount of solvent except when highly compressed. There is a strong repulsive force between the polymer brushes which supports

71

the normal load. However the presence of mobile solvent molecules allows the brushes to move pass each other with minimal shear force.

In addition to the behavior of the lateral forces for brushes under compression, Klein *et al.* [11] also found an interesting coupling between the sliding motion of uncompressed brushes and the normal force. They observed that if the surfaces were either weakly compressed or uncompressed but separated by a small gap, there was an extra contribution to the normal force under oscillatory shear. These effects only occurred above a critical shear rate, suggesting they are related to the relaxation rates of the end-grafted chains and were interpreted as arising from an increase in the uncompressed layer thickness when fluid flows past the layer. This interpretation was supported by several [12–14] theoretical predictions that were based on the Alexander-de Gennes model [15, 16] of a polymer brush in which the density profile of the brush is assumed to be a step function and all chain ends are at the outer surface. Using the same model, however, Rabin and Alexander [17] found that the brush height should not be affected by the shear. The latter result was supported by two Monte Carlo (MC) simulations [18, 19] which treated the solvent as a continuum and modeled the shear flow by modifying the Metroplis transition probability to account for the effective force of the moving solvent on the brush chains. Here we address the question of how a polymer brush behaves in a steady state shear flow using molecular dynamics simulations.

The SFA is a powerful and sensitive technique for measuring the forces between surfaces separated by tens to hundreds of angstroms. However the technique does not give any spatial information on the conformation of the polymer chains or how much they interpenetrate, which is important if one is to understand the experimental results of Klein *et al.* [3, 4] and Granick *et al.* [5]. Because of the small distances involved, it is difficult to obtain such information using additional experimental methods. One technique which has already proven to be valuable for understanding the properties of polymer brushes, including the normal forces between them is computer simulations [20]. Earlier work by Murat and Grest [21] found that simulations for a simple bead-spring model were in excellent agreement with the experimental normal force versus separation profiles obtained by Taunton *et al.* [2] for polystyrene in toluene. These simulations have shown that for many properties of tethered chains it more than sufficient and often desirable to use a simple coarse grained model instead of a detailed atomistic model because of the long length and time scales involved. Using that same model, I show here that simulations can give considerable, new insights into the motion of polymer brushes under steady shear flow.

In the next section, the model and method will be briefly reviewed. In the subsequent section, the flow of a molecular solvent past a surface containing end-grafted polymers will be presented. Unlike previous studies [18, 19, 22], in which the solvent was treated as a continuum, here the solvent is included explicitly. For large shear rate $\dot\gamma$, some but not all of the chains are stretched in the direction of flow and the brush height decreases slightly. Results for the shear force between two surfaces bearing end-grafted polymer as they are brought into contact is then be presented and compared to the SFA experiments of Klein *et al.* [3, 4]. Finally, a brief discussion and summary of the results is presented.

MODEL AND METHOD

To simulate the SFA, a planar Couette geometry is used as shown in Figure 1. Linear polymer chains of $N + 1$ mers are end-grafted at random at a coverage ρ_a on two smooth, solid surfaces parallel to the xy plane. The surfaces are square with area $\mathcal{A}$ and the distance between them is D. Edge effects are minimized by applying periodic boundary conditions within this plane. The chain molecules are simulated using a bead-spring model, in which mers separated by a distance r interact through a truncated Lennard-Jones 6-12 potential
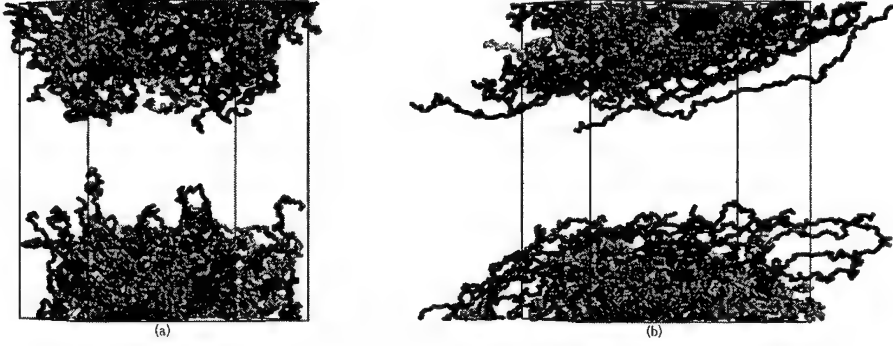
Figure 1: Typical configurations of a brush of chain length $N = 100$ immersed in a melt of $N_f = 2$ dimers for $\rho_a = 0.03\sigma^{-2}$. The solvent is not shown for clarity. The shear velocity is $v_w = 0$ (a) and $0.2\sigma/\tau$ (b). The dimensions of the cell are $\mathcal{A} = 40.8^2\sigma^2$ and $D = 64.9\sigma$. The figures were rendered by Raster3D [23] using sticks to better visualize the polymer chains.

[20, 24],

$$
U_{LJ}(r) = \begin{cases} 4\epsilon \left[\left(\frac{\sigma}{r}\right)^{12} - \left(\frac{\sigma}{r}\right)^6 - \left(\frac{\sigma}{r_c}\right)^{12} + \left(\frac{\sigma}{r_c}\right)^6 \right] & \text{if } r \leq r_c; \\ 0 & r > r_c, \end{cases} \tag{1}
$$

characterized by energy and length scales ϵ and σ, respectively. The cut-off distance is taken as $r_c = 2^{1/6}\sigma$, such that the potential is purely repulsive. Mers not grafted to the surface interact with the two confining plates with a Lennard-Jones potential with a weak attractive, short range component. The parameters for the wall-mer interaction are chosen such that the attractive contribution are much less than $k_B T$ so that the potential is dominated by the repulsive component. Adjacent mers along the chain are coupled through an anharmonic potential [20, 24], the values of which are chosen to eliminate (unphysical) bond crossing or breaking. The average bond length between connected mers is 0.97σ. All of the results presented here are for 50 end-grafted chains of length $N = 100$ per surface. However unlike previous work [22], in which the solvent molecules were not included explicitly, in the present study free chains of $N_f = 2$ mers are included so that the overall mer number density $\rho = 0.85/\sigma^3$. The free and end-grafted chains are identical except for their length. The only previous MD simulation of a polymer brush in an explicit solvent was for chains of length $N = 20$ in a solvent of single mers [25].

Shear is imposed by sliding the top surface at a fixed velocity v_w in the x-direction. The simulations are performed in an ensemble in which the total number of polymer brush and solvent chains, the surface coverage ρ_a, and the separation of the plates D are held constant. For the shear velocities studied here, the increase in the normal load $P_\perp$ under shear is small enough that fixing $P_\perp$ instead of D would change the results only slightly. This is in contrast to previous studies [26] for monomeric and short oligomer fluids confined between plates, which found that D increased significantly for large shear velocities. In these studies, the constant load and constant volume simulations gave quantitatively different results for the dependence of the shear force f on v_w for large v_w. The main difference between the present simulations and these earlier studies is that for the grafted polymer case, the plate separations are larger.

Constant temperature was maintained by coupling some or all of the mers to a thermal reservoir. Using molecular dynamics methods, this was done by introducing viscous damping and random noise terms to the equations of motion for those mers i which are coupled to

the reservoir,

$$m\frac{d^2\mathbf{r}_i}{dt^2} = -\nabla_i U - m\Gamma\frac{d\mathbf{r}_i}{dt} + \mathbf{W}_i(t). \tag{2}$$

Here m is the mass of each mer and Γ is the friction coefficient that couples the mers to the heat bath. The random part of the mer-heat bath coupling is given by a white-noise term $\mathbf{W}_i(t)$ which satisfies the fluctuation-dissipation theorem. For equilibrium studies with zero shear velocity, all three components of the velocity were coupled to the thermal reservoir. However to avoid any possible biasing of the flow in the shear direction (x), only the y component of the velocity was coupled to the reservoir for $v_w \neq 0$. Thus Langevin noise and frictional terms were added to the equations of motion in all three directions for $v_w = 0$, though only in the y-direction for nonzero shear velocities. The equations of motion of the mers were integrated using a velocity-Verlet algorithm [27] with a time step Δt. In most of the runs, all of the mers were coupled to the thermal reservoir with a friction coefficient $\Gamma = 0.5\tau^{-1}$, where $\tau = \sigma(m/\epsilon)^{1/2}$. The time step in this case was either $\Delta t = 0.010$ or 0.012τ, depending on the shear rate. The larger time step was used in most of runs, though at very high shear rate Δt was reduced to keep the algorithm stable. However since introducing a viscous damping screens hydrodynamic interactions [28], some runs were made in which only the first 10 mers of each grafted chain and none of the solvent chains were coupled to the thermal reservoir. In this case, the time step was reduced to $\Delta t = 0.006\tau$. No significant differences in the two cases were observed. Further details on the algorithm can be found elsewhere [20].

The initial states were generated as described in ref. [29]. In the presence of explicit solvent molecules, equilibration was extremely slow [29]. For nonzero values of v_w, long runs of $6 - 30 \times 10^5 \Delta t$ were made to assure steady state had been reached. A number of quantities were then determined from the simulation including the brush height h, the brush mer number density profile from the grafting surface $\rho(z)$, the number density of free ends of the brush chains $\rho_e(z)$, and the mean square end-to-end distance $\langle R^2 \rangle$ and the mean squared radius of gyration $\langle R_G^2 \rangle$ of the chains. These are discussed in more detail in the next two sections.

FLOW PAST A POLYMER BRUSH

In this section the results for flow of a small molecule solvent past a polymer brush are discussed. First, however, let us briefly review the predictions from scaling and free-energy balance arguments for a brush of chain length N in a solvent of free chains of length N_f. De Gennes [16] was the first to obtain the theoretical phase diagram for such a system. He found that as either ρ_a or N_f increases, the free chains are progressively expelled from the brush. The presence of long solvating chains screens the excluded volume interactions between the brush chains, thus shrinking the brush. A Flory-type theory predicts that $h \sim N^{3/5}N_f^{-1/5}$ for low coverage and small N_f (the so-called mushroom regime) while $h \sim N(\rho_a/N_f)^{1/3}$ in the intermediate overlap regime [16,30,31]. This latter scaling relationship gradually breaks down at high coverage and/or large N_f, as the free chains are almost completely expelled from the brush.

Simulating the solvation of a polymer brush by a molecular solvent is very demanding. This is because the number of free chains that must be included is significantly larger than the number of brush chains, even in mer units. Therefore, a larger fraction of the computation time goes to the free molecules, making the computation costly (read hundreds of processor hours). Systems with N_f ranging from single monomers to 40-mers were studied in ref. [29] for intermediate values of ρ_a and D sufficiently large that end-grafted polymers from opposite surfaces did not come into contact. Results for h were is very good agreement with the theoretical predictions. Most of the runs in this study were for three values of the surface
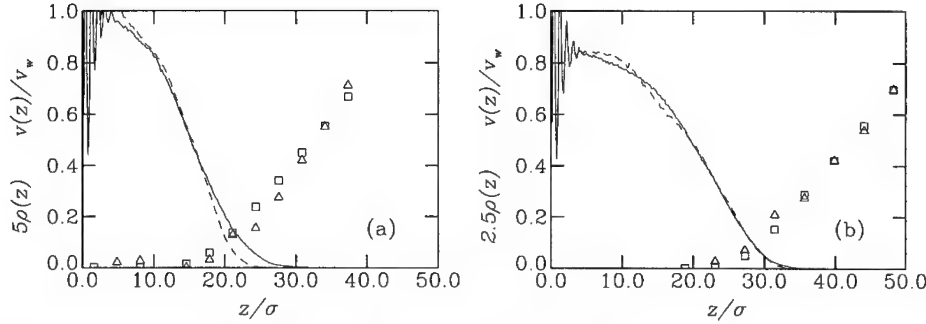
Figure 2: Solvent velocity profile (points) and brush density profile (curves) for a polymer brush under shear flow. The coverage is (a) $\rho_a = 0.03$ and (b) $0.07\sigma^{-2}$. The chain length of the brush is $N = 100$, while that of the solvent is $N_f = 2$. Results are shown for $v_w = 0.02\sigma/\tau$ (solid line and triangles) and $0.2\sigma/\tau$ (dashed line and squares). $\rho(z)$ has been multipled by a factor of 5 and 2.5, respectively, to put the data on the same scale.
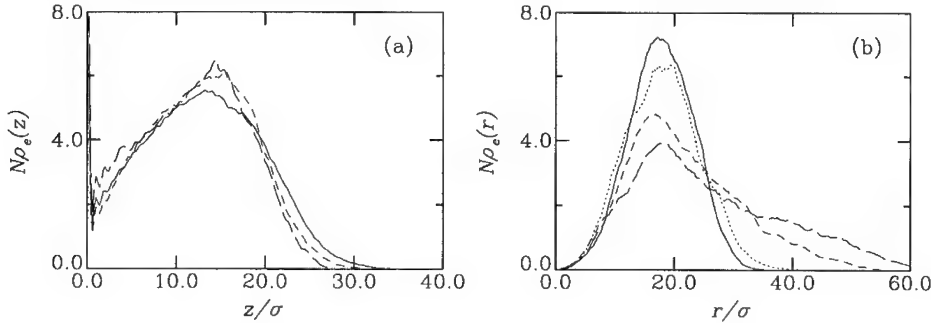
Figure 3: Free end distribution for brushes of length $N = 100$ in a shear flow as a function of the height z above the grafting surface and distance r from the grafting point. The shear rate $\dot{\gamma} = 0.0$ (solid line), 7.2×10^{-4} (dotted line), 3.6×10^{-3} (short dashed line), and $7.2 \times 10^{-3}\tau^{-1}$ (long dashed line). Results are for $\rho_a\sigma^2 = 0.03$.

coverage $\rho_a = 0.03$, 0.07, and $0.10\sigma^{-2}$, which for $N = 100$, are in the intermediate coverage regime, $h \sim N(\rho_a/N_f)^{1/3}$. In this paper, results are presented for a brush immersed in a solvent of dimers, $N_f = 2$, under steady state shear flow for the same three values of ρ_a.

In Figure 1, typical configurations of a polymer brush are shown for $\rho\sigma^2 = 0.03$ for $v_w = 0$ and $v_w = 0.2\sigma/\tau$, which turns out to be a fairly large shear. For $v_w \lesssim 0.02\sigma/\tau$, there is no detectable change in the brush profile or end-to-end distance of the grafted chains. For larger velocities however, the brush chains become strongly stretched along the direction of flow, as v_w increases. As can be seen from Figure 1(b), this also has the effect of slightly decreasing the brush height. There was no difference in the results for the two methods for coupling the system to the thermal reservoir. The small decrease in the brush height for large v_w can also be seen from the density profiles for $v_w = 0.02$ and $0.2\sigma/\tau$ in Figure 2. Note that even though some of the chains become very stretched for large v_w, the mer density for the brush depends only weakly on the shear rate. That only some of the chains are stretched is seen clearly in Figure 3, where results for the end density distributions $\rho_e(z)$ and $\rho_e(r)$ are shown.
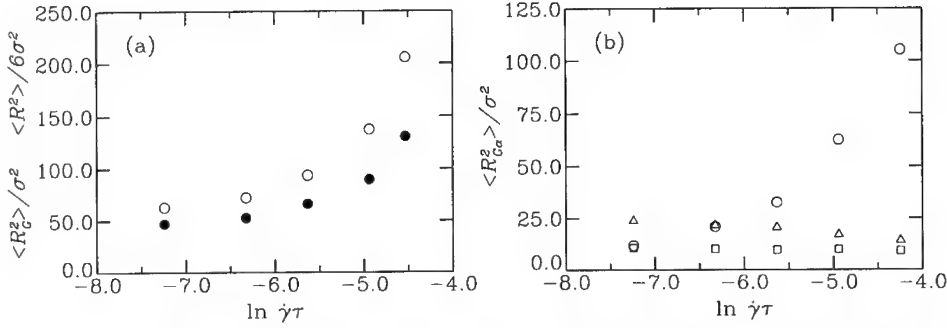
Figure 4: (a) Mean squared radius of gyration $\langle R_G^2 \rangle$ ($\bullet$) and end-to-end distance $\langle R^2 \rangle$ ($\circ$) and (b) components of the mean squared radius of gyration, $\langle R_{Gx}^2 \rangle$ ($\circ$), $\langle R_{Gy}^2 \rangle$ ($\square$), and $\langle R_{Gz}^2 \rangle$ ($\triangle$) as a function of the shear rate $\dot{\gamma}$ for a single brush in a shear flow. Results are for $\rho_a \sigma^2 = 0.03$.

Here z is the height above the grafting surface and r is the distance from the grafting point. A large fraction of the chain ends are buried deep inside the brush and do not feel the effect of the shear even for large v_w. The results shown in Figure 3 quantify the visual observation of Figure 1(b).

The solvent velocity profiles are shown in Figure 2. Away from the brush, the velocity profiles are linear as expected. From this region, the shear rate $\dot{\gamma}$ can easily be determined from the slope of $v(z)$. In the vicinity of the brush, the solvent velocity decays very rapidly, consistent with the predictions by Milner [32] based self-consistent field theory and with previous MD simulations by Peters and Tildesley for short chains [25]. The increase of the chain dimensions with shear rate is shown in Figure 4. As seen in Figure 4(b), all of the increase in the mean squared radius of gyration $\langle R_G^2 \rangle$ comes from the component in the direction of shear flow, x. The other two components remain relatively constant ($\langle R_{Gy}^2 \rangle$) or decrease slightly ($\langle R_{Gz}^2 \rangle$) compared to the large increase in $\langle R_{Gx}^2 \rangle$. Similar results are found for $\rho_a \sigma^2 = 0.07$ and 0.10.

The fact that the chains stretch predominantly along the direction of flow and the brush height is only weakly dependent on the shear rate are in very good agreement with earlier lattice, bond-fluctuation MC simulations by Lai and Binder [18] and off-lattice MC simulations by Miao et $al.$ [19] of a polymer brush in a velocity field. Though neither of these simulations treat the solvent explicitly, they accurately describe the properties of a dense polymer brush in a flow field by modifying the standard Metroplis MC transition probability to take into account the effective force acting upon the brush chains by the moving solvent. Apparently, the rapid decay of the solvent velocity into the brush makes it possible to treat the solvent in this way, provided that the screening of the velocity field is determined self-consistently with the brush density profile $\rho(z)$ [18,19].

Theoretically the situation is less clear. The results of this simulation as well as the MC simulations [18, 19] for a brush in a steady state shear flow differ considerably from some recent theoretical predictions by Barrat [12], Kumaran [13], and Harden and Cates [14]. All of these theories suggest that the height should increases under shear. The only theoretical prediction which found that the height does not increase under shear is that by Rabin and Alexander [17]. However all of these models are based on the Alexander-de Gennes model [15,16] in which the brush density profile is assumed to be a step function and all the free ends are at the outer surface of the brush. While this simple model gives the correct scaling behavior for the brush height h, it appears to be inadequate to describe the shear
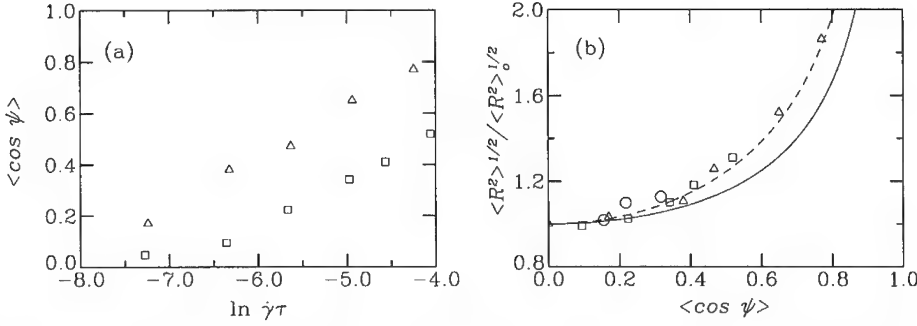
Figure 5: (a) Dependence of $\langle\cos\psi\rangle$ on the shear rate $\dot{\gamma}$ for $\rho_a\sigma^2 = 0.03$ ($\triangle$) and 0.07 ($\square$) for $N = 100$. (b) Scaled average end-to-end distance of a chain as a function of the average inclination of the center of mass to the x axis. Data points are for $\rho_a\sigma^2 = 0.03$ ($\triangle$), 0.07 ($\square$), and 0.10 ($\circ$). The prediction of Rabin and Alexander [17] (solid line) and Barrat [12] (dashed line) are also shown.

rate dependence of h. There has been no theoretical prediction for the properties of a brush under shear using the self-consistent field approach, which correctly predicted not only the scaling dependence of h on chain length N and coverage ρ_a, but also that $\rho(z)$ is parabolic and the ends are distributed throughout the brush.

Experimentally, the only direct measure of the brush height has been the recent neutron reflectivity measurements by Nguyen *et al.* [33]. These results are in agreement with the present simulations in that they find that the height of the polymer brush is not affected by shear for the range of shear rates studied. The original experiment by Klein *et al.* [11] using the SFA found that if the surfaces were either weakly compressed or uncompressed but separated by a small gap, that there was an extra normal force at high velocity. These experiments suggested that an uncompressed layer increases its thickness when a fluid flows past and that the increase occurs above a critical shear rate. However since these experiments were carried out at oscillatory frequencies of a few hundred hertz and not at steady state shear as in the present simulations, direct comparison of the two is not possible. Further simulations under oscillatory shear are needed to explore the interplay between the relaxation times of the end-grafted chains and the shear flow.

Finally, the effect of the shear flow can also be characterized by how much the chains are inclined in the direction of flow. The inclination $\cos\psi$ for each chain can be defined as [18]

$$\cos\psi = \hat{\mathbf{R}}_{\rm cm}\cdot\hat{\mathbf{x}}, \tag{3}$$

where $\hat{\mathbf{R}}_{\rm cm}$ is the unit vector in the direction from the grafting point to the center of mass of the chain and $\hat{\mathbf{x}}$ is the unit vector in the flow direction (x). Figure 5(a) shows $\langle\cos\psi\rangle$ versus the shear rate for two values of the coverage, $\rho_a\sigma^2 = 0.03$ and 0.07. As expected, $\langle\cos\psi\rangle$ increases with increasing shear rate. For a given shear rate, the higher the coverage, the less the inclination. In Figure 5(b), the end-to-end distance $\langle R^2\rangle^{1/2}$, normalized by it's value at zero shear rate, is shown as a function of $\langle\cos\psi\rangle$ for three values of ρ_a. Also shown are the Rabin and Alexander [17] prediction $\langle R^2\rangle/\langle R^2\rangle_o = (1-\cos^2\psi)^{-1}$ and the Barrat [12] prediction, $(1+\cos^2\psi)^{2/3}/(1-\cos^2\psi)$. While the former fits the data very well, this must be fortuitous since both of these theories are based on the Alexander-deGennes model [15,16] in which all the ends are at the outer surface. As seen from Figure 3 this is clearly not the case as the free ends are distributed through out the brush. Lai and Binder [18] found a
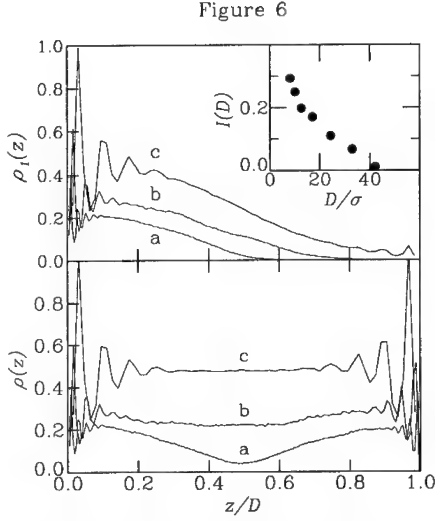
Figure 6: Brush mer number density profile versus distance from the grafting surface z for polymers of length $N = 100$ and solvent of length $N_f = 2$ at $\rho_a \sigma^2 = 0.03$ for (a) $D = 42.1\sigma$, (b) $D = 24.3\sigma$, and (c) $D = 12.6\sigma$. The total brush mer number density $\rho(z)$ is shown in the lower panel and the mer density $\rho_1(z)$ for one brush is in the upper panel. The inset shows the amount of interpenetration $I(D)$ versus D.
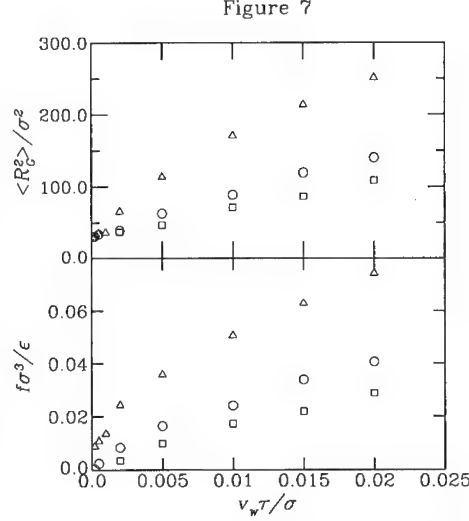
Figure 7: Shear stress f per unit area and mean squared radius of gyration $\langle R_G^2 \rangle$ as a function of the relative velocity v_w of the two surfaces for $N = 100$ and $N_f = 2$. The data is for $\rho_a \sigma^2 = 0.03$ and $D = 24.2\sigma$ ($\square$), $D = 17.1\sigma$ ($\circ$), and $D = 8.1\sigma$ ($\triangle$).

similar scaling result from their MC simulations of a brush in a flow field, though their data fell below the Rabin-Alexander prediction.

COMPRESSED BRUSHES UNDER SHEAR FLOW

Now consider what happens as the two surfaces in Figure 1 are brought into contact. In the experimental SFA, two crossed cylinders bearing end-grafted polymers are brought into contact by increasing the external load. As this occurs, a fraction of the small molecular solvent present in the gap between the surfaces is expelled into the reservoir in which the apparatus is immersed. The experimental system is open and the solvent is at fixed chemical potential with that of the reservoir. The simulations, as discussed above, are in a closed system, in which the number of solvent molecules is fixed. To model the experimental SFA as the distance between the surfaces D is decreased, solvent molecules are removed from the simulation cell so as to maintain a constant overall mer number density $\rho = 0.85\sigma^3$. While this ensemble is slightly different from the experimental situation, in which the overall density of the system may change slightly as the surfaces are brought into contact, the results for the shear force for the two should be qualitatively very similar. However, there is one important difference between the open and closed system and that is the effect of an external load. In the latter, since the number of mers is fixed, increasing the external load increases the density, while in an open system, solvent molecules are expelled. Thus when comparing the normal forces in the two cases, one needs to compare the osmotic pressure in the closed system, i.e. the pressure due to interactions between only end-grafted chains, to the external

78
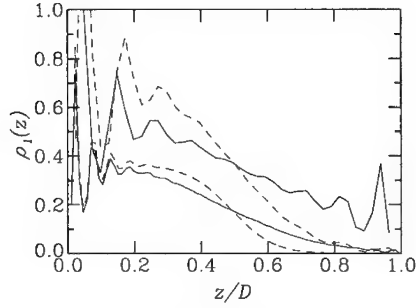
Figure 8: Monomer density profile $\rho_1(z)$ versus distance from the plate z for $D = 8.1\sigma$ (upper pair of curves) and for $D = 17.1\sigma$ (lower set of curves) for $v_w = 0$ (solid line) and $v_w = 0.02\sigma/\tau$ (dashed line) for $N = 100$ and $\rho_a\sigma^2 = 0.03$.

normal load in an open system. In previous simulations [21, 22] in which the solvent was treated as a continuum, this was not an issue, since only brush chains were present.

In Figure 6, the results for the mer number density profiles are presented for three values of D for $v_w = 0$ for $\rho_a\sigma^2 = 0.03$. In this case, the mers from opposite surfaces first begin to overlap at $D \simeq 60\sigma$. In addition to $\rho(z)$, the mer density from only one surface $\rho_1(z)$ is also shown. For very small D, layering occurs near the surface due to the finite volume of each mer. In the inset, the amount of interpenetration $I(D)$, given by the integral of $\rho_1(z)$ from $z/D = 0.5$ to 1.0, is shown. At the highest compression, 30% of the mers connected to one surface are on the opposite half of the midplane. These results are very similar to those obtained previously using a continuum solvent [22].

The shear stress f is obtained from the xz component of the microscopic pressure-stress tensor, $f = -P_{xz}$. The fluctuations in the shear force are much larger than the average force f, requiring long runs. The uncertainty in f is difficult to estimate precisely because long runs for much larger systems is not possible due to limitations on computer time. However from examing the results of runs starting from different conditions and of varying length, the uncertainty in f is estimated to be approximately 10%, compared to about 1% for the normal osmotic pressure $\Pi_\perp$. In Figure 7, the dependence of the shear force f on sliding velocity is shown for three values of D. For small v_w and large D, f was found to increase approximately linearly as would be expected for a Newtonian fluid. In this regime there is little change in $\langle R_G^2 \rangle$ (Figure 7) or $\langle R^2 \rangle$ (not shown). There is also no change in $\rho_1(z)$ compared the results shown in Figure 6 for $v_w = 0$. Beyond the Netwonian-like regime, f increases sublinearly for large v_w, in analogy to earlier observations [26,34] for small molecule systems confined between two plates. One may call this the non-Newtonian regime. As seen from the mean-squared radius of gyration $\langle R_G^2 \rangle$ the chain stretch in this regime and there is some disentanglement of polymers from the two surfaces, particularly for small D and large v_w, as shown in Figure 8. For $D = 8.1\sigma$, $I(D)$ decreases from 0.29 for $v_w = 0$ to 0.27 for $v_w = 0.002\sigma/\tau$ while increasing v_w by a factor of 10 ($v_w = 0.02\sigma/\tau$) decreases $I(D)$ by factor of 2 (0.14). While the amount of interpenetration decreases significantly for large v_w, the normal osmotic pressure actually decreases by about 1%.

Comparison of the normal osmotic pressure and the shear force in this regime for three values of v_w is presented in Figure 9(a) for $\rho_a\sigma^2 = 0.03$. These results are in qualitatively good agreement with the experiments of Klein et $al.$ [3] shown in Figure 9(b). The SFA experiments found that f was below their resolution limit for large D and increased rapidly for high compressions. The simulation results do not increase quite as rapidly with decreasing
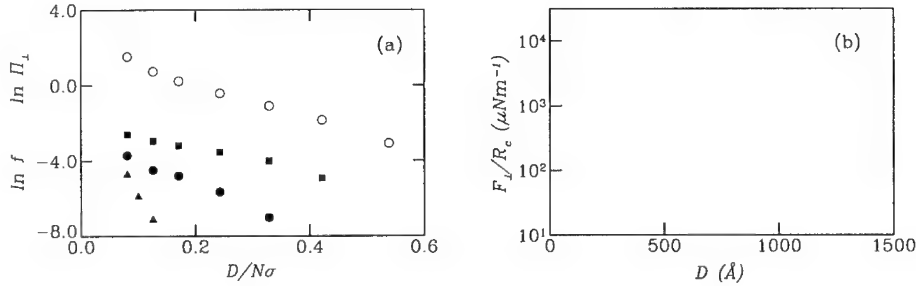
Figure 9: (a) Semilog plot of the normal osmotic pressure $\Pi_\perp$ ($\circ$) and shear force f versus the plate separation D between polymer brushes of 100-mers at $\rho_a = 0.03\sigma^{-2}$. The shear force is shown for $v_w = 2.0 \times 10^{-4}$ ($\blacktriangle$), 2.0×10^{-3} ($\bullet$), and $2.0 \times 10^{-2}\sigma/\tau$ ($\blacksquare$). (b) Experimental results of Klein *et al.* [3] for the normal (upper set of points) and shear (lower set) forces for mica surfaces bearing polystyrene (140 000 molecular weight) in toluene. The experimental force is normalized by the radii of curvature R_c (~ 1 cm) of the surface. Results from several different experiments are shown.

plate separation. As the shear force f is a continuously varying function of velocity even for high shear rates, a true coefficient of friction cannot be defined. However treating the shear-to-normal ratio of the forces as an effective coefficient of friction (as Klein *et al.* did), $\mu_b \simeq 0.005 - 0.007$ for $D \lesssim 20\sigma$ for $v_w = 0.002\sigma/\tau$ and actually decreases slightly as D decreases in agreement with experiment [4]. This is because the normal force increases more rapidly than the shear force as D decreases. The effect is very strong for large v_w. For example, for $v_w = 0.02\sigma/\tau$, μ_b is largest for large D ($\mu_b = 0.05$) and decreases to 0.014 for $D = 7\sigma$. It is important to remember that since the surface forces experiments are for two crossed cylinders and the simulations are for flat plates, the two cannot be compared directly [35]. In the Derjaguin approximation, the interaction energy per unit area, $E(D) = \int_{2h_{max}}^{D} P_\perp(D')\,dD'$, between two flat surfaces is proportional to the normal force $F_\perp$ divided by the radius of curvature R_c, $F_\perp/R_c$, for two crossed cylinders [35]. The relationship between the shear forces in the two systems is less clear. Note that the range of D over which f is large enough to detect is also larger than that observed experimentally. This is presumably due to the fact that the velocities used here are much larger than those in the experiment. Comparing Figures 9(a) and (b), the experiments are best fit by the lowest velocity, $v_w = 2.0 \times 10^{-4}\sigma/\tau$. Thus it is likely that the present experimental results on the SFA are only in the low velocity Newtonian-like regime. However since there is presently no experimental data available for the velocity dependence of f for small D, it is not possible to determine for certain which part of the shear force-velocity curve the experiments access.

In an earlier study [22], results for the shear and normal forces between two surfaces bearing end-grafted chains were presented for a continuum solvent. In Figure 10, the shear force f is presented for the present case in which the solvent is included explicitly and the earlier results in which it is treated as a continuum. Qualitatively the results for the two case are quite similar. Both show the Newtonian-like regime for small v_w and the sublinear increase in f for large v_w. For small D, where the number of solvent molecules is small, the results for the two cases are very close. The difference in the two cases are what one would expect for two solvents with intrinsically different viscosities.

CONCLUSIONS

The findings presented here provide new insight into the interfacial sliding of polymer brushes under shear. For uncompressed brushes, the flow of the solvent stretches some chains
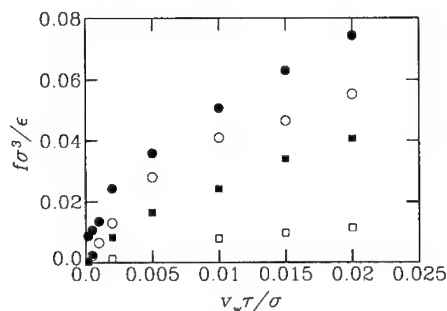
Figure 10: Comparison of the shear stress f per unit area for the continuum solvent (open symbols) and explicit solvent of length $N_f = 2$ (closed symbols) as a function of the relative velocity v_w. The data is for $\rho_a \sigma^2 = 0.03$ and $D = 8.1\sigma$ (circles) and $D = 17.1\sigma$ (squares).

in the direction of shear flow but leaves many unstretched. At least for steady state shear, this leads to a slightly decrease in the brush height with increasing shear rate in contrast to several theoretical models which predict an increase. The solvent velocity field decays very rapidly into the brush as predicted by self-consistent field theory. Further simulations for the case of oscillatory shear are needed to study the interplay of the relaxation of the brush with the shear rate. When these two are on the same time scale, it is possible that the brush height may increase as suggested by the SFA experiments of Klein *et al.* [11].

When two surfaces bearing end-grafted polymer are compressed, the brushes interpenetrate only weakly and easily slide pass each other with immeasurably small shear force at low compression. For higher compressions two regimes were identified, depending on the shear rate. For low shear rates, the mer number density profile and chain conformation are unperturbed even for large compressions. In this Newtonian-like regime, the shear force increases approximately linearly with velocity. However for large shear rates, the chains become strongly stretched and the shear force increases sublinearly with shear velocity. Results for the present simulations which treat the solvent explicitly are in very good agreement with earlier simulations [22] in which the solvent is treated as a continuum. To date, all simulations for the lateral forces have been for good solvent. These should be extended to address the effect of solvent quality which was observed to play an important role [5], particularly for high compression. Experimentally it is important to extend the previous studies to a range of shear rates to determine the shear force-velocity curve, particularly to check for the sublinear rise in the shear force with velocity. A direct measurement of the chain stretching, presumably by scattering, is also very important in understanding how two polymer brushes slide pass each other.

ACKNOWLEGMENT

I thank M.-D. Lacasse for a critical reading of the manuscript.

REFERENCES

1. S. S. Patel and M. Tirrell, Ann. Rev. Phys. Chem. **40**, 597 (1989).
2. H. J. Taunton, C. Toprakcioglu, L. J. Fetters, and J. Klein, Nature **332**, 712 (1988); Macromolecules **23**, 571 (1990).
3. J. Klein, E. Kumacheva, D. Mahalu, D. Perahia, and L. J. Fetters, Nature **370**, 634 (1994); J. Klein, E. Kumacheva, D. Perahia, D. Mahalu, and S. Warburg, Faraday Discuss. **98**, 173 (1994).

4. J. Klein, Ann. Rev. Mat. Sci. **26**, 581 (1996).

5. S. Granick, A. L. Demirel, L. L. Cai, and J. Peanasky, Israel J. Chem. **35**, 75 (1995); L. L. Cai, J. Peanasky, and S. Granick, Trends Polym. Sci. **4**, 47 (1996).

6. F. P. Bowden and D. Tabor, *The Friction and Lubrication of Solids* (Clarendon, Oxford, 1950).

7. D. Tabor, *Friction* (Doubleday, New York, 1973).

8. M. L. Gee, P. M. McGuiggan, J. N. Israelachvili, and A. M. Homola, J. Chem. Phys. **93**, 1895 (1990).

9. J. van Alsten and S. Granick, Langmuir **6**, 877 (1990).

10. P. A. Thompson and M. O. Robbins, Science **250**, 792 (1990); M. O. Robbins and P. A. Thompson, *ibid.* **253**, 916 (1991).

11. J. Klein, D. Perahia, and S. Warburg, Nature **352**, 143 (1991).

12. J.-L. Barrat, Macromolecules **25**, 832 (1992).

13. V. Kumaran, Macromolecules **26**, 2464 (1993).

14. J. L. Harden and M. Cates, Phys. Rev. E **53**, 3782 (1996).

15. S. Alexander, J. Phys. (Paris) **38**, 983 (1977).

16. P.-G. de Gennes, Macromolecules **13**, 1069 (1980).

17. Y. Rabin and S. Alexander, Europhys. Lett. **13**, 49 (1990).

18. P.-Y. Lai and K. Binder, J. Chem. Phys. **98**, 2366 (1993).

19. L. Miao, H. Guo, and M. J. Zuckermann, Macromolecules **29**, 2289 (1996).

20. G. S. Grest and M. Murat, in *Monte Carlo and Molecular Dynamics Simulations in Polymer Science*, edited by K. Binder (Oxford University Press, New York, 1995), p. 476.

21. M. Murat and G. S. Grest, Phys. Rev. Lett. **63**, 1074 (1989).

22. G. S. Grest, Phys. Rev. Lett. **76**, 4979 (1996).

23. D. J. Bacon and W. F. Anderson, J. Molec. Graphics **6**, 219 (1988); E. A. Merritt and M. E. P. Murphy, Acta Cryst. **D50**, 869 (1994).

24. G. S. Grest and M. Murat, Macromolecules **26**, 3108 (1993).

25. G. H. Peters and D. J. Tildesley, Phys. Rev. E **52**, 1882 (1995); Phys. Rev. E **54**, 5493 (1996).

26. P. A. Thompson, G. S. Grest, and M. O. Robbins, Phys. Rev. Lett. **68**, 3448 (1992); P. A. Thompson, M. O. Robbins, and G. S. Grest, Israel J. Chem. **35**, 93 (1995).

27. M. P. Allen and D. J. Tildesley, *Computer Simulation of Liquids* (Clarendon, Oxford, 1987).

28. B. Dünweg, J. Chem. Phys. **99**, 6977 (1993).

29. G. S. Grest, J. Chem. Phys. **105**, 5532 (1996).

30. E. Raphaël, P. Pincus, and G. H. Fredrickson, Macromolecules **26**, 1996 (1993).

31. M. Aubouy, G. H. Fredrickson, P. Pincus, and E. Raphaël, Macromolecules **28**, 2979 (1995).

32. S. T. Milner, Macromolecules **24**, 3704 (1991).

33. D. Nguyen, C. J. Clarke, Y. S. Yu, A. Eisenberg, M. H. Raifailovich, J. Sokolov, and G. S. Smith, unpublished (1996).

34. S. Granick, Science **253**, 1374 (1992).

35. J. Israelachvili, *Intermolecular & Surface Forces* (Academic, London, 1994).

Wall Slip of a Polymer Melt on a Polymer Brush

E. Durliat, H. Hervet, L. Léger
Laboratoire de Physique de la Matière Condensée, URA CNRS 792
Collège de France, 11 place Berthelot, 75231 Paris cedex 05, France

Abstract

We have investigated simple shear flows of poly-dimethyl-siloxane (PDMS) melts on PDMS brushes with well controlled grafting density Σ, using optical techniques based on near field laser anemometry to measure the local velocity of a polymer melt at a solid interface. We have observed a slip transition from a weak slip regime to a strong one as the shear rate crosses a critical value $\dot{\gamma}^*$. The influence of the molecular weight of the melt M_m, of the molecular weight of the brush chains M_b and of Σ on $\dot{\gamma}^*$, has been investigated to elucidate the molecular mechanisms. The results are compared with an existing molecular model.

Introduction

Dynamics of polymer melts play a major role in a lot of industrial processes. The underlying molecular mechanisms for several dynamic properties are nevertheless not always fully clarified. This is the case for the onset of flows with wall slip, which is of great importance because it is supposed to be at the origin of some extrusion problems like stick-slip instabilities or the shark-skin effect.

Recently the velocity at the interface has been investigated experimentally in simple shear flows of PDMS melts on low density adsorbed layers of PDMS on octadecyltrichlorosilane (OTS) monolayers [1, 2]. A slip transition from a regime of weak wall slip to a regime of strong wall slip has been found. This transition has been explained by a microscopic model[3] developed for low density brushes (chains chemically grafted, by only one end, on a non-adsorbing solid surface), and is related to the friction induced by entanglements between the flowing melt and the chains of the brush. In these early experiments[1, 2], the anchored chains were not grafted but adsorbed and the grafting density was small but uncontrolled.

To understand more thoroughly the molecular mechanisms of the dynamic interaction between a flowing melt and a brush, we have investigated simple shear flows of high molecular weight PDMS melts on brushes with well controlled grafting densities. The influence of the molecular parameters of the system, molecular weight of the melt M_m, molecular weight of the chains of the brush M_b, and grafting density Σ of these chains has been systematically investigated in order to test the validity of the molecular model[4].

Experimental system

The experimental setup has already been described[1, 2]. We only recall here its important features. A drop of PDMS melt (M_m= 500, 610, 790 and 970 kg/mol, polydispersity $\mathcal{I} \approx 1.2$) is sandwiched between two smooth surfaces made of fused silica, maintained at a distance d=8μm by mylar spacers. The bottom surface is that of a prism covered with the brush under investigation. The top surface is a moving plate which can be translated at a chosen constant

velocity V_p, thus inducing a simple shear flow. We measure the velocity of the melt, V_s, near the bottom surface using optical techniques based on Near Field Laser Anemometry[1, 2]. We have checked that the velocity of the melt near the moving plate is equal to V_p because the melt adsorbs on the bare silica of the top plate into a pseudobrush[5] on which wall slip is very low in the range of shear rates we have investigated here[6]. We can then define the apparent shear rate $\dot{\gamma} = (V_p - V_s)/d$ and the extrapolation length to zero of the velocity profile, b, which is equal to $b = V_s/\dot{\gamma}$.

Monodisperse α-*sec*-butyl, ω-vinyl PDMS (molecular weights M_b=5, 96, 124, 170, 200 and 263 kg/mol, polydispersity $\mathcal{I} \leq 1.15$) has been synthesized by anionic polymerization[7]. The vinyl ends of such polymers, in an octane solution with volumic fraction ϕ, can be grafted on the SiH groups of a monolayer of chloro-octamethyl-tetrasiloxane (Cl-(Si(CH$_3$)$_2$O)$_3$-Si(CH$_3$)$_2$H) previously self-assembled on the silica prism. The monolayer prevents adsorption of PDMS on silica and functionalizes the surface for grafting[8]. The dry thickness h of the grafted layer is controlled by adjusting the volumic fraction ϕ and the molecular weight M_b[8], and is related to the adimensionnal grafting density Σ by $\Sigma = mh/aM_b$, where $m \approx 74$ g/mol is the mass of a monomer and a is the monomer size ≈ 0.5nm. The range of Σ for these brushes (type I) was 0.00025 to 0.032. We have also formed brushes from a mixture of two melts. One has a molecular weight equal to M_1=5 kg/mol and a radius of gyration $h_1 \approx 4$ nm. As the mass between two entanglement is M_e=7,400 g/mol for PDMS, one can expect that these small grafted chains will behave as an ideal surface with no dynamic interaction with the melt. The other melt of the mixture has a molecular weight $M_b \gg M_1$ and the grafting density of these longer chains in the brush is $\Sigma = (h - h_1)/(a\,M_b/m)$, where h is the dry thickness of the brush. h and Σ are controlled by adjusting the volumic fraction ϕ of the smaller molecular weight in the mixture. Due to the higher diffusion coefficient of the smaller chains, h is always much smaller than the expected value for an ideal mixture, $\phi h_1 + (1 - \phi)a(M_b/m)^{1/2}$ even for small values of ϕ. So the range for Σ with these brushes (type II) was never larger than 0.010. These type II brushes are however interesting because the underlying layer of grafted short chains provides a far more efficient barrier for melt chains adsorption than the self-assembled octamethyltetrasiloxane monolayer.

Results

We have investigated melt flows on brushes of type I and II grafted on the prism surface as described above. In all cases, a slip transition from a weak slip regime to a strong one occurs at a critical slip velocity $V^\star$ as the shear rate is increased, as already observed for adsorbed chains[1, 2]. As shown on fig. 1, at small slip velocities $V_s \leq V^\star$, the extrapolation length b has a value b_0 independent of V_s while the shear rate $\dot{\gamma}$ increases linearly with V_s which remains small compared to V_p. At high slip velocities $V_s \geq V^\star$, b becomes a linear function of V_s and $\dot{\gamma}$ becomes independent of V_s and locked to its value at the transition, $\dot{\gamma}^\star$. At very high slip velocities, b saturates and $\dot{\gamma}$ increases linearly with V_s again. Experimentally, b_0 and $\dot{\gamma}$ are determined independently and $V^\star$ is deduced through the relation : $V^\star = b_0\dot{\gamma}^\star$.

The influence of Σ on $\dot{\gamma}^\star$ has been investigated for $M_m = 970$ and 790 kg/mol. With brushes of type I ($M_b = 96$ kg/mol) (fig. 2a), at high densities $\Sigma \geq \Sigma_1 \approx 0.010 \geq \Sigma^\star$ with $\Sigma^\star$ the overlap threshold density, $\dot{\gamma}^\star$ decreases for both values of M_m. At small grafting densities $\Sigma \leq \Sigma_1$, $\dot{\gamma}^\star$ is constant for $M_m = 790$ kg/mol, while for $M_m = 970$ kg/mol, it is first constant then increases linearly with Σ. We have then checked that there is no dynamic interaction
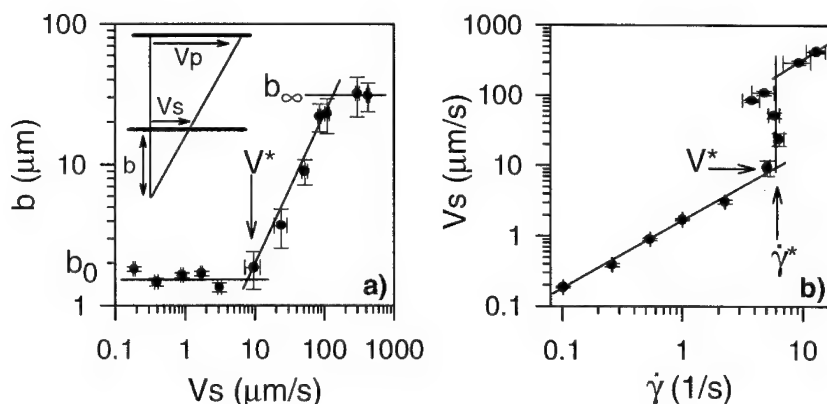
Figure 1: **a)**the extrapolation of the velocity profile to zero, b, versus the slip velocity, V_s, and **b)**V_s versus the shear rate $\dot{\gamma} = V_s/b$, for a PDMS melt (molecular weight $M_m = 1000$ kg/mol) against a PDMS brush (molecular weight $M_b = 96$ kg/mol and grafting density $\Sigma = 0.0055$).

between the melts and a brush of small chains (5 kg/mol). Indeed, b remains constant and high ($\approx 100\mu$m) in the whole range of slip velocities : the surface almost behaves as an ideal one. Thus with brushes of type II, the evolution of $\dot{\gamma}^\star$ versus the grafting density Σ of the longer chains, can be investigated, without being affected by either the short grafted chains or the residual adsorption of a few melt chains on the surface. For $M_b = 96$ and 170 kg/mol, $\dot{\gamma}^\star$ is independent of Σ at very small densities $\Sigma \leq 0.001$. At higher densities $0.001 \leq \Sigma \leq \Sigma_1$, $\dot{\gamma}^\star$ is a linear function of Σ and reaches the values obtained on brushes of type I (fig. 2b).

With brushes of type II, we found that $\dot{\gamma}^\star$ is independent of M_b at small grafting densities $0.001 \leq \Sigma \leq \Sigma_1$ (fig. 2b). With brushes of type I, we found that $\dot{\gamma}^\star$ is decreasing with the weight M_m of the melt under shear flow, and is a non-monotonous function of M_b, at high grafting densities $\Sigma \geq \Sigma_1$ (fig. 3).

The extrapolation length b_0 was found independent of Σ for both types of brushes and of order of 1.8μm, but the influence of M_m and of M_b remains unclear for the moment.

Discussion and Conclusions

We think that the slip transition can be explained in terms of entanglements between the melt and the brush, and thus different regimes can appear depending on the degree of interpenetration between the brush and bulk chains.

For flows on brushes with small grafting densities $\Sigma \leq \Sigma_1$, larger than the limit of the mushroom regime, $\Sigma^\star$, a molecular model has been developed[4]. For $\Sigma \leq \Sigma^\star$, the brush chains are independent. For higher densities $\Sigma^\star \leq \Sigma \leq \Sigma_1$, the brush is totally swollen by the melt, and the brush chains are still independent because the melt screens interactions between brush chains. When the melt flows, each chain of the brush is undergoing both a friction force from the melt, F_v, which tends to elongate the grafted chains into a cylinder of
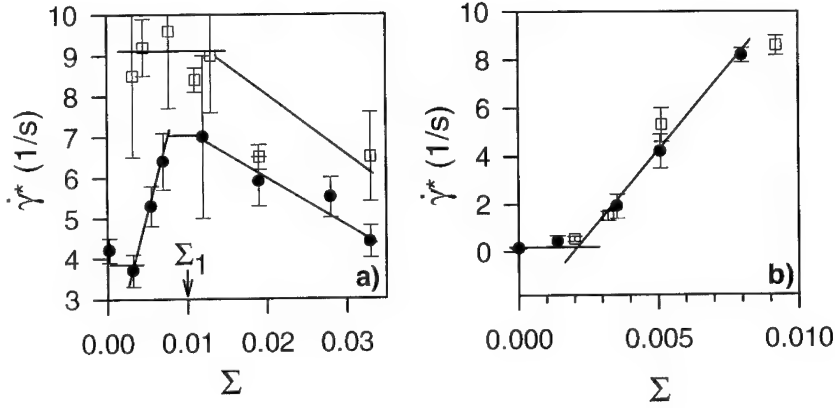
Figure 2: the critical shear rate $\dot{\gamma}^*$ versus the grafting density of the long chains for : a)brushes of type I, M_m=1000 (circles) or 790 (squares) kg/mol and M_b=96 kg/mol, and b)brushes of type II, M_m= 790 kg/mol, M_1=5 kg/mol and M_b= 96 (circles) or 170 (squares) kg/mol.

diameter D, and an elastic restoring force, f_e. D decreases as the shear rate increases, until the brush reaches the threshold of disentanglement : $D = D^*$, with D^* the distance between entanglements. The configuration with $D = D^*$, called the "marginal state", remains stable in a range of slip velocities : indeed, if D decreases further, entanglements will be lost, the friction will be reduced and D will increase so that lost entanglements are recreated. This is possible until the frequency of this mechanism, V_s/D^*, is larger than the reptation frequency $1/\tau_{rep}$. For the larger frequencies, $V_s \geq D^*/\tau_{rep}$, the melt disentangles from the brush, and the extrapolation length b saturates at its value b_∞ on ideal surfaces[9]. One can calculate the forces f_e and F_v and deduce the elastic and friction stresses, σ_e and σ, on the brush :

$$f_e = \frac{kT}{D} \quad \text{and} \quad F_v = Xa\eta_P V_s, \tag{1}$$

with kT the Boltzmann energy, X the number of chains of the melt trapped by each chain of the brush and η_P the viscosity of the melt. If M_b is smaller than M_e^2, X is equal to M_b/M_e[4]. As the chains of the brush are independent, the elastic stress is additive and given by :

$$\sigma_e = \frac{\Sigma}{a^2} f_e = \Sigma \frac{kT}{a^2 D}. \tag{2}$$

To deduce the shear stress, which is also additive, we need the number of chains of the melt trapped by the brush per area unit, $X\Sigma$. It cannot be larger than $P^{-1/2}$, the surface density of melt chains. Thus, for $\Sigma \leq \Sigma_c = X^{-1}P^{-1/2}$, one gets

$$\sigma = \Sigma Xa^{-1}\eta_P V_s. \tag{3}$$

For $\Sigma \geq \Sigma_c$, $X\Sigma$ has its saturated value and

$$\sigma = P^{-1/2} a^{-1}\eta_P V_s. \tag{4}$$
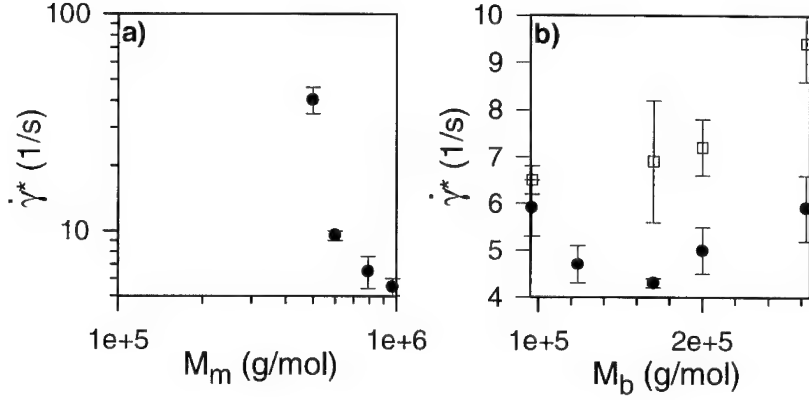
Figure 3: the critical shear rate $\dot{\gamma}^*$ versus **a)**the molecular weight of the flowing melt, M_m, for M_b= 96 kg/mol and Σ= 0.032 $\geq \Sigma_1$, **b)**the molecular weight of the brush chains, M_b, for M_m= 1000 (circles) or 790 (squares) kg/mol and Σ= 0.020 $\geq \Sigma_1$.

Thus, before the marginal state, $b = \eta_P V_s/\sigma$ is independent of V_s and scale as :

$$b_0 = aM_e/\Sigma M_b \quad \text{for } \Sigma \leq \Sigma_c, \tag{5}$$

$$b_0 = aP^{1/2} \quad \text{for } \Sigma_c \leq \Sigma \leq \Sigma_1. \tag{6}$$

In the marginal state, for $\Sigma \leq \Sigma_1$, $\dot{\gamma}$ sticks to its value $\dot{\gamma}^*$ at the transition and scales as

$$\dot{\gamma} = \dot{\gamma}^* = \Sigma \frac{kT}{a^2 \eta_P D^*}, \tag{7}$$

and $b = V_s/\dot{\gamma} = V_s/\dot{\gamma}^*$ is a linear function of V_s.

Experiments indeed show that b has a value b_0 independent of V_s before the transition with b_0 independent of Σ for $\Sigma_c \leq \Sigma \leq \Sigma_1$. In the marginal state, b is linear in V_s and the shear rate locks to $\dot{\gamma}^*$. Both results are different from what was observed for adsorbed layers[1, 2], and we think that this reflects the polydispersity of the tails of the adsorbed chains, which makes the shear rate a slowly increasing function of V_s even in the marginal state[3], whereas the brushes of the present experiments are low-polydisperse grafted chains, and give one clear threshold. With the well controlled brushes of type II, we have shown that, as predicted, $\dot{\gamma}^*$ is a linear function of Σ and is independent of M_b, for $\Sigma \leq \Sigma_1$. At very low densities $\Sigma \leq 0.001 \approx \Sigma^*$ however, we have observed that the shear rate saturates. This can be due to a residual adsorption of a few chains from the melt. This is consistent with the fact that for brushes of type II, the saturated value of $\dot{\gamma}^*$ is much lower than for brushes of type I, where the residual adsorption on the chloro-octamethyl-tetrasiloxane monolayer is not as well reduced as by the protection of the small (5,000 g/mol) grafted chains for type II.

At high grafting densities $\Sigma \geq \Sigma_1$, a slip transition is still observed. There is not yet any model to explain it in details. We can nevertheless say that the dynamic interaction between the melt and the brush is weakened because, as Σ increases, $\dot{\gamma}^*$ decreases. This can be related to the expected progressive expulsion of the melt chains out of the brush as Σ is

increased, an effect which should decrease $\dot{\gamma}^*$. On the other hand, the brush should be less deformable at high densities. The detailed investigation of the dependence of $\dot{\gamma}^*$ with the molecular parameters of the system should provide an insight of the mechanical response of the brush at such high grafting densities, where the brush chains behave in a collective manner. Such a collective behavior of the grafted chains shows up in the new dependences of $\dot{\gamma}^*$ versus M_m and M_b. Let us add that b_0 remains independent of Σ even at high grafting densities.

In conclusion, we have shown that a slip transition from a weak slip regime to a strong one occurs in flows of melts on brushes with well controlled densities, when the shear rate crosses a critical value $\dot{\gamma}^*$. The transition can be described by the extrapolation length b of the velocity profile, which has a value b_0 independent of the slip velocity V_s before the transition and then linearly increases with V_s, and by the critical shear rate $\dot{\gamma}^*$. At small grafting densities Σ, $\dot{\gamma}^*$ has been found to be linear in Σ and independent of the molecular weight of the chains of the brush, as predicted by a recent molecular model which assumes an independent behavior of the chains of the brush. Investigations of higher densities have shown that the chains of the brush do no longer behave independently as they do at low densities, leading to new dependences of the critical shear rate versus the molecular parameters of the system.

Acknowledgment

References

[1] K. B. Migler, H. Hervet, L. Léger, Phys. Rev. Lett. **70**, 287 (1993).

[2] L. Léger, H. Hervet, Y. Marciano, M. Deruelle and G. Massey, Israel J. of Chemistry **35**, 65, (1995).

[3] F. Brochard-Wyart, P.-G. de Gennes, Langmuir **8**, 3033 (1992).

[4] F. Brochard-Wyart, C. Gay, P.-G. de Gennes, Macromol. **29**, 377 (1996).

[5] O. Guiselin, Europhys. Lett. **17**, 225 (1992).

[6] E. Durliat, H. Hervet, L. Léger, Unpublished results.

[7] S. Oulad Hammouch, G. J. Beinert, J. G. Zilliox, J. E. Herz, Polymer **36**, 421 (1995).

[8] J. P. Folkers, M. Deruelle, E. Durliat and L. Léger, To be published.

[9] P.-G. de Gennes, C. R. A. S. Paris **288**, série B, 219 (1979).

Spectroscopic Studies of Confined Molecules

Under Shear

IWAO SOGA
Mitsubishi Chemical Corporation

ALI DHINOJWALA, YOON-KYOUNG CHO, AND STEVE GRANICK
Department of Materials Science and Engineering, University of Illinois, Urbana, IL 61801

ABSTRACT

We introduce two new techniques with the sensitivity to measure spectroscopic properties of confined molecules under shear. One concerns rheo-optics of fluids in micron-sized gaps. The experimental approach consists in applying periodic shear motion to fluid films confined between parallel plates separated by controllable film thickness from 0.1 to 100 micrometers. A key aspect is the concurrent ability to perform spectroscopic experiments (infrared or dielectric spectroscopy, or x-ray or neutron spectroscopy) of these fluids during flow.

The second technique consists in flow field experiments of polymer adsorption and orientation. The experimental approach is to produce one-directional shear, at rates up to 10^4 sec^{-1}, past adsorbed polymer layers of thickness less than 0.01 micrometers. The selective augmentation of vibrational modes oriented preferentially along the chain backbone is then used to probe chain orientation in the direction of flow in a laminar flow field.

INTRODUCTION

New experimental tools open up new fields of investigation. In particular, recent burgeoning interest in confined molecules in shear fields surely finds much of its impetus from the availability of experimental methods to produce shear of liquid films confined between molecularly-smooth solid surfaces. Various experimental devices now afford the capability to measure sliding forces for surfaces separated by fluids as a function of frequency, velocity, and separation between two solid surfaces, the thickness of the confined fluid films being

comparable to molecular dimensions. A review discusses various instrumental approaches and implications for tribology [1]. Computer simulations also enrich greatly the study of confined fluids [2], not least because of the difficulty of achieving direct information about molecular orientation and conformation by other methods.

Experiments with the sensitivity to measure spectroscopic properties of confined molecules under shear are desirable to augment the experimental information that can be obtained from force measurements. In this paper we introduce two techniques under development, for this purpose, in this laboratory:

- Rheo-optics of fluids in micron-sized gaps. The method is based on applying periodic oscillatory motion to fluid films confined between parallel plates at controllable film thickness from 0.1 to 100 micrometers. A key aspect is the concurrent ability to perform spectroscopic experiments of these fluids during flow.

- Flow field experiments of polymer adsorption and orientation. The method is based on producing one-directional shear, at rates up to 10^4 sec^{-1}, past adsorbed polymer layers of thickness less than 0.01 micrometers. The apparatus combines the surface sensitivity and directional resolution of polarized Fourier transform infrared spectroscopy (FTIR), in the mode of attenuated total reflection (ATR), with an adsorption cell designed to provide a laminar flow field.

I. MICRON-GAP RHEOMETER

The goal of the project summarized here was to prepare parallel solid plates at controllable separations from 0.1 to 100 micrometer separation. The resulting large surface area, when plates of diameter 0.1 to 1 cm are employed, should afford sufficient quantity of confined fluid to make possible various spectroscopic or scattering measurements (especially infrared and dielectric spectroscopy, and x-ray and neutron scattering). If metal-coated solid plates are employed, it should be possible to apply an electric field in the direction normal to the surfaces. It should be possible to perform these spectroscopic or scattering experiments in situ while making rheological measurements of shear forces.

A schematic diagram of the micron-gap rheometer, constructed for this purpose [3], is shown below:
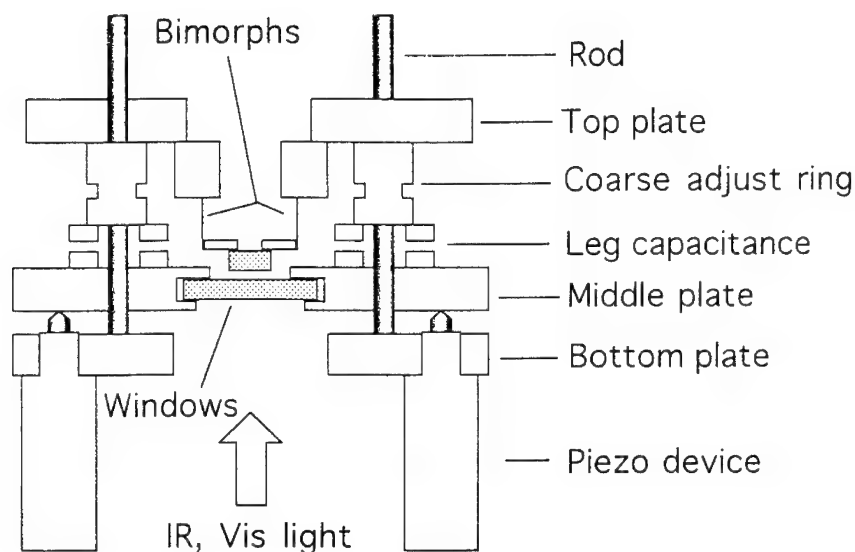
Figure 1:   Apparatus to position solid plates to be parallel at controllable separations while measuring shear rheology of a fluid confined between the plates. Fine adjustment of the plate separation is controlled by piezoelectric devices. Parallelism and magnitude of plate separation are measured either by interferometry (if the plates are translucent) or by capacitance.

Additional information concerning operation of the device, in the mode of transmission infrared (IR) step-scan spectroscopy during shear, is given below. Shear is applied to a top plate by applying voltage to a "sender" bimorph and the resulting motion (amplitude and phase relative to the drive) are detected in a "receiver" bimorph that is mounted symmetrically.   The shear frequency is variable in the range 0.1 to 300 Hz. The shear amplitude is variable from 0.1 nm to 10 micrometers. Parallelism is readily produced, by manipulating a tripod of piezoelectric positioning devices, to a resolution of 1 part in 10^4.   The plates are typically constructed of quartz, germanium, silicon, or metal, polished to the desired quality of surface flatness.
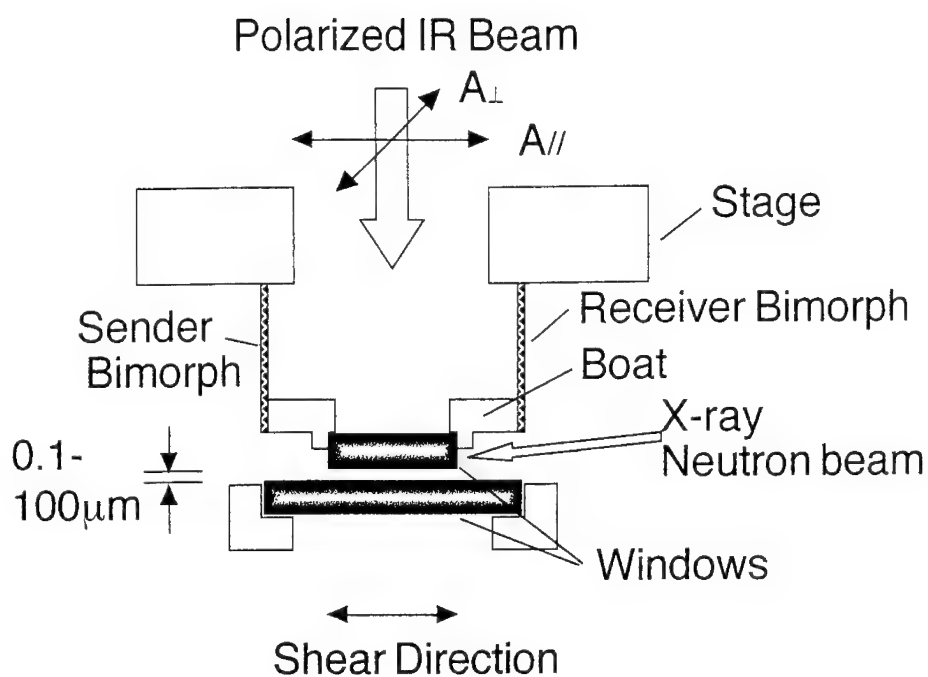
Figure 2: Elements of the rheo-optical configuration. In this example, a polarized infrared (IR) beam enters the sample from the top. For scattering or reflectivity experiments, x-ray or neutron beams enter from the side.

For successful operation of this instrument with opaque surfaces such as metals, a key element is the capability to achieve parallel configuration. As noted above, this relies on sensing capacitance at three points of a tripod attached to one of the surfaces. Comparison of the gap separation (measured by interferometry) with the gap separation (measured by capacitance) is shown in the figure below:
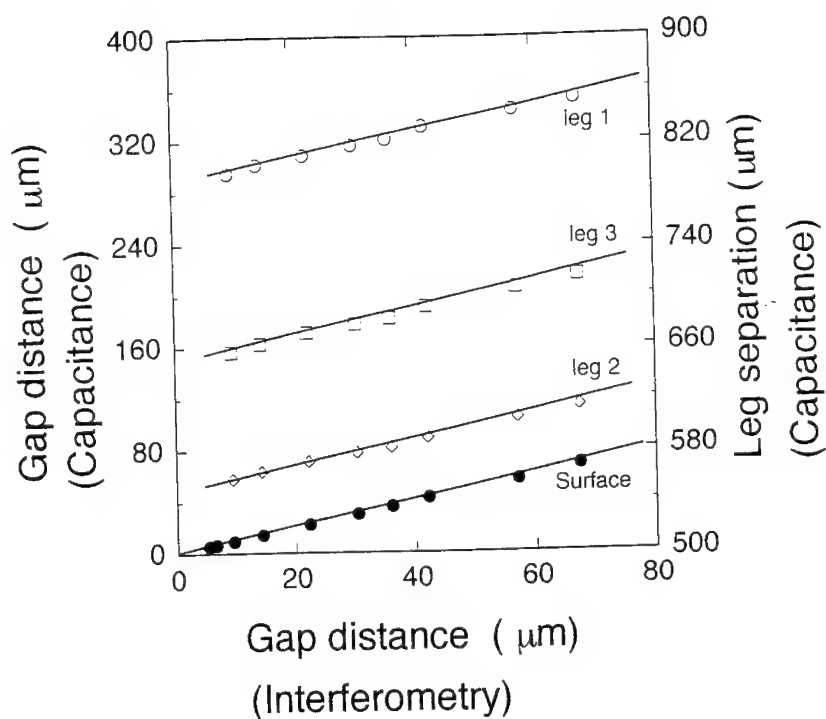
Figure 3: Comparison of interferometric and capacitance sensing of surface-surface separation. The line labeled "surface" shows the numerical agreement between these quantities. The lines labeled "leg 1," "leg 2," and "leg 3" show that the same resolution is obtained when capacitance is measured at the tripod legs on which one surface sits. Note that the closer the surface-surface separation, the higher the accuracy of capacitance measurement.

This apparatus is also designed to permit time-resolved infrared spectroscopy during cycles of periodic shear. The time resolution is variable between 20 microseconds and 1 second. The IR dichroism during the cycle of shear provides a measure of the orientation of various specific functional groups along confined molecules, thus allowing one to determine the molecular alignment at various points during periodic shear motion.
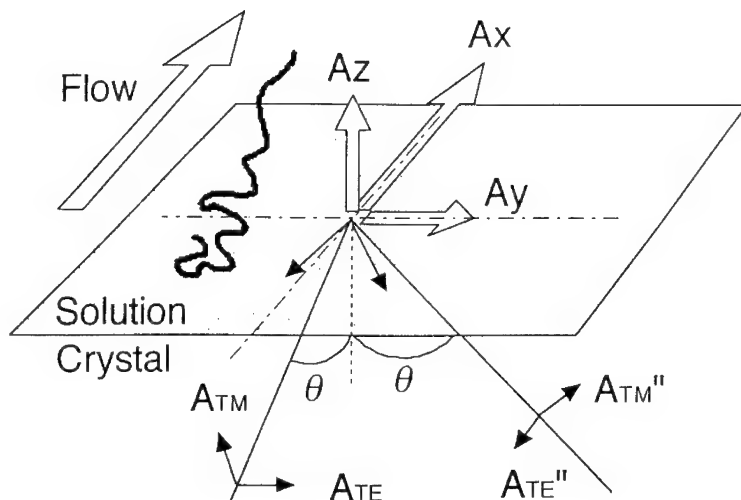
Figure 4: An evanescent IR wave penetrates to a depth of a few microns, and suffers losses due to the excitation of vibrational modes of the material in the surface region. The cell, designed to provide laminar flow up to very high shear rates, is placed in a compartment external to the FTIR spectrometer. The compartment is fitted with well-collimated optics in order to obtain enhanced angular resolution as the infrared beam enters the ATR cell. Solvent flow is provided and controlled by a pump.

Long ago, concurrent with development of the ATR technique, Flournoy and Schaffers described the polarized ATR spectroscopy of anisotropic films [5]. In this work, the ATR intensities (A_{TE} and A_{TM}) for plane polarized radiation are related to the three components of the absorption index, A_x, A_y, A_z Here x indicates the direction of flow, y is in the plane of the solid surface but normal to the flow, and z is the direction normal to the flow.

Considerable effort is required to extricate the three spatial absorption indices from the Flournoy-Schaffers equations. A technique commonly employed by those who study orientations in stretched polymer networks is to rotate the sample by ninety degrees, thus producing a second set of equations with the polarization directions exchanged. This approach has now been implemented for the study of polymer adsorption by use of a motorized rotation stage.

II. ATTENUATED TOTAL REFLECTION WITH A HEMISPHERICAL CRYSTAL

We now describe briefly a second apparatus, also designed to probe molecular alignment during flow processes. The problem here consists to understand polymer adsorption from solution to a <u>single</u> solid surface. The majority of prior analysis of polymer adsorption has focused upon quiescent systems: adsorption from a static solution [4]. Despite its obvious utility as a model system, we believe the quiescent state to be a special case in both nature and technology. Polymer adsorption in the presence of a flow field occurs in such applications as biocompatibility, filtration, enhanced oil recovery, viscometry, lubrication, wastewater treatment, and manufacture of materials. In order to fully understand the surface and rheological properties of polymer layers in these situations, it is essential to understand the parameters that affect conformational changes near the surface.

An apparatus has been constructed to apply a laminar shear field past an infrared prism at shear rates up to 10^4 sec^{-1}. The experiments were performed in a stainless steel, thermostatted flow cell. As shown below, the infrared (IR) beam is directed through a crystal, usually Ge or Si, and reflects at the crystal-solution interface with an angle, theta. The reflected intensity of the IR beam, polarized in the TE and TM directions, is altered by the presence of polymer at the crystal-solution interface and also may be sensitive to flow. The TE and TM intensities can be resolved into intensities in the cartesian coordinates (x, y, and z indicated in the Figure).

As illustrated below, polybutadiene was chosen for this preliminary study because molecular models show that its methylene asymmetric band (2925 cm^{-1}) should be in the direction approximately normal to the backbone of the chain.
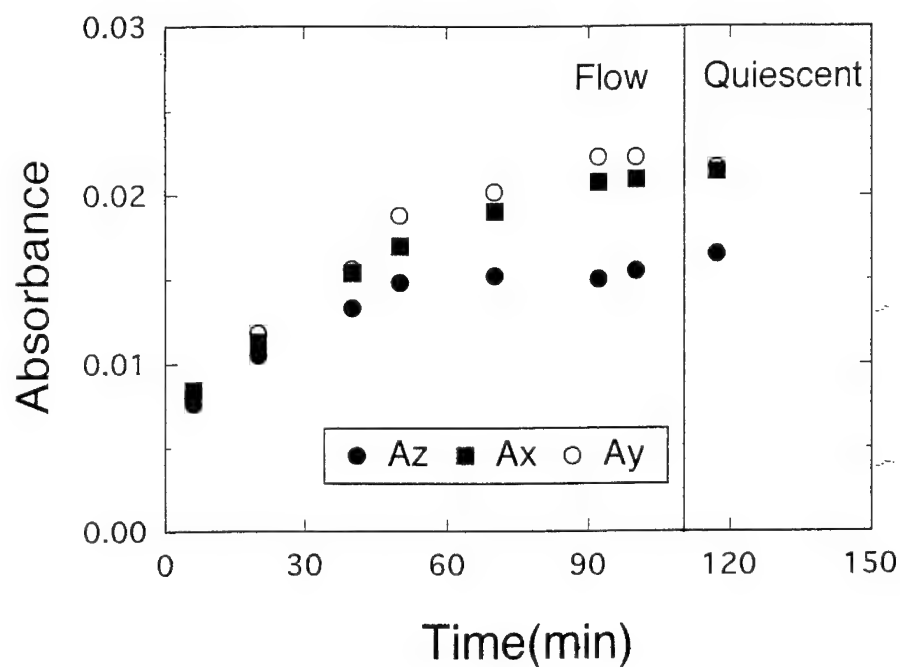
Figure 5: Time-dependent integrated absorbance of the methylene asymmetric band in the x, y, and z directions as 1,2 polybutadiene (molecular weight of the narrow-distribution sample was 1×10^6 g-mole^{-1}) was allowed to adsorb from flowing solution in carbon tetrachloride (0.05 mg-mL^{-1}) onto a Si crystal that had been oxidized in a controlled manner. The shear rate was approximately 10^4 sec^{-1}. The data show surprisingly little alignment in the direction of flow. On the other hand, adsorption in the z direction is significantly less than in the x and y directions. Since the dipole moment is roughly perpendicular to the chain backbone, this indicates that the action of shear was to extend the chains away from the surface. This net orientation persisted after cessation of flow.

REFERENCES

1. G. Luengo, J. N. Israelachvili, A. Dhinojwala, and S. Granick, Wear 200, 328 (1996); and erratum, in press.

2. B. Bhushan, J. N. Israelachvili, and U. Landman, Nature 374, 607 (1995).

3. A. Dhinojwala and S. Granick, submitted to J. Polym. Sci. Polym. Phys. Ed.

4. M. A. Cohen Stuart, T. Cosgrove, B. Vincent, Adv. Colloid Interface Sci. 24, 143 (1986).

5. P. A. Flournoy, W. J. Schaffers, Spectrochimica Acta 22, 5 (1966).

FLUID AND PROTEIN MOTION IN MONOMOLECULAR AND BILAYER FILMS OVERLYING SUBLAYERS OF FINITE DEPTH

H.A. STONE
Division of Engineering & Applied Sciences, Harvard University,
Cambridge, MA 02138, has@stokes.harvard.edu

ABSTRACT

Motion of a monolayer, bilayer or other surface film is affected by the presence of a surrounding fluid phase. Several recent experimental and theoretical studies have examined this viscous coupling with particular attention given to situations where the subphase provides the dominant resistance to motion. This research is summarized and the translation of a membrane-bound particle over a sublayer of finite depth is considered.

INTRODUCTION

There are a variety of dynamical processes that involve the fluid, or fluid-like, response of monolayers, bilayers, or other surface films (e.g. soap films). Examples include translational and rotational diffusion of proteins or other lipid molecules in cell membranes or model bilayers (e.g. [1]), shape changes of two-phase systems in model monomolecular films [2], laminar flow studies for measuring the viscous resistance of surface films (e.g. [3], [4]), laminar flow studies of soap films [5], etc. Several of these configurations are illustrated in figure 1. In this paper we summarize briefly recent studies of the fluid dynamical response of such surface film flows in configurations where resistance of the surrounding (subphase) medium and the presence of a nearby boundary are significant, and in some cases, the dominant sources of resistance to motion.

In each of the examples mentioned above, motion initially occurs in the surface layer and in turn produces motion in the surrounding fluid (typically water or air). This viscous coupling, and the geometries that often accompany the specific applications, make the analytical and numerical solutions more difficult than more common single phase flows. The subsequent dynamical response is characterized by resistance to motion from shearing the surface layer as well as shearing the fluid above and below the surface layer.

For example, suppose that there is flow in a monolayer with characteristic dimension R (e.g. a disk of radius R translates or flow occurs in a surface channel of radius R; see figure 1d), and take the surface film to be of uniform thickness h and have an effective Newtonian viscosity μ_m; the monolayer's viscous resistance is often represented in terms of a surface viscosity $\mu_s = h\mu_m$. Also, the surroundings are a Newtonian fluid with viscosity μ. The viscous forces that act on the circumference of a surface-bound translating disk, moving with speed U, are $O(\mu_m U h)$, while the viscous forces that act over the area $O(R^2)$ in contact with the surroundings is $O(\mu U R)$. Thus, the ratio of the resistance from the
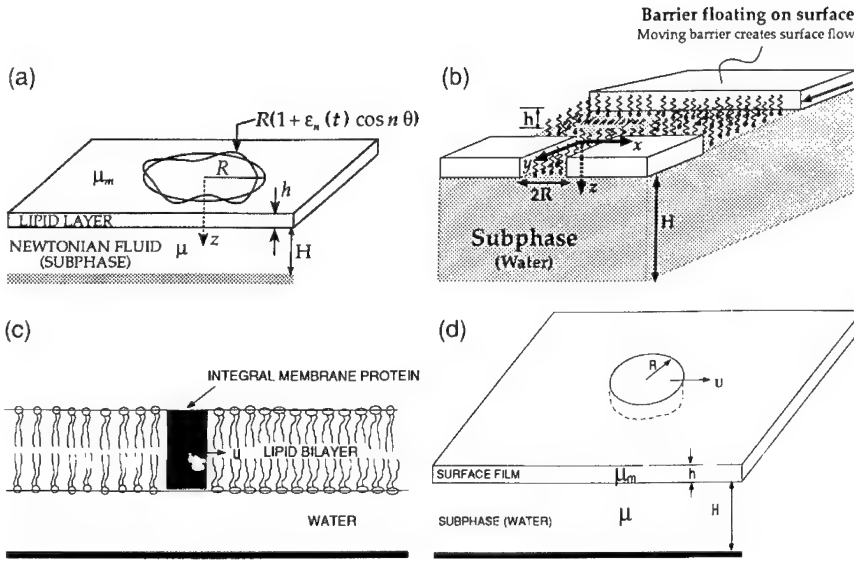
Figure 1: (a) Distorting domain in a two-phase monolayer; (b) pressure-driven flow in a surface channel in a Langmuir trough; (c) model of protein translation in a bilayer; (d) generic model of surface motions with coupling to a sublayer of finite depth.

surroundings to the in-surface resistance is characterized by a dimensionless parameter

$$\Lambda = \frac{\mu R}{\mu_m h} = \frac{\mu R}{\mu_s} \ . \tag{1}$$

Some typical values are $h = O(10\mathring{A})$, and $(\mu_m, \mu) = O(1 \text{ poise}, 10^{-2} \text{ poise})$. On the other hand, R can have a range of values depending on the application. For example, for models of protein diffusion in bilayers $R = O(10 - 50\mathring{A})$, for domain distortions $R = 5 - 50\mu m$, and for the surface channel flow apparatus [3] $R = O(100 - 200\mu m)$. Thus, Λ easily spans the range $10^{-2} < \Lambda < 10^2$. In common experimental configurations there is a sublayer of depth H and so the flow is characterized by Λ and H/R.

A classical example of the ideas of viscous coupling of the surface film to the subphase was provided by Saffman [6] who studied the translation (i.e. diffusion) of a bilayer-bound protein, modelled as a circular cylinder that spans the narrow height h. Saffman examined the limit $\Lambda \ll 1, H/R \gg 1$ and showed how inclusion of the effect of the fluid surrounding the bilayer was necessary to obtain a solution, while Hughes et al. [7] examined arbitrary Λ with $H/R \gg 1$, and Evans and Sackmann [8] investigated the effect of a thin lubricating layer (dynamics associated with thin lubricating films have also been discussed in [9]).

Here we report results for finite H/R and arbitrary Λ.

MECHANICAL AND MATHEMATICAL MODELS

For many monolayers and bilayer flows the sublayer motion is an incompressible low Reynolds number flow (the Reynolds number $\mathcal{R}$ is calculated according to $\mathcal{R} = \rho U R / \mu$, where U is a typical velocity and ρ is the fluid density), $\mathcal{R} \ll 1$, and so satisfies

$$- \nabla p + \mu \nabla^2 \mathbf{u} \; = \; \mathbf{0} \qquad \text{and} \qquad \nabla \cdot \mathbf{u} = 0 \; , \tag{2}$$

where $(\mathbf{u}, p)$ are the velocity and pressure, respectively. The surface layer is assumed to remain flat and uniform with no vertical variations, and so may be treated as a two-dimensional viscous flow with an additional body force $\mathbf{f} = \frac{1}{h} \mathbf{n} \cdot \boldsymbol{\sigma}|_S$ exerted from the sublayer on the surface S ($\mathbf{n}$ and $\boldsymbol{\sigma}$ denote the unit normal directed into the sublayer and the stress tensor, respectively). Denoting the mono- (or surface) layer velocity and pressure, respectively, as $\mathbf{u}^m$ and p^m, the sublayer equations of motion are thus

$$- \nabla p^m + \mu_m \nabla^2 \mathbf{u}^m + \frac{1}{h} \mathbf{n} \cdot \boldsymbol{\sigma}|_S \; = \; \mathbf{0} \qquad \text{and} \qquad \nabla \cdot \mathbf{u}^m = 0 \; , \tag{3}$$

and, in fact, often enter the solution procedure as a boundary condition on the sublayer.

The different problems illustrated in figure 1 may be solved exactly by utilizing (2) and (3) with appropriate boundary conditions. For example, the distortions of an unstable circular domain in a two-phase monolayer (or the relaxation of a distorted shape back towards a circle) may be studied by introducing a delta function forcing into (3) at the location $r = R$ of the original circular boundary. Analytical solutions of the unbounded configuration have been described using Hankel transform methods [10], while the effect of a nearby boundary (finite H/R) required numerical solutions [11] (see [12] for an integral equation approach to this problem). One use of these ideas is to examine the rate of relaxation of distorted domain shapes backs towards a circular equilibrium shape and so estimate the line tension between the two monolayer phases – this approach is discussed for extended "bola" shapes in [13] and examined further for polymer domains in a dilute surface phase in [14].

Also, for a surface channel flow (figure 1b) and models of protein translation (figure 1c) a velocity boundary condition is applied along one region of of the contact area between the surface layer and the subphase while equation (3) is applied along the remainder of the surface. Mathematically, these flow problems therefore have a mixed form of boundary conditions and solutions for arbitrary Λ and H/R require the treatment of dual integral equations (e.g. [6], [7]). An illustration of this idea is given in the next section.

A demonstration of the significant influence of a subphase fluid was provided by Schwartz et al. [3] (for a detailed analysis see [4]) in an experimental study of surface channel flows. Because the subphase resistance was more important than the in-phase resistance to shearing, the velocity profile in the surface channel was slower and more uniform than the possible parabolic (Poiseuille) flow, and by mass conservation the profile

was also broader. Similar profiles showing the flatter, broader structure characteristic of dominant subphase resistance have been documented in laminar falling soap films [15].

APPLICATION TO PROTEIN TRANSLATION IN BILAYERS

The translation of a membrane-bound protein molecule (modelled as a circular cylinder spanning the bilayer or surface film, or equivalently as a thin circular disk, which translates as velocity U) above a sublayer of finite depth was first investigated by Evans and Sackmann [8] for very thin lubricating sublayers. Their work was a natural out growth of detailed investigations of the infinite sublayer limit [6-7]. A solution valid for sublayers of arbitrary depth H relative to R may be developed (the details are to be published). In particular, the velocity field in the surface layer is, in cylindrical coordinates, ($0 \leq r < \infty$)

$$u_r^m(r,\theta) = U\cos\theta \int_0^\infty A(k)\sinh(kH)\left[J_2(kr) + J_0(kr)\right]\mathrm{d}k \tag{4a}$$

$$u_\theta^m(r,\theta) = U\sin\theta \int_0^\infty A(k)\sinh(kH)\left[J_2(kr) - J_0(kr)\right]\mathrm{d}k\ , \tag{4b}$$

where $A(k)$ satisfies the dual integral equations

$$\int_0^\infty A(k)k^{-1}\sinh(kH/R)J_1(kr/R)\mathrm{d}k = \frac{r}{2R} \quad\text{for } r < R \tag{5a}$$

$$\int_0^\infty A(k)k^2\cosh(kH/R)\left[k\tanh(kH/R) + \Lambda\right]J_1(kr/R)\mathrm{d}k = 0 \quad\text{for } r > R. \tag{5b}$$

Equations (5a-5b) can be solved for $A(k)$ and the force $\mathbf{F}$ on the translating disk can be calculated as a function of Λ and H/R. The translational diffusion coefficient D_t of the membrane-bound object is obtained from the Stokes-Einstein relation $D_t = kT/\zeta$, where $|\mathbf{F}| = \zeta U$.

The force on the translating membrane-bound disk is plotted in figure 2 as a function of both Λ and H/R. The dashed curve is the asymptotic approximation developed in [7], valid for small Λ and and an infinitely deep subphase, $H/R \rightarrow \infty$, and the square symbols are our numerical results for $H/R = 10^3$. The agreement is excellent and as indicated in [7] the asymptotic formula is accurate for $\Lambda < 0.6$. We see from figure 2 that decreasing the sublayer thickness to comparable to the particle size increases the force (and so decreases the diffusion coefficient) by about a factor of 2.

Evans and Sackmann [8] studied the resistance produced by a rigid planar boundary in the limit that the sublayer is thin by introducing a friction parameter b_s which arises from shear flow beneath the film and so for thin fluid films $b_s = \mu/H$. Thus, their dimensionless parameter ϵ is given in terms of material parameters by $\epsilon^2 = \Lambda R/H$. Evans and Sackmann's force-velocity relationship [8] may be compared with our numerical results and is in good agreement for $H/R \approx 1$ and small Λ, but the agreement, as might be expected, is not as good for larger H/R. The details of this comparison are in preparation.
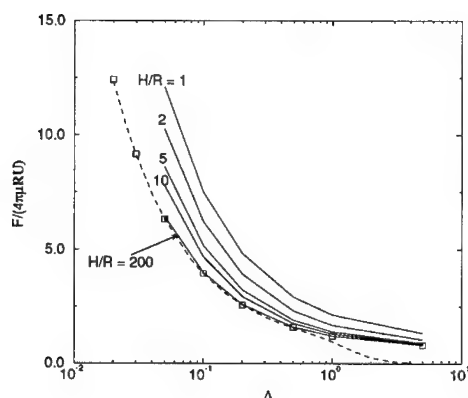
Figure 2: The force on a translating membrane-bound cylindrical particle. The dashed curve is the analytical formula developed in [8], and the squares are the numerical results for $H/R = 1000$. The solid curves are the numerical results for different H/R.

CONCLUDING REMARKS

We close with a brief discussion of other recent applications of similar ideas requiring the viscous coupling of the surface film flow to the motion of surrounding phases. Specifically, the Saffman-Delbrück model for the hydrodynamic features of protein diffusion has been generalized to higher concentrations of membrane-bound objects by accounting for long-range hydrodynamic interactions among the particles [17]. Also, several examples of the hydrodynamics of two-phase liquid monolayers have been examined by De Koker [18], including the effect of shear on a nearly circular domain and the translation of a circular fluid domain. In addition, capillary wave scattering by surface domains with different interfacial properties than the surrounding surface film have been studied by Chou et al. (1994, 1995). We also note that the effect of the surrounding liquid has been shown to be important in hydrodynamics studies of soap films [5, 15]. Finally, an important problem, which has largely been unstudied theoretically, is the effect of a non-Newtonian surface rheology (private communication with G.G. Fuller and D.K. Schwartz).

ACKNOWLEDGMENTS

for describing their recent soap film experiments. The Mendelsohns are thanked for their hospitality during a visit when this paper was written.

REFERENCES

1. P.G. Saffman and M. Delbrück, *Proc. Nat. Acad. Sci. USA* **72**, 3111 (1975).

2. H.M. McConnell, *Annu. Rev. Phys. Chem.* **42**, 171 (1991).

3. D.K. Schwartz, C.M. Knobler and R. Bruinsma, *Phys. Rev. Lett.* **73**, 2841 (1994).

4. H.A. Stone, *Physics of Fluids* **12**, 2931 (1995).

5. M.A. Rutgers, X.-I. Wu, R. Bhagavatula, A.A. Petersen and W.I. Goldburg, *Phys. Fluids* **8**, 2847 (1996).

6. P. G. Saffman, *J. Fluid Mech.* **73**, 593 (1976).

7. B. D. Hughes, B. A. Pailthorpe and L. R. White, *J. Fluid Mech.* **110**, 349 (1981).

8. E. Evans and E. Sackmann, *J. Fluid Mech.* **194**, 553 (1988).

9. D. Andelman, F. Brochard, C.M. Knobler and F. Rondelez in *Micelles, Membranes, Microemulsions, and Monolayers* edited by W.M. Gelbart, A. Ben-Shaul and D. Roux (Springer-Verlag, New York, 1994), p. 559.

10. H.A. Stone and H.M. McConnell, *Proc. Roy. Soc. London* **A448**, 97 (1995).

11. H.A. Stone and H.M. McConnell, *J. Phys. Chem.* **99**, 13505 (1995).

12. D.K. Lubensky and R.E. Goldstein, *Phys. Fluids* **8**, 843 (1996).

13. D.J. Benvegnu and H.M. McConnell, *J. Phys. Chem.* **96**, 6820 (1992).

14. E.K. Mann, S. Hénon, D. Langevin, J. Meunier, and L. Léger, *Phys. Rev. E* **51**, 5708 (1995).

15. M. Rutgers, X.-L. Wu and W. Goldburg, presented at the 1996 APS Fluid Dynamics Meeting, Syracuse, NY.

16. S.J. Bussell, D.A. Hammer and D.L. Koch, *J. Fluid Mech.* **258**, 167 (1994).

17. R.E. de Koker, *PhD thesis*, Stanford University, 1996.

18. T. Chou and D.R. Nelson, *J. Chem. Phys.* **101**, 9022 (1994).

19. T. Chou, S.K. Lucas and H.A. Stone, *Phys. Fluids* **7**, 1872 (1995).

A STUDY OF IMPACTING DROPLETS OF AN EMULSION OR SURFACTANT SOLUTION ON SOLID SUBSTRATES

M. VIGNES-ADLER, B. PRUNET-FOCH, F. LEGAY, N. MOUROUGOU
Laboratoire des Phénomènes de Transport dans les Mélanges du CNRS, SP2MI, F-86960
Futuroscope Cedex, France, adler@io.cnusc.fr

ABSTRACT

Coating of solid surfaces with uniform, thin liquid films occurs in many industrial processes. A common process consists of spraying some liquids or emulsions on a freshly created solid surface. In this context, we have investigated the impact of a single droplet of various emulsions and surface-active solutions on a solid substrate using a high frequency fluorescent visualization technique (1 picture every 0.25 ms). Whatever the materials in presence, the drop spreads and then retracts under the action of inertia and capillarity respectively. Inertia induces spreading and generates a peripheral rim which is unstable to fingering. Then contact line instabilities appear under the form of festoons with pure liquids which are damped with surface-active solutions and amplified with emulsions. When the adsorption kinetics of the surfactant is slow, the equilibrium surface tension is not restored during the duration of the experiment and the drop can bounce back.

INTRODUCTION

Spraying of liquids is now a practical process to coat solid surfaces with liquid films. It is used for example, in painting, steel industry, agriculture, ink jet process, etc... In most applications, the sprayed liquid is never a pure liquid but is rather a solution, a suspension or an emulsion; the major concern is usually to get a regular, uniform, thin coated film without dry patches or blisters. Actually, spraying consists of projecting tiny liquid droplets which reach the surface with a large impact velocity and which are supposed to spread and achieve coalescence, spontaneously or by superimposing some external stress. Hence the basic elementary phenomenon which rules the process is the projection of a single liquid droplet reaching a solid surface with a large kinetic energy and the fate of this impacting droplet is the purpose of the present paper.

The general study of drop impact on solid targets was initiated by Worthington [1] at the end of the last century. Much progress could be made with the development of sophisticated visualization technology and computational methods. A recent literature review on the impact phenomenon has been made by Rein [2]. A typical experiment can be described as follows : when a drop impacts on an unyielding solid target, it spreads under the action of inertia (step I), reaches a maximum wetted area while the contact line presents instabilities related to inertia (step II) and then it retracts due to the capillary forces acting on its free surface (step III). Eventually, it may spread again because of gravity and of the unbalanced capillary forces acting at the contact line between the drop and the solid substrate (step IV). Depending on the substrate properties (e.g. roughness, surface energy and temperature), and on the drop kinetic energy at the impact time, splashes can be observed; depending on the nature of both liquid and substrate, the capillary

forces can be so much amplified that the drop bounces back from the solid substrate and falls again.

To the best of our knowledge, previous investigations have been mainly focused on the drop impact hydrodynamics (analytically [3,4], numerically [5,6] and experimentally [7-10]) i.e. on steps I and II which are basically controlled by the inertial forces assuming that the surface tension remains constant. Our work is rather focused on the following steps of the impact process once forces of physicochemical origin come into play.

Indeed, two key-points must be emphasized for the understanding the present work.
(i) Just before impacting, the droplet is fairly spherical and its surface tension can be considered as equal to its equilibrium value. When the drop has impacted on the target, it becomes essentially like a pancake pushed on the substrate; its total area has extended by one order of magnitude in a few milliseconds. If the liquid is a surface-active solution for example, the drop surface may no longer be in thermodynamic equilibrium with its bulk subsurface and the relevant surface property is no longer the equilibrium surface tension but rather a dynamic one.
(ii) During the drop inertial spreading, the solid surface is wetted by the liquid and this may change its surface energy by specific adsorption of some substances.

These two experimental facts imply major differences with classical wetting experiments where a droplet is carefully deposited on the solid substrate. In this latter case, spreading is driven either by gravity or capillary forces [11], and the droplet spreads on an ever "clean" surface; the liquid surface is usually in equilibrium with its subsurface.

In this paper, recent experimental findings on the impact of non pure liquid drops are presented. Using a high frequency fluorescent visualization technique, surface-active solutions and emulsions are investigated. We show that contact line instabilities develop when the capillary number is sufficiently low; festoons appear with pure liquid, but they are damped with surface-active solutions and amplified to give fingers with emulsions. We measure the dynamic surface tension resulting from a fast dilation of the solution surface by the maximum bubble pressure apparatus and we show that if the adsorption kinetics of the surfactant is slow, the equilibrium surface tension is not restored during the duration of the experiment and the drop can bounce back.

EXPERIMENT

Materials

Experiments were carried out with some pure liquids, water, dimethylnaphtalene (DMN) ..., several surface-active solutions and emulsions. We have used solutions of non ionic surfactants, Soprophor 724P, Rhodasurf 870, Silwett L77, as well as of ionic ones - Sodium Dioctyl Sulfosuccinate (DOS), Sodium Dodecyl Sulfate (SDS), Tetradecyl Trimethyl Ammonium Bromide (TTAB), Cetyl Trimethyl Ammonium Chloride (CTAC). A rather high concentration 10 times the critical micellar concentration (cmc) has been used. The molecular weights of these non-ionic surfactants are rather high with a slow adsorption kinetics while the adsorption kinetics of the ionic ones is fast; besides, Silwett 77 is a superspreader. The investigated emulsion is a 5% wt oil in water (O/W) emulsion. The oil part consists of 92% wt of DMN and 8% wt of oleic acid. A non-ionic polyvinyl emulsifier is used at a concentration of 1% wt in the oil phase.
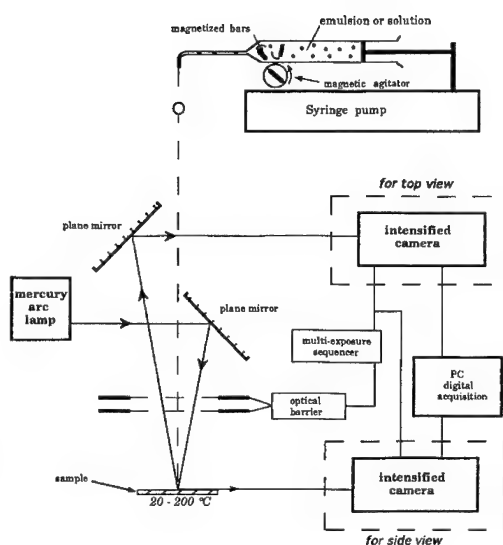
Fig. 1 - Experimental device

The solid substrates were smooth glass plates coated by complexed stearic acid, metallized glass plates and steel plates treated by an antioxidizing; the latter choice has been motivated by engineering applications. The plates surface-energy are about 27 mN/m for the first ones and 40 mN/m for the two others; the glass plates have a very small roughness (Ra ≅ 0,002 μm) and the steel plates have medium and high roughnesses (0.5 μm < Ra < 5 μm).

Methods

A schematic representation of the experimental apparatus is shown in Fig. 1. Drops of 2-3 mm of diameter are formed at the tip of a capillary. These drops fall under gravity from a height of 60 cm onto the solid substrate. At the beginning of its fall, the drop is detected by a first optical barrier which permits the set to zero of the camera scanning, waiting for the shutter trigger. At the end of the fall, the drop passes through two other optical barriers which are connected to an electronic card. The two interruptions trigger the camera electronic shutter with a programmed shot delay: this provides the time $t = 0$ of the spreading after correction and the impact velocity and fixes the time t at which the snapshot is requested. The acquisition system is composed of a high definition tube camera, with a light intensifier, connected to a computer containing a digitization card of 1024x1024 pixels with 256 gray levels.

With this high-speed photographic technique, we take one drop picture at different times t for a series of drops generated in the same experimental conditions. Assuming that the impact is sufficiently reproducible from drop to drop, the evolution of the drop dynamics can be rebuilt. This system can also be used as a double-shot method : each profile picture contains two superimposed exposures of the same drop to determine the impact moment precisely; the first exposure corresponds to the drop in flight and the second exposure, either to the drop later in flight or to the drop spread on the solid surface. The drop volume and its impact velocity can therefore be measured precisely.

A fluorescent dye is dissolved in the solutions and either in the water or in the oil for the emulsion droplets to distinguish between the phases. Top and side views of the droplet are obtained independently on different seies of drops since we are not equipped to get them simultaneously. Top views give information on the aspect of the contact line and on the location of the dyed phase. Side views provide the diameter d(t) of the wetted surface, the apex h(t) and the contact angles of the main drop as functions of time; the spreading factor $\beta(t) = d(t)/d_i$ and the flattening factor $\zeta(t) = h(t)/d_i$ where d_i is the initial drop diameter are easily deduced. The initial

drop diameter depends mainly on the diameter of the capillary tip and on the liquid surface tension.

RESULTS

Typical plots of the spreading and flattening factors are represented in Fig. 2a-b for pure water and surface-active solutions impacting on a glass plate coated by stearic acid, and in Fig. 2c-d for emulsions on a steel plate.
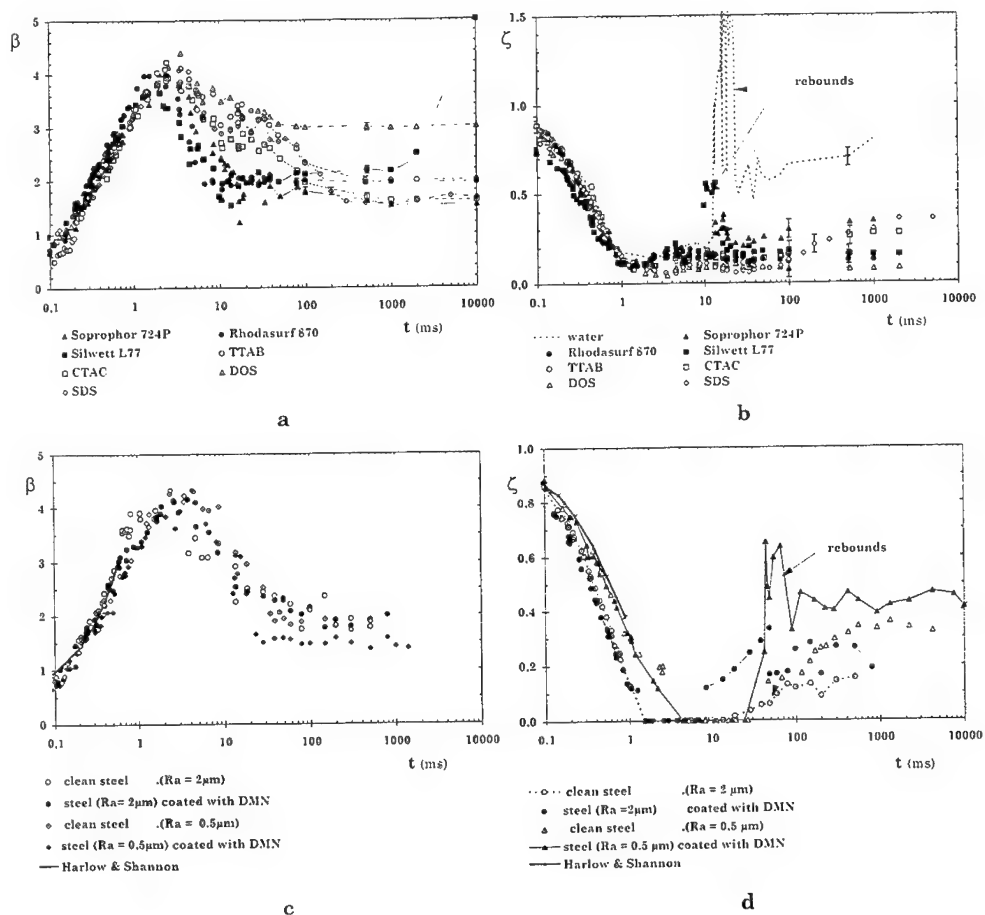
Fig. 2 - Spreading factor β and flattening factor ζ
a, b/ surfactant solutions on smooth glass plate coated by complexed stearic acid,
c, d/ emulsion (5% O/W) on rough steel plate

Some general trends were observed:

(i) As trivially expected, the spreading factor increases while the flattening factor decreases with time (step I). The maximum wetted area is reached at about 3ms and it is 4 or 5 times the initial diameter.

(ii) Splashes are observed on rough or heated steel surfaces just after the impact at $t = 1.5$ ms as it has been already observed for other systems [8]. No splashes are observed on smooth surfaces.

(iii) The radial velocity decreases from 10 to 0 m/s and then reverses its sign ; just before the wetted area of the spread drop is maximum a thicker rim is formed at the periphery of the drop, the radial velocity is almost vanishing and one can observe that instabilities of the contact line have already developed (step II). Festoon instabilities appear with pure liquids and surface-active solutions while fingering instabilities are generated with emulsions (Fig. 3). The festoon amplitude is much smaller for solutions than for pure liquids of comparable viscosity; moreover it decreases when the liquid viscosity increases. Eventually, the festoons wavelength is smaller than the fingers one .

coated by complexed stearic acid $\gamma_{substrate} = 27mN/m$	metallized $\gamma_{substrate} = 50mN/m$

| *Festoons with pure water* | *Festoons with surfactant solutions* | *Festoons with pure water* | *Fingers with emulsions* |
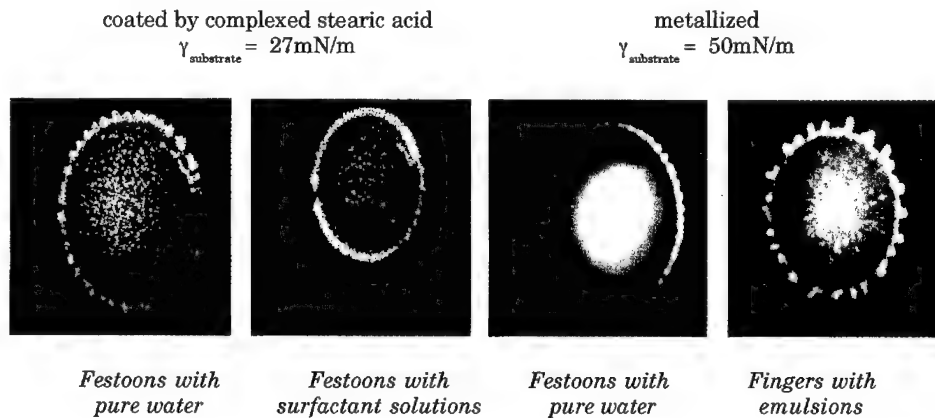
Fig. 3 - Instabilities of the contact line on a smooth glass plate
at : $t_{max} = 2,5 - 3$ ms.

| a | b |
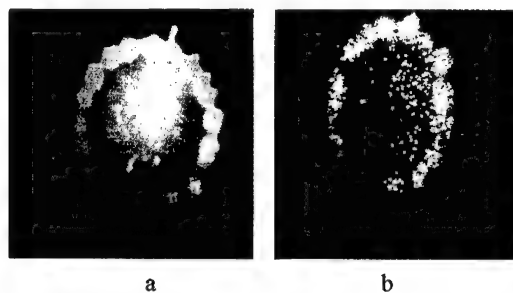
Fig. 4 - Varicosities : drops impacting on rough steel plate (Ra = 2 μm)
a/ dyed water,   b/ 5% O/W emulsion (dyed oil).

(iv) During the retraction phase (step III), one can observe that the festoons or fingers have coalesced at the periphery of the spreading droplet and that they are replaced by varicosities (Fig.4). Then, at t ≅ 10 ms, as retraction proceeds, the varicosities are damped to form an undeformed rim at the periphery of the drop. The whole phenomenon looks like a « reverse » Rayleigh instability.

(v) Major differences also occur as retraction proceeds (Fig. 5). With water or non-ionic surfactant solutions, the capillary waves are strongly amplified at the free surface: this phenomenon is so strong with water on low energy glass plates that the drop bounces back ; this is not true on metallized glass plates which have a higher surface energy. With ionic surfactants solutions and emulsions, this effect does not occur. The retraction is much more intense with water and non-ionic solutions (full symbols) as it is obvious in Fig. 2 where $\zeta(t)$ decreases the fastest.

(vi) At the end, the drop may spread again on a wetted surface depending on the value of the contact angle until the equilibrium of the three phase contact line is restoresd as in classical wetting (step IV).
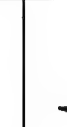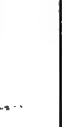
	Glass plate coated by complexed stearic acid			Clean steel plate
	Water	Soprophor 724P	DOS	Emulsion
7-8ms				
10-12 ms				
17-20 ms				
1s				

Fig. 5 - Retraction of the drop on various solid substrate.

DISCUSSION

Obviously, the drop behavior results from the balance between inertia and capillary forces and viscous stresses; this balance is controlled by the Reynolds and capillary numbers based on the velocity of the leading edge which varies as time elapses.

The numerical solution of Harlow and Shannon [5] is given in Fig. 2 who predicted the evolution of the shape of an impacting drop by integrating the Navier equations for a constant liquid volume assuming that the liquid is incompressible and neglecting viscous and surface tension. The experimental curves are fairly well fitted by the numerical solutions until about 500µs, whatever the liquid and the substrate surface properties. This means that inertia controls spreading during step I.

Hence, our discussion is mainly focused on steps III and II when the influences of the capillary forces and inertia forces, that cause retraction and spreading respectively, are of the same order of magnitude.

Analysis of the retraction phase (step III)

As obvious in Fig. 2, the retraction behavior drastically differs depending upon the solutions and emulsions for the same substrate.

While in flight, the drop is spherical and its surface is $S = \pi d^2_i$. When the drop reaches its maximum diameter on the substrate, it looks like a flat pancake of diameter d_{max} and mean thickness H_N. Hence, its surface increases drastically to $S_{max} \cong 1/2 \ (d_{max}/d_i)^2$ in a few ms. The corresponding surface dilational maximum rates λ_{max} range between 250 and 600 s^{-1}. It induces a rapid and large increase of the surface tension because surfactants may have no time to restore its equilibrium value at the free surface for the duration of the experiment. The relaxation time depends on the kinetics of adsorption of the surfactants.

The dynamic surface tension γ_d was measured by the Maximum Bubble Pressure Method (MBMP) which provides a direct measurement of γ_d vs time resulting from a large surface expansion rate $\lambda = \dfrac{1}{S} \dfrac{\Delta S}{\Delta t}$. There are other devices to measure γ_d but the advantage of the MBPM is to provide measurements of γ_d for very short times (< 10 ms) and large λ as in our experimental configuration. γ_d vs λ is plotted in Fig. 6 : the present λ_{max} are in the domain delimited by the hatched strip while the surface tensions measured at low λ are very close to the equilibrium surface tensions γ_e. Obviously, for all the investigated surfactants, γ_d is higher than γ_e, but for the non-ionic surfactants and also for the CTAC it is much higher since it is close to the water surface tension. This can explain why rebounds are observed with the Soprophor 724P and the Silwett 77. However, there is an apparent contradiction with the CTAC for which no rebound is observed. Actually, the non-ionic substances possess a slow adsorption kinetics and the ionic a fast one. This is better appreciated in Fig. 7 where the surface pressure $\Pi = \gamma_{water} - \gamma_d$ is plotted vs $t^{1/2}$. All the ionic surfactants reach a plateau, which means that the equilibrium value is rapidly restored while it is not true for the non-ionic surfactants. This result is somewhat amazing for Silwett 77 if one remembers that it is a superspreader. Its superspreading properties are explained by its very low equilibrium surface tension and they are not correlated to its adsorption kinetics which rules the present phenomenon.

111
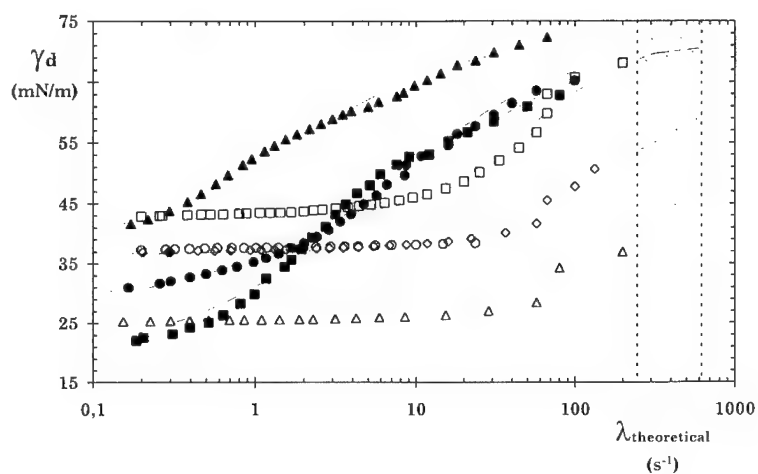
Fig. 6 - Dynamic surface tension of the surfactant solutions.
Δ Soprophor 724P, ■ Silwett L77, o TTAB, Δ DOS, ● Rhodasurf 870, □ CTAC, ◊ SDS.
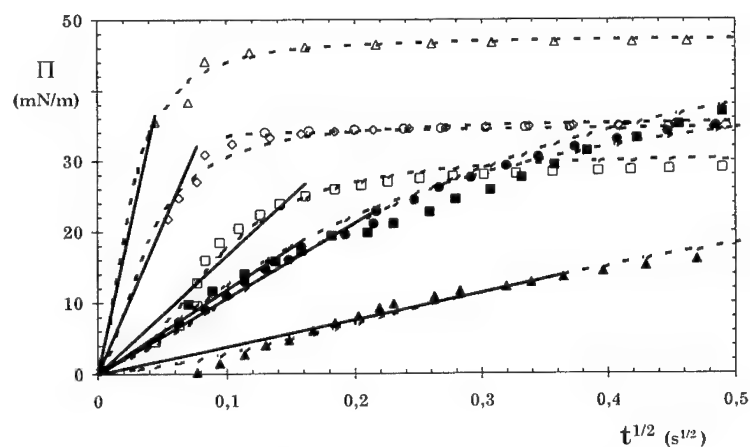
Fig. 7 - Surface pressure of the surfactant solutions
Δ Soprophor 724P, ■ Silwett L77, o TTAB, Δ DOS, ● Rhodasurf 870, □ CTAC, ◊ SDS.

Contact line instabilities (step II)

Let us now discuss the instabilities of the contact line which appear just before β_{max} is attained while the velocity of the contact line is still positive. For pure liquids, they look like festoons. They are damped for the surface active solutions and amplified for the emulsions. Visual

inspection of the photos shows the presence of a thicker rim which does not exist at t = 1.5 ms when the splashes due to the impact are visible. It means that the splashes and the contact line instabilities have not the same origin.

Previous studies have shown that a thin wetting film, in an open geometry, driven by an external body force is unstable to fingering [12]. This was shown in experiments where a broad band of viscous fluid is released so as to flow down a constant slope [13] The instability is maximal in the capillary region near the contact line, where the force due to the surface tension is comparable to the viscous and gravitational forces.

There is a strong similarity with the present case where inertia instead of gravity is acting as an external body force and forces the liquid to spread whereas the capillary forces prevents it. This results in a rim which is unstable to fingering since capillary pressure gradients amplify the growth of the convex portions of the rim. Such instabilities were calculated by Troian et al [12] who have shown that the fingering scales as $1 - H_N (Ca)^{-1/3}$ where H_N is the thickness of the central part of the drop.

The velocity V of the leading edge can be easily obtained from a polynomial fit of $\beta(t)$. We have used V and γ_d to evaluate the capillary number Ca as a function of time. H_N was evaluated assuming that, just before the festoons are developing, the drop has a half doughnut shape. Data give $H_N \simeq 100\mu m$ and $Ca \simeq 10^{-3}$; it gives $l = 1$ mm which is a good order of magnitude of the length of the festoons measured in Fig. 3a for a water drop impacting a low surface energy plate.

Surface-active solutions differ from pure liquids because they usually have a lower surface tension and also because Marangoni effects can be observed. In the present experiment, the origin of the Marangoni effect is the departure from equilibrium surface tension produced by the dilational deformation of the surface [14]. The associated surface tension gradients generate 2D motions in the surface; the latter are always dissipative because of the dragging action of a moving surface layer which induces shear viscous stresses. One can easily understand that, with surface-active solutions, the Marangoni effect damps the rim instabilities by increasing the viscous dissipation.

We have not yet fully understood why with emulsions the festoons are amplified at such a point that they give fingers. Since no Marangoni effect is expected with emulsions, this might be purely inertial in character since the velocity of the thicker part is larger than the thinner part.

CONCLUSION

An important conclusion of this work is the drastic influence of effects of physicochemical nature on the impact of liquid drops onto solid substrates. The large dilational deformation of the surface produces large deviation of the surface properties from their equilibrium value. The fate of the spreading drop is then strongly dependent on the adsorption kinetics of the surface active solutes which controls the dynamic surface tension of the solution and the evolution of the capillary pressure gradients.

REFERENCES

1. A.M. Worthington , Proc. R. Soc. Lond. **A 25**, 261, (1876).

2. M. Rein, Fluid Dyn. Res. **12,** 61, (1993).

3. P. Savic and G.T. Boult, Nat. Res. Council of Canada, Rep. No Mt-26, (1955).

4. A.L. Yarin and D.A. Weiss, J. Fluid Mech. **283,** 141, (1995).

5. F.H. Harlow and J.P. Shannon, J. Appl. Phys. **38** (10), 3855, (1967).

6. J. Fukai, Z. Zhao, D. Poulikakos, C. M. Megaridis, O. Miyatake, Phys. Fluids **A 5** (11), 2588, (1993).

7. J. Fukai, Y. Shliba, T. Yamamoto, O. Miyatake, D. Poulikakos, C. M. Megaridis, Z. Zhao, Phys. Fluids **7** (2), 236, (1995).

8. Z. Levin and P.V. Hobbs, Phil. Trans. R. Soc. Lond. **269,** A1200, 555, (1971).

9. C.D. Stow and M.G. Hadfield, Proc. R. Soc. Lond. **A373,** 419, (1981).

10. S. Chandra and C.T. Avedisian, Proc. .Soc. Lond. **A432,** 13, (1991).

11. A.M. Cazabat, Contemp. Phys. **28**(4), 347, (1987).

12. S. Troian, E. Herbolzheimer, S. A. Safran and J. F. Joanny, Europhys. Lett. **10**(1), 25, (1989).

13. H. E. Huppert, Nature **300,** 427, (1982).

14. L.E. Scriven and C.V Sternling, Nature, **167,** 186, (1960).

NORMAL-STRAIN INDUCED CHANGE IN LATTICE-TYPE FOR CONFINED CYCLOHEXANE FILMS

J.E. CURRY *, J.H. CUSHMAN **
* Department of Soil, Water and Environmental Science, University of Arizona, Tucson, AZ 85721, curry@ag.arizona.edu
** Center for Applied Mathematics, Math Sciences Building, Purdue University, West Lafayette, IN 47907

ABSTRACT

One to three layer cyclohexane films confined between mica-like surfaces are studied to elucidate changes in the films' lattice-type. The laterally confined film is in equilibrium with the bulk fluid that is well into the liquid regime of its phase diagram. Monte Carlo simulations are conducted at constant chemical potential, temperature, and V=Ah, where A is the lateral area and h is the separation between the walls. One and two layers of fluid freeze as h increases. The one layer fluid has a triangular lattice, while the two layer fluid exhibits first a square lattice and then a triangular lattice with increasing surface separation. In contrast to previous studies, solidlike order is induced primarily by the strong fluid-solid interaction and is largely a function of pore width. A shift in the relative alignment of the surfaces perturbs the solidlike fluid structure but does not cause the sudden shear melting transition associated with epitaxial alignment of the fluid atoms with the surface. There is a correlation between the shear stress calculated in the computer experiments and that measured in Surface Forces Apparatus experiments.

INTRODUCTION

Fluids in micropores, (i.e., pores with at least one characteristic dimension on the order of a few fluid molecular diameters), are different from their bulk counterparts, because of the symmetry breaking character of the surfaces [1]. For example, in a slit-pore composed of two plane parallel mica surfaces, Surface Forces Apparatus (SFA) experiments reveal wall-induced layering of fluid films in pores up to ~10 molecular diameters wide [2, 3]. SFA experiments also show that the viscosity of a fluid in a slit-pore may increase by several orders of magnitude due to local ordering within the fluid layers [4, 5].

Computer simulations of confined fluids also show fluid layering parallel to the walls and, additionally, reveal translational order within the layers depending on the relative alignment of the surfaces [6 - 8]. Translational order causes a decrease in the inplane diffusion coefficient and can cause the fluid to become solidlike or "freeze". The fluid displays complex character, such as shear melting [7, 9], fluid-solid phase coexistence [10] and phase separation of miscible binary mixtures [11] in corrugated pores. In most of these simulations, however, fluid and solid atoms are the same size and solidlike order induced in the fluid is directly related to epitaxial alignment of the fluid molecules with the solid surface. Solidlike order results when the fluid is able to pack so that epitaxial alignment is achieved with both surfaces. If the surfaces are arranged so that epitaxial alignment with both surfaces is not possible then the fluid is liquidlike.

In many microporous systems of interest it is likely that the fluid molecules and solid surface atoms will not be the same size. Epitaxial alignment will be less important if the fluid and solid atoms are of different size, particularly if the solid atoms are much smaller. The fluid properties will then be more dependent on the strength of the interaction between the fluid and the solid. In this work we use grand canonical ensemble computer simulations to study a fluid in

a slit-pore where the fluid molecule is much larger than the atoms comprising the solid surface. We study, in particular, the structure and shear stress properties of cyclohexane confined between mica surfaces, a system that has been extensively studied in SFA experiments [3]. The fluid molecules are represented as spherical Lennard-Jones molecules with diameter and mass of cyclohexane. The surfaces are atomically structured with the size and mass of the surface atom and arrangement chosen to represent the first layer of oxygen atoms on a mica surface.

Even though epitaxial alignment is not as important as in previous studies [9-11], we observe solidlike order for one and two layer fluids at certain pore widths. Solidlike order is induced primarily by the strong fluid-solid interaction and is largely a function of pore width. We observe two lattice types, triangular and square, that alternate as a function of the normal strain. A shift in the relative alignment of the surfaces perturbs the solidlike fluid structure but does not cause the sudden shear melting transition associated with epitaxial alignment of the fluid atoms with the surface. Solidlike order in the pore fluid depends primarily on the pore width and secondarily on the relative alignment of the surfaces. There is a positive correlation between the shear stress calculated in the computer experiments and that measured in SFA experiments.

EXPERIMENT

Model and Computational Method

The slit-pore model consists of a simple fluid confined transversely by flat walls that possess structure at the atomic level. The fluid in the open slit pore is in equilibrium with its bulk phase counterpart that is in the liquid state at 1 atm and 303K. Fluid and wall atoms are spherical, non-polar, Lennard-Jones (LJ) atoms characterized by diameters σ_i and interaction energies ε_i where i indicates fluid (f) or wall (w) atom. Following Somers et al. [12], we choose the molecular diameter, mass and interaction strength parameters so that the fluid molecules represent cyclohexane, $\sigma_f = 5.4$ Å and $\varepsilon_f = 4.473 \times 10^{-21}$J, and the wall atoms represent oxygen, $\sigma_w = 2.71$ Å and $\varepsilon_w = 1.629 \times 10^{-21}$J. The reduced chemical potential, μ/ε_f, as calculated by Somers et al. [12] is -14.935.

The distance between the pore walls, h, is measured from the center of the wall atoms. The relative lateral alignment of the walls in the x-direction, or registry, α, is given in terms of the coordinates of the corresponding atoms: $x_i^{(2)} = x_i^{(1)} + \alpha l$; $y_i^{(2)} = y_i^{(1)}$; $z_i^{(2)} = z_i^{(1)} + h$ where superscripts (1) and (2) refer to the lower and upper walls respectively and l is the lattice constant in the x-direction which is taken to be $1.985\sigma_w$. Note that the walls are kept permanently aligned in the y-direction. We set α to zero when the walls are precisely in registry and to 0.5 when they are completely out of registry.

The total potential energy of the confined fluid is approximated as a pairwise sum of LJ (12,6) interactions with cylindrical cutoff $\sigma_{ij} = 1/2 (\sigma_i + \sigma_j)$. The interaction energy between atoms i and j is thus given by

$$u(r_{ij}) = 4\varepsilon_{ij}\left[\left(\frac{\sigma_{ij}}{r_{ij}}\right)^{12} - \left(\frac{\sigma_{ij}}{r_{ij}}\right)^6\right] \qquad (1)$$

where $\varepsilon_{ij} = (\varepsilon_i\varepsilon_j)^{1/2}$. The potential energy cutoff radius is $3.5\ \sigma_{ij}$. Corrections due to the cutoff are calculated and added according to Schoen et al. [13].

The slit pore walls are constructed to represent mica surfaces (See Fig. 1). Each surface consists of layers of oxygen atoms with a density, ρ_s, of 0.12 Å^{-2}. The size of the simulation cell is 91.46 Å in the x direction and 93.18 Å in the y direction. The layer in contact with the fluid is a sheet of 1020 discrete oxygen atoms in a hexagonal arrangement derived from x-ray diffraction data for mica [14]. Following Somers et al. [12], the three layers behind the contact layer are treated as uniform sheets of atoms separated by $\Delta z = 2.2$ Å. The average distance between layers beyond the fourth layer is $\Delta z_{far} = 2.5$ Å. The interaction energy between a fluid atom and a single wall is

$$U_{FW} = \sum_{1}^{NS} u\left(r_{fw}\right) + u_B\left(z_{fw}\right) \tag{2}$$

where $u_B(z_{fw})$ is the 10-4-3 potential [15] given by

$$u_B(z_{fw}) = 2\pi\rho_s\varepsilon_{fw}\left\{\sum_{k=1}^{3}\left[\frac{2\sigma_{fw}^{12}}{5(z_{fw}+k\Delta z)^{10}} - \frac{\sigma_{fw}^{6}}{(z_{fw}+k\Delta z)^{4}}\right] - \frac{\sigma_{fw}^{6}}{3\Delta z_{far}(z_{fw}+3\Delta z+\Delta z_{far})^{3}}\right\}. \tag{3}$$
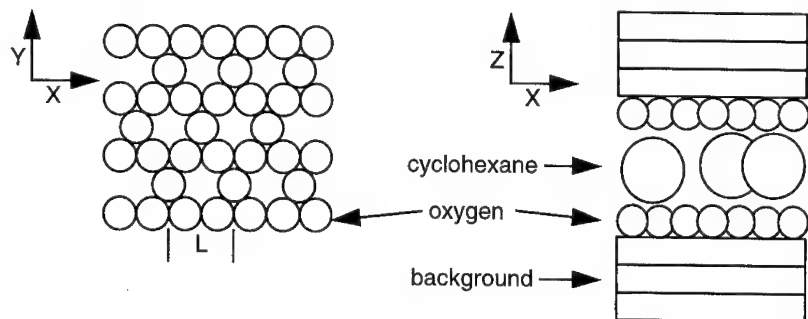
Figure 1. A schematic of a portion of the simulation cell showing an x-y view of one surface on the left and an x-z view of the complete cell on the right. The small circles represent surface oxygen atoms, the large circles represent cyclohexane fluid molecules and the rectangles represent the background oxygen layers. The mineral surfaces consist of four layers of oxygen atoms. The layer in contact with the fluid is modeled as a sheet of discrete oxygen atoms in a hexagonal arrangement. A portion of the contact layer is shown in the x-y view on the left. Each of the three layers behind the contact layer is treated as a uniform sheet of atoms with the oxygen density equal to that for mica. L denotes the unit cell in the x direction.

We examine the behavior of the film confined to the slit pore as the walls are subjected to a shear strain, as they would be in an actual SFA study. That is, we study the behavior of the film as the registry, α, is systematically varied at fixed temperature (T), chemical potential (μ), and pore width (h). Because shear-strain rates used in the actual SFA are extremely small on the molecular scale ($\sim 10^{-9}$ nm/ps), we assume that shearing can be treated as a quasistatic process and apply the grand-canonical ensemble Monte Carlo method as outlined in [10]. By sliding the walls over one another in the x-direction, we vary the registry incrementally from $\alpha = 0.0$ to $\alpha = 0.5$.

Structural features of the pore fluid are presented in terms of an in-plane cylindrical pair correlation function given for each fluid layer by

$$g^{(2)}(z_1, \rho_{12}) = \langle N(z_1, \rho_{12}) \rangle / \left[2\pi \rho_{12} \Delta\rho_{12} \Delta z_{12} \rho^{(1)}(z_1) \right] \tag{4}$$

where $\langle N(z_1, \rho_{12}) \rangle$ is the expected number of fluid atoms in an annulus of radius ρ_{12}, width $\Delta\rho_{12}$ = $0.02\sigma_f$ and thickness Δz_{12} centered on a fluid atom. The increment Δz_{12} is the width of the layer as determined by the density profile, and $\rho^{(1)}(z_1)$ is the average density over the layer with center in the z direction at z_1.

The shear stress is the average force per unit area exerted by the film on either wall in the x direction and is expressed as

$$\tau_{zx}^{k} = \sum_{i=1}^{N} \sum_{j=1}^{N_s^k} \langle x_{ij} u'(r_{ij}) / r_{ij} \rangle / s_x s_y \tag{5}$$

where N is the number of film atoms and N_s^k is the number of solid atoms in wall k (k = 1 or 2).

RESULTS

Fluid structure

Fig. 2 shows the in-plane pair correlation function for pore widths 8.1Å, 11.34Å, and 12.96Å, at registries 0.0, 0.3 and 0.5. Also shown is a configuration snapshot at each pore width for α = 0.0. There is evidence of order in the fluid at each of these pore widths. The fluid structure alternates between triangular and square packing with increasing pore width. At h = 8.1Å there is one layer of fluid molecules between the surfaces. The fluid molecules are arranged in a triangular structure as indicated by the pair correlation function on the left and the configuration snapshot shown on the right. At h = 11.34Å there are two layers of fluid between the surfaces. The center panels of Fig. 2 show that the structure of the fluid has shifted to an ordered square arrangement. With a further increase in pore width to h = 12.96Å, there are still two layers of fluid between the surfaces, but the fluid once again exhibits perturbed triangular structure, as indicated by the lower panels of Fig. 2. Three layer fluids (not shown) are less structured, with the fluid layers next to the surfaces being much more structured than the middle layer. A similar normal strain induced change in lattice type is seen when micron size polystyrene spheres are confined between glass surfaces. Epitaxial alignment is not a factor due to the size difference between the spheres and the granularity of the glass surfaces, but the spheres pack in highly ordered layers. Triangular and square packing arrangements similar to those seen in these simulations alternate with increasing pore width [16].

The fluid structure changes very little when the relative alignment of the surfaces is changed. The subtle differences that do exist are due to epitaxial alignment of the fluid with the surface. There are wells in the surface created by the oxygen rings. The distance between these wells is approximately the diameter of a fluid molecule. Due to the difference in size between the fluid molecules and wall atoms, these wells are not deep enough to lock the fluid molecules in place and therefore epitaxial alignment only weakly contributes to order in the fluid. The strength of the fluid-solid interaction coupled with the space limitations imposed by a specified pore width, is enough to cause the fluid molecules to pack in ordered structures. In previous confined fluid computer simulation studies when the fluid and solid atoms were the same size [9-11], epitaxial alignment strongly influenced order in the fluid. At certain pore widths a change in the relative alignment of the walls caused the fluid to undergo a shear melting transition. This

118

has been linked to the stick-slip phenomena in lubrication [7]. Shear melting is not observed in these simulations.
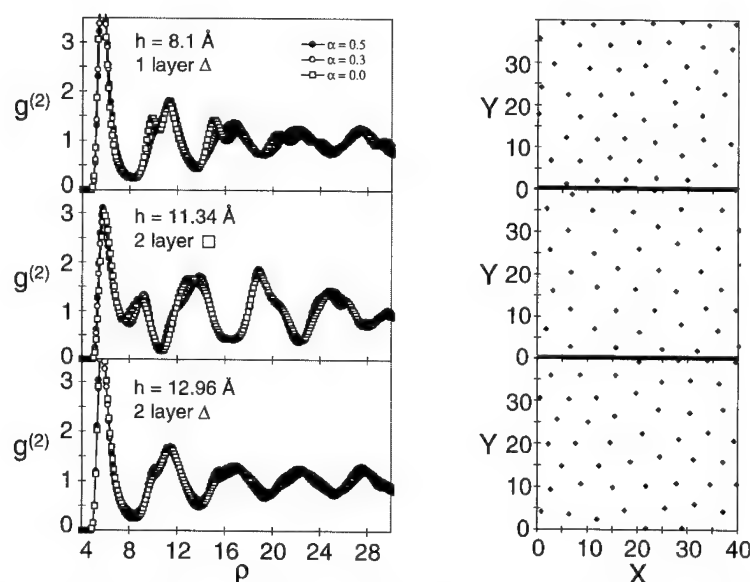
Figure 2. Inplane pair correlation functions for pore widths 8.1Å (top), 11.34Å (center), and 12.96Å (bottom), for registries 0.0 (●), 0.3 (O) and 0.5 (L) are on the left. Corresponding snapshots of a single layer of fluid for pore widths 8.1Å (top), 11.34Å (center), and 12.96Å (bottom), at $\alpha = 0.0$ are shown on the right.

Shear stress

Even though the fluid structure is only slightly perturbed with changes in the relative alignment of the walls, the shear stress changes dramatically with a shift in α. Fig. 3 shows the number of fluid molecules in the pore and the shear stress as a function of pore width. When the walls are either in alignment, $\alpha = 0.0$, or completely out of alignment, $\alpha = 0.5$, there is no stress on the fluid. For intermediate registries the shear stress is a function of pore width. The peaks in the shear stress correspond to pore widths where there is a transition in the number of fluid layers. For instance, the transition from a one layer triangular fluid to a two layer triangular fluid occurs between approximately h = 10 Å and h = 12 Å. Fig. 3 shows the fluid molecule number jumps from ~250 to ~500 and the shear stress goes through two extremes. The maximum at h = 11.34 Å corresponds to the two layer fcc solidlike fluid.

The stress associated with shearing nonpolar liquids between mica surfaces has been measured with the Surface Forces Apparatus. Gee et al. [17] sheared cyclohexane between mica surfaces and found that the force required to initiate sliding, or the yield stress, was 2.3×10^7 N/m^2 for one layer of fluid and 1×10^6 N/m^2 for two layers of fluid. Although a direct comparison is difficult, it is interesting to note that the maximums in the calculated shear stress, 4.5×10^7 N/m^2

at h = 11.34 Å and 3.5×10^6 N/m^2 at h = 15.66 Å corresponding to transitions between one to two and two to three layer triangular structures respectively, are of the same orders of magnitude.
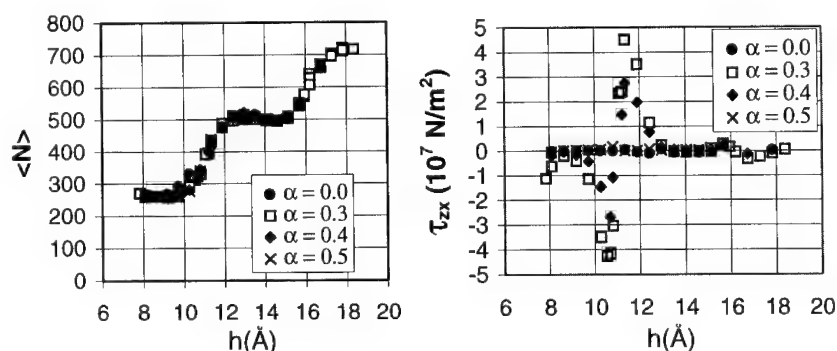
Figure 3. Number of fluid atoms (left) and shear stress (right) as a function of pore width for α = 0.0(●), 0.3(□), 0.4(◆) and 0.5(x).

ACKNOWLEDGMENTS

REFERENCES

1. J.N. Israelachvili, Intermolecular and Surface Forces. Academic Press. San Diego (1991).
2. R. Horn, and J. N. Israelachvili, J. Chem. Phys. **75**, 1400 (1981).
3. H.K. Christenson, J. Chem. Phys. **78**, 6906 (1983).
4. J.N. Israelachvili, P. M. McGuiggan and A. M. Homola. Science. **240**, 189 (1988).
5. J. Van Alsten, and S. Granick. Phys. Rev. Lett. **61**, 2570 (1988).
6. M. Schoen, J.H. Cushman, D.J. Diestler and C.L. Rhykerd, Jr. J. Chem. Phys. **88**, 1394 (1988).
7. P.A. Thompson, and M. O. Robbins. Science **250**, 792 (1990).
8. M. Lupkowski, and F. van Swol, J. Chem. Phys. **95**, 1995 (1991).
9. M. Schoen, C.L. Rhykerd, Jr., D.J. Diestler and J.H. Cushman, Science. **245**, 1223 (1989).
10. J.E. Curry, F. Zhang, J.H. Cushman, M. Schoen and D.J. Diestler, J. Chem. Phys. **101**, 10824 (1994).
11. J.E. Curry and J.H. Cushman, J. Chem. Phys. **103**, 2132 (1995).
12. S.A. Somers, A.V. McCormick, and H.T. Davis, J. Chem. Phys. **99**, 9890 (1993).
13. M. Schoen, D.J. Diestler, and J.H. Cushman, J. Chem. Phys. **87**, 5464 (1987).
14. S.W. Bailey, Crystal structures of clay minerals and their X-ray identification. Mineralogical Society, London (1980).
15. W.A. Steele, Surf. Sci. **36** 317 (1973).
16. P. Pieranski, L. Strzelecki, and B. Pansu, Phys. Rev. Lett. **50**, 900 (1983).
17. M.L. Gee, P.M. McGuiggan, and J.H. Israelachvili, J. Chem. Phys. **93**, 1895 (1990).

DIFFUSION LIMITED WETTING

U. STEINER*,**, J. KLEIN*

*Department of Materials and Interfaces, Weizmann Institute of Science, Rehovot 76100, Israel
**Fakultät für Physik, Universität Konstanz, Postfach 5560, 78464 Konstanz, Germany

ABSTRACT

We have measured the growth with time t of a wetting layer (of thickness $l(t)$) at the surface of a thin film of a binary liquid (polymer) mixture. Over a wide range of experimental parameters, our data is well described by a model of diffusion limited wetting which takes into account the finite film thickness. In this model, $l(t)$ is a function of time which sensitively depends on the nature of the interfacial potential: a detailed comparison shows that long range van-der-Waals forces provide the main driving force for the build-up of the wetting layer .

INTRODUCTION

In many practical applications, the coating of a surface with a liquid film plays an important role. Paints, lubricants, adhesives and thin dielectric layers on semiconductors are a few examples where a surface is modified by a homogeneous macromolecular film. Together with a growing technological interest, there is an increasing activity in experimental and theoretical studies which try to elucidate the thermodynamic origin of wetting phenomena and thin film stability [1-15]. For the surface modification of a of a polymeric surface by a macromolecular layer, for example, thin film stability may be a problem [16,17] Following Cahn's argument [18], this may be related to the intrinsic immiscibility of binary polymer liquids (α, β): starting from Young's equation [19], which relates the contact angle θ of a liquid α with a surface to the three surface tensions $\gamma_{\alpha s}$, $\gamma_{\beta s}$ and $\gamma_{\alpha\beta}$:

$$\cos(\theta) = \frac{\gamma_{as} - \gamma_{\beta s}}{\gamma_{\alpha\beta}} \qquad (1)$$

the balance between the three surface tensions determines whether a liquid α forms a continuous film on a surface s ($\gamma_{\alpha\beta} >= \gamma_{\alpha s} - \gamma_{\beta s}$) or whether such a film is unstable ($\gamma_{\alpha\beta} < \gamma_{\alpha s} - \gamma_{\beta s}$). As the critical temperature T_c for phase separation is approached, both terms ($\gamma_{\alpha\beta}$, $\gamma_{\alpha s} - \gamma_{\beta s}$) approach zero. But whereas the interfacial energy of the liquid–liquid interface vanishes with the critical exponent of the bulk correlation length $\gamma_{\alpha\beta} \sim (T_c - T)^{1.3}$, the difference of the liquid-surface interfacial energies scale with a critical surface exponent ($\gamma_{\alpha s} - \gamma_{\beta s}$) $\sim (T - T_c)^{0.8}$. Since the numerator of Eq. (1) approaches zero more rapidly than the denominator, a transition from partial wetting (drops of the α-phase on the surface) to complete wetting (a thick continuous film of the α-phase on the surface) is expected to occur. Inversely, immiscible liquids far from their critical point T_c are likely to be in the partial wetting regime, and continuous films delimiting a macromolecular bulk from a surface are unstable and tend to break-up [16].

The Cahn argument, however, is valid in this simplified version only if short-range interactions are the dominant driving forces at the surface. Competing long- and short range interfacial forces may suppress complete wetting near the critical point, or lead to a wetting layer even far from T_c [2]. The question whether long-range forces contribute to the wetting layer formation may therefore be of considerable importance when investigating thin film stability of polymer layers. The integrated amount of one of the coexisting phases near a surface (surface excess) yields some information on the thermodynamics of the surface layer [6,20]. The predictions based on these measurements concerning the wetting transition, however, are dependent on the theoretical model used in the data analysis. In particular, there is no

121

unambiguous way to extract in a model independent way the type of surface interaction (long-range or short-range) from an equilibrium absorption experiment.

A novel approach which provides information on the nature of the surface potential is the measurement of the build-up of a surface layer with time [21]. Theoretical studies of diffusion limited wetting layer growth predict different functional forms for the growth of the surface layer thickness with time, depending on the surface potential that drives the process [11,12]. While measurements of dynamic properties in liquids are difficult to perform, since the presence of convectional effects and gravitational fields complicate the surface layer kinetics, these effects are negligible for small polymer melt samples. This allows the application of models which assume strictly diffusion-limited growth in order to extract surface potentials.

Here we report the experimental observation of a wetting layer build-up from a binary polymer mixture with time. We develop a theoretical model to describe the diffusion limited growth of a wetting layer in a confined geometry. In the last section, we describe the analysis of the experimental data in the framework of this theory.

EXPERIMENT

Materials and Sample Preparation

The polymers used in this work are statistical copolymers made of ethylene and ethyl-ethylene monomers (PE-PEE): $([C_4H_8]_{1-x} - [C_2H_3-(C_2H_5)]_x)_N$. Binary mixtures of such polymers (A, B) with values of $\Delta x = x_A - x_B$ from 0.9 to 0.14 and molecular weights N from 1510 – 2030 have been shown to be partially miscible with critical temperatures in the range from 33 – 223°C [22]. For such couples the higher-x containing polymer shows a pronounced enrichment at the free (air) interface, and complete wetting of the sample surface by this component has been found for several binary pairs [6,22]. To allow detection by the experimental technique described in next paragraph, the higher-x component was partially deuterated. The details of the polymers used are summarized in Table I. Two polymer couples were used in this study: $d88/h78$ and $d66/h52$. The bulk properties of these couples have been studied before. Their critical temperatures are: $T_c = 127°C$ ($d88/h78$) and $T_c = 204°C$ ($d66/h52$) [22].

Samples were prepared by spin-coating a film from toluene solution onto a polished silicon surface, which in some cases was covered by a thin gold layer to improve thin-film stability. A second film was similarly spin-cast onto freshly cleaved mica. To obtain bilayers, the film was floated from mica onto the first film. Since the PE-PEE polymers are liquid at room temperature (their glass transition temperature is < –40 °C), a jig was developed for depositing the film from the mica onto the substrate (Fig. 1). As the jig is lowered below the water surface, water intercalates between the polymer film and the mica and the film is pushed onto the substrate. Thus, at each instant, only a very short segment of the film is suspended from the mica surface. This avoids the shrinking and thickening which occurs when a hyrophobic liquid film is floated entirely onto a water surface prior to being transferred to the other surface.

Sample series were annealed in a vacuum oven (< 10^{-2} Torr) at temperatures T between 45 – 163 °C (± 0.3 °C), for times t from 15 min. to 1 month. After annealing, the samples were quenched in liquid nitrogen and stored at -80°C. Each sample was annealed once only for a given time t, and its concentration profile was analyzed by nuclear reaction analysis.

TABLE I. Characteristics of the $([C_4H_8]_{1-x} - [C_2H_3-(C_2H_5)]_x)_N$ .statistical copolymers. x is the ethyl-ethylene content, N the degree of polymerization and f_D the fractional deuteration.

Sample	x	N	f_D
$d88$	0.88	1610	0.34
$h78$	0.78	1290	0.00
$d66$	0.66	2030	0.40
$h52$	0.52	1510	0.00

Silicon
Mica
Glass Slides
Polymer Films
Water
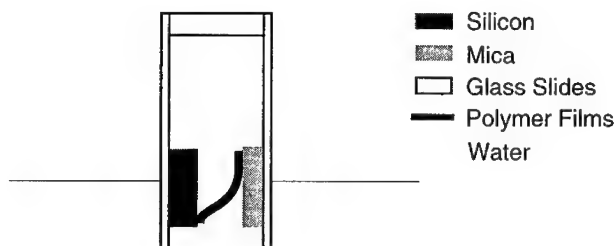
Fig. 1. Jig to create bilayers from polymers which are liquid at room temperature. As the jig is lowered into the water, the polymer film floats off the mica and is immediately brought into contact with the film on the silicon substrate. The separation between the silicon and mica substrates is typically less than 1 mm.

Nuclear Reaction Analysis

To obtain the concentration-depth profiles $\phi(z)$ of the deuterated polymer species, nuclear reaction analysis (NRA) was employed [23]. NRA is based on the $^3\text{He} + {}^2\text{H} \rightarrow {}^4\text{He} + {}^1\text{H} + 18.35$ MeV nuclear reaction. The experimental set-up is schematically represented in Fig. 2. A 900 keV ^{3}He beam is incident on the polymer sample. As the ^{3}He ions penetrate the polymer film, they lose energy due to inelastic electronic interactions. This results in a lowered energy of the ^{4}He particles as compared to a nuclear reaction which takes place at the sample surface. The outgoing α-particles additionally lose energy traversing the film *en route* to the detector, and the overall energy loss is directly related to the depth z at which the reaction has taken place. By measuring the energy spectrum of the high energy $^4\text{He}^{++}$ ions, a concentration-depth profile $\phi(z)$ can directly be computed, after correcting for the reaction cross-section of the $^2\text{He}(^3\text{He},^4\text{He})^1\text{H}$ nuclear reaction.

^{3}He Beam   15°   30°

Magnetic Field
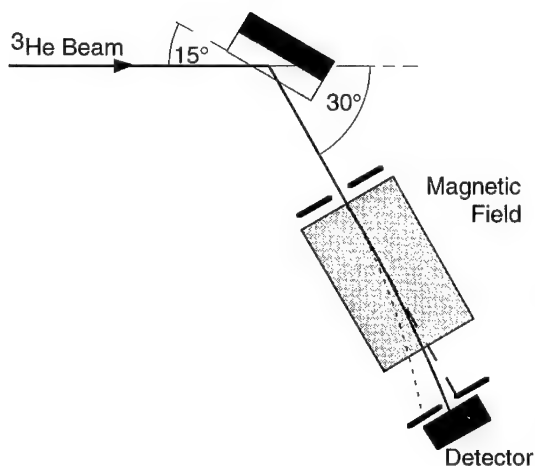
Detector

Fig. 2. Schematic representation of the nuclear reaction analysis experiment. A ^{3}He beam is incident onto the sample where the $^3\text{He}+^2\text{H}\rightarrow^4\text{He}+^1\text{H}$ nuclear reaction takes place. A magnetic filter admits only the $^4\text{He}^{++}$ ions to the detector. The $^4\text{He}^{++}$ energy spectrum can directly be converted into a depth-concentration profile of the deuterated polymer in the sample.

RESULTS

Concentration-depth profiles of an annealing series are shown in Fig. 3 for $d66/h52$ bilayers at an annealing temperature of $T = 110$ °C. In the unannealed sample the polymer layer which is higher in PEE content is initially on the silicon substrate, and is thus excluded from the air-surface, where the wetting layer is expected to form, by the PEE-poorer layer (Fig. 3a). Upon annealing for $t = 18$ h (Fig 3b), the two layers have partially interdiffused and the two coexisting concentrations $\phi_1 \approx 0.75$ and $\phi_2 \approx 0.25$ are established, separated by an interface whose width is given by the correlation length ξ (≈ 22 nm). At the same time, a narrow surface peak of the phase rich in $d66$ (the surface-preferred component) appears at the air interface. For increasing annealing times ($t = 190$ h (Fig. 3c) and $t = 720$ h (Fig 3d)), the width l of the surface peak increases, forming a wetting layer of composition $\phi_s \approx \phi_1$. The formation of a surface layer of width $l \gg \xi$ is direct evidence for complete wetting, and the growth of the wetting layer is only limited by the overall material available to be incorporated into the surface layer. In this experiment, the $d66$ layer next to the substrate surface acts as a reservoir, which supplies the $d66$ chains which are incorporated into the wetting layer. A sample consisting of a uniform film of composition ϕ_1 would quickly be depleted to a concentration $\phi < \phi_1$ for $z \gg l$ and the increase of l would come to a stop. It should be mentioned that gravitational effects are negligible for these thin films, and convectional flow is suppressed by the high viscosity of the polymer melts.

In Fig. 4, the raw data of the wetting layer thickness l versus annealing time t is displayed on double logarithmic scales for the $d88/h78$ couple [Fig 4(a)] and the $d66/h52$ couple [Fig. 4(b)]. In Fig. 4(a), the diffusion temperature was kept constant at $T = 110$ °C, but the thicknesses of the $h78$ layer of the unannealed sample was varied. In Fig. 4(b), the sample layer thicknesses, as well as the annealing temperatures was varied in the different data sets. While a direct interpretation of these raw data seems difficult in the case of Fig. 4(b), a model which takes the
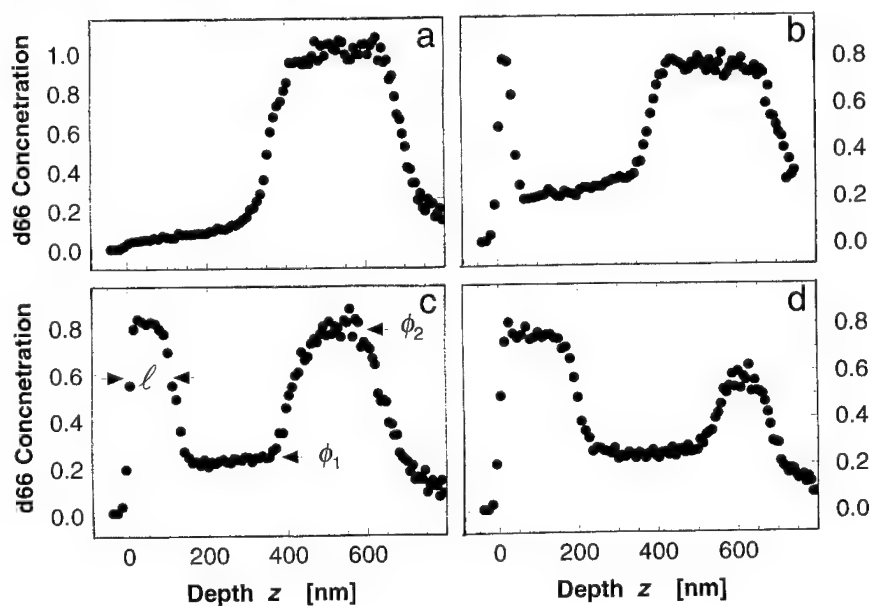
FIG. 3. Concentration-depth profiles for the $d66/h52$ couple annealed at 110°C, determined by nuclear reaction analysis; (a) unannealed, (b) after 18h, (c) after 190h and (c) after 720h. The glass transition temperature for this couple is ca. -60 °C, and some interdiffusion can be observed in the unannealed sample due to the sample handling at room temperature.
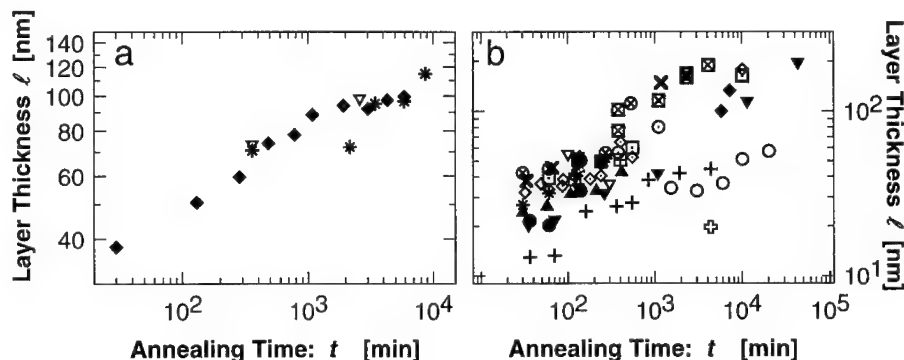
FIG. 4. Wetting layer thickness l vs annealing time t; (a) $d88/h78$ annealed at 110°C. The different symbols refer to varying sample geometries d: $*$, $d = 315 - 530$ nm; $\triangledown$, $d = 360$ nm; $\blacklozenge$, $d = 270 - 340$ nm. (b) $d66/h52$. The different symbols refer to varying sample geometries d and varying temperatures: $\times$, $T = 163$ °C, $d = 345$ nm; $\clubsuit$, $T = 160$ °C, $d = 340$ nm; $\otimes$, $T = 154$ °C, $d = 215$ nm; $\oplus$, $T = 151$ °C, $d = 130$ nm; $\boxminus$, $T = 150$ °C, $d = 590 - 670$ nm; $\diamond$, $T = 150$ °C, $d = 500 - 680$ nm; $\circ$, $T = 150$ °C, $d = 500 - 650$ nm; $\square$, $T = 150$ °C, $d = 545$ nm; $\triangledown$, $T = 150$ °C, $d = 510$ nm; $\diamond$, $T = 150$ °C, $d = 310$ nm; $\triangle$, $T = 150$ °C, $d = 250$ nm; $\square$, $T = 149$ °C, $d = 325$ nm; $*$, $T = 140$ °C, $d = 120 - 250$ nm; $\blacktriangledown$, $T = 110$ °C, $d = 335$ nm; $\blacklozenge$, $T = 110$ °C, $d = 315$ nm; $\blacktriangle$, $T = 110$ °C, $d = 175$ nm; $\bullet$, $T = 110$ °C, $d = 130$ nm; $+$, $T = 90$ °C, $d = 330$ nm; $\circ$, $T = 70$ °C, $d = 275$ nm; $\oplus$, $T = 45$ °C, $d = 260$ nm.

diffusion limited growth of the wetting layer into account is developed in the following section.

DIFFUSION LIMITED WETTING LAYER GROWTH

Excluding the initial stages, where bulk-equilibrium is established, and the initial interfacial build-up occurs, we consider three different regions in the composition profile, as indicated schematically in Fig. (5): (I) The wetting layer of plateau concentration $\phi_s \approx \phi_2$ and thickness l; (II) the non-wetting phase adjacent to (I) of width d and compositions ranging from ϕ_d to ϕ_1; (III) the "reservoir" phase of composition ϕ_2. In our model, we take the material transport to be diffusion limited, but make the reasonable assumption that the wetting layer (I) is in local equilibrium with the immediately adjacent region of concentration ϕ_d. That is, the transfer of material from to the wetting layer from the immediately adjacent region is rapid compared with the flux of material from the reservoir to the wetting layer. When the wetting layer is formed, the adjacent region is depleted, resulting in a concentration gradient in region II, and the growth of the wetting layer is fed by the flux through region II. Since the form of the interfacial composition gradient between region II and III is fixed by the bulk-thermodynamic parameters, mass-transport through region II can occur only by translating the II–III interface towards greater values of z. For a wetting layer thickness l larger than the bulk-correlation length ξ, the composition of the wetting layer ϕ_s becomes approximately equal to ϕ_2. Since $\phi_d \approx \phi_1$, conservation of mass requires that the width of region II, d, be conserved, as indeed seen from the composition profiles in fig. 3. Mass–transport with time is then given by the flux-equation, which relates the increase with time of the surface excess to the flux through region II:

$$\frac{d}{dt}\left[\left(\phi_2 - \phi_1\right)\left(l(t) - l(0)\right)\right] = \frac{D(\phi_1, T)}{d}\left(\phi_1 - \phi_d\right) \tag{2}$$

125
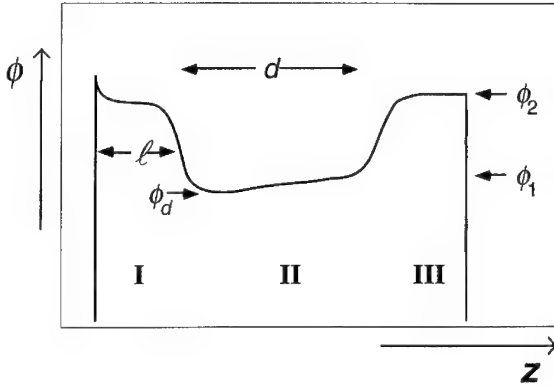
FIG. 5. Schematic representation of the model presented in the text. The composition profile is divided into three regions: (I) the wetting layer of thickness l in local equilibrium with the adjacent phase of composition ϕ_d; (II) the diffusion gradient $\phi_1 - \phi_d$; and (III) the reservoir phase of composition ϕ_2. The increase of the wetting layer takes place by diffusion of polymers from the reservoir phase (III) via the concentration gradient (II) into the wetting layer (I).

where $D(\phi, T)$ is the mutual diffusion coefficient. Since $\phi_d \approx \phi_1$, diffusion takes place in the close vicinity of the phase boundary, and thermodynamic slowing down of diffusion has to be taken into account, leading to a composition dependent diffusion coefficient. To eliminate ϕ_d from Eq. (2), $(\phi_1 - \phi_d)$ can be expressed in terms of the relative chemical potential [11]:

$$\left(\phi_1 - \phi_d\right) = \left[\mu(\phi_1, T) - \mu(\phi_d, T)\right]\left(\frac{\partial \mu}{\partial \phi}\right)^{-1}_{\phi=\phi_1} \tag{3}$$

The chemical potential difference can be related to the interfacial potential $V(l)$ per unit area [11]:

$$\rho\left(\phi_2 - \phi_1\right)\left[\mu(\phi_1, T) - \mu(\phi_d, T)\right] = -\frac{\partial V}{\partial l} \tag{4}$$

where $\rho = (1/a^3)$ the monomer number density with a is the statistical segment size. Eqs. (2) - (4) can be combined to yield a differential equation which describes the growth with time of the wetting layer as a function of the derivative of the surface potential:

$$\frac{dl}{dt} = -\left(\left.\frac{\partial \mu}{\partial \phi}\right|_{\phi_1} \left(\phi_2 - \phi_1\right)^2\right)^{-1} D(\phi, T)\frac{1}{\rho d}\frac{\partial V(l)}{\partial l} \tag{5}$$

Equation 5 can be simplified by writing out expressions for $D(\phi)$ and $\partial \mu / \partial \phi$. An expression for the diffusion coefficient which takes the thermodynamic slowing-down into account is given by [24,25]:

$$D(\phi) = \Omega(\phi)\left[\chi_s(\phi) - \chi\right] \tag{6}$$

$\Omega(\phi)$ is a mobility term:

$$\Omega(\phi) = 2\phi(1 - \phi)\left[D_a^* N_a(1 - \phi) + D_b^* N_b \phi\right] \tag{7}$$

and $\chi_s(\phi)$ is the value of the Flory-Huggins interaction parameter χ on the spinodal:

$$\chi_s(\phi) = \frac{1}{2}\left(\frac{1}{N_a\phi} + \frac{1}{N_b(1-\phi)}\right) \tag{8}$$

N_a and N_b are the polymerization indices of the two polymers, and D_a^* and D_b^* their respective tracer diffusion coefficients.

The chemical potential can be evaluated from the standard Flory-Huggins energy functional for polymer mixing to yield the chemical potential derivative [26]:

$$\frac{\partial\mu}{\partial\phi} = \left[\frac{1}{N_a\phi} + \frac{1}{N_b(1-\phi)} - 2\chi\right]k_BT \tag{9}$$

where k_B is Boltzmann's constant. Equations (6) – (9) define an effective mobility Ω_{eff}:

$$\Omega_{\text{eff}}(\phi_1,\phi_2,T) = \left(\frac{\partial\mu}{\partial\phi}\bigg|_{\phi_1}(\phi_2-\phi_1)^2\right)^{-1}D(\phi,T) = \frac{\phi_1(1-\phi_1)\left[D_a^*N_a(1-\phi_1) + D_b^*N_b\phi_1\right]}{k_BT(\phi_2-\phi_1)^2} \tag{10}$$

Equation (5) then becomes:

$$\frac{dl}{dt} = -\frac{\Omega_{\text{eff}}}{\rho d}\frac{\partial V(l)}{\partial l} \tag{11}$$

Note that by combining Eqs. (6) and (9), all explicit references to the interaction parameter χ cancel, reducing Eq. (11) to a diffusion problem which depends only on the surface potential $V(l)$ and the diffusion geometry as indicated in Fig. 5.

To analyze our experimental data in the framework of the present model, we consider three different forms for $V(l)$:

$$V(l) = -\frac{A_s}{a^2}\exp\left(-\frac{l}{\zeta}\right) \qquad \text{(short range)} \tag{12a}$$

$$V(l) = -\frac{A_{nr}}{12\pi l^2} \qquad \text{(non-retarded vdW)} \tag{12b}$$

$$V(l) = -\frac{aA_r}{l^3} \qquad \text{(retarded vdW)} \tag{12c}$$

where the coefficients A_s, A_{nr} and A_r have units of energies and are the effective surface interaction potentials. Equation (12a) describes a short-range surface interaction which decays exponentially with a decay length which is expected to be short-ranged, i.e. $\zeta \approx a$. A_s is often given by an expansion [27]: $A_s = 1/\zeta\,(\mu_1\,\phi_s + 0.5\,g\,\phi_s^2)\,k_BT$, with μ_1 a chemical potential difference, favoring the component which forms the wetting layer, and g a prefactor to the quadratic term in ϕ_s, which takes changes of interactions due to the presence of the surface ("missing neighbors") into account. Equation (12b) represents non-retarded van der Waals interactions (vdW) with A_{nr} the non-retarded Hamaker constant. For large values of l, retardation effects are expected to play a role and a potential for retarded vdW interactions [Eq. (12c)] must be used, with an effective retarded Hamaker constant A_r. Substitution of Eqs. (12) into Eq. (11) yields the time dependence of the wetting layer growth:

127

$$\frac{1(t)}{a} = \log\left(\frac{-A_s a \Omega_{eff} t}{d\zeta^2}\right) \qquad \text{(short range)} \qquad (13a)$$

$$\frac{1(t)}{a} = \left(\frac{-2A_{nr}}{3\pi}\frac{\Omega_{eff}t}{da}\right)^{\frac{1}{4}} \qquad \text{(non-retarded vdW)} \qquad (13b)$$

$$\frac{1(t)}{a} = \left(\frac{-A_r}{15}\frac{\Omega_{eff}t}{da}\right)^{\frac{1}{5}} \qquad \text{(retarded vdW)} \qquad (13c)$$

Note that Eqs. (13) predict a qualitative difference for the case of short-range interactions (logarithmic growth-law) and long-range vdW interactions (power-law). The derivation of the present theoretical model follows the treatment by Lipowski and Huse (LH), for wetting from a semi-infinite phase of composition ϕ_1 (i.e. $d \to \infty$ in Fig. 5) [11,12]. While their predictions for the short-range case also features a logarithmic time dependence of the wetting layer, their exponents in the case of vdW interactions differ from the results in Eqs. (13): LH find exponents of $1/8$ and $1/10$ for non-retarded and retarded vdW interactions respectively, to be contrasted with our values of $1/4$ and $1/5$. This is a consequence of the different model geometries. In the LH model the depletion zone which establishes the diffusion gradient extends spatially with time to depths $z \approx \sqrt{(Dt)}$, and is quite inappropriate for the present thin film geometry [28]. In contrast, the diffusion distance in the present model between reservoir and wetting layer is fixed, leading to an accelerated material transport.

DISCUSSION

The form of Eqs. (13) suggests the use of transformed the length and time coordinates: $l \to l/a$ and $t \to \Omega_{eff}t/ad$. The use of these rescaled coordinates allows us to superimpose data sets measured at different temperatures and samples of different sample geometry (i.e. d values). In Fig 6 we plot the data from Fig. 4 using rescaled coordinates. In Fig. 6(a) and (c), the wetting layer thickness l is plotted versus a reduced time t/d for the $d88/h78$ data sets. Here, annealing was carried out at a fixed temperature of 110 °C, leading to a constant value of the effective mobility Ω_{eff}, and only the value of d was varied in a range from 270 to 530 nm.

In the case of the $d66/h52$ couple [fig. 6(b) and (d)], the temperature as well as diffusion distance d was varied and the coordinate transformation as mentioned above (l/a vs. $\Omega_{eff}t/ad$) was used. For the data reduction, values for the statistical segment length a were taken from ref. [29], and the mobility Ω_{eff} was computed from Eq.(10). The required parameters in Eq. (10), ϕ_1 and ϕ_2 could in principle be obtained directly from the composition profiles, but more precise values from ref. [22] are used. The tracer diffusion coefficients D^* were estimated via their mutual diffusion coefficients D^{mut} (e.g. for tracer diffusion of $d66$ in $h52$: $D^*_{d66} \approx D^{mut}_{h52}$). The mutual diffusion coefficients for $d66$ and $h52$ have been measured by analyzing the diffusion profiles of $d66/h66$ and $d52/h52$ at room temperature [30]. To obtain the values of D^{mut} at the annealing temperatures of this study, a WLF extrapolation was performed, using the WLF parameters from ref. [30].

Comparing Fig. 4(a) and Fig 6(a) and(c) only a minor reduction of the scatter in the data is detected, when using reduced coordinates. In Fig. 6(d), however, the large scatter in fig. 4 collapses strikingly to give a single master curve which includes all data. To compare the experimental data to Eqs. (13), the data are plotted on log-linear [Fig. 6(a) and 6(b)] and on a double logarithmic scale [Fig. 6(c) and 6(d)]. For $d88/h78$, within the small range in reduced time (2 orders of magnitude), the data is equally well described by a linear relation for both representations. This is a general feature of weak power laws, which resemble logarithmic laws unless a sufficient dynamic range of variables is available. The $d66/h52$ data set exhibits a linear representation only on a double logarithmic scale (Fig. 6d), while the log-linear plot [Fig. 6(b)]
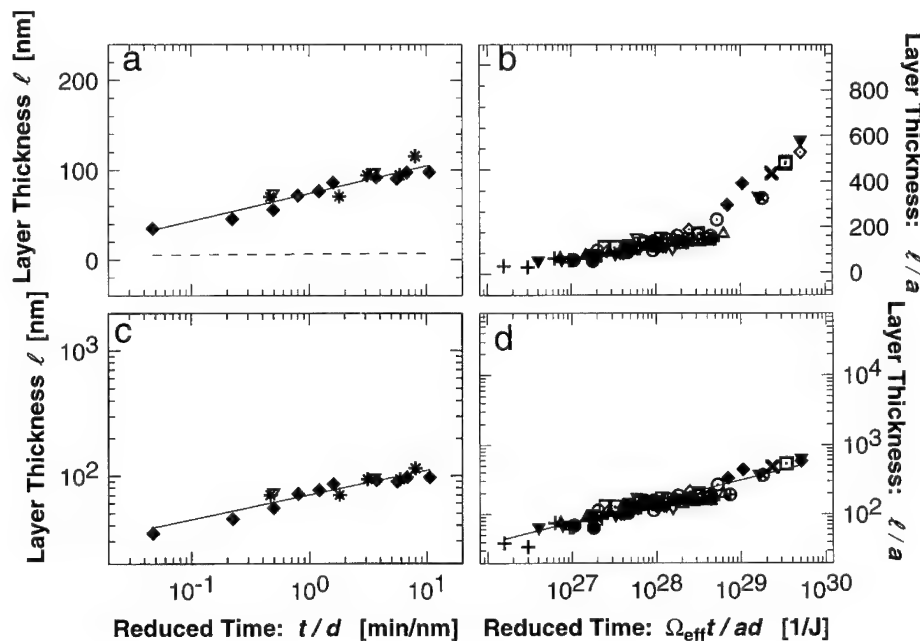
FIG. 6. Time dependence of wetting layer thickness from Fig. 4 in reduced coordinates (the symbols are the same as in Fig. 4): (a) and (c): l vs t/d for the $d88/h78$ couple; (b) and (d): l/a vs $\Omega_{eff}t/da$ for the $d66/h52$ couple. Plot (a) and (b) are in a log $-$ linear representation, (c), (d) on a double-logarithmic scale. The solid line in (a) is a fit to the relation $l \propto \log(t/d)$, the dashed line is the theoretically predicted variation of l with time (see text). The solid line in (c) and (d) are the power-law relations: (c) $l \propto (t/d)^{0.20}$ and (d) $l/a \propto (\Omega_{eff}t/da)^{0.30}$.

shows a distinct curvature, indicating that a long-range surface interaction [Eqs. (12b) and (12c)] rather than a short range potential better describes the experimental data.

To proceed, power-law fits were performed on the data of Fig. 6(c) and (d) (straight lines in the double-logarithmic representation). The solid line in Fig 6(c) corresponds to a power-law relation: $l \sim (t/d)^\kappa$, with $\kappa = 0.20 \pm 0.05$. In Fig. 6(d), the corresponding power-law fit: $l/a \sim (\Omega_{eff}/ad)^\kappa$ yields $\kappa = 0.30 \pm 0.05$. While the power-law exponent κ of the fit in Fig. 6(c) is close to the prediction of Eqs. (13b) or (13c), the uncertainty in the exponent κ is too large to distinguish between the two cases. In any event, one does not expect a sharp crossover in behaviour when non-retarded go over to retarded interactions. The exponent κ for the $d66/h52$ data set [Fig. 6(d)] lies somewhat above the values predicted by Eqs. (13b) and (13c). This discrepancy may be due to the uncertainties in the values of the parameters used in the data reduction (a, ϕ_1, ϕ_2, and Ω_{eff}). In particular the temperature extrapolation of the tracer diffusion coefficients D^*, which enter in the calculation of Ω_{eff} is likely to introduce some error in Ω_{eff} for the higher temperatures. Fitting the data in Fig 6(c) and 6(d) with the non-retarded power-law from Eq. (13b) (the exponent $\kappa = 0.25$ lies within the error margin of both fits described above), using the Hamaker constant A_{nr} as adjustable parameter, we obtain values for $-A_{nr}$ in the range from 10^{-20} to 10^{-21} J, with the uncertainty resulting from the scatter in our data. These values of

A_{nr} compare well with Hamaker constants of non-polar liquids. Taken together with the power law fit to the data, this strongly implicates long-range forces as driving the growth of the wetting layer.

A similar analysis can be performed for Fig. 6(a), but in this case a very different picture emerges. We find that despite the apparent fit to a logarithmic variation $l \propto \log(t)$ (Fig. 6a), the *slope* of the data, using the decay length ζ as a fit parameter of the data to eq. (13a), yields a value $\zeta \approx 31$nm. Since eqs. (12a) and (13a) correspond to a short range interfacial potential, ζ must be comparable to a monomer size or the statistical segment length $a \approx 6$ Å. Thus eqs. (12a) and (13a) *cannot* provide a consistent quantitative description of the $l(t)$ data.

Previous experimental studies on the equilibrium properties of surface enriched layers of the $d66/h52$ couple also find deviations from the Cahn model of wetting which assumes a short range interfacial potential [7,20]. One of these studies provide an estimation for the short-range interaction strength for two PE-PEE systems [20]. Using their published data we obtain an estimate for A_s: $A_s \approx -0.05 k_B T$, and taking the decay-length $\zeta = a \approx 6$Å, a prediction for the growth of a wetting layer which is driven uniquely by short-range interactions [Eq. (12b)] can be calculated The result of this calculation is indicated by the dashed line in Fig. 6(a). The theoretically predicted growth of the wetting layer $l(t)$ lies significantly lower than the data points. After 6 days, the longest annealing time for the $d88/h78$ couple, the theoretically predicted value $l \approx 7$ nm is smaller than the bulk correlation length which sets a lower limit to the validity of our model. In order to attain a 100 nm layer in the framework of this model, using the experimental parameters listed above, cosmological times (10^{60}–10^{120} years) would be required. Thus, while it may well be that short range effects contribute to surface segregation and enrichment of the surface-preferred species, they can play only a negligible role in driving the growth of the wetting layer.

CONCLUSIONS

Using a ion-beam depth-profiling technique, we have investigated the growth with time of a wetting layer from binary polymer mixtures. In the absence of gravitational effects and convectional flow, we propose a model in which the growth of the wetting layer is limited by diffusion from a reservoir at a fixed distance. Since this model makes no *a priori* assumptions on the interaction potential, it is possible to distinguish unambiguously between different surface potentials which drive the formation of the wetting layer.

Applying this model to our experimental data, measurements taken with a variety of different experimental parameters collapse to a single master curve. The functional form of the master curve: $l(t) \sim t^\kappa$ is a signature of a wetting layer formation driven by van der Waals forces; while discrimination between this form and a logarithmic variation (indicating short-ranged forces) is possible, the dominance of long-ranged fields is strongly corroborated by a quantitative analysis which yields a Hamaker constant in the order 10^{-20} – 10^{-21} J, a value which is common for non-polar liquids. We show that any short-ranged interactions (which act on the length scale of a monomer size) play only a minor role, and contribute negligibly to the build-up of the wetting layer.

Since most surface aggregation experiments from binary polymer mixtures exhibit similar parameters for the short-range surface free energy, the present model suggests that van der Waals interaction are essential to form macroscopic wetting layers.

Finally, we point out that the study of the dynamics of wetting layer formation provides an tool which allows assess the precise form of surface potentials in polymeric liquids. This technique could complement equilibrium absorption studies[20], where such a distinction between different surface potentials is more difficult to achieve.

ACKNOWLEDGEMENTS

REFERENCES

1. R. F. Kayser, M. R. Moldover, and J. W. Schmidt, J. Chem. Soc. Faraday Trans. II **82**, 1701 (1986).

2. S. Dietrich, in *Phase Transitions and Critical Phenomena* , edited by C. Domb, and J. L. Leibiwitz (Academic Press Limited, New York, 1988), Vol. XII, p. 1-218.

3. X. L. Wu, M. Schlossman, and C. Franck, Phys. Rev. B **33**, 402 (1986).

4. P. Guenon, and D. Beysens, Phys. Rev. Lett. **65**, 2406-2409 (1990).

5. P. Wilzius, and A. Cumming, Phys. Rev. Lett. **66**, 3000 (1991).

6. U. Steiner, J. Klein, E. Eiser, A. Budkowski, and L. Fetters, Science **258**, 1126-1129 (1992).

7. F. Bruder, and R. Brenn, Phys. Rev. Lett. **69**, 624 (1992).

8. B. Q. Shi, C. Harrison, and A. Cumming, Phys. Rev. Lett. **70**, 206 (1993).

9. B. M. Law, Phys. Rev. Lett. **72**, 1698 (1994).

10. U. Steiner, J. Klein, and L. J. Fetters, Phys. Rev. Lett. **72**, 1498-1501 (1994).

11. R. Lipowsky, Phys. Rev. B **32**, 1731 (1985).

12. R. Lipowsky, and D. A. Huse, Phys. Rev. Lett. **57**, 353-356 (1986).

13. K. K. Mon, K. Binder, and D. P. Landau, Phys. Rev. B **35**, 3683 (1987).

14. R. A. L. Jones, L. J. Norton, E. J. Kramer, and F. S. Bates, Phys. Rev. Lett. **66**, 1991 (1991).

15. G. Krausch, C.-A. Dai, E. J. Kramer, and F. S. Bates, Phys. Rev. Lett. **71**, 3669 (1993).

16. F. Brochard-Wyart, and F. Daillant, J. Canad. J. Phys. **68**, 1084 (1990).

17. G. Reiter, Phys. Rev. Lett. **68**, 75 (1992).

18. M. Schick, in *Liquids at Interfaces* , edited by J. Charvolin, and J.-F. Joanny (North Holland, Amsterdam, 1990), Vol. p. 419-497.

19. T. Young, Phil. Trans. Roy. Soc. London **95**, 65 (1805).

20. F. Scheffold, A. Budkowski, U. Steiner, E. Eiser, J. Klein, and L. J. Fetters, J. Chem. Phys. **104**, 8795 (1996).

21. U. Steiner, and J. Klein, Phys. Rev. Lett. **77**, 2526 (1996).

22. F. Scheffold, E. Eiser, A. Budkowski, U. Steiner, J. Klein, and L. J. Fetters, J. Chem. Phys. **104**, 8786 (1996).

23. U. K. Chaturvedi, U. Steiner, O. Zak, G. Krausch, G. Schatz, and J. Klein, Appl. Phys. Lett. **56**, 1228-1230 (1990).

24. R. J. Composto, E. J. Kramer, and D. M. White, Nature **328**, 234 (1987).

25. A. Losch, D. Wörmann, and J. Klein, Macromolecules **27**, 5713-5715 (1994).

26. P. J. Flory, *Principles of Polymer Chemistry* (Cornell University Press, Ithaca, 1953).

27. I. Schmidt, and K. Binder, J. Phys. II(Paris) **46**, 1631 (1985).

28. U. Steiner, J. Klein, E. Eiser, A. Budkowski, and L. J. Fetters, Berichte der Bunsengessellschaft für Physikalische Chemie **98**, 366 (1994).

29. N. P. Balsara, L. J. Fetters, N. Hadjichristidis, D. J. Lohse, C. C. Han, W. W. Graessley, and R. Krishnamoorti, Macromolecules **25**, 6137 (1992).

30. A. Losch, R. Salomonovic, U. Steiner, L. J. Fetters, and J. Klein, J. Polym. Sci., Polym. Phys. **33**, 1821-1831 (1995).

INTERFACIALLY CONFINED POLYMERIC SYSTEMS STUDIED BY ATOMIC FORCE MICROSCOPY

René M. Overney[*], Lantao Guo[**], Hirono Totsuka[**], Miriam Rafailovich[**], Jonathan Sokolov[**], Steven A. Schwarz[***]

[*] Department of Chemical Engineering
University of Washington, Box 351750, Seattle, WA 98195-1750
[**] Department of Materials Science,
State University of New York at Stony Brook, Stony Brook, N.Y. 11794-2275
[***] Department of Physics, Queens College, Flushing, N.Y. 11765

ABSTRACT

Within the last few years, a surface science technique, the atomic force microscopy (AFM), has evolved to be capable of simultaneously measuring tribological (friction, wear, adhesion) and rheological (elastic moduli, viscosity, hardness) properties and topography on the nanometer scale. Particularly for thin polymeric films, the AFM can be efficiently used for studying surface mechanical properties which are of fundamental importance to help predict stress and frictional behavior of interfacially confined ultrathin films.

In this paper, the following aspects will be discussed: (a) mechanical properties of ultrathin homopolymer and copolymer films, (b) dewetting dynamics of interfacially confined phase-separated homopolymers, and (c) the influence of graft-copolymers on the wetting and dewetting characteristics of homopolymers.

INTRODUCTION

The confinement studies of polymers at solid substrate interfaces are of great importance for various fields in polymer science, e.g., wetting and dewetting characteristics of thin polymer films, blend compatibilization, polymer mobility and polymer elastohydrodynamics. It is crucial to know more about changes introduced by interactions that occur at interfaces, especially, if the technological process of interest depends on the mechanical and stress properties of thin polymer films.

In recent years, considerable effort has been spent on achieving a basic understanding of the flow and dewetting behavior of simple and complex fluids [1-4]. Model systems of interest were ultrathin films of high molecular weight polymers on solid and liquid substrates [2-7]. It was demonstrated for homopolymer films on solid substrates that dewetting can be initiated by conformational constraints [5]. Interfacial tensions were found to play an important role in wetting of polymer blends [8]. The effect of an attractive solid interface on polymer mobility was investigated and found to decrease diffusion significantly [7, 9].

One technique that seems to be a good candidate in addressing local surface mechanical properties is the atomic force microscope (AFM) [10]. This fairly new scanning technique has been repeatedly applied to polymer surfaces because of its real space imaging capability [11,12]. One of the early desires has been to analyze quantitatively surface properties on the nanoscale. In that respect, the AFM encountered two improvements - the capability to measure lateral shear forces and viscoelastic properties simultaneously with topography while scanning a surface on the submicrometer scale [13]. A variety of nanorheological problems have been attacked so far by AFM; e.g., the interplay between competing forces of polymer dynamics and hydrocarbon interaction [13,14], phase separation of polymer blends at surfaces [15], elastohydrodynamic behavior of end-grafted polymer chains in solution [16], and dewetting and nucleation of binary polymer systems [7].

In the present paper, we demonstrate the connection between polymer mobility and mechanical properties. Two cases are considered; (a) The polymer mobility is constrained by pinning approximately $N^{1/2}$ random points along a chain at an interactive hard surface. In this situation we can show that polymer-substrate interfacial interactions can strongly affect the

rheology at the polymer/polymer interface over distances corresponding to several radii of gyration. (b) The mobility is constrained by forming interconnected micelle layers with rigid cores and flexible backbones. This latter configuration is analogous to that found in a cross linked network, where the cross linking density is controlled by varying the size of the loop between glassy interconnecting segments. In the present case we chose a graft copolymer system with an elastomeric backbone and glassy legs. In a graft copolymer system complications such as free chain ends or excess cross linker which can segregate to the surface and change the surface properties do not occur . This is a great advantage over standard cross linked polymers.

EXPERIMENT

Two binary systems are discussed, (a) 13 nm polystyrene (PS) films on 4-400 nm thick polyethylene-copropylene films, and (b) polyethylene acrylate (PEA) films on 50 nm thick deuterated polyethylene acrylate polystyrene block copolymer (PEA-xPS, x=1,3,5).

PEP and PEA-xPS are spin coated directly onto Si(001) wafers from toluene solution. Beforehand the silicon substrates are HF treated [17]. The films are annealed and dried at 110 $^\circ$C. PEP films and PEA-xPS films serve as substrates for the homopolymers PS and PEA, respectively. In the PS/PEP dewetting study, a 5 nm thick poly(vinyl pyridine) (PVP) film is used as a low interaction surface between silicon and PEP. Glass temperatures and molecular weights can be drawn from Table I. The film thickness of the single component films is determined by ellipsometry.

Table I: Molecular weight and glass temperature of the polymers used.

POLYMER	MOLECULAR WEIGHT (M_w) [g/mol]	GLASS TEMPERATURE (T_g) $^\circ$C
PEP	290k	-62
PS	220k	100
PVP	245k	142
PEA-xPS	150k-x15k	-
PEA	150k	-20

PS (13 nm) and PEA (100 nm) films are also prepared by spin casting and floated from water on the PEP and PEA-xPS substrates, respectively. The substrates are partially kept free from the floating film in order to study relative differences in the scan images, and to determine the film thickness of the polymer top layer after annealing.

PEP/PS stacks are annealed at 110-130 $^\circ$C in high vacuum (10^{-6} Pa) between 15 and 30 minutes. PEA/PEA-xPS stacks are annealed at 180 $^\circ$C under the same conditions for 24 hours. Finally the binary films are quenched to room temperature and studied in air upon their dewetting characteristics by AFM.

Surface mechanical properties of single component films and dewetted binary film systems are probed under ambient conditions at room temperature on the submicrometer scale by AFM. The experimental set-up, a modified commercial AFM (*Explorer* from Topometrix, Inc.), is based on the beam-deflection detection scheme [18-20]. With this set-up lateral shear forces, that are directly related to acting torsional forces on the cantilever, are measured in registry with the surface topography. The cantilever is additionally modulated normal to the sample surface, Figure 1.

The in-phase and out-of-phase modulation response is fed into a two-phase lock-in amplifier and the elastic modulus and viscosity determined [21]. Lateral force and force modulation results are normalized by the acting equilibrium load, the sum of applied load and adhesion. The equilibrium load is determined on sample areas of different material by force displacement curves, Figure 2.

Lateral force and elastic moduli are compared between different samples and sample regions and plotted in relative representations. Absolute representations strongly depend on the chosen theoretical model (Hertzian model, JKR-model, DMT model, Maxwell model, etc.) [14, 16, 21-24]. Hence, there are no absolute values reported in this paper. The frequencies of the force modulation are kept below the first resonance frequency of the system (around 4 kHz) between

300-3000 Hz. Comparisons in-between samples are made at the same frequency (1 kHz or 2 kHz) and rms amplitudes of 5.5 nm while scanning with 1 Hz in the x,y plane at a velocity of 50 μm/s.
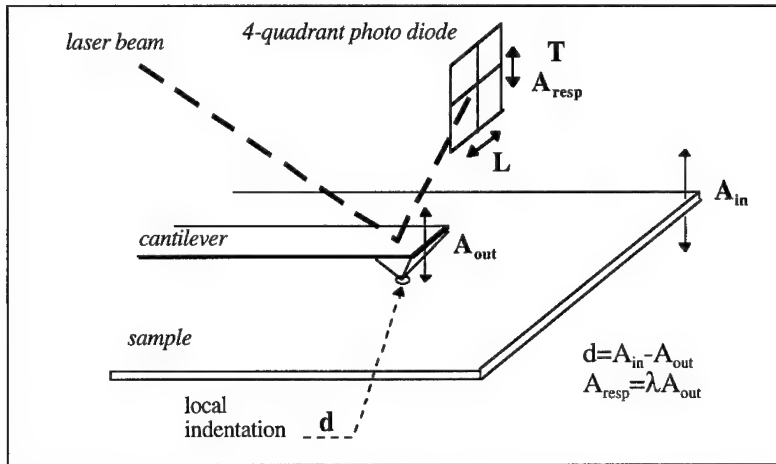
Figure 1: Laser Beam Detection Scheme of a 3-fold AFM Set-up. Topography (T), lateral forces (L) and viscoelastic response (A_{resp}) are measured simultaneously while scanning the cantilever. The input modulation (A_{in}) is either applied at the sample stage (sketched) or cantilever stage. The force modulation response amplitude is calibrated with λ. Amplitude and phase relation between the modulation signals provide local information about the viscoelastic properties of the sample surface.
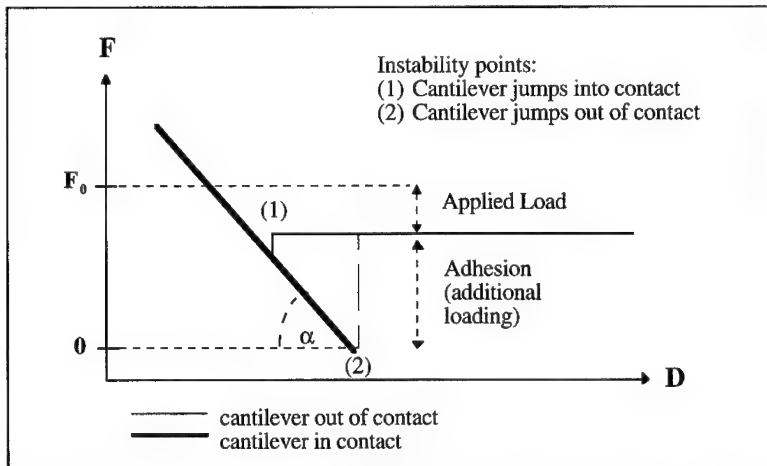
Figure 2: Force-Displacement Curve. The equilibrium load F_0 is the sum of applied load and adhesion and is chosen by the operator. Because of adhesion it is possible to apply a negative load as long as the equilibrium load remains positive. The applied load corresponds to the equilibrium load in case of zero adhesion (Hertzian contact). The slope α is a measure for the convoluted stiffness of cantilever and sample.

Bar and triangular shaped cantilevers with spring constants of 0.01-30 N/m are used. Equilibrium loads on the order of 10^{-8} N are applied for imaging. Measurements are conducted in dry nitrogen environment and compared to measurements in ambient atmosphere. Although the

loading regime under ambient conditions was on average an order of magnitude higher than in a dry nitrogen environment, the normalized (i.e., adhesion corrected) forces and moduli were found to be in good correspondence.

Dynamic secondary ion mass spectrometry (SIMS) measurements are conducted on the deuterated PEA-xPS films where the volume fraction of deuterium is detected as a function of distance from the vacuum interface. SIMS measurements are used to determine the degree of ordering in the films and ascertain the chemical component, in this case the deuterated PEA, on the surface.

RESULTS AND DISCUSSIONS

Dewetting dynamics of interfacially confined homopolymers

In a previously published experiment of PS/PEP stacks on silicon, we found unexpectedly that the depth of the dewetting holes exceeded by far the thickness of the top PS film [7] (see Figure 3). Film thickness and hole depth measurements at PS/PEP-PEP edges confirmed that dewetting occurs deep inside the liquid PEP film. As long as the PEP film is thicker than 200 nm and the PS film thickness is 13 nm the dewetting holes are 25±4 nm in depth.

For PEP films thinner than 200 nm on silicon, we reported decreased dewetting hole depths [7]. The holes decrease with decreasing PEP film thickness, although the silicon interface is significantly further away (more than one order of magnitude larger than the radius of gyration of PEP). Another difference between thick and thin PEP films was found in the lateral size of the dewetting holes. Whereas for thick PEP samples the holes emerged into each other and extended over microns during an annealing time of 15 min., in very thin PEP samples of less than 10 nm thickness, the holes are isolated, circular in shape and less than 500 nm in diameter. Rims were found only around the dewetting holes for thin films. Measurements of dewetting velocities, Figure 4, correspond with the lateral size measurements reported earlier.
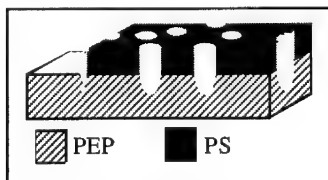
Figure 3: The edge of the PS film on top of PEP. Sketch: Top view and side view of the PS film edge. The dewetting holes are inside the PEP phase, 25 nm in depth
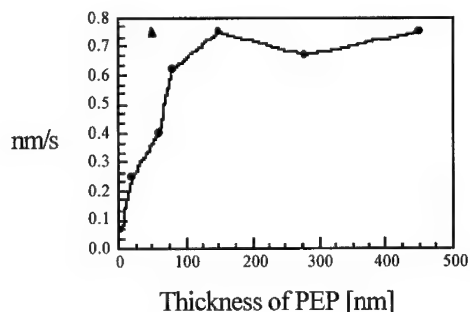
Figure 4: Dewetting Velocities and Dewetting Hole Depths of PS/PEP System. The dewetting velocity is decreasing for a PEP film thickness below 200 nm and silicon as a substrate (●). No decrease in the dewetting velocity is observed in case of a PVP substrate (▲).

Lateral force and viscoelasticity measurements reveal constant mechanical properties of PEP, as long as the PEP film thickness is larger than the above found critical film thickness of 200 nm. However for films thinner than 200 nm, the surface viscoelastic properties are changing, Fig. 5. The thinner the PEP films, the more glassy and less viscous the surfaces behave. This is observed in both modes of operation, the lateral force mode and the normal force modulation mode.

The functional behavior of the lateral forces with the PEP film thickness, Figure 5, corresponds qualitatively with the measured dewetting velocities, Figure 4. Both results combined suggest an overall shift of the rubbery state of bulk PS towards a more glassy behavior of ultrathin PEP films. The loss in molecular mobility is causing smaller dewetting holes in all three dimensions as shown in Figure 6.
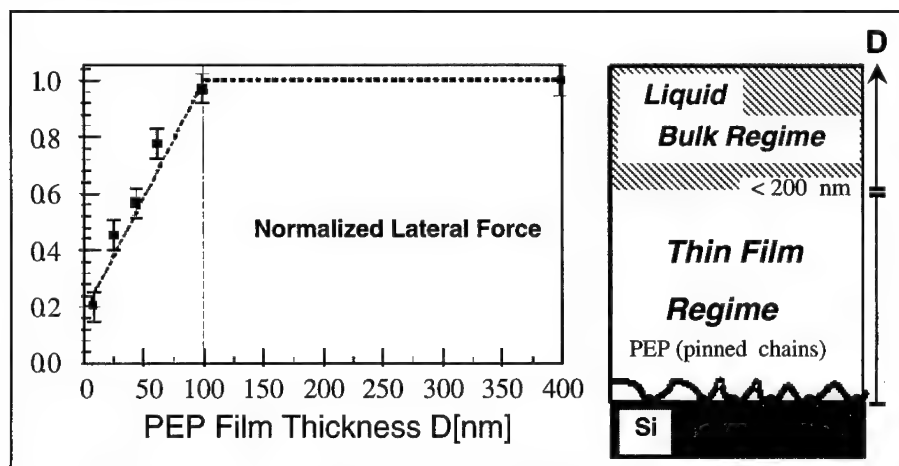
Figure 5: Change in surface mechanical properties of ultrathin PEP films on silicon. Lateral forces - as a measure for surface viscoelastic properties - on PEP films are decreasing with thinner film thickness below 100 nm.
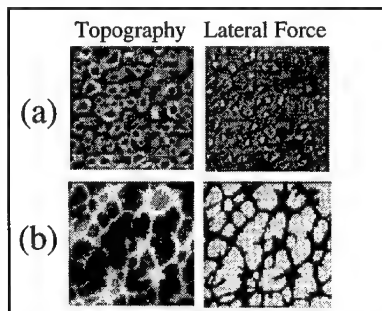
Figure 6: Dewetting influenced by the change in the mechanical properties. AFM topography and lateral force images on 13 nm PS on top of PEP films after 30 min. annealing at 125 °C. (a) 5×5 μm², 4 nm PEP film; small dewetting holes (dark), about 13 nm in depth, surrounded by rims. (b) 20×20 μm² 400 nm PEP film; huge dewetting holes (dark) 25±4 nm in depth.

Rims around dewetting holes are formed if dewetting occurs faster than material can be dispersed. In the thick PEP film, the dewetting plane (we will further refer to it as shear plane) is located about 10 nm in the low viscosity regime of the bulk PEP film. Because of the lower bulk

viscosity of PEP compared to PS, and the considerable large volume which is involved during the annealing process, material can be dispersed fast enough. No rims are formed for thick PEP substrates. For thin PEP films (thinner than 200 nm), PEP become more glassy, hence, the location of the dewetting shear plane is moved towards the PS and PEP interface. Because PS has a higher viscosity phase than PEP, and the molecular mobility in PEP is decreased, dewetting occurs slower and rims are formed.

So we find that dewetting of PS/PEP films is strongly influenced by the mechanical properties of PEP. On the other hand we observe for ultrathin PEP films that the mechanical properties are strongly dependent on the film thickness. Dewetting velocity measurements of PS/PEP films on PVP, a low interaction substrate, expose the silicon surface (a high interaction surface) responsible for the change in the viscoelastic properties of PEP, Figure 4. It is reasonable to assume that pinning forces are accountable for a decrease in the molecular mobility of PEP in the vicinity of the silicon substrate. Hence, there is a viscoelastic property gradient of PEP towards a high interaction substrate.

In order to discuss the location of the dewetting shear plane we use two simplified one-dimensional models depending on the shear regime.

In the shear regime of a thick PEP film (film thickness above 200 nm) we consider diffusion and the PS/PEP interdiffusion zone responsible for the shear plane formation deep inside the PEP phase. Neutron reflection measurements exhibit an interdiffusion zone of around 4 nm at the PS/PEP interface. Hence, a no-slip condition between PS and PEP can be assumed. It is further assumed that PS impulsively opens up and the flow is driven by the motion of the boundary, and density and viscosity of thick PEP films are constant. These assumptions are reasonable for thick films. Hence, the velocity $u(y,t)$ in the PEP film satisfies the classical diffusion equation which is in one-dimension

$$\frac{\partial u}{\partial t} = v \frac{\partial^2 u}{\partial y^2}$$

with y as the coordinate normal to the PEP film surface, and v the kinematic viscosity. It is known that in such a system the effects of the motion are largely confined to a distance on the order of $(vt)^{1/2}$ [25]. The thickness of the boundary layer δ is therefore roughly estimated by

$$\delta^2 = vt^*$$

where t^* is the characteristic time of the momentum diffusion through the boundary layer [25]. The diffusion model of viscous boundary layer provides the characteristic time of diffusion, or if known, the location of the shear plane - assuming the shear plane coincides with the bottom of the boundary layer. Measurements of the time of diffusion are still in progress. There is however a missing experimental observation . No gradual opening of the dewetting holes (i.e., finite slope at the edges) could be measured so far even for long dewetting times. This suggest a instantaneous crack propagation in the liquid PEP phase without flow and is still under investigation.

For ultrathin PEP films, i.e., thicknesses smaller than 200 nm, the Bingham model is used to determine the interplay of a strong interaction substrate. A fluid which is described by the Bingham model, i.e.,

$$\tau_{yx} = -\eta \frac{du_x}{dy} \pm \tau_o \text{ if } |\tau_{yx}| \geq \tau_o$$

$$\frac{du_x}{dy} = 0 \text{ if } |\tau_{yx}| < \tau_o$$

remains rigid when the shear stress τ_{yx} is of smaller magnitude than the yield stress τ_o but flows somewhat like a Newtonian fluid when the shear stress exceeds τ_o (u_x represents the one dimensional velocity in x direction) [26]. Zero shear stress and no slip is assumed at the strong interaction interface, silicon. A boundary layer at the silicon surface can be defined with the shear stress τ_o necessary to open up the PEP film. The boundary layer thickness is determined by the critical shear stress τ_o whereas τ_o is set by the local mechanical properties of the material, PEP.

While the diffusion model would not need the Bingham model to explain shear inside a thick PEP film, the Bingham model is essential for a crack propagation model. Without a gradient in the shear response rate, the shear plane would be established at the PEP/silicon interface.

Confinement effect of compatibalizer on dewetting

The 3-fold measuring AFM technique [14] (simultaneous measurement of topography, lateral forces and viscoelasticity) is used to study the forced wetting and dewetting of PEA-xPS graft copolymer by a thin layer of PEA homopolymer. In figure 7, a partially uncovered area of a PEA-5PS film is shown. As presented in topography and sketched in Figure 7(d), the PEA-xPS film consists of a bilayer base with bilayer islands on top. Constant lateral force values on the uncovered area (i.e., the island do not provide different contrast) suggest that only one molecular species of the PEA-5PS copolymer is exposed to the air interface, Figure 7b. Because there is just a very slight variation in the elastic modulus, Figure 7c, which is not visible in the lateral force mode, lateral forces provide on the bare PEA-5PS substrate a qualitative measure of constant non-conservative tip-sample interaction forces (friction) [27, 28]. This is in correspondence to SIMS measurements, Figure 8, which manifest a bilayer stacking of PEA-5PS↔5PS-PEA. Hence, the PEA-5PS substrate exhibits a chemically uniform surface of PEA which is a perfectly compatible surface for PEA homopolymers.
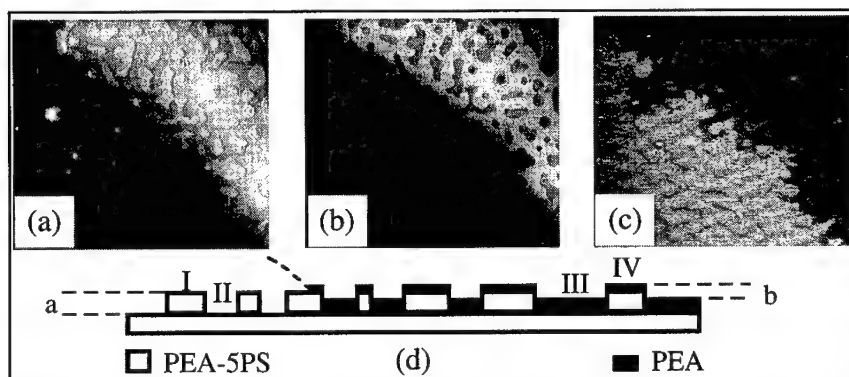
Figure 7: Partial coverage of PEA-5PS by PEA homopolymer. 40×40 μm² 3-fold AFM measurement before annealing. Brighter contrast refer to higher values in topography, lateral force and Young's modulus (stiffness). The upper right triangular area is PEA homopolymer covered. The lower left triangular area is the bare PEA-5PS graft copolymer surface. (a) Topography image. (b) Lateral force image. (c) Elastic response exhibits stiffer graft copolymers (*bright*) than homopolymers (*dark*). (d) Sketch: Represents a topographical cross-section. The left and right side corresponds to the measured bottom and top triangular AFM area, respectively. The height differences are a = 28 ± 2 nm and b = 8 ± 2 nm. Areas are distinct with Roman numbers (c.f. Table II).

The PEA homopolymer covered PEA-5PS area reveals a flattened surface topography before annealing, Figure 7a. PEA preferentially fills the voids while only a thin film (<2 nm in thickness) remains on top of the islands. Even in the case spin coated PEA films thicker than the island height of 28 ± 2 nm, the islands are visible in topography. In figure 7, the PEA-5PS substrate is partially covered with a PEA film of about the substrate's island height size. The PEA covered area reveals a significantly reduced stiffness of a factor of 1.5-2 compared to the graft copolymer substrate. Two regimes of recognizable elastic differences are measured on the PEA homopolymer area. This result if compared to topography reveals that the thinner PEA homopolymer films on top of the PEA-5PS islands are stiffer than the thicker PEA films which fill the voids. The relative values of elastic responses measured are found in Table II.

Lateral force measurements also reveal two distinct regimes in the PEA homopolymer area, Figure 7(b). This is in correspondence with the elastic information. In this particular case, the lateral forces are a measure of the shear mechanical properties of the sample.

Summarized, three lateral force regimes are differentiable on the non-annealed sample, which is found by SIMS as chemically homogeneous, Figure 8.

Table II: Variation in lateral forces and elastic response on PEA/PEA-5PS.

AREA (FIG. 7)	LATERAL FORCE	ELASTIC RESPONSE
I	1 (Norm)	1 (Norm)
II	1	1* ± 0.1
III	4.2 ± 0.2	0.5 ± 0.1
IV	2.8 ± 0.2	0.8 ± 0.1

* variation within uncertainty of measurement

Lateral force measurements also reveal two distinct regimes in the PEA homopolymer area, Figure 7(b). This is in correspondence with the elastic information. In this particular case, the lateral forces are a measure of the shear mechanical properties of the sample.
Summarized, three lateral force regimes are differentiable on the non-annealed sample, which is found by SIMS as chemically homogeneous, Figure 8.
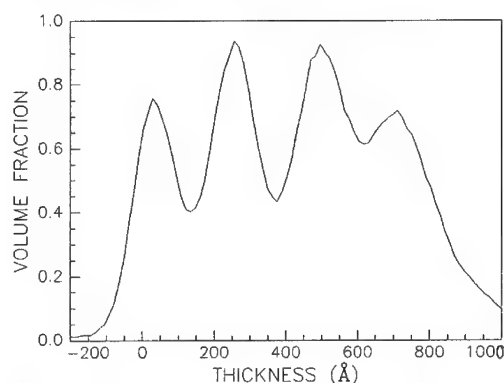
Figure 8: SIMS Measurements on PEA-5PS copolymer. Volume fraction measurements with SIMS exhibit a cylindrical structure of PEA-3PS graft copolymer films with the inclusion of PS between PEA. A lamellar structure is found for x=5.

The reason for lateral force variations are due to strong variations in the mechanical properties. Note, however, that there are no distinct lateral force aberrations on the bare PEA-5PS substrate despite variations in the Young's modulus. Therefore, it is possible to conclude that on this specific area, non-conservative tip-sample interaction forces dominate shear force variations. As expected, the graft copolymers are stiffer than their backbone homopolymers which are, at room temperature, in a rubbery phase. It is interesting to note that the PEA films floated on top of the ordered PEA-xPS substrates flow such that material is spread only thinly on top of island structures and pooled inside the hole morphologies. In a manner similar to that previously observed for the PS/PEP system, the lateral force is lower and the elastic response is higher in the thinner regions on top of the islands and vice versa in the thicker regions at the bottom of the holes. In this case the confining force is the self-adhesion (or cohesion) between PEA homopolymer and the PEA backbones of the block copolymer.

AFM measurements reveal, after annealing at 180 °C for 24 hours, increased height differences in the PEA homopolymer covered area. Lateral force and viscoelasticity measurements suggest that the trapped PEA homopolymers diffused out of the voids on top of the islands, leaving back a mechanically stiffer PEA surface layer. This is supported by topography measurements at PEA homopolymer film edges and will be discussed in more detail elsewhere [29].

After annealing, relatively smooth PEA homopolymer surfaces are found if the PEA spin cast film is around 130 nm thick, Figure 9. On one hand, the homopolymer film is thick enough to cover the island of PEA-5PS, and on the other hand, thin enough to study the effect of surface confinement.

Lateral force and viscoelastic measurements reveal a stiffer elastic response of the annealed PEA film at the location of the substrate's islands, Figure 9. Considering that there is still a height difference of about 5 nm on the PEA/PEA-5PS stack, the relative height variation in the thickness of the PEA film is about 15%. As expected from the measurements of PEP, the 15% thinner areas of PEA, which are located above the substrate islands, are measured to be stiffer in their mechanical response than their surroundings, Figure 9.

(a)   (b)
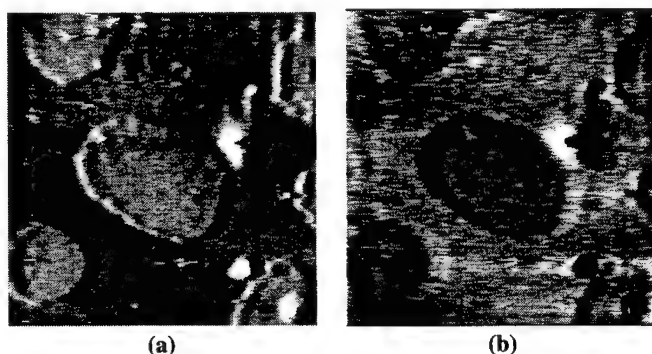
Figure 9: PEA/PEA-5PS stacks annealed. 25×25 μm² 3-fold AFM measurement after annealing. (a) Topography reveals islands of 5 nm height. (b) Lateral forces are lower on top of the islands.
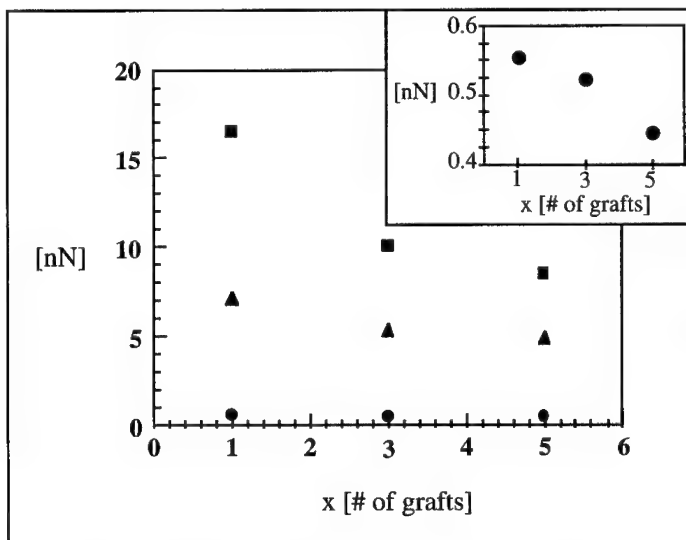
Figure 10: Backbone bending flexibility of PEA-xPS. ■ Adhesion forces provide information about stiffening of graft copolymer surface with increased grafting density. ▲ Absolute lateral forces are adhesion influenced. ● Lateral forces, adhesion corrected. *Inset:* Magnification of adhesion corrected lateral forces.

Mechanical properties, film morphologies and dewetting characteristics are also studied as functions of grafting densities x=1,3,5 of the PEA-xPS substrate. It is found in lateral force and viscoelastic measurements that the graft copolymers stiffens with increasing grafting density,

Figure 10. Note, however, that the stiffening effect is by far not as dramatic as the adhesion dependent lateral force variation, Fig. 10. High adhesion forces are measured for a PEA 1-graft substrate, and considerable declining values for higher grafting densities.

SIMS measurements reveal that with the change in the grafting density, structural changes occur. In 1-, 3- and 5-graft systems, the copolymers form spheres, tubes and lamellae, respectively. Hence, the AFM tip encounters different wetting capabilities of the sample which gives rise to variation in the adhesion. The wetting capability is a measure for flexibility of the polymer structure. In that regards, the 1-graft system is much more flexible than the 3- or 5-graft system. A significantly different morphology is found in the 1-graft system compared to 3- and 5-graft systems, Figure 11. There are no island formations on the PEA-1PS substrates and a very complex and, so far not understood, dewetting pattern of the PEA homopolymer film on top.

(a)   (b)
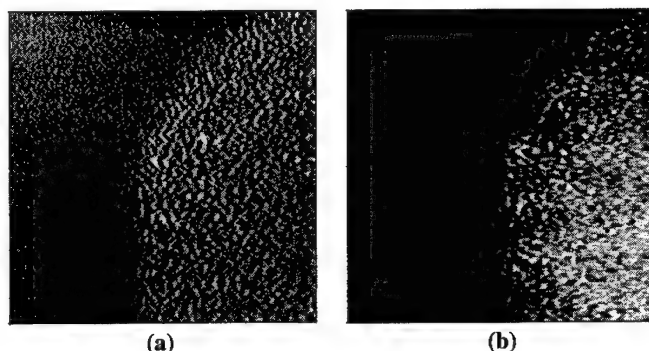
Figure 11: AFM maps of PEA-1PS graft copolymer. 50×50 μm^2 3-fold AFM measurement after annealing. (a) Topography reveals no islands. The dark area corresponds to the bare PEA-1PS substrate. (b) Lateral force scans contain convoluted shear mechanical properties and adhesion values.

CONCLUSIONS

Dewetting has been studied on ultrathin liquid homopolymer films with high and low glass temperature polymers. The substrates were either solids, low glass temperature polymers, or graft copolymers. A general finding is that the mechanical properties of polymers in their liquid phase strongly depend on the interfacial interaction to the substrate. In closest vicinity to the substrate interface, the liquid phase of the polymer on top is shifted towards a more glassy state. A phase gradient is found for PEP on silicon up to a distance of more than 100 nm from the silicon substrate. The interfacially induced confinement of the liquid polymers has been discovered to be the reason for changes in the dewetting behavior. In the PS/PEP system, it is found that the dewetting velocity is significantly decreased for PEP films thinner than about 200 nm. It can be concluded from studies on low and high interaction interfaces that dewetting of ultrathin films can be controlled with the choice of the substrate.

Graft copolymers have been chosen as substrates because of the potential to influence mechanical properties by varying the grafting density without modifying the chemistry. However, only a slight dependence of the shear mechanical properties on the grafting density has been found. A much more significant dependence has been established between polymer backbone bending flexibility and the grafting density. Mechanical properties of PEA homopolymers on chemically identical PEA-xPS graft copolymer surfaces revealed liquid polymer phase gradients as found on the PEP/silicon system.

It has been mentioned that ultrathin PEA films dewet PEA surfaces formed by the graft copolymer. This unusual process of self-dewetting is of great interest because it predicts a negative

spreading coefficient. More research especially in respect of nanomechanical properties and crosslinking density of liquid phase polymers is in progress and will be published soon.

The concept of adhesion correction for lateral force measurements was introduced for the first time. Nanomechanical properties have been determined with the state of the art sinusoidal perturbation technique but also with lateral force measurements. It is important to note that lateral forces measurements resemble not only conservative forces, but also describe irreversible processes, which are determined by adhesion forces between sample and tip. If elastic properties dominate the lateral force response, or the lateral force signals are adhesion corrected, lateral force measurements can provide important information about the surface mechanical properties of the sample. Adhesion measurements, on the other hand, were shown to be useful in determining backbone flexibilities of graft copolymers. Finally, note that with measurements of interaction forces (adhesion: chemical interactions or physisorption) or lateral force measurements alone, conclusions about the surface chemical composition are doubtful.

ACKNOWLEDGMENTS

REFERENCES

[1]   P. G. de Gennes, *Rev. Mod. Phys.*, vol. 57, 827, 1985.
[2]   F. Brochard-Wyart, P. Martin, and C. Redon, *Langmuir*, vol. 9, 3682, 1993.
[3]   G. Reiter, *Langmuir*, vol. 9, 1344, 1994.
[4]   W. Zhao, M. H. Rafailovich, J. Sokolov, L. J. Fetters, R. Plano, M. K. Sanyal, S. K. Sinha, and B. B. Sauer, vol. 70, 1453, 1993.
[5]   Y. Liu, M. H. Rafailovich, J. Sokolov, S. A. Schwarz, X. Zhong, A. Eisenberg, E. J. Kramer, B. B. Sauer, and S. Satija, *Phys. Rev. Lett.*, vol. 73, 440, 1994.
[6]   P. Lambooy, K. C. Phelan, O. Haugg, and G. Krausch, *Phys. Rev. Lett.*, vol. 76, 1110, 1996.
[7]   R. M. Overney, D. P. Leta, L. J. Fetters, Y. Liu, M. H. Rafailovich, and J. Sokolov, *J. Vac. Sci. Technol.*, vol. B 14, 1276, 1996.
[8]   D. Gersappe, D. Irvine, A. C. Balazs, Y. Liu, J. Sokolov, M. H. Rafailovich, S. Schwarz, and D. G. Pfeiffer, *Science*, vol. 265, 1072, 1994.
[9]   X. Zheng, B. B. Sauer, J. G. Van Alsten, S. A. Schwarz, M. H. Rafailovich, J. Sokolov, and M. Rubinstein, *Phys. Rev. Lett.*, vol. 74, 407, 1995.
[10] G. Binnig, C. F. Quate, and C. Gerber, *Phys. Rev. Lett.*, vol. 56, 930, 1986.
[11] M. C. Goh, *Advances in Chemical Physics, vol XCI*, 1-82, eds. I. Prigogine and S.A. Rice, John Wiley & Sons, New York, 1995.
[12] R. M. Overney, *TRIP*, vol. 3, 359, 1995.
[13] R. M. Overney, H. Takano, and M. Fujihira,*Europhys Lett*, vol. 26, 443, 1994.
[14] R. M. Overney, E. Meyer, J. Frommer, H.-J. Güntherodt, M. Fujihira, H. Takano, and Y. Gotoh, *Langmuir*, vol. 10, 1281, 1994.
[15] T. Kajiyama, K. Tanaka, I. Ohki, S.-R. Ge, J.-S. Yoon, and A. Takahara, *Macromolecules*, vol. 27, 7932, 1994.
[16] R. M. Overney, D. P. Leta, C. F. Pictroski, M. H. Rafailovich, Y. Liu, J. Quinn, J. Sokolov, A. Eisenberg, and G. Overney, *Phys. Rev. Lett.*, vol. 76, 1272, 1996.
[17] G. S. Higashi, Y. J. Chabal, G. W. Trucks, and K. Raghavachari, *Appl. Phys. Lett.*, vol. 56, 656, 1990.
[18] G. Meyer and N. M. Amer, *Appl. Phys. Lett.*, vol. 56, 2100, 1990.
[19] G. Meyer and N. M. Amer, *Appl. Phys. Lett.*, vol. 57, 2089, 1990.
[20] O. Marti, J. Colchero, and J. Mlynek, *Nanotechnology*, vol. 1, 141, 1990.
[21] M. Radmacher, R. W. Tillmann, and H. E. Gaub, *Biophys. J.*, vol. 64, 735, 1993.
[22] K. L. Johnson, K. Kendall, and A. D. Roberts, *Proc. Royal Soc. A*, vol. 324, 301, 1971.
[23] K. L. Johnson, *Contact Mechanics*: Cambridge University Press, Cambridge, 1985.

[24] M. Radmacher, R. W. Tillmann, M. Fritz, and H. E. Gaub, *Science*, vol. 257, 1900, 1992.

[25] D. J. Acheson, *Elementary Fluid Dynamics*: Clarendon Press, Oxford, 1992.

[26] R. B. Bird, W. E. Stewart, and E. N. Lightfoot, *Transport Phenomena*: John Wiley & Sons, New York, 1960.

[27] R. M. Overney, E. Meyer, J. Frommer, D. Brodbeck, R. Lüthi, L. Howald, H. J. Güntherodt, M. Fujihira, H. Takano, and Y. Gotoh, *Nature (London)*, vol. 359, 133, 1992.

[28] C. D. Frisbie, L. F. Rozsnayai, A. Noy, M. S. Wrighton, and C. M. Lieber, *Science*, vol. 265, 2071, 1994.

[29] Work in progress.

SPONGE PHASE UNDER SHEAR

H. F. MAHJOUB*, C. BOURGAUX$^{\&}$, K. M. M^{C}GRATH*#, J.F. TASSIN§, M. KLEMAN*
*Laboratoire de Minéralogie-Cristallographie de Paris, Université P.-&-M. Curie, T 16, case 115, 4 pl Jussieu, 75252 Paris cédex 05, France
&LURE, Batiment 209D, Centre Universitaire 91405 Orsay Cedex -France.
#Department of Physics, Princeton University, Princeton, NJ 08544
§Laboratoire de Physico-Chimie Macromoléculaire, Université du Mans, avenue O. Messiaen, BP 35, 72017 Le Mans cédex, France

ABSTRACT

The L_3 phase under shear transforms to a lamellar phase L_α^* above some critical shear rate. We study the sequence of successive states (rheothinning, flow birefringence, transition region, lamellar) with simultaneous rheooptical methods, in situ X-ray scattering, and light microscopy observations. The transition region is biphasic, and the two phases display epitaxial relationship immediately after shearing is ceased.

INTRODUCTION

We report on a series of experiments relating to the structural modifications which affect the sponge phase L_3 under shear. The symmetric sponge phase, according to the most popular view, is an optically isotropic 3-D random multiply connected bilayer of surfactant molecules, dividing the solvent into two equivalent subvolumes [1]. We adopt this view, which is probably correct for the system under study (consisting of: a quaternary ammonium surfactant, cetylpyridinium chloride – CPCl, H_2O content 1mol/mol – ; hexanol; and brine – 1% wt NaCl – as a solvent) in the solvent wt fraction range $0.85 < \phi_s < 0.95$. Different conclusions are valid for other ranges of solvent concentration, yielding the possibility of various sponge phases [2]. This point will not be discussed here.

The most conspicuous macroscopic property of the L_3 sponge phase is its large flow birefringence under gentle shaking. A few investigations of the rheological properties of L_3 are reported in the litterature [3, 4, 5]. Experimentally Diat and Roux have found a regime of flow birefringence above some shear rate threshold for a quaternary system which differs from ours (it is based on SDS surfactant), housed in a rotating Couette cell, using observations made in an orientation perpendicular to that adopted here; these authors state that it would be necessary to go to higher shear rates than those experimentally available to obtain dynamic lamellar L_α^* domains under shear (we use a star exponent for the phase which appears under shear); other authors have found experimental evidence that the L_3 phase is not unstable under shear, while the L_α phase is [5]. These contradictory results are also reflected in the theoretical literature [6, 7]. The results we present here originate from different methods of investigation: rheo-optical measurements, SAXS data, on one hand, optical observations of the textures of the samples just after shear and during relaxation, on the other. They are valid for the system which is under study, and should not be extended without caution to other systems, in the present state of our understanding of the sponge phase. We do not know of any previous optical observations of textures coupled to a phase transition under shear.

EXPERIMENT

Methods

All rheoptical work was performed using a Rheometer Optical Analyzer (ROA of Rheometrics; $\dot{\gamma}_{max} = 500$ s^{-1}), equipped with a Couette cell (gap between cylinders 1mm, outer radius 16mm), which allows the measurement of birefringence Δn in the plane of the flow (plane $\mathbf{V}$, $\nabla\mathbf{V}$), angle of extinction χ, and transmitted light intensity I/I_0, while shearing the sample. The observation of the shape of the transmitted light spot is also possible and of interest.

X-ray scattering experiments were conducted at the D24 beam line of the LURE-DCI synchrotron radiation facility in Orsay. A Couette cell has been specially designed to carry out simultaneously in situ X-ray scattering and optical microscopic observations of complex fluids under shear flow (gap between cylinders 0.5mm or 1mm, outer radius 10 mm or 16 mm). The shear rate $\dot{\gamma}$ ranges between 0.05 s^{-1} and 900 s^{-1}. The cell is made of polymethylmetacrylate, known for its good transparency to X-rays and light. The X-ray beam can be chosen parallel either to the shear gradient (radial geometry) or to the velocity (tangential geometry). An optical microscope is fitted to this cell perpendicular to the X-ray beam to allow simultaneous observation of the sample. The light beam crosses the center of the cell perpendicularly to the X-ray beam, in the horizontal plane. Observations were carried out between crossed polars.

Results

Table I summarizes some of the important material constants as a function of composition of the L_3 phase; d_3 (characteristic length of the L_3 phase, measured at the maximum in the intensity of the X-ray scatter), B (the time constant of the flow birefringence $\Delta n = B\dot{\gamma}$), η (the kinematical viscosity) and d_α^*, the repeat distance in the L_α^* lamellar phase. Some of these results are extracted from a former publication [8] dealing mostly with rheo-optical measurements. Most of the results relate to 2 compositions, sample **a**: $\phi_S = 0.85$, h/c = 1.12, sample **b**: $\phi_S = 0.90$, h/c = 1.15. Here h/c is the wt ratio of the cosurfactant (h: hexanol) and the surfactant (c: CPCl) present in the bilayers.

Table I

	h/c (wt ratio)	ϕ_S (wt fraction)	d_3 (nm) at rest	10^9 B (s)	η (cP) $\dot{\gamma} = 20$ s^{-1}	d_α^* (nm) peak 2	d_α^* (nm) peak 3	d_α^* (nm) peak 4
a	1.12	0.85	22	2.03	7.4	16.5	16.8	18
b	1.15	0.90	33	4.86	5.7	23.7	24.0	26.1
	1.225	0.95		11.9				

Two regimes can be distinguished <u>at low shear rates</u>. In the range $0 < \dot{\gamma} < \dot{\gamma}_0$, the birefringence is small, close to 10^{-9}, strongly fluctuates; above $\dot{\gamma}_0$ and up to some value $\dot{\gamma}_1$, Δn shows a steady linear increase with the shear rate, and the characteristic time B varies as $\phi^{-\alpha}$, with $\alpha \sim 1.8$ to a good approximation (here ϕ is the volumic fraction of the bilayers), close to the value $\alpha = 2$ expected from scaling arguments [9]. At the same time the X-ray scattering shows an isotropic diffuse ring at $q = 2\pi/d_3$ which does not differ significantly from its rest value, to the precision of our measurements. After shearing is ceased in the $\dot{\gamma} > \dot{\gamma}_0$ range, the sample relaxes with a well defined relaxation time τ_0 of the order of $\dot{\gamma}_0^{-1}$ (fig. 1).

Table II

	$\dot{\gamma}_0$ (s^{-1})	τ_0 (ms)	$\dot{\gamma}_1$ (s^{-1})	$\dot{\gamma}_c$ (s^{-1})
a	~10	~150	25-30	40-50
b	~5	200	12	20-30
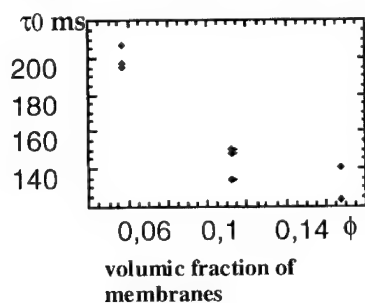
fig. 1: relaxation time τ_0 as a function of ϕ.

<u>At high shear rates</u>, above the critical threshold $\dot{\gamma}_c$ obtained experimentally in [9] (see Table II for values of $\dot{\gamma}_0$, $\dot{\gamma}_1$, $\dot{\gamma}_c$), L_3 transforms completely to a lamellar phase L_α^* (curve 4 in fig. 2; see table I for the 'terminal' d_α^* values), whose orientation is mostly parallel to the boundaries of the
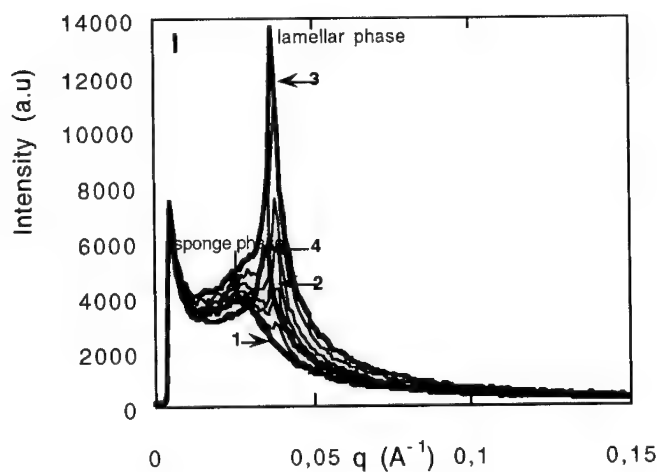
fig. 2: sample **a**, X-ray spectra in radial geometry, at different shear rates:
peak1: $\dot{\gamma} \approx 15$ s^{-1} peak2: $\dot{\gamma}=35$ s^{-1} peak3: $\dot{\gamma}=40$ s^{-1} peak4: $\dot{\gamma}=50$ s^{-1}

cell, but with some disorder probably due to a partition in domains slightly disoriented one with respect to the other, elongated in the direction of the velocity. Their shape and size, roughly 20μm, are deduced from the shape and size of the light beam after traversal of the cell. The X-ray spectrum (curve 4 in fig. 2) shows a smectic peak which is less intense than in the intermediary states, due to a change of orientation (see below). The relaxation of the phase requires long durations; at first, immediately after ceasing the shear, the birefringence *increases*, the lamellar character seems to increase, the whole area observed between crossed polars is remarkably homogeneous, without defects; then after a few hours (sample **a**) a number of focal toric domains (of the first species, i.e. with negative Gaussian curvature), whose size is in the 10μm range, appear.

We have studied the <u>intermediary shear range</u> (above the limit $\dot{\gamma}_1$ of the linear streaming birefringence range of shear rates, below the threshold $\dot{\gamma}_c$ for complete transition) in much more detail. Fig. 2 (radial geometry) displays several situations (sample **a**) labelled 1, 2, 3, 4, corresponding to increasing shear rates and/or increasing shear. The sample is biphasic in states 2, 3 (the L_α^* peak intensity increases from 2 to 3, at the expense of the L_3 peak intensity), then turns rather quickly in a well-defined L_α^* phase at a shear rate for which the L_3 phase completely disappears, and the orientation changes. And indeed the L_α^* layers have a strong component parallel to the **V**, ∇**V** plane in 2 and 3, while they are mostly parallel to the cylinder boundaries in 4 (fig. 3). This is to be compared to the theoretical predictions in [10].

At the same time the L_α^* periodicity increases steadily from 1 to 4 (terminal periodicity). See table I for data. I(q) scales asymptotically as q^{-2} as expected for a layered structure and the Caillé

1)   2)
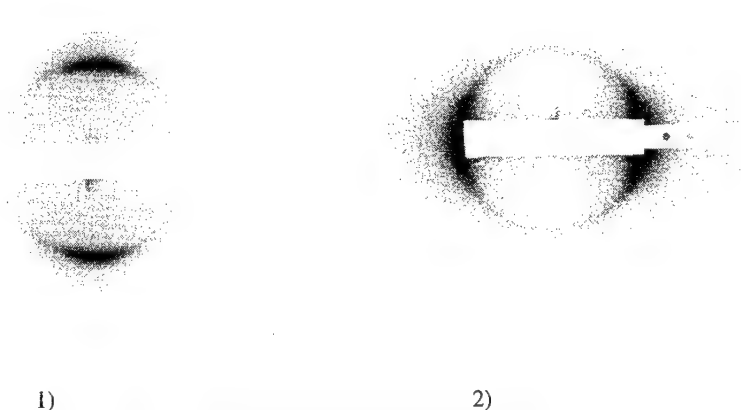
fig. 3: X-ray patterns in tangential geometry, sample **a**;
1)- L_α^* phase oriented perpendicularly to the Couette boundaries, $\dot{\gamma}=35$ s^{-1}
2)- L_α^* phase oriented mostly parallel to the Couette boundaries, $\dot{\gamma}=60$ s^{-1}.

exponent [11] is of the order of 1.06, in good agreement with the theory. These results are corroborated by our optical microscopy observations, made through the transparent walls of the Couette cell immediately after ceasing shear. Fig. 4 shows L_α^* phase nuclei slowly shrinking in the L_3 matrix (between 2 and 3): their shape is somewhat similar to that observed in the biphasic domain L_α - L_3 at rest – logarithmic spirals –, showing that the L_α layers make a constant angle with the boundary [12]; this has been interpreted in terms of epitaxy between L_α and L_3 – matching of the characteristic lengths d_3 and d_α at the interface. Fig. 5 shows L_3 nuclei growing in a L_α^* matrix where oriented focal conic domains are visible; the L_3 nuclei grow perpendicular to the length of the focal domains with an acute angle whose bisector is parallel to the L_α^* layers, indicating the same phenomenon of epitaxy as above [13]. More details about the rheo-optical properties of this complex intermediary regime can be found in [8].

fig. 4

fig. 5

fig. 4: sample **a**, polarizing microscopy; between states 2 and 3 of fig. 2: L_α^* domains in epitaxy with L_3 matrix; $\dot{\gamma}$=30s^{-1}; bar: 100 µm.

fig. 5: sample **b**, polarizing microscopy; state 4 of fig. 2: L_3 domains in epitaxy with L_α^* matrix; focal conic domains perpendicular to the lamellae; angular oriented shape of the L_3 domains; $\dot{\gamma}$= 30s^{-1}; bar: 100 µm.

DISCUSSION

We adopt the interpretation of ref. [3] for the first two ranges: 1)- below $\dot{\gamma}_0$, topological relaxation has time to take place, i.e. passages have time to 'fuse' after 'strangling', such that the structure of the sponge phase fluctuates about its structure at rest, yielding therefore no average birefringence; 2)- above $\dot{\gamma}_0$ and up to some value $\dot{\gamma}_1$ the system experiences flow birefringence, and obeys the scaling laws proposed in [9], see also [3] and [8]; the measured relaxation time (ca. 200ms) is comparable to the value estimated by Waton & Porte [14] for their τ_3 times (relaxation of

connectedness fluctuations) from T-jump experiments In this second range, as above $\dot{\gamma}_1$, there is in principle no change in the topology (passages remain, no new passages are created); this seems to be corroborated by the constancy of the viscosity above $\dot{\gamma}_0$; note that contrarywise the viscosity shows a shear-thinning behavior below $\dot{\gamma}_0$.

The intermediary regime (two-phases regime) shows remarkable characters which are not entirely understood; according to the above discussion, the L_α^* layers should be full of passages; the increase of the periodicity under shear leads us to think that the passages decrease in size, if not in number, and tend to close. Freeze-fracture observations are in progress to investigate this point. If we believe that the L_α^* nuclei observed immediately after shear was ceased are also present during shear (this seems to be in agreement with optical measurements of domain size in this regime), they are certainly not in strict epitaxy equilibrium with the sponge matrix, and dislocations of epitaxy are present. The L_α^* phase is well formed in each nucleus; when these nuclei grow, they come into contact, and do not easily match; this could be at the origin of the desorientation of the L_α^* phase above $\dot{\gamma}_c$.

REFERENCES

1. M. E. Cates, D. Roux, D. Andelman, S. T. Milner, and S. A. Safran, Europhys. Lett. **5**, p. 733 (1988).

2. D.Roux, C.Coulon, M.E.Cates, J.Phys.Chem. **96**, p.4174-4187 (1992).

3. O. Diat, and D. Roux, Langmuir **11**, p. 1392 (1995).

4. P. Snabre and G. Porte, Europhys. Lett. **13**, p. 642 (1990).

5. R. J. Plano, C. R. Safinya, E. B. Sirota, and L. J. Wenzel, Rev. Sci. Instrum. **4**, p. 1309 (1993).

6. M. E. Cates, and S. T. Milner, Phys. Rev. Lett. **62**, p. 1356 (1989).

7. R. F. Bruinsma and I. Rabin, Phys. Rev. A **45**, p.994 (1992).

8. H. F. Mahjoub, K. M. McGrath, and M. Kleman, Langmuir **12**, p. 3131 (1996).

9. G. Porte, M. Delsanti, I. Billard, M. Skouri, J. Appell, J. Marignan, and F. Debeauvais , J. Phys. II France **1**, p. 1101 (1991).

10. M. Goulian, and S. T. Milner, Phys. Rev. Lett. **74**, p. 775 (1995).

11. A. Caillé, C. R. Acad. Sci. Paris **B274**, p. 891 (1972).

12. C. Quilliet, C. Blanc and M. Kleman, Phys. Rev. Lett. **77** p. 522 (1996).

13. C. Blanc, private communication

14. G. Waton, and G. Porte, J. Phys. II France **3**, p. 515 (1993).

15. O. D. Lavrentovich, C. Quilliet, and M. Kleman, J. Phys. Chem. in press

INITIAL DISTRIBUTION EFFECTS ON DIFFUSION-LIMITED REACTIONS IN CONSTRAINED GEOMETRIES

KATJA LINDENBERG *, A. H. ROMERO ** and J. M. SANCHO †
*Department of Chemistry and Biochemistry and Institute for Nonlinear Science, University of California at San Diego. La Jolla, CA 92093-0340
**Department of Chemistry and Biochemistry and Department of Physics, University of California at San Diego, La Jolla, CA 92093-0340
†Departament d'Estructura i Constitutents de la Matèria, Universitat de Barcelona, Av. Diagonal 647, E-08028 Barcelona, Spain

ABSTRACT

We present a study of the effects of the initial distribution on the kinetic evolution of irreversible binary reactions in low dimensions. We focus on the role of initial density fluctuations and, in particular, on the role of the long wavelength components of the initial fluctuations, in the creation of the macroscopic patterns that lead to the well-known kinetic anomalies in this system. The frequently studied random initial distribution is but one of a variety of possible distributions leading to interesting anomalous behavior. Our discussion includes initial distributions that suppress and ones that enhance the initial long wavelength components.

INTRODUCTION

Diffusion-limited binary reactions in low dimensions exhibit kinetic anomalies (deviations from law of mass action behavior) whose physical origin is by now well understood. The laws of mass action assume an efficient mixing mechanism, that is, one that is rapid relative to the local reaction rate; anomalies arise because diffusion in low dimensions is not an efficient mixing mechanism. For example, consider the irreversible $A + B \rightarrow 0$ reaction starting from an initially random distribution of equal amounts of A and B. Such a distribution exhibits local density fluctuations, that is, certain regions of the system are relatively rich in species A while others are relatively rich in species B. Efficient mixing (by whatever mechanism) rapidly suppresses such local fluctuations. If mixing is not efficient as, for example, in a diffusion-limited reaction in low dimensions, then the reaction causes the local minority species to be eliminated extremely rapidly by the local majority species, and diffusion is not able to homogenize the system. This leads to the evolution of spatial regions in which essentially only one or the other of the species is present, and any attempt of the minority species to diffuse into this region leads to its rapid disappearance by reaction. The reaction eventually takes place only at the interfaces of aggregates of different species. As time proceeds (and the concentrations of reactants decrease), the regions in space that are occupied by reactants of essentially only one species grow in size, and the total interface area at which the reaction occurs decreases. This leads to ever more effective spatial segregation of the species and an associated slowing down of the reaction relative to its rate in a homogeneous mixture. The global density $\rho(t)$ of either species evolves through a hierarchy of anomalous kinetic behaviors that includes the behavior $\rho(t) \sim t^{-d/2}$ characteristic of the formation of a "depletion zone" of one species around the other [1, 2] and asymptotic arrival at the so-called Zeldovich regime [3, 4] characterized by the time dependence $\rho \sim t^{-d/4}$ for $d < 4$. This behavior then continues until finite system size effects set in, or until the species disappear altogether.

This discussion punctuates three interesting features of these irreversible diffusion-limited reactions in constrained (low dimensional) geometries. One is that the initial distribution determines the evolution of the system for all time: the future of the reaction is imprinted in the spatial distribution at one given ("initial") moment. A second is the fact that it is necessary to start with *disorder* in order to produce an *ordered* state at a later time: the formation of ever larger aggregates of a single species is a direct consequence of initial fluctuations that are not homogenized. A third is the realization that a random distribution is but one of many possible initial distributions, and it is certainly not the most easily realized in practice. The historical focus on the random distribution has perhaps obscured the fact that other initial distributions lead to other behaviors, some "less anomalous" and others even "more anomalous"

than the Zeldovich law $\rho \sim t^{-d/4}$ in their deviation from classical kinetics. It is this last point that we focus on in this report. Our work expands on previous concern with this problem by a number of authors [2, 5, 6, 7, 8, 9].

THEORETICAL FRAMEWORK

Our work (both theoretical and numerical) is based on the reaction-diffusion equations for the local densities $\rho_i(\vec{x}, t)$, $i = A, B$, of the two species:

$$\partial \rho_A / \partial t = D\nabla^2 \rho_A - K\rho_A \rho_B, \tag{1}$$

and similarly for ρ_B. The global densities are defined as the volume averages of the local densities,

$$\langle \rho_A(\vec{x}, t) \rangle \equiv V^{-1} \int d\vec{x}\, \rho_A(\vec{x}, t) = \langle \rho_B(\vec{x}, t) \rangle \equiv \rho(t). \tag{2}$$

D is the diffusion coefficient, which we assume to be the same for both species, K is the local reaction rate constant, and $V = L^d$ is the system volume. A strictly diffusion-limited reaction requires $K \to \infty$. With finite K (we take $D/K \ll 1$) the reaction eventually becomes reaction- rather than diffusion-limited when the density is sufficiently low.

The local densities $\rho_i(\vec{x}, t)$ evolve from initial configurations $\rho_i(\vec{x}, 0)$; if these initial configurations are chosen from a distribution of different configurations (e.g., a random distribution), it is appropriate to perform an average over initial distributions. We denote the average of a quantity $f(\vec{x}, t)$ over the initial distribution by a bracket, $\langle f(\vec{x}, t) \rangle$. We also use a single bracket notation to denote an average over volume. In our examples it is redundant to take both averages - one suffices (i.e., the average over the initial distribution yields $\vec{x}$-independent densities).

It is convenient to work with the difference and sum variables

$$\gamma(\vec{x}, t) = [\rho_A(\vec{x}, t) - \rho_B(\vec{x}, t)]/2, \qquad \rho(\vec{x}, t) = [\rho_A(\vec{x}, t) + \rho_B(\vec{x}, t)]/2. \tag{3}$$

The difference variable satisfies a linear diffusion equation that can be solved exactly and that captures the variations and fluctuations in the spatial distribution of the species [2]. If the system is thoroughly mixed, this variable is everywhere small; if the species are segregated, then the variable is positive in regions where A predominates and negative where B predominates. Its variability contains information about the sizes of such regions.

The sum variable $\rho(\vec{x}, t)$ is the density without consideration of species identity, and it is in general expected to be a smoother function than the difference variable. Averaging the reaction-diffusion equation over the initial distribution and/or the volume one finds that the average density (which is the same as the global density) satisfies the equation

$$d\rho(t)/dt = -K \left[\langle \rho^2 \rangle - \langle \gamma^2 \rangle \right]. \tag{4}$$

The remaining analysis is based on the behavior of $\langle \gamma^2 \rangle$ (which is known exactly) and the relation between $\langle \rho^2(\vec{x}, t) \rangle$ and $\rho(t)$. For the latter, it should be noted that in general $\langle \rho^2(\vec{x}, t) \rangle \neq \rho^2(t)$, although the equality *does* hold for a homogeneous distribution and also for a segregated distribution (these two "opposite" distributions share this second moment property). For a random distribution $\langle \rho^2(\vec{x}, t) \rangle = \rho^2(t) + \rho_{max}\rho(t)$, where ρ_{max} is the "maximum density." (From a molecular viewpoint ρ_{max} is the inverse of the volume of one molecule; in a lattice approach it is the maximum number of walkers that can simultaneously occupy each lattice site.)

The most important quantity in determining the kinetic behavior of the system is the "driver" $\langle \gamma^2 \rangle$. It is this driver that causes deviations from classical $\rho(t) \sim t^{-1}$ behavior; a homogeneous distrbution of reactants is characterized by a vanishing difference variable and hence by a vanishing driver. The behavior of this quantity for *all times* and, in particular, how rapidly it vanishes at long times, is completely determined by the *initial* configuration of reactants:

$$\langle \gamma^2 \rangle = V^{-1} \sum_{\vec{k}} S(\vec{k}) e^{-2Dtk^2} = (2\pi)^{-d} \int d\vec{k}\, S(\vec{k}) e^{-2Dtk^2} \tag{5}$$

where $k = |\vec{k}|$. For periodic boundary conditions $\vec{k} = 2\pi\vec{n}/L$ and $\vec{n}$ is a d-tuple of integers. The second equality in (5 corresponds to the infinite volume limit. Here $S(\vec{k})$ is the structure function of the initial configuration, and is given by the Fourier transform of the initial correlation function,

$$S(\vec{k}) = \int d\vec{x}e^{-i\vec{k}\cdot\vec{x}} \left\langle \gamma(\vec{x},0)\gamma(\vec{0},0) \right\rangle. \tag{6}$$

For $t > t_a$, where $t_a \equiv (Dk_a^2)^{-1}$, $\left\langle \gamma^2 \right\rangle$ is essentially determined by the behavior of the structure function for $k < k_a$. In other words, the long-time behavior of the driver is dictated by the long-wavelength components of the initial distribution (note also that this behavior is entirely determined by diffusion and is not influenced by the reaction). In general, if $S(\vec{k}) \sim k^\alpha$ for $k < k_a$, then a rescaling of variables in Eq. (5) immediately shows that for $t > t_a$, $\left\langle \gamma^2 \right\rangle \sim t^{-(\alpha+d)/2}$. Note that α may be positive or negative (or zero). If α is sufficiently large (indicating a drastic cutoff of the long wavelength components), specifically if $\alpha > 4 - d$, then the driver decays more rapidly than t^{-2} and it quickly ceases to play a role in the kinetics. The behavior then becomes classical [8, 9]. Conversely, any initial distribution that emphasizes the long wavelength components in the density difference leads to a slower decay of the driver ($\alpha < 0$) and hence to greater deviations from classical behavior.

Ultimately we are constrained by the finite systems in which our numerical work is carried out; this means that eventually the driver vanishes exponentially, reflecting the fact that there are no contributions to it whose wavelengths are longer than the size of the system. The kinetics then become classical.

The results of our analysis of the reaction-diffusion equations are checked against direct numerical integration of Eq. (1), carried out by discretizing the volume V into N^d cells of size $(\Delta x)^d$ ($V = (N\Delta x)^d$) and time into intervals Δt. The Laplace operator is represented in the standard symmetrical form with respect to the mesh size Δx, and the time integration follows a standard first order Euler algorithm. Parameters are chosen so as to clearly illustrate the behaviors under consideration. Throughout we set $\Delta x = 1$ and $\Delta t = 0.01$ except for early time calculations where on occasion we use smaller values of Δt for the first few hundred integration steps. Initially an amount ρ_0 of reactant A is placed in some cells and not in others, according to a specified distribution. Similarly for reactant B. If each reactant is initially placed in $n^d \leq N^d$ cells, the initial global density is $\rho_{init} = n^d\rho_0/N^d$. Note that the maximum initial density possible is then $\rho_{max} = \rho_0$, which occurs if every cell is initially occupied by both reactants. An average over different initial realizations is taken if necessary.

VARIOUS INITIAL DISTRIBUTIONS

The random initial distribution of reactants has been the most thoroughly studied and serves as the benchmark for the understanding of the importance of initial fluctuations in the asymptotic kinetic behavior of the $A + B \rightarrow 0$ system. The random distribution in an infinite volume is characterized by the structure function $S(\vec{k}) = const$ for $k > 0$. In an infinite volume Eq. (5) then leads to the driver $\left\langle \gamma^2 \right\rangle = Q(Dt)^{-d/2}$, where Q is a constant proportional to the initial density. With this form in (4) we can now deduce the kinetic behavior of the system. At the very earliest times, of order K^{-1}, the system is reaction limited and the kinetic behavior is classical [1, 9]. Beyond this, at early times, when the distribution of reactants is still nearly random, we noted earlier that $\left\langle \rho^2 \right\rangle$ is proportional to $\rho(t)$. For $d < 2$ the dominant terms are those on the right side of the equation and consequently one finds that $\rho(t) \sim t^{-d/2}$. This decay is characteristic of the formation of a depletion zone around each reactant. For $d > 2$ the kinetic behavior is classical in this regime ($d = 2$ is the critical dimension: the kinetics is almost classical with logarithmic correction). Deviations from randomness set in quickly [1, 2] and segregation begins. The moment relation changes so that now $\left\langle \rho^2 \right\rangle \sim \rho^2(t)$. For $d < 4$ the dominant terms are again those on the right hand side, and the global density now decays as

$$\rho(t) \sim t^{-d/4} \tag{7}$$

(Zeldovich regime). Figure 1 shows a typical evolution of the global density for a one-dimensional systems with a random initial condition. The slow decay in the Zeldovich regime (which is the predominant "anomalous" regime) is clearly seen. This decay would continue forever in an infinite system. The figure shows the eventual more rapid (classical) decay due to the finite size of the system in our simulations.

An example of an initial distribution in which the long wavelength components of the initial density difference are suppressed relative to those of the random case is that of randomly oriented, randomly
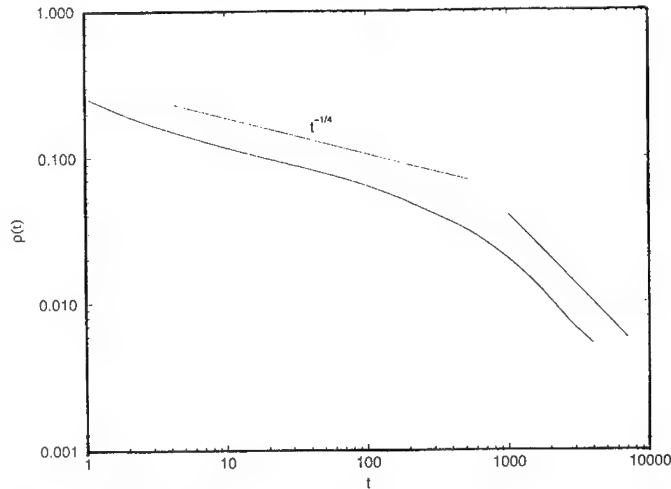
Figure 1: Decay of the global density in one dimension from an initially random distribution of reactants with $N = 512$, $K = 10$, and $D = 2$. The curves are the numerical solutions of the reaction-diffusion equations. Straight lines: $t^{-1/4}$ and t^{-1}.

positioned $A - B$ pairs of particles separated by a fixed distance c. After this initial placement, the particles diffuse independently of one another. The structure function for small k in this case is $S(\vec{k}) \sim k^2$ and the associated driver in an infinite volume is $\langle \gamma^2 \rangle = Q(Dt)^{-d/2} \left[1 - \exp(-c^2/8Dt)\right]$. At times smaller than $t_c \equiv c^2/8D$ the driver is the same as that of the random system, but at times greater than this, $t \gg t_c$, we now have $\langle \gamma^2 \rangle \sim t^{-(d+2)/2}$. The detailed kinetic behavior of the system depends on whether species segregation does or does not set in before time t_c (and this, in turn, depends on c and on the initial density). In any case, even if segregation does begin before this time (with a consequent decay $\rho(t) \sim t^{-d/4}$), the kinetic behavior changes around time t_c and the decay becomes more rapid. For $d < 2$ the decay is of the form

$$\rho(t) \sim t^{-(d+2)/4} \tag{8}$$

and for $d > 2$ the decay is classical ($d = 2$ is the critical dimension). This faster decay is a reflection of the fact that aggregates cannot grow beyond size $\sim c$ because of the initial correlations. The initial constraints on the long wavelength components of the fluctuations thus lead to a behavior "less anomalous" than in the case of random initial conditions. This behavior is illustrated in Fig. 2. Eventually finite system size effects lead to classical behavior in any dimension. The suppression of initial fluctuations at long wavelengths and the associated suppression of anomalous behavior are also evident in two dimensions with initial patterns of finite size such as folded lamellae and spherical droplets [9].

Consider now an initial distribution in which the long wavelength components of the difference variable are *enhanced* relative to the random initial distribution [10]. This initial distribution in one dimension is generated as follows in our numerical integration: the number N of cells in a row is chosen to be a power of 3, $N = 3^n$. We divide N by 3, thereby generating $N/3$ domains (each containing many cells). One of the three domains, chosen at random from among the three, remains empty and is discarded from further consideration. The other two domains are each subdivided into three subdomains, and one of each group of three subdomains again remains empty and is set aside, while the other two are again subdivided. The process continues in this way until the selected domains are as small as possible, that is, of size Δx. An initial density ρ_0 of one of the reactants is placed in each of the selected elementary cells. The process is repeated for the second reactant, and these two distributions are superimposed. In the limit $N \to \infty$ this leads to a fractal geometry of occupied cells of dimension $D_f = \ln 2/\ln 3 = 0.63$ [11]. The difference variable γ is also characterized by the same initial fractal dimension, and the structure function for small

154
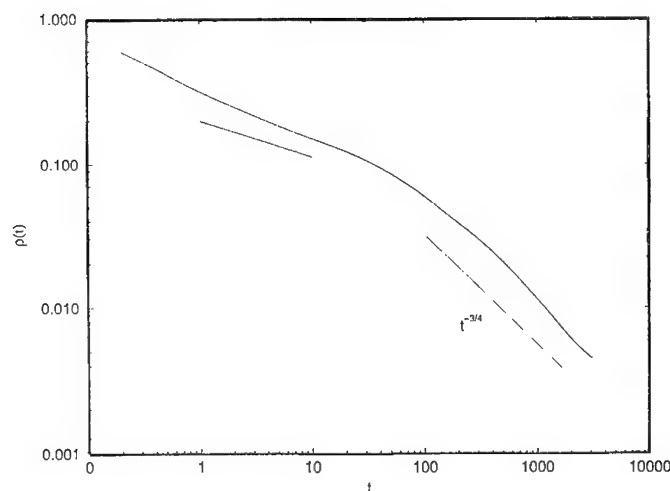
Figure 2: Kinetics for initially correlated pairs in one dimension. $N = 4096$, $K = 10$, $D = 2$, and $c/\Delta x = 32$. The curve is the numerical solution of the reaction-diffusion equations. Straight lines: $t^{-1/4}$ and $t^{-3/4}$.

k behaves as a power law with an exponent given by the fractal dimension, $S(k) \sim k^{-D_f}$. Note that the exponent is negative, i.e., the long wavelength components are enhanced relative to those of a random initial distribution.

Initially one expects rapid (classical) reaction activity due to nearby reactants, but once this reaction-limited activity is completed (on a time scale of order K^{-1}), there will be a quiescent period because occupied regions of space are quite separate. During this quiescent period the distribution is rather segregated but the sum variable is becoming spatially homogenized through diffusion; hence one expects the moment relation $\langle \rho^2 \rangle \sim \rho^2(t)$. The balance of the dominant terms in (4) then leads to the asymptotic decay

$$\rho((t) \sim t^{-(d-D_f)/4}. \tag{9}$$

Note that this decay is *even slower* than the Zeldovich behavior. This decay continues until finite size effects take over.

In Fig. 3 we show the results of the numerical integration of the reaction-diffusion equations and the prediction (9). It should be noted that our initial patterns are not "ideal" fractals because we stop the subdivision at a finite cell size. Our systems have $N = 81$, so we only go through four generations of subdivisions. Nevertheless, the predicted results are clearly apparent in the figures. We see the slow decay of the form $t^{-0.092}$ expected for an initial distribution of fractal dimension $D_f = 0.63$, followed by the abrupt decrease in the global density associated with finite system size effects. The eventual approach to classical behavior is beyond the time scale of this figure.

A similar enhanced anomaly relative to the random initial distribution is also seen in two dimensions [9].

SUMMARY AND CONCLUSIONS

We have presented a study of the effects of initial distributions on the behavior of the irreversible reaction $A + B \rightarrow 0$ under stoichiometric conditions. We have focused on the effects of the initial pattern of fluctuations of the density difference and have stressed that this pattern determines the subsequent

155
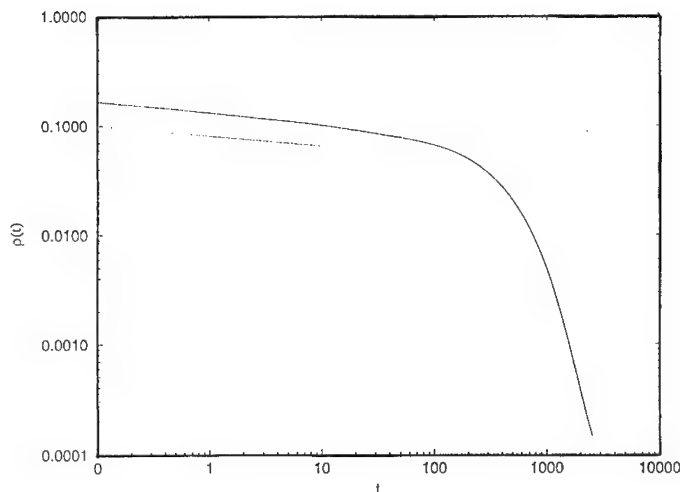
Figure 3: Kinetics for the fractal-like initial pattern in one dimension described in the text, with $N = 81$, $K = 10$, and $D = 0.5$. The curve is the numerical solution of the reaction-diffusion equation. The straight line is proportional to $t^{-0.092}$.

evolution of the system. In particular, the long-wavelength components of the initial difference distribution determine the asymptotic decay of the reactant densities. Thus, this system constitutes a temporal "mirror" that reflects the instantaneous initial spatial pattern.

An initially random distribution of reactants leads to well-known segregation of species and the associated slowing of the reaction. In an infinite system the asymptotic decay of the reactants in this case is described by the "Zeldovich law" $\rho \sim t^{-d/4}$, which is distinctly different from the classical law-of-mass-action behavior $\rho \sim t^{-1}$ for $d < 4$. Initial distributions that limit the long wavelength components of the difference fluctuations lead to constraints on the macroscopic segregation effects and to rate laws closer to the classical. We reviewed a particular example of such an initial distribution, namely, one containing initially correlated $A - B$ pairs. On the other hand, initial distributions that enhance the long wavelength components lead to even greater deviations from the law of mass action. For instance, an initial fractal difference pattern of dimension D_f leads to the very slow decay $\rho \sim t^{-(d-D_f)/4}$.

It would be interesting to observe in detail not only the time evolution of the reactant densities but also the spatial patterns associated with this evolution for the different initial distributions that we have studied. We plan to do so in the future.

ACKNOWLEDGEMENTS

REFERENCES

1. P. Argyrakis, R. Kopelman, R. and K. Lindenberg, Chem. Phys. **177**, 693-707 (1993).

2. K. Lindenberg, P. Argyrakis, and R. Kopelman, in *Noise and Order: The New Synthesis*, ed. M. Millonas, Springer, New York, 1996, pp. 171-203.

3. A. A. Ovchinnikov and Y. B. Zeldovich, Chem. Phys. **28**, 215-218 (1978).

4. S. F. Burlatskii, A. A. Ovchinnikov and G. S. Oshanin, Phys. Lett. A **139**, 245-248 (1989) and references therein.

5. G. Abramson, A. Bru Espino, M. A. Rodriguez and H. S. Wio, Phys. Rev. E **50**, 4319-4326 (1994).

6. G. Abramson, Cinética anómala en sistemas bimoleculares de reacción-difusión, PhD thesis (1995).

7. K. Lindenberg, P. Argyrakis and R. Kopelman, J. Phys. Chem. **98**, 3389-3397 (1994).

8. A. G. Vitukhnovsky, B. L. Pyttel and I. M. Sokolov, Phys. Lett. A **128**, 161-165 (1988).

9. J. M. Sancho, A. H. Romero, K. Lindenberg, F. Sagués, A. Reigada and A. M. Lacasta, to appear in J. Phys. Chem. (1996); K. Lindenberg, A. H. Romero and J. M. Sancho, submitted for publication (1996).

10. Fractal initial conditions have been considered in the context of aggregation phenomena in A. Provata, H. Takayasu and M. Takayasu, Europh. Lett. **33**, 99-104 (1996).

11. Vicsek, T. *Fractal Growth Phenomena* 2nd edition, World Scientific, Singapore, 1992, pp. 24-25.

REVISITING EXPERIMENTAL TESTS OF THE
LAPLACE-KELVIN EQUATION

FRANK VAN SWOL * and LAURA J. DOUGLAS FRINK *
*P.O. Box 5800, MS 1111, Sandia National Laboratory, Albuquerque, NM 87185-1111

ABSTRACT

In this paper we focus on two experimental techniques for testing predictions made by Laplace-Kelvin theory (LKT). The first technique employs the surface forces apparatus (SFA) to measure pull-off forces, the second uses a beam bending (BB) technique to determine the bending forces in a microporous film produced with a sol-gel technique. We use density functional theory (DFT) to analyze the two experiments. We find that the pull-off force in a crossed cylinder geometery contains a minimal solid-liquid contribution, which can explain why the LKT result is found at saturation. We demonstrate that a pore size distribution essential to produce a bending stress that is always compressive and has a dependence on the vapor pressure that coincides with LKT.

INTRODUCTION

Laplace-Kelvin theory (LKT) [1, 2] describes the adsorption behavior and the associated solvation forces of confined fluids. The confinement can occur when fluid is adsorbed into a porous material, or when it is placed between two (mica) surfaces as in the SFA. The basic assumption underlying LKT is that the confined fluid has the properties of uniform bulk fluid. The LKT can be used to predict the point of capillary condensation. This aspect has already received considerable attention in the 1980's [1], and is therefore not the focus of this paper. The conclusion reached was that LKT can only predict capillary condensation in the limit of infinitely large pores. For small pores, of the order of 10 times the molecular diameter LKT prediction for capillary condensation is in serious error. Our main interest lies with the LKT predictions for the force per unit area that the confined fluid exerts on the confining walls. This force per unit area is essentially the solvation force, f_s, provided we subtract the pressure of the bulk fluid with which the confined fluid is in equilibrium. LKT predicts that the solvation force is zero at saturation, and proportional to $ln(p/p_0)$ as long as the confined fluid is in a liquid state. The slope is related to the density of the bulk liquid at saturation, ρ_l.

For small pores one would certainly expect the LKT predictions to be in error. However, pull-off measurements with the SFA [3, 4], and more recently, beam bending experiments [5] performed with microporous sol-gel films seem to suggest that the LKT predictions work remarkably well for geometries as small as a few molecular diameters. To understand these surprising observations we have undertaken a molecular modeling approach to solvation forces in confined geometries.

We find that accounting for a distribution of pore sizes is key to the BB experiment. Our calculations for the pull-off force measurement indicate that the crossed cylinder geometry is the likely reason for observing LKT behavior. This paper is arranged as follows, we first describe the modeling approach, and then illustrate how it is applied to BB and SFA experiments. The conclusions are summarized at the end of the paper.

MOLECULAR THEORY AND LKT PREDICTIONS

To test the LKT predictions we must obviously model the confined fluid in a way that avoids the assumption of a uniform confined fluid. In other words, the main requirement is that our approach accounts for the effects of the confining external field and the packing constraints faced by fluids in narrow geometries. This can be accomplished by more than one approach - e.g. molecular simulation, integral equations and Density Functional Theory (DFT). Of these we consider DFT to be the most straightforward, as it fixes the chemical potential, and provides direct access to the (grand potential) free energy Ω_s as well as its derivatives with respect to the external field, f_s.

We use the functional due to Rosenfeld [6, 7]. Further details can also be found in references [8, 9, 10]. The important point to note is that for the applications discussed here, DFT is always in excellent agreement with molecular simulation [10]. We use a simple 12-6 Lennard-Jones(LJ) potential for the fluid-fluid and a 9-3 LJ potential for the fluid-wall interactions. The direct wall-wall interactions are modelled with a 8-2 LJ potential. These three potentials are characterized by three energy parameters, ϵ, ϵ_{wf} and ϵ_{ww} respectively. Both the fluid-fluid potential and the fluid-wall potential were cut and shifted at 10 diameters (σ). The reduced temperature , T^* was 0.74, close to the triple point.

The LKT predictions express the solvation force in terms of the liquid-vapor (lv) surface tension γ_{lv}, the contact angle θ, and the separation at wich the capillary condensation transition takes place, h_t. All these quantities depend on the temperature (T). In addition h_t is also a function of the chemical potential (μ) or equivalently, the bulk pressure p. Thus, for a slit-like geometry

$$f_s(\mu, T)/A = \begin{cases} 0 & ; h > h_t \\ -2\gamma_{lv}(T)\cos\theta(T)/h_t(T,\mu) & ; h \leq h_t \end{cases} \tag{1}$$

Assuming the vapor is an ideal gas, $cos\theta = 1$ (for a hydrophilic or completely wetting surface) and use the LKT prediction $h_t = -2\gamma_{lv}cos\theta/\rho_l kT \ ln(p/p_o)$, we obtain

$$f_s(\mu, T)/A \approx \begin{cases} 0 & ; h > h_t \\ kT\rho_l ln(p/p_o) & ; h \leq h_t \end{cases} \tag{2}$$

Here ρ_l denotes the density of the bulk saturated liquid which is at the saturation pressure p_o.

Similarly, using the Derjaguin approximation for the crossed-cylinder (or sphere-plate) geometry of the SFA we have for the liquid-vapor contribution

$$F_{lv}(\mu, T, D) \approx \begin{cases} 0 & ; D > h_t \\ 4\pi R\gamma_{lv}cos\theta + 2\pi RDkT\rho_l ln(p/p_o) & ; D \leq h_t \end{cases} \tag{3}$$

Here D denotes the distance of closest approach and R is the radius of curvature of the cylinders. The total force, F, can be approximated [9] as the sum of the lv and the solid-liquid (sl) contributions: $F = F_{sl} + F_{lv}$. F_{sl} can be expressed in terms of the work of adhesion required to separate two surfaces in a liquid, W_{sls}. For the crossed cylinders we have $F_{sl} = 2\pi RW_{sls}$. Note that within DFT we obtain F directly, and hence we can test the division into lv and sl contributions [9]. The comparisons indicate that the division of contributions works extremely well once the adsorption effects are properly accounted for [9].

We shall distinguish two separate predictions. One concerns the value of force at saturation. For the BB experiments which we model with slits we have $f_s = 0$, whereas the SFA
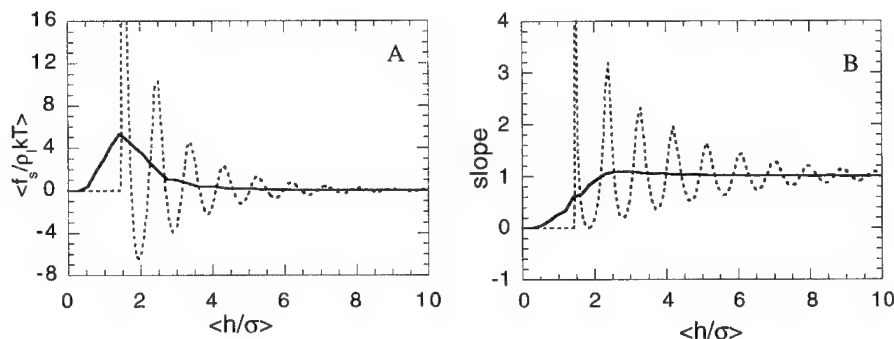
Figure 1: The reduced solvation force (A) and the derivative of the solvation force (B), $\partial f_s \sigma^3 (kT)^{-1}/\partial ln(p/p_o)$ as a function of average pore size, for a LJ fluid at saturation ($T^* = 0.74$). The dashed lines are the results of monodisperse pores ($t = 0$), the solid curves show the results for a gaussian pore size distribution ($t = 0.5$).

experiment gives $F_{lv} = 4\pi R \gamma_{lv} cos\theta$. The other is the dependence of the force on the bulk pressure. For both the BB and the SFA experiments we expect linear behavior with $ln(p/p_o)$ (see equations 2 and 3). We will demonstrate that for the BB experiments only the second prediction is accurate. For the SFA experiments the situation is slightly more complicated. The first prediction is borne out by the experiment, but the second prediction fails for very strong wall-fluid interactions.

RESULTS: BENDING STRESSES

We start by considering the bending stress measurements in microporous sol-gel films [5]. It can be shown that the measured bending stress is proportional to the solvation force. From adsorption measurements the pore size is estimated to be approximately 6.4$\overset{\circ}{A}$. The stress measurements show a positive (compressive) solvation force at saturation, contrary to LKT. As p is lowered from its saturation value, f_s decreases linearly with $ln(p/p_0)$, in agreement with LKT.

Neither one of the experimental observations is expected for a monodisperse network of pores. A single slit-like pore exhibits a solvation force that is oscillatory around zero with wall-wall separation h, not exclusively positive (figure 1A). Similarly, the slope at saturation is oscillatory around the infinite separation (LKT) limit which is given by the liquid density (figure 1B).

The key to understanding the experimental results lies in accounting for polydispersity and/or surface roughness. If we consider a gaussian distribution with a standard deviation t around a mean pore size we do indeed obtain a solvation force at saturation that is consistently positive for small pores (figure 1A). For large average pores the solvation force is zero and we recover the LKT result. The positive nature is a reflection of the very large peak around $h = \sigma$ indicating the very large resistance to squeezing out the last layer of fluid.

We now turn to the variation of the force with p (figure 1B). The effect of the pore size distribution on the slope is to average out the oscillations to a value that is very close to the limiting LKT value, $\rho_l kT$ - within 10 % for average pores larger than about 1.5σ (figure 1B). Notice that the width of the distribution is small, between 0.3 and 0.5 σ, yet wide enough to
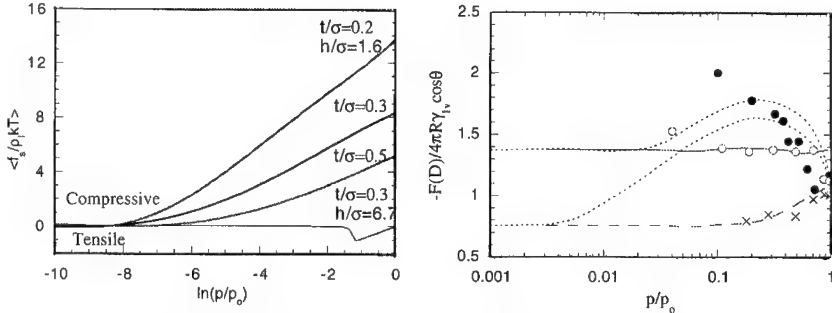
Figure 2: Left: The solvation force as a function of vapor pressure. The DFT results are labeled with the average pore size (h) and the standard deviation (t) of the gaussian pore size distribution. The $h = 6.7\sigma$ result demonstrates that complete LKT tensile behavior is obtained for large pore sizes. Right: The pull-off force normalized by $4\pi R\gamma_{lv}cos\theta$ between a sphere and a plate as a function of the relative vapor pressure (plotted on a log scale). The experimental results are those of Christenson [14]: n-hexane ($\bullet$), water in contact with hydrogen mica ($\circ$), and water in contact with potassium mica ($\times$). The DFT predictions for the water cases are $\epsilon_{wf}/\epsilon = 3.5$ and $\epsilon_{ww}/kT = 5.5$ (dashed line), $\epsilon_{wf}/\epsilon = 3.5$ and $\epsilon_{ww}/kT = 10$ (solid line). Two cases are shown for the n-hexane case. They both have $\epsilon_{wf}/\epsilon = 5$ with $\epsilon_{ww}/kT = 5.5$ and 10 respectively.

smear out the oscillations in both the force and the slope. For wide distributions, i.e. large t, the force at saturation will decrease and eventually reach zero. In figure 2 we show the behavior of the solvation force over a complete range of pressures.

The use of a molecular theory and a pore size distribution allows us to characterize a microporous film, but it cannot pinpoint the physical origin for the distribution. Clearly, the distribution can be interpreted as stemming from polydispersity in pore size of the porous network. However, we have recently found that surface roughness can also be accurately described by a pore size distribution [10]. Specifically, we performed grand canonical Monte Carlo (GCMC) simulations of fluids confined between rough tiled surfaces. The simulations revealed that even when the tiles are of order σ, the solvation force could still be accurately predicted from a distribution of solvation forces for *smooth* walls. Thus, the pore size distribution envoked here can just as well be attributed to surface roughness.

RESULTS: PULL-OFF FORCES

Our DFT calculations are performed for flat plates and directly give us the total force per unit area, $f(h)$, and the surface free energy per unit area. To describe the crossed cylinder or sphere plate geometry we then use the Derjaguin approximation,

$$F(D) = \int_{h=D}^{h=\infty} dx \ 2\pi x f(h) \tag{4}$$

It is helpful to consider pull-off measurements for the sphere-plate geometry of the actual SFA experiments as well as for the more hypothetical slit geometry. In figure 3 we show the DFT results for the force contributions as well as the total force at a vapor pressure below p_o. For flat plates the lv force is a step-function and the sl force contribution shows the familiar oscillations with a period $\approx \sigma$. The step discontinuity approaches the LKT prediction $kT\rho_l ln(p/p_o)$ as $p \to p_o$. In a pull-off measurement one measures the value of the
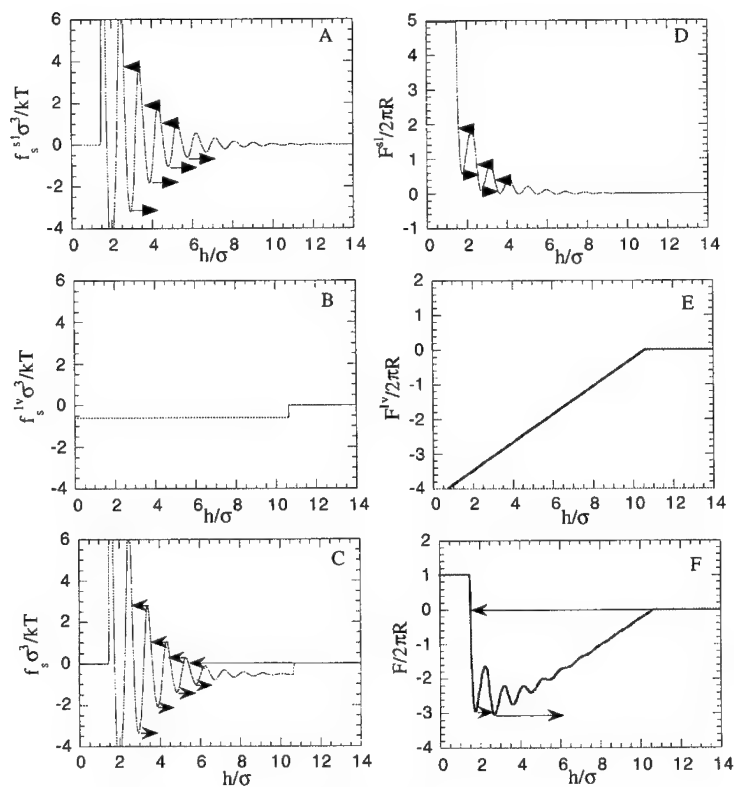
Figure 3: Contributions to the pull-off force for two plates (on the left) and a sphere and a plate (on the right). The *sl* contribution is shown in the top row (A,D), the *lv* contribution appears in the middle row (B,E). The last row (C,F) shows the total force, which is the sum of the two previous rows. The arrows indicate the locations of mechanical instabilities that are manifested by jumps exhibited by the SFA (assuming a very small spring constant).

total force at one of the local minima (see the arrows in figure 3 C and D). In principle one can explore any of the minima by moving the plates in and out. It is clear that for flat plates owing to the oscillatory behavior of f_{sl}, the pull-off force can be dramatatically different form the LKT value. In the example shown, the LKT prediction is only measured when the pull-off distance $\approx 11\sigma$.

We now turn to the sphere-plate geometry. The *lv* contribution is sloped, and the *sl* contribution is oscillatory. The key observation is that F_{sl} is very close to zero at the local minima. Hence, at the local minima of the total force the *sl* contribution virtually vanishes! As a result the pull-off force experiment essentially measures only the *lv* contribution. As $p \to p_o$ this contribution approaches the LKT prediction.

Comparing the flat-plate and the sphere-plate geometry it becomes clear that observing

the LKT result at $p = p_o$ in an SFA pull-off experiment is to a large extent an accident. It does not imply that LKT theory holds for fluids confined to small geometries in general. We note that it would be interesting to consider surface deformations in the analysis of the SFA measurements. This is however outside the scope of the present paper.

We can also test the second prediction of LKT, namely the variation of the pull-off force with $ln\ p$, near saturation. From equation 3 the derivative of F_{lv} wrt to $ln\ p$ should be $2\pi RDkt\rho_l$ which is positive. In experiments and from DFT (figure 2), both positive and negative slopes are observed for the *total* force. The DFT calculations indicate that the outcome depends on the strength of the wall-fluid interactions.

CONCLUSIONS

Molecular modeling provides an ideal way to test the various predictions of LKT. In this paper we have focused on experimental measurements of the solvation force in confined geometries. The analysis of the BB experiments shows that observing the LKT slope for f_s with $ln\ p$, for microporous systems is associated with polydispersity in pore size and/or surface roughness. Even though the LKT fails dramatically for small individual pores, a pore size distribution will produce LKT slope behavior. This is true even when the mean pore size is small and the distribution narrow. Howver, although the slope is close to the LKT result, the sign of the bending stress is opposite to the LKT prediction, which only predicts tensile stresses. Thus only one of the LKT predictions holds for the sol-gel films.

The modeling of the pull-off SFA experiments demonstrates that observing the LKT prediction for the force at saturation would appear to be a geometrical accident - at the local minima of the total force the solid-liquid contribution virtually vanishes for a crossed cylinder geometry. For a flat plate geometry the deviations from LKT would be large. The LKT prediction for the variation of the pull-off force with vapor pressure near saturation is found for some experimental systems, but not all. The DFT results indicate that negative slopes are expected for fluid-wall interactions that are strong relative to the fluid-fluid interaction.

REFERENCES

1. R. Evans, U. Marini Bettolo Marconi, J. Chem. Phys., **86**, 7138-7148 (1987).
2. J.N. Israelachvili, *Intermolecular and Surface Forces*, 2nd ed.,
3. L.R. Fisher and J.N. Israelachvili, Chem. Phys. Lett., **76**, 325-328 (1980).
4. H.K. Christenson, J. Colloid and Interface Sci., **121**, 170, (1988).
5. J. Samuel et al. in *Thin Films: Stresses and Mechanical Properties VI*, editors Gerberich, W. W., Gao, H., Sundgren, J-E., and Baker, S. P., Materials Research Society (1996).
6. Rosenfeld, Y., Phys. Rev. Lett., **63**, 980 (1989), J. Chem. Phys., **98**, 8120 (1993).
7. Kierlik, E. and M.L. Rosinberg, Phys. Rev. A **42**, 3382 (1990), **44**, 5025 (1991).
8. Douglas Frink, L. J. and F. van Swol, J. Chem. Phys., **105**, 2884 (1996).
9. Douglas Frink, L. J. and F. van Swol, J. Chem. Phys., (1996) in press.
10. Douglas Frink, L. J. and F. van Swol, (1996) submitted.

HYSTERESIS PHENOMENA IN NANOCONFINEMENTS:
DENSITY FUNCTIONAL THEORY AND EXPERIMENTS

A.V. NEIMARK[1,2] and P.I. RAVIKOVITCH[2]
[1]TRI/Princeton, 601 Prospect Av., Princeton, NJ, 08542-0625, aneimark@triprinceton.org
[2]Chemical Engineering/Yale University, New Haven, CT, 06520-8286

ABSTRACT

Hysteresis phenomena are observed in many nanoporous environments during adsorption/desorption isothermal quasiequilibrium cycles. A non-local DFT model has been developed for predicting adsorption/desorption isotherms in nanopores of different geometries in the wide range of pore sizes (0.5 - 10 nm) based on given intermolecular fluid/fluid and fluid/solid potentials. Depending on the confining geometry and the intermolecular potentials two types of hysteresis phenomena are occurred: *capillary condensation/evaporation* that implies volume filling of pores with a liquid-like matter, and *layering adsorption/desorption* that implies sequential step-wise formation of adsorption layers. It is shown that the DFT model qualitatively describes these phenomena and is in a reasonable quantitative agreement with some of the experiments.

INTRODUCTION

Adsorption/desorption hysteresis phenomena in pores were first discussed in terms of different mechanisms of meniscus formation in the adsorption process and meniscus evaporation in the reverse process of desorption due to the capillary action on liquid/vapor interfaces of different curvature [1, 2]. A qualitative scheme of condensation/desorption in cylindrical pores has been described by Everett [3]. Derjaguin [4] has shown noted that capillary hysteresis is caused by interactions between capillary forces on curved interfaces and adsorption forces in thin films. Corresponding thermodynamic theories, based on a supposition of additive contribution of capillary and adsorption forces in the chemical potential of the adsorbate (so-called Derjaguin equation), have been developed at different levels of detail for slit-shaped, cylindrical and spherical pores [4, 5].

At present, modern methods of statistical thermodynamics, such as Density Functional Theory (DFT) , Monte Carlo (MC) simulations and Molecular Dynamics (MD), are employed for quantitative studies of hysteresis in individual pores of different geometries for different fluid/solid systems (see, e.g. [6-13].

In our earlier papers, it was shown that the results of DFT calculations were in a satisfactory agreement with experimental adsorption/desorption isotherms of nitrogen in nanopores of MCM-41 [14-16]. In this paper the non-local density approximation (NLDFT) due to Tarazona [6] is employed for studies of hysteresis effects in nanopores. We address not only *condensation/desorption hysteresis* but also *phase transitions in adsorption multilayers* which may be an additional cause of hysteresis [10,12, 18-21].

CAPILLARY CONDENSATION/DESORPTION HYSTERESIS IN NANOPORES

We studied N_2 and Ar capillary condensation hysteresis on a newly synthesized mesoporous molecular sieve of MCM-41 type, which possesses an array uniform hexagonal pores with diameter ca. 0.4 nm. Details of the experimental procedure and the NLDFT model for N_2 and Ar adsorption on MCM-41, are given elsewhere [15-17, 22]. We note, that the fluid-fluid interaction parameters of the NLDFT model have been fitted to reproduced the bulk thermodynamic properties of N_2 and Ar at low temperatures. These parameters ensure the correct estimate of the liquid-gas coexistence densities and pressure, and also the liquid-gas interfacial tension. The pores of MCM-41 were modeled as infinitely long cylindrical pores. Parameters of the solid-fluid interactions have been chosen to reproduce the standard N_2 and Ar isotherms on non-porous silica surface [23] in the multilayer adsorption region.

In Fig. 1 and 2, we present a comparison of the NLDFT theoretical isotherms of Ar at 87K and 77K with the experimental isotherms on the MCM-41 sample. Similar comparison of N_2 isotherms at 77K on the same MCM-41 sample have been published elsewhere [15].
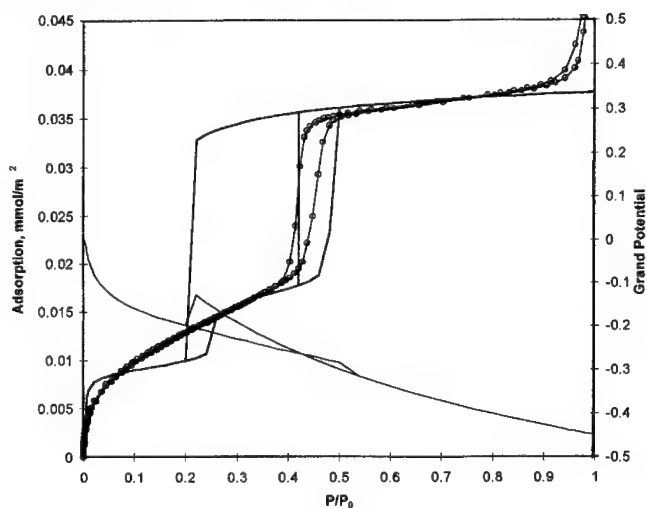
Fig. 1 Comparison of the NLDFT isotherm of Ar at 87 K in a 14 σ_{Ar-Ar} cylindrical pore with the experimental isotherm on MCM-41 (internal pore size is 0.43-0.45 nm). The thin solid curves show the changes in the grand potential along the adsorption and desorption branches (grand potential isotherms).
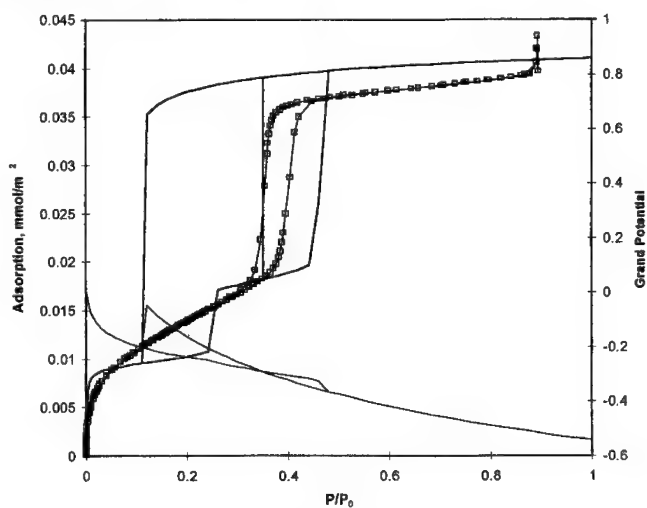
Fig. 2 Comparison of the NLDFT isotherm of Ar at 77 K in a 14 σ_{Ar-Ar} cylindrical pore with the experimental isotherm on MCM-41 (internal pore size is 0.43-0.45 nm). The saturated vapor pressure of the supercooled liquid was used in the experimental isotherm.

The theoretical isotherms have metastable adsorption and desorption branches of the hysteresis loop, which are tracing the equilibrium states characterized by smaller values of the grand potential. The equilibrium thermodynamic transition may occur between the states of equal grand potential. Thus, the intersection of the grand potential adsorption and desorption isotherms corresponds to the point of the equilibrium transition, which is indicated by a vertical line. Comparison with the experimental hysteresis loop clearly shows that the experimental desorption branch is very close to the equilibrium transition, while the experimental adsorption branch is placed within the loop formed by the metastable theoretical adsorption isotherm and the equilibrium transition line.

The experimentally observed transition is smoothed in comparison with the theoretical prediction for a single pore because of some degree of pore size heterogeneity in MCM-41. However, we conclude that in this type of nanoporous materials with predominantly cylindrical pore channels, evaporation occurs at the point of equilibrium transition predicted theoretically. This conclusion is consistent with the traditional mechanistic model of evaporation from an open cylindrical pore [3], which assumes that the pore emptying takes place at constant relative pressure and is associated with the displacement of the equilibrium meniscus formed initially at the pore edge. The may not be observed experimentally because of the fluctuations of the adsorbed film-gas interface and the presence of impurities, which could initiate the system transition toward the state of lower energy. The DFT predicts the upper and lower bounds for the experimental adsorption isotherm.

It worth noting, that for Ar at 77 K (Fig. 2) the good comparison with theoretical calculations has been obtained by considering Ar confined in nanopores at 77 K as a supercooled liquid rather then a solid [17]. The results obtained for N_2 [16, 17] and Ar at two temperatures on the same sample of MCM-41 are consistent, and indicate that the NLDFT model quantitatively estimates capillary condensation/desorption phenomena in cylindrical nanopores. Based on the theoretical NLDFT isotherms, a method for calculating the pore size distributions in silica-based nanoporous materials has been developed [16, 17].

LAYERING ADSORPTION HYSTERESIS

Layering transitions had been studied previously by means of DFT by Ball and Evans [11] and Peterson et al [13], who had also done MC simulations. They found hysteresis associated with individual layering transitions. The transitions were found to be of the first order with small metastable regions [11], and it had been concluded that these states are unlikely to be observed experimentally.

Experimental adsorption-desorption hysteresis isotherms with layering transitions have been reported by Inaba and Morrison [18] for methane adsorbed on graphite. Similar hysteresis loops have been obtained later for Ar, Kr, and CH_4 by Goodstein and coworkers [19-21]. In these works the observed hysteresis effect was attributed to the capillary condensation in gaps and cracks, which are inevitably present on the surface.

The capillary condensation may indeed affect the film adsorption experiments, and may give a significant contribution to the adsorption/desorption hysteresis. However, we argue here that the capillary condensation is not the only cause of the hysteresis in multilayer adsorption. The experimental isotherms show, that the individual layering transition steps on the desorption branch are sometimes shifted to lower pressures with respect to the corresponding steps on the adsorption branch [18]. This observation indicates that hysteresis may be associated with each of the consequential layering transitions. This conclusion is supported by our NLDFT calculations performed for Kr adsorbed on graphite.

Modeling Kr adsorbed on graphite at 90K, we employed the NLDFT model described above. The Kr-Kr interaction parameters for the Lennard-Jones (12-6) potential were $\varepsilon_{Kr-Kr}/k_B = 164.5K$, and $\sigma_{Kr-Kr} = 0.36$ nm. The WCA prescription for the attractive potential is used. The diameter of hard spheres at 90 K, $d_{HS} = 0.3649$ nm has been taken from the temperature dependence for Kr given by Lee et al [24]. The cutoff distance for the Kr-Kr potential was $6\sigma_{Kr-Kr}$. With this set of parameters, the mean-field DFT predicts the saturated vapor pressure of bulk Kr at 90K of ca. 19 Torr, which is quite close to the experimental value for the supercooled liquid Kr. The Kr-graphite interactions were modeled with the 10-4-3 potential of Steele [25].

The isotherm in a slit pore of $H=14\sigma_{Kr-Kr}$ have been calculated using parameters for the Kr-graphite potential obtained from the combining rules (Fig. 3). Starting calculations from low pressures, we have observed 3 layering transitions on the adsorption branch of the isotherm, and then, at a relative pressure very close to the saturation, - the spontaneous capillary condensation. On the desorption branch, the system remained in the condensed state down to a very low pressure (ca. 1 Torr), forming a

wide hysteresis loop with the adsorption branch. The point of the equilibrium transition from the desorption branch to the adsorption branch is ca. 8 Torr. Based on our previous experience with capillary condensation hysteresis in nanopores, we may argue that in experiments evaporation should occur in the vicinity of this transition.
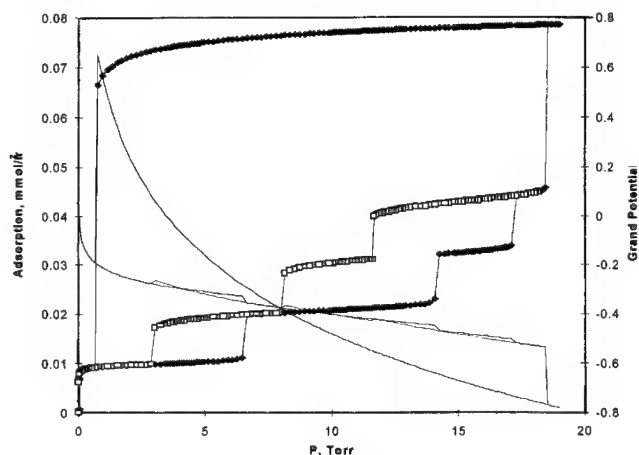
Fig. 3 NLDFT isotherm of Kr adsorbed on graphite in a 14 σ_{Kr-Kr} slit pore at 90 K. The lower curve (diamonds) is the adsorption branch of the isotherm which exhibits 4 layering transitions. The upper curve (diamonds) is the desorption branch after the capillary condensation transition. The central curve (open squares) is the scanning desorption branch which begun from the 4-th adsorbed layer at pressure just below the capillary condensation. The thin solid curves show the changes in the grand potential along these 3 branches of the isotherm.
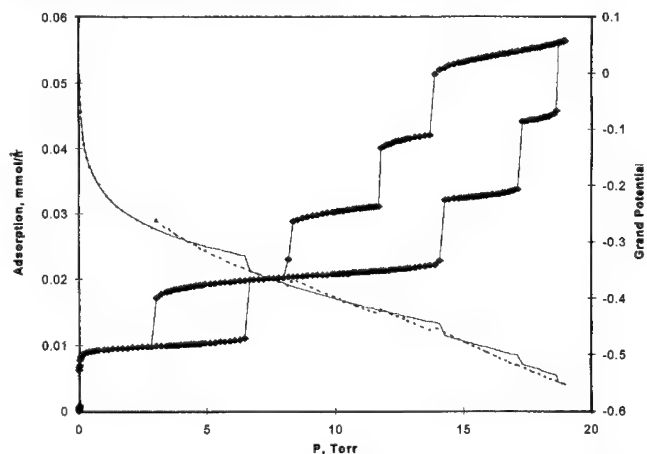
Fig. 4 NLDFT isotherm of Kr adsorbed on graphite in a 23 σ_{Kr-Kr} slit pore at 90 K. The lower curve (diamonds) is the adsorption branch of the isotherm with 5 layering transitions. The upper curve (diamonds) is the desorption path from the 5-th layer. Thin solid line - the grand potential along the adsorption branch, thin dashed line - the grand potential along the desorption branch.

To display hysteresis effects, which are not related to the capillary condensation, we have built a scanning desorption isotherm starting from some point on the adsorption branch corresponding to the 4-th adsorbed layer (ca. 18 Torr). We have obtained (Fig. 3) a secondary hysteresis loop associated with the layering transitions exclusively. The 4-3 layering transition on the desorption branch occurred at ca. 12 Torr, and that is instructive, the desorption branch did not join the adsorption branch at this pressure. With further decrease of pressure, the desorption branch exhibited one more transition and joined the adsorption branch at ca. 8.5 Torr. The hysteresis loop of the 1-2 layering transition was observed at pressures from ca 2.5 to 7 Torr.

In order to completely eliminate the effect of the capillary condensation observed in the 14 σ_{Kr-Kr} pore, we have performed calculations in a wider pore, H=23σ_{Kr-Kr}, (Fig. 4). The presence of the second pore wall at the distance of 23σ_{Kr-Kr} did not affect the layering transitions in the first 4 layers. Moreover, the adsorption branches of the isotherms up to 4-th layer in 14 and in 23σ_{Kr-Kr} pores reduced per unit area were identical. In the 23σ_{Kr-Kr} pore, we have not observed the capillary condensation (we did not extend calculations to pressures above the bulk saturation pressure), but rather the formation of the 5-th adsorbed layer. The desorption isotherm started from this layer, exhibits a wide hysteresis loop with 3 layering transitions. The desorption branches of the isotherms in 14 and in 23σ_{Kr-Kr} pores coincided below 12 Torr. The hysteresis loop in the wider pore included additional 5-th layer.

To explore the effect of the substrate strength on the layering transitions and hysteresis, we provided calculations with the fluid-solid energy reduced by 10%, ε_{Kr-C}/k_B=60.3 K. Results of calculations in the 14σ_{Kr-Kr} pore are presented in Fig. 5. As expected, we observed the shift of all layering transitions toward higher pressures. The desorption branch started from the 4-th layer joined the adsorption branch only on monolayer coverage, at pressure of ca. 4 Torr. This type of hysteresis loop is quite similar to that observed in some experiments. Thus, NLDFT calculations predict that the multilayer isotherms may form the hysteresis loops of different shape, step-wise adsorption and desorption branches.
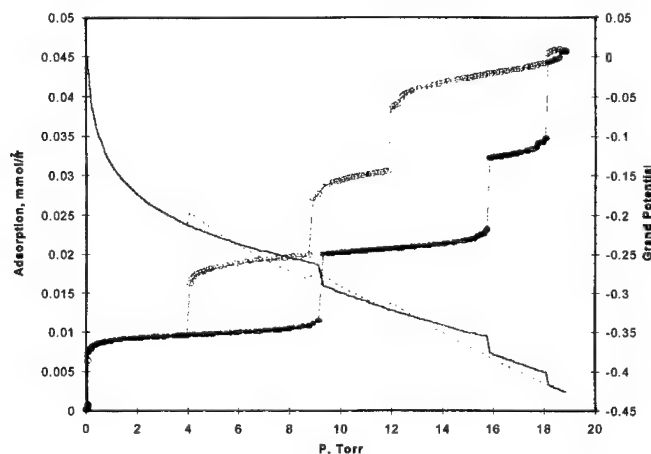
Fig. 5 NLDFT isotherm of Kr adsorbed on graphite in a 14 σ_{Kr-Kr} slit pore at 90 K. The well depth of the Kr-graphite interaction potential has been reduced by 10 %. The lower curve (filled circles) is the adsorption branch of the isotherm with 4 layering transitions. The upper curve (open circles) is the desorption path from the 4-th layer. Thin solid line - the grand potential along the adsorption branch, thin dashed line - the grand potential along the desorption branch.

CONCLUSIONS

NLDFT is a suitable tool for studying the hysteresis phenomena in nanopores. The theory is in a quantitative agreement with the experimental measurements for N_2 and Ar adsorption in cylindrical pores of MCM-41 type of materials at temperatures near and below the normal boiling point of the adsorptive.

The calculations of layering transitions in nanopores, performed with the example of the Kr-graphite system at 90K, show that the hysteresis observed in some experiments on multilayer adsorption at low temperatures (below bulk triple-point) is related to the phase transitions in metastable adsorption films, which may or may not be accompanied by the capillary condensation.

REFERENCES

1. L.H. Cohan, *J.Amer.Chem.Soc.*, **60**, 433 (1938)
2. A.V. Kiselev, *Uspechi Khimii*, **14**, 367 (1945)
3. D.H. Everett, *The Solid-Gas Interface*, Vol.2, edited by E.A.Flood, Dekker: New York, 1967
4. B.V. Derjaguin, *Acta Phys. Chem URSS*, **12**, 181 (1940)
5. J.C.P. Broekhoff, J.H. de Boer, *J.Catalysis*, **9**, 8 (1967); ibid. **10**, 368 (1968)
6. P. Tarazona, *Phys.Rev.A*, **31**, 2672 (1985)
7. R. Evans, U. Marini Bettolo Marconi, P. Tarazona, *J.Chem.Soc.Faraday Trans. 2*, **82**, 1763 (1986)
8. B.K. Peterson, J.P.R.B. Walton, K.E. Gubbins, *J.Chem.Soc.Faraday Trans. 2*, **82**, 1789 (1986)
9. B.K. Peterson, K.E. Gubbins, G.S. Heffelfinger, U. Marini Bettolo Marconi, F. van Swol, *J.Chem.Phys.*, **88**, 6487 (1988)
10. G.S. Heffelfinger, F. van Swol, K.E. Gubbins, *J.Chem.Phys.*, **89**, 5202 (1988)
11. P.C. Ball, R. Evans, *J.Chem.Phys.*, **89**, 4412 (1988)
12. P.C. Ball, R. Evans, *Langmuir*, **5**, 714 (1989)
13. B.K. Peterson, G.S. Heffelfinger, K.E. Gubbins, F. van Swol, *J.Chem.Phys.*, **93**, 679 (1990)
14. P.E. Balbuena, K.E. Gubbins, *Fluid Phase Equilibria*, **76**, 21 (1992)
15. P.I. Ravikovitch, A.V. Neimark, S.C.Ó Domhnaill, F. Schüth, K.K. Unger, *Langmuir*, **11**, 4765 (1995
16. A.V. Neimark, P.I. Ravikovitch, S.C.Ó Domhnaill, F. Schüth, K.K. Unger, in *Fundamentals of Adsorption*; LeVan, M.D., Ed.; Kluwer: Boston, 1996; p. 667
17. A.V. Neimark, P.I. Ravikovitch, M. Grün, F. Schüth, K.K. Unger in *Characterization of Porous Solids IV*, 1996, in press
18. A. Inaba, Y. Koga, J.A. Morrison, *J.Chem.Soc.Faraday Trans. 2*, **82**, 1635 (1986)
19. M.J. Lysek, M. LaMadrid, P. Day, D. Goodstein, Langmuir, **8**, 898 (1992); **9**, 1040 (1993)
20. P. Day, M. LaMadrid, M.J. Lysek, D. Goodstein, *Phys.Rev.B*, **47**, 7501 (1993)
21. P. Day, M.J. Lysek, M. LaMadrid, D. Goodstein, *Phys.Rev.B*, **47**, 10716 (1993)
22. A.V. Neimark, *Langmuir*, **11**, 4183 (1995)
23. S.J. Gregg, K.S.W. Sing, *Adsorption, Surface Area and Porosity*; Academic Press: New York, 1982
24. D.D. Lee, M.M. Telo da Gama, K.E. Gubbins, *Mol.Phys.*, **53**, 1113 (1984)
25. W.A. Steele, *The Interactions of Gases with Solid Surfaces*, Pergamon: New York, 1974

STRUCTURE AND PHASE TRANSITIONS IN PARTIALLY CONFINED SMECTIC LIQUID CRYSTALS

L. J. MARTINEZ-MIRANDA*,**, YUSHAN SHI** AND SATYENDRA KUMAR**
*Dept. of Materials and Nuclear Eng., University of Maryland, College Park, MD 20742-2115,
martinez@eng.umd.edu
**Dept. of Physics and Liquid Crystal Institute, Kent State University, Kent, OH 44242-0001

ABSTRACT

We present the results of an X-ray scattering study on partially confined smectic-A (layered) LC films. This partial confinement is achieved by placing the LC material inside the open grooves of a glass grating. Samples prepared in this manner are confined in the direction perpendicular to the gratings. Samples in which the LC is contained entirely inside the grooves develop an induced molecular tilt, which results in a compression of the smectic layers. The molecular tilt varies as the amount of the LC material increases, eventually forming a thin overlayer film above the gratings. As the thickness varies, a second region develops in the films. The layer spacing in this region is close to the bulk layer spacing. This structural evolution is coupled to a variation in the nematic-to-smectic-A phase transition temperature of the samples from the bulk. In addition, the nature of the phase transition is driven first order. The effects of partial confinement on a sm-C* LC film is discussed briefly.

INTRODUCTION

A liquid crystal (LC) material constrained between two aligning substrates[1-5] or inside a small cavity[6-12], or in the presence of air[13] can exhibit properties that vary significantly from the bulk properties of the material. A number of confined LC systems have been studied and modeled, including free standing smectic films[13-15], nematic and smectic LC's contained in cavities of different sizes[6-12] as well as nematic[6-12,17] and smectic[1-5,13,18-25] LC cells and films of varying thickness. Confinement of a LC, or its proximity to diverse surfaces affects the LC's thermal behavior[10, 13-15]. The thermal behavior depends on the history of the sample[4,26]. In addition, when a smectic LC is confined between two competing aligning surfaces, the film can divide into regions or multilayers of varying smectic layer orientation[1-5]. This is a result of the requirement that the ordered layers rotate to satisfy the boundary conditions at each surface. The size and number of these regions depend on the type of liquid crystal, the film thickness, the film temperature and the type of aligning surfaces

In this paper we present preliminary results of a temperature dependent structural study of a partially confined smectic A liquid crystal, octylcyanobiphenyl (8CB), close to the smectic A to nematic transition. The partial confinement is obtained by depositing the LC inside the open grooves of an open glass grating. The interactions due to confinement are varied by systematically adding LC material to obtain a thin overlayer film above the gratings. We have found that partial confinement results in a tilting of the smectic layers, an effect which is not observed in the bulk material. This compression of the smectic layers is coupled to a change in the nature of the smectic A to nematic phase transition. For thicker samples, a second, non-tilted LC region is observed. The presence of these regions changes the nature of the smectic A to nematic phase transition, as well as the value of the transition temperature of the sample. In addition, we present preliminary results on a partially confined tilted smectic LC material.

EXPERIMENTAL

Octylcyanobiphenyl (8CB), the LC material used in this study, is a LC material available from British Drug House, which has a room temperature sm-A phase and a second order sm-A - nematic transition at 33.5°C. The bulk layer spacing for 8CB is 31.6Å. The materials were deposited on photolithographed glass gratings, with an average grating period of 10 μm, and a depth of 2 μm. The grating preparation method is discussed elsewhere[1-3]. Samples contained within the grooves were prepared by allowing the material to flow by capillary force in the

isotropic phase. The thickness of the overlayer film sampled was varied systematically with the use of a high precision 0.1μl resolution pipette set to dispense 0.5μl of material at a time[1]. The samples were carefully spread in the isotropic phase over the grating area (1.00 cm^2) using a warm wire or a piece of Teflon tubing. 8CB samples were allowed to cool slowly before mounting in the x-ray diffractometer. The mx5112 samples were fast cooled into the sm-C* phase.

The samples were placed inside a single stage oven capable of controlling temperature in steps on 0.05°C. The oven was in the center of a Huber four-circle goniometer. The x-ray scattering measurements were performed using a Rigaku 18kW rotating anode source, using Cu $K_{\alpha 1}$ radiation ($\lambda = 1.5405$Å) , and a Si-Si monochromator - analyzer configuration with a resolution of 4×10^{-4}Å^{-1}, located at Kent State University. The experiments measured the signal from LC planes parallel to the surface of the glass substrate.

RESULTS AND DISCUSSION

Figure 1 shows the variation of the transition temperature as a function of sample thickness for 8CB, expressed in terms of the difference of the measured transition temperature from the ideal bulk transition temperature. The transition temperatures were measured at the center of the hysteresis loop. The figure also shows the observed hysteresis as a function of sample size. This latter quantity was measured from the values of the intensity of the smectic LC signal and the value of the full width at half maximum (FWHM), Δq, as a function of temperature. The transition temperature is higher than the bulk temperature in the smaller samples, where the liquid crystal is contained within the gratings. As the sample size increases, and 8CB forms an overlayer above the gratings, the transition temperature decreases slightly below the bulk transition temperature, and settles close to the value of the bulk transition temperature above a thickness of 4 μm. The width of the hysteresis loop varies up to values of 0.5°C when 8CB is contained within the gratings, and is almost zero when 8CB forms an overlayer above the gratings. Table I shows the evolution of the layer spacing at 29°C as a function size for the 8CB samples presented above. All samples exhibit a compression of the smectic layers, which varies between 0.7% and 1.4%.
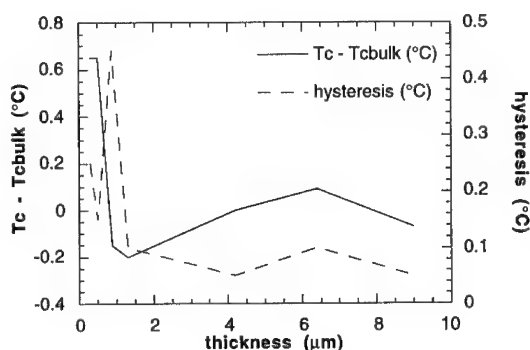
Figure 1. Evolution of the phase transition temperature difference and the hyteresis loop width as a function of sample size for 8CB.

Two of the samples exhibit two peaks corresponding to two different layer spacings at 29°C, as seen from Table I. The two peaks persist over the entire temperature range below the transition, as shown in Figure 2a for the 0.88 μm sample. This figure also shows that the lattice

parameter evolution is coupled to the hysteresis loop. Thicker samples exhibit two peaks at higher temperatures, as shown in Figure 2b for the 9 μm sample, as a function increasing temperature. These latter samples exhibit a very small hysteresis at the smectic A - nematic transition, as shown in Figure 1; however, they exhibit a hysteresis in the region where the split into two peaks appear, below the transition. In the case of the 9 μm, this value is 0.38°C.

Table I. Layer spacing as a function of increasing sample size for 8CB.

Sample size (μm)	first peak(Å)	second peak (Å)
0.3000	31.192	
0.5000	31.280	
0.8800	31.203	31.392
1.3000	31.280	
4.2000	31.159	31.369
6.4000	31.247	
9.0000	31.214	
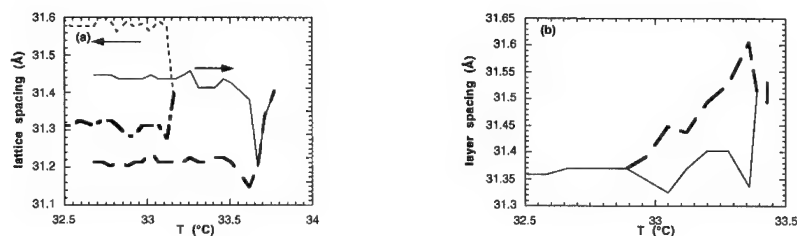
Figure 2. Values of the LC smectic layer spacing as a function of temperature: a) 0.88 μm, shown as a function of increasing as well as decreasing temperature; b) 9 μm, shown as a function of increasing temperature for clarity.

We now discuss briefly the results above. Models of cylindrically confined smectic A materials[26] as well as previous experimental studies on confined nematic LC materials[7, 27], indicate that these confined systems exhibit hysteresis. The result of this is that structures inside the cavities do not correspond to a minimum of the free energy system[27]. Sample preparation history also influences the structures formed in these cavities, as well as in thicker smectic films[4].

In the partially confined samples presented in this paper, the structures formed satisfy both the requirement that the smectic layers rotate to satisfy the boundary conditions at each surface[1-4], as well as the requirement of minimization of the bending deformation energy[26]. The structures are the result of the competition between the air-LC boundary conditions, and the grating wall-LC boundary conditions in the contained samples. The structure of samples consisting of an overlayer film also experience the effects of the grating - grating interaction, which in thicker films results in the complete rotation of the smectic layers in the direction perpendicular to the gratings[1-4].

The grating walls may result in a structure with tilted smectic A layers[26,27]. In Ref. 27, the tilt is accompanied by the formation of a chevron structure, in order to conserve the volume of each layer in the closed cell. Complementary optical observations on the samples in this study did not show evidence of the presence of chevron structures. On the other hand, the air-LC interface results in smectic layers aligned parallel to the surface of the LC, with a smectic layer spacing equal to the bulk spacing. The competition between these two boundaries results in the formation of

temperature dependent domains characterized by different layer spacings within the samples. Samples consist of a tilted component, which arises from the interaction of the samples with the walls of the gratings, and an untilted component, which results from the air-LC interaction. The influence of the latter surface is most notable close to the smectic A - nematic transition, where the nematic bending deformation results in the melting of the tilted smectic A layers allowing the top layer to propagate into the sample.

The interactions affect the transition temperature of the samples. The samples in this study that exhibit a considerable deviation from the bulk transition temperature are samples contained almost completely within the gratings. Surface anchoring at the three grating walls are responsible for the increase in the transition temperature in the smaller samples. The presence of melted smectic layers, most likely in the region separating the tilted and untilted regions in the sample decrease the transition temperature in samples that have a very small overlayer. As the overlayer increases, the transition temperature of the entire sample approaches that of the bulk smectic A - nematic transition temperature. We note that these larger samples may be characterized by two ordering temperatures, as seen in Figure 2b: the smectic A - nematic transition, and a tilting transition below the phase transition.

The presence of multilayers is not limited to smectic A, polar materials such as 8CB[27], nor to samples smaller than 10 μm thick[1-5,28]. We have performed a preliminary structural study on a room temperature smectic C* LC mixture, mx5112. This LC mixture, available from Displaytech, has the following phase transitions,

$$S_3 \text{ -----------------> } sm\text{-}C^* \text{ --------------> } sm\text{-}A .$$
$$20.65°C \qquad\qquad 49.5°C$$
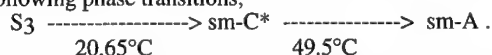
We have observed a persistence of the smectic A layer spacing over the entire smectic C* temperature range samples contained within the gratings. At room temperature (25°C), we measured layer spacings corresponding to all three phases presented above.

CONCLUSIONS

We have presented preliminary results of the temperature dependence of the structure of partially confined samples of 8CB. The smectic A phase of these samples is characterized by tilted layers, corresponding to a compression in the order of 0.7 - 1.4%. The samples may consist of both of tilted and untilted domains, depending on sample size and temperature. This latter observation is the result of the competition between the LC - grating wall interface, and the air-LC interface.

REFERENCES

1. E. Smela and L.J. Martínez-Miranda, J. Appl. Phys., 73, 3299-3304 (1993).

2. E. Smela and L. J. Martínez-Miranda, Liq. Cryst., 14, 1877-1883, 1993.

3. E. Smela and L. J. Martínez-Miranda, J. Appl. Phys.,77, 1923 (1995).

4. E. Smela and L. J. Martínez-Miranda, J. Appl. Phys., 77, 1930 (1995).

5. L. J. Martínez-Miranda, E. Smela and H. Liu, SPIE Vol. 2175, 1994.

6. J. T. Mang, K. Sakamoto and S. Kumar, Mol. Cryst. Liq. Cryst., 223, 133 (1992).

7. G. P. Crawford, D. W. Allender and J. W. Doane, Phys. Rev. A, 45, 8693 (1992).

8. G. P. Crawford, R. Ondris-Crawford, S. Zumer and J. W. Doane, Phys. Rev. Lett. 70, 1838 (1993).

9. G. S. Iannacchione, J. T. Mang, S. Kumar and D. Finotello, Phys. Rev. Lett., 73, 2708 (1994).

10. G. S. Iannacchione, A. Strigazzi and D. Finotello, Liq. Cryst., 14, 1153 (1993).

11. S. Krajl, S. Zumer and D. W. Allender, Phys. Rev. A, 43, 2943 (1991).

12. P. Drzaic, private communication (1995).

13. See, for example, B. M. Ocko, A. Braslau, P. S. Pershan, J. Als-Nielsen and M. Deutsch, Phys. Rev. Lett, 57, 94 (1986); B. D. Swanson, H. Stragier, D. J. Tweet and L. B. Sorensen, Phys. Rev. Lett., 62, 909 (1989).

14. See, for example, J. Collett, P. S. Pershan, E. B. Sirota and L. B. Sorenson, Phys. Rev. Lett., 52, 356 (1984).

15. B. M. Ocko, Phys. Rev. Lett., 64, 2160 (1990).

16. See, for example, P. Guyot-Sionnest, H. Hsiung and Y. R. Shen, Phys. Rev. Lett, 57, 2963 (1986); H. Hsiung and Y. R. Shen, Phys. Rev. A, 34, 4303 (1987); X. Zhuang, L. Marrucci and Y. R. Shen, Phys. Rev. Lett., 73, 1513 (1994).

17. O. D. Laurentovich and V. M. Pergamenshchik, Phys. Rev. Lett., 73, 979 (1994).

18. N. Kothekar, D. W. Allender, and R. M. Hornreich, Phys. Rev. E, 49, 2150 (1994).

19. X. Zhuang, L. Marrucci and Y. R. Shen, Phys. Rev. Lett., 73, 1513 (1994).

20. N. A. Clark, Phys. Rev. Lett., 55, 292 (1985).p

21. See, for example, M. A. Handschy and N. A. Clark, Ferroelectrics, 59, 69 (1984).

22. A. D. L. Chandani, Takashi Hagiwara, Yoshi-ichi Suzuki, Yuchio Ouchi, Hideo Takezoe and Atsuo Fukuda, Japanese Journal of Applied Physics, 27, L729 (1988).

23. Y. Shi, B. Cull and S. Kumar, Phys. Rev. Lett., 71, 2773 (1993).

24. W. Chen, M. B. Feller, and Y. R. Shen, Phys. Rev. Lett. 63, 2665 (1989).

25. Moses, T., Ouchi, Y., Chen, W. and Shen, Y. R., Mol. Cryst. Liq. Cryst. 225, 55 (1993).

26. S. Kralj and S Zumer, Phys. Rev. E, 54, 1610, (1996).

27. Y. Takanishi, Y. Ouchi, H. Takezoe and A. Fukuda, Japanese Journal of Applied Physics, 28, L487 (1989).

28. L. J. Martínez-Miranda, Yushan Shi and Satyendra Kumar, Molec. Cryst. Liq. Cryst, in press (1996).

PHOTON CORRELATION SPECTROSCOPY OF LIQUID CRYSTALS CONFINED IN POROUS MATRICES WITH DIFFERENT STRUCTURE AND PORE SIZE

F.M. ALIEV and I.V. PLECHAKOV
Department of Physics and Materials Research Center, PO BOX 23343, University of Puerto Rico, San Juan, PR 00931-3343, USA

ABSTRACT

We present the results of photon correlation spectroscopy investigations of the influence of confinement, interface, porous matrix structure, pore size and shape on the dynamic behavior of nematic liquid crystals (LC) dispersed in porous matrices with randomly oriented, interconnected pores (porous glasses) and parallel cylindrical pores (Anopore membranes). Investigations of LC in cylindrical pores together with studies in random porous matrices, makes it possible to separate the role of random structure and domain formation from the contributions due to existence of LC - solid pore wall interface and pure finite size effect in relaxation of order parameter or director fluctuations. In the temperature range below nematic - isotropic phase transition temperature we observed two overlapping relaxational processes which are satisfactorily described by the decay function $f(q,t) = a \cdot exp(-t/\tau_1) + (1-a) \cdot exp(-x^z)$, where $x = ln(t/\tau_0)/ln(\tau_2/\tau_0)$ and $\tau_0 = 10^{-8}s$. For LC in 100 Å random pores the second term describing the slow process dominates, whereas for 200 Å and 2000 Å cylindrical pores as well as 1000 Å random pores the contribution from the first term (fast process) is more visible. Since the slow relaxational process which does not exist in the bulk LC and broad spectrum of relaxation times $(10^{-6} - 10)s$ appear not only for LC in random pores but in cylindrical as well, we conclude that differences in dynamical behavior of confined LC from that in the bulk are mainly due to the existence of the interface.

INTRODUCTION

The understanding of new phenomena arising in confined liquid crystals is important for the fundamental physics of interfaces and finite systems. This stimulated intensive research of liquid crystals confined in different geometries. A variety of new properties and phenomena such as the modification of phase transitions, orientational order, elastic properties, director field, has been studied [1-9] both experimentally and theoretically for liquid crystals confined in random porous networks and cylindrical pores. Although great success in the understanding of the physical properties of liquid crystals confined in porous media with different size, shape of pores and different structure of porous matrix was achieved, little work has been done to characterize the influence of confinement on different aspects of dynamical behavior of confined LC.

In this paper we present the results of investigations of the influence of the confinement and interface on the dynamic behavior of nematic liquid crystals (LC) dispersed in porous matrices having different pore structure and pore size using static and dynamic (photon correlation spectroscopy) light scattering.

EXPERIMENT

We performed photon correlation measurements using a 6328 Å He-Ne laser and the ALV-5000/Fast Digital Multiple Tau Correlator (real time) operating over delay times from 12.5 ns up to 10^3 s with the Thorn EMI 9130/100B03 photomultiplier and the ALV preamplifier. In addition we used ALV/LSE unit which allows simultaneously with photon correlation measurements monitoring of the laser beam intensity and stability of its space position as well

as the intensity of scattered light integrated over all frequencies (static light scattering). The depolarized component of scattered light was investigated. In the dynamic light scattering experiment, one measures the intensity-intensity autocorrelation function

$$g_2(t) = \langle I(t)I(0)\rangle/\langle I(0)\rangle^2. \tag{1}$$

The intensity-intensity autocorrelation function $g_2(t)$ is related to dynamic structure factor f(q,t) of the sample by

$$g_2(t) = 1 + k f(q,t)^2, \tag{2}$$

where k is a contrast factor that determines the signal-to-noise ratio and $q = 4\pi n \sin(\Theta/2)/\lambda$, ($n$ is refractive index, and Θ - the scattering angle). We found that for 5CB in porous glasses the intensity-intensity autocorrelation functions were q independent, and almost independent for 5CB in cylindrical pores. All dynamic light scattering data we discuss below were obtained at $\Theta=30^o$.

We used matrices with randomly oriented, interconnected pores (porous glasses with average pore sizes of 100 Å and 1000 Å) and parallel cylindrical pores (Anopore membranes with pore diameters of 200 Å and 2000 Å). The nematic liquid crystal we used was pentyl-cyanobiphenyl (5CB). The phase transition temperatures of 5CB in the bulk are $T_{CN} = 295K$ and $T_{NI} = 308.18K$.

STATIC LIGHT SCATTERING IN CONFINED 5CB

From static light scattering experiments we obtained that the nematic - isotropic phase transition in 1000 Å random pores, 200 Å and 2000 Å cylindrical pores is smeared out, the transition is not as sharp as in the bulk LC, it occupies finite temperature region, and the temperature of this transition is depressed compared to that bulk value. The temperature dependence of the intensity of scattered light (I_{sc}) for 5CB in pores is presented in Fig. 1. It
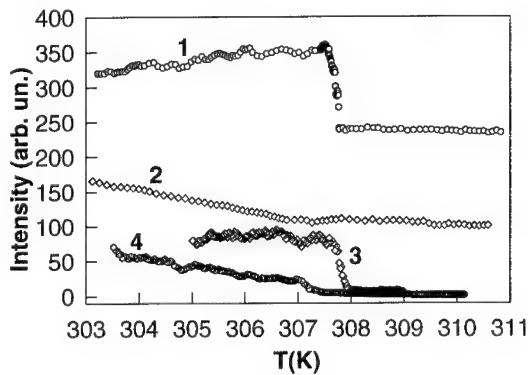
Figure 1: Temperature dependence of the intensity of scattered light for 5CB in pores: (1) - 1000 Å random pores, (2) - 100 Å random pores, (3) - 2000 Å cylindrical pores and (4) - 200 Å cylindrical pores.

is clear that in 100 Å pores (curve 2 in Fig. 1) there is no well defined phase transition from ordered phase to the phase in which long range order is completely absent, or opposite from disordered phase to the phase with perfect long range orientational order. The temperature dependence of (I_{sc}) in isotropic phase of confined LC is different from that in the bulk. In pores I_{sc} is almost independent of temperature (Fig.1) in the temperature range corresponding to the isotropic phase. In the bulk isotropic phase this intensity is temperature

dependent and exhibits the mean-field theory critical exponent expected near a second-order transition at a temperature T^* preempted by a first order phase transition at T_{NI}, namely: $I_{sc} \sim 1/(T - T^*)$.

In determination of phase transition temperature in finite systems the difficulty is that the transition region occupies a finite temperature interval and it is unclear what should be regarded as the transition temperature. The combination of static and dynamic light scattering methods is very useful to determine the phase transition temperature of LC in pores. In dynamic light scattering experiment, only one relaxational process due to fluctuations of order parameter should be observed in isotropic phase. In nematic phase the decay of $g_2(t)$ is due to director fluctuations. The difference in relaxation times of these two processes is of three orders of magnitude, and it is very easy to identify the nature of relaxational process and the phase correspondingly. We determine the nematic-isotropic phase transition temperature for LC in pores as a temperature above which there is no visible decay due to order parameter fluctuations (see next section). These temperatures coincide with temperatures at which rise in the intensity of scattered light (when temperature decreases) finishes (see curves 1, 3 and 4 in Fig. 1). We determine nematic- isotropic phase transition temperatures for 5CB in pores as: 307.5 K (1000 Å random pores), 307.6 K (2000 Å cylindrical pores) and 307.0 K (200 Å cylindrical pores).

PHOTON CORRELATION SPECTROSCOPY OF CONFINED 5CB

Dynamic light scattering in bulk nematic liquid crystals is very well understood [10], and the main contribution to the intensity of scattered light is due to the director fluctuations. In uniformly oriented nematic sample, there are two modes determined by these fluctuations. The first mode is determined by a combination of splay and bend distortions and the second mode by a combination of twist and bend distortions, and each of these modes is described by single exponential decay function. If for the simplicity we assume that six Leslie coefficients
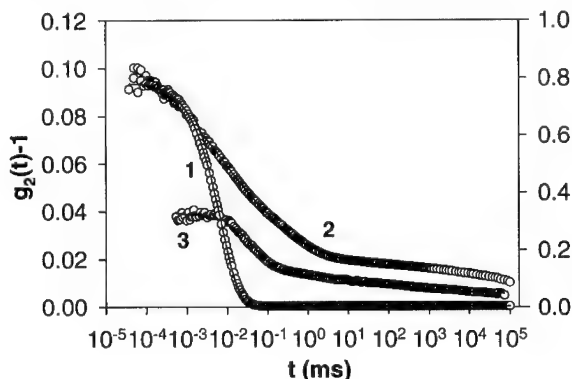
Figure 2: Intensity/intensity autocorrelation functions for 5CB: (1) - bulk 5CB, T=306.2 K (right scale), (2) - in 100 Å random pores, T=295.8 K (left scale), (3) - in 200 Å cylindrical pores, T=306.9 K (left scale). Opened circles-experimental data, solid lines-fitting.

have the same order of magnitude and are $\sim \eta$ (η is an average viscosity), and three elastic constants (bend, splay and twist) are equal (K) then the relaxation time is $\tau = \eta/Kq^2$ and has the same order of magnitude $\sim 10^{-5}s$ for the both modes. The corresponding decay function is exponential decay function:

$$f(q,t) = a \cdot \exp(-t/\tau). \tag{3}$$

The relaxation time $\tau = 1.4 \cdot 10^{-5}s$ which corresponds to the curve 1 (Fig. 2) is in agreement with the theory [10]. The difference between the dynamic behavior of bulk nematic multidomain 5CB and 5CB in 100 Å random pores as well as in 200 Å cylindrical pores can be seen by comparison of curves (1), (2) and (3) in Fig. 2. Slow relaxational process which does not exist in the bulk LC and a broad spectrum of relaxation times $(10^{-8} - 10)s$ appear for 5CB in both random and cylindrical pores if LC is in anisotropic phase. It is clear from the Fig. 2 that the relaxation processes in 5CB confined in the both matrices are highly nonexponential, and the long time tail of relaxational process for 5CB in pores can not be described using standard form of dynamical scaling variable (t/τ). It is reasonable for so slow dynamics and such a wide spectrum to use ideas [1] of activated dynamical scaling with the scaling variable $x = lnt/ln\tau$. We are not able to find the correlation function (or a superposition of correlation functions) which would satisfactorily and quantitatively describe the whole experimental data from $t = 10^{-4}ms$ up to $t = 10^{6}ms$. However we found that in the time interval $10^{-3}ms - 10^{3}ms$ (6 decades on the time scale) decay function :

$$f(q,t) = a \cdot exp(-t/\tau_1) + (1 - a) \cdot exp(-x^z), \qquad (4)$$

where $x = ln(t/\tau_0)/ln(\tau_2/\tau_0)$, and in our case $\tau_0 = 10^{-8}s$ provides suitable fitting for 5CB in narrow (100 Å and 200 Å) pores. For 5CB in 100 Å random pores the second term in relationship (4) dominates, whereas for 200 Å pores the contribution from the first term is much more visible. The fitting parameters corresponding to curves (2) and (3) in Fig. 2 are: (2) - z=2.3, τ_2=0.04 ms (exponential decay is neglected); (3) - τ_1=0.07 ms, z=3.6, τ_2=3s.

The relaxation time of slow process for 5CB in 100 Å pores strongly increases when temperature decreases from 300 K up to 270 K varying from 1.7×10^{-4} s to 14 s in this temperature range. The data analysis shows [5, 8] that the temperature dependence of the relaxation times for 5CB in 100 Å random pores, in the temperature interval (270-300) K, follows the Vogel-Fulcher law: $\tau = \tau_0 exp(B/(T - T_0))$ with parameters: $\tau_0 = 1.4 \cdot 10^{-11}s$, $B = 847K$ and $T_0 = 246K$.

The dynamical behavior of 5CB confined in large pores (1000 Å and 2000 Å) was closer to the bulk behavior as we expected. However slow decay was observed in anisotropic phase. The dynamic behavior of 5CB in 2000 Å cylindrical pores at different temperatures is illustrated in Fig. 3 and Fig. 4. At T = 307.9 K, which is below bulk T_{NI} but above T_{NI}
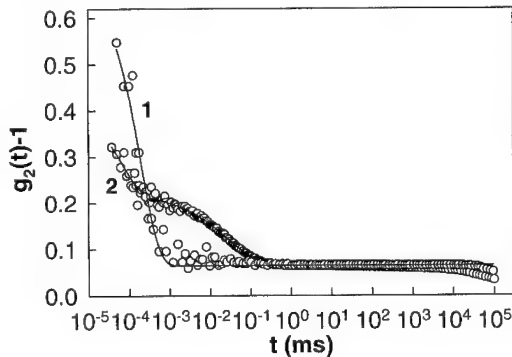
Figure 3: Intensity/intensity autocorrelation functions for 5CB in 2000 Å cylindrical pores. (1) - T = 307.9 K; (2) - T = 307.7 K. Opened circles-experimental data, solid lines-fitting.

in pores, only fast decay due to the order parameter fluctuations is observed. This decay is single exponential with relaxation time τ=3.8×10^{-7} s. With decreasing the temperature (but still above T_{NI} in pores) the contribution from order parameter fluctuations decreases

and visible second decay (curve 2 in Fig. 3) due to director fluctuations appears. The existence of this decay in transitional region is an experimental conformation of the formation of
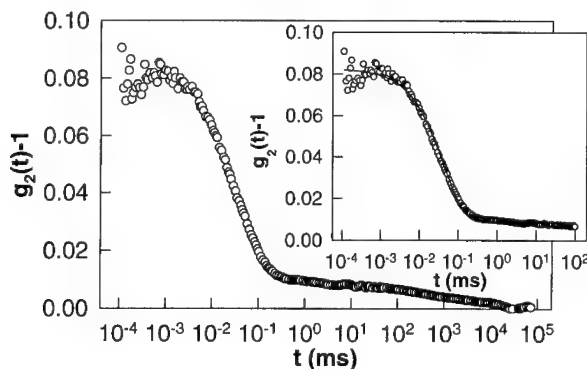
Figure 4: Intensity/intensity autocorrelation functions for 5CB in 2000 Å cylindrical pores at T = 307.3 K. Inset - comparison of the experiment and fitting. Opened circles-experimental data, solid lines-fitting.

ordered phase preceding phase transition in confined LC. This ordered (paranematic) phase has features of nematic phase. However, decay corresponding to the director fluctuations in confined LC is not single but is stretched exponential. So the second term in the formula (4) should be replaced by $(1 - a) \times exp(-(t/\tau_2)^\beta)$. The superposition of single exponential and stretched exponential decays adequately describes experimental data in transitional temperature region. The parameters for the curve (2) are: $\tau_1 = 10^{-7}$s, $\tau_2 = 0.09$ ms and $\beta = 0.56$. In nematic phase fast decay due to order parameter fluctuations vanishes, stretched
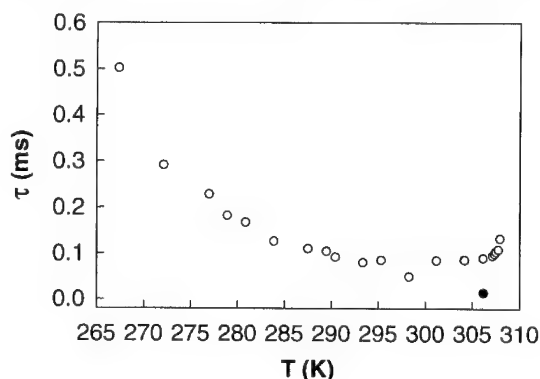
Figure 5: 5CB in 2000 Å cylindrical pores. Temperature dependence of relaxation times of director fluctuations - open circles. Closed circle - relaxation time for bulk 5CB at T=306.16K.

exponential decay due to director fluctuations dominates, and slow decay, origin of which still is under question (see [1-5, 8]) appears (Fig. 4). In order to obtain an information on temperature dependence of relaxation times of director fluctuations we neglect slow decay and restrict time range by $t < 0.1$ s. In this time range the experimental data are satisfactory described by stretched exponential decay function. The data presented in the inset

of Fig. 4 have parameters $\tau = 0.1$ ms and $\beta = 0.8$. The temperature dependence of the relaxation times obtained by using this procedure is presented in Fig. 5. Noticeable increase in relaxation times at low temperatures $(T < 280K)$ corresponding to solid phase in bulk 5 CB is caused by viscosity increasing due to supercooling of LC in pores.

CONCLUSION

The static light scattering and photon correlation experiments show significant changes in physical properties of liquid crystals confined in porous media. Nematic-isotropic phase transition temperature T_{NI} of LC is depressed in 1000 Å random, 200 Å and 2000 Å cylindrical pores compared to that bulk value and this phase transition was not detected at all in 100 Å random pores. We found that even about $20°C$ below bulk crystallization temperature the relaxational processes in confined LC were not frozen. Slow relaxation process which does not exist in the bulk LC and wide spectrum of relaxation times $(10^{-8} - 10)s$ appear in both random and cylindrical pores. This slow process observed in the dynamic light scattering experiments can not be described using standard form of dynamical scaling variable (t/τ) but they obey activated dynamical scaling with the scaling variable $x = lnt/ln\tau$. The slow dynamics in anisotropic phase of confined LC and extremely wide spectrum of relaxation times still remain unexplained.

ACKNOWLEDGEMENTS

REFERENCES

1. X-l. Wu, W.I. Goldburg, M.X. Liu, and J.Z Xue, Phys. Rev. Lett. **69**, 470, (1992).

2. W.I. Goldburg, F.M. Aliev, X-l. Wu, Physica A **213**, 61, (1995).

3. T.Bellini, N.A.Clark, D.W.Schaefer, Phys. Rev.Lett. **74**, 2740, (1995).

4. Z. Zhang and A. Chakrabarti, Phys.Rev. **E52**, 4991, (1995).

5. F.M. Aliev and V.V. Nadtotchi in: Disordered Materials and Interfaces, edited by H.Z. Cummins, D.J. Durian, D.L. Johnson, and H.E. Stanley, (Mater. Res. Soc. Proc. **407**, Pittsburgh, PA, 1996), pp. 125-130.

6. D. Finotello and J. Iannacchione, Int. Journ. Mod. Phys. **B9**, 109, 1995.

7. G.P. Crawford and S. Zumer, Int. Journ. Mod.Phys. **B9**, 331, 1995.

8. F.M. Aliev, in Access in Nanoporous Materials, edited by T.J. Pinnavaia and M.F. Thorpe, (Plenum Press, New York, 1995), pp. 335-354.

9. G.P. Crawford and S. Zumer, Liquid crystals in complex geometries, (Taylor & Francis, London, 1996).

10. P.G. de Gennes and J. Prost, The Physics of Liquid Crystals, 2nd ed. (Clarendon Press, Oxford, 1993).

PHASE TRANSITIONS OF ORGANIC FLUIDS CONFINED IN POROUS SILICON

C. FAIVRE, G. DOLINO, D. BELLET
Laboratoire de Spectrométrie Physique, Université J. Fourier, Grenoble-I, CNRS, (UMR 5588); BP 87; 38402 Saint Martin d'Hères Cedex; France; faivre@spectro.grenet.fr

ABSTRACT

This paper reports experimental data on both the solid-liquid and liquid-vapour phase transitions of an organic fluid confined in the pore network of porous silicon, by using respectively differential scanning calorimetry and X-ray diffraction. Due to the nanometric pore sizes of this material, the surface effects have a strong influence, shifting the transition parameters (lower melting temperature and lower condensation vapour pressure respectively). In particular, the effect of chemical dissolution on the pore size distribution of porous silicon layers has been investigated.

INTRODUCTION

The study of the thermodynamic properties of ultra-fine particules or of confined phases in various host matrices, has been much studied for a long time, and is still a subject of current interest [1, 2]. Thermodynamic properties are modified relative to the bulk values when the size of the particle is in a few nanometer range. Several studies have been devoted to the confinement effects of different fluids (alkanes, water, rare gases...) mainly in porous glasses. Melting temperature depression is observed (often by using Differential Scanning Calorimetry (DSC)), and in a first approximation the temperature shift is proportionnal to the inverse of the pore size [3,4]. Such experiments have even been proposed as a tool for estimating the pore size distribution inside a porous body, a technique called thermoporosimetry [5].

We report in this paper a DSC investigation of fluids confined in the pore network of porous silicon (PS). This material, discovered fourty years ago, was mainly studied for its application in microelectronics technology. Recently a new increase of interest appeared when luminescent properties were observed at room temperature [6,7]. The origin of these luminescent properties is still debated, however the quantum confinement of the carriers inside the nanometric silicon cristallites is often mentionned [8].

Porous silicon is formed through an electrochemical etching of a doped silicon wafer, in a HF solution, resulting in the formation of a porous silicon layer with depth proportionnal to the etching time. The main electrochemical parameters are the doping type and level, the HF concentration of the etching solution and the current density. The control of these parameters enables to get PS layers with different porosities (ranging typically from 20 to 90%), various thicknesses (from a few nanometers up to hundreds of micrometers) and different pore size distributions [9]. The pore size is often in the order of a few nanometers, corresponding to a surface area of a few hundreds of square meters per cubic centimeter : such a large surface plays a key role in any physical properties of porous silicon.

Anyhow, as the interactions between porous silicon and fluids are often encountered, the investigation of such interactions is then important to improve our knowledge on this material, but PS can also be considered as a rather peculiar host matrix on which original experiments can be performed. For instance in spite of its porosity, PS is a nearly perfect single crystal, as revealed by high resolution X-ray diffraction experiments [10]. This property enables one to measure in-situ the elastic strains induced by vapour adsorption, as described below.

The three phase diagram of the fig.1a. presents the two phase transitions studied for confined fluids : the liquid-vapour transition is investigated by X-ray diffraction for vapour pressure variations (at constant temperature) and the solid-liquid transition by DSC for temperature variations.
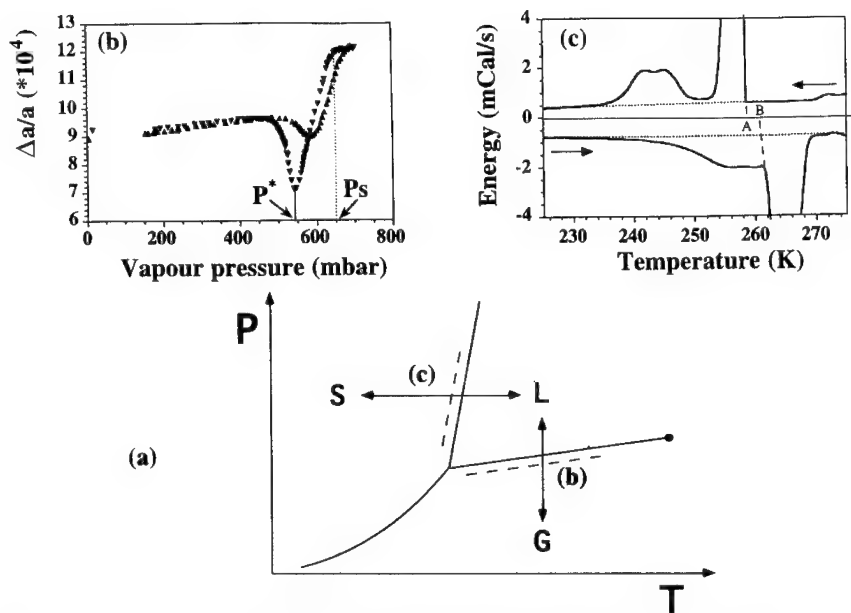
Fig.1 (a): A typical three phase (solid, liquid, gas) diagram of a fluid in bulk state (————) or confined in a porous matrix (- - - -);
    (b) : X-ray measurement of the lattice parameter mismatch of a p+ type PS sample of 80% porosity as a function of the adsorbed pentane vapour pressure;
    (c) : A typical curve of a DSC investigation of the solid-liquid transition of dodecane with a p+ type PS sample of 60% porosity.

EXPERIMENTAL CONDITIONS

X-ray adsorption measurements

The PS layers were obtained by anodization of boron-doped (001) silicon wafers. The p+ type PS layers were fabricated from highly doped Si wafers with 10^{-2} Ω.cm resistivity, under electrochemical conditions leading to a 10 micron thick layer of 80% porosity (electrolyte composed of 15% HF, 35% water and 50% ethanol, current density of 80 mA/cm² and etching time of 220 s).

In the X-ray diffraction experiments, performed with a high resolution diffractometer (Philips MRD), two narrow Bragg peaks are observed, associated with the substrate and the porous layer [10]. From the angular splitting between the two peaks, the lattice mismatch parameter $\Delta a/a$ can be calculated accurately.

X-ray data were obtained at room temperature, with the sample in a vacuum cell with a beryllium window, allowing to control the vapour pressure of pentane between 0 and the saturation vapour pressure, $P_S = 650$ mbar.

DSC measurements:

The p+ type PS layers were prepared with conditions corresponding to 60% porosity (electrolyte composed of 25% HF, 25% water and 50% ethanol, current density of 180 mA/cm² and etching time of 700 s). The 100 micron thick layers were then detached from the substrate by

changing the electrolyte composition to 5% HF, 45% water and 50% ethanol, with a current pulse of 600 mA/cm^2 during 10 seconds.

Chemical dissolutions were performed by leaving the PS layers in the 5% HF solution under dark conditions, for time varying from zero to 100 minutes. Some samples were thermally oxidized at 300°C under oxygen atmosphere for 20 minutes allowing then water to penetrate the pore network as the PS specific surface becomes hydrophilic after thermal oxydation.

The DSC experiments were performed with PS layers filled with different liquids : cyclohexane (a commonly used liquid in DSC technique [4] which presents two phase transitions), dodecane (because of its high latent heat of transition) and water. It is known that alkanes perfectly wet the porous layer (as shown by X-ray diffraction experiment [10]), while the PS layers should be oxidized to become hydrophilic for the water freezing experiment.

The scanning temperature rates were 2.5, 5 or 10 K/min : this is slow enough to avoid any thermal diffusion problems since the Full Width at Half Maximum (FWHM) of the confined peaks were the same for the different scanning rates.

LIQUID-VAPOUR TRANSITION

Using X-ray diffraction, the lattice parameter mismatch was measured as a function of pentane vapour pressure [11]. This dependance is plotted on fig.1(b). At $P = 0$, the lattice expansion of the PS layer, $\Delta a/a$, is $8.9*10^{-4}$, the same value as in air. With increasing vapour pressure there are only little variations of the rocking curve shapes, up to $P \approx 550$ mbar where the porous Bragg peak broadens and shifts toward the substrate peak, reaching its maximum at $P \approx 590$ mbar. Around saturation vapour pressure, $P_s = 650$ mbar, the porous Bragg peak has shifted back and has nearly reached the position found for full immersion in the liquid. With decreasing pressure i.e. during controlled drying, a strain hysteresis is clearly observed : the decrease of the lattice parameter occurs at a smaller value, $P^* \approx 540$ mbar, than for increasing pressure. These lattice parameter variations are attributed to capillary condensation. Then the vapour pressure P^* is related to the pore radius r, via Kelvin equation [11]:

$$P^* = P_s \exp\left(\frac{-2\,\gamma_{LV}V_m}{r\,R\,T}\right) \qquad (1)$$

where V_m is the molar volume of the liquid, γ_{LV} the liquid surface tension and T the temperature (assuming that the contact angle is zero). By replacing $P^* = 540$ mbar and $P_s = 650$ mbar in this equation, we find the mean pore radius to be around 7 nm for a p$^+$ type sample of 80% porosity. This result is coherent with previous results [7] as well as with the mean pore radius calculated below, from DSC curves.

THERMODYNAMIC OF SOLID-LIQUID TRANSITION

A typical DSC scan of dodecane in p$^+$ type PS sample is shown on fig.1(c). One notes the presence of dodecane in excess, since the temperature scan presents two peaks for the solid-liquid transition: some of the dodecane is confined inside the pore network of the PS layer (and therefore gives rise to a down shifted broad peak), and some is outside behaving as bulk dodecane and giving an intense narrow peak. The peak corresponding to the confined liquid is larger than the bulk one and much less intense; the peak is broaden by the pore size distribution of the porous layer (while its intensity depends on the latent heat and on the amount of fluid involved in the transition). For a bulk transition, the tangent to the peak represents the beginning of the nucleation process, i.e. the transition temperature (as considered usually for transitions that are isothermal). However, in order to describe the broaden peak corresponding to the confined fluid, we have to consider the transition temperature which is related to the mean pore radius and the FWHM of the confined peak which can be related to pore size distribution width.

On fig.1b, a small hysteresis for the bulk peak (T_A-T_B) of 5 K is clearly observed. This hysteresis can be understood by considering a small nucleation delay for the freezing of a pure liquid. Usually the bulk melting temperature is identified with the true equilibrium transition

temperature. For the confined peak a larger hysteresis of about 14 K is observed. To explain these results, we have to review briefly the different thermodynamic behaviours of fluid confined in nanometric pores.

For decreasing temperature, first the liquid around the sample freezes, so that an external solid film is present outside the pore aperture. Then freezing in the pores occurs through the penetration of a freezing front with a solid-liquid meniscus. Following Scherer [12], the meniscus is always spherical. Then the transition in the pores occurs at the temperature corresponding to the stability limit of this solid-liquid meniscus, where the meniscus radius is equal to the pore radius. The temperature shift when compared to the bulk transition temperature is :

$$\Delta T = \frac{-\alpha \, \sigma_{LS} \, V_l \, T_0}{L_0 \, r} \tag{2}$$

where α is a coefficient equals to 2 for a spherical meniscus, σ_{LS} is the solid-liquid interfacial free energy, V_l the molar volume of the fluid, T_0 the bulk transition temperature, L_0 the latent heat of the transition and r the pore radius. In this situation, the limiting factor for the meniscus penetration is the pore aperture size and not the actual pore radius. For cylindrical pores, the aperture radius is the same than the pore radius but for spherical pores, we probably underestimate the real pore radius.

We now focus on the melting transition : starting at low temperature, bulk and confined fluids are in solid state. A liquid layer of a few angströms thick must nucleate at the pore surface. This surface melting occurs at a temperature between thermodynamic equilibrium and the stability limit of the surface liquid layer [13]. We will suppose, as it is often considered in the literature, that the measured temperature is closer to the stability limit of the nucleated liquid layer. The relationship between this temperature and the pore radius depends on the pore geometry (spherical or cylindrical). This relation is the same than equation (2) but in this case, $\alpha = 1$ [3,5]. For a cylinder, this variation of coefficient ($\alpha = 2$ for freezing and $\alpha = 1$ for melting) can explain the origin of the large hysteresis of the p^+ type PS samples which have a cylindrical pore morphology.

With these assumptions, one can evaluate a pore radius for the studied samples, calculated from the melting or freezing DSC curves. In principle, we should find the same pore radius if the assumption concerning the origin of the hysteresis is correct.

DSC RESULTS

From the temperature depression observed for the two peaks of fig.1(c), one calculate the pore radius of the p^+ type PS sample from equation (2) and find the two mean pore radii (when considering freezing) to be 3.5 and 4.5 nm. When considering the single melting peak, we find a mean pore radius around 4 nm.

We then performed dissolution experiment by leaving the sample in HF solution, under dark conditions, during time varying from 0 to 100 minutes, to characterise the effect of chemical dissolution on the pore size. The DSC measurements were performed with cyclohexane, which presents two transitions (solid-liquid and solid-solid) which allows two calculations of the pore radius using the latent heat of fusion and surface free energy values of the two transitions [4]. When calculating the resulting pore radius as a function of dissolution time, we obtain the results presented on fig.2(a) where it is shown how the mean pore radius increases from 4 nm to more than 7 nm after 100 minutes in HF. For each dissolution time, the two pore radii calculated for melting ($\alpha = 1$) or freezing ($\alpha = 2$) are very similar if we consider the solid-liquid transition. On the other hand for the solid-solid transition, the hysteresis is larger than predicted by the change from $\alpha = 1$ to 2 in equation (2). In this case it is dubious whether the meniscus penetration in the pore network can be used for a solid-solid transition.

We notice the evolution of the shape of the confined peak presented on fig 2(b) for the two transitions when decreasing temperature and for two different time dissolution. The width of this peak, related to the pore size distribution, decreases when time in HF increases : the chemical dissolution seems to happen preferentially for small pores leading to a narrower size distribution.
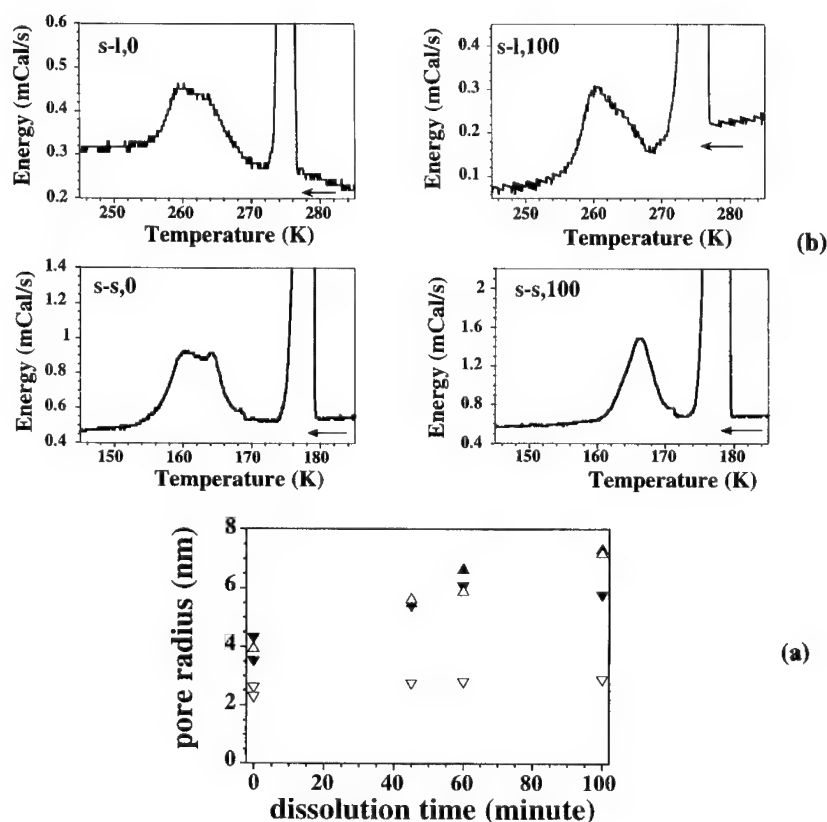
Fig.2(a) : The pore radius of a p^+ type PS sample of 60% porosity, with cyclohexane, as a function of dissolution time in a HF solution; the symbols ($\Delta \nabla$) correspond to the pore radii calculated from the solid-liquid transition and the symbols ($\blacktriangle \blacktriangledown$) to the ones calculated from the solid-solid transition of cyclohexane. The symbols are up ($\blacktriangle \Delta$) for increasing temperature and down ($\blacktriangledown \nabla$) for decreasing temperature.

(b) : DSC freezing curves showing the solid-liquid transition (s-l) and the solid-solid transtition (s-s) of cyclohexane confined in PS sample, either as formed (0) or after a chemical dissolution in HF for 100 minutes (100).

Fig.3a shows the results for water confined inside the same p^+ type PS sample of 60% porosity : for temperature decreasing there is only a single freezing peak. This could be explain by the nucleation hysteresis of pure water (more than 10K); when the excess bulk water freezes, it induces immediately the freezing of the confined water, giving therefore a single freezing peak. For increasing temperature, the confined ice melts first, followed by the bulk water around 272K. To observe water freezing inside the pores, we increased temperature until all the confined water had melted (i.e. for a temperature between the two peaks) and we then decreased the temperature. The resulting DSC scan is presented on fig.3b : the excess bulk water was still frozen outside the pore network and then, we only observed the freezing of the confined water with "double-peak" shape usually observed for this kind of p^+ sample .
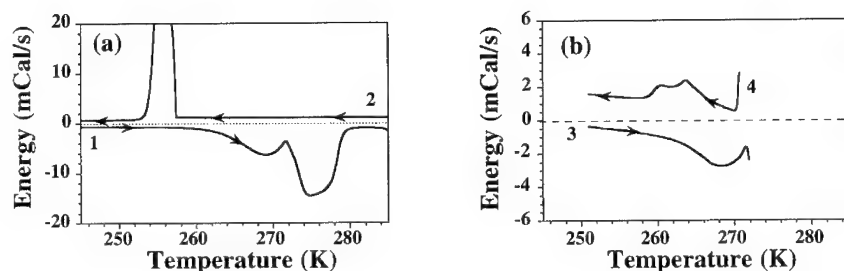
Fig.3 : DSC curves for water and a p$^+$ type PS sample of 60% porosity, thermally oxidized :
(a) for increasing (1) and decreasing temperature (2),
(b) for increasing temperature between the two peaks (3) and then decreasing temperature (4).

CONCLUSIONS

The shift of phase transition of fluids confined in porous silicon (PS) has been clearly observed either as a function of vapour pressure from X-ray determination of adsorpion strains or as a function of temperature from Differential Scanning Calorimetry measurements. Simple thermodynamics considerations give coherent values for the pore radius.

This work can provide a better knowledge of PS material. This is important for the drying of PS, since when the thickness or porosity is too high a cracking is observed [14] . One method to decrease this cracking is for instance the freeze drying technique [15], but as shown by these results, cautions should be considered due to large shifts of the freezing temperature [16].

One can mention the original situation of a single crystal porous structure, in which accurate measurements of strains induced phase transition can be performed. The next step would be to investigate in-situ the induced strains when a solid-liquid transition of the confined fluid occurs : a problem often met for porous material filled with water in nature.

REFERENCES

[1] R. Defay, I. Prigogine, A. Bellemans and D.H. Everett, *Surface tension and adsorption* (Longmans, Green & Co, London, 1966)
[2] P. Buffat and J-P. Borel, Phys. Rev. A13 (1976)
[3] K.M. Unruh, T.E. Huber and C.A. Huber, Phys. Rev. B48, 12, 9021 (1993)
[4] R. Mu and V.M. Malhotra, Phys. Rev. B44, 9, 4296 (1991);
[5] J.F. Quinson J. Dumas and J. Sereghetti, J. of Non-Cryst. Solids 79, 397 (1986)
[6] L.T. Canham, Appl. Phys. Lett. 57, 1046 (1990).
[7] A. Halimaoui, C. Oules, G. Bomchil, A. Bsiesy, F. Gaspard, R. Herino, M. Ligeon and F. Muller, Appl. Phys. Lett. 59, 304 (1991); N. Koshida and H. Koyama, Appl. Phys. Lett. 60, 247 (1991).
[8] *Porous silicon: Material, Technology and Devices*, edited by R. Herino, W. Lang and H. Munder, Thin Solid Films, Vol. 276 (1996).
[9] M.I.J. Beale, N.G. Chew, M.J. Uren, A.G. Cullis and J.D. Benjamin, Appl. Phys. Lett. 46, 86 (1985); R. Herino, G. Bomchil, K. Barla, C. Bertrand and J.L. Ginoux, J. Electrochem. Soc. 134, 1994 (1987).
[10] D. Bellet and G. Dolino, Thin Solid Films 276, 1 (1996);
[11] G. Dolino, D. Bellet and C. Faivre, Phys. Rev.B, to be published (1996).
[12] G.W. Scherer, J. Non-Crystall. Solids 155, 1 (1993)
[13] P.R. Couchman and W.A. Jesser, Nature 269, 481 (1977)
[14] O. Belmont, D. Bellet and Y. Bréchet, J. Appl. Phys. 79, 7586 (1996).
[15] G. Amato and N. Brunetto, Mat. Lett. 26, 295 (1996)
[16] C. Faivre, D. Bellet and G. Dolino, Thin Solid Films, to be published (1997)

TRANSLATIONAL DIFFUSION OF LIQUIDS CONFINED IN NANOPORES

J.-P. KORB*, M. WHALEY**, R. G. BRYANT**
*Laboratoire de Physique de la Matière Condensée, CNRS, Ecole Polytechnique, 91128 Palaiseau, France
**Department of Chemistry, University of Virginia, Charlottesville, VA 22901

ABSTRACT

We present a theory of nuclear spin relaxation and experiments to probe the microdynamics of polar solvents at the surface of calibrated microporous glass beads. The theory is tested using the magnetic field dependence of the proton spin-lattice relaxation rate recorded with a field-switched magnetic relaxation dispersion spectrometer.

INTRODUCTION

Nuclear magnetic relaxation methods offer a variety of opportunities for characterizing the molecular dynamics in confined environments [1-3]. Systems of interest are high surface area materials including biological tissues, chromatographic supports, heterogeneous catalytic materials and natural microporous materials such as clay minerals and rocks.

The magnetic field dependence of the nuclear spin relaxation rate is a rich source of dynamical information [4, 5]. Varying the magnetic field changes the Larmor frequency, and thus, the fluctuations to which the nuclear spin is sensitive. Moreover this method permits a more complete characterization of the dynamics than the usual measurements as a function of temperature at fixed magnetic field strenghts because many common solvent liquids have freezing temperature that may significantly alter the character of the dynamics over the temperature range usually studied. Further, the magnetic field dependence of the spin-lattice relaxation rate $1/T_1$ provides a good test of the theories that relate the measurement to the microdynamical behavior of the liquid. This is especially true in confinement where effects of low dimensionality such as reencounters of spin-bearing molecules occur freequently .

In the present study we are interested in high surface area materials such as microporous glass beads, which contain significant contaminant concentrations of paramagnetic centers (iron ions) that may alter the nature of the relaxation significantly. In particular, the paramagnetic centers provide a large magnetic moment and local dipolar field in which the diffusing liquid spins move. The effects on the nuclear relaxation of the moving spins are large and dominate unambiguously the proton spin-lattice relaxation particularly at low magnetic field strenghts.

Our aim is to describe theoretically as well as experimentally these effects on the proton nuclear spin relaxation rates $1/T_1$, of polar liquid embedded in nanoporous glass beads in presence of Fe(III) paramagnetic impurities fixed at the surface of the pores. The unique properties of the magnet field dependences of these relaxation rates provide a direct measurement of translational diffusion in close proximity of the paramagnetic centers at the pore surface.

THEORY

We consider an ensemble of a large number of nuclear spins I=1/2 (protons) of uniform density which diffuse within an infinite layer of finite thickness d between two flat solid surfaces, in the presence of a constant magnetic field, $\mathbf{B}_0$, oriented at the angle β from the normal axis, $\mathbf{n}$. We consider also the presence of a small quantity of fixed paramagnetic species of spins, S, uniformly distributed on these two solid surfaces with a surface density σ_S. This layered geometry simulates the simplest type of pore, the slit or channel pore, which is sufficient to account for the quasi-two-dimensional characteristics implied by the observed logarithmic magnetic field dependence of the proton spin-lattice relaxation rates in the calibrated porous glass beads (Fig.1).

Due to the large magnetic moment of the paramagnetic species ($\gamma_S = 658.21 \, \gamma_I$), there is no ambiguity about the relaxation mechanism of the diffusing proton spins, I, which is the intermolecular dipolar relaxation process induced by fixed spins S and modulated by the translational diffusion of the mobile spins, I, in close proximity to these surfaces. The nuclear spin-lattice relaxation rate of the diffusing spins, I, is thus given formally by the general expression $1/T_{1I}$ [6]:

$$\frac{1}{T_{1I}} = \frac{2}{3}(\gamma_I \gamma_S \hbar)^2 S(S+1)\left[\frac{1}{3}J_L^{(0)}(\omega_I - \omega_S) + J_L^{(1)}(\omega_I) + 2J_L^{(2)}(\omega_I + \omega_S)\right] \tag{1}$$

where the spectral densities in the laboratory frame J_L (related to $\mathbf{B}_0$) are related to the one in the lamellar frame J_M (related to $\mathbf{n}$) by :

$$J_L^{(m)}(\omega) = \sum_{m'=-2}^{+2}\left|d_{-m,m'}^{(2)}(\beta)\right|^2 J_M^{(m')}(\omega) \tag{2}$$

with the $d_{mm'}$ being the usual Wigner coefficients. Here, the spectral density $J_M^{(m)}$ are the exponential Fourier transform of the pairwise correlation function $G_M^{(m)}$ {$m\in(-2,+2)$} :

$$G_M^{(m)}(\tau) = \left\langle F_M^{-m}(0)F_M^{-m}*(\tau)\right\rangle \tag{3}$$

of the dipolar field $F_M^{(m)} = \sqrt{(6\pi/5)} \, Y_2^m(\rho, z)/(\rho^2+z^2)^{3/2}$ between spins S and I, where the (ρ, z, φ) are the cylindrical coordinates of the interspin I-S vector $\mathbf{r}$, and Y_2^m are the second order spherical harmonics expressed in cylindrical coordinates. The notation <> stands for the ensemble average over all the positions of the spins I at times 0 and τ. This average can be replaced by their usual integral average over the normalized conditional probability P which is the solution of a diffusion equation.

When considering translational diffusion of spin-bearing molecules in this quasi two-dimensional geometry, we have shown for homonuclear dipolar relaxation [2] that the anisotropy of the dynamics is described by an unbounded diffusion perpendicular to the normal axis, $\mathbf{n}$, and a bounded diffusion parallel to this axis. According to this diffusion model, P is defined as a

product of a bounded $P_{//}$ and unbounded $P_\perp$ terms, whose expression are given in Eq. (4) of Ref. [2]. Here we extend our former calculation of this integral average to an heteronuclear dipolar relaxation with one of the spin species (S) fixed on the pore wall.

For a polar liquid in contact with a solid surface, it is known that there are two distinct phases in fast exchange : a surface-affected liquid phase of thickness about a molecular diameter, δ, and a bulk liquid phase. Our earlier NMR studies [1-3] proved the applicability of this biphasic fast exchange model. We now introduce the distance of minimal approach, δ', between spins I and S at the pore surface. Typically, δ' is comparable to the radius of the molecules, $\delta/2$. A typical choice is $\delta'=\delta/(2\,n)$, with n being a parameter of the order of unity. This parameter takes into account a variable distance of minimal approach at the surface between the spin-bearing molecules and does not affect the essential features of our results. In consequence, we have separated the calculations of Eq. (3) in two spatial regions. In the first region, the spin I is restricted to the bulk part of the pore ($\delta' \leq z \leq d-\delta'$; $0 \leq \rho < \infty$) and in the second region the spin I is restricted to the surface layer of the pore ($0 \leq z \leq \delta'$; $\delta' \leq \rho < \infty$). As we are only interested in the nuclear relaxation rates at low frequency, one can focus only on the long-time dependence of $G_M^{(m)}(\tau)$. After some calculations, one finds that, at long times ($\tau \gg \tau_\perp$), the surface contributions dominate the correlation for $G_M^{(0)}(\tau)$, while the bulk contribution dominate the correlation for $G_M^{(1)}(\tau)$ and $G_M^{(2)}(\tau)$:

$$G_M^{(0)}(\tau) \approx \frac{3}{8}\frac{\pi\sigma_S}{d^2\delta'^2}\left(\frac{\tau_\perp}{\tau}\right), \quad G_M^{(1)}(\tau) \approx \frac{1}{4}\frac{\pi\sigma_S}{\delta'^4}\left(\frac{\tau_\perp}{\tau}\right)^2, \quad G_M^{(2)}(\tau) \approx \frac{1}{16}\frac{\pi\sigma_S}{\delta'^4}\left(\frac{\tau_\perp}{\tau}\right)^2. \tag{4}$$

These power-laws show that the persistences of the pairwise dipolar correlations are dominated by the unbounded modes of diffusion parallel to the pore walls. These modes are characterized by a correlation time, $\tau_\perp$, necessary to make a single random molecular jump parallel to the pore wall, $\tau_\perp = \delta^2/(4\,D_{\perp\perp})$. One sees that $G_M^{(0)}(\tau)$ dominates the dipolar correlation at long times. Its slow time decay ($1/\tau$) is coherent with a logarithmic frequency dependence of the spectral density $J_M^{(0)}(\omega)$ at low frequency. Physically this comes from the back and forward motion of the moving spins I in close proximity to the fixed spin S.

We made similar analytic calculations for $J_M^{(m)}(\omega)$ and after a powder average over the angle, β, of the resulting Eqs. (2) and (1) and with $\omega_S = 658.21\,\omega_I$, one obtains a theoretical expression for $1/T_{1I}$ valid at low frequency ($\omega\tau_\perp \ll 1$):

$$\frac{1}{T_{1I}} = \frac{\pi}{15}\sigma_S(\gamma_I\gamma_S\hbar)^2 S(S+1)\frac{\tau_\perp}{d^2\delta'^2}\left\{10\ln\left[\frac{d}{\delta'}+1\right]-31+\frac{1}{4}\left[7\ln\left(1+\omega_S^{-2}\tau_\perp^{-2}\right)+3\ln\left(1+\omega_I^{-2}\tau_\perp^{-2}\right)\right]\right\}.$$
$$\tag{5}$$

The bilogarithmic magnetic field dependence will permit the verification of the uniqueness of the present model. The ratio of 10/3 between the slopes of the linear portions of the semilogarithmic plots shown in Fig. 1 results from the usual coefficients of the required spectral densities in the basic relaxation equation [7]. This factor agrees with the data of Fig.1. Moreover such an analytical expression identifies clearly the influence of the pore size, d, and the diffusion constant, $D_{\perp\perp}$, on the frequency dependence of $1/T_{1I}$. In the next section we apply this model to probe the microdynamics of different polar solvents at the surfaces of microporous systems.

COMPARISON WITH EXPERIMENTAL RESULTS AND DISCUSSION

Proton nuclear magnetic relaxation rates were measured using a home-built instrument that switches current in a copper solenoid that is immersed in liquid nitrogen. Spins are polarized in a field corresponding to a ^{1}H Larmor frequency of 30 MHz, then the field is switched to a field of interest for a variable relaxation period after which the field is switched to a ^{1}H Larmor frequency of 7.25 MHz where the magnetization is detected by a Hahn spin echo. This field switching technique permits measurement of spin-lattice relaxation rates from 0.01 to 30 MHz with nearly constant signal-to-noise ratios. Samples are contained in 10 mm pyrex tubes closed with both a rubber stopper and a screw cap. Temperature was controlled by a Neslab RTE-8 system using perchloroethylene as the cryogeneic fluid.

Controlled pore chromatographic glass was purchased from Sigma Chemical Company with mean pore diameters of 75Å and 159Å and specific area of 140m^2/g and 90.9 m^2/g, respectively. Reagent grade acetone, acetonitrile, N,N-dimethylformamide (DMF) and dimethylsulfoxide (DMSO) were obtained from Mallinkrodt Chemical and J.T. Baker Chemical companies and were used without further purification. Samples were prepared gravimetrically by depositing a known mass of glass beads in a 10 mm pyrex glass sample tube, fitted with a screw cap, then filled with the solvent of interest, and the tube shaken vigorously. The glass beads were permitted to settle, excess solvent removed by pipet, and the total mass recorded. Sample tubes were finally doubly sealed with rubber stoppers and a screw cap.

The magnetic field dependence of the proton spin-lattice relaxation rates are reported in Fig. 1 for fields corresponding to ^{1}H Larmor frequencies from 0.01 MHz to 30 MHz for acetone, acetonitrile, dimethylformamide and dimethyl sulfoxide at 5, 15, 25, 35 and 45°C contained in samples of 75Å and 159Å controlled pore chromatographic glass beads. One observes clearly the bilogarithmic character of these dependences and the ratio between their slopes is indeed 10/3. This proves the validity of our theoretical model. These data dependences have been fitted with Eq. (5). The surface densities σ_S of paramagnetic spins (S=5/2 for Fe) was obtained from from EPR and chemical analysis giving 45 ppm and 36 ppm of Fe(III) in the 75Å and 159Å glasses, respectively. From the specific area and assuming that all the iron is at the pore surface, one finds $\sigma_S = 3.46 \ 10^{11}$ Fe/cm^2 and 4.27 10^{11} Fe/cm^2 for d=75Å and 159Å, respectively. The molecular sizes have been obtained from the molecular modeling program Insight2, which fits the different molecules into spheres with diameters $\delta = 6.12$Å, 6.18Å, 7.50Å and 7.06Å for acetone, acetonitrile, DMF and DMSO, respectively. There are only two free parameters : δ' and $D_{\perp}$. We estimate δ' based on reasonable hydrogen bonding geometries between the polar solvents and the Fe-OH groups present at the pore surface.

The best fits of our experiments obtained with Eq. (5) are displayed in (Fig. 1) as the continuous lines. One finds that δ' is larger than $\delta/2$ for the 75Å glass and smaller than $\delta/2$ for the 159Å. The translational diffusion coefficients $D_{\perp}$ obtained for the different polar solvents are about an order of magnitude smaller than in the bulk and increase with pore size
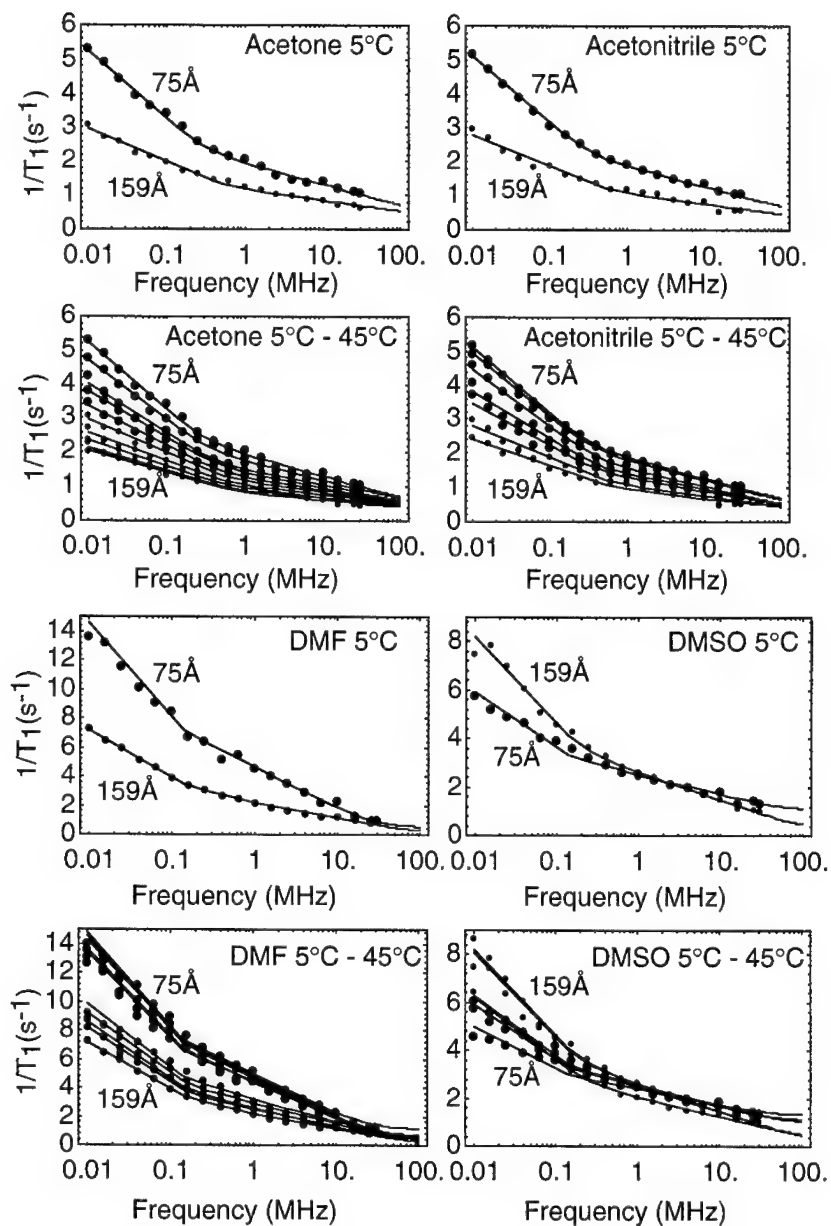
Fig.1 The magnetic field dependencies of proton spin-lattice relaxation rates of four polar solvents embedded in calibrated porous glasses beads at increasing temperatures. The small and large experimental black points correspond to glasses of 75 and 159 Å pore sizes, respectively. The continuous lines correspond to the best fits obtained with Eq. (5). The field strength is shown at the [1]H Larmor frequency.

In Fig. 2, we have plotted these coefficients as a function of the inverse of the molecular size $1/\delta$ for increasing temperatures. The quasi linear variation obtained in each case is consistent with the Stokes law, $D_{I\perp} \propto kT/\delta$, and strongly supports the approach of the model. That these coefficients increase when enlarging the pore size (Fig. 2) is reasonable. Finally we have displayed the temperature dependencies of $D_{I\perp}$ on an Arrhenius plot (Fig. 3). The straight lines observed confirm that the translational diffusion at the surface of the pores is an activation process whose activation energy is about 2 to 3 kcal/mol which seems to decrease when enlarging the pore size.
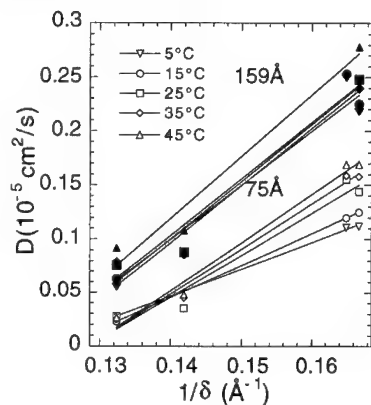
Fig.2 Translational diffusion coefficient $D_{I\perp}$ as function of the inverse of the molecular size δ for increasing temperatures and for glasses of pore sizes 75 and 159Å. $D_{I\perp}$ is found from the fits of Figs. 1 with Eq. (5).
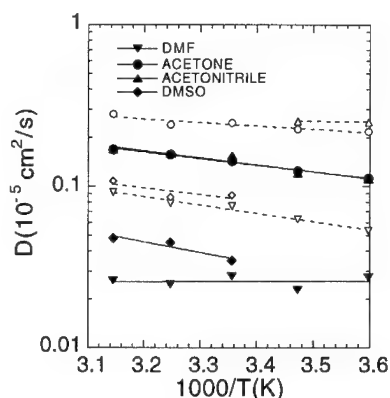
Fig.3 Translational diffusion coefficient $D_{I\perp}$ as function of the inverse of the temperature for different polar molecules. The filled and open experimental points correspond to glasses of pore sizes of 75 and 159Å.

CONCLUSION

A theoretical model of proton nuclear spin relaxation of a polar liquid diffusing at proximity of paramagnetic species fixed at the pore surface allows to interpret the proton dispersion curves of polar solvents embedded in calibrated microporous glass beads. This approach has allowed a direct measurement of the translational diffusion of polar solvent at the surface of the pores.

REFERENCES

1. J.-P. Korb, L. Malier, F. Cros, Shu Xu, and J. Jonas, Phys. Rev. Lett. **77**, 2312 (1996).
2. J.-P. Korb, Shu Xu, and J. Jonas, J. Chem. Phys. **98**, 2411 (1993).
3. J.-P. Korb, A. Delville, Shu Xu, G. Demeulenaere, G. Costa, and J. Jonas, J. Chem. Phys. **101**, 7074 (1994).
4. S. Stapf and R. Kimmich, J. Chem. Phys. 103, 2247 (1995).
5   M. Whaley, A.J. Lawrence, J.-P. Korb, and R. G. Bryant, Solid State Nuclear Magn. Reson., (in press).
6. A. Abragam, "The Principles of Nuclear Magnetism", (Oxford at the Clarendon Press, 1961), Ch VIII.
7. I. Solomon, Phys. Rev. **99**, 559 (1955); N. Bloembergen and L.O. Morgan, J. Chem. Phys. **34**, 842 (1961).

BROAD-BAND DIELECTRIC SPECTROSCOPY OF LIQUID CRYSTALS CONFINED IN RANDOM AND CYLINDRICAL PORES

G.P. SINHA and F.M. ALIEV
Department of Physics and Materials Research Center, PO BOX 23343, University of Puerto Rico, San Juan, PR 00931-3343, USA

ABSTRACT

Using dielectric spectroscopy in the frequency range 0.1 Hz-1.5 GHz, we investigated the influence of confinement on the dynamic properties of polar nematic liquid crystals (LC) dispersed in porous matrices with randomly oriented, interconnected pores as well as in parallel cylindrical pores with different pores sizes. The confinement has a strong influence on the dielectric properties of LC which resulted in the appearance of a low frequency relaxational process ($f \leq 10$ KHz) absent in bulk and a strong modification of modes due to the molecular rotation around short axis and librational motion. The differences between bulk and confined behavior are: (a) - the dielectrically active modes in confined LC are not frozen even at temperatures about 20 degrees below the bulk crystallization temperature; (b) - in the temperature range corresponding to the anisotropic phase in pores, $ln\tau$, where τ is the relaxation time corresponding to the molecular rotation around short axis, is not a linear function of $1/T$ and there is an evidence for smectic type order formation at sufficiently low T; (c) - the retardation factor $g = \tau/\tau_{is}$ is $\simeq 1.5$, where as the typical value of g in bulk nematic liquid crystals is $\simeq 4$; (d) - smooth and small changes in τ at phase transition in pores suggest that the "isotropic" phase of LC in pores is not bulk like isotropic phase with complete disorder in molecular orientations, and some degree of orientation order still persists.

INTRODUCTION

The understanding of new phenomena arising in confined condensed matter is important for the physics of interfaces and finite systems. This has stimulated intensive research of solids, liquids and liquid crystals confined in different geometries. A variety of new properties and phenomena were discovered and studied in these materials.

Although there has been great success in the investigations of the physical properties of confined fluids [1] and liquid crystals [2], there are still open questions in the understanding of the influence of confinement on the dynamical behavior of both ordinary and anisotropic liquids. In this paper we present the results of investigations of the influence of confinement and interface on the dynamic behavior of nematic liquid crystals (LC) dispersed in porous matrices, which have different pore structure, using broad-band dielectric spectroscopy.

Dielectric spectroscopy method contribute significantly to overall characterization of porous materials [3] in general, and investigations of condensed matter confined to porous matrices [4-9] in particular. Applications of dielectric spectroscopy to confined liquid crystals [4,8,9] and glass-forming liquids [5-7] revealed new information on changes in molecular mobility, broadening of the distribution of relaxation times as well as changes in phase and glass transition temperatures.

We have investigated two alkylcyanobiphenyls (pentylcyanobiphenyl - 5CB and octylcyanobiphenyl - 8CB) confined in porous glasses with interconnected randomly oriented pores, and in Anopore membranes with parallel cylindrical pores. Analysis of results obtained for 5CB suggests that there is some evidence for the formation of a smectic phase in 5CB in random pores although bulk 5CB does not have a smectic phase. This smectic type phase could be formed at the pore wall - liquid crystal interface due to surface induced ordering. In order to verify the existence of this surface induced phase we studied 8CB confined in the same porous matrices. We chose 8CB because it has both nematic and smectic phases in the bulk. The dielectric properties of these liquid crystals have been investigated thoroughly

[10-13]. In the dielectric investigations [10-13] of nematic phase of bulk 5CB and 8CB, one relaxational process attributed to the rotation of polar molecules around their short molecular axis with relaxation times $\tau \sim 10^{-8}s$ was clearly observed, and data analysis based on fitting procedure showed that for 8CB there is a second hidden relaxational process at the frequencies $f > 50$ MHz. This process was observed for an orientation of the electric field perpendicular to the director [11-13]. One of the suggested explanations [12] of the origin of this high frequency relaxation was given in terms of librational motion of molecules.

We found that confinement has a strong influence on the dielectric properties of LC which resulted in the appearance of a low frequency relaxational process ($f \leq 10$ KHz) absent in bulk and a strong modification of the modes due to the molecular rotation around short axis and librational motion.

EXPERIMENT

Measurements of the real (ϵ') and the imaginary (ϵ'') parts of the complex dielectric permittivity in the frequency range 0.1 Hz - 3 MHz were carried out at different temperatures using a computer controlled Schlumberger Technologies 1260 Impedance/Gain-Phase Analyzer. For measurements in the frequency range 1MHz - 1.5GHz we used HP 4291A RF Impedance Analyzer with a calibrated HP 16453A Dielectric Material Test Fixture. We used matrices with randomly oriented, interconnected pores (porous glasses with average pore sizes of 100 Å and 1000 Å) and parallel cylindrical pores (Anopore membranes with pore diameters of 200 Å and 2000 Å). The samples were porous glass plates, of dimension $2cm \times 2cm \times 0.1cm$ and Anopore membranes 60 μm thick impregnated with 5CB and 8CB. The temperatures of phase transitions of 5CB in the bulk are T_{CN}=295 K and T_{NI}=308.27 K and for 8CB the bulk phase transition temperatures are: T_{CSm}=294.2 K, T_{SmN}=306.6 K and T_{NI}=313.9 K. Both matrices have practically negligible electrical conductivities, and their dielectric permittivities are independent of temperature and frequency over a wide range of frequencies.

RESULTS AND DISCUSSION

The dielectric behavior of confined LC that we investigated is different from it's bulk behavior. We observe at least three identified relaxational processes: low frequency (1 Hz - 10 KHz), a very clear process in MHz frequency range and the last one in the frequency range $f >$30MHz. In Fig. 1 the low frequency process is illustrated for 5CB dispersed in 100 Å random pores at T = 13.0 °C, which is below the bulk crystallization temperature. We found that at temperatures at least 20 °C below the bulk crystallization temperature the dielectric behavior of confined LC is very different from the behavior expected for solid state: all dielectrically active modes were not frozen. The two other high frequency relaxational processes are shown in Fig. 2. This figure represents frequency dependencies of the real and imaginary parts of the dielectric permittivity as well as the Cole - Cole diagrams for 5CB and 8CB in 1000 Å pores, and 5CB in 200 Å cylindrical pores. We call the process with the relaxation in MHz range as "bulk-like". We believe that this relaxational process with $\tau \sim 10^{-8}s$ corresponds to the rotation of the molecule around the short axis.

The data analysis shows that the best description of the experimental results is provided by the Debye equation for complex permittivity ϵ^*, modified by Cole and Cole [14]. According to Cole and Cole the frequency dependence of complex dielectric permittivity of a system which has more than one relaxational process is described by the equation:

$$\epsilon^* = \epsilon_\infty + \sum_{j=1}(\epsilon_{js} - \epsilon_\infty)/(1 + i2\pi f\tau_j)^{1-\alpha_j} - i\sigma/2\pi\epsilon_0 f^n, \tag{1}$$

where ϵ_∞ is the high-frequency limit of the permittivity, ϵ_{js} the low-frequency limit, τ_j the mean relaxation time, and j the number of the relaxational process. The term $i\sigma/2\pi\epsilon_0 f^n$
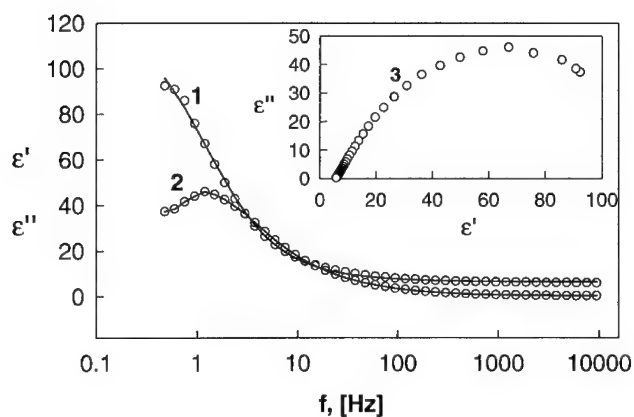
Figure 1: Low frequency relaxation of 5CB in 100 Å random pores, T = 13.0 °C. (1) - ϵ', (2) - ϵ'' and (3) - Cole-Cole plot. Open circles - experimental data, solid lines - fitting.
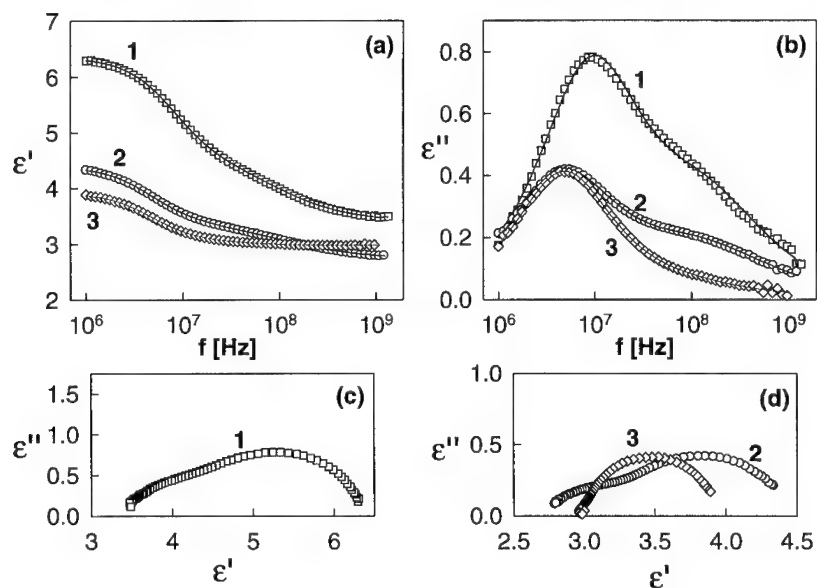
Figure 2: Real (a) and imaginary (b) parts of dielectric permittivity, and Cole-Cole plots (c and d) for 5CB and 8CB in pores. (1) - 5CB in 1000 Å random pores at T = 31.6 °C; (2) - 8CB in 1000 Å random pores at T = 31.6 °C; (3) - 5CB in 200 Å cylindrical pores at T = 22.0 °C. Open symbols - experimental data, solid lines - fitting.

takes into account the contribution of conductivity σ and n is a fitting parameter ($n \simeq 1$). The solid lines in Fig.1 and Fig.2 represent the results of using formula (1) for the description of the observed dielectric spectra. In Fig.1 the parameters describing the low frequency relaxational process are: $\tau = 0.13s$, $\alpha=0.2$. The data analysis shows [8] that the temperature dependence of the relaxation times of the first (slow) relaxational process in both random pores, in the temperature interval (275-295) K for 1000 Å pores and in (275-305) K for 100 Å pores, follow the Vogel-Fulcher law: $\tau = \tau_0 exp(B/(T - T_0))$, and this is a relaxation of interfacial polarization not due to Maxwell-Wagner effect but rather due to a formation of the surface layers with polar ordering on the pore wall.

In Fig. 2 the parameters corresponding to fitting lines are: $\tau_1 = 1.8 \cdot 10^{-8}s$, $\alpha_1=0.06$, $\tau_2 = 1.1 \cdot 10^{-9}s$, $\alpha_2 = 0.2$ for 5CB in 1000 Å pores, $\tau_1 = 3.4 \cdot 10^{-8}s$, $\alpha_1=0.08$, $\tau_2 = 1.3 \cdot 10^{-9}s$, $\alpha_2=0.3$ for 8CB in 1000 Å pores, and $\tau_1 = 3.4 \cdot 10^{-8}s$, $\alpha_1=0.03$, $\tau_2 = 2.0 \cdot 10^{-9}s$, $\alpha_2 = 0.3$ for 5CB in 200 Å pores. The temperature dependence of relaxation times corresponding to the rotation of molecules around short axis for 5CB and 8CB in 1000 Å random pores is presented in Fig. 3. The process with $\tau \sim (10^{-9} - 10^{-10})$s could be related to the librational motion of the molecules. This last process was much more visible in random pores than in cylindrical pores as can be seen in Fig.2.
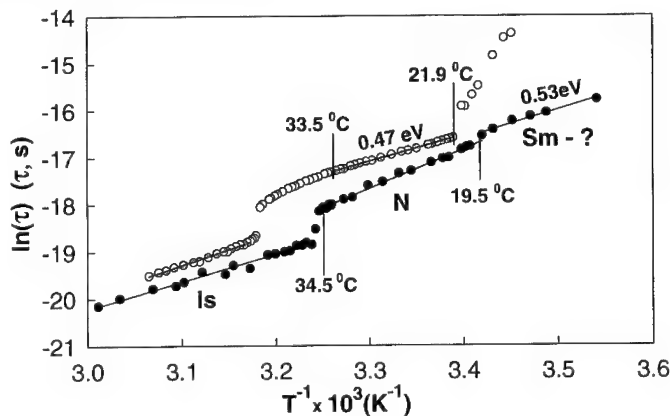
Figure 3: Temperature dependence of relaxation times corresponding to the molecular rotation around short axis for 5CB and 8CB in 1000 Å random pores. Solid circles - 5CB and open circles - 8CB, solid lines correspond to fitting according to Arrhenius formula.

The temperature dependence of these relaxation times corresponding to the molecular rotation around short axis for LC in pores (Fig. 3) is different from the bulk behavior. First of all, for 5CB, in the temperature range corresponding to the anisotropic phase ($T < 34.5°C$) in pores, $ln\tau$, is not a linear function of $1/T$. This means that the temperature dependence cannot be described by Arrhenius formula: $\tau = \tau_0 exp(U/kT)$, where U is the activation energy and k is the Boltzmann constant. However if we consider the temperature regions $34.5°C < T < 20°C$ and $19.5°C < T < 9°C$ separately then $ln\tau = f(1/T)$ in each of these regions is reasonably well approximated by a linear function and the corresponding activation energies are $U_1 = 0.74eV$ and $U_2 = 0.53eV$. The first activation energy U_1 is greater than the activation energy of bulk nematic phase ($U_b = 0.61eV$) but $U_2 < U_b$. We attribute the temperature range $34.5°C < T < 20°C$ to nematic phase. The activation energy in pores in nematic phase is greater because the pore wall imposes additional potential due to pore wall - molecule interaction. This potential is 0.13 eV ($2 \cdot 10^{-13}erg$), and taking into account that number of molecules per unit area is $(2 - 3) \cdot 10^{14}cm^{-2}$ we estimate surface potential of molecule-wall interaction $U_{surf} \sim 50erg/cm^2$. The fact that $U_2 < U_1$ at the temperatures

below 19.5°C is an evidence for the smectic type order formation in this temperature range. This value of the activation energy is very close to the value corresponding to 8CB in the same pores in the temperature range $21.9 < T < 33.5$, which corresponds to the smectic phase. In the whole temperature range corresponding to the anisotropic phase of 8CB in pores the temperature dependence of relaxation times also does not obey Arrhenius formula.

The activation energies of isotropic phase of 5CB in 1000 Å pores is 0.51 eV, and 0.58 eV for 8CB. The relaxation times for 8CB are greater than for 5CB as seen in Fig.3 because 8CB is more viscous than 5CB. We also observe that the changes in relaxation times at nematic-isotropic phase transition in pores are not as sharp as in the bulk, and the relaxation times in pores at the transition do not change as much as in the bulk. The retardation factor $g = \tau/\tau_{is}$ at nematic-isotropic phase transition temperature for both investigated LC in pores is $\simeq 1.8$, where as the corresponding typical value of g for bulk nematic liquid crystals is $\simeq 4$. The temperature dependencies of g for 5CB and 8CB in 1000 Å pores are presented in Fig. 4. The sharp increase in the relaxation times, and correspondingly in g at T<20 °C could be related to the sharp increase in viscosity due to supercooling of LC in pores much below crystallization temperature.
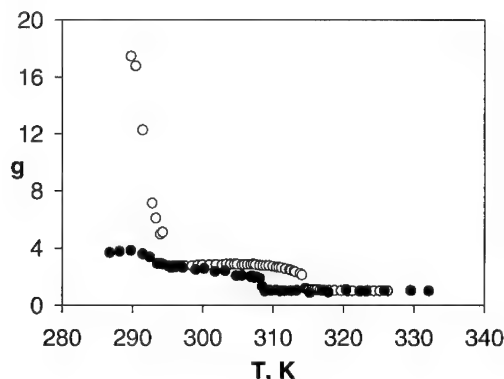
Figure 4: Temperature dependence of retardation factor for 5CB and 8CB in 1000 Å random pores. Solid circles - 5CB and open circles - 8CB.

Relatively smooth and small changes in τ at phase transition in pores suggest that the "isotropic" phase of LC in pores is not bulk like with complete disorder in molecular orientations, and some orientational order still persists.

The relaxational process at the frequencies $f > 50$ MHz was observed [13-15] in alkylcyanobiphenyls for an orientation of the electric field perpendicular to the director. In random pores, there are always molecules oriented perpendicular to the electric field regardless of the molecular alignment inside pores. So we suppose that the mode observed in the frequency range $f > 30$ MHz has the same origin as was found earlier for bulk alkylcyanobiphenyls. The difference is that in our experiments for random pores, as it is clearly seen from Fig. 2, the existence of this mode is obvious even without deep analysis, where as for bulk alkylcyanobiphenyls the conclusion about high frequency relaxation was made [11-13] on the basis of fitting procedure. It is surprising that this process was present in cylindrical pores as well. For the Anopore membrane with cylindrical pores, the applied electric field was parallel to the pore axis. Since at frequencies greater than 1 MHz the process corresponding to the rotation of the molecules around short axis dominates, we conclude that majority of the molecules are oriented along the pore axis. However due to the fact that the high frequency process (at $f > 30$ MHz) is also present, we assume that small fraction of molecules presumably at the pore walls are tilted with respect to the pore axis direction.

CONCLUSION

The spatial confinement has a strong influence on the dielectric properties of LC. Slow relaxational process which does not exist in the bulk phase was observed. The dielectrically active modes were not completely frozen even at temperatures at least 20 °C below the bulk crystallization temperature. The difference between dielectric behavior of 5CB in random pores and in the bulk can be explained by the assumption of the formation of a smectic type ordering on the wall of a pore. This assumption is in agreement with the results obtained for 8CB in smectic phase.

ACKNOWLEDGEMENTS

REFERENCES

1. Molecular Dynamics in Restricted Geometries, ed. by J. Klafter and J.M. Drake (Wiley, New York, 1989).

2. G.P. Crawford and S. Zumer, Liquid crystals in complex geometries, Taylor & Francis, London, 1996).

3. R. Hilfer, Phys. Rev. B **44**, p. 60 (1991).

4. F.M.Aliev, M.N.Breganov, Sov. Phys. JETP **68**, p. 70 (1989).

5. J. Schuller, Yu.B. Mel'nichenko, R. Richert, and E.W. Fischer, Phys. Rev. Lett. **73**, p. 2224 (1994).

6. M. Arndt and F. Kremer in: Dynamics in Small Confining Systems II, edited by J.M. Drake, J. Klafter, R. Kopelman, S.M. Troian, (Mater. Res. Soc. Proc. **363**, Pittsburgh, PA 1995), pp. 259-263.

7. Yu. Mel'nichenko, J. Schuller, R. Richert, B. Ewen and C.-K. Loong, J. Chem. Phys. **103**, p. 2016 (1995).

8. F.M. Aliev and G.P. Sinha in: Electrically based Microstructural Characterization, edited by R.A. Gerhardt, S.R. Taylor, and E.J. Garboczi (Mater. Res. Soc. Proc. **411**, Pittsburgh, PA 1996), pp. 413-418.

9. S.R. Rozanski, R. Stanarius, H. Groothues, and F. Kremer, Liquid Crystals **20**, p. 59 (1996).

10. P.G. Cummins, D.A. Danmur, and D.A. Laidler, MCLC **30**, p. 109 (1975).

11. D.Lippens, J.P.Parneix, and A. Chapoton, J. de Phys. **38**, p. 1465 (1977).

12. J.M. Wacrenier, C. Druon, and D. Lippens, Molec. Phys. **43**, p. 97 (1981).

13. T.K. Bose, R. Chahine, M. Merabet, and J. Thoen, J. de Phys. **45**, p. 11329 (1984).

14. B.K.P. Scaife, Principles of Dielectrics, (Clarendon Press, Oxford, 1989).

DYNAMICS OF SPONTANEOUS SPREADING WITH EVAPORATION FOR THIN SOLVENT FILMS

ANNE D. DUSSAUD and SANDRA M. TROIAN
Department of Chemical Engineering, Princeton University, Princeton NJ 08544-5263

ABSTRACT

We have investigated the spreading behavior of solvent droplets on a bulk water support using solvents with different vapor pressures and spreading coefficients. Instead of seeding the surface with tracer particles, as is usually done to track moving fronts, we employ laser shadowgraphy to visualize the entire surface of the spreading film including the leading edge. For non-volatile systems it has previously been shown that the leading edge advances in time as $t^{3/4}$. We find that volatile systems with positive initial spreading coefficients exhibit two spreading fronts, both of which demonstrate power law growth but with exponents closer to $1/2$. Surprisingly, differences in the liquid vapor pressure or the spreading coefficient seem only to effect the speed of advance but not the value of the exponent. We are presently investigating the behavior of the subsurface flow to determine the mechanism leading to the smaller spreading exponent.

INTRODUCTION

Processes ranging from the casting of membranes from spread films to the advance of oil slicks during the late stages of a spill all require detailed knowledge of the spreading dynamics of solvent films along the surface of a bulk liquid support. Spontaneous spreading is generally ruled by the spreading coefficient, S, first defined by Harkins [1] to be $S = \gamma_1 - \gamma_2 - \gamma_{12}$ where γ_1 denotes the surface tension of the uncontaminated liquid or solid substrate, γ_2 the vapor/liquid surface tension, and γ_{12} the interfacial tension between the spreading film and the liquid or solid support. Spontaneous flow induced by variations in surface tension gives rise to Marangoni flow so-named after Carlo Marangoni, who first realized that the spreading coefficient determines whether a liquid will spread spontanously over a supporting surface (S ≥ 0) or remain in equilibrium with the support by assuming a lenticular shape ($S < 0$) [2]. Much of the work devoted to Marangoni spreading has focused almost exclusively on pure, immiscible and non-volatile surface films. In such cases, a simple scaling analysis proposed by Fay [3] outlines the scaling analysis which determines the location of the advancing front of the spreading film, $L(t)$. Assuming that the spreading film remains coherent from the source of deposition to the leading edge and that the thin spreading film undergo plug flow, a force balance at the film surface, $z = 0$, determines the position of the advancing front for both unidirectional or axisymmetric flow. Fay reasoned that the spreading coefficient reflects the net surface force per unit length, F_S, created by the Marangoni stress at the surface such that $F_S = \int_0^{L(t)} \frac{\partial \gamma}{\partial x} dx = S$. The viscous drag from the sublayer creates a surface shear stress per unit length $F_V = \int_0^{L(t)} \mu [\frac{\partial u}{\partial z}]_{z=0} \, dx$, where the coordinates x and z represent the horizontal and vertical directions, respectively. Estimating this viscous drag to be $\mu \frac{UL}{\delta}$ and substituting from boundary layer theory the surface velocity, $U = L/t$, and the boundary layer thickness $\delta = (\frac{\mu}{\rho} t)^{1/2}$, leads directly to the relation $L(t) = K \frac{S^{1/2}}{(\mu\rho)^{1/4}} t^{3/4}$. The subphase viscosity and density are denoted by μ and ρ. This relation determines the position of the

201

Mat. Res. Soc. Symp. Proc. Vol. 464 ®1997 Materials Research Society

leading edge of a thin surface active film supplied from an infinite reservoir and spreading along a thick liquid support of higher tension under the action of Marangoni forces. Since there has been surprisingly little study of spreading phenomena in the presence of evaporation, we present a systematic experimental study of the spreading kinetics of several volatile but immiscible hydrocarbon films advancing over a bulk water support. We performed these studies to determine whether or not there exists some universal behavior that describes the advance of a spreading film undergoing evaporation. As we show below, there does appear to exist a power law advance with a smaller temporal exponent even for systems experiencing significant mass loss during spreading.

EXPERIMENT

Materials

In order to separate the effects due to the strength of the spreading coefficient and the effects due to vapor pressure of the spreading film, four immiscible solvents with significantly different volatilities and spreading coefficients were chosen to vary the range of spreading behaviors. The four solvents, used as received, were toluene (99.8%, Aldrich), p-xylene(99+, Aldrich), 2,2,4 trimethylpentane (99.9%, Aldrich) and n-heptane (spectrophotometric grade, Mallinckrodt). Pure silicone oil (1000 mPa.s, Fluka) was chosen as the control sample in our studies since previous work has shown that silicone oil spreading on water exhibits model Marangoni spreading with a 3/4 exponent and a coefficient that agrees well with theoretical predictions [4]. The physical and interfacial properties of these spreading fluids are presented in Table I. The supporting liquid was distilled and deionized ultra pure water ($18 M\Omega \cdot cm^{-1}$).

Table I: Physical and interfacial properties of spreading solvents

Spreading liquid	Boiling point (°C)	Vapor pressure (mm Hg) 25° C	S ± 0.2 mN.m^{-1} 23° C
Toluene	110.6	30	8.2
p-Xylene	138.4	8.7	7.4
Trimethylpentane	99.2	49	4.1
Heptane	98.4	45.7	2.3
Silicone oil	-	0	9.4

Visualization Technique

The experiments were performed in a circular glass dish of 16 cm diameter and 8 cm depth fit specifically with an optically flat bottom. The oil spreading over the water surface was visualized by laser shadowgraphy, a method especially well suited to detecting surface deflections in liquid films. The glass cell is illuminated from below by a beam of monochromatic light from a 1 mW He-Ne laser. The beam is expanded by first passing through a spatial filter and then through a collimating lens to provide a uniformly lit area of 9 cm diameter with which to visualize a significant portion of the spreading film. Shadows created from any surface deflections are formed onto a projection screen of ground glass and recorded onto SVHS tapes by a high resolution CCD camera. The video images were analyzed to deduce the temporal advance of any regions of high curvature. The leading edge of the spreading film was detected by the presence of the well-known Thoreau-Reynolds ridge as observed by

McCutchen [5] and Scott [6] who studied in detail the spreading of non-volatile organic films on water. This ridge is produced by the very high surface shear stress at the leading edge of the boundary layer and corresponds to the variable $L(t)$ introduced above.

Procedure

All parts in contact with the liquids were carefully cleaned using solvents and sulfochromic acid and rinsed with copious amounts of distilled water. The cell was filled with ultrapure water to a depth of 3 cm. During the experiment the cell remained completely open to the atmosphere to provide fully unsaturated conditions for the solvent vapor in order to maximize evaporation from the spreading film. A small and precise volume (2-4 μl) of solvent was carefully deposited onto the pure water surface. One droplet was deposited every 40 seconds, a time period during which we determined the solvent film completely evaporates from the water surface, thereby returning the water to its original high surface tension value (see Ref. 7 for more details). Three runs of ten successive depositions were performed for each solvent.

RESULTS

Since laser shadowgraphy has not previously been used to visualize spreading rates of thin films, we tested our apparatus by studying the leading edge of silicone oil spreading on a water film. A typical shadowgraph of the spreading of a silicone oil droplet is shown Fig.1a along with a sketch of the surface profile in Fig.1c. The outside bright ring, denoted by L, is used to track the propagation of the leading edge, $L(t)$, as plotted in Fig. 2. The bright ring in the inner region, denoted by R, corresponds to the periphery of the droplet reservoir that feeds the advancing film. As shown in Fig. 2, the data for $L(t)$ for the silicone oil, which
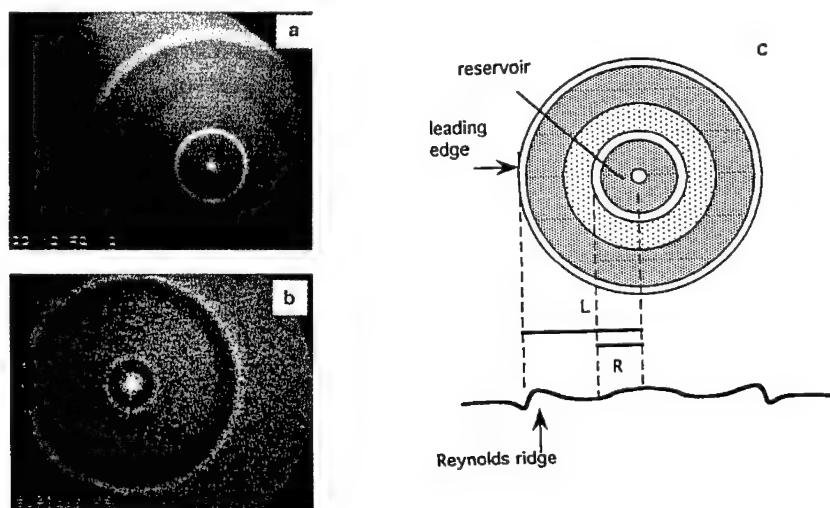

Figure 1 : Typical shadowgraph of the spreading of silicone oil (a) and toluene (b) at t=0.30 s. (c) Sketch of the surface profile corresponding to a shadowgraph.

neither evaporates nor dissolves in water, allows a fit to a power law with an exponent of 0.74, in excellent agreement with the theoretical value of 3/4. We note that these control experiments with silicone oil establish that in spite of the small range of available observation times for the spreading dynamics, the temporal advance of the spreading film is well characterized by the appropriate power law. As shown in Fig. 1b, the surface spreading profiles of the solvent films appear similar to the spreading of silicone oil. We detect, however, two fronts of high curvature corresponding to the leading edge and to the periphery of the droplet reservoir. We have observed that after this initial spreading regime which lasts on order of 1.5 sec, the reservoir edge R stops growing and achieves a plateau in time. At this point the reservoir becomes unstable and undergoes a peculiar dewetting instablity followed by a period of turbulent mixing and retraction [8]. We are presently studying this instability in order to determine the mechanism for film rupture and recession. We have only presented here results from the initial stage of spreading, $t \leq 2$ sec, during which the reservoir is well behaved and stable.

The evolution of $L(t)$ for the solvents toluene, xylene, heptane and trimethylpentane is shown Fig. 2.
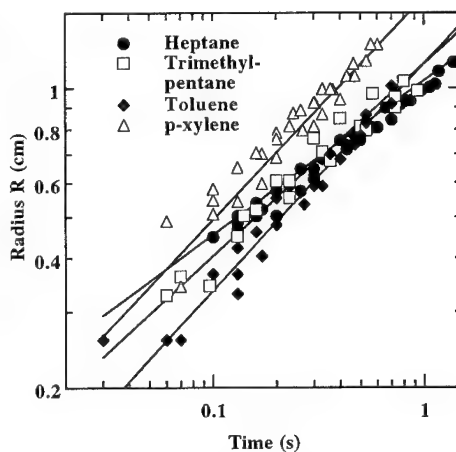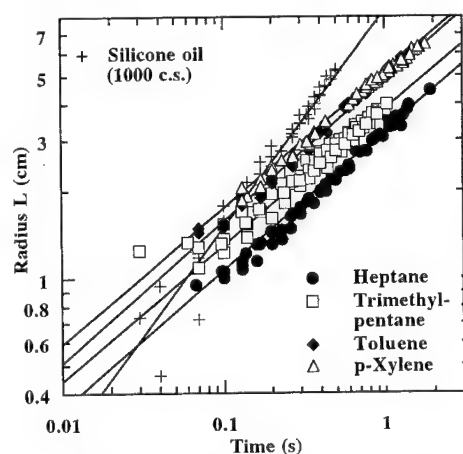
Figure 2: Radius of leading edge $L(t)$ Figure 3: Radius of reservoir edge $R(t)$

Table II shows the results of power law fits to the data with k and α as adjustable parameters. Each entry represents the average over N independent spreading events. The standard deviation for the location of the advancing fronts for each solvent tested is approximately $\pm$ 8% indicating good reproducibility between runs. As seen from the values in Table II, the spreading exponent for the leading edge is approximately 1/2, irrespective of the solvent used. This value is significantly lower than the 3/4 value observed for the spreading of non-volatile and immiscible surface films. To determine the dependence of k on some spreading parameters, we plot in Fig. 4 the value of k vs. the spreading coefficient S. Clearly the speed of propagation of the leading edge increases with S. This suggests that the spreading of the front is driven by Marangoni forces. The experimental values for k seem approximated by the empirical relation $k \simeq S^{0.36}$. Several other volatile solvents with a wider range of spreading coefficients must necessarily be tested to confirm this tendency.

Table II: Results of fitting data to the form $\bar{r} = kt^{\alpha}$. $\bar{r}$ denotes the spreading distance, α the spreading exponent, and k the overall coefficient. N is the number of droplets deposited in total on one surface, and r, the mean value of the linear correlation coefficient.

Solvent	Leading edge L				Reservoir R			
	N	α	k	r	N	α	k	r
Toluene	10	0.49± 0.05	4.86± 0.27	0.9986	20	0.53± 0.05	1.14± 0.10	0.9935
Xylene	10	0.47± 0.02	5.15± 0.16	0.9986	20	0.52± 0.05	1.63± 0.13	0.9904
Trimethyl - pentane	10	0.47± 0.03	3.83± 0.15	0.9972	11	0.45± 0.03	1.14± 0.11	0.9908
Heptane	13	0.48± 0.04	3.22± 0.11	0.9925	13	0.36± 0.02	1.04± 0.07	0.9963

In particular, it remains unclear whether xylene and toluene propagate at the same speed since although their spreading coefficients are very close, their vapor pressures are fairly different. The time evolution of the reservoir periphery $R(t)$ is plotted in Fig. 3. The reservoir spreads 3 to 4 times more slowly than the leading edge. The data were fitted by a power law with an exponent ranging between 0.35 and 0.53. The coefficient for the reservoir periphery k vs. S is not described by a power law in contrast to the behavior of the leading edge shown in Fig. 3. The reservoir spreading seems affected by the volatility of the spreading material. Indeed, the reservoirs of the three solvents, toluene, trimethylpentane and heptane, which have rather similar vapor pressures, spread almost all at the same speed. The reservoir for xylene, which is the least volatile solvent, spreads significantly more rapidly.
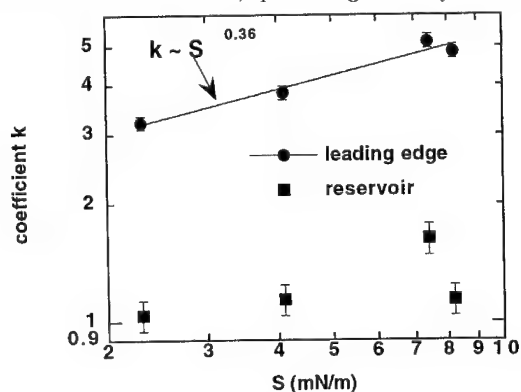

Figure 4: Coefficient k versus the spreading coefficient.

It can easily be shown that if the reservoir spreading is driven by the balance of capillary and viscous forces, then the reservoir advances with an exponent of $3/4(2+\alpha)$ for rectilinear ($\alpha = 1$) or axisymmetric geometry ($\alpha = 2$) [7]. Surprisingly, the velocities as well as the exponents we obtained (0.35-0.53) are all higher than the values typically attained by capillary driven spreading on a thick liquid support indicating the dominant effect of Marangoni forces.

CONCLUSIONS

In lieu of the usual technique of surface tracer particles which can only track an advancing liquid front, we have used laser shadowgraphy to monitor the entire spreading profile of thin immiscible volatile films spreading along the surface of a bulk water support. Because the volatile films have a surface tension lower than that of pure water, the films spread spontaneously and rapidly under the action of Marangoni forces. Using different volatile solvents, we have uncovered that the leading edge exhibits a spreading behavior well characterized by the relation $L(t) = kt^\alpha$ with $\alpha \approx 1/2$, irrespective of the spreading coefficient or vapor pressure of the volatile liquid used. The coefficient k appears to increase with the value of the spreading coefficient S. There also appears power law growth in a second advancing front associated with the reservoir droplet periphery, though the speed of advance in this regime appears controlled by the volatility of the liquid studied. We are presently characterizing a mechanism which may be responsible for the decrease in exponent of the leading edge from 3/4 to approximately 1/2 associated with a subsurface instability created by the significant surface cooling induced by the rapid spreading [7]. There appears to develop a Bénard-like cellular roll under the Thoreau-Reynolds ridge which systematically slows the advance of the spreading film. A discussion of this aspect of the flow as well as some scaling suggestions to determine the 1/2 exponent can be found in the upcoming publication in Ref. 7. We hope these and similar studies can help improve present forecasting models for the areal coverage of a contaminant spill when only Marangoni and viscous forces determine the extent of spreading.

ACKNOWLEDGMENTS

REFERENCES

1. W. D. Harkins in The Physical Chemistry of Surface Films, Reinhold Publishing. Corp., New York (1952).
2. C.G.M. Marangoni, Nuovo Cim. **2**, p. 239, (1872).
3. J.A. Fay in Oil on the sea edited by D. Hoult, Plenum Press, New York (1969).
4. D.W. Camp and J. C. Berg, J. Fluid Mech. **184**, p. 445, (1987).
5. C.W. McCutchen, Science **170**, p. 61, (1970).
6. J. C. Scott, J. Fluid Mech. **116**, p. 283, (1982).
7. A.D. Dussaud and S.M. Troian, submitted to Phys. Fluids.
8. S.M. Troian and J. M. Drake, in preparation.

Molecular dynamics simulations of sliding friction of Langmuir-Blodgett monolayers

Asako Koike, Makoto Yoneya, Yutaka Ito
Hitachi Research Laboratory, Hitachi, Ltd.
7-1-1 Omika, Hitachi, Ibaraki 319-12, Japan

Abstract

Molecular dynamics simulations have been performed to study friction in Langmuir-Blodgett monolayers of perfluorocarboxylic acid, semifluoro acid and hydrocarboxylic acid on SiO_2. The frictional coefficient of perfluorocarboxylic acid is about three times as large as that of hydrocarboxylic acid, while the frictional coefficient of semifluorocarboxylic acid is about two times as large as that of hydrocarboxylic acid. The qualitative aspects of these simulation results are consistent with known experimental results. In order to interpret the difference in the frictional coefficient, a series of simulations have been carried out by changing molecular potential parameters. The simulation results suggest that the 1,4-van der Waals interaction is the main cause of the larger frictional force for perfluorocarboxylic acid than that for hydrocarboxylic acid. Further frictional coefficients of semifluorocarboxylic acid are found to change by the fluorination ratio. The results also show that frictional force is roughly proportional to the excess r.m.s. fluctuation of the potential energy under shear from the equilibrium. The relation between the frictional force and the energy needed for molecular deformation under shear conditions is also discussed.

1. Introduction

Thin organic films are widely used as lubricant molecules to reduce friction between two surfaces. With the development of technological devices, such as magnetic storage devices, demands to develop a low friction, durable and thinner lubricant film are increasing. Therefore, it is necessary to elucidate the tribological mechanism of thin organic films.

Langmuir-Blodgett (LB) films, which are highly ordered, minute films, have been widely used to investigate frictional force and molecular structures by SFA (surface force apparatus) and the SFM (scanning force microscopy). In particular, the frictional coefficient of perfluorocarbons, semifluorocarbons, and hydrocarbons are extensively investigated. For example, Overney and co-workers [1-3] measured the LB film of phase separated mixtures of C_9F_{19} -C_2H_4 -O-C_2H_4COOH and $C_{19}H_{39}COOH$ on an Si surface. Although the frictional force was sensitive to film conditions such as pH, the friction on fluorocarbon areas was about three or four times as large as on carbon areas. Briscoe and Evans[4] measured the friction of LB films of carboxylic acids (C14-C22) and $C_7F_{15}C_{10}H_{20}COOH$ by SFA and found that the frictional force divided by the real contact area on partially fluorinated carboxylic acids was about five times as large as that of carboxylic acids. Other experiments[5-6] also showed that the frictional coefficients of perfluorocarboxylic acids and semifluorocarboxylic acids were larger than those of carboxylic acids. Judging from the above experimental results, as far as LB film are concerned, the frictional coefficients of the fluorocarbons are higher than those of carbons, although perfluoro polymers are widely used as lubricants. However, the cause of the difference in the frictional coefficients and the relationships between the frictional coefficients and the molecular structures are not well understood. In this study, we have performed molecular dynamics simulations of LB films of carboxylic, semifluorocarboxylic, and perfluoro carboxylic acids in order to understand the frictional mechanism of LB films and to clarify the causes for the difference in the sliding frictional force on fluorocarboxylic and carboxylic acids.

2. Molecular Model and Simulation Methods
2.1. Molecular model

We employed the CVFF (Consistent Valence Force Field) [7] and the parameters used are summarized in the previous paper [8]. A quartz-type SiO_2 (0 0 1) surface was used as base and slider surfaces and SiO2 surfaces were simulated as rigid two layers. Simulated monolayers were composed of 36 chains of each kind of molecule adsorbed on the SiO_2 surface.

The areas per molecule of $C_{14}F_{29}COOH$, $C_8F_{17}C_{10}H_{20}COOH$, and $C_{14}H_{29}COOH$ monolayers were $0.265nm^2$, $0.310nm^2$, and $0.221nm^2$, respectively. These areas per molecule correspond to those at 20-40mN/m experimental surface pressures. [5,9] In the close packed condition which we considered in the simulations, there are almost no gauche defects in any of molecular films. [10] Thus all initial configurations of the molecules were set to be *trans*.

2.2 Simulation procedure

The simulations were carried out in three steps. First the monolayer films were equilibrated for 50ps. Next the sliders were compressed in the < 0 0 1 > direction at a constant velocity of 0.1nm/ps from 1.0nm above the film. Finally the sliders were moved in the < 0 1 0 > direction at a constant velocity of 0.1nm/ps under a constant load of 6.0nN for 4.0nm (40ps) as shown in Fig. 1. The load was calculated as a sum of the normal forces to the slider surface.

A leapfrog algorithm was used to integrate Newton's equations of motion. In the equilibrium step, we used a time step of 0.5fs and in the compression and sliding steps, 0.4fs. The average temperature was maintained at 300K by use of a

Fig. 1. Initial configuration showing the compressing and sliding directions.

weak coupling to an external bath, i.e., Berendsen's thermostat. The initial velocities of each atom were sampled from Maxwell-Boltzmann distributions. Periodic boundaries were imposed in the in-plane direction. The cut-off length of the non-bonding interaction was set at 0.9nm. The particle positions were stored every 125 time steps and then analyzed.

3. Results and Discussions
3.1 Frictional force difference between carboxylic acid and fluorocarboxylic acids

The frictional force was stabilized within 10-15ps in every system. Thus the trajectory for 20-40ps was used for the analysis.

The average frictional forces of $C_{14}F_{29}COOH$, $C_8F_{17}C_{10}H_{20}COOH$, and $C_{14}H_{29}COOH$, are 2.07nN(frictional coefficient is 0.345), 1.56nN(0.26), and 0.659nN(0.11), respectively in the simulations. The frictional force is the total lateral force needed for the slider to move at a constant velocity. The frictional coefficient of $C_{14}F_{29}COOH$ is about three times as large as that of $C_{14}H_{29}COOH$, while the frictional coefficient of $C_8F_{17}C_{10}H_{20}COOH$ is about two times as large as that of $C_{14}H_{29}COOH$. The frictional coefficient of hydrocarbons is about 0.1 and that of fluorocarbons is about 0.4 in the SFM experiment [3]. The frictional coefficients of perfluorocarbons, semifluorocarbons, and hydrocarbons by the repeating sliding apparatus are 0.16, 0.13, and 0.06, respectively [5]. Although the slider and the sliding velocity differ between the experiments and the simulations, the simulated results qualitatively correspond to experimental results.

The differences in the frictional coefficients between fluorocarbons and hydrocarbons have been experimentally discussed from various viewpoints, such as cohesive energies between the slider and LB film, elasticity of the film, and molecular stiffness [1,2,4]. However the causes of the differences have remained elusive. The cohesive energies between the slider and LB film in carbons and perfluorocarbons are -396kJ/mol and -459kJ/mol, respectively, and those between the base and LB film are -718kJ/mol and -611kJ/mol, respectively, in these simulations. The cohesive energies difference is too small to be the main reason, at least in this simulations. Therefore, a difference in the molecular stiffness, such as due to differences of the torsion potential barrier and the bond angle bending barrier, or a difference in the inter-molecular interaction of each molecule are probable causes for the differences in the frictional coefficients.

3.2 Relation between frictional force and molecular stiffness

We have carried out three types of virtual model molecules to investigate the relation between molecular stiffness and frictional force. The changed parameters of the models are as follows:
1) Model molecule HstiffF; the torsion and bond angle potential parameters of carbons were changed so as to reproduce the torsion and bond angle potential surfaces of fluorocarbons. In detail, the term $12.0\cos\theta$ (kJ/mol) was added to the torsion potential parameter and the angle potential parameters were replaced by those of fluorocarbons. That is to say, the carbon molecules were stiffened as highly as fluorocarbons molecules.
2) Model molecule FstiffH; the L-J, coulomb, and angle potentials of the fluorocarbons were changed to give the torsion and bond angle potential surfaces of carbons. In detail, carbon angle bending parameters were used instead of those of fluorocarbons. The L-J and Coulomb parameters of only the 1-4 interactions were 0.13 and 0.08 times the original ones, respectively. Namely the stiffness of the fluorocarbon molecules was lowered to that of the carbon molecules.
3) Model molecule Fstiff/t; the L-J potential parameters of only 1-4 interactions were made 0.13 times the original ones. Namely, only the torsion potential barriers were lowered.

Since no large conformational changes of the films were induced by the changing the parameters, it is reasonable to compare the results. Table 1 summarizes the frictional forces of the above models averaged for 20-40ps. Comparing the average frictional force of the model FstiffH with that of the original fluorocarboxylic acid shows that the frictional force is lowered by lowering the stiffness of the molecules. On the other hand, comparing the frictional force average of the model HstiffF with that of the original carboxylic acid shows that the frictional force is lowered by increasing the stiffness of the molecules. From these results, it is impossible to interpret the largeness of the frictional force only from the viewpoint of molecular stiffness. The rest probable reason for the frictional coefficient difference as mentioned above is the intra-molecular interaction of the films. However, the film structure is largely changed by changing the parameters of the intra-molecular interaction. Accordingly, attention was turned to the root mean square (r.m.s.) fluctuations of potential energy based on the following idea. The frictional work (frictional energy) derived from the frictional force is converted into thermal energy after being saved once as potential energy. Thus the excess potential energy fluctuation under the shear condition, as compared to the equilibrium condition, is expected to have some correlation with frictional force.

Table 1 The averaged frictional force of each molecule.

molecule type	average of the frictional force(nN)	molecular type	average of the frictional force(nN)
$C_{14}H_{29}COOH$	0.659	$C_{14}F_{29}COOH$	2.07
HstiffF	0.427	FstiffH	0.813
		Fstiff/t	0.887

3.3 Relation between r.m.s. fluctuations of the potential energy and frictional force

Fig. 2 shows the relation between average frictional force and r.m.s. fluctuations of potential energy difference between shear and equilibrium conditions. In the simulations of the equilibrium conditions, the slider was kept at a constant load of 6.0nN for 40ps without sliding. In order to investigate the influence of the frequency of potential energy dissipation, the r.m.s. fluctuations of the total potential energy of the system are calculated in two ways. The open circles in Fig. 2 were calculated to take account of lower frequencies as follows. The r.m.s. fluctuations of potential energy were calculated for 20-40ps. Hereinafter the r.m.s. fluctuations of the potential energy of the equilibrium condition are referred to as

Fig. 2. The relation between the frictional force and the averaged r.m.s. fluctuations of total potential energy difference $< \Delta E >$ between shear and equilibrium conditions.

$< E_E >$ and those of the sliding condition as $< E_S >$. Further, the value of the equilibrium condition was taken as thermal fluctuation minus that of the shear condition; that is, the open circles represent $< E_S > - < E_E >$. The filled circles were calculated to reduce the influence of low frequencies as follows. The r.m.s. fluctuations of the potential energy for 20-40ps were calculated at an interval of 0.5ps and then averaged. Hereinafter, the averaged value of the equilibrium condition is referred to as $< E_{SE} >$ and that of the sliding condition as $< E_{SS} >$. The filled circles represent $< E_{SS} > - < E_{SE} >$. Fig. 2 indicates that the frictional force is roughly proportional to $< E_{SS} > - < E_{SE} >$ and $< E_S > - < E_E >$. This indicates that the frictional energy dissipates as thermal energy after being saved once as potential energy.

Since the potential energy contains the film potential energy and the nonbonding interaction energy between the slider and the film, we can put the above proportional relation in other words; that is, the frictional energy represents how much energy is necessary for deformation of the film and for the slider to overcome the local maximum of interfacial interaction between the film and slider when the slider moves. Therefore, the energy term which has the largest fluctuation under the shear condition as excess over the thermal fluctuation is expected to be the main cause for the

frictional force. Fig. 3 shows the averaged r.m.s. fluctuations of each energy difference between the shear and equilibrium conditions calculated so as to reduce the influence of the low frequencies. Fig. 3 shows that the r.m.s. fluctuations of the nonbonding interaction energy between the slider and the film represented by interfacial interaction are not very large compared to the other r.m.s. fluctuations of the film. Thus, interfacial interaction
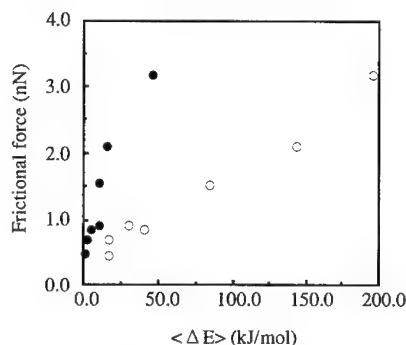

Fig. 3. The averaged r.m.s. fluctuations of each potential energy difference $< \Delta E >$ between shear and equilibrated conditions.

is not expected to correlate with the frictional force in these simulations.

Fig. 3 shows that in all energy terms in the film, except the torsion angle term, the r.m.s. fluctuations of energy of perfluorocarboxylic acids are larger than those of carboxylic acids, which indicates that the fluctuation of the potential energies of perfluorocarboxylic acid is mainly dominated by the Lennard-Jones (L-J) term. Furthermore, because the average of the r.m.s. fluctuations of the intra-molecular L-J energies difference is 30.0kJ/mol and that of the inter-molecular L-J energies difference is 15.0kJ/mol, it is concluded that the fluctuation of the L-J energy of the perfluorocarboxylic acid is dominated by intra-molecular interaction. Considering the fluctuation of the intra-molecular L-J term is almost completely caused by those of the 1,4-nonbonding interactions, it is expected that the main cause of the high frictional coefficient of the perfluorocarboxylic acids is the L-J of the 1,4-nonbonding atoms interaction. Certainly the frictional coefficient of Fstiff/t, in which only the L-J interactions of 1,4-nonbonding atoms are lowered, is significantly lower than that of the original perfluorocarboxylic acids. Thus it is concluded that the main reason for the high frictional coefficient of the perfluorocarboxylic acids is 1,4-L-J(van der Waals) interaction.

3.4 Relation between frictional force and fluorination ratio

As discussed above, the frictional coefficients of the perfluoro carbons are higher than those of hydrocarbons in LB films. However, from the viewpoint of low reactivity and good hydrophobic properties, perfluorocarbons are good for lubricants. Next, we investigated the influence of the partial fluorination of hydrocarboxylic acid on the frictional coefficient.

The molecules of LB films used are $C_{18}F_{37}COOH$(the are per molecule is $0.31nm^2$), $C_{12}F_{25}C_6H_{12}COOH$($0.31nm^2$), $C_8F_{17}C_{10}H_{20}COOH$($0.31nm^2$), $C_5F_{11}C_{13}H_{26}COOH$($0.31nm^2$), $C_3F_7C_{15}H_{30}COOH$($0.265nm^2$), and $C_{18}H_{37}COOH$($0.221nm^2$), which were simulated similarly.

The frictional coefficients of the molecules are in the same order: 0.31, 0.31, 0.26, 0.26, 0.18, and 0.12, respectively. The proportional relation between frictional force and potential energy fluctuations as seen in Fig. 2 are observed. In order to get further insight into the difference in frictional coefficients, r.m.s. fluctuations of each potential energy difference between shear and equilibrium conditions were investigated, as shown in Fig. 4. These were calculated in the same manner as in Fig. 3.

Fig. 4 shows that the largeness of the fluctuations of $C_{18}F_{37}COOH$ and $C_{12}F_{25}C_6H_{12}COOH$ are comparatively similar. On the other hand, the fluctuations of each energy in $C_8F_{17}C_{10}H_{20}COOH$ are significantly small when these are compared with those of $C_{12}F_{25}C_6H_{12}COOH$. Since the van der Waals radius of the hydrogen atom is smaller than that of the fluorine atom and it is easy for softer parts, i.e. hydrocarbons, to move due to the mixture of two kinds of molecular stiffness parts (fluorocarbons and hydrocarbons), it becomes easy for the hydrocarbons to move a lot. Thus the coordinate fluctuations and energy fluctuations of the hydrogen parts in semifluorocarboxylic acids are larger than those of hydrocarboxylic acid. Accordingly, we expect
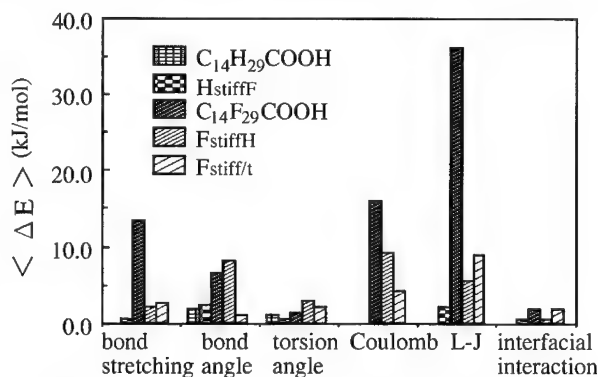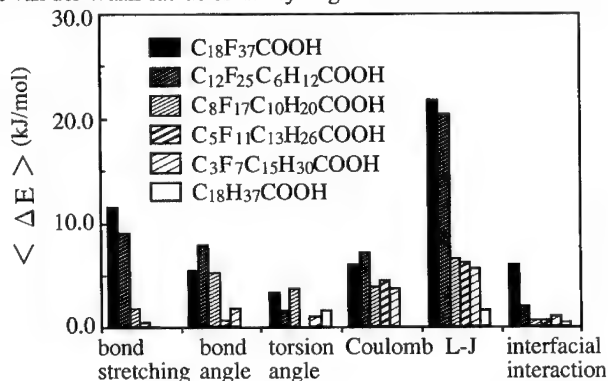

Fig. 4. The averaged r.m.s. fluctuations of each potential energy difference $< \Delta E >$ between shear and equilibrated conditions.

that for $C_{12}F_{25}C_6H_{12}COOH$, the effect in the decrease in the energy fluctuations due to a replacement of fluorine atoms by hydrogen atoms is almost the same as the effect of increasing the energy fluctuation of the hydrogen parts. On the other hand, in semifluorocarboxylic acids except $C_{12}F_{25}C_6H_{12}COOH$, because the hydrogen parts are long enough, the effect of replacing fluorine atoms by hydrogen atoms is larger than the effect of increasing the energy fluctuations of the hydrogen parts.

Fig. 4 also shows that the differences in the fluctuations between $C_8F_{17}C_{10}H_{20}COOH$, $C_5F_{11}C_{13}H_{26}COOH$ and $C_3F_7C_{15}H_{30}COOH$ are small. This may be caused by the fact that the film deformation, which causes the large potential energy fluctuations, occurred mainly in the film surface. In addition, the differences in each energy fluctuation for $C_5F_{11}C_{13}H_{26}COOH$ and $C_3F_7C_{15}H_{30}COOH$ are small, although the frictional coefficient of the $C_3F_7C_{15}H_{30}COOH$ is smaller than that of $C_5F_{11}C_{13}H_{26}COOH$. This is believed to be caused by the fact that the energy needed for the slider to move is not large enough to clarify the difference in the energy fluctuations in the two molecules. If we simulated these molecules by heavier load in a similar manner, the energy needed for the slider to move would increase and the differences between the two molecules would be clear.

Conclusions

Molecular dynamics simulations were performed to understand the frictional mechanisms of the Langmuir-Blodegtt (LB) films and the causes of the frictional coefficient differences between perfluorocarboxylic acid and hydrocarboxylic acid. The simulation results, that is, that the frictional coefficient of perfluorocarboxylic acid was about three times as large as that of hydrocarboxylic acid while the frictional coefficient of semifluorocarboxylic acid was about two times as large as that of hydrocarboxylic acid, qualitatively corresponded to the experimental results. The results indicated that the frictional force difference between perfluorocarbons and hydrocarbons was mainly caused by the difference of 1,4-van der Waals interaction and that the frictional force was roughly proportional to the difference of potential energy fluctuation between the shear and equilibrium conditions. Further, from the proportional relations, we conclude that the frictional energy represents how large energy is required for deformation of the film and for the slider to overcome the local maximum of interfacial interaction between the film and slider when the slider moves. By modeling the molecules so as to decrease this required energy for the films and the slider, we can achieve low frictional films.

References

1) R. M. Overney, E. Meyer, J. Frommer, D. Brodbeck, R. Lüthi, L. Howald, H.-J. Güntherodt, M. Fujihira, H. Takano and Y. Gotoh, Nature, **359**, 133 (1992).

2) R. M. Overney, E. Meyer, J. Frommer, H.-J. Güntherodt, M. Fujihira, H. Takano and Y. Gotoh, Langmuir, **10**, 1281 (1994).

3) E. Meyer , R. Overney, R. Lüthi, D. Brodbeck, L. Howald, J. Frommer, H.-J. Güntherodt , O.Wolter, M. Fujihira, H. Takano, and Y. Gotoh, Thin Solid Films, **220**, 132 (1992).

4) B. J. Briscoe and D. C. Evans, Proc. R. Soc. Londn. A **380**, 389 (1982).

5) T. Kato and M. Kameyama , private communications.

6) O. Levine and W. A. Zisman, J. Phys. Chem. **61**, 1188 (1957).

7) P. Dauber-Osguthorpe, V. A. Roberts, D. J. Osguthorpe, J. Wolff, M. Genest, A. T. Hagler, Protein:Structure, Function and Genetics, **4**, 31 (1988).

8) A. Koike and M. Yoneya, J. Chem. Phys. **105**, 6060 (1996).

9) S. W. Barton, A. Goudot, O. Bouloussa, F. Rondelez, B. Lin, F. Novak, A. Acero, and S. A. Rice, J. Chem. Phys., **96**, 1343(1992).

10) S. Shin, N. Collazo, and S. A. Rice, J. Chem. Phys. **96**, 1352 (1992).

11) O. Levine and W. A. Zisman, J. Phys. Chem. **61**, 1188 (1957).

STM INVESTIGATIONS OF CONFINED TRANSITION METAL CHALCOGENIDE COLLOIDAL PARTICLES

F. KIVUITU and S. P. KELTY*
Department of Chemistry, Seton Hall University, South Orange NJ 07079

ABSTRACT

The chemical reactivity of catalytic surfaces often arises from a unique crystal or electronic structure confined to the first few atomic layers. Scanning Tunneling Microscopy (STM) is particularly well suited to studying the spatially confined structural properties of such systems. In this paper, I report recent advances in the characterization of colloidal layered transition metal chalcogenides using STM. These particles mimic the surface (layer edge) properties of bulk catalytic materials. It is found that the materials adopt distinct equilibrium chemical and electronic structures as compared to the bulk. The possible significance of these novel structures in regard to the bulk catalytic functionality of the parent material will be briefly discussed.

INTRODUCTION

A great deal of interest has been generated in the preparation and characterization of colloidal semiconducting particles driven by the unique optical and electronic properties of these nano-engineered materials. The layered transition metal chalcogenides (LTMC) MoS_2 and WS_2 exhibit a wide variety of structure types including disordered and inorganic fullerene nanostructures.[1-10] A particularly interesting and novel polytypic LTMC is nano-structured MoS_2 consisting of platelets less than 100 nm in diameter. Recent optical studies of these materials indicate size dependent quantum confinement.[3,11] Rubtsova, et al., observed size dependent exciton localization energies in nano-structured MoS_2 but were unable to unambiguously establish whether this size quantization was associated with the basal plane (x-y) or to the stacking dimension (z). Using the effective mass approximation, they observed quantum confinement in particles of several nm in overall size.[3] Starting from size-fractionated MoS_2 nano-particles, Wilcoxon and Samara investigated optical properties of <4.5 nm and >2.5 nm-sized MoS_2.[11] The excitonic structure of <4.5 nm particles was also found to exhibit a size dependent blue-shift from bulk-derived exciton structure. Significantly, the excitonic structure in the smaller >2.5 nm particles could not be directly correlated with further size dependent blue shifts of the bulk exciton. These results indicate an alternate crystal structure in particles smaller than 2.5 nm with a unique excitonic structure. The observations are constant with the Bohr radius of the MoS_2 bulk exciton being ca. 2.0 nm and that particles larger 3 or 4 nm are larger than the exciton.[12, 13] Wilcoxon and Samara have argued that the "cut-off" size from bulk to molecule-like electronic properties is determined by the exciton Bohr radius in nanocluster MoS_2.[9,10]

The interpretation of the above optical studies would benefit greatly from a direct determination of the local structural properties of the nanoparticles. Scanning Tunneling Microscopy (STM), being inherently sensitive to local structural details which may profoundly influence the electronic properties, is ideally suited for investigating MoS2 nanoparticles. Consequently, an STM study was undertaken to characterize local edge and near-edge properties of MoS_2 nanoparticles.

MoS$_2$ crystallizes in the P6$_3$/mmc space group consisting of two layers per unit cell (Figure 1). The layers are composed of hcp molybdenum layers sandwiched between trigonal prismatic coordinated sulfur layers. Adjacent S-Mo-S layers are bound by van der Waals forces. The bulk lattice parameters are $a = b = 3.16$ Å, $c = 12.29$ Å (two layers) and $\gamma = 120°$. MoS$_2$ is a semiconductor with a 1.97 eV indirect band gap.[14] The bulk valance and conduction bands are dominated by the Mo d electron density with minor contributions from the sulfur s and p atomic orbitals.[15]
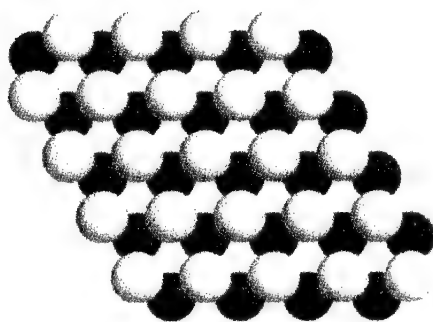
Figure 1. MoS$_2$ basal plane showing top sulfur (light) and Mo (dark) layers.

EXPERIMENTAL DETAILS

Nanoparticles of MoS$_2$ were prepared by ultrasonication of bulk MoS$_2$ single crystals in N-methylformamide.[16] A flake (approximately .5 x .5 x .01 cm) of natural MoS$_2$ was placed in a vessel containing HCONHCH$_3$ and ultrasonicated for 24-30 hours until a stable suspension was prepared. Colloidal suspensions made by this techniques have been shown to be stable for many months.[16] Larger particles were removed with centrifugation. 10-20 μL of this colloidal suspension was deposited onto a clean HOPG graphite surface after which the HCONHCH$_3$ solvent was evaporated. All STM and AFM images were obtained using commercial scanning probe microscopes (either Digital Instruments Nanoscope II or Park Scientific Instruments Model CP) under ambient air conditions at room temperature. Mechanically-sharpened Pt-Ir (80:20) tips were used for STM, and Au-coated Si$_3$N$_4$ probes were used for AFM. Atomic-scale images were recorded in the height and current imaging modes for STM, and in the height and force imaging modes. The images presented in this paper are typical of numerous images taken over a several month period. Some image analysis was performed using the public domain image analysis programs NIH Image (U.S. National Institutes of Health) and UTHSCSA ImageTool (University of Texas Health Science Center at San Antonio, Texas).

RESULTS AND DISCUSSION

Bulk MoS$_2$ has been previously characterized using STM and AFM.[17,18] When the tip-surface interaction is negligible (for a large tip-to-surface distance, r_0), STM images in the constant height mode are proportional to the partial electron density $\rho(r_0, e_f)$ of the sample surface.[19, 20] Despite the large contribution of d-electron density to the valence and conduction bands, STM images of LTMCs are dominated by atomic state density of the top chalcogenide layers and are essentially images of that layer.[21-23] Contact-AFM images of LTMCs, have also been successfully modeled as topographs of the total electron density, $\rho(r_0)$, of the surface. In the present work, preliminary STM and AFM investigations of colloidal MoS$_2$ nanoparticles are reported.

The top-most layer in bulk MoS_2 is composed of a flat hcp sulfur atom sheet with 3.2 Å S-S separation. Shown in Figure 2 is a typical STM image of bulk MoS_2 which is characterized by the typical 3.2 Å interatomic separation expected for this material.

Graphite is a convenient substrate for the nanoparticles as it is an inert semimetallic surface exhibiting large micron size atomically flat regions. Graphite also provides an internal distance calibration standard (C-C distance = 2.46 Å). Figure 3 shows a typical low resolution AFM image of dried MoS_2 colloid. It is evident that the particles do not, in general, self-assimilate and remain monodisperse when deposited on the substrate. The particles vary in size from a few nm to a few hundred nm. The overall shape did not appear to exhibit "magic number" size distributions in this size regime.

High resolution images of the nanoparticles were more easily obtained using STM. Typical gap resistances used during STM imaging were approximately 200MΩ. This allowed detailed studies of the particles while simultaneously imaging the substrate for length calibration. In Figure 4 is shown an STM image of the near edge region of a single MoS_2 crystallite of total size 30-40 nm. The height of this particle above the graphite substrate (approximately 6-9 Å) indicated that it is a single layer thick. Toward the right of the image is the bulk of the crystallite and the

Figure 2. STM image of bulk MoS_2 basal plane.
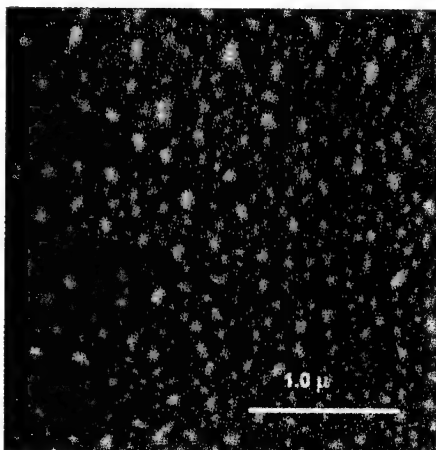
Figure 3. AFM image of MoS_2 colloidal particles.

edge is seen at the left. In the bulk area, the normal 3.2 Å period hcp sulfur lattice is observed similar to that seen in Figure 2. Toward the left of the image, near the particle edge the 3.2 Å hcp lattice normally observed in this material undergoes a perturbation typified by the formation of a superstructure which increases in amplitude with decreasing proximity to the edge. A number of local super-periodicities can be discerned although the most common appears to be a $(\sqrt{3} \times \sqrt{3})R30°$. This new structure does nor appear to involve loss of sulfur atoms. It is suspected that certain of the LTMCs might undergo sulfur loss near the edge. The new superstructure appears to extend about 30-40 Å into the particle. It is well known that corrugation heights measured in STM may not be reliable on an absolute scale due to an
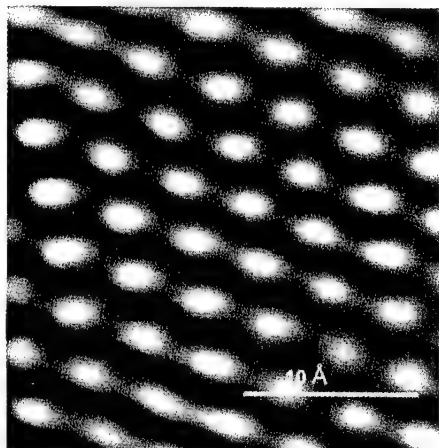
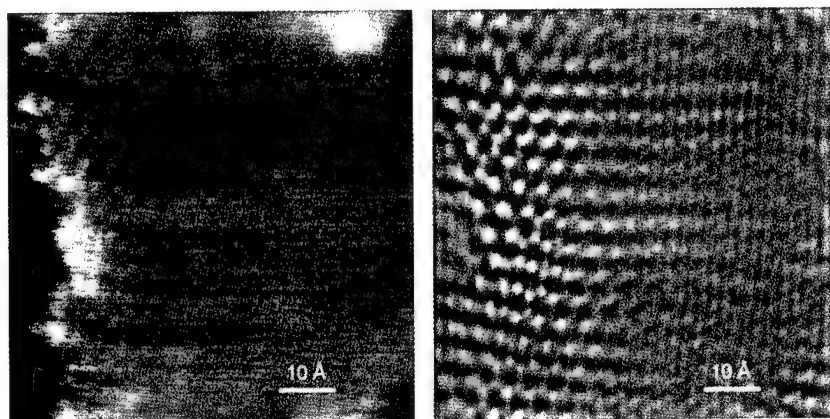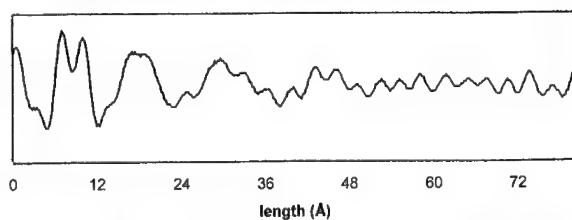Figure 4. Raw and 2DFFT filtered STM image of MoS₂ nanoparticle.

Figure 5. Height corrugation crossection from Fig 4.
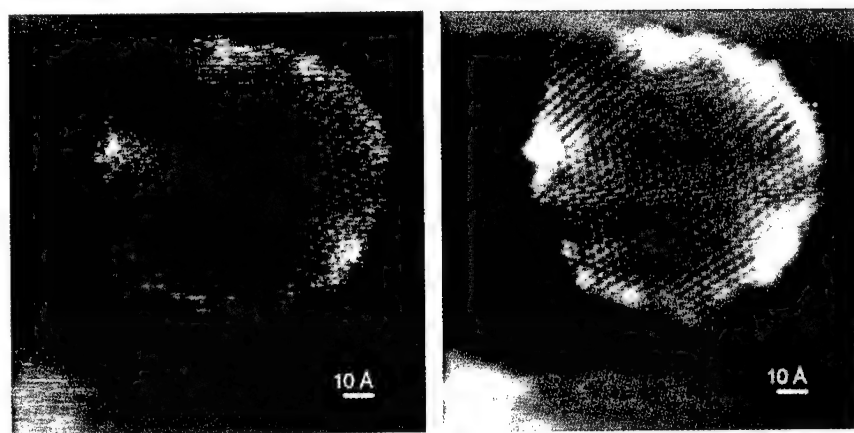

Figure 6. Raw and 2DFFT filtered STM image of MoS₂ nanoparticle.

inherently irreproducible tip morphology, but variations in relative height can be used to indicate local variations in electronic or crystal structures. In this sample, the height corrugation was found to increase by about a factor of 5-6 from the right of the image (bulk side) showing the typical 3.2 Å corrugation to the left (edge side).(Figure 5) The details of this superstructure are currently under investigation. Figure 6 shows a smaller 40-50 Å diameter particle in which the entire lattice exhibits a similar superstructure in the height corrugation. The size of this particle corresponds to an "all-edge" portion of the particle in Figure 4. It is apparent that this particle is sufficiently small that it is entirely encompassed by the new structure. One would not expect that the methods used here to prepare the colloids would lead to a great deal of consistency in the chemical composition of the edges from one particle to another. Nevertheless, similarities in the superstructure are clearly evident. In both images, local areas of ($\sqrt{3}$ x $\sqrt{3}$)R30 superstructure are observed. The consistency of this superstructure indicates that it more a function of the particle size (or proximity to the edge) rather than any random consequence of local edge structure.

It is significant that the size of the perturbation is consistent with that observed in the size dependent optical studies.[11] Specifically, the lower size limit defined by Wilcoxon and Samara for observation of bulk-like excitonic structure correlates with the observed perturbation in the near-edge region. We believe that the transition from bulk-like to cluster or molecular orbital electronic structure occurs when the particle size is smaller than 30-40 Å independent of the details of the edge termination chemistry. This size corresponds to about twice the Bohr radius of the exciton.

It is tempting albeit speculative to correlate the observed novel structure with gap states that have been previously reported for MoS_2 edge planes.[24] These gap states which are confined to the edge region have been correlated with the hydrodesulfurization catalytic activity. It is clear that further details concerning the chemical composition of the edges are required to make such a connection.

REFERENCES
[1] R. R. Chianelli, E. B. Prestridge, T. A. Pecoraro, J. P. DeNeufville, Science **203**, p. 1105 (1979).
[2] M. Gutierrez, A. Henglein, Ultrasonics **27**, p. 259 (1989).
[3] N. A. Rubtsova, R. F. Khairutdinov, S. B. Kosta, Colloid J Russ Acad Sci-Engl **55**, p. 446 (1993).
[4] Y. Feldman, E. Wasserman, D. J. Srolovitz, R. Tenne, Science **267**, p. 222 (1995).
[5] S. Mulley, A. Sironi, A. DeStefanis, A. A. G. Tomlinson, Journal of Materials Chemistry **6**, p. 661 (1996).
[6] M. Homyonfer, Y. Mastai, M. Hershfinkel, V. Volterra, J. L. Hutchison, R. Tenne, Journal of the American Chemical Society **118**, p. 7804 (1996).
[7] T. Xu, Z. J. Zhang, J. Z. Zhao, Q. J. Xue, Materials Research Bulletin **31**, p. 345 (1996).

[8]   M. JoseYacaman, H. Lopez, P. Santiago, D. H. Galvan, I. L. Garzon, A. Reyes, Applied Physics Letters **69**, p. 1065 (1996).

[9]   P. Joensen, R. F. Frindt, S. R. Morrison, Mat. Res. Bull. **21**, p. 457 (1986).

[10]   X. R. Qin, D. Yang, R. F. Frindt, J. C. Irwin, Phys. Rev. B **44**, p. 3490 (1991).

[11]   J. P. Wilcoxon, G. A. Samara, Physical Review B   Condensed Matter **51**, p. 7299 (1995).

[12]   B. L. Evans, P. A. Young, Proc. Royal Soc. London A **198**, p. 74 (1967).

[13]   R. F. Frindt, A. D. Yoffe, Proc. Royal Soc. London A **273**, p. 69 (1963).

[14]   J. A. Wilson, A. D. Yoffe, Adv. Phys. **18**, p. 193 (1969).

[15]   W. Jaegermann, H. Tributsch, Prog. Surf. Sci. **29**, p. 1 (1988).

[16]   E. Lu, P. D. Persans, A. F. Ruppert, R. R. Chianelli, Mater. Res. Soc. Symp. Proc. (1990).

[17]   X. L. Wu, C. M. Lieber, Prog. Inorg. Chem. **39**, p. 431 (1991).

[18]   R. V. Coleman, Z. Dai, W. W. McNairy, C. G. Slough, C. Wang, in G. Benedek (Ed.): *Surface Properties of Layered Structures, Vol. 16*, Kluwer Scientific Publishers, Dordrecht, Boston, London 1992, p. 27.

[19]   J. Tersoff, D. R. Hamann, Phys. Rev. B **31**, p. 805 (1985).

[20]   J. Tersoff, Phys. Rev. Lett. **57**, p. 440 (1986).

[21]   B. A. Parkinson, J. Ren, M. H. Whangbo, J. Am. Chem. Soc **113**, p. 7833 (1991).

[22]   J. Ren, M. H. Whangbo, H. Bengel, H. J. Cantow, S. N. Magonov, Chem. Mater **5**, p. 1018 (1993).

[23]   S. P. Kelty, A. F. Ruppert, R. R. Chianelli, J. Ren, M. H. Whangbo, J. Am. Chem. Soc **116**, p. 7857 (1994).

[24]   C. B. Roxlo, R. R. Chianelli, H. W. Deckman, A. F. Ruppert, P. P. Wong, J. Vac. Sci. Technol., A **5**(4, Pt. 1), p. 555 (1987).

IRREVERSIBLE ADSORPTION OF POLYMER MELTS

U. SAWHNEY, C.J. DURNING AND B. O'SHAUGHNESSY
Department of Chemical Engineering,Materials Science and Mining Engineering
Columbia University, New York, NY 10027, USA
G.S. SMITH AND J. MAJEWSKI
MLNSC, Los Alamos National Laboratory, Los Alamos, NM 87545

ABSTRACT

We studied the equilibrium architecture of polymer layers strongly adsorbed from the melt. Immobilized layers of poly-(methyl methacrylate) (PMMA) were produced by the following method: 1) The polymer was spin-coated onto silanol bearing surfaces of single crystal and fused quartz, and annealed at melt conditions, 2) The annealed layer was quenched to room temperature (below the glass transition temperature) in order to "freeze in" the melt structure near the substrate, 3) Unbound material was leached away in good solvent (benzene) to leave a residual, strongly-adsorbed layer. The architecture of this layer was studied by neutron reflection. Data on dried adsorbed layers indicates a dense PMMA film whose thickness gradually increases with annealing time in the melt from a minimal value. Evidently, annealing gradually relaxes a rather flat non-equilibrium structure produced by spin-coating. The thicknesses, h, in a series of dry layers annealed long enough to achieve equilibrium conditions in the melt scale as $h \sim N^{1/2}$. Data on swollen layers suggest a dilute, extended layer, but the preliminary results cannot give a definitive confirmation of the brush structure predicted by Guiselin.[1]

INTRODUCTION

Flexible, high molecular weight polymers can adsorb on solid surfaces very strongly. This results from the amplification of even a very small favorable segmental sticking energy per monomer to a huge sticking energy per chain for high molecular weights. Consequently, polymer adsorption often appears to be irreversible on experimental time-scales with adsorbed layers exhibiting persistent non-equilibrium architecture. In this paper, we report preliminary results on the non-equilibrium layers resulting when flexible polymers adsorb strongly from the melt, including conditions where the adsorbed layer structure is expected to have a number of universal features.

Besides the fundamental importance in polymer physics, adsorption from the melt is of considerable practical importance in a number of applications. For example, the appearance of flow instabilities in extrusion processes depends sensitively on nature of interactions between the melt and internal machine surfaces near the die exit.[2] Also, the understanding of the structure of a melt or concentrated solution near a solid surface is important in the formation, characterization and control of ultra-thin polymer films useful for advanced coatings and information storage media.

Relatively little work has been done to understand adsorption from the melt. De Gennes[3] showed that the static screening length in polymer melts in contact with a hard-core repulsive wall reduces to the monomer size. This means that

at equilibrium, essentially random walk statistics are maintained near a hard-core repulsive wall since the effect of the wall is screened out beyond a distance of order the monomer size. Based on this observation, Guiselin[1] showed that if a melt was brought into contact with an inert wall and strong favorable interaction suddenly "switched on", removal of unbound material would result in a dry residual adsorbed layer of height $h \sim N^{1/2}$. If this layer were swollen with good solvent, a brush-like structure should result, whose height $h_{swollen}$ scales $h_{swollen} \sim N^{5/6}$, and whose segment density profile $\phi(z)$ scales $\phi(z) \sim z^{-2/5}$.

Auvray[4] et. al. published verification of Guiselin's theoretical predictions. However the system that they studied (poly-(dimethyl siloxane) (PDMS) on silica) is complex: polydisperse polymer ($M_w/M_n = 1.2$) adsorbed on irregular porous particles and protracted aging effects after first contact,[5] leading to some doubt whether Guiselin's 'thought experiment' had been achieved. We revisit the Guiselin layers, but with a much simpler system for studying the situation: nearly monodisperse polymer on a single flat surface with the direct interrogation of the resulting layer structure using neutron reflection. The preliminary data demonstrate that the contacting conditions used realize Guiselin's thought experiment.

EXPERIMENTAL

Materials: Nearly monodisperse poly-(methyl methacrylate) (PMMA) (polydispersity 1.05 - 1.10) of molecular weight ranging from 25K to 345K was obtained from two sources: Polymer Laboratories Ltd., Church Stretton, U.K. and Polymer Sources Inc., Montreal, Canada. The glass transitions quoted by the suppliers are in the range of $105^o - 115^oC$. Single crystal and fused quartz blocks (variation in refractive index $\Delta n \leq 10^{-6}$) were obtained from Heraeus Amercil Inc., GA and polished by Virgo Optics, FL. The polishing specifications are as follows: long range waviness less than $\lambda/4$; surface quality better than 10/5. To prepare polymer solutions and as the leaching solvent, HPLC grade or ACS reagent grade benzene was used. Deuterated benzene was obtained from Cambridge Isotope Laboratories, MA and was 99.6% pure.

Substrate preparation: Before contacting the PMMA with the quartz, the substrates were cleaned and functionalized by a protocol which gave very reproducible results. First, the substrates were immersed in aqua regia (3 : 1 hydrochloric : nitric acid) for $4 - 6$ hours followed by a millipore filtered, deionized (18.2 $M\Omega$) water rinse, followed by UV-ozone plasma oxidation for 120 minutes. This procedure effectively removes organic contaminants. This was followed by immersion in concentrated hydrochloric acid for 2 hours to hydroxylate the surface. The surface was finally rinsed with millipore filtered, de-ionized ($18.2M\Omega$) water to yield a clean hydrophilic surface evidenced by an immeasurably low water contact angle.

Adsorbed layer formation: Semi-dilute solutions (10-20 wt.%) of PMMA in benzene were prepared by slow stirring of the as-received polymer in warm solvent ($\approx 40^oC$) for 24 to 48 hours. The solution was then spun onto the quartz at $2000 - 3000$ rpm to produce thin coatings of order 1μ in thickness. Then the coated samples were annealed at $165^oC \pm 1^oC$ in an argon purged oven for various lengths of times. The annealing step drives off residual casting solvent and liquifies

the overcoating of PMMA, allowing the melt to equilibrate against the hydroxylated quartz surface. The annealed samples were then quenched to room temperature and subsequently leached three times in baths of benzene. Each leach concluded with $5-10$ minutes of ultra-sonication to aid stripping the unbound material. Finally, the sample was either dried on a hot plate ($70-80^oC$) to remove traces of benzene from the adsorbed layer and analyzed against air, or contacted with d-benzene in a sample cell to analyze the swollen layer structure.

Neutron reflection: The majority of the analyses were performed on the SPEAR reflectometer at the Los Alamos Neutron Science Center (LANSCE), Los Alamos, NM. A few experiments were performed at the High Flux Beam Reactor H9A' reflectometer at the Brookhaven National Laboratory, Upton, NY. In order to observe the structure of the dried layer, reflection was performed in upright geometry against air; a few experiments on dried layers were also performed in inverted geometry in a sample cell against D_2O (The inverted geometry is necessary to avoid passing the neutron beam through liquid, where the attenuation is unacceptably large). Attempts to observe the swollen layer structure also employed inverted geometry.

For analysis of reflectivity data we employed a least square fitting method. A FORTRAN program implements Marquard's weighted least square fitting, allowing one to determine optimal parameters for any given scattering length density profile. Roughness of the interfaces was treated by the convolution of the assumed profile with Gaussian smearing functions.[6] For the preliminary data discussed here, the simplest possible box-models were employed. More refined calculations are presented elsewhere.

RESULTS AND DISCUSSION

The functionalized surfaces are extremely hydrophilic; for example the contact angles for water were immeasurably low. The silanol (-OH) density is expected to be in the range of $1-8nm^{-2}$ based on estimates for powdered silica treated similarly in the literature.[7] The substrates we used are also very flat; Fig.1 shows a reflectivity profile typical for our bare quartz surface against air plotted q^4R vs q, where R is the reflectivity and q is the momentum transfer. The plot demonstrates an almost horizontal region at intermediate q in keeping with Porod's law for a perfect flat edge: $R \sim q^{-4}$ for $q >> q_{crit}$. Least squares fits for the bare edges gave consistent values of roughnesses of $5-6A$.

The differential segmental sticking energy for the PMMA/silica/benzene system was estimated by Johnson and Granick[8] to be approximately $4kT$ at room temperature. One expects that spin-casting of the PMMA from benzene onto this strongly adsorbing surface produces a non-equilibrium adsorbed layer. This is equilibrated by the annealing step. Subsequent quenching to below the glass transition temperature freezes in the equilibrium structure, and rinsing with benzene removes unadsorbed polymer while imposing a high differential sticking energy, preventing desorption or reorganization of adsorbed chains. In principle, long enough annealing should result in the Guiselin layer.
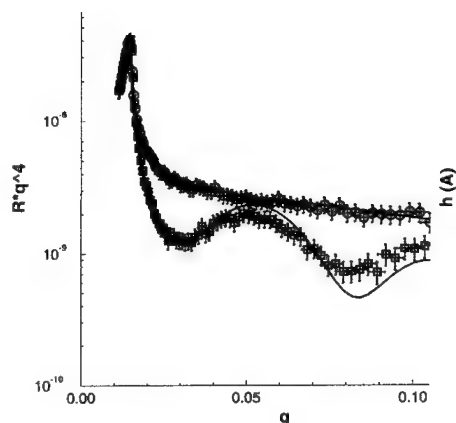
Fig.1 q^4R vs q: for a bare quartz edge against air (circles) and for an adsorbed dry layer of PMMA on quartz (M.W.= 216K; annealed for 120 hours) against air (squares). The lines are box model fits.
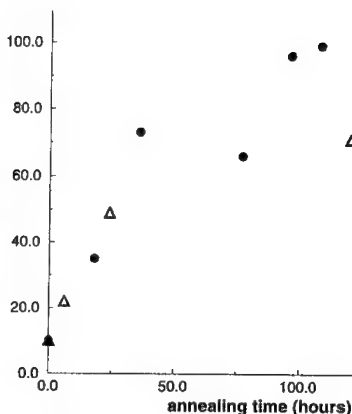
Fig.2 Adsorbed layer height h, vs annealing time for dry adsorbed layers of 345K (bullets) and 70K (triangles) PMMA.

Dried adsorbed layers of PMMA with molecular weights ranging from $25K$ to $345K$ were analyzed via neutron reflection against air. Fig. 1 shows a typical profile for this situation. The sharp peak gives the position of the critical edge which is, of course, a function only of the difference between the scattering length density of quartz and air. This peak coincided for all measured curves and showed good agreement with the theoretical value, $q_{crit} = (16\pi\Delta b/V)^{1/2} = 0.0145A^{-1}$, where $\Delta b/V$ is the relevant scattering length density difference. As seen in Fig.1, the reflectivity profiles for coated substrates differ qualitatively from the bare edge curves in that they exhibit fringes indicative of a thin film on the substrate. The fringe width Δq provides an estimate of the layer thickness, $h \approx 2\pi/\Delta q$.

We used the simplest one-box model to analyze all the dry adsorbed layer data. Roughness of the substrate was set from the corresponding bare edge measurement, as indicated above. The fitting procedure optimized values of the layer's scattering length density and thickness. A variable normalization was also allowed. All such fits gave dense PMMA layers, of scattering length density comparable $(0.85 - 1.10.10^{-6}A^{-2})$ to that expected for PMMA melts. The thicknesses of these layers, however, vary systematically with molecular weight and annealing time.

We measured the dry adsorbed layer thickness as a function of annealing time in the melt for two values of molecular weight, 70K and 345K; Fig.2 shows the result. In both cases, a very thin layer ($\sim 10A$) results from spin-casting alone. This is far less than the thickness expected for either polymer. The data also show a gradual increase in the thickness with annealing towards an equilibrium value corresponding to that expected from Guiselin's thought experiment [1]. The time-scale for relaxation

---

[1]For example, for the 70K molecular weight, N=700 and a=3 gives $R_g = N^{1/2}a/\sqrt{6} \approx 33A$.

to the equilibrium thickness increases with molecular weight; a detailed analysis of this effect will be presented elsewhere. Analysis of dry layers against heavy water, a non-solvent for PMMA, using inverted geometry, gave essentially the same results as the corresponding analyses against air for this range of molecular weight.
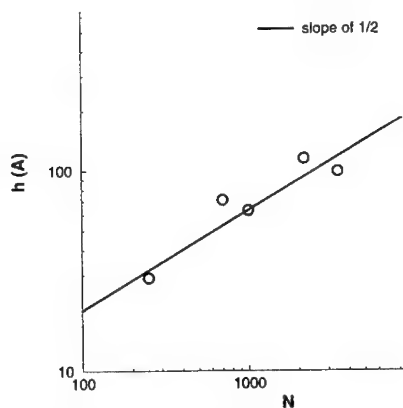
Fig.3 Adsorbed layer height, h vs degree of polymerization, N for PMMA layers on quartz.
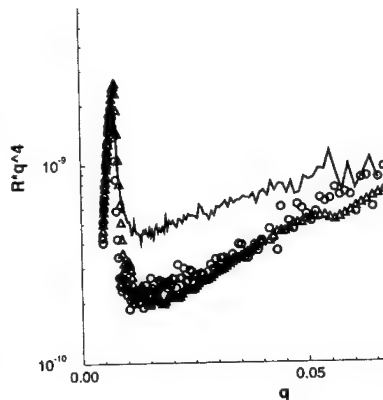
Fig.4 q^4R vs q: for a 330K PMMA layer annealed for 8 hours and swollen with d-benzene (circles); two-box best fit (triangles); and corresponding bare quartz edge against d-benzene (line).

The extremely small initial thicknesses observed could be the result of initial contact of the polymer with the surface under semi-dilute conditions. In this situation, one expects that a large number of adsorption sites are not immediately covered with polymer. Subsequent collapse of initially formed loops onto the surface to fill the vacant sites would result in a layer flat relative to the Guiselin picture. The shear field produced during spin-coating could also have a flattening effect on the layer.

Figure 3 shows a log-log plot of the dry adsorbed layer thicknesses vs degree of polymerization for very long annealing times $(96-120$ hours) where an equilibration of the melt against the substrate is expected. The plot indicates $h \sim N^{1/2}$ in accordance with Guiselin's prediction, suggesting we have achieved equilibrium melts for the range of molecular weight and annealing conditions employed, and effectively immobilized the melt structure by quenching and rinsing in good solvent.

Figure 4 shows data for an adsorbed layer swollen in d-benzene, together with the corresponding plot for the bare edge against d-benzene. The bare edge curve indicates the presence of a thin $(\approx 10A)$ hydrogenous layer on the quartz surface against d-benzene, which is most likely a water layer. This feature has been observed previously for quartz edges against organic solvents,[9] and may be exacerbated here due to the hygroscopic nature of d-benzene.

Despite this complication, a swollen polymer layer is clearly observed [2] from the qualitative differences between the swollen layer and bare surface data. The swollen layer data can be modelled successfully within the framework of a two-box model composed of a thin layer of polymer, solvent and water, and a thick layer of polymer and solvent. The suppression of reflectivity at low q values and the shift of the first minimum towards lower q relative to the bare edge profile are consistent with the presence of a thick (~ 1000 A), dilute layer of polymer. However, verification of the power law profile predicted by Guiselin requires more refined measurements.

CONCLUSION

PMMA adsorbs strongly from the melt onto hydroxylated quartz. Dry adsorbed layer thicknesses scale as $h \sim N^{1/2}$ provided equilibriation of the melt against the solid surface is achieved by annealing. The residual layers, when swollen in good solvent exhibit a highly extended structure, although unambiguous verification of Guiselin's power-law requires more refined measurements.

References

[1] O. Guiselin, Europhys. Lett., 17 (3), 225 (1992).

[2] M.M. Denn, in Theoretical and Applied Rheology: Proc. XI Ind. Cong. Rheol., Moldenaers and Kevnings eds., Elsevier, Amsterdam (1992).

[3] P.G. deGennes, C.R. Acad. Sc. Paris, 290, 509 (1980).

[4] L. Auvray, P. Auroy and M. Cruz, J. Phys. (Fr.) I, 2, 943 (1992).

[5] J.V. de Groot, C.W. Macosko, T. Kume and T. Hashimoto , J. Coll. Int. Sci., 166, 404 (1994).

[6] T.P. Russell, Mater. Sci. Reports, 5, 171 (1990).

[7] K. Kobayashi, K. Araki and Y. Imamura, Bull. Chem. Soc. Jpn., 62, 3421 (1989).

[8] H.E. Johnson and S. Granick, Science, 255, 966 (1992), and references therein.

[9] J. McCarney, J.R. Lu, R.K. Thomas and A.R. Rennie, Coll. Surf. A: Phys. Eng. Aspects, 86, 185 (1994).

---

[2] The annealing time for the layer in Fig.4 (8 hrs) is clearly not long enough to achieve the equilibrium thickness; data for a similar molecular weight (Fig.2) indicates that equilibration for this system requires greater than 100 hours of annealing at $165^{\circ}C$. Therefore, the swollen layer in Fig.4 is probably not a fully developed "Guiselin brush".

Experimental Investigations of the Kinetics of a Catalytic Trapping Reaction in Confined Spaces

Mark S. Feldman, Anna L. Lin, Raoul Kopelman
Dept. of Chemistry, University of Michigan
Ann Arbor, MI 48109-1055 USA

Abstract

We investigate the anomalous kinetics in one dimension of a diffusion limited catalytic trapping reaction, $A + T \rightarrow T$, by measuring the oxidation of glucose. The reaction is carried out in a thin capillary tube, and the depletion of oxygen in the vicinity of the reaction front is monitored by the fluorescence of a Ru(II) dye. Theoretical results and simulations have predicted an asymptotic $t^{1/2}$ dependence for the rate coefficient. We observe a depedence on $t^{0.56}$, with what appears to be an asymptotic behavior approaching $t^{1/2}$.

Introduction

Many chemical reaction processes are heterogeneous; that is, they take place at interfaces of different phases and on solid, viscous or porous media, where particles are effectively not free to roam in three dimensions. Examples of this include industrial surface catalysis, enzymatic reactions and atmospheric reactions. Under these sorts of conditions it is often difficult to obtain complete convective stirring, thus resulting in a reaction that is limited by diffusion and for which self-stirring is inefficient.

Theory (1-17) and simulations (2, 7, 13, 18-20) have established that kinetics of all diffusion-limited reactions are highly affected by the spatial dimensions in which the reactions occur; many types of bimolecular elementary reactions such as $A+B\rightarrow C$, $A+A\rightarrow A$ and $A+T\rightarrow T$ exhibit "non-classical" behavior, i.e. they exhibit rate laws which do not follow the rules of classical reaction kinetics. The $A+T\rightarrow T$ "trapping" reaction has been examined by physical exciton annihilation experiments (21-22) and was shown to obey the theoretical predictions of non-classical behavior. Here, we use glucose and oxygen together as the reactant A and an acrylamide polymer as the catalytic trap T in an effort to observe this behavior experimentally via an actual chemical reaction:

$$glucose + O_2 + H_2O \rightarrow gluconic\ acid + H_2O_2$$
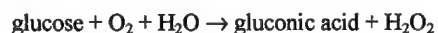
The depletion of oxygen is monitored by the fluorescence quenching of a molecular Ru(II) complex known to respond linearly to O_2 concentrations of 12 ppm (air saturation) and below (23).

Classically, the $A+T\rightarrow T$ reaction obeys the pseudo-first order rate law

$$-d[A]/dt = k[A][T] \approx k'[A] \qquad (1)$$

where $k' = k[T]$ is approximated as a constant because the trap T is not consumed. This leads to the integrated expression

$$\ln([A]/[A]_0) = -k't \qquad (2)$$

However, in non-classical kinetics for dimensions less than two, the rate constant k' is replaced in the differential form of the rate law by $k_1 t^{-h}$, where h, the "heterogeneity coefficient," is equal to $1-d_s/2$, where d_s is the spectral dimension (14). This spectral dimension is related to the probability that a random walker in an n-dimensional space will return to its origin after a certain time t. For Euclidean (non-fractal) spaces, $d_s = d_n$, the more familiar "dimension" of that space. In one dimension, h=1/2, and thus a non classical rate coefficient of $k_1 t^{-1/2}$ is predicted in the differential rate law. Integration then leads to a dependence of $\ln([A]/[A]_0)$, which will hereafter be referred to as "Y" for brevity's sake, on $t^{1/2}$ in one dimension.

$$Y = -k_1 t^{1/2} \qquad (3)$$

It is this dependence which we test here experimentally for a catalytic oxidation of glucose. Finally, we must note that all of the non-classical behavior we have just described is an asymptotic result.
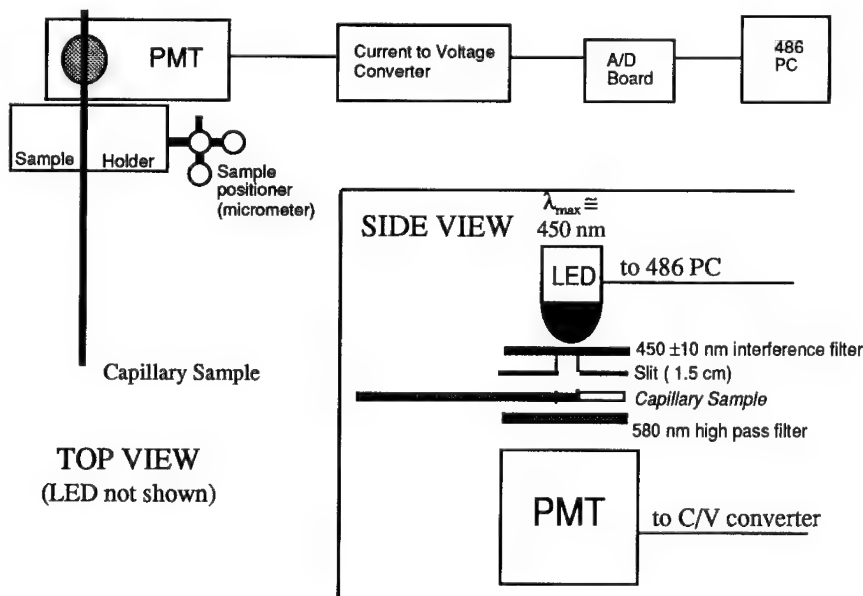
Figure 1 - Data Collection Set-up

Experimental

Preparation of the Trap. The polyacrylamide matrix was similar to that used by Rosenzweig et. al. for submicrometer optical fiber oxygen sensors (23). A 6.5 pH, 0.1 M phosphate buffer solution was prepared with 0.4 mM tris(1,10-phenanthroline)ruthenium(II) chloride, 27% acrylamide and 3% N,N-methylenebisacrylamide as cross-linker. The polymerization was carried out by adding as catalysts 1 µL triethylamine and 20 µL 10% ammonium persulfate. The polymer was washed three times with 2 mL of tris(hydroxy-methyl)aminomethane hydrochloric acid buffer and then soaked in 5 mL of 20 mM 6.5 pH phosphate buffer / 135 mM NaCl solution for at least an hour. The acrylamide was obtained from Gibco. All other chemicals were obtained from Aldrich Chemical Co.

Experimental Set-up. A 16 mM glucose solution was prepared in a phosphate buffer of pH 7.6, 5 mM in $H_2PO_4^-$, and 2 mM in HPO_4^{2-}. For blank experiments, the glucose was left out. This solution was inserted into a glass capillary tube with a diameter of 0.53 mm. One end of the tube was then sealed with Krytox teflon grease. The other end was pressed into the trap, which had been soaking for about 10 minutes in the 7.6 pH phosphate buffer to equilibrate. The end of the tube with the trap was sealed and the tube positioned quickly so readings could start within five minutes. The capillary tubes were obtained from Sutter Instrument Co. The grease was obtained from DuPont Chemical Co.

The data collection system, shown in figure 1, included a blue LED as excitation source which passed through a slit of 1.5 cm width, the sample, and a 580 nm high pass filter. The detector was a photomulitiplier tube, the signal from which was converted to voltage and sent to an IBM PC-486. The tube was positioned so that the slit was directly over the volume of the glucose solution closest to the trap. The trap - solution interface was at the far end of the slit. The fluorescence of the Ru(II) was monitored in arbitrary intensity units over 24 hours, and readings were taken at 20 second intervals. The fluorescence was binned over 500 msec. and averaged over 1 sec. for each data point. All solutions were air saturated.

Results and Discussion

We consider oxygen to be the reactant A and monitor the oxygen depletion by the increase in fluorescence of the Ru(II) complex. We can define a quantity "Z" to be analogous to Y with respect to the fluorescence intensity. Thus, Z will be equal to $\ln(I/I_0)$, and it is proportional to Y because the fluorescence intensity (I) increases linearly as $[O_2]$ decreases. In addition, the minus sign in equation 3 should disappear when Z is substituted for Y. Therefore, we expect to observe an increase in fluorescence such that Z varies with the square root of time asymptotically.

Since we choose to measure $[O_2]$ depletion, we must find a way to observe the concentration profile in the vicinity of the trap for the one dimensional $A + T \rightarrow T$ system[3], shown in figure 2. The slit is positioned directly over the "depletion mass," that is the volume where the reactant's concentration is decreasing. We are assuming an infinite source of reactant, which is essentially true, given the following: The reason the slit is 1.5 cm wide is so that we can 'see' all of the reactants being depleted. Einstein's diffusion equation, $x = (2Dt)^{1/2}$, is applied to

O_2. Using $D = 2.6 \times 10^{-5}$ cm^2/s for a time of 12 hours, a result of 1.5 cm is calculated. This means that as long as the slit is this wide, we need not worry about the oxygen migrating out of the volume of the tube under the slit. This is crucial, since if it did migrate into other parts of the tube, we would not be measuring all of the depletion mass. We also need not worry about the source of O_2 getting used up, since the tube is 10 cm long, thus acting as a reservoir.
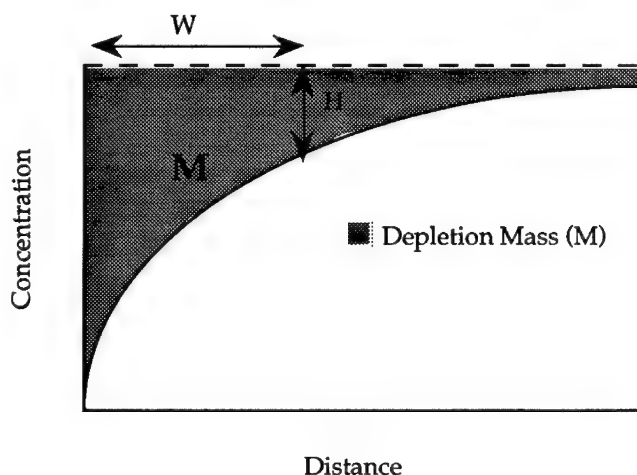
Figure 2 - Depletion Mass Under 1.5 cm Slit

The area M in figure 2 represents how much O_2 has been depleted. This area has been shown by simulation (18) to vary as $t^{1/2}$, so the quantity Z with respect to Ru(II) fluorescence should behave likewise. Figures 3a and 3b are plots of Z vs. time, the latter being a log-log plot. The data with glucose was averaged over several experiments, and the data without glucose was then subtracted. In addition, the data was run through a computer program that sampled points in such a way as to give equal weight to all points on a logarithmic scale.

The behavior observed was an increase with t to the power 0.57. One may note after a closer look at figures 3a-b that the data appear to be falling away from the best fit line. This is to be expected, since the $t^{1/2}$ behavior is theoretically an infinite time result, so the actual power law at smaller time intervals along the way ought to be approaching 1/2, which it is (see the solid line in figure 3b). In addition, the fact that the power law is approaching $t^{1/2}$ from above as opposed to below makes sense. Simulations of the trapping reaction with different reaction probabilities (that is, the probability that a given collision between a reactant particle and the trap will result in a reaction) have been done (18). For probabilities less than 1, the data fit powers of t that are >1/2 and <1 at early time, but as $t \to \infty$ the reaction probability becomes effectively 1 and the $t^{1/2}$ dependence is eventually obtained. This is in agreement with our observations of powers greater than 1/2 but gradually approaching 1/2.
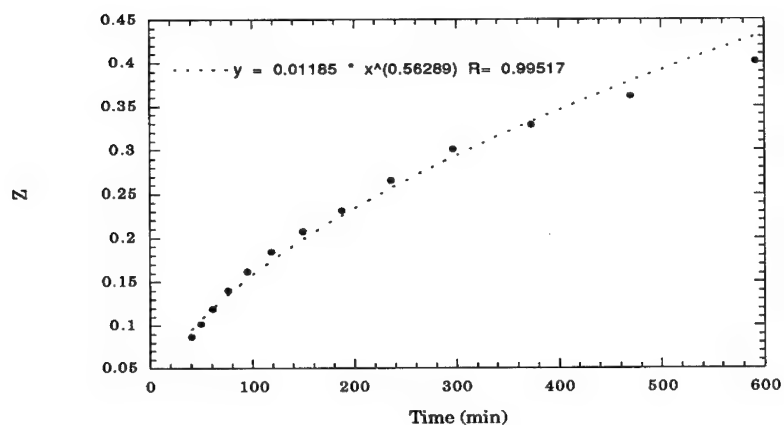
Figure 3a - Z vs. Time Plot
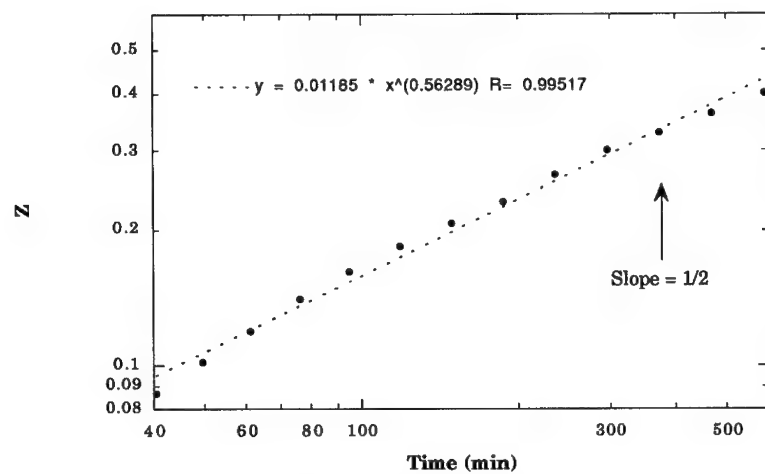
Figure 3b - lnZ vs. ln(t) plot

We are currently investigating the details of the reaction that is resulting in this behavior. Future work will also include attempts to model other types of elementary diffusion-limited reactions experimentally.

Acknowledgements

References

(1) A. A. Ovchinnikov and Y.G. Zeldovich, *Chem. Phys. B*, **28**, 215 (1978).

(2) R. Kopelman and P. Argyrakis, *J. Chem. Phys.*, **72**, 3053 (1980).

(3) A. Blumen, J. Klafter and G. Zumofen, *Phys. Rev. B*, **27**, 3429 (1983).

(4) P.G. de Gennes, *Compt. R. Acad. Sci. Paris*, **296**, 881 (1983).

(5) P. Evesque, *J. Phys. (Paris)*, **44**, 1217 (1983).

(6) P.W. Klymko and R. Kopelman, *J. Phys. Chem.*, **87**, *23*, 4565-7 (1983) and references therein.

(7) D. Toussaint and F. Wilczek, *J. Chem. Phys.*, **78**, *5*, 2642-7 (1983).

(8) K. Kang and S. Redner, *Phys. Rev. Lett.*, **52**, 955 (1984).

(9) K. Kang, P. Meakin, J. H. Oh and S. Redner, *J. Phys. A*, **17**, L665 (1984).

(10) K. Kang and S. Redner, *Phys. Rev. Lett A*, **32**, 435 (1985).

(11) G. Zumofen, A. Blumen and J. Klafter, *J. Chem. Phys.*, **82**, 3198 (1985).

(12) K. Lindenberg, B.J. West and R. Kopelman, *Phys. Rev. Lett.*, **60**, 1777 (1988).

(13) D. ben-Avraham, *J. Chem. Phys.*, **88**, 941 (1988).

(14) R. Kopelman, *Science*, **241**, 1620 (1988).

(15) G. Weiss, R. Kopelman and S. Havlin, *Phys. Rev. A*, **39**, 466 (1989).

(16) E. Clement, R. Kopelman and L.M. Sander, *Europhys. Lett.*, **11**, 707 (1990).

(17) H. Taitelbaum, R. Kopelman, G. H. Weiss and S. Havlin, *Phys. Rev. A*, **41**, 3116 (1990).

(18) R. Schoonover, PhD Thesis, University of Michigan, Ann Arbor, MI (1993).

(19) K. Lindenberg, P. Argyrakis and R. Kopelman, *J. Phys. Chem.*, **99**, 7542 (1995).

(20) A. Lin and R. Kopelman, Anomalous Kinetics of the Trapping Reaction in One Dimension Under Steady State Conditions, *Proceedings of the Materials Research Society Symposium*, Boston, Mass., 27-30 Nov., **407**, 137 (1995).

(21) R. Kopelman, S. J. Parus and J. Prasad, in *Excited State Relaxation and Transport Phenomena in Solids*, edited by J. L. Skinner and M.D. Fayer, special issue of *Chem. Phys.*, **128**, 209 (1988).

(22) R. Kopelman and A. Lin, Experimental Invesitgations of Molecular and Excitonic Elementary Reaction Kinetics in One Dimension, Non-equilibrium Statistical Mechanics in One Dimension, V. Privman, ed., Cambridge University Press (1996).

(23) Z. Rosenzweig and R. Kopelman, *Anal. Chem.*, **67**, 2650 (1995).

Critical Current Fluctuations in Disordered Superconducting Wire Networks

Carlos Bonetto and N. E. Israeloff,

Dept. of Physics, Northeastern University, Boston , MA 02115

Abstract

We report results of an investigation of magnetic-field dependent critical currents in artificially disordered superconducting Al wire networks well below T_c. Aperiodic but reproducible variations with field are found, in sharp contrast with the periodic oscillations observed close to T_c. Critical currents also exhibited strong variations on cycling the current at low fields reflecting variations in frozen-in metastable vortex patterns. Both the variations in field and on cycling vanished above a critical field set by the disorder strength.

Introduction

Superconducting wire networks provide well controlled systems for studying vortex dynamics and cooperative phenomena in general. The field-dependent critical current in periodic grid networks was studied theoretically for the regime very close to the mean-field critical temperature, T_c, using linearized Ginzburg -Landau [1] theory. In this regime the properties of wire networks are closely related to those of Josephson junction arrays. In the case of wire networks the depairing current determined the critical current and gives rise to sharp periodic maxima at applied fields corresponding to low-order rational numbers of flux-quanta filling each cell. The temperature dependence of the critical current was predicted to follow $I_c = I_c (0) \tau^{3/2}$, where $\tau = (T_c-T)/T_c$ is reduced temperature. All of these predictions agreed well with experiments [2].

At temperatures well below T_c several theoretical difficulties arise. The non-linear Ginzburg Landau theory must be used. Significant variations of the amplitude of superconducting wave function are expected on the network. Thus the physics may depart further from that of a josephson-junction array. The strength of the superconductivity in the wires produces significant pinning of the vortices. Thus metastable patterns of vortices which are highly defected versions of the predicted ground state patterns are easily quenched in, even in ordered networks. This was clearly demonstrated in recent imaging studies of Nb wire networks [3]. Thus the physics in this regime may be more connected with other non-equilibrium many-body systems such glasses or granular assemblies.

The purpose of this work is to study the behavior of the critical current at temperatures well below T_c where vortex dynamics dominates, and to understand the role played by positional disorder in these arrays. Previous studies have focused on the disappearance of T_c oscillations with field in networks with correlated disorder above a critical field set by the areal disorder of the cells in the network. Above the critical field the network periodicity is no longer apparent since the spatially fluctuating random component of flux per cell becomes of the order of one flux quantum (about 1/3 was observed) [4]. In the case of uncorrelated positional disorder as we

study here, the regime above the critical field is analogous to the gauge glass model in which vortex plastic flow is observed in simulations [5].

Experimental Methods

The networks studied consisted of square Al wire grids of 200 x 100 wires. The Al thickness was 30 nm and the wire width 270 nm, the lattice constant (wire spacing) was $a = 2$ μm. The positional disorder is achieved by random displacement of the nodes $\mathbf{r}/a = (n_x+\delta_x, n_y+\delta_y)$ with $n_{x,y}$ integers and $\delta_{x,y}$ a random uniform number in the range $[-\Delta, \Delta]$. Figure 1 (inset) shows an electron micrograph of one sample. The samples used in these studies were made at the Cornell Nanofabrication Facility. Electron beam lithography and lift-off techniques were used to pattern Al films evaporated onto oxidized silicon substrates. To ensure current uniformity, we used large Al current contact pads with Au/Ti overlay, each covering the entire edge of the network. Multiple closely spaced voltage leads were patterned on each side of the network, with a separation of three or ten cells.

The measurements were carried out in a liquid ^{3}He cryostat with a base temperature of 300 mK. The magnetic field was produced with a small copper solenoid. The critical temperature was measured using a 4-probe technique with an ac current bias of 1 μA and lock-in detection. The mean-field $T_c(H)$ was measured by holding the resistance fixed at half its normal-state value by feeding the sample voltage into a temperature controller (LR-130) while the field was slowly swept.

In order to determine the critical currents, current-voltage characteristics (I-V) were measured. The current was ramped with a sawtooth pattern at 5Hz and the voltage was recorded after amplification via an SRS preamp. At a fixed magnetic field and temperature the current was ramped up and down typically 400 times. At temperatures well below T_c the I-V's were hysteretic due to heating effects. The critical currents were defined by the sharp voltage jump on the increasing portion of the current sweep.

Results and Discussion

In figure 1 we show the experimentally determined superconducting-normal phase boundary for a disordered network with $\Delta = .05$. There are sharp maxima at integral flux quanta per cell. We see that the amplitude of the oscillation decreases with increasing field. The critical field above which the oscillations are suppressed and disorder dominates appears to be approximately 40 G. In addition to the oscillations a background increase in T_c with field was observed at low fields while at high fields T_c decreased. This low-field T_c increase or negative magneto-resistance has been observed before [6] in Al microstructures when large current densities were used. In those instances the effect was attributed to non-equilibrium superconductivity. But in our case this effect is observed even at quite low current densities at which no such effect is expected nor previously reported in arrays [7]. We are now testing whether this effect is a property of the Al or the network geometry. Based on the quadratic field dependence of T_c at higher fields we calculate [8] the zero temperature coherence length to be $\xi_0 = 83$ nm for these networks.
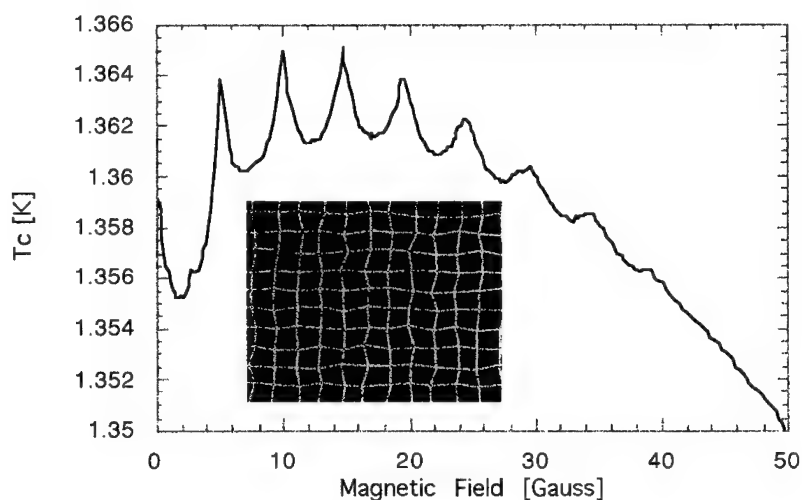
Figure 1. Superconducting-normal phase boundary for a disordered Al wire network, $\Delta=0.05$. Inset: SEM micrograph of a disordered network with 2 μm wire spacing and $\Delta=0.15$.

In fig. 2(a) and 2(b) we plot the I-V curves at 0.7 K for fields below and above the critical field. At each field the sample has been cooled through the transition with zero magnetic field. The critical current was extracted from the sharp jump in voltage on the increasing portion of each IV curve. On each current cycle the array has been driven (and heated) to effectively the normal state. The striking feature is the lack of reproducibility of the critical current at low fields and low temperatures. At higher fields the critical current becomes quite reproducible.

At each field the mean value of the critical current, $\langle I_c \rangle$, and the standard deviation of the critical current $\sigma(I_c)$ is calculated from 400 I-V cycles. These are plotted as a function of field in figures 3(a) and 3(b). Several surprising features are observed. First, aperiodic fluctuations are observed in the mean critical current as a function of field. These field-dependent fluctuations are much larger than the expected mean standard deviation, $\sigma(I_c)/20$, and furthermore they are *reproducible*. These contrast with the periodic oscillations observed close to T_c, as shown in the inset of fig. 3(a). These fluctuations decrease and finally disappear above the critical field of about 40 G. Second, the fluctuations in critical current at fixed field shown in fig. 3(b) are large at low fields but again diminish and disappear above the critical field. The larger fluctuations observed in $\sigma(I_c)$ as a function of field are aperiodic but reproducible.
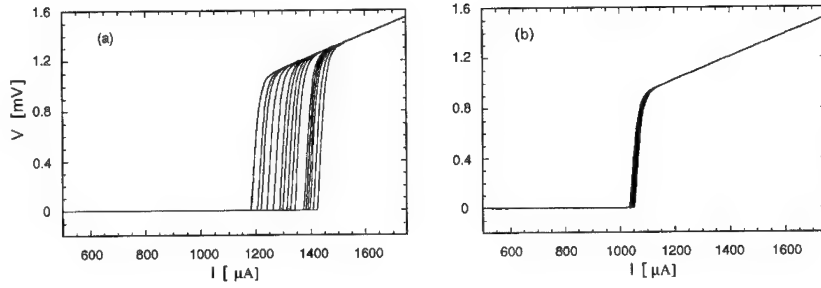
Figure 2: Repeated measurements of the I-V characteristics of a disordered wire network (Δ =0.05) at T=0.7 K for (a) H = 4 G and (b) H= 47 G are shown.
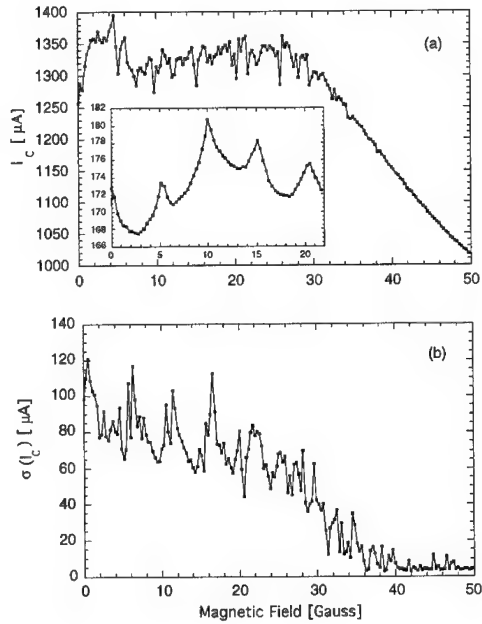

Figure 3. (a) Mean critical current vs magnetic field for the disordered array (Δ=0.05) at 0.7 K. Each point is obtained from 400 I-V measurements. Inset: Critical current at 1.3 K (close to T_c.) (b) Critical current standard deviation vs magnetic field at 0.7 K

One possible source of these fluctuations at fixed field is external noise. The $\sigma(I_c)$ did not appear to change significantly with ramp frequency or manual ramping with a battery current source. But magnetic field noise could explain why $\sigma(I_c)$ decreases with field in the same way as the field-dependent fluctuations in $<I_c>$. We ruled this out by switching to a low-noise battery source for the magnet power-supply, and using substantial Pb and mu-metal shielding. In addition, on several I-V cycles in which no jump in voltage had yet occurred up to the mean-value of critical current, we stopped the current ramp at a value slightly above the mean and waited for up to 30 minutes. In these cases, no jumps ever occurred during the waiting period. This suggests that the critical current is not determined by external noise, but rather is set by the particular realization of the vortex configuration quenched-in after cycling from the normal state.

It is surprising that little periodic structure in critical current is seen at low temperatures as it is at high temperatures. But the fact that both the field and quench dependent fluctuations in critical current vanish above the same critical field at which the mean-field T_c oscillations vanish is striking. This suggests that the network geometry which determines the field above which disorder dominates is important.

Why then do these fluctuations disappear at higher fields in the disorder dominated regime? One possibility is that below the critical field, metastable locally commensurate states are important to the pinning even at irrational fields. In ordered networks metastable configurations of vortices can locally mimic nearby rational states. For vortices imaged in ordered Nb wire networks, Hallen et. al. [3], reported a variety of different metastable vortex patterns at a given f value after quenching. Even at f= 1/2 the famous checkerboard pattern had considerable "defects". At f values between 1/3 and 1/2 small "grains" of 1/2 like or 1/3-like order were typical. Disordered grain boundaries were observed. Above the critical field there are no nearby commensurate states. Completely disordered vortex patterns are expected. This regime may in fact be a pinned liquid.

The critical current measured in our experiment may not depend on the global average of the free-energy as does T_c, but instead on the local region of weakest pinning in the sample set by the degree of local commensurability. This may be why the critical current does not exhibit the periodicity of T_c (H). We speculate that the collective pinning strength might have much larger spatial variations in the low-field order-dominated regime where large commensurate grains are surrounded by disordered grain boundaries. Inhomogeneous vortex plastic flow and large fluctuations result [5,7].

In simulations of disordered Josephson junction arrays, Dominguez [5] found that different realizations of the disorder gave different critical currents. Different quenched vortex configurations for fixed disorder *may* have a similar effect since both contribute in a similar way to the (linearized) GL free energy. In the simulations the sample to sample fluctuations of the critical current decreased with increasing sample size. In the largest samples with 64 x 64 cells, the critical current standard deviation was about 5 % of the mean in the high field or gauge-glass limit. In our case, variations of critical current as a function of quench were observed in 100 x 200 cell samples. The standard deviation averaged 6 % (3-8 % range), but only at low fields. Suprisingly at high fields (gauge glass regime) the variations became very small, about 0.5%.

Conclusions

In conclusion we have measured the critical current of disordered wire networks at a temperature well below the T_c. We observed aperiodic field and cycle dependent fluctuations in the critical currents due to metastable quenched vortex configurations. Both types of fluctuations vanish above a critical field set by the network disorder. We speculate that strong spatial variations in collective pinning due to locally commensurate vortex states are important at low fields resulting in large critical current variations. At high fields the behavior is that of a pinned liquid. Further theoretical and numerical work and spatially resolved measurements on ordered and disordered networks are needed to quantitatively understand these effects.

Acknowledgments

References

1) Y.Y. Wang, B. Pannetier and R. Rammal, J. de Physique **49**, 2045-2057 (1988).
2) O. Buisson, M. Giroud and B. Pannetier, Europhys. Lett. **12**(8), 727-733 (1990).
3) H.D. Hallen *et al.*, Phys. Rev. Lett. **71**, 3007 (1993).
4) M. A. Itzler, A. M. Behrooz, C. W. Wilks, R. Bojko, and P.M. Chaikin, Phys. Rev. **B42**, 8319 (1990).
5) D. Dominguez, Phys. Rev. Lett. **72**, 3096 (1994).
6) I.N. Zhilyaev, I.A. Sosnin, k. Fossheim, Phys. Rev. **B54**, 9658 (1996).
7) F. Yu *et al.*, Phys. Rev. Lett. **68**, 2335 (1992). X.S. Ling *et al.*, Phys. Rev. Lett. **76**, 2989 (1996).
8) *Introduction to Superconductivity*, Michael Tinkham, (McGraw-Hill, New York, 1996).
9) A.E. Koshelev, V.M. Vinokur, Phys. Rev. Lett. **73**, 3580-3583 (1994).

DYNAMICS AND STABILITY OF SURFACTANT COATED THIN SPREADING FILMS

OMAR K. MATAR and SANDRA M. TROIAN
Department of Chemical Engineering, Princeton University, Princeton NJ 08544-5263

ABSTRACT

Within lubrication theory, we investigate the hydrodynamic stability of a thin surfactant coated liquid film spreading strictly by Marangoni stresses. These stresses are generated along the air-liquid interface because of local variations in surfactant concentration. The evolution equations governing the unperturbed film thickness and surface surfactant concentration admit simple self-similar solutions for rectilinear geometry and global conservation of insoluble surfactant. A linear stability analysis of these self-similar flows within a quasi steady-state approximation (QSSA) yields an eigenvalue problem for a single third-order nonlinear differential equation. The analysis indicates that a thin film driven purely by Marangoni stresses is linearly stable to small perturbations of all wavenumbers. The insights gained from this calculation suggest a flow mechanism that *can* potentially destabilize the spreading process.

INTRODUCTION

The spontaneous spreading of surface active solutions along a liquid support of higher surface tension, so called Marangoni spreading, plays a significant role in processes from industry to daily life, including detergency, optical coating manufacture, lubrication, and aerosol delivery of bronchodilating drugs. As an example of a Marangoni spreading process, many premature infants develop a respiratory distress syndrome at birth if their lungs have not sufficiently matured to produce adequate quantities of pulmonary surfactant. This substance reduces the surface tension of the liquid which lines the alveoli and lung airways and its deficiency can give rise to respiratory difficulties associated with airway closure, decreased lung compliance and mechanical damage of the airway linings. An effective technique for the treatment of this condition is to deliver surfactant externally through inhalation of surfactant in aerosol form [1]. This process can accurately be modeled as surface active liquid droplets spreading along a thin water based film [2-5].

Marangoni driven spreading occurs spontaneously and rapidly. Variations in the concentration of surface active material produce surface tension gradients at the air-liquid interface. Such gradients create surface stresses which induce motion in the spreading film and liquid support in the direction of increasing surface tension. It has been shown experimentally and theoretically that such stresses lead to the formation of a thinned region near the surfactant deposition point and a subsequent film thickening at the advancing front [2-10]. Within the past few years, the description of the unperturbed uniform spreading process has been the subject of considerable interest. The base state equations have been expanded to include many of the forces affecting thin film flow including Marangoni stresses, surface diffusion, capillarity, gravity, solubility and van der Waals forces [2-5]. In addition, the spreading process has been extended to several geometries and to cases for which the surfactant reservoir can provide either a finite or infinite amount of material.

Experiments have revealed the existence of a new fingering instability near the point of deposition [6-10] and at the advancing front [11] of thin surfactant coated water films spreading on a thin water support. Though modeling efforts have concentrated on the uniform spread-

ing process, the stability of the system of equations describing spontaneous Marangoni driven spreading has received surprisingly little attention. We would like to determine whether linear stability analysis can uncover unstable flow and subsequent finger formation near the thinned region upstream of the initial advancing front. A much simplified linear stability analysis within a long wavelength approximation has suggested that Marangoni driven films are susceptible to perturbations in the thinned region [5]. In this work the unperturbed flow was modeled as a spherical cap of liquid coated with insoluble surfactant spreading on an uncontaminated layer of the same liquid. Allowing only concentration disturbances and assuming that the surfactant reservoir provided unlimited material, the flow was shown to be unstable to perturbations near the surfactant deposition point. Within this model, both Marangoni and capillary effects were included.

The work presented below provides a more complete and rigorous linear stability analysis without the approximations used previously. We investigate flows driven strictly by Marangoni stresses (with no capillary effects) in order to isolate the dominant source of unstable flow. The possibility of an instability arising solely from Marangoni flow and not capillary driven flow is studied by considering the spread of a surfactant monolayer. With only one mechanism present, the base flow profiles demonstrate simple and analytical self-similar form. The linear stability analysis of these profiles includes fluctuations in the film thickness *and* surfactant concentration, both of which are treated self-consistently. We show below that such self-similar profiles are stable to linear perturbations of all wavenumbers. With the insight gained from this analysis, we propose a mechanism which can enhance disturbances in the flow to destabilize the system.

PROBLEM FORMULATION

Base State

Consider a thin Newtonian liquid layer of viscosity μ^* and density ρ^* partially covered with surfactant and resting on a solid substrate. The asterisk denotes dimensional quantities. The aspect ratio of initial film thickness, H_o^*, to the horizontal extent of the initial surfactant distribution, L^*, is denoted by ε, the small parameter characteristic of the lubrication approximation. The difference in surface tension between the surfactant free, σ_o^*, and contaminated liquid surfaces, σ_m^*, is given by the spreading coefficient $\Pi^* = \sigma_o^* - \sigma_m^*$. Initial gradients in surface tension of order Π^*/L^* generate a shear stress at the interface of order $\mu^* U^*/L^*$ that drives the spreading. From the shear stress balance at the interface emerges the velocity scaling $U^* = \varepsilon \Pi^*/\mu^*$. The horizontal and transverse coordinates, x^* and z^*, are scaled by L^* while the vertical coordinate y^* is scaled by H_o^*. The axial and transverse velocities, u^* and w^*, are scaled by U^* and the vertical velocity, v^*, by εU^*. Time is rescaled by $\mu^* L^*/\varepsilon \Pi^*$ and pressure by Π^*/H_o^*. The lubrication approximation dictates that $\varepsilon << 1$ and $\varepsilon Re << 1$, where $Re \equiv \frac{\rho^* U^* H_o^*}{\mu^*} = \frac{\varepsilon \rho^* \Pi^*}{\mu^{*2}}$ is a modified Reynolds number. The dimensionless surface tension is taken to be $\sigma = (\sigma^* - \sigma^*_m)/(\sigma^*_o - \sigma^*_m)$.

Introduction of the above scalings into the equations of mass and momentum conservation yields the following dimensionless evolution equations to leading order in ε:

$$u_x + v_y + w_z = 0. \tag{1}$$

$$P_x = u_{yy} + O(\varepsilon Re, \varepsilon^2), \tag{2}$$

$$P_y = 0 + O(\varepsilon^2), \tag{3}$$

$$P_z = w_{yy} + O(\varepsilon Re, \varepsilon^2). \tag{4}$$

238

The no slip boundary condition at $y = 0$ demands that $u = v = w = 0$, while the tangential and normal stress conditions at the interface $y = H(x, z, t)$, demand that $u_y = \sigma_x$, $w_y = \sigma_z$, and $\vec{p} = 0 + O(\varepsilon^2)$. Integration of Eqs. (2) and (4) subject to the boundary conditions yields a simple Couette type velocity profile for the spreading film. Mass conservation for the liquid support and insoluble surfactant require $H_t + \nabla \cdot \vec{Q} = 0$ and $\Gamma_t + \nabla \cdot (\Gamma \vec{u_s}) = \frac{1}{Pe_s} \nabla^2 \Gamma$, where $\vec{Q}$ represents the dimensionless liquid flux, $\Gamma(x, z, t)$ is the surface surfactant concentration and $\vec{u_s}$ is the surface velocity vector. Substitution of the velocity profile into these equations yields the evolution equations for the film thickness, $H(x, z, t)$, and the surfactant concentration, $\Gamma(x, z, t)$ where $\sigma_\Gamma = \partial\sigma/\partial\Gamma$:

$$H_t \;\; + \;\; \frac{1}{2} \nabla \cdot (H^2 \sigma_\Gamma \Gamma_x) = 0, \tag{5}$$

$$\Gamma_t \;\; + \;\; \nabla \cdot (\Gamma H \sigma_\Gamma \Gamma_x) - \frac{1}{Pe_s} \nabla^2 \Gamma = 0. \tag{6}$$

The linear equation of state, $\sigma = 1 - \Gamma$, suitable for dilute concentrations couples the two equations. More complex equations of state can be introduced for concentrated solutions. The modified Peclet number, $Pe_s \equiv \frac{U^* L^*}{\mathcal{D}_s^*} = \frac{\Pi^* H_o^*}{\mu^* \mathcal{D}_s^*}$ represents the ratio of bulk Marangoni convection to surface diffusion. Since the convection process always dominates spreading by surface diffusion, we consider the limit $\frac{1}{Pe_s} \to 0$. For a finite surfactant reservoir, then, Eqs.(5) and (6) admit the following self-similar solutions for rectilinear geometry [4]:

$$H_o(x, t) = h(\xi) = 2 \xi \quad \Gamma_o(x, t) = \frac{g(\xi)}{R(t)} = \frac{\lambda}{2 \, R(t)}(1 - \xi) \; . \tag{7}$$

The self similar variable $\xi \equiv \frac{x}{R(t)}$ where $R(t) = (3\lambda t)^{\frac{1}{3}}$. The parameter $\lambda = 4M_o$ where M_o is the total mass of surfactant deposited on the liquid support. Inspection of this solution reveals that the rates of change of $h(\xi)$ and $g(\xi)$ decrease as $t^{-4/3}$. This observation justifies the use of the quasi steady-state approximation in the linear stability analysis.

Linear Stability Analysis and Quasi-Steady State Approximation (QSSA)

We appeal to linear stability analysis and propose a normal mode form for the applied perturbations. Since the base flow solutions change with position and time, the meaning of the stability of this system remains somewhat ambiguous. As is normally done with such flows, we first investigate the stability within the QSSA for which the perturbations are assumed to evolve on a faster time scale than the base state. The normal mode perturbations of wavenumber K, chosen as $\widetilde{H}(x, z, t) = \Psi(\xi, t)e^{iKz}$ and $\tilde{G}(x, z, t) = \frac{\Phi(\xi, t)}{R(t)} e^{iKz}$, are substituted into Eqs.(5) and (6). The coupled pair of PDE's governing the disturbances therefore becomes

$$\Psi_t \;\; = \;\; \frac{\dot{R}}{R} \xi \Psi_\xi + \frac{1}{2R^3} \left(h^2 \Phi_\xi + 2hg_\xi \Psi \right)_\xi - \frac{K^2}{2R} h^2 \Phi, \tag{8}$$

$$\Phi_t \;\; = \;\; \frac{\dot{R}}{R} (\xi \Phi)_\xi + \frac{1}{R^3} (gg_\xi \Psi + hg_\xi \Phi + hg\Phi_\xi)_\xi - \frac{K^2}{R} hg\Phi. \tag{9}$$

In accordance with the assumptions of the QSSA, we choose a time t_{qs}, sufficiently far from $t = 0$ for memory of initial conditions to be lost, beyond which the base flows remain frozen in time. The time dependent coefficients in Eqs.(8) and (9) are therefore evaluated at $t = t_{qs}$.

The disturbances Ψ and Φ are therefore only spatially inhomogeneous and assume the form $(\Psi, \Phi)(\xi, t) = e^{\sigma(K, t_{qs})t}(\psi, \phi)(\xi, t_{qs})$ where σ is the quasi-static growth constant. Combination of this form with Eqs.(7), (8) and (9) and the variable transformations $\sigma \rightarrow \sigma R(t_{qs})^3$, $K \rightarrow (K R(t_{qs}))^2$, and $\psi \rightarrow \lambda\psi$, gives a single nonlinear third order equation for the rescaled dimensionless surfactant concentration:

$$\frac{1}{2}\xi^2(1-\xi)\phi_{\xi\xi\xi} + \xi(2 - \frac{5}{2}\xi - (\sigma+1)(1-\xi))\phi_{\xi\xi} \ +$$

$$(1 - 2\xi - \frac{1}{2}K\xi^2(1-\xi) - (\sigma+1)(1-2\xi))\phi_{\xi} \ +$$

$$(\sigma(\sigma+1) - K\xi(1 - \frac{3}{2}\xi - (\sigma+1)(1-\xi))\phi \ = \ 0 \tag{10}$$

Eq.(10), which has regular singular points at $\xi = 0$ and $\xi = 1$, must be solved numerically subject to regularity conditions at the boundaries [12]. Removing the singular point at the origin by substituting the transformation $\phi(\xi) = \xi^{2\sigma+1}Y(\xi)$ into Eq.(10) gives

$$a(\xi)Y_{\xi\xi\xi} + b(\xi)Y_{\xi\xi} + c(\xi)Y_{\xi} + d(\xi)Y = 0 \tag{11}$$

where the coefficients are defined by $a(\xi) = \xi^2(1-\xi)$, $b(\xi) = \xi(5 - 6\xi + 4\sigma(1-\xi))$, $c(\xi) = 4(\sigma+1)^2 - 2(\sigma+1)(2\sigma+3)\xi - K\xi^2(1-\xi)$ and $d(\xi) = 2\sigma(\sigma+1) - K\xi(1-2\xi)$. The quantity $2\sigma + 1$ represents the so-called indicial exponent in Frobenius expansions. Numerical solutions of Eq.(11) are constructed for different values of K using a standard shooting method by shooting away from the boundaries to a fitting point within the domain. Continuity of Y, Y_{ξ} and $Y_{\xi\xi}$ at the fitting point yields the conditions which form the basis for iterative solutions to the eigenvalue σ.

RESULTS AND DISCUSSION

Fig. 1 shows the relation between the quasi-static growth rate, σ, and the wavenumber of the perturbation, K. Since $\sigma < 0$ always, the spreading process is stable to perturbations of all K within the approximations used. An interesting feature of these stable eigenfunctions is the complementary relation that develops between ψ and ϕ near the origin as shown in Fig. 2. In particular, as the disturbance film thickness increases, the disturbance surfactant concentration decreases. The physical reason for this inverse relation is that regions of greater film thickness experience a larger mobility thereby facilitating surfactant transport and decreasing the local surfactant concentration. Apparently the disturbances readjust so as to stabilize any perturbations in film thickness or surfactant concentration.

In order to visualize the three-dimensional flow, the perturbations are superimposed upon the base state and extended periodically in the z direction. The amplitude of the perturbations is exaggerated in order to emphasize the formations created by the disturbances. The corrugated flow profiles shown in Figs. 3, 4, 5 and 6 resemble fingering-like instabilities in other systems but for this situation, the flow is stable. As shown in Figs. 4 and 6, large wavenumber disturbances become increasingly localized near the origin. This is consistent with the transformation $\phi = \xi^{2\sigma+1}Y$ which requires that both ψ and ϕ become increasingly singular at the origin as σ becomes more negative. (The interested reader can find more details of this analysis in a forthcoming publication [12].)
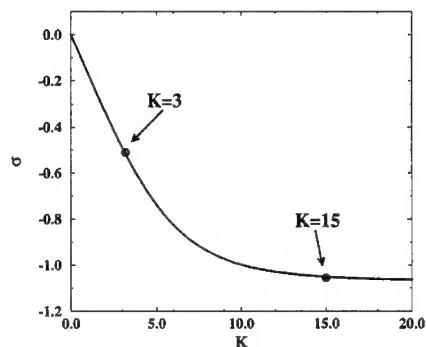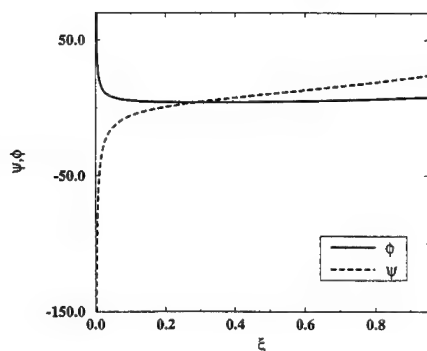
Fig. 1 Partial eigenvalue spectrum.

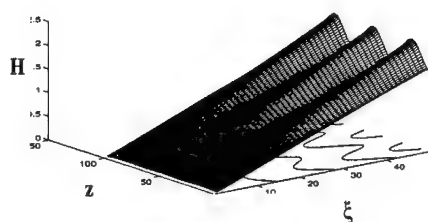Fig. 2 Illustration of the complementarity relation between ψ and ϕ near $K = 6$.

Fig. 3 Total film thickness, H ($K=3$).
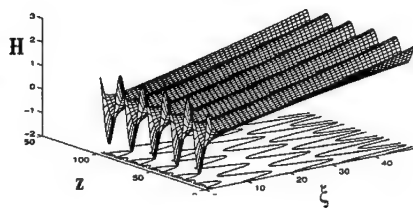
Fig. 4 Total film thickness, H ($K=15$).
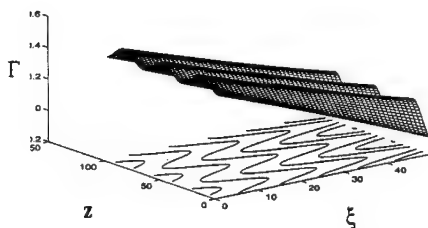
Fig. 5 Total surfactant concentration, Γ ($K=3$).
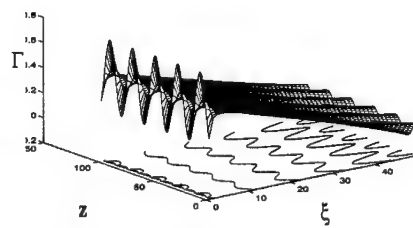
Fig. 6 Total surfactant concentration, Γ ($K=15$).

It proves instructive to consider the average velocity of the disturbance flow, $\tilde{u}(\xi) = \frac{\psi}{4} - \xi\phi_\xi$. Examination of this equation suggests a mechanism for destabilizing the flow profiles. Regions in which *both* $\psi > 0$ and $\phi_\xi < 0$ can enhance the local film velocity $\tilde{u}$ thereby advancing any protrusions in the flow. Inspection of Fig. 2 reveals that the above condition is never satisfied. In particular, both $\phi_\xi < 0$ and $\psi < 0$ near the origin while both $\phi_\xi > 0$ and $\psi > 0$ downstream. The dominant terms, $\psi < 0$ near the origin, and $\phi_\xi > 0$ downstream, are therefore very effective in stabilizing the flow. We have also performed an energy analysis to

241

determine which terms in the disturbance flux enhance perturbations and which terms retard them [12]. Not surprisingly, perhaps, Marangoni convection in the streamwise direction can destabilize the flow while Marangoni convection in the transverse flow direction always stabilizes the fluid redistribution. The energy analysis confirms the requirements cited above for conditions under which the flow will be unstable.

CONCLUSIONS

A linear stability of the self-similar profiles governing the long time spreading behavior of insoluble surfactant on a thin liquid support has been shown to be stable for all wavenumbers within a QSSA. The Couette-like velocity profiles studied here do not contain an appropriate mechanism for destabilizing the spreading process. The disturbance flow, nonetheless, produces surface corrugations resembling fingering instabilities in other flow phenomena. Flow profiles for which the disturbance film thickness is positive while the surfactant concentration gradient is negative could create unstable flow. We are investigating such a possibility by probing the stability characteristics at earlier times than those studied here and by including the effects of capillarity and surface diffusion.

ACKNOWLEDGMENTS

REFERENCES

1. D. L. Shapiro, Surfactant Replacement Therapy, New York: A. RL. Liss., 1989.

2. M. E. Borgas and J. B. Grotberg, J. Fluid Mech., **193**, p. 151 (1988).

3. D. P. Gaver and J. B. Grotberg, J. Fluid Mech., **213**, p. 127 (1990).

4. O. E. Jensen and J. B. Grotberg, J. Fluid Mech., **240**, p. 259 (1992) and Phys. Fluids, **5**, p. 58 (1993).

5. S. M. Troian, E. Herbohlzheimer and S. A. Safran, Phys. Rev. Lett., **65**, p. 333 (1990).

6. A. Marmur and M. D. Lelah, Chem. Eng. Comm., **13**, p. 133 (1981).

7. S. M. Troian, X. L. Wu and S. A. Safran, Phys. Rev. Lett., **62**, p. 1496 (1989).

8. G. D. Nadkarni and S. Garoff, Langmuir, **10**, p. 1618, (1994).

9. B. Frank and S. Garoff, Langmuir, **11**, p. 87, (1995).

10. S. He and J.B. Ketterson, Phys. Fluids, **7**, p. 2640, (1995).

11. A. Pereira and S. M. Troian, unpublished.

12. O. K. Matar and S. M. Troian, submitted to Phys. Fluids.

Random walks, trapping and reactions in quasi-one dimensional lattices

Panos Argyrakis
Department of Physics, University of Thessaloniki,
54006 Thessaloniki Greece.
E-mail: argyrakis@physics.auth.gr

Anna L. Lin and Raoul Kopelman
Department of Chemistry, University of Michigan,
Ann Arbor, Michigan 48109-1055
E-mail: alin@chem.lsa.umich.edu, kopelman@umich.edu

We performed Monte Carlo simulations of diffusion processes on baguette-like lattices, which have very small width and height, but long length, in effect providing quasi-one dimensional systems. This is done by investigating random walk properties of single particles, and also the well known model bimolecular reactions $A + A$ and $A + B$. We monitor the number of distinct sites visited, as a function of time, and also the survival probability in the presence of static traps. For the reaction systems we monitor, as usual, the decay of the particle density. The expected one-dimensional behavior is recovered, in the long time limit, for all cases studied. Our interest here is in the crossover time, from 3- (or 2-)dimensional behavior (early time) to one-dimensional (long time). We find that this crossover time scales with respect to the baguette's short dimension. However, this scaling deviates significantly from a mean square displacement law, and it is specific to both tube dimensionality and reaction type (e.g. $A + A$ or $A + B$). Specifically, instead of an expected power of 2, the exponents range between 1 and 4. The densities of the $A + B$ reactions at the dimensional crossover are compared to the densities at the segregation crossover in regular lattices at all three dimesnions. As expected, the time evolution of the $A + A$ reaction parallels the behavior of the average number of distinct sites visited.

Non-classical reaction kinetics in quasi one-dimensional systems with one-dimensional rate-law characteristics have been clearly demonstrated experimentally for several systems [1–3], including bimolecular reactions in solution filled pores [4,5] and binary exciton annihilation in crystalline media embedded inside pores [6–8], as well as for exciton annihilation on isolated guest chains [9] in polymer blends. The dynamics of the diffusion controlled photochemical and photophysical processes in most of these systems, including the well characterized nucleopore membranes [2], revealed cylindrical pore structures. These cylindrical systems exhibited crossover times dependent on width or, alternatively, cross-over widths for given experimental time scales.

The non-classical, anomalous behavior of the $A + A$ elementary reaction [1–12] has been shown [3,8–12] to be caused by the anomalously large, and continuosly growing kinetic depletion zones, i.e. fluctuating mesoscopic domains, where the reactants have been depleted. Even more dramatic non-classical effects have been demonstrated for elementary $A + B$ reactions [3,13–15] where kinetic self-segregation between A and B, the Ovchinnikov-Zeldovich effect [13], has been demonstrated for an initially random sys-

tem, as well as for steady state conditions [16,17]. This purely kinetic self-segregation of reactants in an elementary reaction has not yet been observed experimentally. The Ovchinnikov-Zeldovich rate law deviates from classical kinetics only slightly in three dimensions, more in two, and most prominently in one dimension. Searching for experimental realizations of this effect, one dimensional cases should yield the clearest results. While strictly one-dimensional reaction systems are hard to come by experimentally, it is much easier to find or to construct systems that are effectively one-dimensional, such as capillaries, pores or tubules. Such systems are, or can be made to be, immune to convection currents that otherwise might frustrate [18] the Ovchinnikov-Zeldovich effect. Towards this goal, we performed here simulations of such tubular systems, using "baguette-like" lattices, with the aim of quantifying the conditions necessary for the experimental observation of the Ovchinnikov-Zeldovich effect. Since in the short time regime (too short to reach the Ovchinnikov-Zeldovich effect) the $A + B$ reaction mimicks the behavior of the $A + A$ reaction [19], we have also simulated the $A + A$ case. Also, as the $A + A$ reaction generally follows the scaling of the number of distinct sites visited, we also simulated this case. For completeness, we have simulated two-dimensional "flat" tube reactions to compare with the three-dimensional square tube results.

The dimensional sensitivity of non-classical kinetics implies crossover times that depend on tube diameter. Previous work [14,19–21] has effectively used scaling arguments based on the mean square displacement law (Einstein diffusion) to describe the time dependence of diffusion controlled reaction kinetics. The latter law has also been found [15,19] to describe correctly the crossover times for the onset of finite size effects in regular lattices (1,2, and 3-D). To determine if this law is also relevant to the crossover times resulting from the finite width of the tube, Monte-Carlo simulations were performed here for elementary $A + A$ and $A + B$ irreversible reactions, and for the average number of distinct sites visited, in two and three dimensional baguette-like lattices. The boundary conditions for these lattices were reflective in the shorter dimension(s) and cyclic in the long dimension. The simulation methods have been detailed before [15,22].

Seen in Fig. 1 are data representing each of the three processes which we discuss here: the number of distinct sites visited, S_N; the elementary reaction process $A + A \rightarrow 0$; and the elementary reaction process $A + B \rightarrow 0$. The latter two are both measured in terms of the reaction progress, $< \rho(t) >^{-1} - \rho_o^{-1}$, where ρ_o is the initial A particle density. In Fig. 1, the solid line fits to the $A + A$ data represent how we determined the crossover time, t_c, between the early time and asypmtotic time behavior of the $A + A$ and the $A + B$ reactions. To determine t_c for the single random walker, we utilized analytical expressions to fit the data before and after the dimensional crossover.

The analytical expressions for the behavior of S_N in the asymptotic limit of $N \rightarrow \infty$, where N is the number of steps, have been given by Montroll and Weiss [23]. In 1-D, S_N follows a $t^{1/2}$ power law:

1-D:

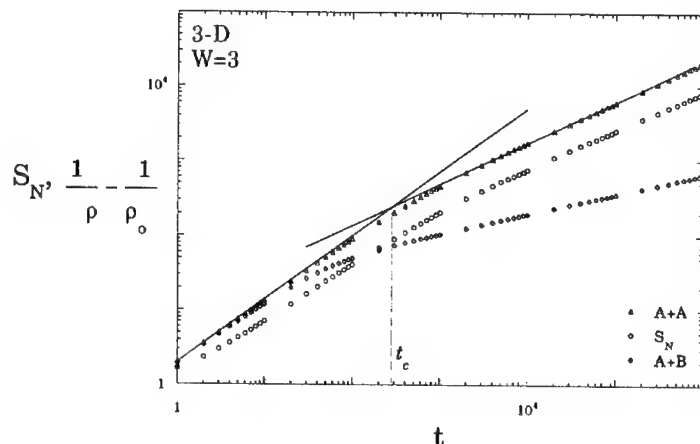$$S_N \sim (\frac{8N}{\pi})^{1/2} \qquad N \rightarrow \infty \qquad (1)$$

FIG. 1. Representative data plots for three processes: S_N, the average number of distinct sites visited (200 runs averaged), and the reaction progress of both $A + A \rightarrow 0$ (25 runs averaged) and $A + B \rightarrow 0$ (7 runs averaged), as measured by $< \rho(t) >^{-1} - \rho_o^{-1}$, vs. time, all occurring on a spatially anisotropic, "baguette-like" lattice of size $3 \times 3 \times 10^5$. The initial density, ρ_o, is 0.8 *particle/site* for the $A + A$ simulations and 0.4 in each species for the $A + B$ simumlations. The crossover time, t_c, from 3-D behavior at early times to 1-D behavior at asymptotic times is found from the intersection of the two solid lines, which are drawn as best straight line fits to the data at early and asymptotic times.

Correction terms to the asymptotic solutions, which add accuracy to the early time behavior [23,24], have also been determined. In 2- and 3-D these analytical expressions are:

2-D (ref. [24]):

$$S_N = \frac{AN}{\ln(BN)} \sum_{j=0}^{\infty} \frac{-\delta_\beta}{lnBN}^j \big|_{\beta=2} [1 + O(\frac{1}{N})] \tag{2}$$

3-D (ref. [23]):

$$S_N = 0.65946267N + 0.573921N^{1/2} + 0.449530 + 0.40732N^{-1/2} + \ldots \tag{3}$$

where A and B in (2) are constants. The crossover time, t_c, defined as the point in time at which the system changes its effective behavior from that in 2- or 3-D to that in 1-D, is calculated separately for every curve. We implement eqns. (1), (2) and (3) to compare the behavior of S_N on isotropic lattices to that observed on our anisotropic, baguette-like lattices. We also use these expressions to determine the crossover time, t_c, of S_N from 3-D or 2-D behavior, into 1-D behavior, by fitting eqns. (2) and (3) to the early time region of the S_N vs. N curves in 2- and 3-D, respectively, while fitting eqn. (1) to the asymptotic region of those curves. The time axis value corresponding to the intersection of these two curve fits is defined as t_c. The other method, which we employ to determine the crossover time, t_c, for the $A + A \rightarrow 0$ and $A + B \rightarrow 0$ processes, involves drawing "best" linear fits to both the early time and the asymptotic time portions of the curve. Again, the corresponding time axis value where these two

straight lines intersect is defined as t_c (see Fig. 1). Utilizing both methods to determine t_c for the S_N or the $A + A$ data results in different absolute values of t_c for a given process. However, if each method is applied in a self-consistent manner, the resulting scaling relations agree, within the associated errors given in *Table 1*. The single random walker simulations were done on baguette-like lattices with ample lengths, such that site revisitations, due to finite size effects, did not occur in the length direction.

In Fig. 2, the crossover times, t_c, for S_N and for the reaction progress of the $A+A \to 0$ and $A + B \to 0$ reactions, are plotted as a function of tube width, W, revealing the existence of scaling relations between these two parameters. The complex pattern of these scaling relations is possibly the most interesting behavior exhibited in these two- and three-dimensional tube-like lattices. We write this scaling relation in the form

$$t_c \sim W^x \tag{4}$$

where x is the crossover time scaling exponent. *Table 1* lists these exponents. We see a dependence on both the dimensionality of the problem and the specific nature of the reaction. (Note that S_N represents directly some trapping reactions [25,26]).
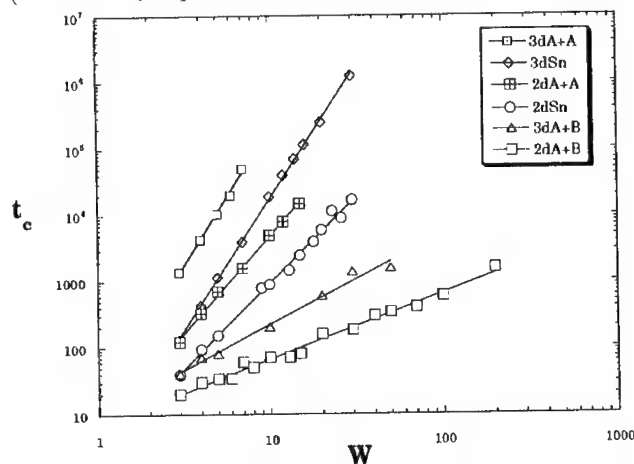
FIG. 2. The plot of t_c vs. W for S_N and for the progress of the two reactions, $A+A \to 0$ and $A + B \to 0$, on spatially anisotropic, "baguette-like" lattices, showing the scaling relation between the width, W, and the time, t_c, at which the process exhibits a crossover from its behavior in 2- or 3-D lattices to that in a 1-D lattice.

TABLE I. Dimensional Scaling Exponents for the Relation between t_c and W ($\pm$ designates estimated accuracies)

	S_N	$A + A$	$A + B$
$2 - D$	2.6 ± 0.4	2.8 ± 0.8	1.0 ± 0.2
$3 - D$	4.0 ± 0.4	4.2 ± 1	1.4 ± 0.3

Based on an analogy to the finite size effect crossovers found for isotropic lattices [19], one might have expected a universal crossover power of 2 in eqn. (4), i.e., $x = 2$ or $t_c \sim W^2$, in analogy to the Einstein mean-square displacement diffusion law. Indeed, current arguments concerning both depletion zone growth in time (for trapping and $A + A$ reactions) and aggregate size growth in time (for $A + B$ reactions) are usually based on this mean square scaling law [14,19–21,27]. Furthermore, we note that in classical chemical reaction kinetics there is no dependence of any elementary reaction progress on dimensionality. The reaction progress, measured by $< \rho(t) >^{-1} - \rho_o^{-1}$, is simply linear in time at all times and thus no crossover time can be defined (in a scaling sense).

In contrast to the above expectations, we see from *Table 1* that even the simplest case, S_N, does not scale as the mean square displacement law (x=2) but rather exhibits anomalous scalings on these 2- and 3-D spatially anisotropic lattices. Within the associated errors, the crossover times of the $A + A \to 0$ reaction process follow (at least roughly) those of S_N. The $A + A$ data are found only over a relatively narrow range of widths because the $A + A$ reaction process occurs quickly in these baguette-like lattices and finite size effects set in (the particle density becomes too dilute) before the dimensional crossover can be reached for lattices with $W > 20$ in 2-D and with $W \geq 10$ in 3-D, approximately.

We emphasize that the powers of S_N and of the 3-D $A + A$ reaction are significantly *larger* than two. On the other hand, the crossover powers for the $A + B \to 0$ processes are significantly *smaller* than two in both 2-D and 3-D baguette-like lattices. We also note that while the precision of scaling exponents is very high, the accuracy of the values listed (*Table 1*) is less certain. Still, all but one of the values of these scaling exponents are well away from two.

In Fig. 3, we plot vs. W the ratio , $\frac{\rho_c}{\rho_o}$, which is the density of A particles remaining on the lattice at t_c, normalized by ρ_o, for the $A + B$ process occurring in 2- and 3-D, respectively. We note that, in general, $\frac{\rho(t)}{\rho_o}$ is the "survival probability", at time t, of the original particles. For comparison we plot another "survival probability", $\frac{\rho'_c}{\rho_o}$, namely, the normalized densities at $t = t'_c$, where t'_c is the crossover time to the segregated (Ovchinnikov-Zeldovich) time regime in *isotropic*, linear, square and cubic lattices, found in earlier work [15,19], where this ratio was called f_d (d=1,2,3). These values are, of course, unrelated to the "baguette" width, W, in our baguette-like lattices, and are represented in Fig. 3 by horizontal, W independent lines, for d=1,2, and 3. ¿From this plot one can observe that, for $W \leq 10$, the density ratios, $\frac{\rho_c}{\rho_o}$, at the times of the dimensional crossovers (t_c) in the 2- and 3-D baguette-like lattices, occur well above the density ratios needed for crossover into the Ovchinnikov-Zeldovich regime, given by $f_d = \frac{\rho'_c}{\rho_o}$, where d is the dimension of the isotropic lattice [19], i.e. $t_c < t'_c$ for "thin baguettes". This implies that aggregates of like particles begin to form within the first few time steps on our narrow baguette-like lattices [1]. This aggregation also seems to result in a slowing down of the reaction process and the deviation from the $A + A$ type behavior (see Fig. 1) in these baguettes, in contrast to the behavior observed for the $A + B$ reaction, at early times, on isotropic lattices [15,19]. Furthermore, the scaling of t_c with W appears to be universal on the length scales we studied — for both the

---

[1]This can be seen visually in our simulation movies of the A and B particles "diffusing" and "reacting" on 2-D "tube" lattices.

small W lattices, where $\frac{\rho_c}{\rho_o} > f_d$, and the large W lattices, where $\frac{\rho_c}{\rho_o} < f_d$.
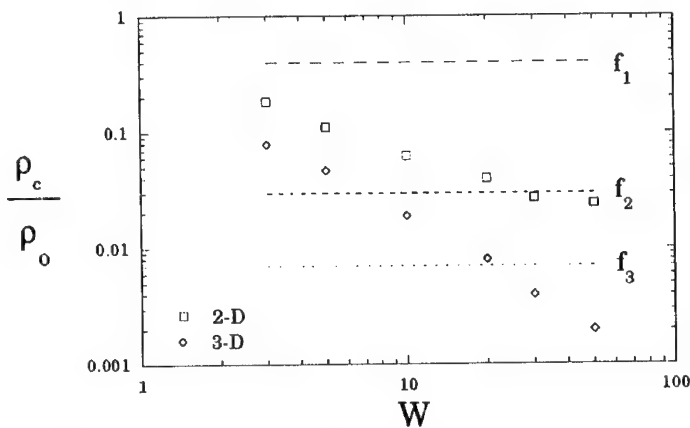

FIG. 3. The density of particles remaining on the baguette-like lattice at the dimensional crossover time normalized by the initial particle density, $\frac{\rho_c}{\rho_o}$, as a function of lattice width, W. For comparison, the horizontal lines represent the normalized density of particles, f_d, remaining on a regular, isotropic lattice at the crossover to the Ovchinnikov-Zeldovich regime. The values of f_d, where d is the dimension 1,2, or 3, are taken from [15,19].

In Figure 4 we show the results of trapping in these lattices, in the presence of static traps. Here we generate 2-D baguette-like lattices of size 10×10^6 and 3×10^6, and include a trap concentration of 10^{-3}. Single particles are allowed to perform a random walk until they get trapped irreversibly by a single trap site. At this point the walk stops and the time to trapping is recorded. The distribution of these times-to-trapping is formed first. Then, the survival probability at time t is calculated by subtracting the area under the curve (from 0 to t), from the area under the entire curve (from 0 to ∞). This is the standard survival probability, S [28]. In the same plot we show the known analytical results for 1-D and 2-D lattices [29,30], which are asymptotic at long times. We notice that for the case of the regular 2-D lattice we get very good agreement, while the baguette-like lattices show "parallel" behavior with the 1-D at long times, as expected, and in line with the other results in the present work. Quantitatively, the width $W = 3$ is closer to the 1-D than the $W = 10$, as expected. Notice that the analytical expressions for these curves is not a simple scaling law, but a far more complicated combination [29,30]. Thus, here we simply show that for the usual trapping problem there is a crossover effect, analogous to the number of sites visited, and the density of the reacting species.
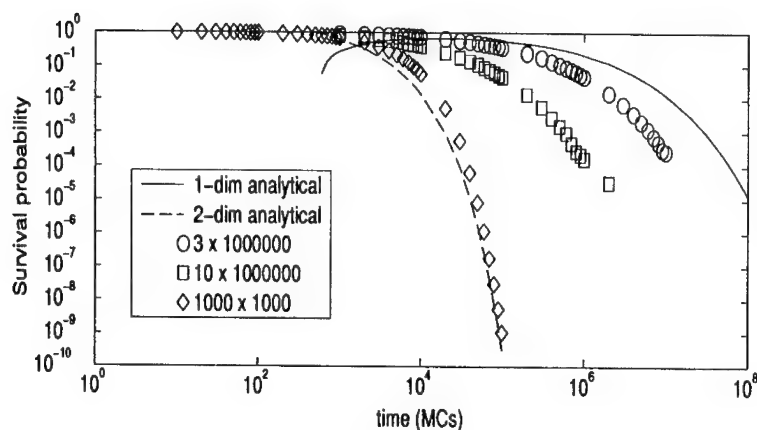
FIG. 4. The survival probability of particles diffusing in a lattice in the presence of traps. The trap concentration here is 10^{-3}. Three different lattice sizes are shown, as marked.

In summary, we find that the crossover times, t_c, do scale with lattice width, but with unexpected powers. Their values range from one to four, compared to the expected value of two. At times well beyond the crossover time, the number of distinct sites visited, S_N, as well as both the $A+A$ and the $A+B$ reactions, display the characteristic, asymptotic, non-classical behavior of a one-dimensional system. Finally, trapping in such quasi one-dimensional lattices is found to also display a crossing from the 2-D to the 1-D behavior, with decreasing tube width, as shown from the calculated survival probability.

[1] *Molecular Dynamics in Restricted Geometries*, eds. J. Klafter, J. M. Drake, John Wiley and Sons (1989).

[2] Chs. 20 and 21, *Nonequilibrium Statistical Mechanics in One Dimension*, ed. V. Privman, Cambridge University Press, (in press).

[3] R. Kopelman, Science **41**, 1620 (1988).

[4] J. Prasad and R. Kopelman, Chem. Phys. Lett. **157**, 535 (1989).

[5] J. Prasad and R. Kopelman, J. Phys. Chem. **91**, 265 (1987).

[6] R. Kopelman, S. J. Parus, and J. Prasad, in *Excited State Relaxation and Transport Phenomena in Solids*, eds. J. L. Skinner and M. D. Fayer, special issue of Chem. Phys., **128**, 209 (1988).

[7] R. Kopelman, S. Parus, J. Prasad, Phys. Rev. Lett., **56**, 1742 (1986).

[8] R. Kopelman, S. J. Parus, and J. Prasad, Chem. Phys., **128**, 209 (1988).

[9] R. Kopelman, Z.-Y. Shi and C. S. Li, J. Lumin. **48** and **49**, 143 (1991).

[10] S. J. Parus and R. Kopelman, Phys. Rev. B **39**, 889 (1989).

[11] C. R. Doering and D. Ben-Avraham, Phys. Rev. A **38**, 3035 (1988).

[12] C. R. Doering and D. Ben-Avraham, Phys. Rev. Lett. **62**, 2563 (1989).

[13] A. A. Ovchinnikov and Y. G. Zeldovich, Chem. Phys. B, **28**, 215 (1978).

[14] D. Toussaint and F. Wilczek, J. Chem. Phys. **78**, 2642 (1983).

[15] A. Lin, R. Kopelman, and P. Argyrakis, Phys. Rev. E., **53**, 1502 (1996).

[16] L. W. Anacker and R. Kopelman, Phys. Rev. Lett. **58**, 289 (1987).

[17] K. Lindenberg, B. J. West, and R. Kopelman, Phys. Rev. Lett. **60**, 1777 (1988).

[18] P. Argyrakis and R. Kopelman, J. Phys. Chem., **91**, 2699 (1987).

[19] P. Argyrakis, R. Kopelman, and K. Lindenberg, Chem. Phys. **177**, 693 (1993).

[20] K. Kang and S. Redner, Phys. Rev. Lett. **52**, 955 (1984).

[21] K. Kang and S. Redner, Phys. Rev. A, **32**, 435 (1985).

[22] P. Argyrakis, Computers in Physics, **6**, 525 (1992).

[23] E. W. Montroll and G. H. Weiss, J. Math. Phys. **6**, 167 (1965).

[24] F. S. Henyey and V. Seshadri, J. Chem. Phys. **76**, 5530 (1982).

[25] R. Kopelman and P. Argyrakis, J. Chem. Phys., **72**, 3050 (1980).

[26] P. G. de Gennes, Chem. R. Acad. Sci. Paris **296**, 881 (1983).

[27] F. Leyvraz and S. Redner, Phys. Rev. A, **46**, 3132 (1992).

[28] G.H. Weiss, *Aspects and Applications of the Random Walk* Elsevier, Amsterdam (1994).

[29] J.K. Anlauf, Phys. Rev. Lett., **52**, 1845 (1984).

[30] L.K. Gallos and P. Argyrakis, in Proceedings of Surface diffusion: atomistic and collective processes, Rhodes, Greece (1996).

Reaction Dynamics and Chemical Pattern Formation in Capillary Tubes Resulting from the Competition Between Two Elementary Complex Formation Reactions

Anna L. Lin, Andrew Yen, Yong-Eun Lee Koo, Baruch Vilensky, Haim Taitelbaum and Raoul Kopelman
Department of Chemistry, University of Michigan, Ann Arbor, MI 48109-1055 and
Department of Physics, Bar-Ilan University, Ramat-Gan 52900, Israel

Abstract

A system of competing elementary reactions is investigated experimentally using the reaction of xylenol orange with Cr^{3+} in aqueous solution. The two reagents are initially separated in a long, thin capillary tube and meet in the center, forming a reaction front (s). The geometry of the reactor and the initial separation of the reagents makes the system effectively one-dimensional. Aqueous Cr^{3+} solution has a very rich chemistry and provides two different chemical Cr^{3+} reactants which compete to react with xylenol orange. Rich spatio-temporal patterns are observed experimentally and are explained by a reaction-diffusion model. Results from exact enumeration simulations predict that when the concentrations of the competing species are very different and the microscopic rate constants of the competing species are such that the majority species reaction rate is much faster than the reaction rate of the minority species, the reaction front splits into two distinct regions. The spatio-temporal patterns generated by theory and experiment agree quantitatively. Also in agreement with the theory are the experimental early time and asymptotic time global rate behaviors, which exhibit multiple crossovers.

Introduction

The simplest forms of chemical reaction fronts have been investigated in a series of recent theoretical and experimental papers. It has been shown that, even for a single bimolecular reaction, elementary reaction-diffusion systems with initially separated reactants can exhibit very unusual dynamic properties[1-4].

We present here results obtained from an experimental and theoretical investigation of a slightly more complex reaction front, one in which there are two competing chemical reactions. We observe a splitting of the chemical reaction front in a capillary. The resulting dynamic patterns in both real and reaction spaces are accounted for by our model. The effectively one dimensional experimental set-up, together with the non-classical rate laws, enable us to extract the relative reaction probabilities of the chromium ion monomer and higher oligomers.

The first theoretical work on the reaction-diffusion system with initially separated components was done by Galfi and Racz[1] on the irreversible $A+B \rightarrow C$ reaction, for which they predicted the *asymptotic* behavior of the reaction front. In their model, reactant A, with concentration a_o, and reactant B, with concentration b_o, are initially separated. They meet at time 0, forming a reaction front.

The following set of mean-field type reaction-diffusion equations for the local concentrations a, b has been assumed to describe the system:

$$\frac{\partial a}{\partial t} = D_a \nabla^2 a - kab$$

$$\frac{\partial b}{\partial t} = D_b \nabla^2 b - kab \qquad (1)$$

where D_a and D_b are the diffusion coefficients, and k is the microscopic reaction constant. The equations are subject to the initial separation condition along the separation axis, x:

$$a = a_o H(x) \qquad b = b_o [1-H(x)] \qquad (2)$$

where a_o and b_o are the initial concentrations and $H(x)$ is the Heaviside step function. Galfi and Racz used a scaling analysis to study the asymptotic behavior of the dynamic properties of the reaction front. Their study shows that the center of the reaction front (x_f) and the width (w) of

the front scale with time, as $x_f \sim t^{1/2}$ and $w \sim t^{1/6}$ respectively, while the local production rate of C at x_f is proportional to $t^{-2/3}$, in the asymptotic regime. The global rate, $R(t)$, which is defined as the integral of the local rate over space, scales as $t^{-1/2}$ asymptotically. The early time behavior of the system was studied by Taitelbaum et. al[4] using perturbation analysis. They predicted that the global rate and width will scale as $t^{1/2}$ at early time.

The case of two competing reactions is the first stage of complexity beyond the model of simple, independently acting elementary reactions. We model such a system based on the existence of two species on one side of the initially separated system. The two species, A_1 and A_2, which do not react with each other, are on one side of the system while the species B, which reacts with both A_1 and A_2, is on the other side. The reaction scheme is represented as

$$A_1 + B \rightarrow C_1 \tag{3a}$$
$$A_2 + B \rightarrow C_2 \tag{3b}$$
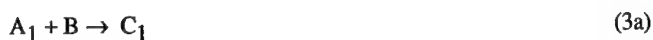
where (3a) and (3b) take place simultaneously. Thus, A_1 and A_2 compete to react with B. The products, C_1 and C_2, are assumed to be either identical or experimentally indistinguishable, and thus the local reaction rate of the system can be written as:

$$R(x,t) = k_1 \rho_{a1}(x,t)\rho_b(x,t) + k_2 \rho_{a2}(x,t)\rho_b(x,t) \tag{4}$$

We chose the following reactions [7-9] for our experiment:

$$Cr^{3+} \text{ (monomer)} + \text{xylenol orange} \quad \rightarrow \quad \text{1:1 complex} \tag{5a}$$
$$Cr^{3+} \text{ (oligomer)} + \text{xylenol orange} \quad \rightarrow \quad \text{1:1 complex} \tag{5b}$$

The source of Cr^{3+} and XO were $CrCl_3$ and the sodium salt of xylenol orange, respectively. Reactive species of Cr^{3+} present in aqueous solution have been shown to be highly dependent on pH. Stunzi et al. studied the polymerization of Cr^{3+} in aqueous solution. The Cr^{3+} ions bind with H_2O, $-OH$ and other Cr^{3+} ions in solution to form monomeric, dimeric and higher order oligomeric species of Cr^{3+}. At pH 4.5, approximately 3% of the Cr^{3+} in aqueous solution is in monomeric form and approximately 97% is in the form of higher order oligomers . The monomeric form of Cr^{3+} plays the role of the fast reacting, low concentration species, A_1 of the theoretical model and the higher order oligomers together constitute the slow reacting, high concentration species, A_2 of the model. We expected the microscopic rate constant of the monomer to be higher than that of the higher order oligomers because the monomer is less sterically hindered.

In our experimental system , aqueous solutions of Cr^{3+} and XO at pH 4.5 are injected into opposite ends of a capillary. Product formation with time is measured via optical absorption measurement[2]. The optical absorbance of the accumulated product versus position was measured at fixed time intervals. According to the Beer-Lambert law, the optical absorbance of the product is directly proportional to the concentration of the product. From the differences of the absorbance of the total product, measured at consecutive times, we obtained subtraction-profiles. The subtraction-profiles give the spatial distribution of product formation between times t and $t+\Delta t$. Normalized by proper time intervals, they gave us information that is equivalent to $R(x,t)$ vs. position, x. From the normalized subtracted profiles, we determined the time exponents for the dynamic properties of the reaction front.

The reaction front width was measured as the width at the half height of each subtraction profile. The global rate was determined experimentally from the baseline corrected integrated area of the differential peak, divided by the appropriate time intervals.

Figure 1 shows results for the temporal evolution of the spatial distribution of the product formation per time in terms of the change in absorbance, (ΔA), over a time interval, (Δt), versus position: $\Delta A/\Delta t$ vs. x. We can clearly see the splitting of the reaction front into two localized reaction fronts, starting at t = 29 minutes. As time progresses, the left peak diminishes while the right peak becomes the dominant peak in the $\Delta A/\Delta t$ vs. x plot. Due to this splitting behavior we were unable to determine precisely the exponents for the width after early times. However, we were still able to calculate the global rate, as shown in Figure 2.
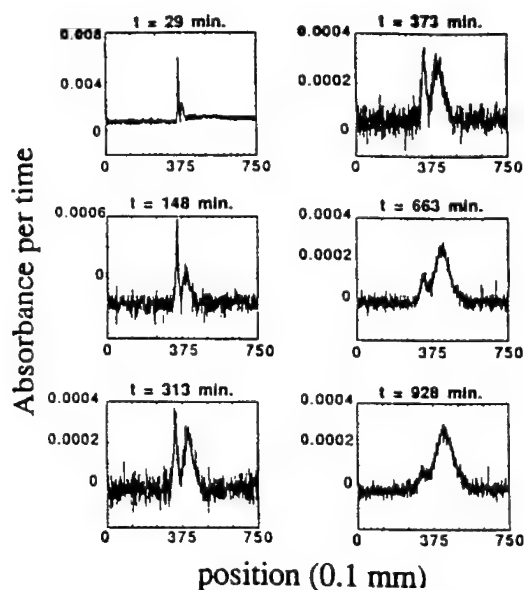

FIG. 1. Experimental profiles of the product absorbance per time at various times.
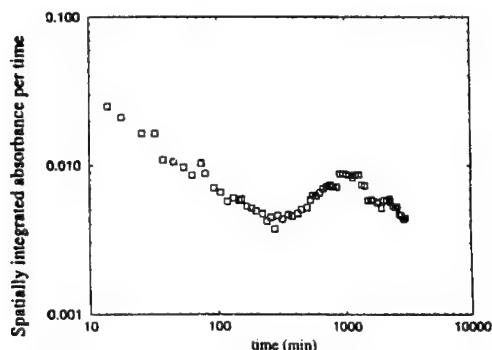

FIG. 2. Experimental results of the spatially integrated absorbance per time, which is proportional to the global reaction rate $R(t)$. The results are in accord with the theoretical results shown in Fig. 2.

253

We measured the critical exponents of the width and of the global rate from log-log plots, shown in Figures 3 and 4, respectively, for the reaction of Cr^{3+} with XO. At early time, there exists a clear crossover of the scaling laws for both the width and for the global reaction rate. The first crossover time, t_{c1}, for both properties, occurs at approximately 45 minutes. Figure 2 shows the scaling of the global rate, which has more than one crossover in time, over the entire time scale of the experiment. For this run, no data were taken before about t=15 minutes, approximately, so for the early time crossover regime of the global rate, we refer to Figure 3. The first crossover time for the global rate is shown in Figure 2 and occurred at 45 minutes. The second and third crossover times for the global rate occur at approximately 270 minutes and at approximately 1,100 minutes, respectively.

All three crossovers can be explained if one considers the conditions of the model for two competing reactions, one due to the chromium monomer and the other due to the higher order oligomers. The second crossover results from a "changing of the guard" of the fast reaction process and the slow reaction process-- the fast reaction process, which dominates the global rate behavior at early time, is overtaken by the slow reaction process, which begins its global rate ascent at later times. Because the reactant which contributes to the fast reaction has a much lower initial concentration, the fast reaction process eventually becomes negligible and the slow reaction, which results from the high initial concentration reactant species, begins to dominate the reaction front behavior at later times. Eventually, the slow reaction process also crosses over, as the fast reaction process did, into its asymptotic, regime, causing the third crossover in time.
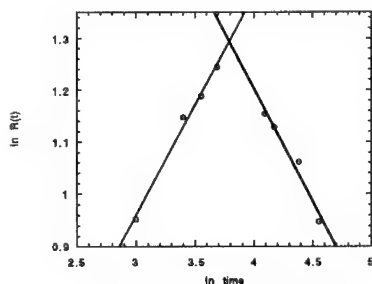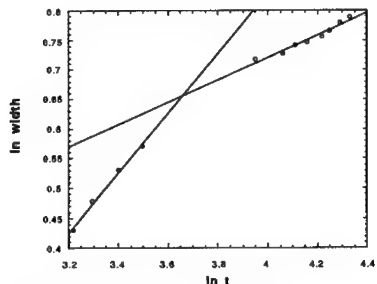

Fig 3. ln global rate vs. ln t at early time

Fig 4. ln width vs.ln t at early time

The first crossover time, from the early time to the late time behavior of the first, faster reaction process (due to the monomer) is shown in Figure 2 and occurred at t=45 minutes. The second crossover time, shown in Figure 3, resulted from the kinetics of the second, slower reaction process (due to the higher order oligomers) and occurred at t=1,100 minutes. It has been predicted analytically that the crossover time of the global rate, from the early time $t^{1/2}$ to the asypmtotic time, $t^{-1/2}$, follows[4]

$$t_c \sim \frac{C_o}{C_1 k (a_o b_o)^{1/2}} \tag{6}$$

where t_c is the crossover time and C_0 and C_1 are constants. Thus, the crossover times observed in our experiments can be used to determine the relative rates of reaction for the two types of Cr^{3+} (monomers vs. higher order oligomers) with XO. Taking into account the different initial concentrations used to obtain the results shown in Figures 2 and 3, we calculate the relative rates of the two reactions to be $k_1/k_2 \cong 250$.

We studied this system via a simulation method based on a discrete version of the evolution equation. At each time unit, n, all species perform a discrete diffusion step, using the exact enumeration method, followed by reaction events according to scheme (1). Finite probabilities of reaction replace the reaction constants k_1 and k_2. We have assumed equal diffusion coefficients for all species, and have studied a wide range of microscopic reaction constants and different fractions of the A_i's density out of the total A density.

It was shown that under conditions where k_1 and k_2 differ by several orders of magnitude, and where the faster reacting A_1 species is only a small fraction of the total density of A ($A = A_1 + A_2$), the reaction front splits in two. Furthermore, the global reaction rate is nonmonotonic in time, first increasing, then decreasing, then increasing again in time and finally decreasing asymptotically as

$t^{-1/2}$, the same as the asymptotic behavior exhibited for the simple A+B→C elementary reaction.

Figures 5 and 6 show simulation results for the reaction-diffusion system of two competing reactions with rate constants k_1=1 and k_2=10^{-4} and initial densities a_1=3% and a_2=97% of the total

A density. The inset figure in Figure 6 shows R(t) vs. t for the conditions: k_1=0.1, k_2=10^{-4} and a_1=4%, a_2=96% of the total A-density.

Figure 5 shows the spatio-temporal evolution of the product formed over given time intervals, Δt.: $\Delta P/\Delta t$ vs. x. As can be seen, the experimental data and the simulation results are in agreement with each other. The overall behavior is characteristic for competition between a dilute, but fast reacting, component vs. a concentrated, but slow-reacting, component. For the opposite relative reaction speeds, the contribution of the dilute component is masked by that of the high concentration component.
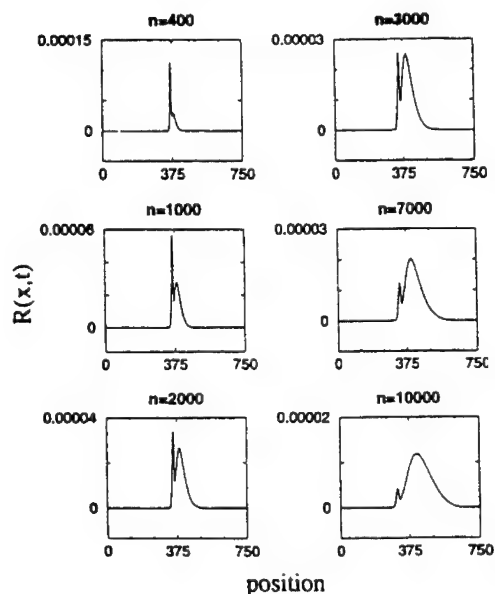

FIG. 5 Numerical results for the time evolution of the spatial profile of the local production rate $R(x.t)$, for $k_1 = 1$, $k_2 = 10^{-4}$, and $a_1 = 3\%$, $a_2 = 97\%$ of the total A density. The front's initial position is at 375.
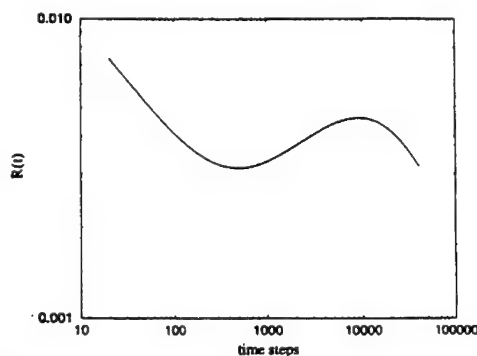

FIG. 6 Numerical results of the global rate $R(t)$ as a function of time for the double-reaction scheme of Eq. (3), for the same parameters as in Fig. 1.

Figure 6 shows the temporal evolution of the global reaction rate, $R(t)$, seen with the simulation by integrating the superposition of the two processes over x, according to the scheme for competing reactions (equation 4). In the competing reaction system, the faster reaction, which is the main contributor to the global rate at early time, begins to decay, while the slower reaction becomes the main contributor to the global rate of the system. The qualitative agreement between experiment and simulation is quite good, as can be seen by comparing Figures 1 and 2 to Fig 5 and 6.

We believe that the splitting of the chemical reaction front which we observed was the direct result of the reaction-diffusion kinetics of two competing reactions and that Cr^{3+} is the analog of the A_i species in our simulation model. For two competing reactions under initially separated conditions, where the major component reacts slowly and the minor component reacts quickly, we observed interesting spatio-temporal patterns. Our experiment yielded spatial patterns similar to those generated from a computer model for this system of competing reactions. We observed at early time a crossover for the global reaction rate and width, as predicted by perturbation theory for a simple $A+B \rightarrow C$ reaction, since a single reaction, the fast reaction, dominates the early kinetics of the system. At later times, when the slower reaction begins to influence the kinetics, we observed front splitting and non-monotonic behaviors of the global rate exponents. At even later times we saw the slow component take over and exhibit the same rise and decline in rate as the fast component did earlier. From the ratio of the crossover times, corrected for initial concentrations, we are able to determine a value that expresses the relative reaction rates of the two competing reaction processes. The reaction probability of the chromium ion monomer is about 250 times greater than that of the average higher chromium ion oligomer. This information stems from the non-classical rate laws encountered for such a low-dimensional reactor. As seen in the simple $A+B \rightarrow C$ case, the persistence of reactant segregation was also observed in the asymptotic regime for the competing reactions, where the slower reaction dominated. As a result, the global reaction rate decreased approximately with $t^{-0.5}$ the value predicted and observed experimentally for the asymptotic rate of the elementary $A+B \rightarrow C$ type reaction. All together, the global reaction rate crossed over twice from a reaction limited $t^{0.5}$ slope to a diffusion limited $t^{-0.5}$ slope. Overall, with no free parameters, the theoretical and simulation models are consistent with the complex spatio-temporal patterns and the unusual scaling laws observed experimentally. An interesting and self-consistent temporal pattern of scaling exponents and crossover behaviors emerged.

References

(1) Galfi, L.; Racz, Z. *Phys. Rev. A* **1988**, *38*, 3151.

(2) Koo, Y-E. L.; Kopelman, R. *J. Stat. Phys.* **1991**, *65*, 893. Koo, Y-E. L.; Li, L.; Kopelman, R. *Mol. Cryst. Liq. Cryst.* **1990**, *183*, 187.

(3) Taitelbaum, H; Havlin, S.; Kiefer, J. E.; Trus, B.; Weiss, G. H. *J. Stat. Phys.* **1991**, *65*, S73.

(4) Taitelbaum, H.; Koo, Y-E. L.; Havlin, S.; Kopelman, R.; Weiss, G. H. *Phys. Rev. A* **1992**, *46*, 2151.

(5) Taitelbaum, H.; Vilensky, B.; Lin, A.; Yen, A.; Koo, Y. E; Kopelman, R. *Phys. Rev. Lett.* **1996**, 77, 1640.

(6) Stunzi, H.; Spiccia, L; Rotzinger, F.P.; Marty, W. *Inorg. Chem.* **1989**, *28*, 66.

(7) Snell, F. D. *Photometric and Fluorometric Methods of Analysis*, Part 1; Wiley: New York, 1978.

(8) Valci, O.; Nemcova, I.; Suk, V. *Handbook of Triarylmethane and Xanthene Dyes*, CRC Press, 1985.

The Anomalous Diffusion-limited Reaction Kinetics of a Phototrapping Reaction

Eric Monson[†], Anna L. Lin[*] and Raoul Kopelman[*†]
[*]Department of Chemistry, University of Michigan, Ann Arbor, Michigan 48109-1055
[†]Applied Physics Program, University of Michigan, Ann Arbor, Michigan 48019-1055

Abstract

A focused laser beam acts as both a "phototrap", bleaching fluorophore molecules which diffuse into the beam path, and as a confocal probe, detecting the excited, unbleached fluorophore molecules still present in the trap. With this focused laser beam, we observe anomalous asymptotic rate laws similar to those predicted for a diffusion-controlled elementary trapping reaction, $A + T \rightarrow T$, in one and two dimensions. One dimensional diffusion-limited trapping kinetics are approached in capillaries with $10 \ \mu m$ diameters while two dimensional diffusion limited trapping kinetics are observed with unstirred samples having a quasi 2-D geometry. In the presence of stirring, the 2-D samples exhibit the classical, constant trapping rate over time.

1 Introduction

The dimension dependent kinetic rate laws of diffusion-limited pseudounary elementary reaction processes have been predicted [6, 7, 8] to exhibit an anomalous time dependence. in the absence of convection. The reaction rate may be diffusion-limited if the reaction process is fast enough. For the pseudounary trapping reaction, $A + T \rightarrow T$, in dimensions $d < 2$, this non-classical behavior results from the creation of a zone around the trap in which the reactant is depleted. This depletion zone grows in time with a particular time dependence, which is proportional to the rate of change of the reaction rate in time [9]. This is in contrast to the traditional kinetic rate law for pseudounary reactions, which assumes that the depletion zone is of constant size over the entire time course of the reaction, and thus implies stirring or other convective forces are present.

It is predicted theoretically [5, 6, 7, 8, 9] that the asymptotic rate law of the diffusion-limited $A + T \rightarrow T$ trapping reaction has a time *dependence* in $d < 2$. This is in contrast to the time *independent*, mean-field rate law,

$$R \sim Const., \tag{1}$$

assumed valid in all dimensions, where R is the *reaction rate*. In three dimensions, the rate of diffusion-limited trapping does follow the predicted mean-field rate law, as it also does in two dimensions, the critical dimension, except for a logarithmic correction term [8],

$$R \sim \frac{Const.}{logt} \qquad (d = 2). \tag{2}$$

In 1-D geometries, an asymptotic time dependence

$$R \sim t^{-0.5} \tag{3}$$

257

is predicted for both perfect [6] and imperfect [7] trapping reactions. Previous experimental investigations of trapping reactions [10] have been done in the condensed phase [11, 12, 13] and in solution phase [13, 14], but the reaction kinetics observed for trapping were not experimentally separated from a binary $A + A \rightarrow 0$ reaction process, which occurred simultaneously, and the effect of stirring on the reaction processes studied in these experiments was not investigated.

In this work, we measured the trapping rate of fluorescein free acid in pH 7.6 phosphate buffer solutions contained in 10 μm I.D. capillary tubes (quasi 1-D). For comparison, we also measured the trapping rate of the same solution confined between a cover slip and a microscope slide and in a cylindrical trough. The combined geometry of the sample and the focused beam caused the latter two systems to be quasi 2-D. The trap in these experiments is a focused laser beam "phototrap", which photobleaches the fluorophores diffusing into it. Here, we consider the photobleaching of the fluorophore to be the trapping process since it renders the fluorophore invisible to our dection system, and thus is "annihilated". Because the fluorophore does not necessarily bleach as soon as it diffuses into the beam path, the "phototrap" is an imperfect trap. The relative number of fluorophores in the phototrap, measured via confocal fluorescence detection, was monitored as a function of time.

2   Methods

Experimental

Fused silica capillaries(Polymicro Technologies Inc.) with 10 μm I.D.'s and 150 μm O.D.'s were used as quasi 1-D reaction vessels. We cut the capillary into pieces with lengths of approximately 10 to 15 cm and burned an optical window in the fluorescent polyimide outer coating of the capillaries by soaking a central portion of the length of the capillary in 100°C fuming sulfuric acid for 1 hour.

The 'reactant' solutions consisted of a known concentration of the free acid form of fluorescein in pH 7.6 phosphate buffer aqueous solution. The buffered pH 7.6 solution was necessary for complete dissolution of the Fluorecein at a concentration of $1x10^{-5}$ M and also provides a stable ionic environment for the fluorescein free acid. Fluorescein free acid is in its neutral form at pH 7.6, thus we didn't have the double layer effect which can occur between ions in solution and the capillary walls. Spectroscopic grade fluorescein free acid was purchased from Aldrich and used without further purification. The phosphate buffer solution was prepared using distilled water and monobasic and dibasic potassium phosphate, both purchased from Aldrich. To fill a 10 μm I.D. capillary with the aqueous fluorophore solution, we inserted it into the end of a 21 gauge syringe needle and sealed it inside of the needle with glue. A 5 cc syringe was then used to suck the solution into the capillary.

We also confined a drop of the same fluorescein solution between a 22 x 22 mm^2 Corning No. 1 coversip and a Gold Seal microscope slide. A clear acrylic shelack was applied to the edges of the coverslip which sealed the coverslip to the microscope slide. We measured the thickness of the solution to be approximately 3 to 8 microns.

The other sample geometry employed was a cylindrical trough with a flat bottom, dimensions 1.3 cm x 2.1 cm. The wall of the trough was made of pyrex glass tubing and the bottom of the trough was a glass microscope slide. For the experiments, the trough was filled approximately two-thirds full with the standard buffered $1x10^{-5}$ fluorescein free acid solution. Gelled samples were prepared by adding 0.5% $wt : wt$ low melting temperature agarose to the fluorescein solution. The purpose of gelling some of the solutions was to determine if there was any convection present in the trough samples which was strong enough to override diffusion as the primary form of mass transport in these experiments. This was accomplished by comparing the trapping rate in gelled versus non-gel samples. Some of the non-gelled samples were vigorously stirred by blowing N_2 gas over the top of the the solution.

The experimental set-up is depicted in Fig. 1. We used lenses to expand and then refocus the beam of an Ion Laser Technology model No. 5490AWC-0 Ar^+ laser, which was then sent to the back port of an
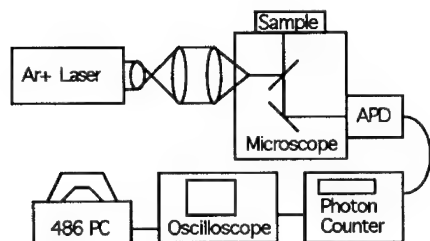
Figure 1: Schematic of experimental set-up.

Olympus IX70 inverted optical microscope configured for epi-illumination, to create a confocal image plane in which the 488 nm Ar^+ laser line was focused to approximately a 2 ± 1 μm diameter and then defocused to approximately a 10 ± 1 μm diameter. The sample sat in the image plane such that the focus of the beam was approximately in the center of the capillary. A high numerical aperture 60X objective, $N.A. = 1.4$, was used with index of refraction matching oil, $n = 1.47$, to minimize aberrations of the beam shape passing through the capillary. The use of this high numerical aperture objective necessitates that the $O.D.$ of the capillaries be $< 200\mu m$. For the coverslip and trough samples, a 40X and 4X objective, respectively, were used in place of the 60X objective. Fluorescence was detected by an EG&G model No. SPCM-200 avalanche photodiode(APD) which has a $100\mu m$ active area diameter. The APD is connected in series to a photon counter (EG&G, Model No. 1109) and a Tektronix model No. TDS 420 digital ocsilloscope. The signal collected from the APD was processed by the photon counter as a logarithmic value of counts/second and then converted to a voltage. This voltage output was grabbed by the digital ocscilloscope in 100 ms time bins. The ocsilloscope stored the output over the time course of the experiment. The data was then acquired from the oscilloscope by a 486 PC computer using the associated TEKDIG software, for storage and analysis.

The Ar^+ laser was used at 20 mW power. Thus the beam had a power density which varied from $6.3\frac{mW}{\mu m^2}$ to $0.03\frac{mW}{\mu m^2}$, approximately, as we defocused the beam from $2 \pm 1\mu m$ to $30\mu m$, for example. In the capillaries, the beam traverses the diameter of the tube. The focus of the beam was expanded such that it filled the entire cross-sectional area of the capillary and thus rendered the trapping kinetics effectively 1-D. In the remaining samples, those created by sandwiching sample solution between two glass slides and those created by filling a trough with regular or gelled sample solution, the confocal beam is directed through the center of the sample, perpendicular to its largest plane. This geometrical arrangement results in effectively 2-D trapping kinetics for those samples.

Data Analysis

Data was collected linearly in time. Since we are interested in determining the power law dependence of the trapping rate, R, as a function of time, and we are measuring the instantaneous population of fluorophores at the trap which is proportional to the rate, we choose to plot the data on a log-log scale. To obtain a properly weighted fit, we wrote a C language code which averaged the linearly collected data over logarithmically increasing time ranges, resulting in 10 data points per decade. The data were then fit with a linear least squares fitting program. No data was "thrown out" using this method.

3   Results

2-D Experiments

Figs. 2a-d show data of intensity vs. time obtained under the different 2-D trapping geometries described in Section 2. All data are plotted on a log-log scale and the axes are the same for all 4 subfigures.
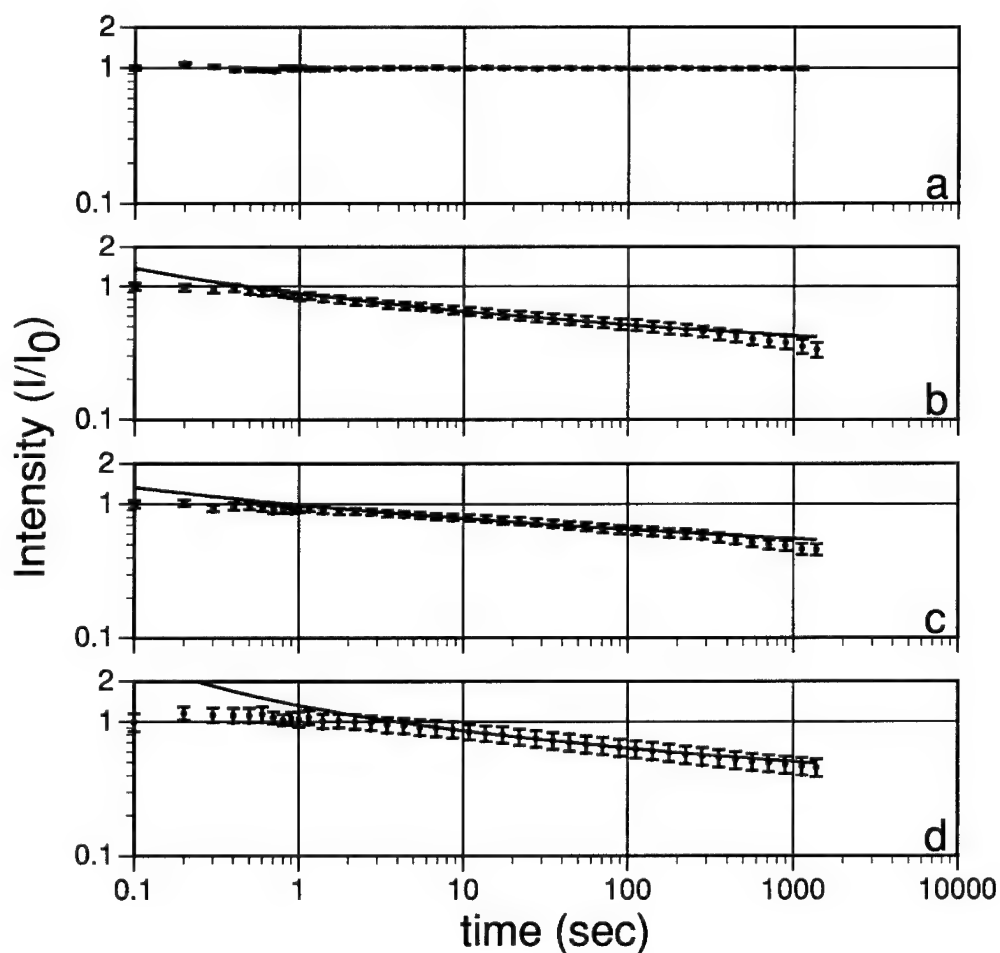
Figure 2: Intensity vs time data for 2-D phototrapping experiments. The subfigures show the normalized, averaged fluorescence intensity obtained from (a) stirred trough samples (6 runs) (b) non-gel trough samples (7 runs), (c) gelled trough samples (6 runs), and (d) coverslip samples (11 runs). See text for explanation of sample types. Points are experimental data. Lines are the theoretical fits (eq. 2).

Fig. 2a is a plot of intensity vs. time acquired when the phototrap was directed through a cylindrical, flat bottomed trough filled with stock fluorescein solution. The solutions were *stirred* over the entire timescale of the experiment. The data points represent the average of 6 independent runs in which the normalized fluorescence intensity at the trap is recorded as a function of time. The slope of the averaged data is 0.0020 ± 0.0004. Fig. 2b is also a

plot of intensity vs. time for data acquired at the phototrap directed through the trough. However, the trough was filled with fluorophore solution which was *not* stirred. The data points are the average of 7 runs and and have a least-squares fit slope of 0.09 ± 0.02. The solid line in Subfigs 2b-d is the function $y = (Const.)/log x$. Fig. 2c is a plot of intensity vs. time of data acquired at the phototrap when it was directed through samples indentical to those used to obtain the data shown in Fig. 2b, *except* that the solution was gelled to assure the absence of convection. The data points are the average of 6 runs and the least squares fit of this data has a slope of 0.13 ± 0.02. Fig. 2d is a plot of intensity vs. time of data that was acquired when the confocal phototrap was directed through a thin layer of fluorophore solution sandwiched between a coverslip and a microscope slide. The data points are the average values from eleven runs and the linear least squares fit of this data has a slope of 0.11 ± 0.02.

Because the geometry of the phototrap is conical and it traverses the short dimension of our samples, perpendicular to the largest plane of the coverslip and trough samples, both of of these samples are effectively 2-D with respect to trapping kinetics. In Figs. 2b-d the fluorescence intensity shows a weak power law dependence in time asymptotically, as can be seen by their fit to the log corrected time solid line curves at late times, plotted in Figs. 2b-d. A weak power law dependence is indicative of a logarithmic correction to a constant time dependence of the trapping rate (see eqn. 2) which is the functional form of the 2-D trapping rate law predicted theoretically [8]. In contrast to the above, the stirred system essentially exhibits the classical, time independent rate law predicted for a trapping reaction which occurs under reaction-limited conditions.

1-D Experiments

Plotted in Fig. 3 is intensity vs. time, measured at a 10 μm confocal light trap in a 10 μm *I.D.* capillary. The fluorescence intensity is measured in arbitrary units and the circles in Fig. 3 are the normalized, averaged values of seven independent runs.
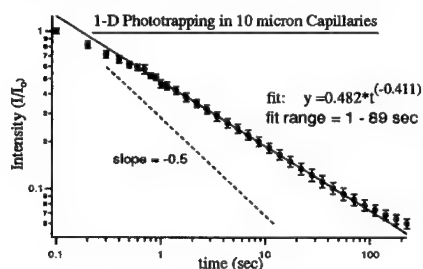

Figure 3: Intensity vs time data for 1-D phototrapping experiments. Points are experimental data. The solid line is the algebraic fit and the dashed line has a slope of -0.5.

The solid line is the linear least squares regression of the data, $y = 0.48 * t^{-0.41}$, fit over the range $t = 1 - 89$ *sec* and the dashed line, for comparison, has a slope of -0.5. The early time data of Fig. 3 show a shallower slope than the longer time data, used to obtain the fit, probably because of the imperfect photobleaching (trapping) of the fluorophore by the focused laser beam trap. The deviation of the last few data points from the fit is probably the result of an experimental limiation(s), i.e. lower S/N at later times. Since we are able

to observe a constant trapping rate in time for the well stirred phototrapping reaction (Fig. 2a), it seems reasonable to attribute the time dependent, $R \sim t^{-0.41}$, trapping rate of the photobleaching reaction observed in the capillaries to dimension-dependent diffusion-limited trapping kinetics. We do not observe the asymptotic $\sim t^{-0.5}$ time dependent trapping rate predicted [6, 7] theoretically for 1-D. This may be because we are unable to extend the timescale on which we take measurments for technical reasons (i.e. background signal begins to dominate, sample movement.) However, we do observe behavior which is substantialy different than that observed in the 2-D systems, for both the stirred and the unstirred samples, and the data exhibits the predicted trend.

References

[1] A. A. Ovchinnikov and Y. G. Zeldovich, *Chem. Phys. B*, **28**, 215 (1978).

[2] P. G. de Gennes, *Chem. R. Acad. Sci. Paris* **296**, 881 (1983).

[3] K. Kang and S. Redner, *Phys. Rev. Lett.* **52**, 55 (1984).

[4] P. Argyrakis and R. Kopelman, *J. Theor. Biol.* **73**, 205 (1978).

[5] R. Kopelman, *Science* **41**, 1620 (1988).

[6] G. Weiss, R. Kopelman and S. Havlin, *Phys. Rev. A* **39** 466 (1989).

[7] H. Taitelbaum, R. Kopelman, G. Weiss, S. Havlin, *Phys. Rev. A* **41** 3116 (1990).

[8] S. Havlin, H. Larralde, R. Kopelman, G.H. Weiss, *Physica A* **169** 337 (1990).

[9] R. Schoonover, Ph.D. Thesis, University of Michigan, Ann Arbor (1993).

[10] Molecular Dynamics in Restricted Geometries, J. Klafter and J.M. Drake, eds., John Wiley and Sons (1989).

[11] R. Kopelman, S.J. Parus, J. Prasad, *Chem. Phys.* **128** 209 (1988).

[12] R. Kopelman, Z.Y. Shi, C.S. Li, *J. Lumin.* **48 and 49** 143 (1991).

[13] Non-equilibrium Statistical Mechanics in One Dimension, V. Privman, ed., Cambridge University Press (1996).

[14] J. Prasad and R. Kopelman, *J. Phys. Chem.* **91** 265 (1987).

TEMPERATURE-DEPENDENT DYNAMICS OF MICROCONFINED CS$_2$

B. J. LOUGHNANE, R. A. FARRER, L. A. DESCHENES and J. T. FOURKAS
Eugene F. Merkert Chemistry Center, Boston College, Chestnut Hill, MA 02167

ABSTRACT

Femtosecond optical-heterodyne detected Raman-induced Kerr effect spectroscopy (OHD-RIKES) has been used to study the reorientational dynamics of CS$_2$ in microporous glasses over a wide range of temperatures. Microconfinement is shown to affect the behavior of the liquid at all the temperature studied. The results are interpreted in terms of a two-state model of the confined liquid.

INTRODUCTION

Microconfined liquids are ubiquitous in nature and are of importance in many areas of technology, and as such have received considerable attention in recent years. Microconfinement can alter the dynamics of liquids considerably, due to geometrical constraints, large surface to volume ratios, and correspondingly large interactions with the surfaces of the confining material. A number of experimental techniques have been employed in an effort to evaluate the influence of these factors on dynamics, including NMR [1,2], Raman scattering [3,4], dielectric spectroscopy [5], neutron scattering [6] and ultrafast spectroscopy [7,8].

Based on evidence from a number of these techniques, it has been suggested that there are two distinct populations of liquid molecules within the pores [1,2,4,7]. Molecules in the centers of the pores have the same dynamics as molecules in the bulk liquid, whereas molecules at the surfaces of the pores experience a greater effective viscosity than in the bulk. The strength of this effect and the thickness of the altered layer depend on the relative polarity and hydrogen-bonding capability of the liquid and of the confining surface. For instance, ultrafast spectroscopic techniques have been used to study a non-wetting liquid (CS$_2$) and a wetting liquid (nitrobenzene) in pores with a diameter of 44 Å [7]. In both liquids an exponential decay was observed whose time constant matched that of the bulk liquid. However, the nitrobenzene data exhibited a second, slower decay, which was interpreted as arising from the surface layer [7].

The general features of the two-state model for microconfined liquids have been supported by a diverse array of experimental techniques. For instance, Jonas and co-workers have used NMR to study the effects of confinement on the spin-lattice relaxation time (T$_1$) of a number of deuterated liquids [1,2]. Since T$_1$ is inversely proportional to (and generally much longer than) the orientational correlation time, the NMR experiments are analyzed under the assumption that each molecule samples the bulk-like and surface regions statistically in a time much shorter than T$_1$. The effective T$_1$ for each molecule is thus given by the population-weighted average of the spin-lattice relaxation times for each environment. This so-called two-state fast-exchange (TSFE) model has been successful in describing the relaxation behavior of a wide variety of liquids [1,2].

Wallen *et al.* have recently used Raman spectroscopy to examine the behavior of CS$_2$ confined in pores of different sizes [4]. In contrast to previous Raman [3] and ultrafast [7] spectroscopic studies, Wallen *et al.* found the reorientational rate of CS$_2$ to be dependent on pore size, and were able to analyze their data successfully in terms of the TSFE model [4]. Reorientational motion affects the Raman linewidths directly, which implies that exchange between the surface and bulk-like populations of molecules must be faster than the reorientational times for the TSFE

model to be valid for Raman data. Since the reorientational time constant of bulk CS_2 at room temperature is less than 2 ps, it is surprising that the TSFE model does such a good job of explaining the data. To further investigate the dynamics of this liquid under microconfinement, we have used OHD-RIKES to study its temperature-dependent behavior in pores 24 Å in diameter.

EXPERIMENT

Sol-gel glasses were prepared from tetraethyl orthosilicate following standard procedures for acid-catalyzed hydrolysis [9]. Small pore sizes were achieved by adding a minimal concentration of base after the hydrolysis reaction. The gels were allowed to dehydrate for one month following preparation, after which they were cured in a furnace whose temperature was ramped to 600 °C over a period of several days. Nitrogen BET analysis of several samples gave an average pore diameter of ≈24Å, with a variance of approximately 10 Å in the pores size for a single sample and with a sample-to-sample variance of 3-4 Å in the average diameter. Small-angle neutron scattering yielded similar results, with an average pore size of approximately 21 Å. The monolithic samples, which are approximately 8 mm in diameter, were sanded down to a thickness of 2-3 mm and then polished to optical quality. After polishing, the samples were cleaned and baked a second time to remove any adsorbed water. Upon removal from the oven, the sol-gel glasses were filled immediately by immersion in CS_2 for a period of 24 hours. The liquid was distilled and filtered before use.

The sample is placed in a cell that is specially constructed for use in a constant-flow liquid-nitrogen-cooled vacuum cryostat. The cell consists of a cylindrical Teflon ring that is clamped between two glass windows in a brass sample holder. Before use, the cell is assembled and heated to a high enough temperature that the Teflon becomes soft and conforms to the surfaces of the windows. To load the cell, the rear window is removed and the microporous glass sample, which fits snugly inside the cylinder, is pressed up against the front window. Extra liquid is added, and then the cell is reassembled and attached to the cold finger of the cryostat. To ensure the quality of the seal at low temperatures, the cell holder is clamped with spring-loaded screws.

OHD-RIKES has been described in detail elsewhere [10], and so we will only briefly summarize the technique. Our experiments are performed using a Ti:sapphire oscillator, which produces nearly transform-limited 30-fs pulses with a center wavelength of approximately 800 nm. The output of the laser is split to produce two pulses: a pump pulse that is polarized vertically and a weak probe pulse that is polarized at 45°. The two beams intersect in the sample cell, either in the microporous glass or the bulk liquid depending on the position of the cryostat. The pump beam creates a transient birefringence in the sample by causing a small net alignment of the anisotropically polarizable liquid molecules. After the sample, the probe beam is incident on an analyzer polarizer set at -45°, such that any depolarization of the probe pulse can be detected. To increase the detection sensitivity, before the sample the probe beam passes through a quarter-wave plate whose fast axis is slightly non-collinear with the probe polarization, thereby creating a heterodyne pulse that is 90° out of phase with the probe pulse. By monitoring the intensity of the depolarized light as a function of the time delay between the two pulses, the reorientational diffusion of the liquid can be observed directly. The pump and probe beams are mechanically chopped at different frequencies, and the leakage through the analyzer polarizer is detected at the sum frequency by a photodiode and lock-in amplifier. At each temperature, data were obtained for both the microconfined and bulk liquid out to long enough delay times to accurately determine the reorientational diffusion times. Data were taken at a wide range of temperatures (165 K to 290 K), and the temperature was held constant to within a fraction of a degree for each data set.

264

RESULTS

At all temperatures, the bulk CS_2 sample exhibited single-exponential decays at delay times longer than five to ten picoseconds (at shorter times, low-frequency Raman scattering contributes to the signal). In contrast, the microconfined sample exhibited non-exponential decays at all temperatures. With the idea of testing the two-state model, the data from the microconfined liquid were fit to the sum of two exponentials. The decay constant for one exponential was constrained to match that of the bulk liquid, leaving one decay constant and two amplitudes as adjustable parameters. Excellent fits were obtained in each case. Representative data, obtained from bulk and microconfined CS_2 at 165 K, are shown in Figure 1 along with the fits. The differences in the decays are particularly evident at times greater than 20 ps.

The data are summarized in Table 1 and Figure 2. The bulk-like decay time is almost a factor of three faster than the surface decay time at room temperature, and increases to a factor of almost four faster as the temperature is decreased to 165 K. In terms of the amplitudes of the two exponentials, the bulk-like molecules are always the major contributor to the decay. However, because the alignment that can be created is proportional to the viscosity, in the absence of exchange the contribution of each type of molecule to the signal is given by the population of that type of molecule divided by its reorientational decay time [11]. Thus, an advantage of OHD-RIKES is that the relative populations of bulk-like and surface molecules can be extracted directly from the data by multiplying the ratio of the amplitudes of the two exponentials by the ratio of their decay times. The results of this analysis are given in Table 1. While the majority of the molecules are bulk-like at 290 K, at 165 K these molecules are slightly in the minority.
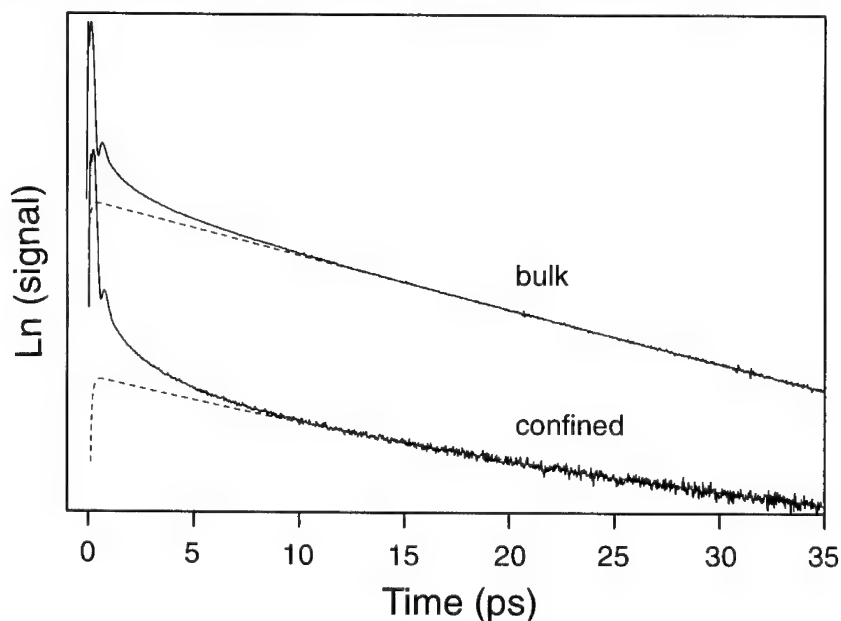
Figure 1. Logarithm of OHD-RIKES data in bulk CS_2 (top trace) and microconfined CS_2 (bottom trace) at 165 K. Dashed lines are fits of the long-time portion of the data (see text).

Table 1. Parameters from fits of the microconfined CS_2 data.

Temperature (K)	Bulk-Like Decay Time (ps)	Surface Decay Time (ps)	Bulk/Surface Amplitude Ratio	Bulk/Surface Population Ratio
165	11.2	43.1	2.56	0.67
175	8.88	33.5	3.00	0.80
190	6.71	23.2	3.13	0.91
210	4.83	15.8	3.57	1.09
230	3.56	11.5	4.13	1.28
250	2.76	8.2	4.52	1.52
270	2.23	6.5	4.81	1.65
290	1.84	5.2	5.17	1.83
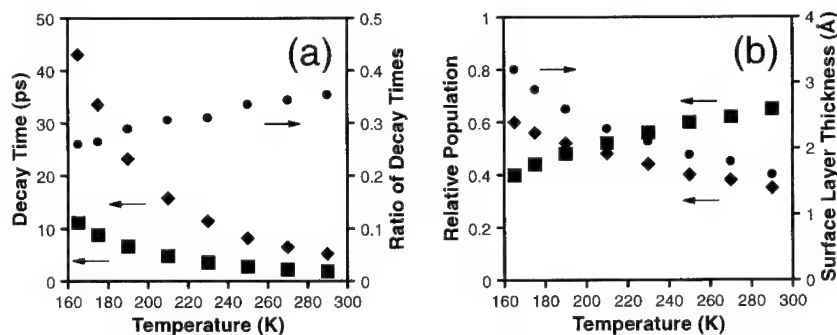
Figure 2. Results of analysis of CS_2 data. (a) Reorientational relaxation times for the bulk-like (squares) and surface molecules (diamonds) and ratio of the relaxation times (circles); (b) Relative populations of the bulk-like (squares) and surface (diamonds) molecules and thickness of the surface layer (circles).

Our data lend support to the idea that there are two distinct populations of molecules in the pores, which is in accord with the results of [4] but in apparent disagreement with those of [3] and [7]. However, although the data of [4] were analyzed using the TSFE model, our data indicate unambiguously that any exchange between surface and bulk-like molecules is not fast compared to reorientational diffusion. Our analysis yields a surface decay time of 5.2 ps at 290 K, as opposed to the estimate of 3.3 ps obtained by applying the TSFE model to the Raman data [4].

The relative populations of the surface and bulk-like molecules can be used to estimate the thickness of the surface layer. By assuming that the pores are spherical, we can calculate the maximum thickness of this layer (see Figure 2b). We find that the thickness of this layer is 1.6 Å at 290 K, and increases to 3.2 Å at 165 K. Both of these distances are smaller than the molecular diameter of CS_2, which was estimated to be the thickness of the surface layer in [4]. There are several possible explanations for this result: (1) Only a fraction of the surface molecules in each pore experience a higher effective viscosity; (2) Only those molecules in the smallest pores in the distribution or in the throats between pores experience a higher effective viscosity; and (3) The effects of exchange are not negligible. An investigation of the effects of pore size will help to differentiate among these possibilities. It is also possible that the molecules at the surfaces experience a reduced polarizability anisotropy, leading to an underestimate of the surface population. This effect would be most likely to occur in the neighborhood of charged surface groups, and so should be strongly affected by surface modification of the pores. We believe that the fact

that Wallen *et al.* saw little change in their Raman data after hydrophobizing their pores severely limits the possible magnitude of any such effect. The relatively small difference in activation energies for reorientation between the surface and bulk-like molecules (*vide infra*) also supports this view.

Given the measured decay times and an estimate of the surface layer thickness, we can calculate the decay rate predicted by the TSFE model. At 290 K we predict a reorientational time of 2.2 ps, which is significantly shorter than the reorientational time of 2.7 ps measured in similar pores in [4]. If we assume that exchange is negligible and that the thickness of the surface layer is independent of pore size, we can also compare our results to those of previous ultrafast spectroscopic experiments [7]. Using our layer thickness, we find that four out of five molecules in pores of a 44-Å diameter are bulk-like. Assuming that the surface reorientational time is also independent of pore size, we would estimate that the contribution of the surface molecules to the signal in these pores would be less than one part in twelve, which may account for the conclusion of [7] that the reorientational dynamics of CS_2 are unaffected by confinement in pores of this size.

The temperature dependence of the reorientational rates can be used to find the effective activation energy for reorientation in the bulk-like and surface layers in the pores. As shown in Figure 3, the data for both types of molecules yield linear Arrhenius plots. The activation energies for reorientation derived for the bulk-like and surface layers are 1.37 and 1.61 Kcal/mole, respectively. The 0.24 Kcal/mole difference in activation energy between the two populations is relatively modest, suggesting that the strength of the interactions between the surface and the liquid is not particularly strong, as one would expect for a non-wetting liquid such as CS_2. In contrast, for acetonitrile, which does wet the surfaces of the pores, Zhang and Jonas have estimated a 1.14 Kcal/mole difference in the activation energy for reorientation between the bulk-like and surface layers [2].
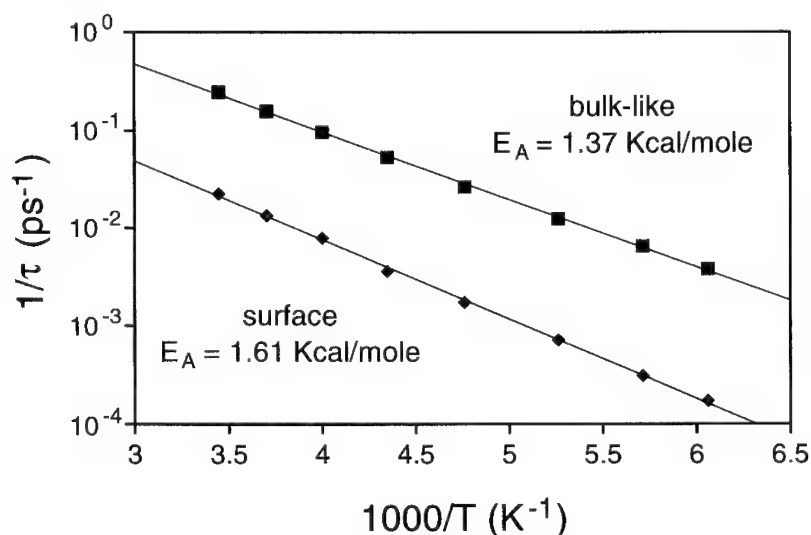
Figure 3. Arrhenius plot of reorientational rates of bulk-like and surface CS_2 molecules. Solid lines are linear regression fits to the data.

CONCLUSIONS

We have studied the dynamics of CS_2 confined in 24 Å pores at temperatures ranging from 165 K to 290 K using OHD-RIKES. The data at all temperatures are consistent with a two-state model of the confined liquid, in which the liquid in the centers of the pores is bulk-like and the liquid at the surfaces exhibits a higher effective viscosity. Our experimental technique is able to provide quantitative information on the relative populations in the two states. At all temperatures, we find that only a fraction of the molecules at the surface have properties that differ from those of the bulk-like molecules. Our data are not consistent with the TSFE model, but it remains possible that exchange at an intermediate rate affects our results. Further experiments are in progress to help resolve these issues.

ACKNOWLEDGMENTS

REFERENCES

1. G. Liu, Y. Li and J. Jonas, J. Chem. Phys. **95,** p. 6892 (1991).

2. J. Zhang and J. Jonas, J. Phys. Chem. **97,** p. 8812 (1993).

3. L. Nikiel, B. Hopkins and T. W. Zerda, J. Phys. Chem. **94,** p. 7458 (1990).

4. S. L. Wallen, L. Nikiel, J. Yi and J. Jonas, J. Phys. Chem. **99,** p. 15421 (1995).

5. P. Pissis, J. Laudat, D. Daoukaki and A. Kyritsis, J. Non-Cryst. Solids **171,** p. 201 (1994).

6. M.-C. Bellisent-Funel, J. Lal and L. Bosio, J. Chem. Phys. **98,** p. 4246 (1993).

7. J. Warnock, D. D. Awschalom and M. W. Schafer, Phys. Rev. B **34,** p. 475 (1986).

8. F. W. Deeg and G. Schwalb in <u>Dynamics in Small Confining Systems II</u>, edited by J. M. Drake, J. Klafter, R. Kopelman and S. M. Troian (Mater. Res. Soc. Proc. 366, Pittsburgh, PA 1995), p. 213-224.

9. C. Jeffrey Brinker and George W. Scherer, <u>Sol-Gel Science: The Physics and Chemistry of Sol-Gel Processing</u>, Academic Press, San Diego, 1990.

10. Dale McMorrow and William T. Lotshaw, J. Phys. Chem. **95,** p. 10395 (1991).

11. Yong-Xin Yan and K. A. Nelson, J. Chem. Phys. **87,** p. 6240 (1987).

MOLECULAR CONFIGURATIONS AND SOLVATION FORCES OF CONFINED *i*-TETRADECANE

JEE-CHING WANG and KRISTEN A. FICHTHORN
Department of Chemical Engineering, The Pennsylvania State University, University Park, PA 16802

ABSTRACT

This work is a molecular-dynamics simulation study of the influence of chain branching on the molecular configuration in confined tetradecane thin films. Simulations of layered interfacial films of *n*- and *i*-tetradecane on Pt(111) show, in contrast to experiments, that a side methyl group does not impart sufficient asymmetry to alter the solvation force law from oscillatory to non-oscillatory. Based on previous experimental findings, a novel vertical structure resembling a self-assembled monolayer, is proposed for confined, long-chain iso-alkanes. Simulations show that *i*-tetradecane in this structure is stable over the time scales that can be probed by molecular dynamics and that vertical films have a lower energy per molecule than layered films. With this structure, many experimental features, including the non-oscillatory solvation forces, of confined iso-alkanes are explainable and will be discussed in this paper.

INTRODUCTION

A good understanding of the structural and dynamical properties of nanoscopically confined fluids is important in a variety of fields, such as boundary lubrication (nanotribology), fluid flow through small, confining areas (nanorheology) such as those in microporous solids and microelectromechanical devices, and the stability of colloidal systems. When a fluid is confined in a highly restricted space, its properties become quantitatively and qualitatively different from those of the unconstrained bulk. One interesting feature associated with nanoscale fluid confinement is the appearance of "structural" or "solvation" forces between the two confining surfaces. In experimental studies with the surface force apparatus (SFA) it is found that when the confined fluid consists of spherical molecules or symmetric chain molecules, the solvation forces are oscillatory with surface separation, varying between attractive and repulsive over a period approximately equal to a molecular diameter [1,2,4]. In contrast, non-oscillatory solvation forces are observed for asymmetric chain molecules with methyl side branches [3,4]. Continuum theories, such as the DLVO theory, cannot describe these phenomena [1-4]. It is believed that solvation forces are a signature of molecular ordering induced by the confining surfaces. However, this hypothesis cannot be directly verified with current experimental methods.

Computer simulation methods, such as Monte Carlo (MC) and molecular dynamics (MD), have proven to be a useful tool for probing the origins of solvation forces. Recent computer simulations [5-11] have successfully reproduced some of the results of experimental SFA studies and provided an explanation for the oscillatory solvation force laws. These studies show that confining walls can induce spherical or symmetric molecules near them to lie parallel and form quasi-discrete layers over a range of several molecular diameters. The layered molecules give a decaying, oscillatory density profile with a periodicity close to the mean molecular diameter. At separations corresponding to an integer number of layers, the system is near mechanical equilibrium with a zero solvation force. When the surface separation is reduced, the number of confined molecules changes in a stepwise fashion, such that a whole layer of molecules is squeezed out, during which the film undergoes a sort of solid-liquid transition and exerts repulsive as well as attractive forces on the confining walls. From the results of simulation studies of various confined liquids, the consensus has emerged that if confined molecules are able to be ordered into discrete layers, decaying oscillatory density profiles result and, consequently, oscillatory solvation forces will be observed [5-11].

Based on these findings, it has been suggested that confined asymmetric molecules, which do not show oscillations in solvation forces, take on a structure very different from the layered structure of spherical or symmetric chain molecules. However, this structure has yet to be identified. To our knowledge, very few efforts have been made to clarify this issue. Padilla *et al.*

269

[12] studied the density profiles of 4-propyl-heptane and 5-butyl-nonane confined between two solid surfaces and observed layered structures, which are not consistent with non-oscillatory solvation forces. The most relevant work was done by Wang *et al.* [11], who probed the structure and solvation forces in confined *n*-octane and *i*-octane films. They observed that *i*-octane exhibits a layered structure and its solvation force profile shows oscillations as strong as those seen for *n*-octane films. Thus, their findings are also inconsistent with the experimental results.

In this paper, we use MD simulations to probe the origins of non-oscillatory solvation forces in confined *i*-tetradecane films. Similarly to Padilla [12] and Wang [11], we find that if *i*-tetradecane molecules are initially placed in a random orientation near the surface, a layered structure results which is nearly identical to the structure formed for layered *n*-tetradecane. Since studies [11] have shown that this structure cannot explain the non-oscillatory solvation forces in confined iso-alkane films, we have attempted to identify feasible, alternative structures. One possibility is that interfacial *i*-tetradecane films may have a structure similar to alkanethiol self-assembled monolayers (SAMs) on Au(111) [13], in which the molecules adsorb "vertically" with their long, alkyl tails oriented normal to the surface. In this conformation, we expect the branched, isopropyl ends of the molecules to reside in close proximity to the surface and provide extra attraction to stabilize the vertical structure, thus playing a role similar to the thiol end, which chemisorbs to the surface atoms in alkanethiol films on Au(111). A careful review of experimental studies [1-4,14] related to confined *n*- and *i*-alkane films indicates that experimental results could be consistent with a vertical structure for long-chain iso-alkanes. Molecular-dynamics (MD) simulations of layered and vertical *i*-tetradecane films show that the vertical structure is stable over the time scales that can be probed by these simulations and that vertical films have a lower energy per molecule than layered films.

MODEL AND METHODS

Our model systems in this study are free-standing films of both *n*-tetradecane and *i*-tetradecane on a model Pt(111) surface. Since detailed descriptions of our models can be found elsewhere [15], only a brief summary is given here. The surface is represented by a five-layer slab with 22×22 atoms in each layer. In most of our studies, the surface atoms were rigidly fixed to their bulk positions. The methyl and methylene groups in the alkanes were modeled as united atoms [15,16] with interaction centers placed at the positions of the C atoms. Each C-C bond length was constrained to its equilibrium liquid-phase value by applying the SHAKE algorithm [17]. The internal C-C-C bond bending and C-C-C-C torsional motions were also considered by using a simple harmonic potential for the former and a 6-term cosine polynomial potential for the latter [15,16]. We model the collective motions of the five united atoms involved in the iso portion of *i*-tetradecane with four bond bending angles and two torsional angles. The torsional potentials for the iso group were parameterized to reproduce Jorgensen's potential for the internal rotation about the branching site of iso-pentane [11,18]. The Lennard-Jones 12-6 potential was employed to describe the interactions between united atoms in different molecules, or in the same molecule but more than three bonds apart [15,16]. The same type of potential was also used for the Pt-alkane interactions. The dynamical behavior of these model interfacial systems was modeled using MD. The Verlet algorithm [19] was used with a time step of 2 fs to integrate the equations of motion.

We created two types of alkane interfacial films: "horizontal", layered films and "vertical" films with a SAM-like structure. Horizontal films were created by randomly dropping molecules onto the solid substrate and subsequently rescaling the molecular velocities to achieve equilibrium at a temperature of 350K. The horizontal films consisted of 160 *i*-tetradecane or *n*-tetradecane molecules, which are enough to comprise about four interfacial layers. Vertical interfacial films were created by employing an initial condition in which the alkyl tails were oriented perpendicular to the surface. For the *i*-tetradecane films, simulations were initiated with the iso ends of the molecules in close proximity to the surface. Initial velocities in this configuration were selected from a Gaussian distribution and this film was equilibrated to 300K via velocity rescaling. Vertical films with two different interfacial densities were considered. With 121 molecules initially forming a single-layer, vertical film, a density of 0.8 g/cm³ is achieved, which is close to the liquid bulk densities of *n*-tetradecane and *i*-tetradecane [20]. Denser films, consisting of 144 molecules in a single, vertical layer, were also considered. Simulations of the films were run to times greater than 1 ns, while a variety of structural properties were monitored, as discussed below.

RESULTS AND DISCUSSION

Figure 1 shows the segment density profiles for horizontal films of both *n*- and *i*-tetradecane. It is clear that the solid surface imposes a similar layering effect on both alkanes, although it is less pronounced for *i*-tetradecane. The density profile of *n*-tetradecane is comparable to those observed by Xia *et al.* [21] for interfacial films of *n*-hexadecane on Au(100) at the same temperature. Our results also show very good consistency with those observed by Wang *et al.* [11], who found that confined *i*-octane shows much the same layered density profiles, only with its oscillations slightly weaker than those of confined *n*-octane. Similarly to Xia *et al.* [21], we observed that the solid surface induces an in-plane molecular ordering, which reflects the surface geometry. We find that *i*-tetradecane exhibits less in-plane ordering than *n*-tetradecane. Calculations of the molar fraction of the iso group as a function of distance were carried out to see how the side branches distribute under the influence of solid surface. As shown in Fig. 2, we find that the iso groups are predominant in the low-density regions, such as the liquid-vacuum interface and the inter-layer regions, which is also observed by Wang *et al.* [11] for confined *i*-octane. However, Wang *et al.* showed that, in contrast to experiments, the layered *i*-octane films yielded oscillatory solvation-force profiles, which are very similar to those of *n*-octane.

Since the layered structure does not seem capable of explaining non-oscillatory solvation forces for confined *i*-alkanes, we have considered the possibility that a different structure exists. Specifically, we consider the possibility that confined *i*-tetradecane films may form a vertical structure similar to that formed by alkanethiol SAMs. In this structure, molecules are "anchored" to the surface by their isopropyl ends and stabilized in the vertical structure by interactions between the alkyl tails. A review of relevant literature indicates that many experimental features of confined *i*-alkane films are consistent with the vertical structure. For example, when *i*-nonadecane thin films are confined between mica surfaces, the final, repulsive wall in the solvation-force profile occurs at a distance of about 2 nm. In contrast, the repulsive wall in the solvation-force profile for *n*-alkanes confined between mica surfaces occurs at about 5 Å. The larger repulsive-wall distance for *i*-nonadecane could originate from a vertical or quasi-SAM film structure. From viscosity measurements of long *i*-alkanes confined between two mica surfaces, Israelachvili and co-workers found evidence that a thick layer of molecules is effectively pinned at each surface [4]. No evidence for this phenomenon was seen for *n*-alkanes [4]. When nanoscopically confined *i*-alkanes are sheared, a long induction time occurs, which is significantly longer than that seen for *n*-alkanes, before steady-state, slip-stick motion is observed [14]. In contrast to the behavior seen for *n*-alkanes, when sheared *i*-alkanes reach the steady-state slip-stick regime, a significant reduction in the film thickness occurs. These observations are both consistent with the existence of
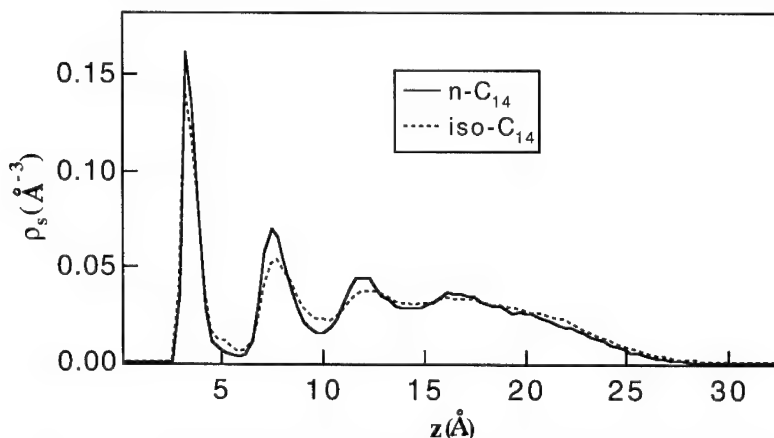

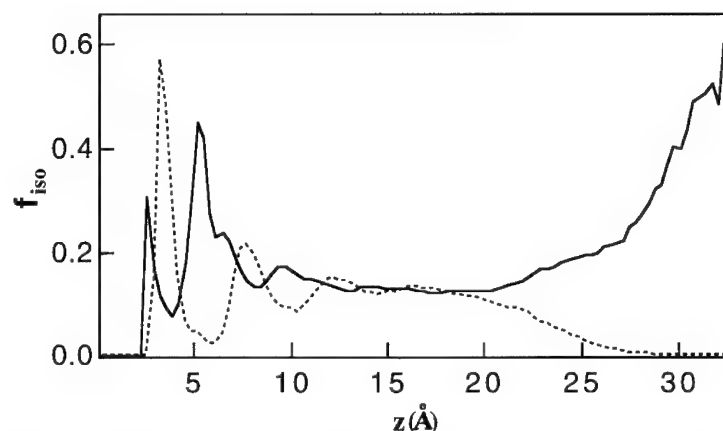Figure. 1. Density profiles of layered *n*-tetradecane and layered *i*-tetradecane on Pt(111) at 350K.

Figure 2. Mole fraction of the iso group in *i*-tetradecane as a function of distance from the surface. The superimposed dashed curve is the density profile of *i*-tetradecane.

an extended interfacial structure for long, confined *i*-alkanes, which breaks down under shear.

Further evidence for a vertical structure can be been in a set of SFA experiments by Israelachvili *et al.* of a series of *i*-alkanes confined between mica surfaces at room temperature [3]. Their results indicate that only molecules longer than *i*-decane exhibit non-oscillatory solvation forces— shorter molecules exhibit solvation-force oscillations. Since we expect alkyl tail interactions to play a role in stabilizing the vertical structure, the transformation of a vertical structure to a layered structure for shorter molecules (as evidenced by oscillatory solvation forces for shorter molecules) is consistent with our picture. Finally, evidence that a vertically oriented interfacial structure can lead to unexpected solvation forces has been seen in the behavior of silica particles grated with octadecyl chains and dispersed in long-chain alkane fluids [22]. These particles exhibit an unexpected, non-van der Waal attraction, which causes their flocculation. It has been speculated that the alkane solvent molecules become aligned into a vertical crystalline state at each surface and that attractive bridging forces mediated by alkanes higher than decane are responsible for the flocculation [4,22].

Thus, although the existence of a vertically aligned interfacial *i*-alkane layer seems to be possible, direct evidence is still needed to justify the possibility of this configuration. As we saw above (*cf.*, Fig. 1) and as has been seen in other studies [11], *i*-alkanes which are initially randomly oriented at a solid surface assume the horizontal, layered structure. It is possible that over times longer than those that can be probed by MD, the *i*-alkanes will reorient themselves into the vertical configuration. However, since it seems that this evolution would require an inordinate amount of computer time, we have chosen an alternate route to determine the tenability of the vertical conformation. Here we begin our MD simulations with molecules oriented in the vertical configuration and we examine the stability of this structure. We aim to show that (1) the vertical structure is stable under experimental temperatures; and (2) the vertical structure is feasible for *i*-alkanes, but not for *n*-alkanes.

As discussed above, one variable in our investigation is the density of the vertical films. Langmuir monolayers form SAM-like structures with surface-area densities between 21 $Å^2$/molecule and ~30 $Å^2$/molecule [23]. Tetradecane films with densities close to the liquid-phase value of ~0.8 g/cm^3 [20] and surface-area densities of 27 $Å^2$/molecule (lower density films) were the subject of our first set of investigations. Since it is reasonable to expect a higher-density layer near the surface than in the liquid phase, films with densities of 22 $Å^2$/molecule (higher density films) were also investigated. Simulations were run for lower density films of both *n*-tetradecane and *i*-tetradecane at 300K. We find that this density is too low to sustain a completely vertically oriented film of either *n*- or *i*- tetradecane. The collapse of the vertical structure is somewhat

revealing. After 640 ps, we find that ~70% of the *i*-tetradecane molecules retain their vertical orientation and initial position — the remaining 30% of the molecules may lay horizontally, with their alkyl tails parallel to the surface, or may displace towards the vacuum. In contrast only 57% of the *n*-tetradecane molecules remain vertical. The more sluggish dynamics of *i*-tetradecane reflect the stronger interaction of the isopropyl end of the molecule with the surface and the greater vertical stability of *i*-tetradecane. The higher density films showed greater vertical stability than the lower density films. After 1.1 ns, both *n*- and *i*-tetradecane films remain vertically oriented. Figure 3 shows density profiles of higher-density *i*-tetradecane films after 400 ps and 1.1 ns of simulation time. The bumpy, segment-density profile shown in Fig. 3(b) is indicative of the vertical structure and is virtually unchanged over the course of the simulation. The center-of-mass density profile [*cf.*, Fig 3(a)] is more revealing and shows that, over the course of a simulation, a few molecules have climbed on top of the vertical structure and one or two molecules have laid down on the surface. Since both *n*- and *i*-tetradecane films remained essentially vertical, it is difficult to make conclusions regarding their relative vertical stabilities. Instead, we have compared the average energies per molecule in layered *i*-tetradecane films to those in vertical films. These calculations show that the average potential energy per molecule is -59 kJ/mol for vertical *i*-tetradecane films, while it is -42 kJ/mol for layered films at 300K. Since the vertical structure is energetically favored, we expect it to be predominant at sufficiently low temperatures. Accurate free-energy calculations could unambiguously indicate whether the vertical conformation is favored at room temperature. Thus, although we cannot unequivocally confirm the predominance of the vertical configuration, we cannot rule it out. Another possibility is that confined *i*-tetradecane films have coexistence between the horizontal and vertical structures. Islands with the vertical structure may produce enough disorder to yield non-oscillatory solvation forces. Future studies in our group will examine the solvation-force profiles of vertical *i*-tetradecane films to examine their consistency with experiment.

CONCLUSIONS

We have investigated the structure of interfacial films of *n*-and *i*-tetradecane on a Pt(111) surface. Our studies of layered tetradecane films yield density profiles in agreement with those seen in earlier studies [5-12]. We found that the side branches of *i*-tetradecane dominate the interlayer regions and the vacuum-liquid interface. In contrast to experimental findings, one single methyl branch introduced into the confined *n*-alkane system does not bring enough asymmetry to eliminate layering and yield non-oscillatory salvation forces [11]. A novel vertical configuration based on suggestive experimental findings is thus proposed. Our simulation results show that this structure is stable and energetically favored over the layered structure. Future studies in our group will focus on quantifying the ramifications of the vertical structure for the solvation forces of confined *i*-tetradecane films.
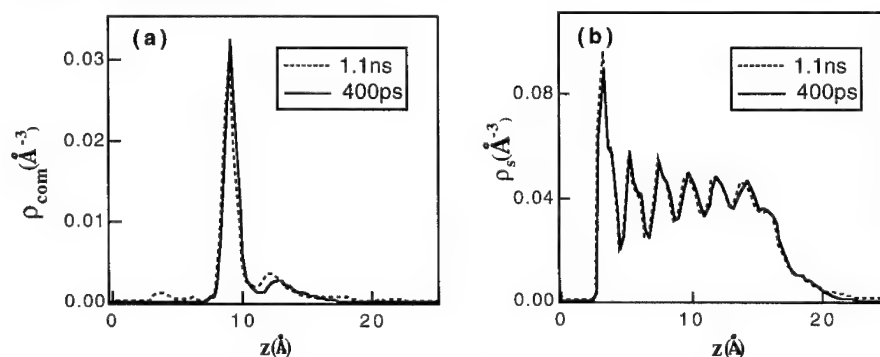

Figure 3. The center-of-mass distributions (a) and the density profiles (b) of higher density *i*-tetradecance films on Pt(111).

REFERENCES

1. R. G. Horn and J. N. Israelachvili, J. Chem. Phys. **75**, p. 1,400 (1981).

2. H. K. Christenson, D. W. R. Gruen, R. G. Horn and J. N. Israelachvili, J. Chem. Phys. **87**, p. 1,834 (1987).

3. J. N. Israelachvili, S. J. Kott amd M. L. Gee, Macromolecules **22**, p. 4,247 (1989).

4. M. L. Gee and J. N. Israelachvili, J. Chem. Soc. Faraday Trans. **86**, p. 4,049 (1990).

5. I. K. Snook and W. V. Megen, J. Chem. Phys. **72**, p. 2,907 (1980).

6. J. J. Magda, M. Tirrell and H. T. Davis, J. Chem. Phys. **83**, p. 1,888 (1985).

7. M. Schoen, D. J. Diestler and J. H. Cushman, J. Chem. Phys. **87**, p. 5,464 (1987).

8. X. L. Chu, A. D. Nikolov and D. T. Wasan, Langmuir **10**, p. 4,403 (1994).

9. A. Yethiraj, , J. Chem. Phys. **101**, p. 2,489 (1994).

10. S. A. Somer and H. T. Davis, J. Chem. Phys. **96**, p. 5,389 (1992).

11. (a) Y. Wang, K. Hill and J. G. Harris, J. Chem. Phys. **100**, p. 3,276 (1993). (b) Y. Wang, K. Hill and J. G. Harris, Langmuir **9**, p. 1,983 (1993). (c) Y. Wang, K. Hill and J. G. Harris, J. Phys. Chem. **97**, p. 9,013 (1993).

12. (a) P. Padilla, J. Chem. Phys. **103**, p. 2,517 (1995). (b) P. Padilla and S. Toxvaerd, J. Chem. Phys. **101**, p. 1,490 (1994).

13. J. Hautman and M. L. Klein, J. Chem. Phys. **91**, p. 4,994 (1989).

14. . M. L. Gee, P. M. McGuiggan and J. N. Israelachvili, J. Chem. Phys. **93**, p. 1,895 (1987).

15. D. Huang, Y. Chen and K. A. Fichthorn, J. Chem. Phys. **101**, p. 11,021 (1994).

16. S. Leggetter and D. J. Tildesley, Mol. Phys. **68**, p. 520 (1989).

17. J. P. Ryckaert, G. Ciccotti and H. T. C. Berendsen, J. Comp. Chem. **23**, p. 327 (1977).

18. W. L. Jorgensen, J. D. Madura and C. J. Swenson, J. Am. Chem. Soc. **106**, p. 6,638 (1984).

19. L. Verlet, Phys. Rev. **159**, p. 98 (1967).

20. S. T. Cui, S. A. Gupta, P. T. Cummings and H. D. Cochran, J. Chem. Phys. **105**, p. 1,214 (1996).

21. T. K. Xia, J. Ouyang, M. W. Ribarsky and U. Landman, Phys. Rev. Lett. **69**, p. 1,967 (1992).

22. J. W. Jansen, C. G. De Kruif and A. Vrij, J. Coll. Int. Sci. **114**, p. 481 (1986).

23. J. P. Bareman, G. Cardini and M. L. Klein, Phys. Rev. Lett. **60**, p. 2,152 (1988).

ELECTRON ESCAPE FROM A QUANTUM WELL

JAMES P. LAVINE* and HARVEY S. PICKER**
*Microelectronics Technology Division
Eastman Kodak Company, Rochester, NY 14650-2008
**Department of Physics
Trinity College, Hartford, CT 06106

ABSTRACT

The quantum mechanical escape rate is calculated for an electron in a one-dimensional potential well. First-order time-dependent perturbation theory is used for the bound-to-bound and the bound-to-free transitions. The bound-to-free transition probability decays exponentially with bound energy. The fraction of one-electron systems in a bound state decays exponentially with time. The characteristic time constant grows exponentially with an increase in the depth of the potential well.

INTRODUCTION

Particles escape confinement within a potential by tunneling or by excitation. Kramers [1] first solved the classical escape problem of a particle that encounters a potential barrier and subsequent developments have been thoroughly reviewed [2]. A variety of quantum mechanical approaches have appeared, which range from general formalisms [3-4] to detailed studies of special cases [5]. Other approaches consider the response of a hydrogen atom to an electromagnetic field [6], as well as the perturbation calculation of the ionization probability of a system [7].

The present work focuses on a straightforward application of perturbation theory to treat escape through excitation. The goal is to determine how the time scale for escape depends on the potential well depth. First-order, time-dependent perturbation theory is applied to a one-dimensional square-well. Previous work [8] considered the bound-to-bound transitions and used *ad hoc* expressions for the bound-to-free transitions. Here, the bound-to-free transition matrix elements are calculated within the same formalism as the bound-to-bound.

Schrödinger's equation is solved for the bound states of an electron in a square-well with an infinite barrier on one side. A time-dependent perturbation causes transitions of the electron between bound states and

between a bound state and the continuum. Recapture from the continuum to a bound state is ignored. The time evolution of an ensemble of one-electron systems is followed through a rate equation approach. That fraction of systems that remain in a bound state is found to decay exponentially with time. The characteristic time constant, τ, for the decay grows exponentially with an increase in the well depth. This functional dependence parallels Kramers' result for the classical escape problem [1].

The model is developed in Section 2 and numerical results are presented in Section 3. The final section summarizes the work.

MODEL FOR ESCAPE CALCULATIONS

Schrödinger's equation is solved for the bound state energies and wave functions for a square-well of depth $-V_0$ and width L. The energy levels for various well depths are shown in Fig. 1 for $L = 0.02 \ \mu$m. Transitions are driven by the perturbation

$$V(x,t) = V_p[x(L-x)/L^2] \ (t/t_0) \ e^{-t/t_0} \quad , \quad (1)$$

or by

$$V(x,t) = V_p[x(L-x)/L^2] \ (\Delta t \ /10) \ \delta(t-\Delta t/2) \quad . \quad (2)$$

These permit closed-form evaluations of the probabilities for bound-to-free and for bound-to-bound transitions [9]. The integrals over time go from 0 to Δt. Here $t_0 = 0.3 \times 10^{-13}$ s, $\Delta t = 1.0 \times 10^{-13}$ s, and $V_p = kT$, the thermal energy at 300 K. These perturbations are intended to simulate thermally driven escape. Figures 2 and 3 show the calculated bound-to-free transition probabilities for Eqs. (1) and (2), respectively, when the free state is represented by a plane wave. There is an approximate exponential decrease in the transition probability as the bound state deepens. Figure 4 presents the bound-to-free transition probability from the shallowest and the next most shallow bound state as a function of the well depth. It is apparent that the probabilities reflect the depths of the bound states as a study of Fig. 1 confirms.

The transition probabilities are used to evolve the ensemble of one-electron systems with a time step of Δt. Spontaneous emission for bound-to-bound transitions is included [8]. All ensembles start with the electron in the deepest bound state at $t = 0$. An explicit numerical rate
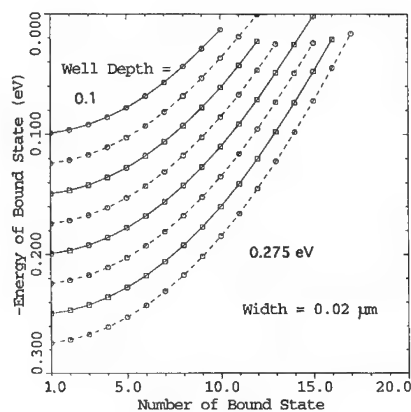
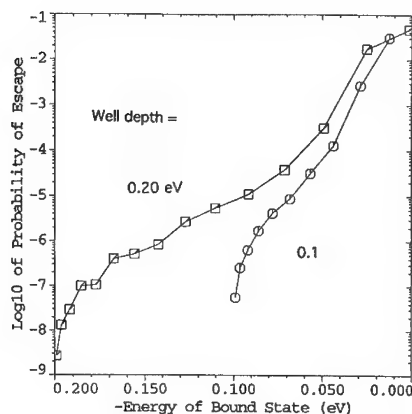Fig. 1. Bound state energies for varying well depth and $L = 0.02$ μm. Successive curves vary by 0.025 eV.

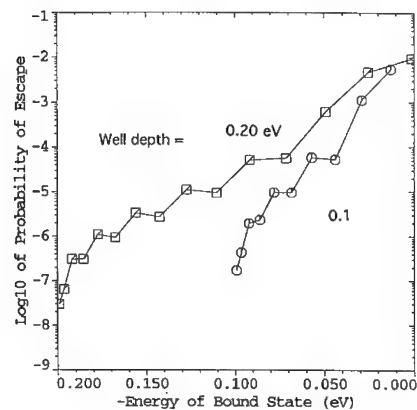Fig. 2. Bound-to-free transition probability versus bound state energy for $V_0 = 0.1$ (o) and 0.2 eV ($\square$) with Eq. (1).

Fig. 3. Bound-to-free transition probability versus bound state energy for $V_0 = 0.1$ (o) and 0.2 eV ($\square$) with Eq. (2).
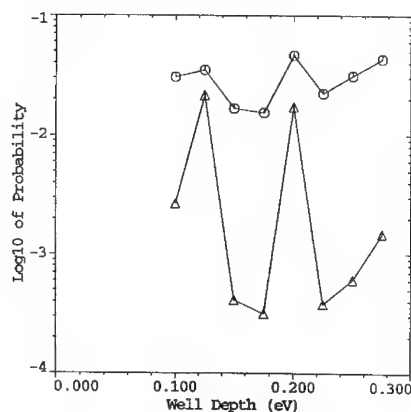

Fig. 4. Bound-to-free transition probabilities versus well depth for Eq. (1). Shallowest level (o), next shallowest (Δ).

equation approach advances the ensemble at each time step, so the fraction of the systems in each bound state is known as a function of time. Electrons that enter the continuum are considered to have escaped.

277

NUMERICAL RESULTS

Figure 5 shows how the fraction of the ensemble with a bound electron decays as a function of time for a series of well depths with $L = 0.02$ μm and Eq. (1). The decay is exponential with time and the slope yields a characteristic time constant, τ, that is plotted in Fig. 6, the open circles, versus the well depth. The classical result [1] is that τ is proportional to $\exp(qV_0/rkT)$ with $r = 1$. The present calculations yield $r = 0.89$ for $V_0 = 0.1$ to 0.175 eV and $r = 1.18$ for deeper wells. These results have a factor of two in the density of states to account for electron spin. Similar calculations without this factor of two provide the filled circles in Fig. 6. The escape is slower and the r-values are close with $r = 0.86$ for the shallower wells and $r = 1.16$ for the deeper wells. Figure 7 shows τ versus the well depth for the perturbation of Eq. (2) with the electron spin included. The slope is quite different with $r = 1.55$ for $V_0 = 0.1$ to 0.175 eV. The curve then grows more slowly with $r = 2.1$.
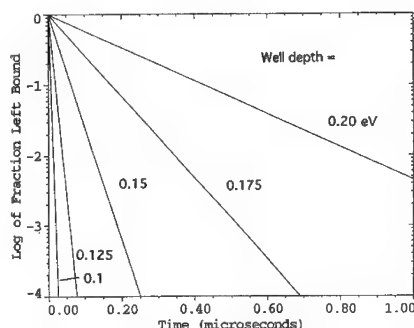
Fig. 5. Fraction left bound versus time. $V_0 = 0.10$ to 0.20 eV from left to right, $L = 0.02$ μm, and Eq. (1).
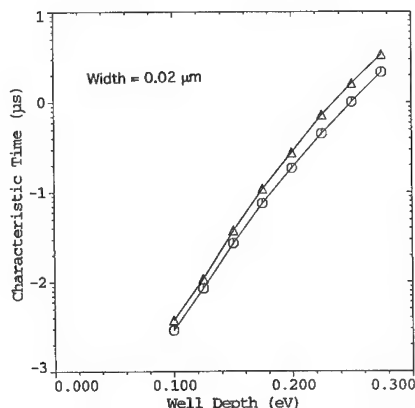
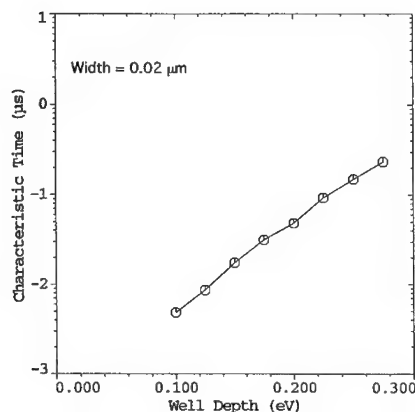Fig. 6. Characteristic time constant versus well depth V_0 with Eq. (1). (o) electron spin in density of states, (Δ) no electron spin.

Fig. 7. Characteristic time
constant versus well depth
V_0 with Eq. (2).

Width = 0.02 μm

SUMMARY

The present calculations continue an exploration of the quantum mechanical escape problem with first-order time-dependent perturbation theory. Probabilities for bound-to-free transitions are calculated for the same perturbations that are used for the bound-to-bound transitions. This improves on the *ad hoc* expressions previously used [8]. The characteristic time constant for escape grows exponentially with an increase in the well depth. However, the slope deviates from the classical 1/kT and changes with the well depth. The extent of the deviation depends on the exact nature of the time-dependence of the perturbation. A change in the density of states provided an approximate scaling of τ. Future work will explore coupled potential wells in an effort to treat escape and recapture on a consistent basis.

REFERENCES

1. H. A. Kramers, Physica **7**, 284 (1940).
2. P. Hänggi, P. Talkner, and M. Borkovec, Rev. Mod. Phys. **6 2**, 251 (1990).
3. V. I. Mel'nikov, Phys. Rep. **2 0 9**, 1 (1991).
4. W. H. Miller, Ber. Bunsenges Phys. Chem. **9 5**, 389 (1991).
5. G. Garcia-Calderón, J. L. Mateos, and M. Moshinsky, Ann. Phys. (NY) **2 4 9**, 430 (1996).
6. M. Luban and B. Nudler-Blum, J. Math. Phys. **1 8**, 1871 (1977).
7. G. Lucovsky, Solid State Commun. **3**, 299 (1965).
8. J. P. Lavine, in *Dynamics in Small Confining Systems II*, edited by J. M. Drake, J. Klafter, R. Kopelman, and S. M. Troian (Mater. Res. Soc. Proc. **3 6 6**, Pittsburgh, PA, 1995) pp. 353-358.
9. W. Greiner, *Quantum Mechanics An Introduction*, Springer-Verlag, Berlin, 1993, Sect. 11-4 and 11-6.

Monte Carlo Study of A+A+A→0 and A+2B→0 Reactions

Andrew Yen and Raoul Kopelman, Department of Chemistry, University of Michigan, Ann Arbor, MI 48109-1055

ABSTRACT

The diffusion-limited annihilation reactions A+A→products and A+B→products have been subject to theoretical, numerical, and experimental study over the past decade. "Anomalous" behaviors have been reported for both reactions, but with different upper critical dimensions (d=2 and d=4 respectively). The critical dimensions and the scaling of the exponents for the generalized reaction nA+mB→products depends on n and m. We present Monte Carlo simulations for two different types of third-order reactions, A+A+A→0 and A+2B→0, on both one and two dimensional lattices. Our numerical results show that for the two-dimensional case the behavior of the reaction follows mean-field theory while in one dimension the result is "anomalous". Our numerical results are in good agreement with theory based on microscopic arguments and scaling analysis.

INTRODUCTION

The past two decades experienced a resurgence of interest in diffusion-limited reaction kinetics[1-6] . The most basic model of this type is given by the irreversible bimolecular reaction A+B→C. Such processes play an important role in many areas in physics, chemistry and biology.

For homogeneous initial conditions, and in low dimensions, the diffusion mechanism is not an efficient stirring mechanism. As a result, a spatial segregation of particles occurs. This results in a slowing down of the reaction rates which is described by rate laws called "anomalous".

In this report we present Monte Carlo simulations for two different types of termolecular reactions, A+A+A→0 and A+2B→0, on both one and two dimensional lattices. Our numerical results show that for the two-dimensional case the behavior of the reaction follows mean-field theory while in one dimension the result is "anomalous". Our numerical results are in good agreement with theory based on microscopic arguments and scaling analysis

THEORY

The generalized reaction nA+mB→products has been studied by Cornell, Droz and Chopard[7]. For n+m≥3 their microscopic arguments predict that for random initial conditions and for

dimensionality $d\geq 2$ and $n+m\geq 3$ that the kinetics is mean-field based and obeys the classical kinetics laws. In one dimension the kinetics is anomalous for $(n,m)=(1,2)$.

The $nA\rightarrow$products reaction under an initial random distribution was studied by Kang and Redner[4]. Their result ,based on scaling arguments, predicts that the density ρ_a scales as $\rho_a(t)\sim t^{d/2}$, for $d<d_c=2/(N-1)$, where d_c is the critical dimension ,and that the mean-field decay of $\rho_a(t)\sim t^{a/(N-1)}$ holds for $d\geq d_c$.

NUMERICAL SIMULATIONS

Simulation Method

We perform Monte Carlo simulations where each particle is treated as a discrete time random walker. At $t=0$ we randomly place all the particles on the lattice. Each time step consist of moving every particle to one of its unoccupied neighboring sites. The diffusion coefficient of all the particles are set to be equal to unity and periodical boundary conditions are applied in all directions. We used two different algorithms to monitor the termolecular reactions. In the first method, called "intermediate", one allows the formation of an infinite life- time intermediate (AA or AB). The intermediate can either be stationary or diffuse on the lattice. In the second method, called the "scanning" method, after walking every particle on the lattice, one checks the vicinity of every A particle. If there are two reactive species next to this A particle, all three particles leave the system. In this case the life- time of the intermediate is zero and the capture radius is one lattice spacing.

Simulation Results

The simulation is performed on regular one and two dimensional lattices. For $A+2B\rightarrow 0$ on a two-dimensional lattice the results are shown in Figs. 1 and 2 . Fig. 1 shows the result obtained from the "intermediate" method and Fig. 2 shows the result from the "scanning" method. Both runs are done on a 200x200 lattice and averaged over 10 realizations. At $t=0$ there are 5000 A and 10,000 B on the lattice. We plotted ln A vs. ln t and the slope gives the exponent . From the fit we get 0.53 for the "intermediate" method and 0.49 for the "scanning" method. Evidently the exponents from both methods agree with the mean-field theory value of 0.5 and thus are in good agreement with Cornell et al's simulation result performed by a Cellular Automata (CA) algorithm.
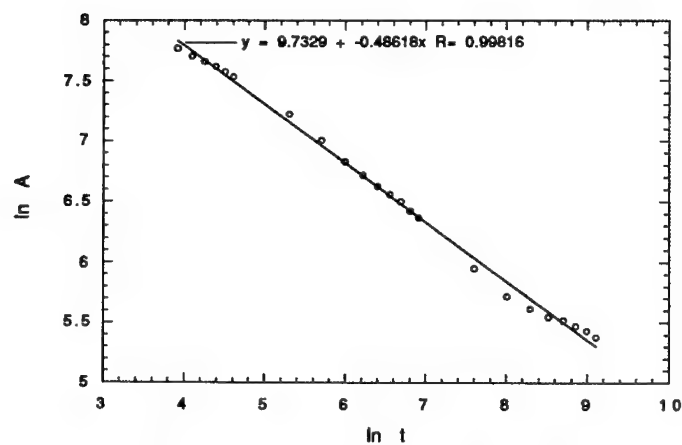
Fig.1 ln A vs. ln t for A+2B→0 reaction using
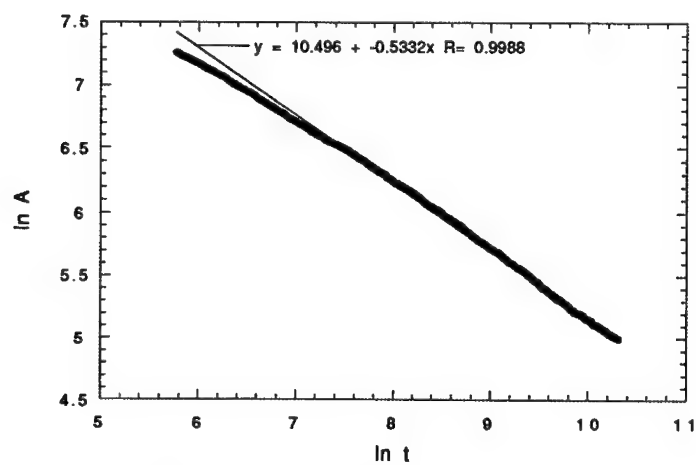the "scanning" method on a 2d lattice.

Fig.2 ln A vs. ln t for A+2B→0 reaction using
the "intermediate" method on a 2d lattice.

For the A+A+A--->0 reaction on a two-dimensional lattice we obtained the following results. We used a "scanning" method where if any two out of four nearest neighbor sites are occupied then all three A particles leave the system. We performed the simulation on a 200x200 lattice with 1000 A particles on the lattice initially. We ran the simulation for 1000 steps and averaged over two runs. The results are shown in Fig.3. The slope is -0.47. For the "intermediate" method, under the same conditions, the ln A vs. ln t plot also show a slope of about -0.47 (Fig4). Both results are close to the value of -0.5 predicted by Kang and Redner [8].
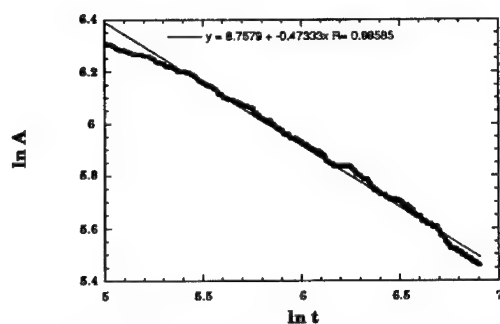
Fig.3 ln A vs. ln t for A+A+A→0 reaction using
the "scanning" method on a 2d lattice.

For the A+2B→0 simulation, using the "scanning method", the power law decay for the A+2B→C case is 0.13. This is smaller than the 0.25 power for the A+B→C case. However, there is little or no reaction going on after 20-30 steps (Fig 5). The result obtained from the "intermediate" method shows similar patterns as Fig 5.
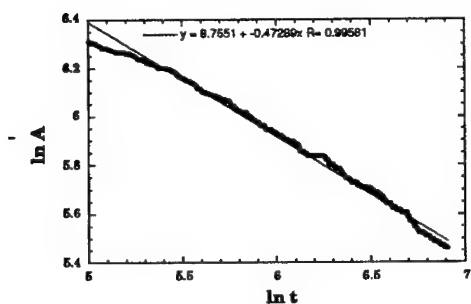
Fig. 4 ln A vs. ln t for A+A+A→0 reaction using
the "intermediate" method on a 2d lattice.

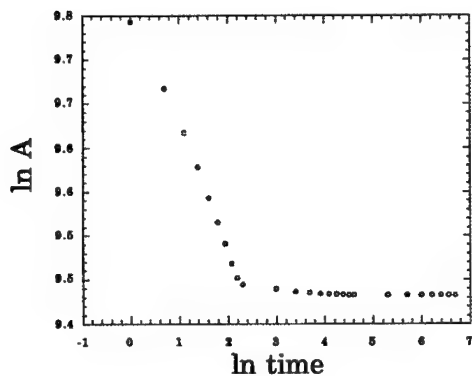Fig. 5 ln A vs. ln t for A+2B→0 reaction using
the "scanning" method on a 1d lattice.

For the A+A+A→C simulation on 1d lattice we get the following results. Fig.6 shows ln A vs. ln t for a 100,000 site lattice with 10,000 initially A particles using the "intermediate" method. It seems to have three different regions . The slope at the early region is -0.44. At the intermediate time regime the slope is -0.17 (Fig. 6).

For the one-dimensional case the termolecular reactions show exponents that differ from those of the mean-field theory. The slower rate may be due to the confinement of one-dimensional geometry and the formation of patches of like particles.
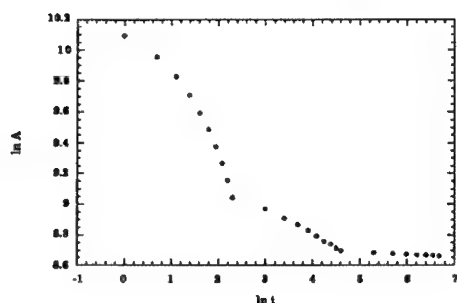
Fig.6 ln A vs. ln t for A+A+A→0 reaction using
the "intermediate" method on a 1d lattice.

Summary

We have performed simulations for two types of termolecular reactions using Monte Carlo
simulations. Two different algorithms were used. In the first one we allow the formation of
intermediates (AA or AB). In the second method we move the particles first and then scan the
lattice to check if there are two reactive species next to the scanned particle.

It is shown that in two dimensions the result is mean-field like and follows classical chemical
kinetics, and that the life time of the intermediate is irrelevant in this case. However, in one
dimension the result is anomalous. The power laws we obtained give a slower particle decay than
the classical predictions .

References

1. A.A. Ovchinikov and Ya. B Zeldovich. Chem. Phys. **28**:215 (1978).
2. D.Toussaint and F. Wilczek, J. Chem. Phys. **78**:2642 (1983).
3. K. Kang and S. Redner, Phys. Rev Lett. **52**:955 (1984)
4. K. Linderberg, B. J West, and R. Kopelman, Phys. Rev Lett. **60**:1777 (1988)
5. R. Kopelman, Science **241**:1620 (1988)
6. C.R. Doering and D Ben-Avraham. Phys. Rev A **38**:3035 (1988)
7. S. Cornell, M. Droz and B.Chopard, Physica A **188** (1992)
8. K. Kang and S. Redner, Phys. Rev A 1985 **32**, 435

LINE TENSION EFFECT ON ALKANE DROPLETS
NEAR THE WETTING TRANSITION

A. D. DUSSAUD* and M. VIGNES-ADLER**
*Department of Chemical Engineering, Princeton University, Princeton NJ 08544
** Laboratoire des Phénomènes de Transport dans les Mélanges du CNRS
SP2MI, Bd 3 Téléport 2, BP 179, F-86960 Futuroscope Cedex, France

ABSTRACT

We have investigated n-octane droplets resting on the surface of sodium chloride solutions as a function of the salt concentration in a saturated, closed cell. For high salt concentration, the system approaches a wetting transition : the contact angles are very small ($\sim 1°$), the macroscopic droplet is unstable, and it breaks up spontaneously into microdroplets. The stable polydisperse population of microdroplets ($5 \, \mu m < r < 250 \, \mu m$) allowed us to analyze the dependence of the contact angle on droplet size. Because of the low contact angle values, accurate measurement of contact angles was obtained by interferometry. Moreover the accuracy of the classical method was significantly improved through the systematic use of three wavelengths. The relationship between the contact angle and the size droplet size indicated a positive line tension, τ, and the order of magnitude of τ was in good agreement with the theoretical prediction. τ varies between $(8.6 \pm 0.9).10^{-11}$ N and $(1 \pm 0.1).10^{-9}$ N and was dependent on the salt concentration. The positive sign of τ and its significant effect on droplet shape were related to the fact that the system was approaching the wetting transition.

INTRODUCTION

Several studies have pointed out the importance of line tension on the behavior of finely dispersed particles at interfaces [1, 2, 3]. For example, Aveyard and Clint recently showed that the line tension can influence the effectiveness of fine particles in rupturing a thin film [4]. It can also play a significant role in heterogeneous nucleation from supersaturated vapors on liquid substrates [5]. In all of these phenomena, the line tension influences the contact angles of the particles at the interfaces by exerting an excess force in the line of discontinuity where three phases meet. Consider an oil droplet resting on a plane water/vapor interfaces (Fig. 1). The mechanical equilibrium of the forces (per unit length) at the contact line can be expressed by Neumann-Young's law. Balancing the horizontal components of these forces leads to

$$\gamma_1 - \gamma_2 \cos\alpha - \gamma_3 \cos\beta - \frac{\tau}{r} = 0 \tag{1}$$

where γ_1 is the surface tension of water, γ_2 is the surface tension of oil, γ_3 is the interfacial tension between water and oil, α and β are the contact angles, τ is the line tension, and r is the radius of the droplet. As the line tension is very small ($\sim 10^{-11}$ N), it plays a significant role on the wettability of particles at interfaces only when the contact line has significant curvature, as for example a tiny droplet with a diameter much less than 1 mm. Line tension can be positive or negative [6], and hence may decrease or increase, respectively, the wettability of the particle. Although theoretical estimates for τ have been available for very long time, the prediction of reliable values for a given system are very difficult to derive due to the variety and complexity of interaction forces in the region where the line tension is exerted. Moreover as the line tension is very small, very few measurements are available in literature. Hence, the development of experimental measurements is crucial to understanding the line tension effect and providing more precise values for the predictions of wetting phenomena involving fine particles. In addition, there is presently

controversy regarding the theoretical aspects of the line tension at a wetting transition [7]. The wetting transition corresponds to the case where the spreading coefficient, defined as $S = \gamma_1 - \gamma_2 - \gamma_3$ goes to zero, or equivalently, when the contact angles α and β go to zero. To the best of our knowledge, no experimental measurement has ever been made on line tension near a wetting transition.

Recently, we investigated the spreading of n-alkane droplets on the surface of sodium chloride solutions as a function of the salt concentration in a saturated closed cell [8]. Among several n-alkanes, we chose n-octane because it has a low spreading coefficient (S = - 0.6 mN/m). By adding a substantial quantity of salt, S becomes greater than zero but remains small. The details of the study of this system are given in [8]. As long as the salt concentration is lower than 1.2 M, the macroscopic droplet (3-8 μl) takes the form of a lens in a stable coexistence with an adsorbed thin film. For salt concentrations of about 3 M or more, spreading is considerably enhanced, and the lens becomes a metastable pancake with a contact angle smaller than 1°. After a few hours, it breaks up into a multitude of stable microdroplets which disappear 24 hr later. In this paper, we report the line tension effect on n-octane microdroplets when the wetting transition is approached, at constant temperature, by substantial addition of salt.
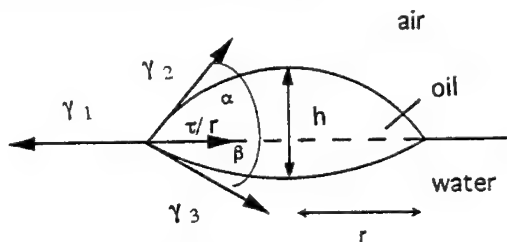

Figure 1: Microdroplet at a liquid interface in the absence of gravity.

EXPERIMENT

Fluids and interfacial properties

The n-octane is purchased from Aldrich (purity 99%) and purified by shaking with alumina followed by washing with milliQ water for 8 hours. The sodium chloride is purchased from Aldrich. Its purity is controlled by the value of the surface tension of the aqueous solutions which must depend linearly on the salt concentration [9]. Next, the n-octane and the NaCl solution are mutually saturated by mechanical stirring for 6 hr at the experimental temperature. Two NaCl concentrations were studied, 3 M and 5 M. The interfacial properties corresponding to the systems octane/pure water and octane/electrolyte solutions are shown table I. γ_{oct}, $\gamma_{oct/wat}$, γ_{wat} denote the surface tension of n-octane, the interfacial tension at the oil/water interface, the surface tension of the aqueous substrate. γ^s_{wat} is the surface tension measured in an atmosphere saturated in n-octane. The decrease of surface tension γ^s_{wat} relative to γ_{wat} shows that n-octane molecules adsorb from the vapor on the aqueous surface. NaCl close to saturation increases the surface tension of water by about 10 %. By increasing the surface energy of the supporting liquid, it facilitates the spreading of n-octane and changes the sign of S at a salt concentration close to 2 M.

Experimental device and procedure

The microdroplets were observed by interferential microscopy. The cell consists of a circular glass Petri dish with a diameter of 60 mm filled with the salt solution and placed inside a larger Petri dish. This cell is placed in a thermo regulated wall chamber (20 ± 0.1° C). The larger Petri dish contains an n-octane layer to saturate the cell atmosphere. All connections of the cell with the

Table I : Interfacial properties of octane/electrolyte solutions

NaCl M	γ_{wat} mN/m 20° C	γ^s_{wat} mN/m 20° C	γ_{oct} mN/m 20° C	$\gamma_{oct/wat}$ mN/m 20° C	S mN/m 20° C
0	72.58	71.58	22.3	50.9	- 0.6
3	78	76.8	22.7	55.1	+ 0.2
5	81.6	79.8	22.7	57.9	+ 1

outside are achieved through holes closed with septa. The cell is placed in the field of a microscope and is illuminated by a reflected monochromatic light. Visualization of the phenomena is made by a CCD camera connected to a tape recorder. The videotapes are processed afterwards using an image analysis system. A small droplet of n-octane (3-8 μl) is formed at the tip of a glass capillary and carefully deposited on the surface of the salt solution. After deposition, the macroscopic droplet remains a metastable pancake for a time varying between 2 and 12 hours. During this stage, the cell is illuminated only intermittently to check regularly the onset of instability. Although the onset of instability was always observed, the time at which the instability began may be due to a requirement for the macrodoplet to evaporate to a critical thickness for the onset of instability. Indeed, near the wetting transition, minor changes in external constraints may induce the instability, in particular if temperature gradients exist. After the spontaneous break-up of the macrodroplet which lasts about 15 min., the microdoplets did not show any instability and were analyzed. One experiment corresponds to the analysis of a population of microdroplets formed from a single initial macroscopic droplet.

Contact angle measurement

The microdroplet diameter is measured on the digitized image. The analysis of the interference pattern provides the microdroplets thickness h, or more precisely an interval for h e.g. $N\lambda_i/8n \pm \lambda_i/8n$ where λ_i is the light wavelength, N is the number of dark fringes observed on the microdroplet image, and n is the refractive index of n-octane. Three wavelengths (λ = 480, 546, 650 nm) were systematically used for each measurement to improve the precision. From the analysis of the three fringe patterns, h is deduced to belong to the intersection of the three intervals corresponding to the three colors. This method allows us to reduce the interval of possible thickness (h_{min}, h_{max}) by about 50 %. In the following, h_{mean} denotes the mean thickness h_{mean} = (h_{min} + h_{max}) / 2. The contact angles of the microdroplets are calculated from the measurement of their thickness h and radius r (5 μm < r < 250 μm). Contact angle calculation for a sessile droplet implies the knowledge of the shape of the lens, which is usually obtained by integrating the Laplace equation for the three interfaces [10]. The present physical situation allows much simplification. For the two interfaces (oct/air, oct/water), the Bond number Bo = $\Delta\rho.g.4\ r^2/\gamma$,which measures the importance of capillary forces [11] for each interface, varies in the following range : $Bo_{air/oil} \sim 10^{-4} - 2.10^{-2}$ and $Bo_{wat/oil} \sim 3.10^{-5} - 7.10^{-3}$, where $\Delta\rho$ is the density difference between air and n-octane or water and n-octane respectively. These two numbers are very small compared to 1. Hence, the effect of gravity on the lens shape can be neglected, and the lens can be assumed to be composed of two spherical caps (Fig. 1). α and β denote the angles of the caps. When they are assumed to be very small, the angles α and β can be derived from the values of h and r and the interfacial tensions. The interfacial tension are obtained independently by tensiometry, and are assumed to be constant. The detailed calculation is presented in [8]. Finally, it can easily be shown that

$$\alpha = \frac{2h_i}{r} \frac{\gamma_{oct/wat}}{\gamma_{oct} + \gamma_{oct/wat}} \quad \text{and} \qquad \beta = \frac{2h_i}{r} \frac{\gamma_{oct}}{\gamma_{oct} + \gamma_{oct/wat}} \tag{2}$$

where $h_i = h_{min}, h_{max}$ or h_{mean} .

RESULTS

The mean values of contact angles α and β are plotted vs. the microdroplet diameters in Fig. 2-3 for the 3 M and 5 M solutions. The contact angles were measured in three independent experiments at 3 M and two independent experiments at 5 M. Two experiments at each salt concentration gave similar results, while experiment 2 at 3 M gave a significantly different plot. For each experiment, the angles increase when the droplet diameter decreases. It must be pointed out that the contact angles of a 30 μm diameter microdroplet are about three to four times larger than the contact angles of a 500 μm microdroplet, for which the line tension is almost negligible.

The quantity $\gamma^* = \gamma_{oct}\cos\alpha + \gamma_{oct/wat}\cos\beta$ was plotted vs. $1/r$ for each salt concentration in Figs. 4-5 to obtain the line tension from the slope ($-\tau$) according to the relation (1). The empty symbols correspond to the value of γ^* calculated from h_{min} and h_{max}, while the filled symbols correspond to the value of γ^* calculated from h_{mean}. The analysis of a large population of microdroplets using three wavelengths clearly shows that γ^* decreases linearly when $1/r$ increases. The slope of γ^* and its ordinate at the origin are obtained by a linear regression from the values of γ^* calculated from h_{mean}. The error on these slopes is less than 10 %. The line tension τ is positive and varies between $(8.6 \pm 0.9).10^{-11}$ N and $(1 \pm 0.1).10^{-9}$ N. It depends on salt concentration, higher values of τ being obtained with the 3 M solution. The values of γ^s_{wat} are 77.7999 and 80.5991 $\pm$ 2.10^{-4} mN.m^{-1} for the 3 M and 5 M solutions, respectively (the accuracy of these values until the 4th decimal results from the resolution of α and β obtained by interferometry, the interfacial tensions being assumed constant). For 3 M, experiments 1 and 3 gave a different slope τ versus experiment 2, while the ordinate at the origin γ^s_{wat} was not modified.

CONCLUSIONS

The orders of magnitude obtained for τ (10^{-10} N-10^{-9} N) agree well with theoretical estimations and available experimental data [2]. Moreover, τ/γ^s ranges between 1.08 nm and 12.9 nm ; it has the order of magnitude of a molecular length and, it is very near the theoretical value as predicted by Kerins and Widom [12].

Positive line tensions are less common than negative ones. This was explained by several approaches in the case of pseudo partial wetting (i.e. coexistence of the droplet with a thin film) [1, 7, 13]. In the present case, as the atmosphere is saturated in octane vapor, the microdroplets are, in fact, in coexistence with a thin film. Thus means, although the contact angles are very small and S is slightly positive, the wetting transition is imminent but not yet reached. Our results show that near the wetting transition, the line tension significantly influences the shape of the n-alkane droplet. The positive line tension tends to contract the microdroplets and prevent them from spreading. This result confirms a prediction given by the mean field theory for the first-order wetting transition [7]. Indeed, the mean field theory predicts that, as the system approaches complete wetting (α and β go to zero), the line tension becomes positive, increases and finally reaches a finite value at S = 0. Therefore, near the wetting transition, the strongest effect of line
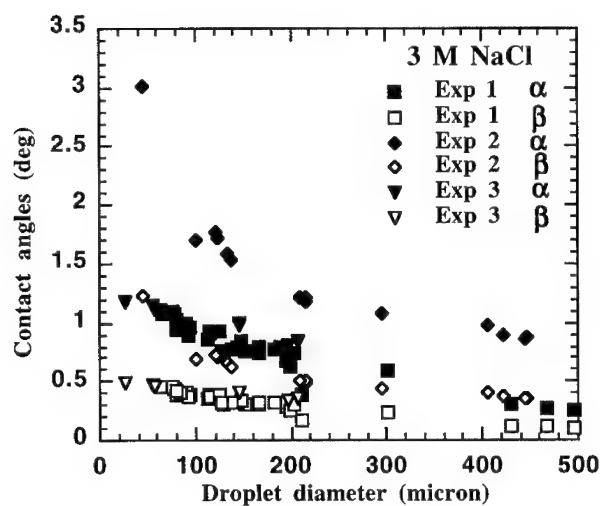
Figure 2 : Contact angles α and β versus the diameter of octane droplet.

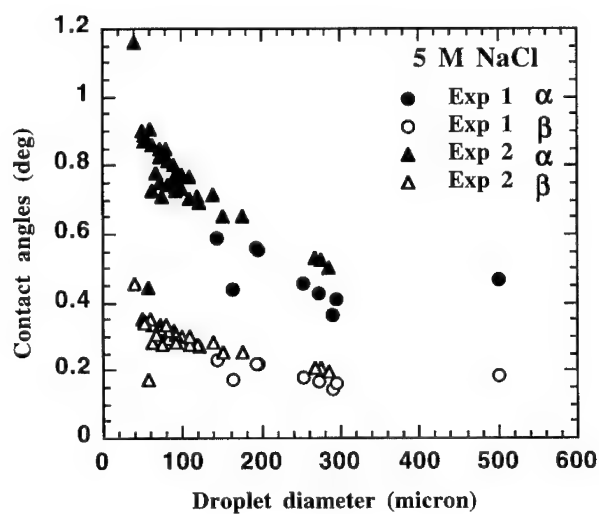Figure 3 : Contact angles α and β versus the diameter of octane droplet.
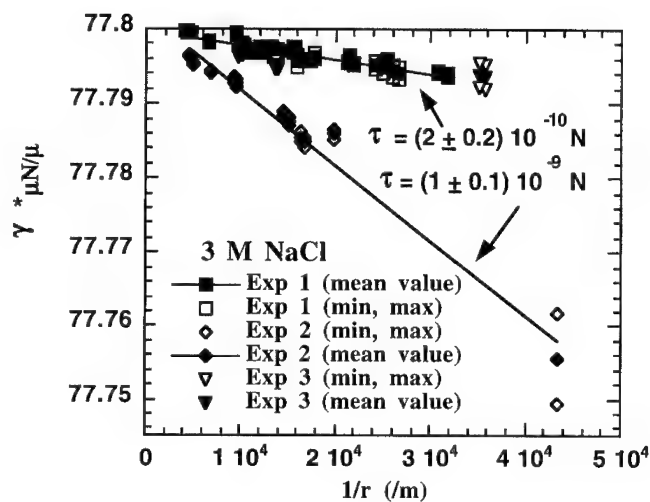
Figure 4 : $\gamma^*=\gamma_{oct}\cos\alpha+\gamma_{oct/wat}\cos\beta$ versus 1/r for octane droplets on the surface of 3 M NaCl solutions.

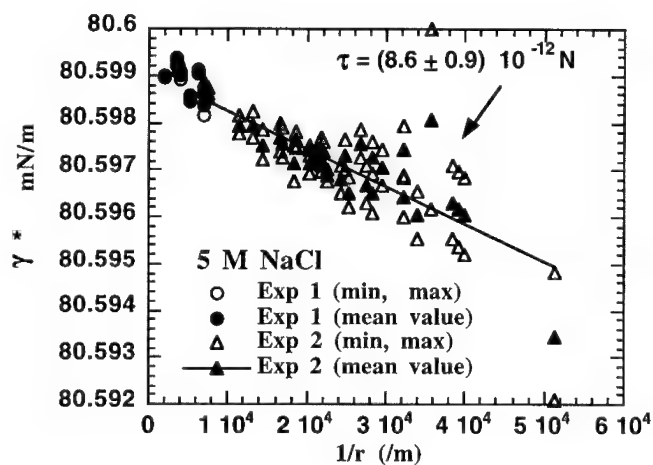

Figure 5 : $\gamma^*=\gamma_{oct}\cos\alpha+\gamma_{oct/wat}\cos\beta$ versus 1/r for octane droplets on the surface of 5 M NaCl solutions.

tension should be expected. Moreover, it is shown that the slope of τ (θ) (θ=contact angle) or $\tau(T)$ (T=temperature) increases significantly as θ goes to 0. This could explain why, at 3 M salt, a very small difference of temperature between experiment 2 and experiment 1-3 may change τ so much (by a factor 10). These results also show that the effect of salt on n-octane spreading is peculiar. Indeed, while it is clear that at constant temperature, salt at high concentration brings the n-octane/electrolyte system close to the wetting transition, it seems more efficient at 3 M than at 5 M, as τ is higher at 3 M.

Another approach is proposed in [8] to explain the positive sign of τ by considering the influence of the interaction free energy on the surface tension near the contact line. This work shows clear experimental evidence of the line tension effect in a system close to the wetting transition. It will be very interesting to pursue the study of this interesting effect of salt at high concentration on n-alkane spreading in order to explore the wetting transition further.

ACKNOWLEDGMENTS

REFERENCES

1. J.A. De Feijter and A.Vrij , J. Electroanal. Chem. **37**, p. 9 (1972).

2. B.V. Toshev, D. Platikanov and A. Scheludko , Langmuir **4,** p. 489 (1988).

3. B. Widom , J. Phys. Chem. **99**, p. 2803 (1995).

4. R. Aveyard R. and J. H. Clint, J. Chem. Soc., Faraday Trans. **92(1),** p. 85 (1996).

5. A. D. Alexandrov, B. Toshev and A. D. Sheludko, Colloids and Surfaces A. **79**, p. 43 (1993).

6. J. S. Rowlinson and B. Widom in Molecular Theory of Capillarity, Clarendon Press, Oxford,1984 p. 240.

7. J. O. Indekeu, Int. J. Modern Phys. B. **8**, p.309 (1994).

8. A. D. Dussaud and M. Vignes-Adler, Langmuir, in press.

9. J.J. Bikerman in Physical Surfaces, Academic Press, New York, 1970.

10. P.R. Pujado ,L. E. Scriven , J. Colloid Interface Sci.**40**, p. 82 (1972).

11. S. Ross and I.D. Morrison in Colloidal Systems and Interfaces, John Wiley & Sons, New-York, 1988.

12. J. Kerins and B. Widom , J. Chem. Phys.**77**, p. 2061 (1982).

13. N. V. Churaev, V. M. Starov and B. V. Derjaguin , J. Colloid Interface Sci. **89**, 1, p. 16 (1982).

PHOTOPHYSICS OF HIGH CONCENTRATION SYSTEMS AT A SOLUTION / SOLID INTERFACE: AN EVANESCENT WAVE STUDY

J.A. ELLIOTT *, G. RUMBLES *, A.J. DE MELLO *, H.L. ANDERSON **
*   Department of Chemistry, Imperial College, London SW7 2AY, UK, j.elliott@ic.ac.uk
** The Dyson Perrins Laboratory, University of Oxford, Oxford OX1 3QY.

ABSTRACT

For many species the study of photophysical behaviour by fluorescence spectroscopy has been confined to low concentration as a result of the influence of the inner filter effect. In this paper we report how the total internal reflection technique of evanescent wave fluorescence spectroscopy (EWIFS) allows both the collection of distortion free steady-state fluorescence emission spectra and quantitative analysis of such species, in 'bulk' solution environment, to significantly higher concentration than can be achieved with a conventional (right-angle) geometry. A study of two species, the laser dye rhodamine 101 and a novel meso-substituted zinc prophyrin is presented.

INTRODUCTION

Fluorescence spectroscopy finds wide application in materials research for study of photophysical properties due to both its high specificity and sensitivity. For a number of important systems, however, the use of both steady-state and time-resolved fluorescence techniques are severely limited by the observation phenomenon known as the inner filter effect (also called self-absorption or re-absorption of fluorescence).

The inner filter effect arises from two processes; attenuation of the excitation radiation through absorption by a sample (primary absorption) and re-absorption of fluorescence emission which passes through the sample on travel from its point of origin to the detector (secondary absorption). In conventional, steady-state, fluorescence spectroscopy such self-absorption causes distortion of the emission spectrum observed for the sample. Such distortion is characterised by both a general decrease in the emission intensity and specific attenuation of the 'blue-edge' of the emission spectrum causing an apparent shift of the emission maximum to higher wavelength and a change in the emission profile. Calculation of fluorescence quantum yields from emission spectra distorted in such a way yields significantly reduced values. Both the qualitative distortion of emission spectra and apparent reduction of fluorescence quantum yield resulting from the inner filter effect can be incorrectly attributed to physical phenomena such as aggregation [1] or excimer formation.

The degree of distortion observed in emission spectra due to the inner filter effect is dependent on: the sample concentration; the absorption and emission properties of the system under study and the geometry of the sample holder. At high concentration, materials showing a small Stokes' shift give greatly distorted fluorescence emission spectra with use of conventional (right-angle) geometry systems with long pathlengths for both excitation and emission. Such materials include the rhodamine laser dyes and many biological systems. The importance of study of these materials at high concentration has led to development of both computational [2-4] and experimental [5-12] methods for reducing and / or correcting for the effects of re-absorption in fluorescence measurements.

Experimental techniques for minimisation of the inner filter effect involving reduction of either, or both, the excitation and emission pathlengths to mm or μm dimensions offer significant improvement for collection of steady-state emission spectra. Many of these, however, still require

complex numerical analysis before distortion free data is obtained, thus making measurement of even a standard fluorescence spectrum time-consuming. With use of the internal reflection fluorescence technique evanescent wave induced fluorescence spectroscopy [13-16] both excitation and emission pathlengths of the order of 10's to 100' s nm can be achieved simultaneously.

EWIFS is now well established for study of the photophysical behaviour of fluorophore species at a solid / solution interface. With selection of appropriate experimental conditions, however, emission from fluorophores located further from the surface of the solid dominates the observed fluorescence, allowing study of species in a 'bulk' solution environment. In steady-state EWIFS, with excitation radiation of constant intensity incident upon the interface at a constant angle, and hence penetration depth, the intensity of fluorescence from evanescent excitation of such species, I_{fluor}, follows

$$I_{fluor} \propto c . \phi_f \tag{1}$$

where both the fluorophore concentration (c) and quantum yield (ϕ_f) are independent of the distance from surface of the solid [15]. According to equation (1), steady-state EWIFS can be used for both quantitative measurement of the concentration of a fluorophore species or study of its photophysical behaviour, via the fluorescence quantum yield. Unfortunately the derivation of equation (1) assumes optical transparency of both of the phases that define the interface. Where the solution absorbs strongly at the excitation wavelength the concentration dependence of the emission intensity becomes more complex [16,17], even for species such as rhodamine 101 where the fluorescence quantum yield has been shown to be invariant up to high concentration [18].

EXPERIMENT

Rhodamine 101 (640 perchlorate - Exciton) and the meso-subsutituted zinc porphyrin 'long monomer' (synthesised by H. Anderson [19] - compound Zn9) were both used without purification. Ethanol (BDH, AnalaR) and dichloromethane (Aldrich, 99.6 %) were tested to ensure the absence of extraneous fluorescence; no further purification was necessary. All measurements on the solutions of the 'long monomer' in dichloromethane were performed on the day of preparation.

Corrected steady-state fluorescence emission spectra were obtained at conventional geometry with a Spex FluoroMax spectrofluorometer, resolution 0.6 mm, using a standard quartz cuvette (10 mm x 10 mm). Corresponding absorption spectra were recorded on a Perkin-Elmer Lambda 2 spectrophotometer. Spectra of the lower concentration solutions were obtained with a standard 10 mm pathlength quartz cuvette; at higher concentrations this was replaced by a 1 mm cuvette.

Full experimental details of the steady-state EWIF spectrometer are described elsewhere [20]. For the study of rhodamine 101 in ethanolic solution excitation (3mW, 488 nm) was provided by an argon ion laser (Spectra Physics 165). This excitation was incident upon a semicircular, cylindrical fused silica TIR element (Spanoptic, refractive index, n_1 = 1.460) at an angle of 71°. In the corresponding study of the 'long monomer' in dichloromethane excitation (13 mW, 625 nm) was provided by a Kiton red dye laser (Spectra Physics 375) pumped by the argon ion laser. In this series of experiments the excitation was incident upon a similar fused silica TIR element at the angle of 80°. Here the incident angles employed correspond to intensity 1 / e penetration depths [13] of 154 nm and 138 nm in the rhodamine 101 and 'long monomer' experiments, respectively, assuming the refractive index of the solvent is unaffected by the solute. For both systems the prism was tested for the absence of extraneous fluorescence prior to use. It

was cleaned thoroughly, with the appropriate solvent, then air-dried at room temperature before addition of each sample.

For each sample, quantitative measurement of the emission intensity at the selected wavelength was performed for a period of 10 s, prior to collection of the qualitative emission spectrum. The intensity of the laser radiation was recorded continuously during collection of both data sets. In the experiments performed here, high intensity incident radiation and long penetration depths were used to minimise the contribution of fluorescence from the surface. In both experiments fluorescence from surface associated species was estimated to account for approximately 1 % of observed fluorescence emission.

RESULTS

Rhodamine 101

Fluorescence emission spectra of solutions of rhodamine 101 in ethanol recorded at conventional geometry, with excitation at 488 nm, exhibit a change in emission profile, maximum and intensity with increasing concentration. At concentrations below 1×10^{-6} mol dm^{-3} the emission profile and maximum are invariant; above this concentration progressive attenuation of the blue-edge of the emission profile and corresponding red-shift of the emission maximum are observed with increasing solution concentration. The dependence of the wavelength of the emission maximum on concentration is shown in figure 1 (a). The intensity of the emission spectrum shows an initial increase with increasing concentration, however, above 1×10^{-4} mol dm^{-3} further increase in solution concentration results in a progressive decrease in the intensity of the emission spectrum recorded. The concentration dependence of the emission intensity observed at 585 nm, for rhodamine 101 in ethanol, is shown in figure 2 (a). Here a decrease in emission intensity is seen at concentrations above of 5×10^{-5} mol dm^{-3}. At this wavelength both the blue-edge attenuation and overall decrease in intensity of the emission spectrum influence the observed fluorescence intensity.

Such concentration dependence of the fluorescence emission spectra of rhodamine 101 is characteristic of the inner filter effect. The invariance of the wavelength of the peak-normalised absorption spectrum with concentration and the linear dependence of absorbance on concentration verify the absence of aggregation of the fluorophore at high concentrations.

With use of the EWIF geometry the influence of the inner filter effect on the emission spectra recorded for high concentration solutions of rhodamine 101 in ethanol is significantly reduced. For concentrations below 1×10^{-4} mol dm^{-3} no attenuation of the blue-edge of the emission profile is observed and variation in wavelength of the emission maximum with concentration does not exceed the limits of experimental precision. At higher concentrations blue-edge attenuation of the emission profile and red-shift of the emission maximum are seen. These, however, are significantly less than observed in the corresponding spectra recorded at conventional geometry. At the concentration 1×10^{-3} mol dm^{-3}, near the solubility limit of rhodamine 101 in ethanol, a red-shift of 12 nm, with respect to the emission maximum at low concentration, is observed for EWIFS; at this concentration a red-shift of 38 nm is observed at conventional geometry. This is shown clearly by comparison of figure 1 (a) and (b). The intensity of the fluorescence emission spectra recorded by EWIFS increases with concentration throughout the range 1×10^{-7} to 1×10^{-3} mol dm^{-3}. This is shown at the observation wavelength 585 nm in figure 2 (b). Here linear dependence of emission intensity on concentration up to 1×10^{-5} mol dm^{-3} can be demonstrated. This concentration is ten times higher than the corresponding limit of linearity observed with the conventional geometry.
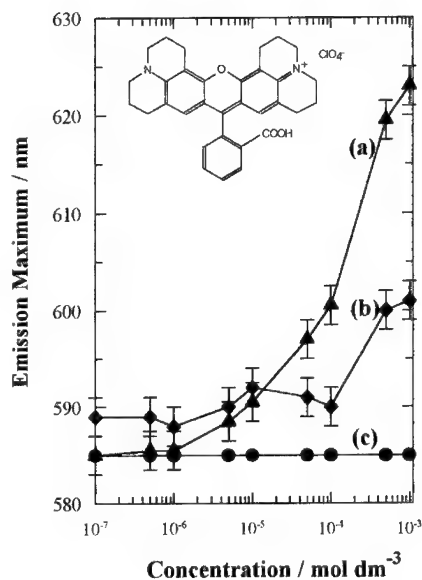
Fig 1. Dependence of the observed emission maximum of rhodamine 101 in ethanol on concentration: (a) conventional geometry, (b) EWIFS (Λ = 154 nm), (c) ideal behaviour.
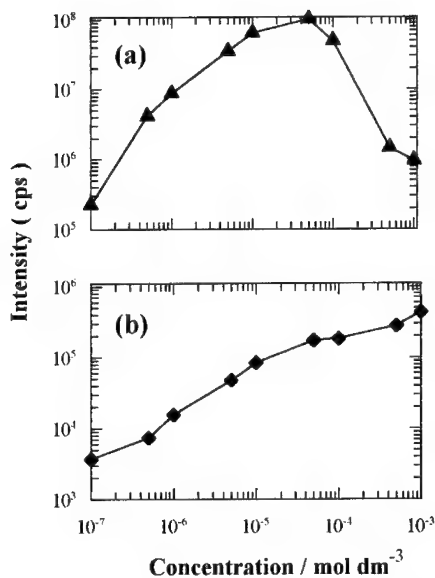
Fig 2. Dependence of the observed emission intensity of rhodamine 101 at 585 nm n concentration: (a) conventional geometry, (b) EWIFS (Λ = 154 nm).

Zinc Porphyrin 'Long Monomer'

Fluorescence emission spectra of solutions of the 'long monomer' in dichloromethane recorded at conventional geometry, with excitation of the Q band at 625 nm, exhibit a change in emission profile, maximum and intensity with increasing concentration similar to that described previously for rhodamine 101. This behaviour is shown in figure 3 (a). Attenuation of the blue-edge of the Q band emission profile, and the red-shift of the emission maximum, is observed at concentrations exceeding 5×10^{-6} mol dm^{-3}. An increase in the intensity of the emission spectrum with increasing concentration is seen up to a concentration of 9×10^{-6} mol dm^{-3}; after this further increase in concentration results in marked decrease of emission intensity. For this species no change in the peak-normalised absorption spectrum with increasing concentration is observed in the corresponding Q band absorption. This suggests that the dominant process causing both the blue-edge attenuation and decrease in intensity of the emission spectrum of the 'long monomer' is the inner filter effect rather than any aggregation, which may be expected [19] at the higher concentrations used in this experiment.

As demonstrated for rhodamine 101, use of the EWIF geometry significantly reduces the distortion of fluorescence emission spectra at high concentration caused by the inner filter effect. This is shown clearly in figure 3, from comparison between (a) and (b). With use of EWIFS minimal blue-edge distortion of emission spectra is observed even at a concentration of 4×10^{-4} mol dm^{-3}; this is accompanied by the absence of significant red-shift of the spectrum with concentration.
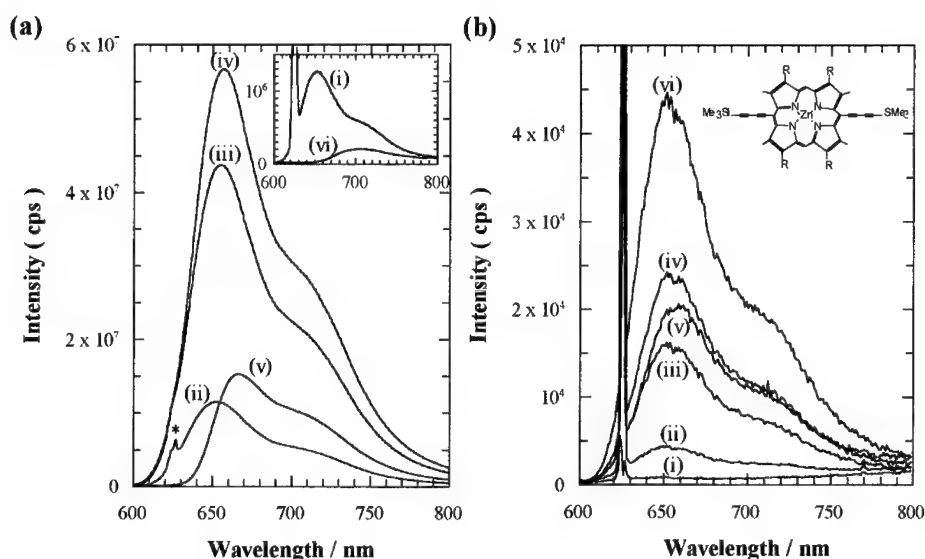
Fig 3. Corrected fluorescence spectra of the 'long monomer' in dichloromethane:
(a) conventional geometry, (b) EWIFS ($\Lambda = 138$ nm) at concentrations of (i) 1×10^{-7}, (ii) 1×10^{-6}, (iii) 5×10^{-6}, (iv) 9×10^{-6}, (v) 6×10^{-5} and (vi) 4×10^{-4} mol dm^{-3}. The feature denoted * represents scatter of the excitation radiation.

For the long monomer in dichloromethane the intensity of emission observed at 650 nm at conventional geometry exhibits a similar dependence on concentration as that shown in figure 2 (a). However, a linear increase in emission intensity with increasing concentration is only observed up to a concentration of 1×10^{-6} mol dm^{-3}; above this, further increase in concentration results in decreasing fluorescence intensity. With use of the EWIF geometry the linear region of such an intensity plot is extended to a concentration of 1×10^{-5} mol dm^{-3}. On further increase of the concentration the observed intensity shows firstly a slight decrease at concentrations of 1×10^{-4} and 6×10^{-5} mol dm^{-3}, followed by a significant increase for the solution of concentration 4×10^{-4} mol dm^{-3}. This behaviour is likely to originate from absorption effects in the TIR regime.

For both rhodamine 101 and the zinc porphyrin 'long monomer' a progressive decrease in the fluorescence quantum yield derived from the EWIF spectra is observed with increasing solution concentration. Although this decrease is significantly smaller than that seen with use of the conventional geometry, it indicates a residual influence of the inner filter effect on the fluorescence emission spectra recorded by this technique. Unfortunately such behaviour has not yet been fully investigated and modelled, and thus, currently prevents a detailed study of the aggregation and photophysics of the 'long monomer'. Even at the highest concentration studied, 4×10^{-4} mol dm^{-3} the degree of aggregation is expected to be relatively low, below 10 % [19], and therefore quite small changes in both the fluorescence intensity and quantum yield are expected. At such concentrations the accuracy and precision that are required for the study of this process are greater than can be currently achieved with EWIFS.

CONCLUSIONS

Use of EWIFS enables collection of fluorescence emission at high concentration, free from distortion due to the inner filter effect obtained using a conventional right-angle geometry. This technique also shows promise as a method for quantitative analysis of bulk solutions, allowing measurement up to concentrations at least ten times greater than can be determined with conventional geometry techniques.

In the EWIFS experiments performed on the long monomer the wavelength of excitation radiation corresponded with the absorption maximum of the Q band. The intensity of fluorescence emission from this species is expected to exhibit a linear dependence on concentration to a higher concentration limit with use of excitation radiation at a wavelength where primary re-absorption effects are smaller [16]. Although the resulting fluorescence emission will be lower in such a case it is expected to enable a photophysical study of this species a region of high concentration.

REFERENCES

1. S. Dhami, A.J. De Mello, G. Rumbles, S.M. Bishop, D. Phillips and A. Beeby, Photochem. Photobiol. **61** (4), 341 (1995).
2. James E. Gill, Appl. Spectrosc. **24**(6), 588 (1970).
3. D.R. Christmann, S.R. Crouch, J.F. Holland and Andrew Timnick, Anal. Chem. **52**, 291 (1980).
4. A. Penakofer and W. Leupacher, J. Luminescence, **37**, 61 (1987).
5. P.R. Hammond, J. Chem. Phys. **70**(8), 3884 (1979).
6. I. Lopéz Arbeloa, J Photochem. **14**, 97 (1980).
7. F. Lopéz Arbeloa, P. Ruiz Ojeda and I. Lopéz Arbeloa, J. Photochem. and Photobiol. A. **45**, 313 (1988).
8. John F. Holland, Richard E. Teets, Partick M. Kelly and Andrew Timnick, Anal. Chem. **49**(6), 706 (1977).
9. D.R. Christmann, S.R. Crouch and Andrew Timnick, Anal. Chem. **53**, 276 (1981).
10. Hans-Peter Lutz and Pier Luigi Luisi, Helv. Chim. Act. **66**(7), 1929 (1983).
11. Mikael Kubista, Robert Sjöback, Svante Eriksson and Bo Albinsson, Analyst, **119**, 417 (1994).
12. Konstantin B. Konstantinov, Prasad Dhurjati, Tina Van Dyk, William Majarian and Robert LaRossa, Biotechnology and Bioengineering, **42**, 1190 (1993).
13. A. J. De Mello, Total Internal Reflection Spectroscopy in Surface Analytical Techniques for Probing Biomaterial Surfaces, edited by J.Davies (CRC Press,1996), p. 1.
14. Daniel Axelrod, Edward H. Hellen and Robert M. Fulbright, Topics in Fluorescence Spectroscopy: Volume 3 - Biochemical Applications, edited Joseph R. Lakowicz (Plenum Press, 1992), p.289.
15. G. Rumbles, D. Bloor, A.J. Brown, A.J. DeMello, B. Crystall, D. Phillips and T.A. Smith, Microchemistry: Spectroscopy and Chemistry in Small Domains, edited H. Masuhara (Elsevier Science,1994), p.269.
16. M. Toriumi and H. Masuhara, Spectrochimica Acta Rev. **14** (5), 353 (1991).
17. M. Toriumi, M.Yanagimachi and H. Masuhara, Appl. Opt. **31** (30), 6376 (1992).
18. J.L. Clark and G. Rumbles, Phys. Rev. Letts **76**(12), 2037 (1996).
19. H.L. Anderson. Inorg. Chem. **33**, 972 (1994).
20. A.J. De Mello, PhD thesis, University of London, 1995.

Imaging Complex Fluids Under Confinement and Flow: Development of Bragg-Fresnel Optics for X-ray Microdiffraction

Youli Li[1], Stefan H.J. Idziak[1&2], Ernie Caine[3], G. Subramanian[1], Evelyn Hu[3], Cyrus R. Safinya[1]

[1]Materials Research Laboratory, Materials Department, Physics Department, Biochemistry and Molecular Biology Program, University of California, Santa Barbara, CA

[2]Current address: Department of Physics, University of Waterloo, Waterloo, Ontario, CANADA

[3]Center for Quantized Electronic Structures (QUEST) and Nanotech, UCSB branch of the National Nanofabrication Users Network (NNUN), UCSB, Santa Barbara, CA

ABSTRACT

We present results of simultaneous efforts to develop: 1.) Bragg-Fresnel Optics (BFO) to be used in X-ray microdiffraction methods, in particular as applied to structural studies of complex fluids and biomaterials under confinement and flow conditions; and 2.) Methodologies for confining complex fluids and biomaterials for in-situ structural studies. Using microelectronics process technology, we have fabricated linear and circular Bragg-Fresnel Lenses (BFL) in Si and III-V compound semiconductor substrates such as InP, GaAs and GaAs heterostructures with outermost zone width to 0.25 µm. X-ray characterization of linear BFLs were performed on a wiggler beamline at Stanford Synchrotron Radiation Laboratory (SSRL) at x-ray energies of 8 keV and 16 keV. A ~5 µm focal spot size was obtained with a 50 µm incident beam, which was determined by the partial coherence of the source. On the confinement techniques, we have developed the X-ray Surface Force Apparatus (XSFA) which allows in-situ x-ray diffraction measurements to be made on fluid thin films confined between two atomically smooth surfaces. A new approach is being pursued to study the effects of confinement and flow on complex fluids and biological materials using microchannels fabricated on glass substrates.

INTRODUCTION

Confinement of complex fluids in thin films between two surfaces or in small pores is expected to strongly alter the collective structure of trapped molecules or molecular assemblies such as polymers, vesicles, biomembranes, or colloidal particles suspended in liquid with or without the presence of flow. The understanding of structures of complex fluids under confinement and flow has many technological implications in fields such as lubrication, the flow of colloidal and biological particles through narrow channels or biological pores, and the processing of ceramic and polymer composite materials. When x-ray diffraction methods are used to probe the structure of complex fluids under geometric confinement at mesoscopic scales, it is essential to use an incident beam with a spatial extent comparable to the linear scale of the confined sample. Moreover, as the confinement gap decreases, the loss of sample volume becomes a limiting factor in obtaining accurate scattering data. Therefore the use of focusing optics which can

enhance the brightness (flux/area) of the incident beam while compressing the beam size is highly desirable.

Conventional geometric x-ray optics such as bent mirrors and crystals, etc., generally do no provide submicron focused beams. With the advent of third generation synchrotron sources with high degree of spatial coherence, diffractive optics such as the Bragg-Fresnel Lenses (BFL), which are Fresnel zones fabricated on the surface of single crystal substrates, as well as refractive lenses, have been demonstrated to be effective x-ray optics for focusing hard x-rays into submicron beams[1-3].

In this paper we present results of our developmental effort to fabricate and characterize BFLs with the goal of using these devices to produce submicron x-ray microbeams for studying complex fluids and biomaterials in confined geometries. We have fabricated linear and circular BFLs with zone width down to 0.25 μm on Si and III-V compound semiconductor materials, which offer many advantages in the fabrication process. We will discuss experiments performed at Stanford Synchrotron Radiation Laboratory (SSRL) to characterize the optical properties of linear BFLs.

We present experimental approaches which would allow in-situ structural study using x-ray diffraction and optical microscopy on complex fluid samples under confinement and flow. Specifically, we discuss incorporation of the BFL-based microbeam diffraction methods in the newly developed X-ray Surface Force Apparatus (XSFA) which confines a fluid sample between two atomically smooth surfaces with a continually variable gap, and in microchannels fabricated on glass surfaces with discrete channel spacings. The latter can be used to study not only the effects of confinement, but also flow; therefore serving as a useful model for studying important biological problems such as blood flow in microscopic vessels.

BRAGG-FRESNEL OPTICS

Fabrication

Fig.1a shows the typical process flow used to fabricate BFLs at UCSB[4]. Fresnel zone patterns were defined on substrates using electron beam lithography and pattern transfer was accomplished using Reactive Ion Etching(RIE) process with an evaporated Ni mask. We developed our own CAD tools to generate the zone patterns for the e-beam machine in order to ensure faithful pattern replication on the substrate, which is critical for focusing. Overall device sizes range from 50 μm - 300 μm with 25 - 150 zones. The smallest outermost zone width that we have used was 0.25 μm. However, devices free from fabrication defects were made generally using 0.5 μm line width. SEM photos of the central and edge zones of a 150 zone circular BFL fabricated on a GaAs (111) substrate are shown in Fig.1b&c. It is easy to see the fact that sixty four sided polygons were used to approximate the rings in circular BFLs.

The technological requirements for the critical etch-transfer process are stringent: straight and smooth etched sidewalls and a precisely defined etch depth that is uniform over the entire device. The continually varying line densities (hence aspect ratios) in a BFL present special challenges in terms of mask integrity and the microloading effect. The relatively thin Ni mask (<1300 Å, above which Ni tends to peel due to stress) can not

withstand prolonged etching which is required for large zone depths; whereas the microloading effect (caused by the local depletion of the etching species for the denser areas of the pattern) reduces the etch rate for high aspect ratio outer zones leading to shallower zone depths in these zones vs. the central zones, which is detrimental to the focusing properties of the BFL. Since the required zone height for a pure phase lens scales inversely with the density of the substrate material[1], it is clearly advantageous to use higher density substrates such as the III-V compound semiconductor materials for fabricating BFLs. Based on these considerations, we have used GaAs and InP (the required zone depths for these materials are less than 50% of that for Si) substrates to fabricate high quality linear and circular BFLs. However, the nonuniformity in etched zone depths still persisted albeit to a lesser extent.

BFL Process Flow
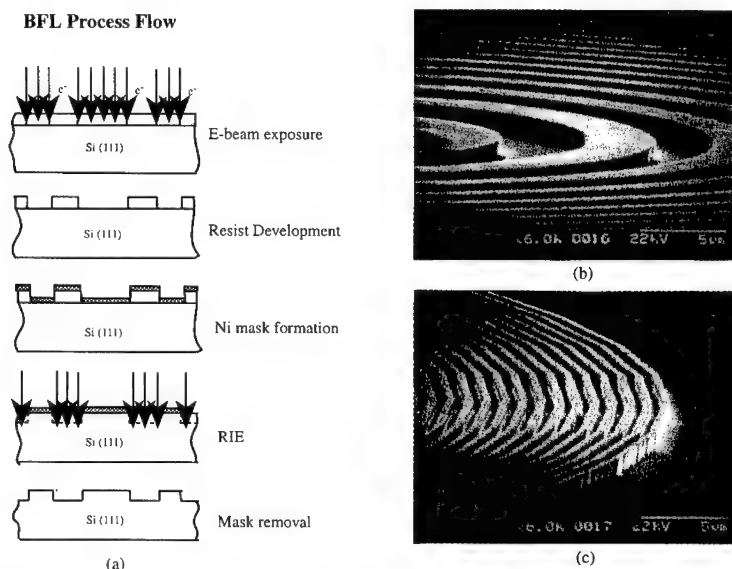
Fig.1 Flow chart of the BFL fabrication process and SEM images of a circular GaAs BFL. The central zone radius = 12.2 μm, outermost zone width = 0.5 μm and aperture size = 300 μm.

To counter this problem we have exploited the availability of heterostructures in the III-V materials (e.g. GaAs/AlAs) which allow us to incorporate highly efficient etch-stop layers into the structures to ensure uniform etched depth in all zones. In particular, we have used a MBE-grown GaAs/AlGaAs/GaAs heterostructure as substrate for fabricating BFLs. The growth started with a 5000 Å GaAs buffer layer on a GaAs (111)B substrate, followed by 1000 Å Al_7Ga_3As, and a thin (20 Å) AlAs layer, followed by a GaAs layer of 5300 Å thickness which is the required zone height for a linear BFL. The AlGaAs/AlAs layer becomes a natural etch stop when small amount of O_2 is introduced during the Chlorine-based RIE of the heterostructure, forming poorly etchable aluminum oxides. In the initial test of this process, we have achieved uniform etched depth over the

303

entire device[4], at the expense of increased surface roughness the cause of which is currently under investigation.

X-ray Characterization

Characterization of Si and GaAs linear BFLs have been conducted at Stanford Synchrotron Radiation Laboratory (SSRL) wiggler beamline 10-2. The objectives of the characterization were to test the focusing properties of the BFLs and develop relevant experimental methods for utilizing these devices in x-ray microdiffraction experiments. Experiments were done using 8 keV and 16 keV x-rays on 150 zone (Aperture = 300 μm) and specially fabricated 25 zone (Aperture = 50 μm) BFLs. Although focusing effects were observed to varying degree from all these devices, we found that the 25 zone device provided the cleanest focusing pattern with the smallest focal spot size (FWHM ~5 μm) because the device size more closely matched the spatial coherence of the incident beam.

(b) focused beam   (c) X-ray beam from Si substrate

(d) focused beam   (e) X-ray beam from Si substrate
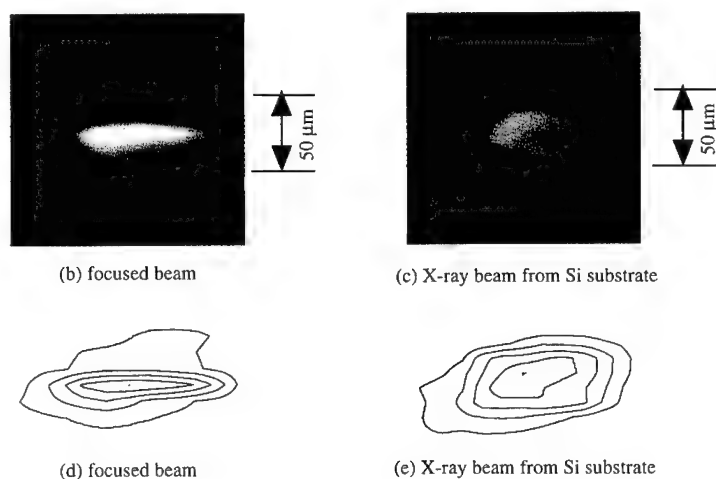
Fig. 2 Greyscale images and contour plots of measured intensity distribution (at 8 keV) of the focused beam and the un-focused beam from the Si substrate. The BFL was a linear Si (111) device with an area of 50 μm (height) x 300 μm (length) and a finest zone width of 0.5 μm.

The experiment was set up as follows. The incident beam was defined by a set of x-ray slits to match the size of the BFL located at 22m from the x-ray source. The BFL was mounted on a translation/rotation stage assembly for positioning the BFL in the x-ray beam and for setting the Bragg angle. The focused beam from the BFL was measured using a scanning pinhole (aperture size = 5 - 10 μm) placed at the focal plane of the lens. Images of the beam were also taken at distances in front and behind the focal plane to determine the true focal length of the lens and to investigate de-focusing effects. For comparison, images of the unfocused x-ray beam were acquired by vertically translating

the BFL by 150 μm so that the incident beam was illuminating the blank Si substrate. Fig. 2 shows images of both the BFL focused beam and the un-focused beam coming from the Si substrate. The focal spot size (~5 μm) and flux/area enhancement (~ a factor of 2), are both far below theoretical expectations, which is indicative of a large spatially incoherent component in the incident beam. By employing upstream apertures to reduce effective source size, and/or utilizing low emittance third generation synchrotron sources, a submicron focal spot size with substantial brightness gain can be achieved. These submicron size x-ray beams will be very useful for probing the structure of materials in confined geometries.

CONFINEMENT TECHNIQUES

We have developed two experimental systems for confining complex fluids and biomaterials while allowing simultaneous measurement of structural properties of the confined material using x-rays, in particular BFL-based microbeams.

The X-ray Surface Force Apparatus (XSFA)

The XSFA, which is schematically shown in Fig. 3a, allows transmission x-ray scattering studies of complex fluid samples confined between two atomically smooth surfaces[5]. The confinement gap can be varied continually from microns down to tens of angstroms with angstrom resolution. Alignment of several liquid crystalline material systems, by shear-flow or direct confinement, were observed using the XSFA at SSRL[5-7]. The smallest confinement gap used in experiments were determined by both the incident beam size and the total flux in the beam. So far we have used gap size ~3000 Å on wiggler beamlines at SSRL with a pinhole-defined 100 μm incident beam. By utilizing BFL-based microdiffraction methods at the Advanced Photon Source (APS), we will be able to reduce the gap size down to nanometer scale so that a single monolayer of molecules could be aligned and studied in the XSFA.

Microchannels for Confinement and Flow Studies

We are currently developing methods to use microchannels fabricated on glass substrates for studying the effects of confinement and flow on liquid crystalline materials and biological systems. One approach is to directly use linear Bragg-Fresnel lenses, such as the one shown in Fig. 3b, for these studies. From center to edge a BFL provides a decent gap range (channel widths: 0.25 μm - 12.2 μm) for observing confinement effects. Flow could be induced using microinjectors. We have also fabricated arrays of uniform spacing microchannels on thin (~ 200 μm) glass cover slips which are designed specifically for studying the structure of confined material using polarized microscopy and x-ray diffraction (both in transmission and reflection). The smallest channel width we used were 0.25 μm, which can be reduced further (possibly to below 50 nm) by using specialized lithographic methods.

<div style="text-align:center">(a)   (b)</div>
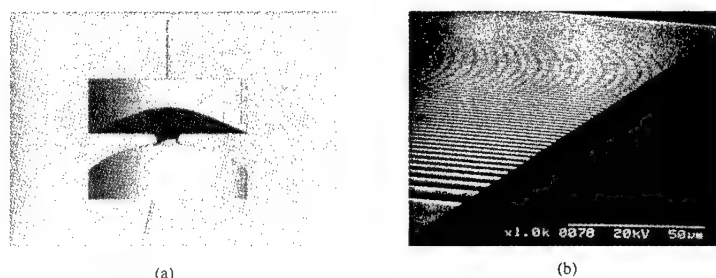
Fig. 3 Two experimental systems for studying structure of complex fluids and biomaterials under confinement and flow. (a) The confining surfaces in the XSFA. The gap size can be varied continually with angstrom steps. (b) A linear BFL on Si. The zone channels, and silmilar structures fabricated on glass substrates, are being used to study confinement and flow of complex fluids and biomaterials.

SUMMARY

We have presented development of Bragg-Fresnel optics on Si and III-V compound semiconductor materials (GaAs, InP and GaAs heterostructures) for x-ray microdiffraction studies of complex fluids and biomaterials in confined geometries. We have also reported development of experiment systems, which include the continually variable gap confinement technique based on the XSFA and discrete gap method based on microchannels fabricated on glass substrates, for in-situ x-ray diffraction and optical microscopy studies of complex fluids under confinement and flow.

ACKNOWLEDGMENT

REFERENCES

1. A.A. Snigirev, *Rev. Sci. Instrum.* **66**(2), 2053-2058, 1995

2. A. Snigirev, V. Kohn, in *X-ray Microbeam Tech. and Appl., Proc. of SPIE,* **2516**, 27-37, 1995

3. A. Snigirev, V. Kohn, I. Snigireva & B. Lengeler, *Nature*, **384**, 49-51, 1996

4. E.J. Caine, S.Shi, E.L.Hu, Y.Li, S.H.J. Idziak, G. Subramanian, C.R. Safinya, to appear in *Microelectronics Engineering*

5. S.H.J. Idziak, C.R. Safinya, R.S. Hill, et al., *Science*, **264**, 1915-1918, 1994

6. S.H.J. Idziak, I. Koltover, J. Israelavhivilli and C.R. Safinya, *Phys. Rev. Lett.* **76**, 1477-1479, 1996

7. I. Koltover, S.H.J. Idziak, P. Davidson, Y.Li, C.R. Safinya, et al, *J. Phys. II,* **6**, 893-907, 1996

INSTABILITY AND FRONTAL BREAKUP IN SUPER-MENISCUS FILMS

DAWN E. KATAOKA and SANDRA M. TROIAN
Department of Chemical Engineering, Princeton University, Princeton NJ 08544-5263

ABSTRACT

Surface tension gradients created by a nonuniform temperature distribution in a thin liquid film can force vertical spreading beyond the equilibrium meniscus [1]. Experiments designed to probe the flow behavior of super-meniscus films have shown that the leading edge can either spread uniformly with complete surface coverage or become corrugated and breakup into long slender rivulets. We show that within linear stability analysis, both the conditions for unstable flow and the most unstable wavelength compare favorably with recent experiments reported in the literature.

INTRODUCTION

Coating processes usually require a forcing mechanism to induce spreading over the surface. Although flows can be driven by a mechanism as simple as tilting or spinning, flows driven by surface tension gradients have the advantages of operating independent of geometry and allowing the substrate to remain stationary.

Temperature gradient driven films of silicon oils on both vertical [2] and horizontal [3] silicon wafers have been shown to spread with a corrugated leading edge. Such unstable flows exhibit a capillary ridge or "bump" at the leading edge. Surprisingly, similar experiments examining the flow of squalane on a vertical silver plate demonstrate that the film climbs with a uniformly straight front [1]. Furthermore, rather than exhibiting the characteristic advancing ridge, these profiles decrease monotonically as the contact line is approached. The two observations seem contradictory: one would expect similar behavior for both liquid-on-solid systems since the liquids completely wet the different substrates.

It has been proposed in the literature [4] that the capillary ridge must be present in order for the instability to occur. We present here a linear stability analysis of films driven by a constant temperature gradient. This analysis indicates a strong correlation between the presence of a capillary ridge in the unperturbed film thickness profiles and the subsequent formation of long rivulets at the advancing front.

PROBLEM FORMULATION

Governing Equations

Lubrication theory is valid for low Reynolds number flows for which the characteristic extent in the direction of flow is much larger than the film thickness. The temperature gradient driven films observed in Refs. [1–3] are therefore governed by the lubrication equations,

$$\eta \frac{\partial^2 u}{\partial z^2} = \frac{\partial p}{\partial x} + \rho g \qquad (1)$$

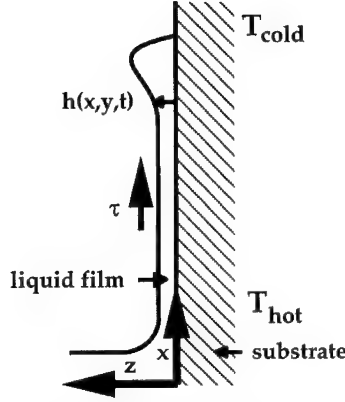$$\eta \frac{\partial^2 v}{\partial z^2} = \frac{\partial p}{\partial y} \qquad (2)$$

307

Figure 1: Coordinate system. The y axis points into the page.

$$\frac{\partial p}{\partial z} = 0, \tag{3}$$

where the x axis is along the vertical flow direction, the y axis is in the transverse flow direction, and the z axis is perpendicular to the surface, as illustrated in Fig. (1). The velocity components u and v represent flow in the x and y directions, while p denotes the local pressure in the fluid. The air-liquid interface is described by $z = h(x, y, t)$, which represents the film thickness resting above the stationary substrate located at $z = 0$. The viscosity, density, and local surface tension of the liquid are given by η, ρ, and γ. In the derivation which follows we assume that the temperature distribution mostly affects the local surface tension, with local viscosity or density undergoing smaller changes which are neglected. The boundary conditions are the no-slip requirement at the solid surface

$$u, v|_{z=0} = 0, \tag{4}$$

and constant shear stress at the air-liquid interface

$$\eta \frac{\partial u}{\partial z}\bigg|_{z=h} = \tau. \tag{5}$$

In regions of the flow where curvature terms become important, we assume relatively small slopes, so that the capillary pressure throughout the film is given by $p = -\gamma \nabla^2 h$. Solving for the height-averaged velocities with contributions from Marangoni flow, capillarity and gravity yields

$$U(x) = \frac{\tau h}{2\eta} + \frac{\gamma}{3\eta} h^2 \nabla \cdot \nabla^2 h - \frac{\rho g h^2}{3\eta} \tag{6}$$

$$V(x) = \frac{\gamma}{3\eta} h^2 \nabla \cdot \nabla^2 h. \tag{7}$$

Substitution of the velocities into the continuity equation

$$\frac{\partial h}{\partial t} + \frac{\partial}{\partial x}(hU) + \frac{\partial}{\partial y}(hV) = 0, \tag{8}$$

308

with the requirement that the leading edge match smoothly onto a prewetting layer located beyond the nominal contact line gives the film height profiles. For horizontal films, the last term in Eqn. (6) is deleted. Moreover, for vertical geometries, this term can be neglected for sufficiently thin films for which the Marangoni driving force is much larger than drainage by gravity, i.e.

$$h \ll \frac{3\tau}{2\rho g}. \tag{9}$$

Scaling

Away from the leading edge, the film is relatively flat and curvature effects can be neglected. Balancing viscous and Marangoni forces in this "outer" region yields the characteristic velocity scale for the system

$$U_c = \frac{\tau h}{2\eta}. \tag{10}$$

Near the spreading front, curvature effects must be included; the interface must curve in order to contact the substrate. Inclusion of capillary effects in the balance with viscous and Marangoni forces gives the characteristic length scale over which the interface curvature is significant

$$l = h_c (3Ca)^{-\frac{1}{3}}, \tag{11}$$

where Ca is the capillary number, defined by

$$Ca = \frac{\eta U_c}{\gamma}, \tag{12}$$

and h_c represents the film thickness at the leading edge of the outer region.

To address the stability of the leading edge which occurs in the vicinity of the capillary region, we must first solve for the unperturbed film thickness profiles in the inner region. We therefore rescale all variables in a manner similar to other driven flow problems [4–6]. This rescaling effectively stretches the appropriate variables in such a way as to balance contributions among all the local forces present in the capillary region. Spatial coordinates are rescaled by l, the film thickness h by h_c, and time by U_c/l. Rescaling of Eqn. (8) yields the appropriate dimensionless evolution equation for the film thickness

$$\hat{h}_{\hat{t}} + (1+b)\hat{h}_\xi \;-\; \frac{\partial}{\partial \xi}\left[\hat{h}^2 - \hat{h}^3(\hat{h}_{\xi\xi\xi} + \hat{h}_{\xi\zeta\zeta})\right]$$
$$+\; \frac{\partial}{\partial \zeta}\left[\hat{h}^3(\hat{h}_{\zeta\xi\xi} + \hat{h}_{\zeta\zeta\zeta})\right] = 0. \tag{13}$$

The solution to (13) must satisfy the two required boundary conditions in ξ,

$$\hat{h} \to 1 \quad as \quad \xi \to \infty \tag{14}$$
$$\hat{h} \to b \quad as \quad \xi \to -\infty. \tag{15}$$

A third boundary condition in ξ is unnecessary; Eqn. (13) lacks explicit ξ dependence and is therefore translationally invariant. Boundary conditions in ζ and an initial condition in $\hat{t}$ are also not needed since the form of the profile disturbance in ζ and $\hat{t}$ will be specified. The

309

variables ξ and ζ are the dimensionless x and y coordinates, and $\hat{h}$ and $\hat{t}$ are the dimensionless film thickness and time. The ξ coordinate has been scaled such that the origin translates with the contact line so that ξ is positive in the upstream direction. The parameter b is the ratio of the precursor film thickness to the characteristic film thickness h_c.

RESULTS

Base Flow

To solve for the base flow profile and perturbation, we expand the film thickness as

$$h(\xi, \zeta, t) = h_0(\xi) + \epsilon h_1(\xi, \zeta, t), \tag{16}$$

where h_0 denotes the unperturbed film profile, h_1 is the disturbance, and ϵ is a small parameter representing the strength of the applied perturbation. (The hats have been dropped for clarity.) We find the shape of the unperturbed film and the perturbation by substituting the expanded form of h into Eqn. (13). The base flow is given by the $O(1)$ equation

$$h_{0\xi\xi\xi} = \frac{1}{h_0} - (1 + b)\frac{1}{h_0^2} + b\frac{1}{h_0^3}, \tag{17}$$

which must satisfy the boundary conditions

$$h_0 \to 1 \quad as \quad \xi \to \infty \tag{18}$$
$$h_0 \to b \quad as \quad \xi \to -\infty. \tag{19}$$

Again, a third boundary condition is unnecessary because (17) is translationally invariant. Numerical solutions to (17) for various precursor thicknesses are plotted in Fig. (2). Note that the height of the capillary ridge decreases with an increase in the precursor layer thickness.
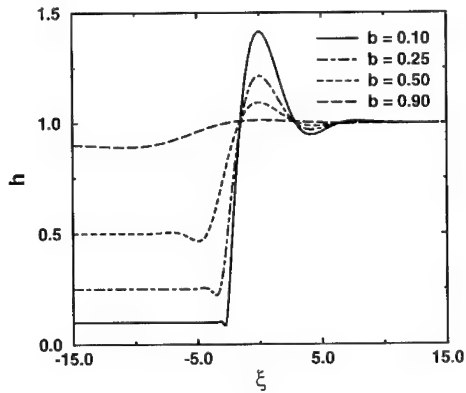
Figure 2: Base flow film profiles for various prewetting layer thicknesses. The profiles have been shifted to align the profile maxima.

<u>Linear Stability Analysis</u>

The shape of the disturbance is given by keeping the $O(\epsilon)$ terms and substituting in the normal mode form for the disturbance

$$h_1(\xi, \zeta, t) = G(\xi) exp(iq\zeta + \beta t), \qquad (20)$$

where q denotes the wavenumber of the disturbance in the transverse flow direction and β is the eigenvalue or growth rate of the perturbation. The resulting linear equation

$$\beta G \;\; + \;\; (1+b)G_\xi - \frac{\partial}{\partial \xi} \left[2Gh_0 - 3Gh_0^2 h_{0\xi\xi\xi} \right.$$

$$\left. -h_0^3 \left(G_{\xi\xi\xi} - q^2 G_\xi \right) \right] + h_0^3 \left(q^4 G - q^2 G_{\xi\xi} \right) = 0 \qquad (21)$$

is subject to decay boundary conditions

$$G, G_\xi \to 0 \quad as \quad \xi \to \infty \qquad (22)$$

$$G, G_\xi \to 0 \quad as \quad \xi \to -\infty. \qquad (23)$$

Numerical solutions to Eqn. (21) for the largest growth rate as a function of wavenumber are illustrated in Fig. (3). Note that the magnitude of the disturbance growth rate decreases with an increase in the precursor film thickness.

DISCUSSION AND CONCLUSIONS

The above theoretical analysis is valid for constant shear stress driven flows for which gravity is negligible. The base flow profiles of these spreading films contain a capillary ridge at the leading edge whose magnitude decreases with an increase in the prewetting layer thickness (Fig. 2). As the capillary ridge decreases or as the precursor layer increases, the flow becomes more stable. As illustrated in Fig. (3), the film becomes marginally stable for a prewetting layer thickness that is about half as thick as the characteristic thickness of the spreading film. This result indicates a strong correlation between the capillary ridge thickness and the linear stability of the film.
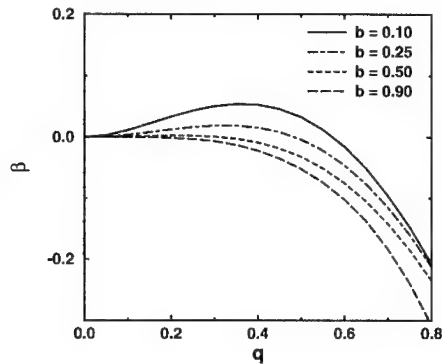
Figure 3: Dispersion relationship illustrating the largest eigenvalue β as a function of wavenumber q for the films illustrated in Fig. (2).

We have compared our predictions with experiments reported in the literature for spreading silicon oil films [2,3]. The climbing films were sufficiently thin to satisfy Eqn. (9), and horizontal films were unaffected by drainage. The theoretical analysis assumes, however, the presence of a prewetted layer ahead of the leading edge. Although the surfaces were not precoated in the experiments, evaporation/condensation, van der Waals forces, or diffusion may have deposited a very thin layer of fluid ahead of the spreading front. The presence of such a prewetting layer was found by Carles et al [7]. It appears therefore that the theoretical predictions for very small prewetting layers most closely resembles the experimental conditions. Small values of b yield relatively large capillary ridge thicknesses, which are in agreement with experimental observations. Furthermore, the observed instability is consistent with the theoretical prediction that flow with large capillary ridges become unstable. In addition, we have found that the most unstable wavelength is $\lambda \approx 18l$, which is in excellent agreement with experiments [8].

In contrast to the silicon oil films, the squalane films reported in Ref. [1] lacked a capillary ridge and spread with a straight front. The small temperature gradients used in these experiments produced films of sufficient thickness for which drainage velocities become comparable to Marangoni velocities. Inclusion of drainage by gravity in the theory is expected to eliminate the capillary ridge to produce theoretical profiles which decrease monotonically as the edge is approached. We are currently investigating the stability of Marangoni driven flows with the inclusion of drainage. If the additional mechanism eliminates the bump and suppresses the instability, this result will provide strong evidence for the link between the presence of the bump and the instability and will elucidate the reason behind the discrepancy between the similar experimental systems.

ACKNOWLEDGMENTS

REFERENCES

1. V. Ludviksson and E.N. Lightfoot, AIChE J. **17**, p. 1166 (1971).

2. A.M. Cazabat, F. Heslot, S.M. Troian, and P. Carles, Nature **346**, p. 824 (1990).

3. J.B. Brzoska, F. Brochard-Wyart, and F. Rondelez, Europhys. Lett. **19**, p. 2 (1992).

4. S.M. Troian, E. Herbolzheimer, S.A. Safran, and J.F. Joanny, Europhys. Lett. **10**, p. 25 (1989).

5. J.A. Moriarty, L. Schwartz, and E.O. Tuck, Phys. Fluids **3**, p. 733 (1991).

6. M.A. Spaid and G.M. Homsy, Phys. Fluids **8**, p. 460 (1996).

7. P. Carles, A.M. Cazabat, and E. Kolb, Colloids and Surfaces A **79**, p. 65 (1993).

8. D.E. Kataoka and S.M. Troian, submitted to J. Colloid Interface Sci.

NMR EXPERIMENTS ON MOLECULAR DYNAMICS IN NANOPOROUS MEDIA: EVIDENCE FOR LÉVY WALK STATISTICS

RAINER K I M M I C H, TATIANA Z A V A D A, SIEGFRIED S T A P F

Universität Ulm, Sektion Kernresonanzspektroskopie, 89069 Ulm, Germany

ABSTRACT

Field-cycling ^{1}H and ^{2}H NMR relaxometry and field-gradient ^{1}H NMR diffusometry were applied to polar and nonpolar liquids filled into porous glasses and fineparticle agglomerates (SiO_2, ZnO, TiO_2, globular proteins). The orders of magnitude of the length scales of the pore spaces ranged from 10^0 to several 10^2 nm. Pronounced differences of the spin-lattice relaxation dispersion for "weak" (nonpolar) and "strong" (polar) adsorption were found. In the latter case, the correlation times of the adsorbate orientation are up to eight orders of magnitude longer than in bulk. Translational diffusion in liquid surface layers was directly studied with the aid of field-gradient NMR diffusometry in systems where the free liquid was frozen. The spin-lattice relaxation dispersion can be explained on the basis of reorientations mediated by translational displacements (RMTD) of adsorbate molecules on the surfaces. This process appears to be enhanced by a Lévy walk mechanism so that the propagator adopts the form of a Cauchy distribution. The evaluated surface correlation functions are characterized by surface correlation lengths in the same order as the pore diameters, that is, up to three orders of magnitude larger than the length scale of dipolar interaction.

INTRODUCTION

Nanoporous media such as those listed in tab. 1 form a class of lacunar systems with a particularly high surface-to-volume ratio which ranges up to 400 m^2/g. The dynamics of solvent molecules confined in the pore spaces of such systems are expected to deviate from the bulk behaviour because of two reasons. Firstly, the random-walk trajectories are restricted by the matrix. This **excluded-volume (or geometry) effect** reduces the diffusivity on length scales beyond the mean pore diameters. Furthermore there is a tendency towards anomalous diffusion behaviour within the correlation length of the pore space.

system	characteristic lengths in nm
porous glasses	3, 4, 8, 30, 50, 68, 96, 208
porous ceramics	38
protein powders	3 ... 9
silica fineparticle agglomerates	7, 20
ZnO fineparticle agglomerates	200 ... 800
TiO_2 fineparticle agglomerates	200 ... 500

Table 1: The nanoporous materials considered in this study

Secondly, molecules confined in pore spaces can be subject to interactions with the pore walls leading to what may be called **adsorption effect**. In case the adsorbate molecules are trapped on the surfaces for a long time, the consequence may be that self-diffusion in

313

pore spaces is further slowed down. On the other hand, surface interaction tends to impose a certain preferential orientation on the adsorbate molecules. That is, molecular reorientations are more or less hindered. The strategy of the present study of the adsorbate dynamics consequently was a) to consider pore spaces with geometries varying on lengthscales from several 10^0 to several 10^2 nm, b) to modify the polar character of the surfaces and to employ adsorbate molecules of different polarity and hydrogen-bonding capacity. In particular we distinguish the "strong" and "weak adsorption" limits as suggested in ref. [1].

METHODS

In the case of ordinary diffusion, the mean squared displacement of adsorbate molecules obeys the relation

$$\langle r^2 \rangle = 6Dt \tag{1}$$

where D is the diffusion coefficient, and t is the time. The geometry effect may cause an anomalous behaviour which can often be represented by a power law

$$\langle r^2 \rangle = \alpha t^\kappa \tag{2}$$

where α is a constant. An exponent κ deviating from one indicates "anomalous diffusion."

Field-gradient NMR diffusometry is a suitable means for studies of either mean-squared displacement law [2,3]. The signal to be detected in such experiments usually is the stimulated echo arising after a three-pulse sequence with intervals τ_1 and τ_2. If the second pulse interval complies to the limit $\tau_2 \gg \tau_1$, which can easily be adjusted using strong steady field gradients [4], the mean-squared displacement can be evaluated from

$$\left\langle r^2(t) \right\rangle = -6 \frac{\ln A_{diff}(k,t)}{k^2} \tag{3}$$

The echo attenuation factor due to diffusion is designated by $A_{diff} = A_{diff}(k,t)$. This is a function of the "diffusion time" $t = \tau_1 + \tau_2$, and of the "wavenumber" $k = \gamma_n G \tau_1$. The quantity γ_n is the gyromagnetic ratio of the resonant nucleus, and G is the (average) gradient in the first pulse interval τ_1.

Apart from self-diffusion we are interested in the reorientational fluctuations of the adsorbate molecules. Any changes should directly reflect the influence of wall interactions. The method of choice is **field-cycling NMR relaxometry** [3]. Combined with conventional pulse methods and suitably carried out, this technique typically probes total frequency ranges $3 \times 10^3 \ldots 3 \times 10^8$ Hz for ^{1}H, and $3 \times 10^2 \ldots 4 \times 10^7$ Hz for ^{2}H resonance.

The spin-lattice relaxation rate of an ensemble of either dipolar coupled two-spin 1/2 systems with a fixed internuclear distance, or quadrupolar coupled spin 1 nuclei is given by (e. g. [3])

$$R_1 \equiv \frac{1}{T_1} = K \left[\mathcal{I}(\omega) + 4\mathcal{I}(2\omega) \right] \tag{4}$$

where K represents constants characteristic for the nuclear species and the couplings. The intensity function is defined by

$$\mathcal{I}(\omega) = \int\limits_{-\infty}^{+\infty} G(\tau) e^{-i\omega\tau} \, d\tau \tag{5}$$

314

For the spin interactions under consideration here, the NMR correlation function reads

$$G(\tau) = \left\langle Y_{2,m}[\vartheta(0), \varphi(0)] \; Y_{2,m}^*[\vartheta(\tau), \varphi(\tau)] \right\rangle \qquad (6)$$

where $Y_{2,m}$ is a spherical harmonics of second rank with $m = 1, 2$. The polar and azimuthal angles ϑ and φ, respectively, characterize the (fluctuating) orientations of the adsorbate molecules.

In the following, we will discuss experimental data for the dispersion of the spin-lattice relaxation rate, $R_1 = R_1(\nu)$. The goal is to extract data for the NMR correlation function $G = G(\tau)$ on the time scale corresponding to the accessible frequency window. These can then be interpreted on the basis of models specific for molecular mechanisms on surfaces. Experimental details on the samples and the instruments can be found in our previous papers [5,6].

THE SELF-DIFFUSION/REORIENTATION PARADOX

Self-diffusion of water and other small liquid adsorbate molecules in completely filled nano-porous materials is characterized by the following findings:

- Apart from special aerogel-like preparations of the matrix [7,8], no indication of anomalous diffusion was found on a time scale restricted by our present experimental limit of $\tau_1 + \tau_2 = 250$ μs. That is, the root mean-squared displacement on this time-scale exceeds the correlation length of the pore space of our porous-glass samples by far.

- The self-diffusion coefficients of polar and non-polar solvents filled into porous glasses is only slightly reduced relative to the bulk values (fig. 1). For the investigated glasses, the reduction appears to be a function of the porosity but depends neither on the solvent polarity nor on parameters such as the pore diameter or the temperature [9].

- Freezing of the free fraction of the confined solvent leaves one or two monolayer thick liquid films on the surfaces. That is, self-diffusion virtually is restricted to these liquid layers. The self-diffusion coefficients measured under such conditions are amazingly high [7,9]. The reduction of typically one order of magnitude relative to the unfrozen system may largely be attributed to the effectively diminished porosity. The adsorbate molecules retain a high translational mobility even when tightly confined to the surfaces. Recently it was even shown that "single-file diffusion" of adsorbate molecules confined in zeolite channels of a quasi one-dimensional structure is extremely fast [10]. Furthermore, a molecular dynamics computer simulation study of acetone diffusion in cylindrical silica pores with diameters as small as 1.5 nm reveals diffusion coefficients in the same order of magnitude as under bulk conditions [11].

The extremely high surface diffusivities are opposed by the time scale of reorientational fluctuations of the adsorbate molecules probed by proton as well as deuteron field-cycling relaxometry. The following findings can be stated:

- The "strong" and "weak adsorption" limits [1] reveal themselves by steep and flat spin-lattice relaxation dispersions [6], respectively.
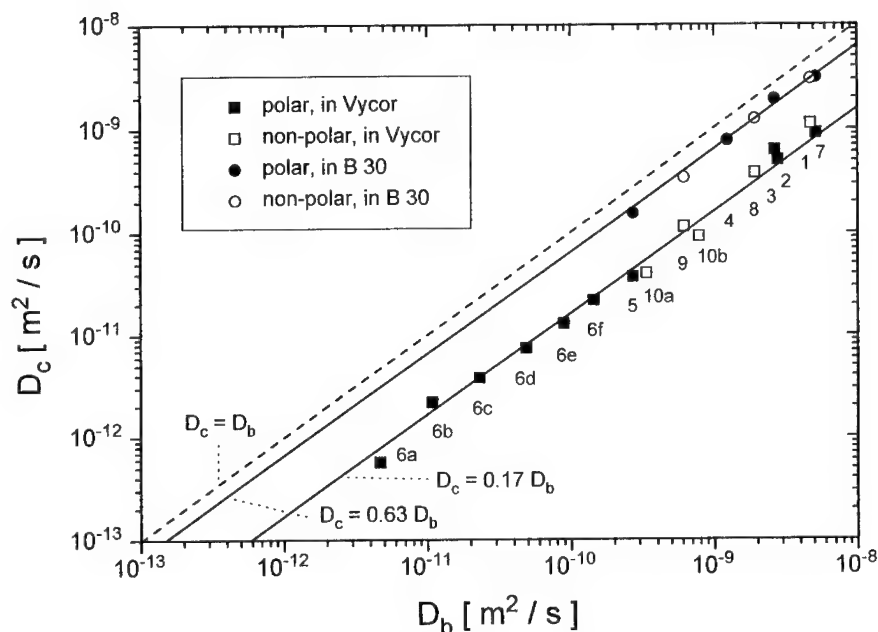
Figure 1:

Diffusion coefficients, D_c, of ten different liquids confined in porous glasses at different temperatures in correlation to the bulk values, D_b. The adsorbates and the temperatures are indicated by numbers and letters: 1, acetone at 303 K; 2, toluene at 303 K; 3, water at 303 K; 4, ethanol at 303 K; 5, hexanol at 303 K; 6a - 6f, glycerol at temperatures between 305 and 378 K; 7, hexane at 303 K; 8, cyclohexane at 303 K; 9, tetradecane at 303 K; 10a and b, octacosane at 343 and 373 K, respectively. The reduction factors common to all liquids are found to be 0.63 and 0.17 for Bioran B30 (porosity 0.67; mean pore diameter 30 nm) and Vycor (porosity 0.28; mean pore diameter 4 nm), respectively.

- In the low-frequency range $\nu < 10^7$ Hz, the spin-lattice relaxation dispersion of H_2O (proton resonance) and D_2O (deuteron resonance) in Bioran porous glass is identical [6]. That is, low-frequency spin-lattice relaxation is dominated by intramolecular spin interactions, and the influence of potential electron paramagnetic impurities can be neglected. ESR studies confirm this conclusion [12].

- In the case of strong adsorption, i. e., polar adsorbates adsorbed at polar surfaces, the low-frequency spin-lattice relaxation dispersion reveals correlation times up to eight orders of magnitude longer than in bulk [5,6,13]. No strong temperature dependence can be stated.

- Freezing of the free adsorbate fraction leaving liquid surface layers converts the spin-lattice relaxation dispersion to a "strong-adsorption-like" behaviour in case it is "weak-adsorption-like" in the unfrozen state, whereas "strong-adsorption-like" behaviour in the unfrozen state is maintained [14].

The combined diffusometry and field-cycling relaxometry results which are of interest in this context may be summarized by the statement: *In the strong-adsorption limit, the rotational degrees of freedom of adsorbate molecules imply components extremely slowed down compared to the bulk, whereas the translational degrees of freedom maintain mobilities in the same order of magnitude.*

REORIENTATIONS MEDIATED BY TRANSLATIONAL DISPLACEMENTS

In previous papers [8,13,15] we have suggested that the slow decay of the NMR correlation function is the consequence of *reorientations mediated by translational displacements* (RMTD). Adsorbate molecules are subject to preferential orientations relative to the local surface while residing in the surface layer [16,17]. Diffusion along curved or rugged surfaces then governs the reorientation rate and, hence, the decay of the NMR correlation function in the limit beyond the time scale of local processes. That is, it is translational diffusion in combination with the surface topology rather than any hindrances by potential barriers which determine the time scale of complete reorientations.

In cases of very low adsorbate concentrations so that all adsorbate molecules in the sample populate the surface layer, or when the free phase is frozen and, therefore, excluded from efficient molecular motions, surface-guided displacements represent the only translational degree of freedom which is measured in NMR diffusometry experiments (see above) and which can act as an RMTD mechanism in principle [7,14]. Under such circumstances, there is no doubt that the low-frequency spin-lattice relaxation dispersion mirrors the surface structure. We have therefore introduced an orientational structure factor for description purposes [13].

In the presence of a "free" adsorbate phase the situation is less clear. If the RMTD mechanism is to apply, a physical reason must exist why the adsorbate molecules stay at or near the surfaces at least as long as the longest orientational correlation time contributing to the spin-lattice relaxation dispersion. Correspondingly high binding energies are chemically unplausible and contradict the translational degrees of freedom experimentally found.

LÉVY WALKS

In order to probe the surface orientation, an adsorbate molecule need not stay all the time directly attached to the surface. For a contribution to the RMTD correlation function it is sufficient if the adsorbate molecule resides initially and finally on surface sites whereas many desorption and readsorption processes may occur in between. In the strong adsorption limit this situation appears to be a general scenario as recently suggested by Bychuk and O'Shaughnessy [1,18]. These authors showed that the effective displacements of adsorbate molecules along a surface can be the consequence of stochastic desorption/readsorption cycles with intermittent excursions in the free phase, and obeys Lévy walk statistics [19].

According to this theory, the effective displacements along the surface are described by the Cauchy distribution in two dimensions,

$$\Psi(s,\tau) = \frac{1}{2\pi} \frac{c\tau}{[(c\tau)^2 + s^2]^{3/2}} \qquad [Q^{-1} < \tau < t_h] \qquad (7)$$

where the two-dimensional displacement on the surface is denoted by s, and the bulk diffusion coefficient by D. The time scale on which this surface propagator applies is limited by the
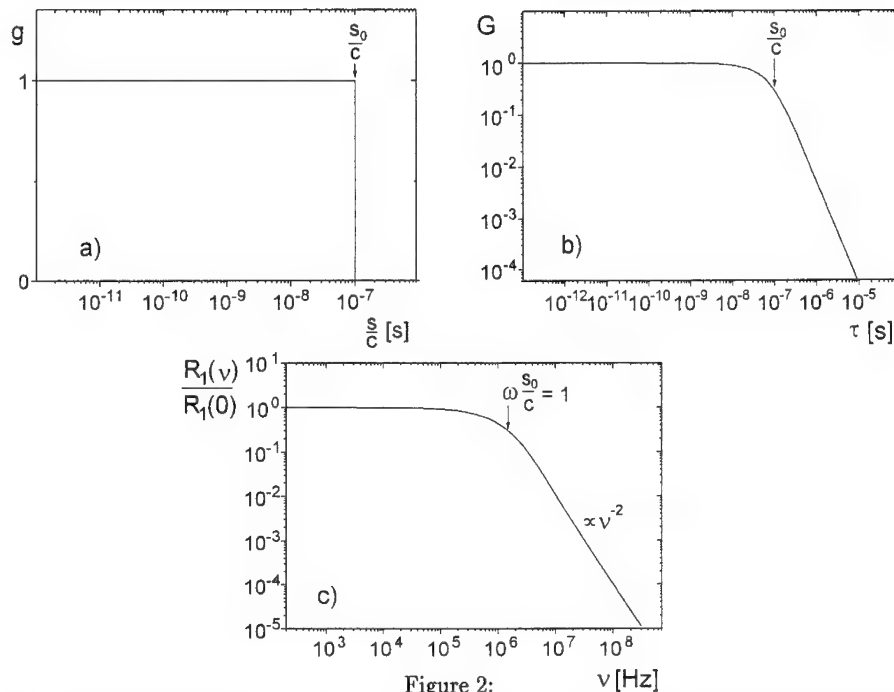
Figure 2:

RMTD correlation function $G(t)$ (b) and spin-lattice relaxation dispersion $R_1(\nu)$ (c) for the Lévy walk modification of the RMTD process calculated for a rectangular surface correlation function $g = g_r(s/c)$ (a).

desorption time Q^{-1} and the "retention time" t_h characterizing the adsorbate occupancy of the surface until complete exchange. The quantity $c = D/h$ has the dimension of a velocity. The length $h \approx \sqrt{Dt_h}$ is called "adsorption depth". The probability, that a particle is displaced a curvilinear distance on the surface within $s \ldots s + \mathrm{d}s$ in a time τ, is then given by $\Psi(s, \tau) 2\pi s \, \mathrm{d}s$.

The surface is visited by a reference molecule at sites forming a "Lévy dust." The RMTD mechanism nevertheless applies. The above surface diffusion propagator has merely to be combined with the surface orientation correlation function $g(s)$, so that the RMTD correlation function reads

$$G(\tau) = \int\limits_0^\infty g(s) \, \Psi(s, \tau) \, 2\pi s \, \mathrm{d}s = c\tau \int\limits_0^\infty \frac{s \, g(s)}{[(c\tau)^2 + s^2]^{3/2}} \, \mathrm{d}s \qquad (8)$$

The surface correlation function $g(s)$ characterizes the variations of the local surface orientation which is imposed on the adsorbed molecules. The distance s is measured curvilinearly along the surface.

The NMR correlation function $G(\tau)$ relevant in this context can be evaluated from the low-frequency spin-lattice relaxation dispersion data of strongly adsorbed liquids. We thus have a direct interconnection between surface structure and spin-lattice relaxation dispersion.
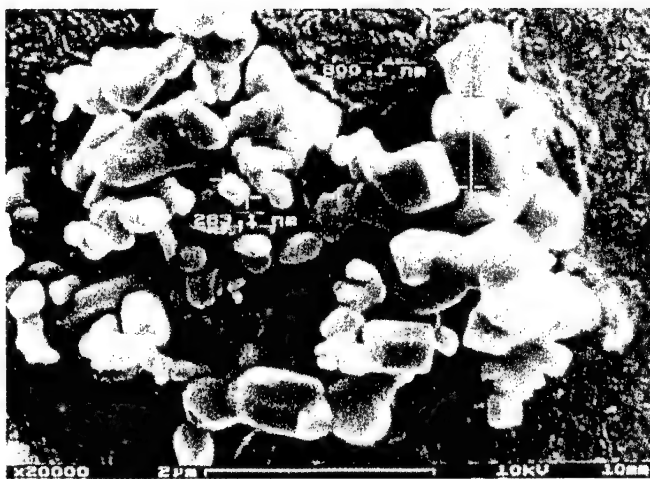
Figure 3:

Scanning electron micrograph of zincoxide fineparticle agglomerates. The length scale of the particle diameters ranges from 200 to 800 nm.

As a simple example let us consider the abruptly decaying surface correlation function

$$g_r(s) = \begin{cases} 1 & \text{for } s \leq s_0 \\ 0 & \text{otherwise} \end{cases} \qquad (9)$$

This corresponds to a polyhedral surface consisting of planar faces with uncorrelated normal vectors. That is, a particle completely loses its memory to the initial orientation when it jumps to another face of the polyhedron. The quantity s_0 may be called surface correlation length.

Inserting the "rectangular" surface correlation function eqn 9 into the expression for the RMTD correlation function eqn 8 gives

$$G_r(\tau) = 1 - \frac{1}{\sqrt{1 + [s_0/(c\tau)]^2}} \qquad (10)$$

The numerical evaluation of eqns 5 and 4 leads to the corresponding spin-lattice relaxation dispersion curve. The three functions $g_r(s)$, $G_r(\tau)$ are juxtaposed in fig. 2. Interestingly, the spin-lattice relaxation dispersion looks rather similar (albeit not identical!) to that for an exponential NMR correlation function with a correlation time $\tau_c = s_0/c$.

THE POLYHEDRAL-SURFACE MODEL

Systems like those listed in tab. 1, imply all sorts of curved and rugged surface topologies. As an approach we model the actual topology by a polyhedral structure with randomly oriented planar faces as mentioned before. However, the surface correlation length s_0 of the

faces is now assumed to be distributed according to a function $P(s_0)$. This is to represent the heterogeneous ("inhomogeneous") character of the pore surface problem. A given surface correlation length defines a subensemble of the polyhedral planar faces generating a certain spin-lattice relaxation dispersion as illustrated in fig. 2c. Figure 3 demonstrates that the "polyhedral-surface model" is adequate for the situation one is dealing with in zincoxide fine particle agglomerates, for instance. In other cases it may serve as an approach.
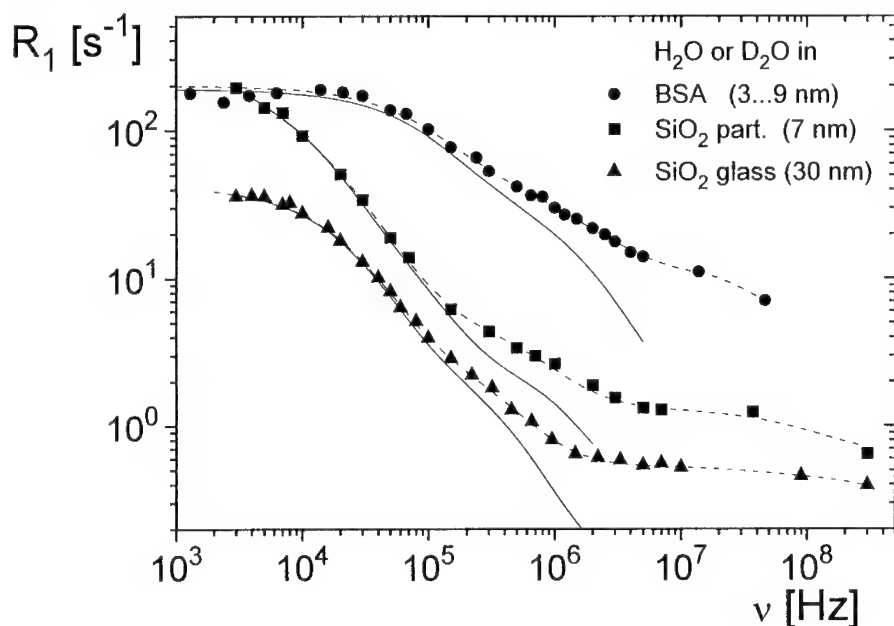
Figure 4:

Field-cycling proton relaxometry data of water filled into porous SiO_2 glass (Bioran B30, mean pore diameter 30 nm), SiO_2 fineparticle agglomerate (Cab-O-Sil EH-5, mean particle diameter 7 nm, 38.3 % H_2O by weight) and a globular-protein agglomerate (bovine serum albumin (BSA), molecular diameter 3...9 nm, 25 % D_2O by weight, deuteron resonance). The solid lines represent the RMTD analysis of the low-frequency part of the spin-lattice relaxation dispersion based on eqn 11 (polyhedral-surface model). The distributions of the surface correlation lengths are given in figs 5 and 6. The dashed lines were calculated assuming local relaxation rate contributions by high-frequency processes in addition.

The adsorbate dynamics is of an ergodic nature: In all samples referred to in this study the spin-lattice relaxation curves were found to decay monoexponentially as far as they can be probed reliably (that is over one decade at least). The explanation is that the root mean squared displacements of the adsorbate molecules on the time scale of spin-lattice relaxation is much larger than any correlation length of the samples. Therefore, an adsorbate molecule faces all surface correlation lengths and all orientations of the polyhedral surface during a period of the order of the spin-lattice relaxation time.

Under such circumstances the total RMTD correlation function is weighted composition

of the independent RMTD correlation functions for the polyhedral faces,

$$G(\tau) = \int\limits_{0}^{\infty} P(s_0) \left(1 - \frac{1}{\sqrt{1 + [s_0/(c\tau)]^2}}\right) ds_0 \qquad (11)$$

where we have combined eqn 10 with the distribution function of the polyhedral-face correlation lengths.

TYPICAL SPIN-LATTICE RELAXATION DISPERSION RESULTS

In our previous work we have already reported field-cycling NMR relaxometry data of polar and nonpolar liquids in porous glasses, proteins, and fineparticle agglomerates [5,6,13]. Figure 4 shows spin-lattice relaxation dispersions typical for fineparticle agglomerates and porous glasses.
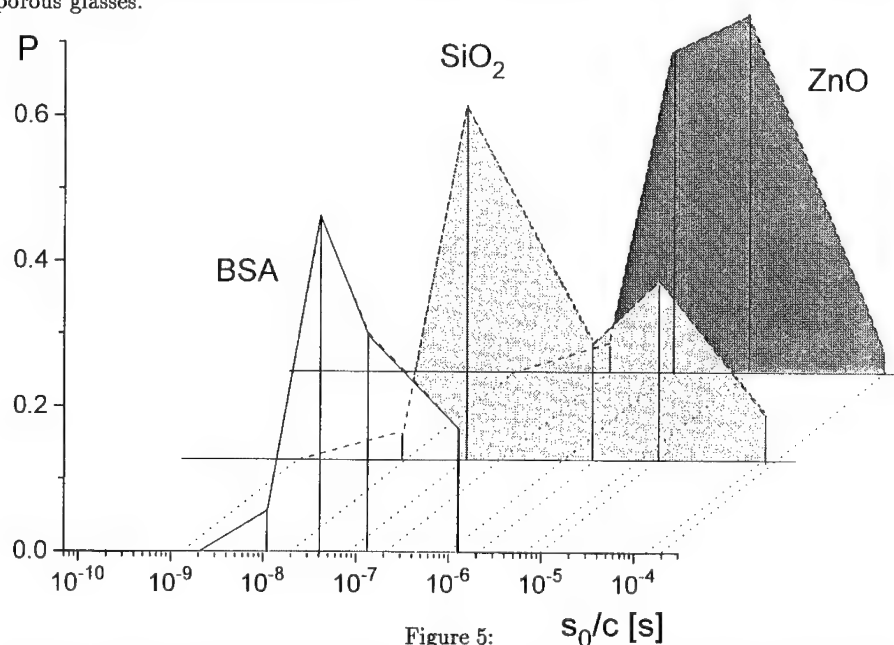
Figure 5: s_0/c [s]

Discrete distributions of the polyhedral-face correlation lengths evaluated from the low-frequency spin-lattice relaxation dispersions of water in fineparticle agglomerates (BSA, $3\ldots9$ nm; SiO_2, 7 nm; ZnO, $200\ldots800$ nm). The data partly correspond to the solid lines in fig. 4 (see eqn 11). The "bar" diagrams (vertical lines) are marked by gray shades for the convenience of the reader.

For the evaluation, the distribution function in eqn 11 was approximated by a discrete distribution. A corresponding data analysis leads to the results plotted in figs 5 and 6.

These distributions directly reflect the low-frequency spin-lattice relaxation dispersions typically measured for $\nu < 10^7$ Hz. At higher frequencies, local reorientations in a restricted solid-angle range tend to influence the dispersion curves. The maximum values of the distributions indicate the most likely polyhedral-face correlation lengths which obviously correlate with the characteristic lengths (mean pore or particle diameters).
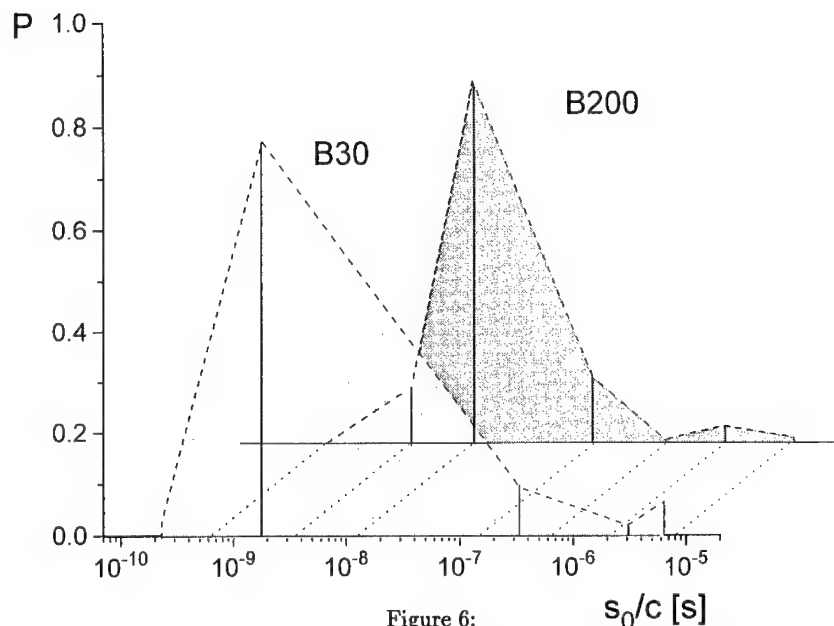
Figure 6:

Discrete distributions of the polyhedral-face correlation lengths evaluated from the low-frequency spin-lattice relaxation dispersions of water in porous glasses with 30 (Bioran B30) and 208 nm (Bioran B200) mean pore diameters. The data were evaluated from the low-frequency relaxation dispersions (see fig. 4) using eqn 11. The "bar" diagrams (vertical lines) are marked by gray shades for the convenience of the reader.

As an order-of-magnitude estimation we consider a room-temperature bulk diffusion coefficient $D \approx 10^{-9}$ m^2/s. Based on the low-frequency field cycling data, the retention time, i. e. the longest time after which an influence of RMTD can be probed in principle, is estimated to be of the order $t_h = 10^{-5}$ s. This means the adsorption length is $h \approx \sqrt{Dt_h} = 10^{-7}$ m. The constant $c = D/h$ is therefore expected to be of the order $c = 10^{-2}$ m/s. This suggests a range of the correlation lengths probed in our field-cycling experiments 10^{-10} m $< s_0 < 10^{-6}$ m . The lower limit is of the order of the adsorbate molecule diameter, the upper limit corresponds to the largest ZnO particle diameter.

In all cases considered so far, the adsorbate molecules are supposed to be in the "strong adsorption" limit. Adsorbates matching the "weak adsorption limit" reveal themselves by rather flat relaxation dispersion curves [6]. This situation arises with nonpolar adsorbate molecules on polar surfaces, for instance. Modifying the surface from "polar" to "nonpolar" by chemical treatment therefore should interchange the dispersion slopes of polar and nonpolar adsorbates.

A corresponding experiment was carried out. The surfaces of the porous glass Bioran B30 were treated with $(CH_3)_3SiCl$ so that the surface -OH groups are converted at least partly into $-OSi(CH_3)_3$. The effect on the spin-lattice relaxation dispersion of cyclohexane (nonpolar) and pyridine (polar) is shown in fig. 7. The polar adsorbate species (pyridine) reveals a flatter spin-lattice relaxation dispersion tending to the behaviour of nonpolar adsorbates at polar surfaces, whereas the nonpolar liquid (cyclohexane) shows the reverse behaviour.
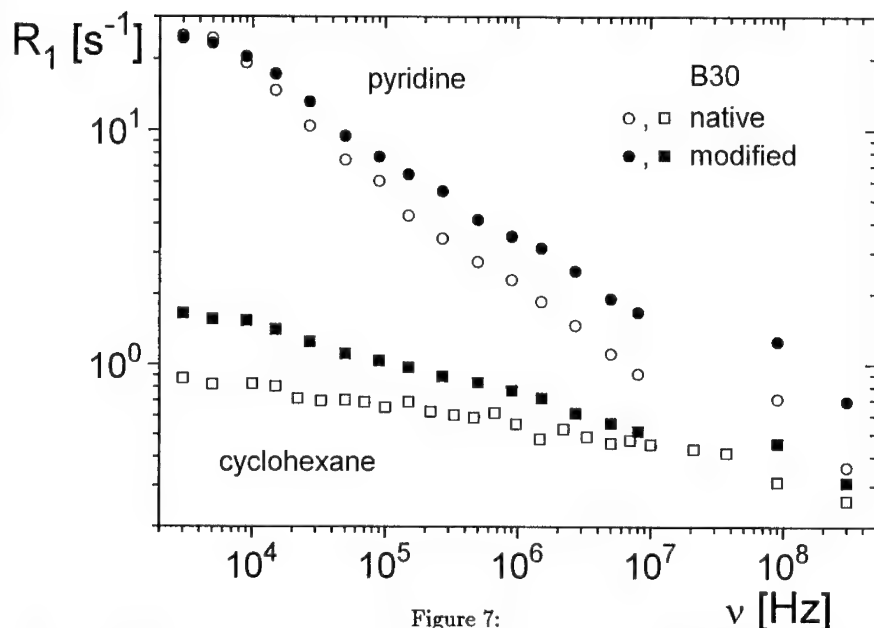
Figure 7:

Proton spin-lattice relaxation dispersion polar (pyridine) and nonpolar (cyclohexane) liquids in porous glass Bioran B30 (mean pore diameter 30 nm) with original (-OH groups) and modified (-OSi(CH$_3$)$_3$ groups) surfaces.

Although the chemical treatment changed the surface polarity only to a certain degree, the spin-lattice relaxation dispersion actually showed the predicted tendencies.

CONCLUSIONS AND DISCUSSION

This study and our previous work on the spin-lattice relaxation dispersion of solvents confined in porous media confirm the "weak" and "strong adsorption" limits predicted by Bychuk and O'Shaughnessy [1]. Polar adsorbate molecules in a polar matrix, for instance, are subject to "strong adsorption." The spin-lattice relaxation dispersion is then much steeper than in the opposite case.

In the strong-adsorption limit, the low-frequency dispersion indicates orientation correlation times eight orders of magnitude longer than in bulk, whereas translational diffusion is scarcely slowed down mainly for reasons of geometrical obstruction. This applies even when practically all adsorbate molecules under investigation are located in layers close to the surfaces.

This self-diffusion/reorientation paradox becomes conceivable when considering Lévy walks effectively taking place along surfaces in the strong adsorption limit. A corresponding RMTD mechanism for NMR relaxation modified by a Cauchy distribution of the surface displacements was established. It permits the perfect description of the field-cycling NMR relaxometry data. Nevertheless, it must be stressed that an RMTD relaxation mechanism based on ordinary surface diffusion with a Gaussian propagator accounts for the data with

the same quality [5]. However, in that case there is no plausible explanation why the adsorbate molecules can diffuse almost without restraint along surfaces while retaining the memory to the initial orientation over such extremely long periods.

The RMTD formalism links dynamic and geometric features. That is, the surface correlation function can be deduced from the experimental relaxation dispersion curves. For this purpose, the "polyhedral-surface model" was introduced as an approach to real surfaces in nanoporous media. The surface orientations eventually are described in the form of a distribution function of polyhedral-face correlation lengths. A peculiar finding of this analysis is that the maxima of those empirical distributions are correlated with the length scale characteristic for the matrix. Larger fineparticles, for instance, reveal a maximum at longer correlation lengths.

References

[1] O. V. Bychuk and B. O'Shaughnessy, J. Chem. Phys. **101**, 772 (1994).

[2] J. Kärger, H. Pfeifer, and W. Heink, Adv. Magn. Reson. **12**, 1 (1988).

[3] R. Kimmich, NMR: Tomography, Diffusometry, Relaxometry (Springer-Verlag, Heidelberg, 1997).

[4] R. Kimmich, W. Unrath, G. Schnur, and E. Rommel J. Magn. Reson. **91**, 136 (1991).

[5] S. Stapf, R. Kimmich, and J. Nieß, J. Appl. Phys. **75**, 529 (1994).

[6] S. Stapf, R. Kimmich, and R.-O. Seitter, Phys. Rev. Lett. **75**, 2855 (1995).

[7] R. Kimmich, F. Klammler, V. D. Skirda, I. A. Serebrennikova, A. I. Maklakov, and N. Fatkullin, Appl. Magn. Reson. **4**, 425 (1993).

[8] R. Kimmich, S. Stapf, R.-O. Seitter, P. Callaghan, and E. V. Khozina, Mat. Res. Soc. Symp. Proc. **366**, 189 (1995).

[9] R. Kimmich, S. Stapf, A. I. Maklakov, V. D. Skirda, and E. V. Khozina, Magn. Reson. Imaging **14**, (1996), in press.

[10] K. Hahn, J. Kärger, and V. Kukla, Phys. Rev. Lett. **76**, 2762 (1996).

[11] A. Bródka and T. W. Zerda, J. Chem. Phys. **104**, 6319 (1996).

[12] J.-P. Korb, private communication.

[13] R. Kimmich and H. W. Weber, Phys. Rev. B **47**, 11 788 (1993).

[14] S. Stapf and R. Kimmich, J. Chem. Phys. **103**, 2247 (1995).

[15] R. Kimmich, W. Nusser, and T. Gneiting, Colloids and Surfaces **45**, 283 (1990).

[16] J.-P. Korb, L. Malier, F. Cros, Shu Xu, and J. Jonas, Phys. Rev. Lett. **77**, 2312 (1996).

[17] S. König, E. Sackmann, D. Richter, R. Zorn, C. Carlile, and T. M. Bayerl, J. Chem. Phys. **100**, 3307 (1994).

[18] O. V. Bychuk and B. O'Shaughnessy, J. Phys. II **4**, 1135 (1994).

[19] J. Klafter, M. F. Shlesinger, and G. Zumofen, Physics Today **49**, 33 (1996).

DISCONTINUITY IN PARTICLE GRANULAR TEMPERATURE OBSERVED IN GAS FLUIDIZED BEDS ACROSS THE GELDART B/A BOUNDARY - IMPLICATIONS FOR STABILITY AND PROPERTIES OF THE GELDART A PHASE

George D. Cody and David J. Goldfarb,
Exxon Corporate Research Laboratory, Clinton Township, Route 22 East, Annandale, New Jersey 08801, e-mail: gdcody@erenj.com

ABSTRACT

We present new experimental data on the properties of monodispersed glass spheres as a function of sphere diameter and gas flow in a gas fluidized bed. The data obtained by a novel non-intrusive probe of the average particle kinetic energy, or granular temperature, at the wall is used to explore and understand the well known empirical distinction between fluidized particles which exhibit a single phase state at initial fluidization (Geldart A powders) and fluidized particles that exhibit gas bubbles at initial fluidization (Geldart B powders). Specifically we show that the experimental "jump" we observe in the granular temperature at the Geldart A/B transition is sufficient to account for the initial stability of the Geldart A phase on the basis of the one dimensional, first order, two wave, stability theory first introduced by Jackson in the early sixties. We present new data on the diameter dependent properties of the glass spheres during bed collapse and bed expansion, which demonstrate the distinction between Geldart A and B behavior for these monodispersed glass spheres. Finally we present a simple Langevin model to account for the dependence of the granular temperature on sphere diameter and gas flow, and discuss the implications of these new experimental data for the fundamental physics of the Geldart A phase.

INTRODUCTION

The widely used distinction between Geldart A particles, which exhibit a regime of stable homogeneous gas fluidization before bubbling, and Geldart B particles, which exhibit bubbles at fluidization[1] has yet to receive a fundamental explanation. Theoretical attempts to understand the stability of the gas fluidized state were begun in the early sixties, initially with simplified models and more recently by direct numerical simulation of the equations of motion[2]. While instability is a broader category than bubbling, it is clear that the Geldart B/A transition should be a feature of any first-principles theory of stability. However, the absence of experimental data on key experimental quantities remains a significant obstacle to evaluating the relevance of these theories to the Geldart classification[3]. The granular temperature, T^*, or steady state mean squared particle fluctuation velocity, can be related, through the kinetic theory of dense gasses, to the pressure, bulk modulus, velocity of sound, and Froude number of the dense phase of the fluidized state[4, 5, 6] all key parameters in current theories of stability and the fundamental significance of the Geldart B/A transition. In this paper, we present new experimental data on the granular temperature at the wall of a gas fluidized bed, as a function of particle diameter and gas flow. It differs from the experimental data and conclusions of our earlier paper only in more precise control and measurement of the fluidizing gas flow. The more accurate data presented here suggests that the Geldart B/A transition for monodispersed glass spheres is a consequence of a remarkable bifurcation in the steady state particle dynamics between the two regions. We explore the implications of the granular temperature data for the properties of the Geldart A and B phases and present new experimental data on the properties of Geldart A mono-dispersed glass spheres, specifically bed collapse time and initial bed expansion as a function of sphere diameter. A major result of this work is the first observation of the scaling of the granular temperature of the dense phase with sphere diameter, D, and gas superficial velocity, U_s. All of our data suggests that for the dense phase, the steady state value of $T^*(D,U_s)$ scales as $U_s^2 D^{-2}$. We present a physical model for the steady state value of $T^*(D,U_s)$, based on a viscous power input into the fluidized bed with energy dissipation modeled by the Langevin equation, that is in reasonable agreement with both this remarkably simple scaling, and the estimated magnitude of the required steady state power.

GRANULAR TEMPERATURE OR MEAN SQUARE FLUCTUATION VELOCITY

We denote the particle velocity as $\vec{c}(r,t)$. The ensemble average of $\vec{c}(r,t)$ defines the *particle drift velocity*, $V(r,t)$, at the location "r", where $V(r,t) \equiv <\vec{c}(r,t)>$. $V(r,t)$ can be an obvious visual feature of a fluidized bed for example, the downward "convective flow" of spheres at the wall. However, the sphere fluctuation velocity, $\vec{w}(r,t) = \vec{c}(r,t) - V(r,t)$, while much too rapid to be a visual feature, is experimentally the major contribution to the granular temperature in the gas range studied in this paper.

The granular temperature, T^*, defined as the ensemble average of the squared fluctuation velocity, is given by $3T^* \equiv <\vec{w}(r,t)^2> = <\vec{c}(r,t)^2> - [V(r,t)]^2$. As noted, $[V(r,t)]^2 << <\vec{c}^2>$ in these experiments, and hence the mean square of the sphere velocity, $<\vec{c}^2>$, dominates the granular temperature, T^*. With the *assumptions of spatial uniformity and isotropy*, T^* can be expressed by one component of $<\vec{c}^2>$. For later convenience, we choose the velocity component normal to the wall, $v_n(r,t)$, and thus write $T^* \equiv (<\vec{w}(r,t)^2>/3) \approx <v_n(r,t)^2> \equiv v_n^2$.

If sphere collisions were elastic we could define the granular pressure, bulk modulus, sound velocity, viscosity and diffusion constant from the kinetic theory of dense gasses. Given inelastic collisions, such an approach is clearly only a first approximation[7]- although comparisons with direct measurements of the relevant quantities suggest it to be a relatively good approximation. Direct measurements of the normal stress of particle impacts on the wall in gas fluidized beds by Campbell and collaborators[8] and by Polashenski and Chen[9] can be interpreted to supply independent data on the granular temperature, as can direct measurements of the particle viscosity by Gidaspow and Huilin[10] The excellent agreement between these direct measurements of the granular temperature and our indirect measurements derived from the kinetic model[5] encourages us to use this model for other kinetic parameters as well. Thus, we will define a granular pressure P^*, granular bulk modulus E^* and granular sound velocity, C^* by the usual expressions from a dense kinetic gas model: $P^* = \rho_s T^*$, $E^* = dP^*/d\ln\rho_s = P^*$, $(C^*)^2 = (E^*/\rho_s) = T^*$. The quantity ρ_s is the density of the dense phase given by $\rho_s = \rho_0 (1-e_s)$ where ρ_0 is the density of the particles and e_s is the voidage of the dense phase.

EXPERIMENTAL

The particles utilized in the present series of experiments[4, 5, 6] are glass spheres (1600 Series, Spacer Grade Microbeads, Cataphote Inc., Jackson, Miss., "90% true" [maximum variation of $\pm$ 6% from average diameter]) of average diameter 297, 210, 149, 105, 88, 74 and 63 microns (μm) and density $\rho_0 = 2.46$ gm/cc. These spheres span "Region B", and extend into "Region A" of the "Geldart Plot" whose boundary at $\rho_0 = 2.46$ is D=120μm These glass spheres differ significantly in size, shape, and surface uniformity, from either sand or cat-cracking catalyst which in the past have often been the particles of choice for experimental studies of fluidization. We will also present some data on catalytic cracking catalyst particles (Quasar 4452) in this paper which have a log normal distribution in particle size and a median diameter of 70μm (σ=30μm).

The force power spectrum at location R_i on the wall of the vessel, $S_F(f,R_i)$ due to acoustic shot noise for glass spheres with diameters in the range D<600μm is a white noise source for frequencies less than 300kHz, well above the 20kHz maximum of the present experiments[5]. We utilize the measurement of the wall acceleration power spectrum, $S_a(f,0)$, at the location R=0, produced by acoustic shot noise excitation of the wall of the fluidized bed by random particle impact to determine the average granular temperature at the wall of the fluidized bed. Since the technique and its validation have been exhaustively discussed in our previous publication, we summarize here only the defining equations. The *wall acceleration power spectrum*, is given, in terms of measured properties of the wall, and the mean squared fluctuation velocity at the wall, v_n, by:

$$S_a(f,0) = <|H(f)|^2> <(2mv_n)^2 \rho_b v_n> A \tag{1}$$

In Eq. (1), the quantity $<|H(f)|^2>$ is the frequency dependent, mean squared "transfer function" of the wall, which is ***experimentally obtained*** by hammer excitation over the wall of the cylinder. The second term is the average of $S_F(f,R_i)$ taken over the cylinder. The quantities "m" and "ρ_b" are the mass of an individual sphere. The mass density, ρ_s, of spheres in the fluidized bed is given by "$\rho_s = m \rho_b$". The quantity "A" is the area of the internal wall of the cylinder.

The measured quantity is the mean-squared acceleration, a_m^2, in the frequency range, 10-20kHz, obtained by a two channel signal processor. In this frequency range, and our experimental apparatus, acoustic shot noise has been shown to dominate other excitation sources[5]. We define the quantity, a^2, as the integral of $S_a(f,0)$ over the frequency range 10-20kHz. In general the measured quantity $a_m^2 \equiv a^2 + a_n^2$ where a_n^2 is determined by an electronic, or vibrational, noise power spectrum that is independent of gas flow. This noise source, $S_n(f)$, is thus assumed to be independent of acoustic shot noise, cylinder transfer function, and gas flow. In our experiments electronic noise was dominant and meets that condition. In what follows we define $a^2 \equiv [a_m^2 - a_n^2]$. Finally we easily obtain from Eq. (1), the above definition of T^*, and the ***assumption of spatial uniformity and isotropy***, the defining equation of the non-intrusive acoustic shot noise probe for the average T^* at the wall of the gas fluidized bed:

$$T^* = \left(\frac{a^2}{4I^2 A m \rho_s} \right)^{2/3} \tag{2}$$

In Eq. (2) the quantity "I" is the integral of $<|H(f)|^2>$ over the range 10-20kHz; all the other quantities have been previously defined.

GELDART POWDER CLASSIFICATION

Fig. 1a, locates the glass spheres studied in the present experiment on the "Geldart Plot" of powder fluidization behavior. The line separating Region A from Region B was originally determined by Geldart[11] through an empirical comparison of the minimum gas superficial velocity for bubbling, U_{mb}, and that for fluidization, U_{mf}. Region A, "aeratable", was empirically defined by $U_{mf} < U_{mb}$, and Region B, "bubbles readily", defined by $U_{mf} > U_{mb}$. In Fig. 1b we exhibit our measurements of U_{mf} determined by the rapid onset of T^*, which agrees with that determined by either bed pressure drop or bed height. Such agreement does not hold for FCCU catalyst, where U_{mf} by the T^* onset is a factor of ≈ 4 larger than the onset determined by either bed pressure drop or bed height[5]. From Fig. 1b we note that the original distinction between Geldart A and B for the glass spheres, fails for Geldart's expression for U_{mb} and our values for U_{mf}. The factor of two increase in U_{mf} across the boundary is consistent with a 15% increase in voidage at U_{mf} suggesting an increase in T* at fluidization

CHANGE IN RMS FLUCTUATION VELOCITY AT THE GELDART B/A TRANSITION

In Fig. 2a we show the RMS fluctuation velocity scaled to the argon superficial velocity U_s, and particle diameter D, for Geldart B glass spheres with D=297, 210, 149μm, and for glass spheres with D=105μm, which lie on the B/A boundary. The scaling length, 110μm, and its implications are discussed exhaustively in our earlier paper [5]. As noted earlier the data for v_n for D≤105μm is quantitatively more accurate due to greatly improved measurement and control of gas flow, but is qualitatively the same as that published earlier. In Fig. 2a, we note a ***factor of 1.5 increase*** in the scaled quantity, $[(v_n/U_s)(D(\mu m)/110)]$ for D=105μm, compared to the Geldart B glass spheres with D=149, 210, 297μm. In Fig. 2b, we note an ***additional factor of 1.5 increase*** in the scaled quantity, $[(v_n/U_s)(D(\mu m)/110)]$ for 63μm≤D≤88μm, compared to the magnitude of $[(v_n/U_s)(D(\mu m)/110)]$ for D=105μm.

Figure 1a

"D"
"Spoutable"

"A"
"Aeratable"

"B"
"Bubbles Readily"

Mono-Dispersed
Glass Spheres:
63, 74, 88, 105μ

Mono-Dispersed
Glass Spheres:
149, 210, 297μ

"C"
"Cohesive"

$\rho_o = [296 * 10^3 / D(\mu)]$

ρ_o = Particle Density (kgm/m^3)

$<D>$ = Average Particle Diameter (μ)

Figure 1b

$U_{mf} = 0.691 \times 10^{-4} D(\mu m)^2$
R=0.935
e_{mf}=0.380

$U_{mf} = 1.1167 \times 10^{-4} D(\mu m)^2$
R=0.941
e_{mf}=0.433

Geldart Empirical
Minimum Bubbling Velocity
$U_{mb} = 88 \times 10^{-4} D(\mu m)$

Geldart A   Geldart B
D=120μm

$$U_{mf} = \frac{e_{mf}^3 D^2 \rho_s g}{150(1-e_{mf})\mu_g}$$

U_{mf}(cm/s), U_{mb}(cm/s)

Sphere Diameter=D(μm)

328

Figure 2a

$(v_n/U_s)(D(\mu m)/110) \equiv W_i(U)$

D=105μm

1.7[1-exp(-4(U-1))

[1+1.6exp(-U/3)]

1.10[1-exp(-8(U-1))

D=297, 210, 149μm

○	#87	149μm Umf=1.6cm/s
▲	#63	210μm Umf=3.7cm/s
▼	#103	210μm Umf=4.0cm/s
□	#65	297μm Umf=5.67cm/s
●	#88	105μm Umf=1.56cm/s

$U=[U_s/U_{mf}]$

Figure 2b

$(v_n/U_s)*(D(\mu m)/110) \equiv W_i(U)$

Geldart A: D= 88, 74, 63μm

2.7[1-exp(-4(U-1))]

[1+6.5exp(-U/2)]

A/B Transition: D=105μm

Geldart B: D=297, 210, 149μm

○	#89	88μm 2,3,4,5 Umf=0.8cm/s
▲	#90	74μm 2,3,4,5 Umf=0.55cm/s
▼	#96	74μm 1,2 Umf=0.58cm/s
□	#97	74μm 1,2 Umf=0.59cm/s
◩	#72	63μm 2,3,2,5 Umf=0.47cm/s
⊞	#91	63μm 2,3,4,5 Umf=0.52cm/s

$U=[U_s/U_{mf}]$

From the fitted curves of Figs. 2a and 2b, it is possible to construct $T^*(D,U)$ where $U=(U_s/U_{mf})$. From the dense phase kinetic model the granular pressure is obtained from $T^*(D,U)$ as $P^*(D,U) =\rho_s T^*(D,U)$, and, as noted, there is excellent agreement between this quantity as inferred from the fluctuation velocity measurements, and its average magnitude obtained by direct measurements at zero frequency [5].

The derivative of $P^*(D,U)$ with respect to voidage, $E^s(D,U)=(-\partial P^*/\partial e_s) =\rho_0 T^*(D,U)$, can be shown to be the bulk modulus of uniform fluidized state, a critical parameter of the first order, one-dimensional model first introduced by Jackson and later collaborators[12, 13, 14] more than 30 years ago. Before we discuss this model in detail, we exhibit in Figs. 3a and 3b the quantity $E^s(D,U)$ as a function of U obtained from the fitted curves of Figs. 2a and 2b, for D=105, 149, and 210µm in Fig. 3a and for D=63, 74, 88, and 149µm in Fig. 3b.

It is easily shown from Figs. 2a and 2b that for increasing U ($U \geq 8$), T^* and E^s are quadratic functions of D. Thus the comparable magnitude of E^s for D=105µm, and D=210µm in Fig. 3a is remarkable! Equally remarkable is the qualitative similarity between the curves for D=105, 149, and 210µm. Clearly, the significant change in the magnitude of E^s for D=105µm exhibited in Fig. 3a, over the Geldart B glass spheres has not been accompanied by a significant change in fludization properties as represented by the U dependence of $E^s(D,U)$. However, we do note a dramatic change in both the magnitude of E^s and its dependence on U, for the Geldart A glass spheres with D=63, 74, 88µm. As shown in Fig. 3b, the **Geldart A glass spheres exhibit three distinct regions of fluidization:** **A-I**, where E^s increases quadratically with U, **A-II** where E^s is approximately constant, and **A-III** where E^s again increases quadratically. It is tempting to identify region A-II with the "two phase" fluidization model of Davidson[15], where the dense phase is assumed to remain at constant gas flow while excess gas flows through bubbles, but clearly the situation exhibited in Figs. 3a and 3b is considerably more complex.

STABILITY OF GAS FLUIDIZED BED

The simplest stability theory starts with a set of equations that satisfy locally averaged momentum and mass balance for the gas and particles that comprise the fluid bed[16]. The time-dependent equation governing one-dimensional, first order perturbations from the uniformly stabilized state is then developed and as noted by Wallis[17], two critical velocities emerge that determine the stability of the fluidized state against small perturbations in voidage. The first, the *"continuity velocity"*, U_e, is given by $U_e(D,U)=-(1-e_s)(dU_s/de_s)$. Utilizing the Richardson-Zaki equation, $U_s=U_t e_s^n$, we obtain, $U_e(D,U) =U_t n e_s^{n-1}(1-e_s)$, where U_t is the Stokes "free fall velocity", $U_t=\rho_0 g D^2/18\mu_g$, g is the gravitational constant and μ_g is the viscosity of the gas. The second critical velocity is the *"dynamical velocity"*, $V_w(D,U)$, which is analogous to a sound velocity for pressure fluctuations in the dense phase, and is given by $V_w(D,U) = (E^s/\rho_s)^{0.5}$.

In general[17, 18] the uniform fluidized bed is stable against small perturbation in e_s, if $V_w(D,U) > U_e(D,U)$. In Fig. 4, we exhibit $V_w(D,U=2)$ as a function of D obtained from Figs. 2a and 2b, and $U_e(D,U=2)$ for argon with $\mu_g =210$µpoise. From Fig. 1a we utilize n = 4.7 for D≥149µm and n=4.85 for D≤105µm. However, it should be noted that the results shown in Fig. 4 are not sensitive to the parameter "n". From Fig. 4 we note that the dramatic increase in the normalized fluctuation velocity v_n shown in Fig. 2b, has the just the right magnitude to make Geldart A glass spheres for D≤ 88µm stable, at $U=[U_s/U_{mf}]=2$!
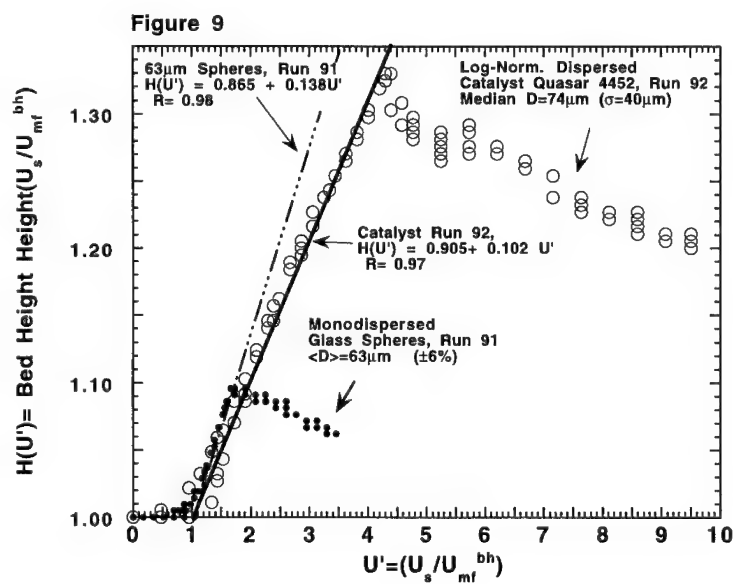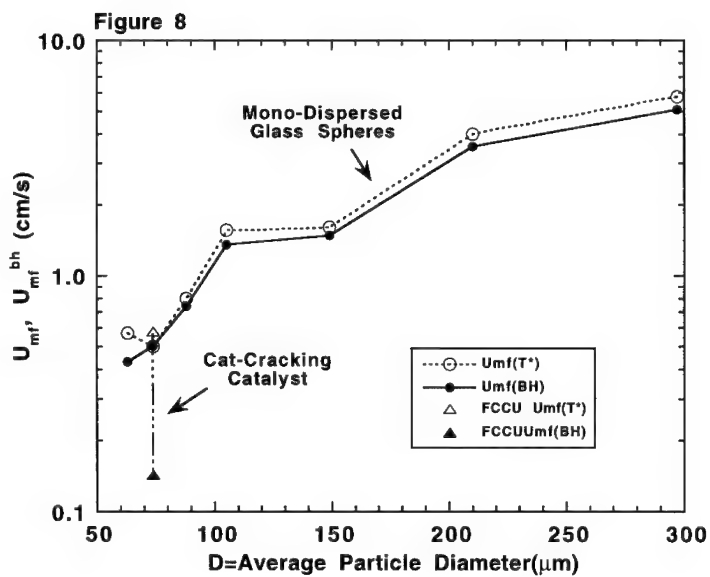
Previous attempts to obtain the magnitude of E^s utilized the bulk modulus of particles in mechanical contact held by suitable "cohesive forces". The early experimental papers of Rietema and collaborators[19] belong to that category, as well as recent theoretical work of Bouillard and Gidaspow [20] . These papers are important in focusing on the potential for particle contact,

Figure 3a

$E^s(D,U) = \rho_o T^\cdot(D,U)$ [dynes/cm²]

D=105μm
U_{mf}=1.2 cm/s

D=210μm
U_{mf}=3.1cm/s

D=149μm
U_{mf}=1.6cm/s

$U = (U_s/U_{mf})$

Figure 3b

$E^s(D,U) = \rho_o T^\cdot(D,U)$ [dynes/cm²]

A-I   A-II   A-III

D=88μm
U_{mf}=0.87cm/s

D=74μm
U_{mf}=0.61cm/s

D=63μm
U_{mf}=0.0.44cm/s

D=149μm
U_{mf}=1.57cm/s

B

(U_s/U_{mf})

Figure 4

$U_e(D,U=2)=U_t n e_s^{(n-1)}(1-e_s)$

1D,1st Order Stability:
$V_w(D,U=2)>U_e(D,U=2)$

Stable

Unstable

$V_w(D,U=2)$ (Experiment)

Geldart A | Geldart B
D=120μm

$U_e(D,U=2)$, $V_w(D,U=2)$(cm/s)

100

10

1

50 60 70 80 100 200 300 400

D(μm)

Figure 5

$U_e(D,U=2)=U_t n e_s^{(n-1)}(1-e_s)$

Foscolo and Gibilaro Theory
$V_w(D,U=2)=[3.2gD(1-e_s)]^{0.5}$

Cody et al, Experiment
$V_w=[T^*(D,U=2)/(1-e_s)]^{0.5}$

Geldart A | Geldart B
120μm

U_e (cm/s), V_w(cm/s)

20

15

10

5

0

0   50   100   150   200   250   300

Sphere Diameter =D(μm)

Figure 6

Start $U_s/U_{mf} \approx 5$

Geldart A Quasar FCCU (4452):
$<D>=70\mu$ ($\pm70\%$, Log Normal)
$BH(t=\infty)$ =24.9cm, U_{mf}=0.65cm/s

Granular Flow?

Geldart A/B Glass Spheres:
$<D>=105\mu$ ($\pm6\%$)
$BH(t=\infty)$=19.7cm, U_{mf}=1.4cm/s

Geldart A Glass Spheres:
$<D>=74\mu$ ($\pm6\%$)
$BH(t=\infty)$=20.6cm, U_{mf}=0.70cm/s

(Bed Height (t)/Bed Height(t=0))

Log (t (sec))

Figure 7

Geldart "A" Quasar 4452 Catalyst
$<D>$ = 72μ, Log Normal Distribution
$BH(t=\infty)$=24.9cm

Geldart "A" Grace Catalyst
$<D>$ = 60μm, Normal Distribution
$BH(t=\infty)$=45.5cm

Geldart "A" Monodispersed
Glass Spheres $BH(t=\infty)$=20cm
$\Delta T_c \approx D^{-3}$

Geldart "B" Monodispersed
Glass Spheres, $BH(t=\infty)$=20cm

ΔT_c =Bed Height Collapse Time (s)

$<D>$ = Average Particle Diameter (μm)

333

Figure 8

Figure 9

particularly in powders such as catalysts which have a broad distribution in particles size, shape and roughness and where there is other experimental evidence for the role of contact forces [21]. However, it is difficult to imagine such particle contact "forces" for the monodispersed Geldart A glass spheres studied in the present paper.

Another approach has been taken by Foscolo, Gibilaro and collaborators [22, 23, 24, 25]. These authors develop a model for the velocity of the kinematic wave based on a "general theory of fluid-particle interaction". The velocity of the kinematic wave, V_w, according to their model is given by $V_w=(3.2gD[1-e_s])^{0.5}$. Finally, Batchelor [26] arrived at an expression for V_w that is similar in form to Foscolo and Gibilaro. His approach focuses on the mean squared particle fluctuation velocity obtained through an analysis of particle diffusion. As we pointed out earlier[5] the average particle diffusion constant is proportional to the granular temperature $T^*(D,U)$, and $T^*(D,U)$ is thus a critical parameter of Batchelor's stability theory[3] as well. Indeed, one of the motivations for our initial research was to respond to Batchelor's observation that "it should be possible to make measurements of....the non-dimensional mean-square particle velocity fluctuation in a uniform fluidized bed...[but] there are few published data".

In Fig. 5 we compare our experimental results for $V_w(D,U=2)$ with the theoretical expression of Foscolo and Gibilaro also at U=2. We note comparable magnitude and functional dependence on sphere diameter D in the Geldart B regime for the two expressions for $V_w(D,U=2)$ which is significant given the experimental support in the literature for the Foscolo and Gibilaro expression [25]. From Fig. 5, we note that the Foscolo and Gibilaro value for $V_w(D,U=2)$ is too low by a factor of 1.2-2 to predict stability for $63\mu m \leq D \leq 88\mu m$, although their value for $V_w(D,U=1)$ does predict stability for $D=63\mu m$.

FLUIDIZATION CHARACTERISTICS OF GELDART A MONODISPERSED GLASS SPHERES

The properties of Geldart A powders have been largely defined by particles such as catalysts which exhibit a wide dispersion in particle shape, surface and diameter, in sharp contrast to the monodispersed glass spheres that have been the focus of the present study. There are significant differences between these two types of "Geldart A" particles in bed collapse measurements. In these experiments the bed height of a fluidized bed is followed in time after the shut-off of fluidization gas. Figure 6 adapted from our earlier paper [5] compares bed collapse data for Geldart A catalyst particles with a mean diameter of 70μm and a log-normal distribution in particle size ($\sigma = 30\mu m$) to glass spheres with D=74μm (Geldart A) and D=105μm (Geldart A/B). The catalyst data is in reasonable agreement with other bed collapse measurements on catalysts [27]. The total collapse times for the Geldart A glass sphere is about 20 times shorter - and might suggest a qualitative difference in behavior for the two "Geldart " particles. However it is apparent from Figure 6 that the collapse time for the catalyst particles exhibits an initial fall which is similar in shape and time scale to the Geldart A glass spheres, indeed the extended "tail" in the bed collapse curve for the catalyst particles may be a "granular" response [28, 29]of the particulate phase. As shown in Figure 7, there is a systematic *increase* in the collapse time ΔT_c for Geldart A glass spheres compared to Geldart B glass spheres. The data is reasonably fit by $\Delta T_c \approx D^{-3}$

In Figure 8 we exhibit another difference between the fluidization characteristics of catalyst particles and the monodispersed glass spheres In this figure we compare the minimum fluidization velocity U_{mf} determined by the onset of the T^* as indicated in Figs. 2a and 2b, with the minimum fluidization velocity U_{mf}^{BH} determined by the on-set of the increase in bed height at fluidization. As noted there is excellent agreement between the two methods for the glass spheres. However for the catalyst particles the two quantities differ by a factor of 4! Moreover the maximum percentage change in bed height for the catalyst particles as shown in Figure 9 is about a factor of 3 times greater than that for the glass spheres of comparable diameter! Both observations suggesting that the initial increase in bed height for the catalyst may be associated with particle mechanical contact as noted in recent experiments of Tsinontides and Jackson [21].

The normalized initial slope of the bed height, $\alpha = [\partial \ln(BH(U))/\partial U]$ at $U=1$ ($U_s = U_{mf}^{bh}$), exhibited in Figure 10, again indicates a significant difference between Geldart A and B monodispersed glass spheres. Indeed as shown in Fig. 10, α for the Geldart A glass spheres is significantly larger for the Geldart A catalyst particles. We note that $\alpha \approx D^{-2}$.

Figure 10

Glass Spheres: D=295→63μm, U_{mf}=5.8→0.57cm/s, ρ=2.5gm/cc.
Polymer Spheres: D=320μm, 650μm, U_{mf}=10.0, 3.5cm/s, ρ=1.04gm/cc.
Catalyst Particles: Med D=70μm, U_{mf}=0.18cm/s, ρ=1.5gm/cc
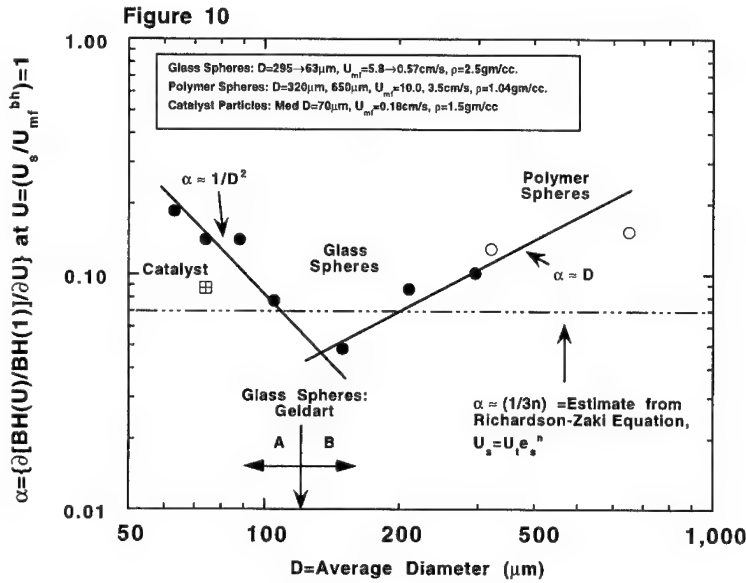
DISCUSSION

Scaling of T* With Sphere Diameter D, and Gas Flow U_s

Critical to all the stability considerations is the experimental dependence of $T^* \approx U_s^2 D^{-2}$ which one of the major results of the present experiments Given the units of T*, the quadratic dependence of T* on the gas superficial velocity, U_s is anticipated. If we scale U_s with respect to U_{mf} ($U=U_s/U_{mf}$) and note that $U_{mf} \approx D^2$, we can restate this result as obtain $T^*(D,U) \approx U^2 D^2$. Is there any theoretical support for such a quadratic scaling of the granular temperature of the dense phase to the sphere diameter; what is the fundamental length scale, D_o, that is introduced?

We employ a Langevin equation for the vector velocity $\vec{c}(r,t)$ to model the random and disipative motion of an individual sphere:

$$m\left(\frac{d\vec{c}(r,t)}{dt}\right) + m\left(\frac{\vec{c}(r,t)}{\tau_p}\right) = \vec{\mathbb{F}}(r,t) \tag{3}$$

where $\vec{\mathbb{F}}(r,t)$ is the random force exerted on the sphere by the fluidizing gas and impact with other particles, m is the mass of the sphere, and τ_p is the velocity relaxation time. Our earlier studies of

336

the time dependence of the granular temperature during bed collapse gave $\tau_p \approx 90\text{-}15\text{ms}$, a magnitude that is quantitatively consistent with a coefficient of restitution for the glass spheres, $e_p = 0.86\text{-}0.92$[5]. In the steady state

$$T^*(D,U) = \frac{<\vec{c}(r,t)\cdot\vec{c}(r,t)>}{3} = \left(\frac{\tau_p}{3m}\right)<\vec{F}(r,t)\cdot\vec{c}(r,t) \tag{4}$$

The power input per unit volume $d\Omega^*/dt$ to maintain $T^*(d,U)$ constant is then given by

$$d\Omega^*/dt = \rho_b <\vec{F}(r,t)\cdot\vec{c}(r,t)> = \left(\frac{3\rho_m T^*(D,U)}{\tau_p}\right) \tag{5}$$

The power per unit volume , $d\Omega^{fb}/dt$ to drive gas of viscosity, μ_g ,through a "fixed bed" of voidage, e_s is readily derived from the Ergun equation [30] as

$$d\Omega^{fb}/dt = (150)\left(\frac{(1-e_s)^2}{e_s^3}\right)\mu_g\left(\frac{U_s^2}{D^2}\right) \tag{7}$$

If we set $d\Omega^*/dt = K \, d\Omega^{fb}/dt$ and define $D_o^2 \approx (\mu_g\tau_p/\rho_o)$, we obtain

$$T^*(D,U) = (50K)\left(\frac{(1-e_s)}{e_s^3}\right)\left(\frac{\mu_g\tau_p}{\rho_o}\right)\left(\frac{U_s^2}{D^2}\right) \equiv D_o^2\left(\frac{U_s^2}{D^2}\right) \tag{8}$$

At $(U_s/U_{mf})=2$ with $\mu_g = 210\mu$poise, $\rho_o=2.5$gm/cc, $\tau_p = 120$ms, e_s from the Richardson-Zaki Equation, and the data of Figs. 2a and 2b, we obtain from Eq. (8) the following estimate for K: for Geldart B glass spheres, K=5% (D=600-150μm and D_o=121μm, n=4.70, e_s=0.439); for Geldart A/B glass spheres, K=20% (D=105μm and D_o=187μm, n=4.85, e_s=0.497); and for Geldart A glass spheres, K=50% (D=88-63μm and D_o=297μm, n=4.85, e_s=0.439).

Increase in $T^*(D,U)$ Across the Geldart A/B Boundary: Cause or Effect?

The remarkable and systematic increase in $T^*(D,U)$ as the Geldart B/A boundary is crossed can be interpreted in two ways. The first would focus on the suppression of bubbles near U=1 for Geldart A glass spheres with the experimental consequence of increasing gas flow through the dense phase compared to Geldart B glass spheres. The rapid, essentially discontinuous increase in $T^*(D,U)$ would thus be an experimental indication of the sharpness of the Geldart B/A transition and, hence, an additional validation of the acoustic shot noise probe. Indeed, such an point of view was taken in our original publication of the early experimental results for Geldart A glass spheres[5]. Unfortunately, the fundamental physical basis for the Geldart B/A transition can not be derived from a comparison of U_{mb} and U_{mf}, given the comparable data on U_{mf} and U_{mb} for Geldart A glass spheres exhibited in Fig. 1b.

Another interpretation for the Geldart A/B transition starts with the evidence of Figs. 2a,b which suggests the onset of a phase transition in the dynamics of the glass spheres as the Geldart B/A boundary is approached and passed. The remarkable increase in $T^*(D,U)$ exhibited in Fig. 3a, for the spheres with D=105μm over the Geldart B spheres (D=149μm), while not sufficient to affect the stability of the fluidized state [e.g. $V_w(D=105\mu m,U=2) < U_e(D=105\mu m,U=2)$], would indicate a significant fundamental change in the particle/gas dynamics. The continuing increase in $T^*(D,U)$, with decreasing D, is sufficient to produces first order stability since, for D≤88μm, $V_w(D,U=2) > U_e(D,U=2)$. The Geldart B/A transition would then be derived from the discontinuous increase in the granular temperature, and not the reverse! However the fundamental

basis for the apparent bifurcation ratio of 1.5 in v_n for D=105μm relative to D=149, 210, 297μm, and the apparent bifurcation ratio of 1.5 in v_n for D=63, 74, 88μm relative to D=105μm, remains a challenge for theory.

ACKNOWLEDGEMENTS

REFERENCES
1. D. Geldart, in *Gas Fluidization Technology*, D. Geldart, Ed., John Wiley, New York, 1986, pp. 11-51.
2. R. Jackson, in *Fluid Particle Technology, AIChE Symposium Series 301*, A. W. Weimer, Ed., vol. 90, American Institute of Chemical Engineers, New York, 1994, pp. 1-30.
3. M. Nicolas, J.-M. Chomaz, E. Guazzelli, *Phys. Fluids*, **6**, (1994) 3936-3944.
4. G. D. Cody, D. J. Goldfarb, G. V. Storch, Jr., A. N. Norris, Particle Granular Temperature in Gas Fluidized Beds, AIChE Annual Meeting 11/12-17/95, Miami Beach, Florida (AIChE, 1995).
5. G. D. Cody, D. J. Goldfarb, G. V. Storch, Jr., A. N. Norris, *Powder Technology*, **87**, (1996) 211-232.
6. G. D. Cody, D. J. Goldfarb, Discontinuity in Particle Granular Temperature Across the Geldart B/A Boundary, AIChE Annual Meeting 11/10-16/96, Chicago, Illinois (AIChE, 1996).
7. D. Gidaspow, *Multiphase Flow and Fludization - Continuum and Kinetic Theory Descriptions*, Academic Press, San Diego, 1994, p. 239-354.
8. C. S. Campbell, K. Rahman, *Meas. Sci. Tech.*, **3**, (1992) 709-712.
9. W. Polashenski, Jr., J. C. Chen, *to be published, Powder Technology*, , (1996)
10. D. Gidaspow, L. Huillin, Collisional Viscosity of FCC Particles in a CFB, AIChE Annual Meeting, 11/12-17/95, Miami Beach, Florida (AIChE, 1995).
11. D. Geldart, *Powder Technology*, **7**, (1973) 285-282.
12. R. Jackson, *Trans. Instn. Chem. Engrs.*, **41**, (1963) 13-21.
13. T. B. Anderson, R. Jackson, *I&EC Fundamentals*, **6**, (1967) 527-539.
14. T. B. Anderson, R. Jackson, *I&EC Fundamentals*, **7**, (1968) 12-21.
15. J. F. Davidson, in *Mobile Particulate Systems*, E. Guazzelli, L. Oger, Eds., Kluwer, Dodrecht, The Netherlands, 1995, pp. 173-220.
16. R. Jackson, in *Fluidization*, J. F. Davidson, R. Clift, D. Harrison, Eds., Academic Press, New York, 1985, pp. 47-72.
17. G. B. Wallis, *One-Dimensional Two-Phase Flow*, McGraw-Hill, New York, 1969, p. 122-242.
18. J. T. C. Liu, *Proc. R. Soc. Lond.*, **A389**, (1983) 331-347.
19. S. M. P. Mutsers, K. Rietema, *Powder Technology*, **18**, (1977) 239-248.
20. J. X. Bouillard, D. Gidaspow, *Powder Technology*, **68**, (1991) 13-22.
21. S. C. Tsinontides, R. Jackson, *J. Fluid Mech.*, **255**, (1993) 237-274.
22. P. U. Foscolo, L. G. Gibilaro, *Chem. Eng. Science*, **39**, (1984) 1667-1675.
23. P. U. Foscolo, L. G. Gibilaro, *Chem. Eng. Science*, **42**, (1987) 1489-1500.
24. P. U. Foscolo, L. G. Gibilaro, S. Rapagna, in *Developments in Fluidzation and Fluid Particle Systems, AIChE Symposium Series 308*, J. C. Chen, Ed., vol. 90, American Institute of Chemical Engineers, New York, 1995, pp. 44-50.
25. L. Gibilaro, P. Foscolo, R. di Felice, in *Two Phase Flow and Waves*, D. D. Joseph, D. G. Schaeffe, Eds., Springer-Verlag, New York, 1990, pp. 56-69.
26. G. K. Batchelor, *J. Fluid Mech.*, **193**, (1988) 75-110.
27. J. R. Grace, in *Fluidized Processes, AICHE Symposium Series 289*, A. W. Weimer, Ed., vol. 88, American Institute of Chemical Engineers, New York, 1992, pp. 1-16.
28. J. T. Jenkins, S. B. Savage, *J. Fluid Mech.*, **155**, (1983) 187-202.
29. H. M. Jaeger, S. R. Nagel, *Science*, **255**, (1992) 1523-1531.
30. D. Kunii, O. Levenspiel, *Fluidization Engineering*, Krieger, Malabar, Florida, USA, 1987, p. 73.

Massively Parallel Molecular Dynamics Simulation of Gas Permeation across Molecular Sieving Porous Membranes

Phillip I. Pohl and Grant S. Heffelfinger
Sandia National Laboratories, Albuquerque, NM 87185-0720

Abstract

In this work we simulate the diffusion of gases in a microporous solid models using a newly developed dual control volume grand canonical molecular dynamics technique. This allows spatial variation of chemical potential and hence an accurate simulation of steady-state pressure driven diffusion. The molecular sieving nature of microporous zeolites are discussed and compared with that for amorphous silica from sol-gel methods. Massively parallel supercomputers allow a quick and insightful study of these microporous structures.

INTRODUCTION

The diffusion of gases in porous solids is governed by physical and chemical features of both the solid and the gas. Computer simulations aid in understanding the structure-property relationships interactions with microporous solids. The diffusion of a species, i, in a direction, x, is related to the gradient of concentration or density, ρ, by Fick's law,

$$J_i^x = -D_i^x \frac{d}{dx} \rho_i(x).$$ (1)

Permeability, F, a more appropriate parameter used in flow across membranes is found by modifying (1) slightly, i.e.,

$$J_i^x = \frac{F}{Ax} \Delta P_i.$$ (2)

Where ΔP is the pressure drop across a membrane of thickness x, per cross sectional area A. If x is not known exactly, then it is absorbed into F and takes the name permeance.

Recently, Xiao and Wei gave a detailed analysis of the diffusion mechanisms of hydrocarbons in zeolites [1]. Their unified diffusion theory describing gaseous, liquid, Knudsen, solid and configurational (molecular sieving) diffusion, has a diffusivity expressed by

$$D = guLe^{-\frac{E}{RT}}$$ (3)

where g is a geometric term, u is a characteristic velocity, L the characteristic path length, and E the activation energy. The activation energy is only used for solid and configurational diffusion, and is cause for the sieving effect important in microporous membrane separations.

To test the assumptions used in arriving at equation 3, we recently employed a number of simulation techniques [2] including molecular mechanics to predict E, grand canonical Monte Carlo (GCMC) to simulate the concentration in model pores and analysis of available pore space for different sized molecules to evaluate porosity/tortuosity effects. The focus of the present work has been an alternative to this three pronged approach. That is, simulate pressure driven gas transport in pores, which is more like the actual experiments carried out in testing zeolite [3]or silica [4] membranes. It is generally known that the chemical potential gradient is the true driving force for diffusion. Hence, simulation in the grand canonical ensemble (constant μVT) is the most appropriate construct. To completely investigate pore diffusion, we have simulated gas movement driven by a chemical potential gradient in microporous silica using a newly developed dual control volume grand canonical molecular dynamics method [5].

POROUS MODEL
The wall atoms, which did not move, were positioned according to the coordinates of a model by expanding an amorphous glass model to a density of 1.5g/cc as in ref 6. The pore size of current generation sol-gel derived silica membranes consists of a distribution and all indications suggest that it may be similar to that of our model (Figure 1). That is, Brinker and Seghal [4] have been able to demonstrate molecular sieving by preparing membranes that exclude CH_4 at

detectable levels, but allow He to permeate at a rate of 2.25×10^{-5} cm^3/cm^2-s-cmHg at 313K. In the present work, the He (modeled as a Lennard-Jones particle at 300K) permeance is determined for the 1.5g/cc silica model.
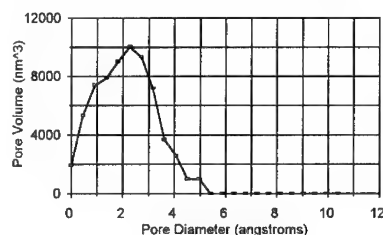
Figure 1 Silica Model Pore Size Distribution

GCMD
The Dual Control Volume Grand Canonical Molecular Dynamics (DCV-GCMD) method has recently been adapted to investigate pressure-driven transport of a pure component fluid through a model zeolite [7]. While the DCV-GCMD method employs molecular dynamics (MD) moves throughout the system, each MD move is followed by a series of GCMC-like insertions and deletions of fluid molecules in each of two control volumes in order to maintain the chemical potential in the control volumes constant at a desired value. By measuring the flux and the gradient of the resulting steady-state density profile, the diffusivity of each fluid component, i, in the presence of a chemical potential or pressure gradient, transport parameter can be determined from equations 1 and 2. While DCV-GCMD has been demonstrated for binary color diffusion [5], in this work we have extended the method to model a fluid experiencing a pressure gradient while confined in a porous system [7] as well as running the code on a massively parallel computer. The pressure gradient is achieved for a pure component fluid simply by choosing chemical potentials in the two control volumes which produce two different fluid densities. Gradient driven gas diffusion simulations in pores is being tried by several others [8,9,10,11].

The fluid-fluid and fluid-wall interactions were modeled with the cut and shifted Lennard-Jones potential, the cut-off distance taken to be 2.5σ for all interactions. The parameters were

taken as those for silica hydroxyl oxygens [12] and He, CH_4 and Ar [13] (σ_O=3.0 Å, ε_O/k=230K; σ_H=2.6 Å, ε_H/k=10K; σ_M=3.8 Å, ε_M/k=148K; σ_A=3.4 Å, ε_A/k=130K;), and Lorentz-Bertholot combining rules used. The Si atoms in the silica model were neglected as they are effectively shielded by the Os making up the tetrahedral network. The densities in the system were initially set only to give ample flux for study but can be controlled to the desired bulk pressure, the temperature was 300K and the MD time step 2.9 fs.

The silica system was $139.0\sigma_H$ long consisting of 8x3x3 of the models described above, thus the x coordinate stretched from 0.0 to $139.0\sigma_H$. Periodic boundary conditions were employed along all planes and at x = 0.0 and x = $139\sigma_H$. Each control volume encompassed the entire pore cross section (Figure 2). While we have positioned the control volumes for both systems outside the pore, they could just as easily have been positioned inside the pore, enabling one to neglect entrance effects.

Figure 2 Schematic of DCV-GCMD Pore System I
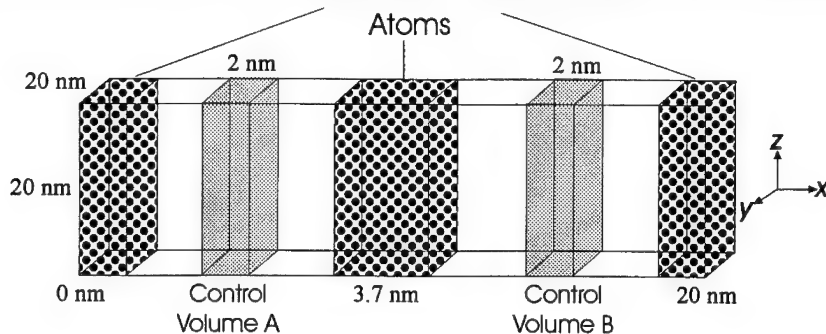
The simulation was equilibrated for 100,000 timesteps after which averages were accumulated for ~1,000,000 steps. The algorithm employed in this work is a massively parallel version of the DCV-GCMD. Briefly, this parallel algorithm employs a superposition of two different parallel algorithms: spatial GCMC and spatial MD. With this parallel DCV-GCMD algorithm, simultaneous insertions/deletions can be attempted in each control volume thus for this work, 64 insertions and/or deletions were attempted in each control volume after each MD step. For this simulation, carried out on 250 processors of Sandia's Intel Paragon, each MD timestep and its associated 64 attempted insertions/deletions in each control volume took ~1 cpu second depending on the number of gas particles.

RESULTS

The axial density profile ($\rho(x)$), determined by averaging the number of fluid molecules in 1 σ_H wide bins is shown in Figure 3. From this figure, we can see that the density in control volumes A and B are $\rho\sigma_H^3$ = 0.010 and 0.001, which correspond to bulk pressures of 20 and 2 atm. respectively. While these conditions are currently unattainable experimentally, the results should still be valid if the Gas-Gas interactions are much fewer than the Gas-Membrane interactions. Based on the low densities, we have assumed this is the case and a concentrations

Figure 3 Axial density profiles in silica membrane model (reduced units)
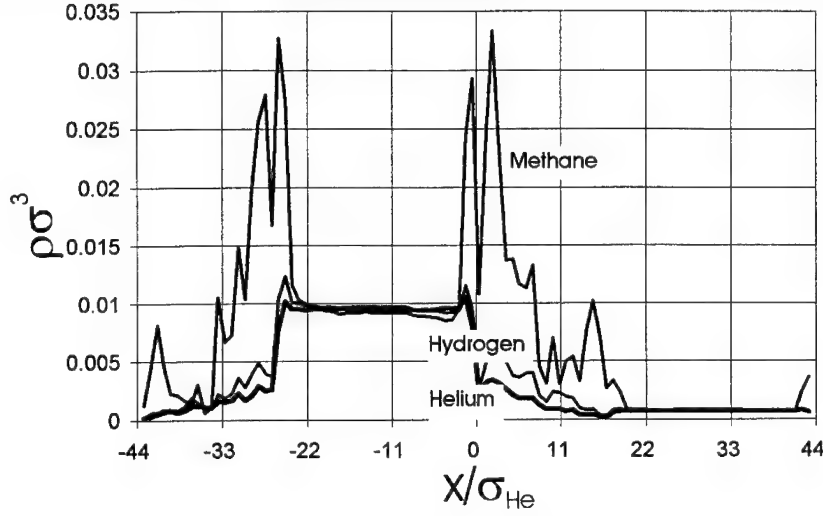
dependence is not expected. The axial density profile in Figure 3 shows approximate Fickian behavior, namely the straight line shape. We have calculated the flux via two different methods [11], the flux plane method and the control volume flux method (J^x and ζ^x, respectively):

$$J^x = \frac{j^{LTR} - j^{RTL}}{\Delta t A_{yz} N_{planes}}, \qquad (4)$$

$$\xi^x = \frac{M(B) - M(A)}{4\Delta t A_{yz} N_{steps}}, \qquad (5)$$

where j^{LTR} and j^{RTL} represent the net number of fluid molecules which move through each flux plane (two were used in this work, one at x = 70.0σ_H and another at the periodic boundary, x = 0 and 140.0σ_H) and N_{planes} is the number of flux planes (2 for this work). $M(B)$ and $M(A)$ are the net number of insertions (accepted insertions - deletions) in control volumes A and B, respectively, Δt is the MD timestep, A_{yz} is the cross sectional area of the model, and N_{steps} is the number of MD timesteps. The fluxes, calculated via both methods (reduced by multiplying by $\sigma_H^3(m_H/\varepsilon_H)^{1/2}$), and the resulting permeabilities computed from equation 2 are shown in Table I.

From Table I we see that the fluxes calculated via the two methods agree quite well and yield a value for the permeabilites, for silica[1]. These values are considerably higher than the experimental values given above at 313K suggest that the density of this particular model is too low for comparison with the molecular sieveing membranes of Brinker et al. [4]. The reason for this

Table I. Fluxes and permeabilities from DCV-GCMD

	$J^x \sigma^3 \sqrt{\dfrac{m}{\varepsilon}}$	$\xi^x \sigma^3 \sqrt{\dfrac{m}{\varepsilon}}$	permeability (Barrers*)
He(450K)	3.6e-5	3.7e-5	3,300
He(300K)	3.5e-5	3.8e-5	3,500
H$_2$(450K)	2.4e-5	1.9e-5	2,300
H$_2$(300K)	3.3e-5	3.2e-5	3,000
Ar(450K)	3.3e-6	3.1e-6	335
Ar(300K)	2.2e-6	1.5e-6	250
CH$_4$(450K)	2.2e-7	5.0e-7	80
CH$_4$(300K)	0.0	3.1e-7	<1
He (Mixed)	1.4e-5	1.3e-5	2,700
CH$_4$(Mixed)	3.0e-5	3.0e-5	<10

*1 Barrer = 10^{-10} cm^3(stp)/cm/cm^2/s/cmHg   **Assuming 1 μm thick membrane

CONCLUSIONS

We have demonstrated the usefulness of DCV-GCMD for investigating the sieving nature of microporous materials by applying the method to a model silica system. Work is currently underway to apply DCV-GCMD to multicomponent fluids under different conditions in other silica and zeolite models. In this work we tried to exhibit the power and usefulness of massively parallel computer simulation in understanding gas flow in microporous solids. The theories in use for zeolites may work well for amorphous silica membranes if the pores are of molecular dimensions. DCV-GCMD simulation allows comparison with the most relevant experiments in membrane research, that is permeation of gases and gas mixtures.

LITERATURE CITED

1. Xiao, J., and J. Wei, "Diffusion Mechanism of Hydrocarbons in Zeolites-I. Theroy", Chem. Engr. Sci., 1992, 47(5), 1123.

2. Pohl, P.I. and D.M. Smith, "Molecular Simulation of Porous Silicates", *Advances in Porous Materials*, MRS Vol 371, 27-33, 1995.

3. Yan, Y., M. E. Davis, and G.R. Gavalas, "Preparation of Zeolite ZSM-5 Membranes by In-Situ Crystallization on Porous a-Al2O3", *Ind. Eng.Chem. Res.*", 34, 1652-1661, 1995.

4. Seghal, R., PhD Dissertation, University of New Mexico, 1995.

5. Heffelfinger, G. S., and F. van Swol, J. Chem Phys., 1994, 100(10), 7548.

6. Pohl, P.I., J.L. Faulon, and D.M. Smith, "Molecular Dynamics Computer Simulation of Silica Aerogels", *J. Non-Cryst. Solids*, 186, 349-355, 1995.

7. Pohl, P.I., G.S. Heffelfinger, and D. M. Smith, "Molecular dynamics computer simulation of gas permeation in thin silicalite membranes", *Mol. Phys.*, 89(6), 347-354, 1996.

8. MacElroy, J.M.D., "Nonequilbrium Molecular Dynamics Simulation of Diffusion and Flow in Thin Microporou Membranes", *J. Chem. Phys.*, 101(6), 5274-5280, 1994.

9. Cracknell, R. F., D. Nicholson, and N. Quirke, "Direct Molecular Dynamcis Simulation of Flow Down a Chemical Potential Gradient in a Slit-Shaped Micropore", *Phys. Rev. Let.*, 74(13), 2463-2466, 1995.

10. Fritzsche, S., R. Haberlandt and J. Kärger, "An MD Study on the Correlation between Transport Diffusion and Self-Diffusion in Zeolites", *Z. Phys. Chem.*(Munich), 189, 211-220, 1995.

11. Ford, D. M. and E. D. Glandt, "Molecular Simulation of the Surface Barrier Effect. Dilute Gas Limit", *J. Chem. Phys.*, 99, 11543-11549, 1995.

12. MacElroy, J.M.D., and K. Raghavan, "|Adsorption and Diffusion of a Lennard-Jones Vapor in Microporou Silica", *J. Chem. Phys.*, 93(3), 2068-2079, 1992.

13. Hirshfelder, J. O., C. F. Curtiss, and R. B. Bird, *Molecular Theory of Gases and Liquids*, John Wiley & Sons, New York, 1954.

14. S. Heffelfinger, "Massively Parallel Dual Control Volume Grand Canonical Molecular Dynamics with LADERA", *in preparation*.

GAS TRANSPORT IN SOL-GEL DERIVED POROUS CARBON AEROGELS

G. REICHENAUER, J. FRICKE
Physikalisches Institut der Universität Würzburg, Am Hubland, D-97074Würzburg,Germany,
reichenauer@physik.uni.wuerzburg.de

ABSTRACT

Due to their high electrical conductivity, their large specific surface area and their high porosity sol-gel derived nanoporous carbons are promising materials for electrodes, e.g. in water desalination systems or fuel cells. In order to optimize their properties with respect to these applications information is needed about transient and steady state transport through the interconnected pores.

Dynamic gas expansion and time resolved permeation measurements allow to determine the relevant quantities, i.e. the permeablilty, the ratio of gas phase to surface diffusion and the volume of dead end pores along with the tortuosity.

Experimental data on nanoporous carbons of different density are presented. All samples investigated were prepared via pyrolysis of resorcinol formaldehyde aerogels. The measurements were performed with different gases below 0.1 MPa.

INTRODUCTION

Sol-gel derived carbons (also known as carbon aerogels or xerogels) are open-porous solids, that can be tailored for different applications. Due to their large inner surfaces and high electrical conductivities compared to compressed carbon black powders, these materials can be used as porous electrodes for supercapacitors, filter systems or reaction cells [1,2,3].

All applications mentioned deal with mass transport through or into the interconnected pores. Only a few experiments with respect to this property have been performed so far [4,5]. Parameters like dead end volume, tortuosity, ratio of gas phase to surface diffusion have not been investigated to our knowledge.

In order to gather more detailed information about the mechanisms of fluid transport in sol-gel derived porous carbons, we used two different experimental techniques as well as a set of gases to determine the diffusion coefficients.

THEORY

In order to classify the fluid transport in a porous medium the following points have to be checked:
1. Is the Knudsen number K, i.e. the ratio of the mean free path of a molecule to the mean distance between the pore walls smaller or larger then 1 ? If $K \ll 1$ the transport in the gas phase is governed by viscous flow, with the permeability P being proportional to p_m/η, where p_m is the mean pressure and η the viscosity of the gas. In case of $K \gg 1$ molecular diffusion dominates, i.e.

$$P \propto (T/m)^{0.5}, \qquad\qquad (1)$$

with T the temperature and m the molar mass of the diffusing gas.

Thus, even without any information about the structure of the sample the question whether molecular diffusion or viscous flow is the predominant transport mechanism can be answered analyzing either the pressure dependence of the permeability or comparing the permeabilities determined for different "non-adsorbable" gases.

2. Can the analysis gas be adsorbed, in a sense that more than 1/4 of a monolayer is covered in the experimental run [6] ? The surface contribution P_s to the total permeability is then given by

$$P_S = D_S \cdot \frac{S}{\tau \cdot L \cdot A} \cdot dV_{ads} / dp, \tag{2}$$

with S the total inner surface, L the length and A the area of the specimen perpendicular to the flow; τ is the tortuosity, i.e. the ratio of the diffusion path to the length of the sample and dV_{ads}/dp is the slope of the adsorption isotherm [7].

There is an additional point, that might be important in the case of strong adsorption, i.e. the fact, that in transient (dynamic) measurements the sample is not isothermal as exothermal effects occur upon adsorption [8].

3. Is the diffusion path tortuous, is a dead end volume present or takes adsorption place in the specimen ?

The tortuosity enters the transient permeablility squared, whereas it affects the steady state permeability only linearily [9]. On the other hand, a dead end volume $V_{dead\ end}$ as well as immobile adsorbed molecules do not contribute to the steady state, but to the transient permeability:

$$P_t \propto [(1 + V_{dead\ end} / V_{open}) \cdot (1 + V_{ads} / V_{pore})]^{-1}, \qquad P_{ss} \propto 1/V_{open} \tag{3}$$

$$\rightarrow \quad P_{ss} / P_t = \tau \cdot (1 + V_{dead\ end} / V_{open})(1 + V_{ads} / V_{pore}).$$

EXPERIMENTAL

Experimental Techniques

Two different methods have been applied :

1. *Steady state experiments (one-dimensional)* : The pressure drop Δp across a disclike sample was recorded with a membran pressure transducer (range 0.1 MPa, accuracy 0.15 %) for different given flow rates J; the flowmeter used to measure this quantity has a range of 100 ccm STP/min and a resolution of 0.1 ccm STP/min. To achieve even better accuracy the flow rate has been alternatively calculated from the pressure increase in a calibrated volume V_C (pressure resol. 1.5 Pa, volume 77 ccm); in order to provide quasi steady state conditions this pressure has to be small compared to the pressure drop along the specimen.

The steady state permeability P_{ss} of the specimen was calculated via the equation

$$J = V_C \cdot dp/dt = - P_{ss} \cdot A \cdot \Delta p/L, \tag{4}$$

with A the area and L the thickness of the sample. Typical values for these quantities were A = 2 cm^2 and L =1.5 mm. The rim of the samples has been sealed with machinable epoxy resin.
If the pressure in V_C is recorded after a rapid pressure gradient change across the sample, the socalled lag time τ_L can be extracted [10]. It is related to the transient permeability P_t via

$$\tau_L = L^2/(6P_t) . \tag{5}$$

2. *Dynamic measurements :* The pressure p in a volume containing the specimen under investigation is raised within 100 ms. As this time scale is too short to allow for the pressure in the pores of the sample to reach the new equilibrium state, one can measure the pressure drop around the sample as a function of time to determine the transient permeability. The experimental procedure as well as the data analysis is described in detail in ref. [11]. The approximative solution [11], well suited for all sample/gas combinations with only minor adsorption has been extended for the case of strong adsorption taking into account the change in boundary conditions numerically . The samples used for the dynamic experiments were cylinders of about 1.5 cm in diameter and about 2 cm in height.
The advantages of the dynamic gas expansion method compared to the steady state set-up are :
- no sealing of the sample is necessary,
- the sceletal volume can be determined if helium is used and
- the amount of gas adsorbed can be measured if adsorption occurs.

Sample Preparation

The sol gel derived carbons studied in this paper were prepared via pyrolysis of resorcinol-formaldehyde aerogels [1]. These precursor aerogels consist of spherical particles forming a three-dimensional network. Their nanometer to micron sized structures develop upon catalyst-controlled polycondensation of resorcinol and formaldehyde in an aqueous solution. While the size of the primary particles is essentially a function of the molar ratio of resorcinol and catalyst (R/C), the total porosity and the average pore size can be controlled via the concentration of resorcinol and formaldehyde in the starting solution (RF number).
After drying the resulting organic aquagel at ambient pressure the resorcinal-formaldehyde aerogels are pyrolized in an Ar-atmosphere at 1050 °C. The result are porous carbon aerogels with the main features of the percursor structure being preserved.
The R/C ratio of all carbons investigated was 1500; the RF number was varied between 30 and 60, yielding sample densities between 320 and 1050 kg/m^3. The ID used for each sample contains the R/C as well as the RF number.

RESULTS

Steady state measurements

A typical curve taken under quasi steady state conditions is shown in Fig.1. After applying a pressure gradient of about 0.004 MPa across the sample the pressure increase at the low pressure

Fig.1 : Pressure change in a calibrated volume, connected to the lower pressure side of sample #1500_50, after a pressure rise at the frontside. The straight line is a fit to the linear part of the curve (steady state); the intercept of this line with the time-axis corresponds to the lag time τ_L (5).
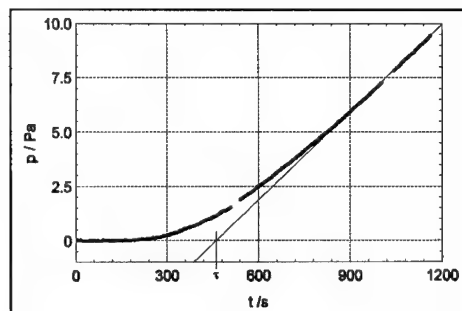
side of the sample has been recorded until steady state conditions were reached (linear part of the curve). In Table 1 the steady state permeabilities P_{ss} as well as the transient quantities P_t calculated via eq. (4) and (5), respectively, are listed.

Dynamic gas expansion

In Fig. 2 the experimental data p(t) for sample #1500_50 are plotted for three different gases : helium, argon and carbon dioxide. The time-scale has been transformed by a factor $\gamma= 1/(V_{ads}/V_{pore} +1)$ in order to take into account the spread of the time scale due to adsorption effects. The curves have been fitted with P_t as a free parameter. The results of the fit are summarized in Tab.1. The experimental procedure allows also for the calculation of the adsorp-tion isotherm or its derivative (Fig.3), respec-tively. According to eq. (2), the latter con-trols the pressure dependence of surface diffusion.
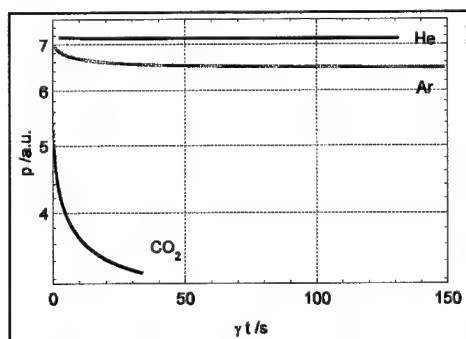
Fig.2 : Pressure as a function of time recorded in a dynamic gas expansion experiment for sample #1500_50 and three different gases. The time scale has been multiplied by the factor γ for each gas.
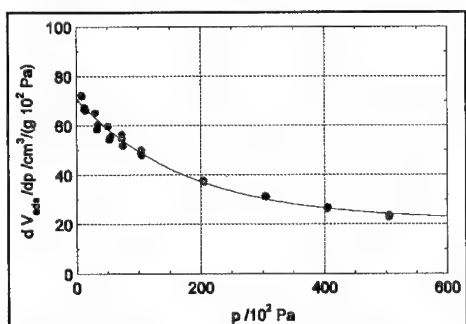
Fig.3 : Derivative of the adsorption isotherm for CO_2 and sample #1500_50 at 297 K.

Table1 . Transient and steady state permeabilities P_t and P_{SS} for three carbon aerogels at different mean pressures p as derived from (quasi) steady state data and dynamic gas expansion experiments. γ is defined as V_{ads}/V_{pore}, i.e. the ratio of gas in the adsorbed state and the gas phase.

				quasi steady state			dynamic gas expansion	
Sample ID	ρ/kg/m³	Gas	p/10² Pa	P_{SS}/10⁻⁶ m²/s	P_t/10⁻⁶ m²/s	P_{SS}/P_t	P_t/10⁻⁶ m²/s	γ+1
1500_30	320	He	18	14.8± 0.05	-	-	-	10
		Ar	18	4.8±0.2	-	-	1.6±0.1	38
			34	4.3±0.4	-	-	1.6±0.1	37
1500_50	720	He	12	0.140 ±0.005	-	-	-	-
			150	0.16±0.03	-	-	-	10
			170	0.144 ±0.005	-	-	-	10
		Ar	14	0.065 ±0.002	0.010 ±0.002	65	-	48
		CO₂	40	0.095 ±0.003	0.00098 ±0.00005	970	-	770
			900	0.075 ±0.005	-	-	-	295
1500_60	1050	He	50-300	-	-	-	0.08±0.01	1

DISCUSSION

Analyzing the data in Table 1 the following facts can be stated :

1. The gas phase transport in the samples investigated obviously is governed by molecular diffusion rather than by viscous flow. This can be deduced from the pressure independent He permeability in case of sample #1500_50 as well as from the scaling of the steady state permeabilities for aerogel #1500_30 with $(1/m_{gas})^{0.5}$.

2. With increasing adsorption, i. e. increasing $(1+\gamma)$, these two findings are no longer fullfilled. E.g. sample #1500_50 exhibits a clearly larger steady state permeability for Ar then for CO_2, although the molar masses for both gases are almost equal.

According to eq. (2) the contribution of surface diffusion increases with the amount of gas adsorbed upon pressure change. The pure gas phase diffusion for CO_2 in aerogel #1500_50 as calculated from the He values via the molar mass relationship should be about 0.043 10⁻⁶ m²/s. Thus the additional transport component decreases by about a factor of two when the mean

pressure is raised from 0.004 to 0.09 MPa. The corresponding factor in dVads/dp taken from Fig.3 is about 3.5. The discrepancy can be explained by a change in the surface diffusion coefficient Ds (eq. (2)), which is a function of the heat of adsorption [7] and thus of the total amount adsorbed at a certain mean pressure (below complete monolayer coverage).

3. According to eq. (3) the ratio of steady state and transient permeability includes the factor $(1+\gamma)$ as well as the tortuosity τ and the ratio of dead end to open pore volume. Dividing the quantity PSS/Pt as derived for the sample #1500_50 by the factor $(1+\gamma)$ yields a value of 1.35 in case of argon and 1.26 for carbon dioxide, respectively. I.e. a factor of about 1.3 is caused by tortuosity of the diffusion path and/or dead end volume.

CONCLUSIONS

Analysing both, the steady state as well as the transient permeabilities of carbon aerogels with respect to different gases is a powerful tool collect detailed information on the transport in porous materials. It allows for the separation of gas phase and surface diffusion and for the extraction of a geometrical factor that includes the tortuosity of the diffusion path as well as the dead pore volume.
For the future we plan more extended investigation in this field.

ACKNOWLEDGEMENT

REFERENCES

1. J.L. Kaschmitter, S.T. Mayer, R.W. Pekala, Supercapacitors Based on Carbon Foam, U.S. Patent No. 5 260 855 (November 1993).
2. C. Frankel, The Environment, IEEE Spectrum, p.76 (January 1996).
3. H. Shi, Electrochimica Acta 41, p.1633 (1996).
4. F.M. Kong, J.D. Le May, S.S. Hulsey, C.T. Alviso and R.W. Pekala, J. Mater. Res. 8, p. 3100 (1993).
5. G. Reichenauer, C.Stumpf, J.Fricke, J.Non-Cryst. Solids, 186, p. 334 (1995).
6. R.K. Smith, A.B. Metzner, J. Phys. Chem. 68, p. 2741 (1964).
7. K.J. Sladek,E.R. Gilliland, R.F. Baddour, Ind. Eng. Chem. Fundam. 13, p.100 (1974).
8. R. Haul, H. Stremming in Characterization of Porous Solids, edited by K.K. Unger, J. Rouquerol, K.S.W. Sing and H. Kral (Elsevier Publishers B.V.,Amsterdam, 1988), p.367.
9. S.Satoh, I. Matsuyama, K. Susa, J. Non-Cryst. Solids 190, p.206 (1995).
10. W.R. Vieth, Diffusion In and Through Polymers (Hanser Publishers, 1979), p.20.
11. C. Stumpf, K.v. Gässler, G. Reichenauer and J. Fricke, J. Non-Cryst. Solids 145, p. 180 (1992).

DYNAMICS OF AIR-WATER CONTACT LINES AND INTERFACES NEAR THE PINNING THRESHOLD

PO-ZEN WONG,* ERIK SCHÄFFER AND DAVID B. PENGRA[†]
Department of Physics and Astronomy, University of Massachusetts, Amherst, MA 01003

ABSTRACT

We report a study of the dynamics of capillary rise of water in glass tubes and glass bead packs. The water column height h is measured as a function of time t by video imaging. Analyzing the late time data in terms of critical pinning, $dh/dt \propto (P - P_c)^\beta$, we find an anomalously large exponent β for interfaces in bead packs and $\beta \approx 1$ for contact lines in capillary tubes. Repetitive rise and fall experiments in capillary tubes suggests that thinning of the wetting film plays an important role in the dynamics. We discuss these findings in light of recent theories and experiments.

INTRODUCTION

Pinning of lines and interfaces occurs in a wide variety of physical systems. Perhaps the most common experience is the observation of rain drops stuck on a window pane. Less direct observations include the hysteretic motion of magnetic domain wall upon the reversal of an applied field [1], and the motion of flux lines in high-T_c superconductors with increasing electric current [2]. In all cases, pinning results from the inherent *disorder* in the system.

It is commonly *postulated* that the pinned state and the moving state are separated by a *dynamical phase transition* that exhibits *universality*, i.e., independent of the details of the systems. For this reason, the problem has attracted considerable theoretical interest in recent years [3, 4]. However, there is so far no clear experimental evidence for any particular model. In this paper, we describe our effort to study the depinning transition by simple capillary rise experiments. The advantage of such experiments is that the stick-slip actions may be visually observed. In addition, no external device is needed to drive the system, so the observed behavior is *self-organized*.

Two types of experiments were carried out. In the first, a glass tube filled with small beads was placed vertically in water. We measured the water level as a function of time and observed how it came to a stop, i.e., reached the pinned state. The object being pinned is the air-water interface. The pinning forces are the random capillary forces acting on the interface due to the different sizes and shapes of the pores. In the second type of experiments, a glass capillary tube is used instead. Here, the object being pinned is the contact line between the air-water meniscus and the interior wall of the capillary tube. Microscopic roughness and chemical inhomogeneities on the wall provide the random pinning forces. As shown below, there are interesting similarities and differences between the two sets of results.

The glass beads results have been presented previously [5, 6] and the capillary tube results are new. Thus our discussion here focuses more on the latter. The readers are referred to the published papers for more details on the former. In the following, we first give an overview of the relevant theories and some previous experiments. This will be followed by a description of our experiment and the main results. A brief conclusion will be given at the end.

THEORETICAL AND EXPERIMENTAL BACKGROUND

Interface pinning in porous media

Koplik and Levine [7] suggested in 1985 that the dynamics of fluid interfaces [8] in random porous media is analogous to that of domain walls in random-field magnets [9]. Assuming that the fluid interface is described by a single-valued function $z = f(\mathbf{x}, t)$, where $\mathbf{x}$ is a $(d - 1)$-component transverse vector, the equation of motion is

$$\frac{\partial f}{\partial t} = P + \nabla^2 f + Y(\mathbf{x}, f) , \tag{1}$$

where P is a uniform driving force, $\nabla^2 f$ is an effective surface tension that minimizes the surface area, and Y represents quenched random capillary forces acting on the interface. They noted that the same equation was used by Bruinsma and Aeppli [10] to study domain wall dynamics in the random-field Ising model (RFIM). The underlying connection is that Eq. (1) is the time-dependent Ginzburg-Landau equation

$$\frac{\partial f}{\partial t} = P - \frac{\delta F}{\delta f} \tag{2}$$

for the RFIM interface free energy derived by Grinstein and Ma [11]

$$F(f) = \int d^{d-1}x \left[\frac{1}{2} |\nabla f|^2 - \int_\infty^f dz Y(\mathbf{x}, z) \right] . \tag{3}$$

For small values of Y, Koplik and Levine find that the interface translates smoothly but, for large values of Y, it can be pinned in rough configurations.

The critical behavior of the depinning transition in the above model has recently been analyzed by Nattermann *et al* [3], and independently by Narayan and Fisher [4]. Essentially the same results were obtained. The physical picture is that the interface fluctuations are correlated over a distance ξ along the interface which diverges as

$$\xi \propto (P - P_c)^{-\nu} \tag{4}$$

at a critical force P_c. The interface width w obeys self-affine scaling

$$w \propto \xi^\alpha \propto (P - P_c)^{-\nu\alpha} \tag{5}$$

with $\alpha = 2 - 1/\nu = \epsilon/3$, where $\epsilon = (5 - d)$. The advance of the interface occurs via avalanches of different sizes. The waiting time τ for an avalanche of size ξ obeys dynamic scaling

$$\tau \propto \xi^z \propto (P - P_c)^{-\nu z}. \tag{6}$$

Consequently, the interface velocity is given by

$$\upsilon \propto w/\tau \propto \xi^{\alpha-z} \propto (P - P_c)^{-\nu(\alpha-z)} \equiv (P - P_c)^\beta \tag{7}$$

where $\beta = (z - \alpha)\nu \approx 1 - \epsilon/9 + O(\epsilon^2)$. In this scaling picture of the transition, there are only two independent scaling exponents, ν and z, or equivalently α and β. For two dimensions, the theoretical predictions are $\alpha = 1$ and $\beta \approx 2/3$, and for three dimensions, $\alpha = 2/3$ and $\beta \approx 7/9$. Experimentally, the exponent α can be determined by analyzing the interface

roughness according to Eq. (5) [12, 13] and β may be determined by analyzing the interface velocity v as a function of the applied force P according to Eq. (7). *This is the main result tested in our experiments.*

In a previous 2D experiment [12, 13], He, Kahanda and Wong (HKW) studied the roughness of water invasion fronts in air-filled porous media. They find that the effective value of α increases towards unity as the flow rate is decreased and, at the lowest flow rates, overhangs begins to develop. This suggests that $\alpha \to 1$ in the limit of $v \to 0$ [13], in agreement with the prediction for two dimensions. β could not be determined in that experiment because the mechanical syringe pump exhibits stick-slip behavior of its own at $v < 10$ μm/s. An earlier experiment by Stokes *et al* [8] suggested that the critical behavior is observable for $v < 100$ μm/s, but the data were too noisy for determining β. In the capillary rise experiment described below, no mechanical device was used to drive the fluid. The interface is allowed to slow down on its own to approach the critical point, i.e., in a *self-organized* manner. We were able to observe the interface movement over a speed range of $0.1 - 1000$ μm/s. This corresponds to capillary numbers $N_{cap} \equiv v\eta/\gamma$ as low as 1.5×10^{-9} and modified capillary numbers $Ca \equiv D_b^2 v\eta/\gamma k$ as low as 10^{-6}. Here, η is the viscosity of water, γ its surface tension, D_b is the diameter of the glass beads and k is the permeability of the bead pack. We find that the value of β is much larger than the theoretical prediction [5, 6].

Contact line pinning

The depinning of contact lines can be modelled by the same scaling idea described above, except that the energy associated with a distorted line is not given by Eq. (3). This is because the contact line is the intersect of three interfaces: vapor-liquid, vapor-solid, and liquid-solid. The distortion of the contact line affects the shapes and areas of all three and their associated interfacial energies. Ertaş and Kardar [14] assumed that the contact line moves on a solid surface with randomly fluctuating interfacial energies with short-range correlations. Their analysis gives $\alpha = 1/3$ and $\beta \approx 2/3$ in three dimensions. Prior to this work, Raphaël and de Gennes [15] considered a contact line passing over pinning defects one at a time sequentially. They predicted $\beta = 3/2$. Joanny and Robbins [16] considered the case in which the contact lines passes over periodic stripes of chemical heterogeneities parallel to the line, and they also found $\beta = 3/2$. A common assumption in these models is that they focus on the interfacial energies and ignore the dissipation due to the viscous flow of the liquid. The reason is that viscous effects usually diminish as the velocity approaches zero. However, Sheng and Zhou [17] argued that the breakdown of the no-slip boundary condition at the contact line can lead to significant dissipation. By analyzing different slip models, they predicted $\beta > 2$, where the exact value depends on the details of the slip action.

Experimental studies of contact line pinning have found a range of values for the exponent β. Stokes et al [18] used an ac method to study the nonlinear response of the meniscus between mineral oil and a glycerol-methane mixture in a capillary tube. Analyzing the harmonics in terms of Eq.(7) gave $\beta \approx 2.5 \pm 0.4$. More recently, Kumar *et al.* [19] used the same technique to study water-decane and water-hexadecane menisci. They found $\beta \approx 5$ instead. Ström *et al.* [20] measured the dynamic contact angle visually by dipping a solid plate into a liquid at different speed v. They found that the data were consistent with $\beta \approx 3/2$ for $N_{cap} < 10^{-4}$. An earlier work of Mumley *et al.* [21] analyzed capillary rise data for various liquid-liquid menisci in glass tubes with treated surfaces. They suggested $\beta \approx 2$ with data in the range of $N_{cap} > 10^{-5}$. The differences in these results suggest that many experimental details such as N_{cap} and the chemical nature of the liquids and solids can all
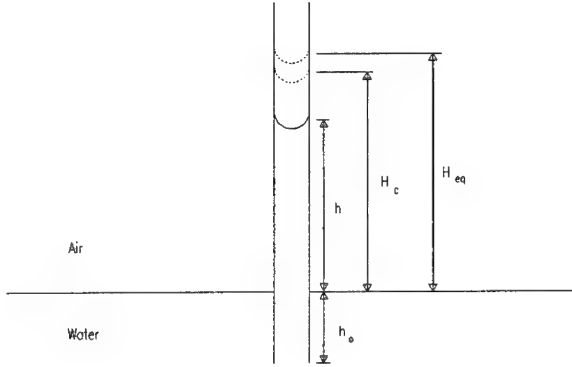
Figure 1: Schematics of a capillary rise experiment.

affect the results. In our experiment, we let N_{cap} reach below 10^{-9} to get as near to the pinning threshold as possible. We used deionized water and cleaned glass tubes to keep the chemistry less complicated. We find $\beta \approx 1$ but there are slight differences between capillary fall and capillary rise, suggesting that the details of the wetting film are important [22].

Capillary rise and the Washburn equation

It is interesting to note that while the theoretical predictions and experimental results give a wide range of values for β, the general form of Eq. (7) is undisputed. Comparing experiments to theories is difficult because the nature of the pinning defects in the experiments are usually unknown and the size of the critical region is also ambiguous. In the capillary rise experiment, the velocity can vary over a wide range. In order to assess the importance of pinning effects, we need to first understand the behavior without pinning [23]. Fig. 1 shows the basic geometry of such an experiment. For a tube of radius r dipped into water, in the absence of pinning, we expect the water column to rise to an equilibrium height $H_{eq} = 2\gamma \cos\theta / r\rho g$ where θ is the contact angle, ρ the water density and g the gravitational acceleration. *Assuming* that θ is independent of velocity, the upward driving pressure is $\rho g(H_{eq} - h)$ at column height h. If we further assume that the resistance to flow comes only from the fluid viscosity and the Poiseuille formula is obeyed, the equation of motion is

$$\frac{8\eta(h + h_o)}{r^2}\frac{dh}{dt} = \rho g(H_{eq} - h) \; , \tag{8}$$

where h_o is the length of the tube submerged in water, as shown in Fig. 1. The LHS of this equation is the viscous pressure drop in the tube and the RHS is the net driving pressure due to surface tension and gravity. This equation ignores the water acceleration which amounts to an overdamp approximation. It can be shown numerically that the assumption is valid for water near room temperature if the tube radius r is less than 0.25 mm [23]. To solve this equation, we define $z = h + h_o$ and $Z_{eq} = h_o + H_{eq}$, giving

$$\frac{8\eta z}{\rho g r^2}\frac{dz}{dt} = Z_{eq} - z \; . \tag{9}$$

354
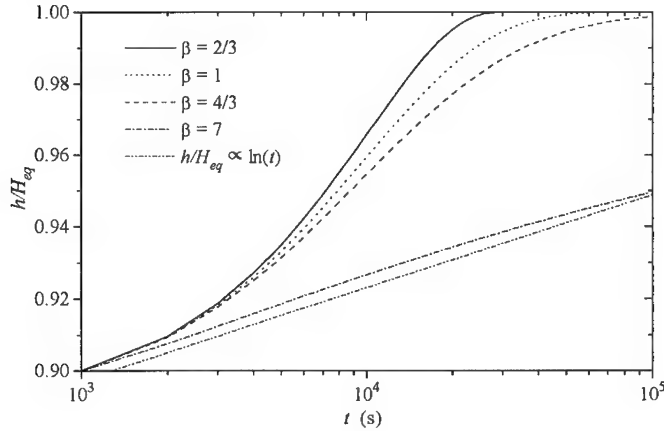
Figure 2: Effects of different values of β on the approach of h to H_c.

Using a normalized height $y = z/Z_{eq}$ and a normalized time $x = t/\tau_w$, where

$$\tau_w = 8\eta Z_{eq}/\rho g r^2 \ , \tag{10}$$

we obtain a dimensionless equation $y(dy/dx) = 1 - y$. Integrating with the initial condition $y = y_1$ at $x = x_1$ gives

$$x - x_1 = -(y - y_1) - \ln\left(\frac{1-y}{1-y_1}\right) \tag{11}$$

or

$$\frac{t - t_1}{\tau_w} = -\frac{h - h_1}{H_{eq} + h_o} - \ln\left(\frac{H_{eq} - h}{H_{eq} - h_1}\right) \ , \tag{12}$$

known as the Washburn equation [24]. It describes *capillary rise* ($h_1 < H_{eq}$) as well as *capillary fall* ($h_1 > H_{eq}$). The motion is characterized by the time constant τ_w given by Eq. (10). The column height h approaches H_{eq} exponentially at long times. The Washburn equation applies to flow in porous media as well. The only modification is that the factor $8/r^2$ in Eq. (8) is replaced by the permeability k [13, 23], and the same applies to Eq. (10).

With pinning effects, we expect the air-water interface to stop at a height $H_c < H_{eq}$ in capillary rise (but $H_c > H_{eq}$ in capillary fall). So the threshold pressure for pinning is $P_c = \rho g(H_{eq} - H_c)$. Eq. (7) leads us to write

$$\frac{dh}{dt} = v_o \left(\frac{H_c - h}{H_{eq} - H_c}\right)^\beta \ . \tag{13}$$

For $\beta \neq 1$, integrating from initial time t_1 and height h_1 yields

$$h(t) = H_c - (H_c - h_1)[1 + A(t - t_1)]^{1/(1-\beta)} \ , \tag{14}$$

where $A = (\beta - 1)v_o(H_c - h_1)^{\beta-1}/(H_{eq} - H_c)^\beta$. If $\beta < 1$, we have $A < 0$, and h reaches H_c after a finite time given by $\tau_o = t - t_1 = -1/A$. If $\beta > 1$, h approaches H_c algebraically as $t \to \infty$. If $\beta = 1$, the integral of Eq. (13) gives,

355
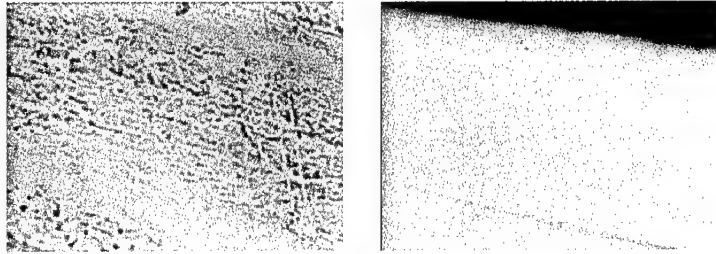
Figure 3: Under a microscope, the interior wall of a fractured 410 μm diameter Type R capillary tube (left) can be seen to have a much higher level of roughness compared to that of a 355 μm diameter Type S tube (right). The size of each image is 110×85 μm^2.

$$h(t) = H_c - (H_c - h_1)e^{-(t-t_1)/\tau_1} \quad , \tag{15}$$

with $\tau_1 = (H_{eq} - H_c)/v_o$. Hence the three cases $\beta < 1$, $\beta = 1$, and $\beta > 1$, give qualitatively different behavior in the way H_c is approached. Fig. 2 illustrates this difference. We note in particular that for $\beta < 1$, h stops at H_c abruptly. For $\beta \gg 1$, the rise is almost logarithmic. Eqs. (12), (14) and (15) are the main expressions we use to analyze our data. As we shall see, the early time data are very well described by the Washburn equation while the late time data fit either Eq. (14) or (15).

EXPERIMENTAL DESIGN

The porous media experiments were carried out with an 8 mm inner diameter glass tube filled with glass beads. Four different bead sizes with diameters D_b ranging from 180 to 510 μm ($\pm15\%$) were used. The beads were rinsed in deionized water several times and air dried. The tube stands vertically in a base container filled with deionized water. The section submerged in water has a length $h_o \approx 4$ cm. A Nylon filter membrane is glued to the bottom of the tube to hold the beads while letting the water through. A video camera records the capillary rise. The video images are digitized at set time intervals to locate the interface position and determine its average height h versus time t. The rms width w of the interface can also be computed. Each capillary rise experiment runs for about 24 hours ($\sim 10^5$ s). To prevent water loss due to evaporation, a small water-containing cap is placed at the top of the tube to provide 100% humidity. This cap has a 1/16-inch escape hole so that the total pressure is the same as the ambient. Capillary fall experiments were not performed because they are known to exhibit percolation patterns which cannot be described by the motion of a single-valued interface profile. Additional experimental details are given elsewhere [5, 23].

The contact line experiments were carried out with glass tubes with diameters between 150 and 410 μm. Figure (3) shows the difference in wall roughness between two types of tubes which we refer to as Types R and S (rough and smooth). Our previous experiments [6, 23] were carried out with R-tubes. They were cleaned immediately before the experiment with the following procedure: 400 ml of 1 M hydrochloric acid is flowed through the tube in about an hour and rinsed with 400 ml of deionized water, then finally boiled in deionized water for
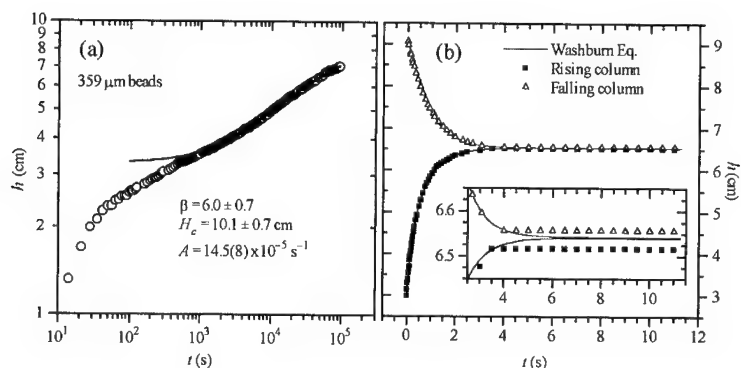
Figure 4: Comparison of the pinning dynamics of (a) a bead pack and (b) a capillary tube with a coarse spatial resolution.

at least 3 hours. Both capillary rise and fall experiments were carried out. A small syringe is used to draw the fluid to an initial height above or below H_{eq}. A three-way valve was used to switch the tube from the syringe to an ambient pressure with 100% humidity. The difference of final heights between the rise and fall experiments is an indication of the pinning effect. Although the basic experimental method is the same as that for porous media, for reasons explained below, each run lasted only about 10^3 s. Much of the movement occurs in the first few seconds, followed by very slow creeping of the meniscus. A microscope was used for the latter. We typically image a field size of 3.2 mm with 640 pixels, giving a resolution of 5 μm/pixel. With this spatial resolution, we found that a change in room temperature ΔT by 1 K would affect the surface tension enough to change the equilibrium height H_{eq} by about 57 pixels (see Fig. 8). Consequently, the apparatus was enclosed in a thermally insulated chamber so that $\Delta T < 0.01$ K during a run and H_{eq} was stable to less than half a pixel.

RESULTS

Porous media

Figure 4a shows an example of the capillary rise data for the 359 μm size beads. The data in the first minute was found to be well described by the Washburn equation, but the water level continued to creep upward several centimeters over many hours. The time constant given by Eq.(10) corresponds to the shoulder in the data. This behavior is typical of all the runs with different bead sizes. We fit the late-time data to Eq. (14). In Fig. 4, the fit covers the period between 15 minutes to 24 hours (about 10^3 to 10^5 s) and gives $\beta = 6.0 \pm 0.7$. Fitting the data from different runs, with different bead sizes, and over different time scales results in an overall estimate $\beta = 6.5 \pm 3.5$, much larger than the prediction of $\beta = 7/9$ based on the theoretical analyses of Eq. (1). It is also interesting to note that the values of H_c obtained from the fits are always well above the experimental range of h. For example, h in Fig. 4a reaches only 7 cm and H_c obtained from the fit is 10.1 cm. This is due to the fact that, for large values of β, it takes very long time to reach the pinning height. The effect is

$$t = c(h_1 - h) - \tau_w \ln\left(\frac{H - h}{H - h_1}\right)$$
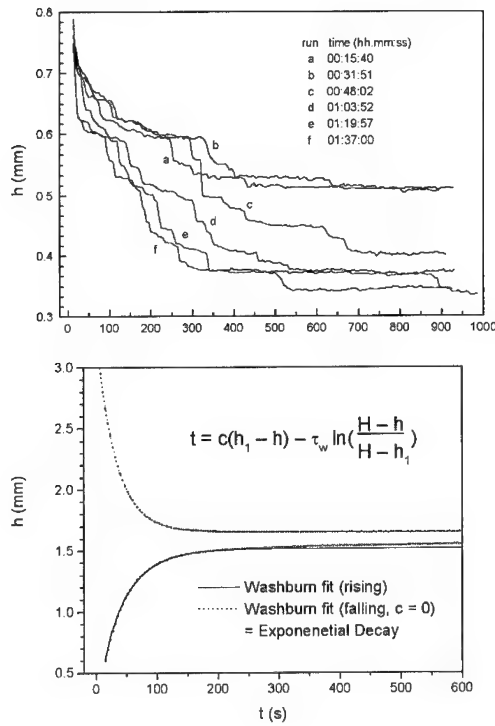
Figure 5: With a fine spatial resolution, (a) the capillary fall data in a 310 μm R-tube show stick-slip behavior and cannot be used to analyze the exponent β. (b) The rise and fall data obtained with a 254 μm diameter S-tube are well described by Eq. (15) in the first 200 s. Only the rise data show noticeable deviation at later times.

illustrated in Fig. 2. More details can be found in Refs. [5], [6] and [23].

Contact lines

The capillary rise experiments for glass tubes were always performed after the tube was prewetted in a capillary fall experiment. Fig. 4b shows the capillary rise and fall data for a 410 μm diameter R-tube without using a microscope. The final heights differ by about 0.4 mm, evident for pinning effects. However, all the data before reaching the pinned height were well described by the Washburn equation, so the exponent β cannot be analyzed. It is interesting to note that time constant τ_w is about 1 s, much less than what is typically found for bead packs. The reason is that the permeability of bead packs is empirically given by $k \approx D_b^2/700$ [13]. Since D_b is comparable to the tube radii r in our experiment, when k is used in place of $r^2/8$ in Eq. (10), the resulting time constant τ_w is about one hundred times longer. This accounts for the large difference in experimental time. To investigate the
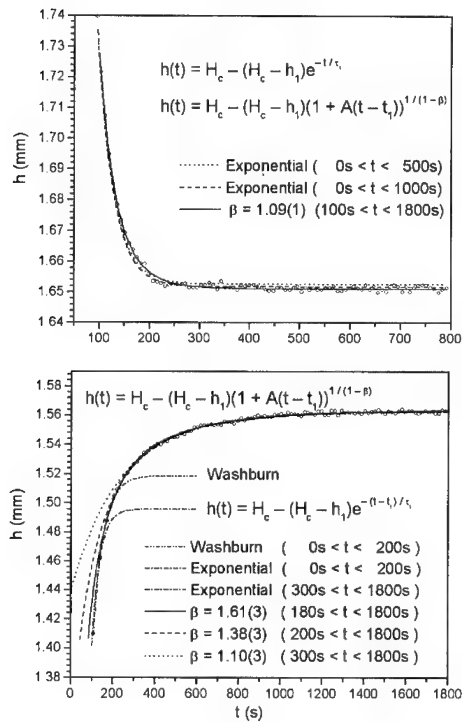
Figure 6: The data for (a) capillary fall and (b) capillary rise are analyzed in terms of Eqs. (14) and (15) for the 254 μm diameter S-tube. Note that the data are all within 200 μm of the pinning threshold.

pinning effect, we used the microscope to enhance the spatial resolution. Fig. 5(a) shows the capillary fall data within 0.5 mm of pinning for a 300 μm diameter R-tube. We can clearly observe stick-slip behavior that is different for each consecutive run. While this shows the qualitative effects of pinning, we cannot fit the data to Eq. (14) to find β. The problem is that the roughness in the R-tube is too large and we do not have adequate statistical sampling to compare with Eq. (14).

To find β, we used the S-tubes with much weaker pinning effects so that the individual avalanche is not resolved by our apparatus. Fig. 5(b) shows the rise and fall data for a 254 μm diameter S-tube. We note that the final height difference is only about 100 μm, which confirms that the pinning effect is weak. The Washburn equation was found to fit the falling data extremely well and the rising data not quite as well. In both cases, the time constant was in the range 30-50 s and the first term in Eq. (12) made little difference to the fit. Without the first term, Eq. (12) is reduced to Eq. (15) which corresponds to $\beta = 1$, so the observed time constant is actually τ_1 and unrelated to τ_w given by Eq. (10). As discussed in conjunction with Fig. 4, the true Washburn time constant τ_w is only of the order of 1 s

359
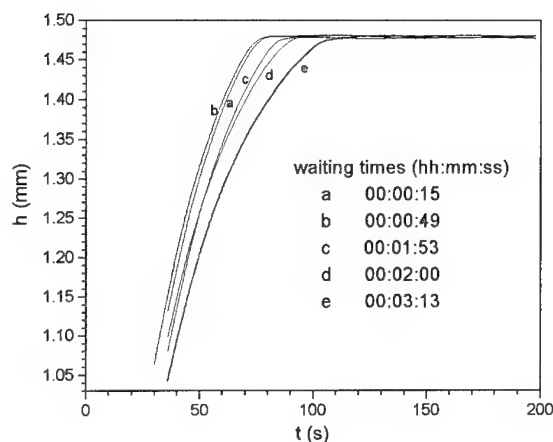
Figure 7: Capillary rise is fastest when it follows immediately after a capillary fall experiment, and the rise is slower if the waiting time Δt after the fall is increased. The data were taken with a 254 μm diameter S-tube.

and that applies to the first several centimeters of meniscus movement. In contrast, Fig. 5 shows the last millimeter of movement. To determine β more precisely in this critical region, it is necessary to test how Eq. (15) compares to Eq. (14) in fitting the data. Fig. 6 shows such a comparison. For the capillary fall data, we find that the best fit to Eq. (14) gives $\beta = 1.09(1)$ with a standard deviation of $\delta = 0.14$ pixel. Similarly, for the capillary rise data, we find $\beta = 1.10(2)$ if the starting time t_1 in Eq. (14) is chosen to be 300 s. The standard deviation is $\delta = 0.17$ pixel. Reducing t_1 to 200 s has the effect of increasing β but δ remains about the same. If Eq. (15) is used to fit the fall data, we find that it works quite well over the entire range in Fig. 6(a) but δ is larger by a factor of 2 to 3. For the two time ranges shown in Fig. 6(a), δ is 0.41 and 0.33 pixels, respectively. For the rise data, Eq. (15) cannot be used to fit the entire range. Instead, the first 200 s data give $\tau_1 = 37$ s and the data after 300 s give $\tau_1 = 269$ s. δ for these fits are about 0.2 pixel, indistinguishable from the fits to Eq. (14).

From the above analysis, we can conclude that the late time data for both capillary rise and fall are best described by Eq. (14) with $\beta \approx 1.10(2)$, but the distinction from Eq. (15) ($\beta = 1$) cannot be made with absolute certainty. As we can see from Fig. 2, small differences in β near $\beta = 1$ can be difficult to resolve. On the other hand, finding the same value between the rise and fall data lends more confidence to this result. What is also interesting is that, when Eq. (15) is used to fit the capillary rise data, the first 200 s and the late time data give very drastically different values for τ_1. This was not observed in the fall data where a single τ_1 sufficed. A plausible cause is that we always carried out a rise experiment following a fall experiment such that the tube wall was prewetted with a thin water film. If this film slides off during the early stage of the rise experiment, then the rise would be slower at the late stage. To test this idea, we performed rise experiments with a variable waiting time Δt following a fall experiment. Fig. 7 shows the result. We note that there is a noticeable
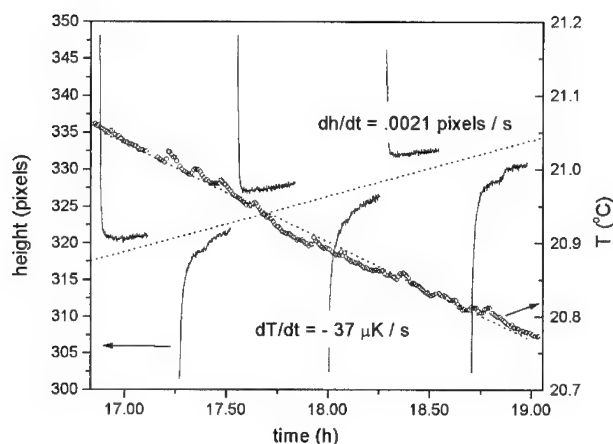
Figure 8: Room temperature change can have a serious effect on the result because the surface tension varies with temperature. For our system, a change of $\Delta T = 1$ K moves the menicus position by about 57 pixels($\approx 283\ \mu$m) which exceeds the size of the critical region analyzed in Fig. 6. The data was taken with a 305 μm diameter S-tube.

slowdown in the rise when the waiting time is increased from 15 s to about 200 s. This suggests that the dynamics of an invisible wetting film affects the macroscopic behavior of the meniscus.

CONCLUSIONS

Our experiments have shown that the pinning dynamics of an air-water interface in porous media is quite different from that of a contact line in capillary tubes. While both fit the general description of Eq. (7), they have very different values for β and different sizes for the critical region. That the value of β for interfaces is much larger than the RFIM prediction of $\beta \approx 7/9$ may be surprising at first glance, but it is quite understandable. The reason is that the volume of fluid is a conserved quantity and the magnetization in the RFIM is not. As a result, while a large cluster of spins can flip all at once to cause an avalanche, a volume of fluid must flow from elsewhere to cause the interface to advance. This naturally slows down the dynamics [25]. The effect should be less severe for a contact line as its motion mainly affects the areas of the three intersecting interfaces. The much smaller value of β for the contact line means that the dynamics are faster. This is intuitively reasonable.

In the contact line experiment, we have found larger values for β compared to previous studies. We believe there are many reasons for the difference. In Fig. 8, we show that the temperature stability can have a very important effect because surface tension is quite sensitive to temperature change. We only used data from runs with total temperature variation below 0.01 K. Many previous experiments were less stringent, e.g., Mumley $et\ al.$ [21], the stated stability is ± 2 K. A second factor is the size of the critical region. We show in Fig. 4 that the Washburn equation works well to less than 1 mm from the pinned height H_c.

The highest velocity in Fig. 6 is only about 2 μm/s, which corresponds to a maximum N_{cap} of 3×10^{-8}. In contrast, many studies did not find Washburn behavior at all and Eq. (7) was used to analyze data at capillary numbers N_{cap} several orders of magnitude higher than ours. A third factor is that many studies used two different liquids with complicated surface interactions. As we inferred from the waiting time effect data in Fig. 7, the draining of an invisible wetting film can influenced the macroscopic observations [22]. Hence the choice of liquid and the protocols for cleaning the tube can all affect the results.

ACKNOWLEDGMENTS

REFERENCES

* Electronic address: pzwong@phast.umass.edu.

† Present address: Department of Physics and Astronomy, Ohio Wesleyan University, Delaware OH 43015

1. J. S. Urbach, R. C. Madison, and J. T. Markert, Phys. Rev. Lett. **75**, 276 (1995).

2. S. Bhattacharya and M. J. Higgins, Phys. Rev. Lett. **70**, 2617 (1993).

3. T. Nattermann et al., J. Physique II **2**, 1483 (1992).

4. O. Narayan and D. S. Fisher, Phys. Rev. B **48**, 7030 (1993).

5. T. Delker, D. B. Pengra, and P.-z. Wong, Phys. Rev. Lett. **76**, 2902 (1996).

6. P.-z. Wong, T. Delker, M. Hott, and D. B. Pengra, in *Disordered Materials and Interfaces*, MRS Symp. Proc. 407, H. Z. Cummins, D. J. Durian, D. L. Johnson and H. E. Stanley, eds., pp. 27–32 (MRS, Pittsburgh, 1996).

7. J. Koplik and H. Levine, Phys. Rev. B **32**, 280 (1985).

8. J. P. Stokes, A. P. Kushnick, and M. O. Robbins, Phys. Rev. Lett. **60**, 1386 (1988).

9. P.-z. Wong and J. W. Cable, Phys. Rev. B **28**, 5361 (1983).

10. R. Bruinsma and G. Aeppli, Phys. Rev. Lett. **52**, 1547 (1984).

11. G. Grinstein and S.-k. Ma, Phys. Rev. B **28**, 2588 (1983).

12. S. He, G. L. M. K. S. Kahanda, and P.-z. Wong, Phys. Rev. Lett. **69**, 3731 (1992).

13. See, e.g., P.-z. Wong, MRS Bull. **19**, No. 5, 32 (1994), and references therein.

14. See, e.g., D. Ertaş and M. Kardar, Phys. Rev. E **49**, R2532 (1994).

15. E. Raphaël and P. G. de Gennes, J. Chem. Phys. **90**, 7577 (1989).

16. J. F. Joanny and M. O. Robbins, J. Chem. Phys. **92**, 3206 (1990).

17. P. Sheng and M. Zhou, Phys. Rev. A **45**, 5694 (1992).

18. J. P. Stokes *et al.*, Phys. Rev. Lett. **65**, 1885 (1990).

19. S. Kumar, D. H. Reich, and M. O. Robbins, Phys. Rev. E **52**, R5776 (1995).

20. G. Ström, M. Fredriksson, P. Stenius, and B. Rodoev, J. Colloid Interface Sci. **134**, 107 (1990).

21. T. E. Mumley, C. J. Radke, and M. C. Williams, J. Colloid Interface Sci. **109**, 398 (1986).

22. D. J. Durian, K. Abeysuriya, S. K. Watson, and C. Franck, Phys. Rev. A **42**, 4724 (1990).

23. T. Delker, Senior Honors Thesis, University of Massachusetts at Amherst (1995).

24. E. W. Washburn, Phys. Rev. **17**, 273 (1921).

25. P. C. Hohenberg and B. I. Halperin, Rev. Mod. Phys. **49**, 435 (1977).

thickness and 1.4 cm in diameter with help of a rotating diamond saw. The pieces were finely sanded to fit exactly the neutron scattering cell. Vycor is easily contaminated, and so several cleaning procedures were tried. The following one was finally adopted. First Vycor was rinsed just by distilled water in a soxhlet extractor. It was then washed in 30% hydrogen peroxide solution and again washed by distilled water in a soxhlet. Afterwards it was gently dried under vacuum at room temperature. The Vycor was then slowly heated to 540°C in order to burn off any hydrocarbon impurities from the glass pores. After this cleaning, the Vycor pieces were immersed for various periods of time in the polymer solutions to be measured.

In one case, we have derivatized the silanol groups on Vycor by reacting them with a 10% solution of trimethylchlorosilane in toluene. This method yields a more hydrophobic surface less prone to adsorption of polymers.

Matching between solvent and vycor

The nominal scattering length density of Vycor based on composition (96% SiO_2, 3% B_2O_3 and <1% Al_2O_3) density of Vycor (1.45g/cm³) and porosity (28%) is 3.2×10^{10} cm⁻². Since Vycor may be not quite homogeneous and have traces of other oxides, the real scattering length density may be slightly different. It was determined by contrast variation experiments using mixtures of hydrogenated and deuterated methanol (CD_3OD), and looking for the minimal value of the scattering intensity extrapolated at vanishing scattering vector. Methanol was chosen because it can be easily evaporated. This enabled us to use the same Vycor piece during the experiment. The minimum value of the best fitting parabola is the matching point realized for 63.3% of CD_3OD. This corresponds to a scattering length density of 3.55×10^{10} cm⁻² close to the nominal value for pure silica with a density of 2.2 g/cm³.

This value determines thus the isotopic composition of the solvent that was used to prepare the polymer solutions. Two solvents were used successively. The study was started with perdeuterated dichloromethane which in practice perfectly matches Vycor. This solvent presents the advantage of minimizing the incoherent background in the scattering experiments. However, dichloromethane is very volatile and the neutron scattering cells were not sealed tightly enough to prevent drying of the Vycor after a few hours. Finally, the solvent was changed to toluene with 55% of deuterated molecules. It was observed that the data were insensitive to this change of solvent.

Polystyrene solutions satisfying the zero average contrast condition

The second condition that was satisfied in order to observe the form factor of the polymer chains inside Vycor is the condition of average contrast matching between the chains and the solvent should equal. The value of the scattering length density of deuterated polystyrene (PSD), $n_{D-pol} = 6.54 \times 10^{10}$ cm⁻², and the one of hydrogenated polystyrene (PSH), $n_{H-pol} = 1.43 \times 10^{10}$ cm⁻², determine the relative proportion of deuterated chains in the mixture which has to be x = 41%. Fortunately, this is close to the value x = 0.5 which maximizes the scattering intensity.

Choice of polymer concentration

In order to choose the polymer concentration such that the chains can enter the pores the scaling picture of semi-dilute solution in terms of a closely packed system of "blobs" was used. The size of a blob is proportional to the correlation length of the solution ξ_{bulk} which can be precisely measured from scattering experiments. One can also precisely define a blob radius ξ_{blob} such that ξ_{blob} becomes equal to the radius of gyration of a dilute chain at the overlap concentration c*, then experimentally $\xi_{bulk} = 0.35 \, \xi_{blob}$. The empirical relation between ξ_{blob} and the polymer volume fraction ϕ_{bulk} is for polystyrene $\phi_{bulk} = 19.8 \, (\xi_{blob})^{-1.3}$ with ξ_{blob} in Å. The ϕ_{bulk} was chosen such that ξ_{blob} was at most equal to the average pore radius 35Å, this yielded $\phi_{bulk} = 0.2$. For such a concentration, the correlation length ξ_{bulk} is about 10Å.

STRUCTURE OF POLYMER CHAINS CONFINED IN VYCOR

JYOTSANA LAL *, SUNIL K. SINHA **, LOIC AUVRAY *
* Laboratoire Léon Brillouin (CEA-CNRS) 91191 Gif sur Yvette, Cedex, France.
** APS, Argonne National Laboratory, Argonne, IL 60439, USA.

ABSTRACT

We observe by Small Angle Neutron Scattering (SANS) the structure of polystyrene chains in semi-dilute solutions confined in model porous medium, Vycor. The size of the free polymer chains in solution is always larger than the pore diameter, 70 Å. The use of a suitable mixture of hydrogenated and deuterated solvents and polymers enables us to directly measure the form factor of one single chain among the others. The penetration of the chain in the porous media is almost complete for the concentration ($\Phi = 20\%$) and the range of molecular weights (35000 $<M< 800000$) used. The measured radius of gyration of confined chains is always smaller than the radius of gyration of free chains in the equivalent bulk solution.

INTRODUCTION

Depending on the physical situation and on the nature of the porous medium, the effect on the chains are calculated theoretically or simulated on computers by studying the statistical mechanics of chains in well-defined model geometries [1] or in random potentials [2]. The case of confinement of polymers by fluid deformable interfaces, liquid droplets [3] or surfactant membranes [4] has also begun to be considered. All these theoretical studies reveal again the well-known analogy between polymer systems and other strongly fluctuating systems as binary mixtures or liquid helium close to their critical point [5]. Depending on the approach in terms of geometry or of random fields they demonstrate in particular the effects of change of spatial dimensionality induced by confinement on the fluctuations, correlations and dynamics of the systems or deals with the effects of localization of the chains induced by a random quenched disorder.

In fact the observation of the structure of the polymer chains confined in Vycor is a complicated problem because in the general case the scattering signal may be dominated not by the polymer in its solvent, but by the porous medium itself. This problem can be solved by matching the scattering length density of the vycor and of the solvent using an appropriate mixture of hydrogenated and deuterated toluene. In order to simplify further the study a suitable mixture of physically identical hydrogenated and deuterated polymer chains was chosen such that the scattering intensity becomes proportional only to the form factor of one chain among the others. Thus the correlations between different chains are ignored. This is known as the method of zero average contrast [6].

Here we describe the systems studied and the experimental conditions. In the last section we present and discuss results obtained as a function of the chain molecular weight and compare it with the theoretical predictions of Daoud and deGennes [1], which are recalled in the course of the discussion.

SAMPLES AND EXPERIMENTS

Porous Material

Vycor was used (Corning Vycor Brand 7930) [7] for confining the polymer solutions. The main scattering feature of this porous solid is the occurrence of a strong correlation peak at $.02\text{Å}^{-1}$ corresponding to a length of 300Å. Vycor was cut into very fine pieces of 1mm in

Samples

Five solutions of a mixture of monodisperse hydrogenated and deuterated polystyrene with increasing molecular weight were prepared, the polymer and the solvent satisfying both their respective contrast matching conditions described above. The mass of the H and D chains in a given sample (respectively, M_w^H = 33500, 71700, 120000, 336000, 781000 and M_w^D = 32700, 75000, 137000, 351000, 795000) were chosen to be as close as possible. The radius of gyration of the deuterated chains in bulk semi-dilute toluene solutions at a volume fraction

Φ = 0.2, can be calculated from known experimental results, the values being 61Å, 92Å, 124Å , 199Å and 300Å respectively. In each case, it is always larger than the pore radius.

The samples of confined polymers were prepared by immersing a dry piece of cleaned but underivatized Vycor in a solutions of appropriate amount of H and D polystyrene chains for various periods of time 3 days, 23 days and 65 days. We observed that the solutions were slowly sucked into the Vycor. The samples, which were initially rather white and opaque become translucent.

The same procedure was used to prepare two test samples with the silanized Vycor, one was immersed in a polystyrene solution made with the 120K, 137K pair of H and D chains at a volume fraction of 20%, the other in a 781K-795K solution at a smaller volume fraction of 10%.

scattering experiments

The scattering experiments were performed in Saclay on the PACE spectrometer. The measurements were done in several different configurations : a first series in the q range 2.89×10^{-3} to 0.1Å^{-1} (wavelength λ=6.47Å, sample-detector distance d=3.0m and λ=14 Å, d=4.67m) and a second series in the q range 3×10^{-3} to 0.3Å^{-1} (λ=5.12Å, d=1.0m and λ=12.15 Å, d=4.5m). Water (which scatters isotropically) was used to normalize the intensities on a absolute scale. In each case was measured the bare Vycor sample in its contrast matching solvent, the bulk solutions of mixed H and D chains and the Vycor samples containing the polymer solutions at zero average contrast. The data of these last samples were treated by substracting the raw intensity of the bare matched Vycor from the raw intensity of the samples in order to eliminate very precisely the incoherent intensity of the solvent and the residual signal of the nominally matched Vycor which can never be completely extinguished.

RESULTS

Figure 1a S(q) versus q for deuterated chains of 351K PSD inside Vycor in CD_2Cl_2 (top) compared with the scattering intensity of the corresponding matched Vycor (bottom).
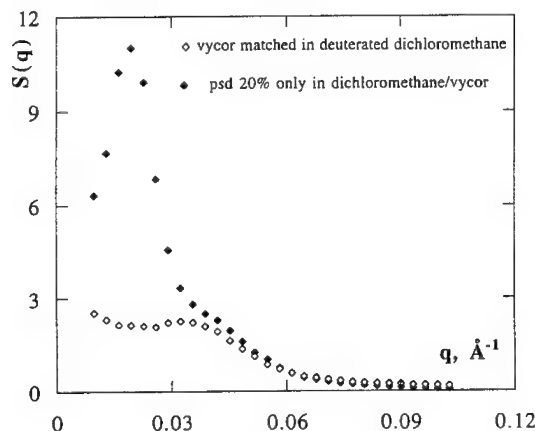
The first immediate, but non trivial result of our experiments is that the polymer chains enter the pores of Vycor (diameter D=70Å) whatever their molecular weight at the concentration of 20%, that was used. This was first evident qualitatively from the macroscopic observation of the samples: The vycor pieces become much more chalk white in colour and more opaque after drying of the samples than they were without having been in contact with a polymer solution. The penetration of polymers is also of course revealed directly and quantitatively by the scattering experiment.

In Figure 1a the results of first scattering experiment are presented where the signal (bottom curve) of a bare Vycor piece matched in deuterated dichloromethane (CD_2Cl_2) is compared with the signal (top curve) of a sample imbibed with a solution of deuterated chains only (M_w = 351K) in the same solvent. Although the Vycor is not perfectly matched due to a cleaning problem at this stage of the experiment, the difference between the two signals is large. On the

Figure 1b S(q) versus q for a mixture of H and D chains of 32.7K satisfying ZAC inside Vycor matched in CD_2Cl_2 (middle) compared to scattering of bare matched Vycor (bottom) and one corresponding to bulk polymer solution (top).
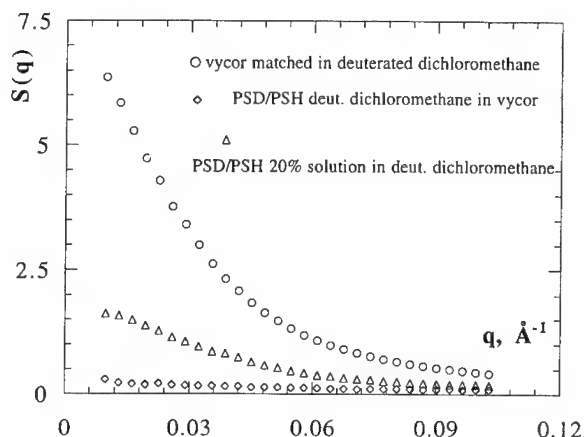
spectrum of the sample containing only deuterated polymer the characteristic peak of non-matched Vycor which is absent in the matched bare Vycor is again observed. Thus it can be concluded qualitatively that indeed the deuterated chains penetrate into the pores and that with this contrast, the main effect of confined polymer chains on the scattering intensity is to reveal the pore structure at large scales, i.e. at low scattering vectors, by breaking the contrast matching with the solvent. This demonstrates also the utility of the zero average contrast method which eliminates the trivial effects of the structure of the porous medium on the scattering intensity.

Indeed more information can be obtained by observing the samples satisfying this zero average contrast condition. As a first example, we consider the case, shown in Figure 1b, of the sample with the smallest molecular weight (M_w^D=32.7K) in deuterated Dichloromethane. The bare Vycor (also in deuterated Dichloromethane) is perfectly matched (bottom spectrum) and yields a much smaller signal than the zero average contrast sample (middle spectrum). It is observed that the scattering intensity is now a smoothly decreasing function of q as the scattering intensity of the bulk corresponding solution (top curve). Both of them as expected look very much like the form factor of a chain. The comparison between these two spectra shows that the ratio of the intensities at large scattering vector of the confined chains and of the bulk solution is about 25%. As this ratio should be proportional to the ratio of polymer volume fraction in the two samples it can be concluded that there is 4 times less polymer in the Vycor samples than in the bulk solution. As the porosity of Vycor is about 28%, we conclude that the penetration of the polymer solution into the Vycor pores is almost complete and that the partition coefficient of the chains between the Vycor and the solution of immersion is practically one.

Similar observations can be made on the other samples prepared from 55% deuterated toluene solutions. The comparison between the spectra of the bulk and confined polymer solutions were done for different samples (molecular weights 32.7K, 75K, 137K, 351K and 795K) (Table I). In Figure 2 are the data are taken after being imbibed for 23 days, when even the chains of 351K have thoroughly penetrated the vycor. The intensities at large scattering vectors shows that the concentration of the chains in the Vycor sample is always about 25% of the bulk concentration which corresponds well with the 28% porosity of Vycor. Within the uncertainty of the intensity measurements and normalization, the concentration of polymer inside Vycor is independent of the chain molecular weight at the used volume fraction of 20%

For chains inside Vycor, we find useful to try to fit also the data to the Debye scattering law. At low q, this is an efficient way of determining the radius of gyration of the chains, as efficient and justified as the Guinier or Lorentzian laws, and at large q, this is a way to reveal the differences with respect to the free chains. Indeed the fits were good only at very low q in a much smaller range of scattering vector (qR_g<1 but not $q\xi_{bulk}$ <1) than for the corresponding free chains.
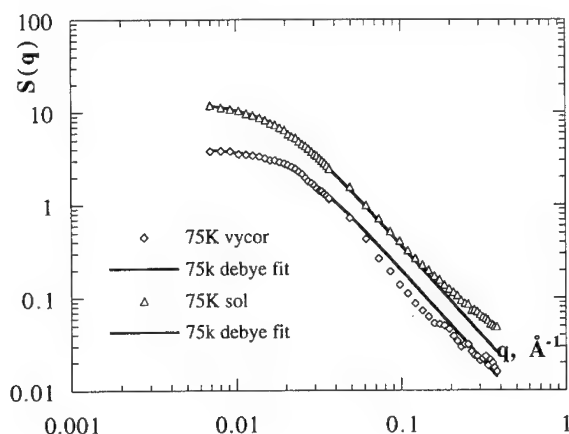
Figure 2 Normalized scattering intensities using averaged matched H and D chains of 75K inside Vycor and in bulk (symbols) and the coresponding Debye fits (full lines) in 55% deuterated Toluene.

Figure 3 The measued effective size of polymer chains in bulk solution and in Vycor as a function of molecular weight
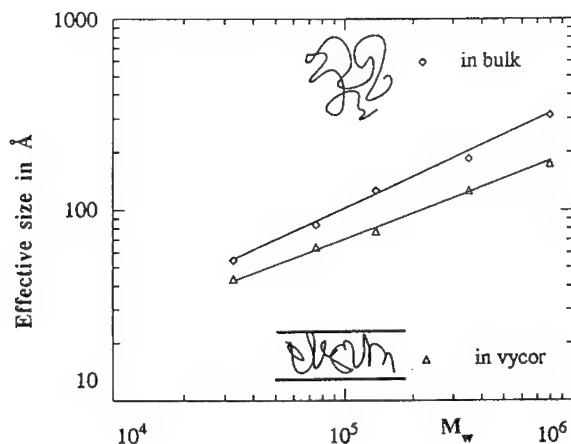
The first observation is that the values of the radii of gyration of the confined chains are smaller than the bulk values. They are plotted on figure 3 together with the bulk values.

The second observation is that there is marked deviation from the classical asymptotic behavior for ideal chains $P(q) \sim q^{-2}$ in the regime of scattering vectors corresponding to distances $R_g \gg q^{-1} \gg \xi_{bulk}$. The intensities decreases more rapidly than $1/q^2$. Power laws greater than 2 are observed by plotting the scattering intensities in logarithmic coordinates. These slopes apparently vary with the molecular weight of polystyrene chains. This could arise due to slight adsorption of chains onto the bare surface of Vycor. We show that silanizing Vycor suppresses this adsorption [8].

Comparison with theoretical predictions

We first confront our data to the predictions of the simplest theories of polymer confinement in a straight cylindrical pore. Briefly one can say according to [1,8] that four main effects govern the behaviour of chains confined in a small cylindrical non adsorbing cylinder : the confinement of the chains by the cylinder walls squeezes the chains laterally, the intrachain excluded volume effect swells the chains and stretches them along the cylinder axis, the entropic elasticity of the chains limits the swelling and stretching, the interchains excluded volume effect screens the intrachain effect but may lead to chains self segregation.

The strength of these different effects depends on the polymer concentration and on the degree of confinement, their competition lead to different regimes (Figure 4) that can be expressed in terms of reduced variables $x=R/D$ and $y=R/\xi$ (D=pore diameter, $R=N^{3/5}$ a is the Flory radius of the excluded volume chain in dilute free solution and ξ is the bulk correlation length of the semi-dilute solution).
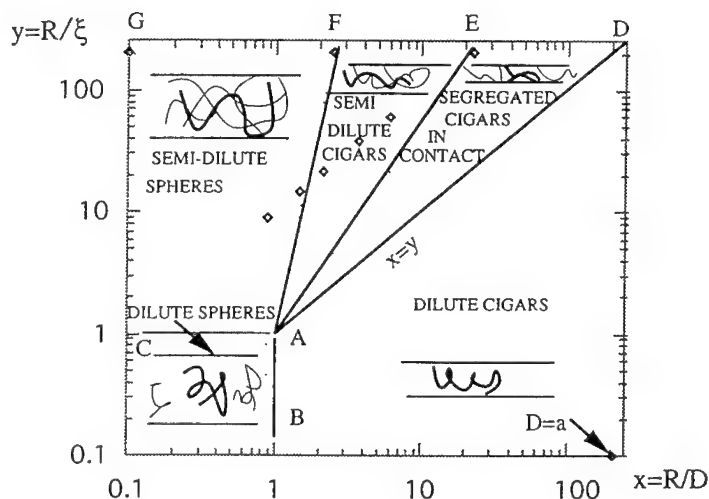
Figure 4 Phase diagram for polymer solutions confined in capillary as a function of reduced variables $x=R/D$ and $y=R/\xi$. The points correspond to the five samples studied.

CONCLUSIONS

We have presented the first direct observation of the structure of polymer chains confined in a porous media [8]. One of the aims of the future experiments should be to explore the numerous regimes and situations that this confinement problem can present.

REFERENCES

1. M. Daoud and P. G. de Gennes, J. De Physique **38**, p. 85 (1977).

2. S. F. Edwards and M. Muthukumar, J. Chem. Phys. **89(4)**, p.2435 (1988).

3. F. Brochard and A. Haperin, C. R. Acad. Sci. Paris Serie II **302**, p.1043 (1986).

4. J. T. Brooks and M. E. Cates, J. Chem. Phys. **99**, p.5467 (1993).

5. F. Brochard and P. G. de Gennes, J. Phys. -Lett. **44**, L-785 (1983).

6. J. S. Higgins and H. C. Benoit, Polymers and Neutron Scattering (Clarendon Press Oxford, 1994) p. 128.

7. P. Levitz, G. Ehret, S. K. Sinha and J. M. Drake, J. Chem. Phys. **95** p. 6151 (1991).

8. J. Lal, S.K. Sinha and L. Auvray to be published soon in J. de Physique.

IMAGING AND RESISTIVITY STUDIES OF SATURATION GRADIENTS IN TWO-PHASE FLOW IN 3-D POROUS MEDIA

E. H. KAWAMOTO AND PO-ZEN WONG
Department of Physics and Astronomy, University of Massachusetts,
Amherst, MA 01003, U. S. A.

ABSTRACT

We have carried out x-ray radiography and computed tomography (CT) to study two-phase flow in 3-D porous media. Air-brine displacement was imaged for drainage and imbibition experiments in a vertical column of glass beads. By correlating water saturation S_w with resistance R, we find that there is a threshold saturation $S^* \approx 0.2$, above which $R(S_w) \sim S_w^{-2}$, in agreement with the empirical Archie relation. This holds true for both drainage and imbibition with little hysteresis, provided that S_w remains above S^*. Should S_w drop below S^* during drainage, $R(S_w)$ rises above the Archie prediction, exhibiting strong hysteresis upon reimbibition. This behavior suggests a transition in the connectivity of the water phase near S^*, possibly due to percolation effects.

INTRODUCTION

When the water saturation S_w in a porous rock is decreased due to the invasion of hydrocarbons, the electrical resistance R increases. Empirical correlations between R and S_w are commonly used in the petroleum industry to estimate oil and gas saturations in reservoirs. In his 1942 paper, Archie [1] found that in brine-saturated sandstones, the *formation factor* F, defined as the ratio between conductivities of pure brine and of brine-saturated rock ($\equiv \sigma_w/\sigma_r$) has a power-law dependence on the rock porosity ϕ: $F \sim \phi^{-m}$, where the "cementation exponent" $m \approx 2$. Hence, he conjectured

$$R = R_o S_w^{-n} \tag{1}$$

where R_o is the resistance for $S_w = 1$, with $n \approx 2$. This is known as the second Archie relation, and is widely used to interpret resistivity logging data from oil fields. It is also sometimes confirmed in laboratory experiments [2]. However, unlike the first Archie relation for which there are simple explanations for the dependence of F on ϕ, Eq. (1) runs counter to our current understanding of two-phase flow phenomena. Recent studies [3] have shown that the fluid distribution for drainage and imbibition processes can be vastly different. *Drainage* refers to a nonwetting fluid displacing a wetting fluid (*e.g.*, oil displacing water), while *imbibition* refers to the opposite process (*e.g.*, water displacing oil). Since electrical conduction depends on how the brine is connected through the pores, one would expect R to depend not only on the value of S_w, but also on how S_w is realized, *i.e.*, the flow history of the fluids. Indeed, previous workers [4] have noted that n depends on how wetting phase saturation was obtained. Thus the dependence of $R(S_w)$ on flow history bears closer examination. In this paper, we report an experiment that uses x-ray imaging to determine S_w for different flow histories while simultaneously measuring the resistance R. This allows us to see if Eq. (1) has any validity.

A common problem in previous studies of Eq. (1) is that only the average S_w and the end-to-end resistance of the sample were measured. The details of the fluid distribution were unknown. Typically, when one fluid displaces another, we expect the saturation to vary monotonically between the inlet and outlet so that the sample does not have a unique value of S_w. This problem has been
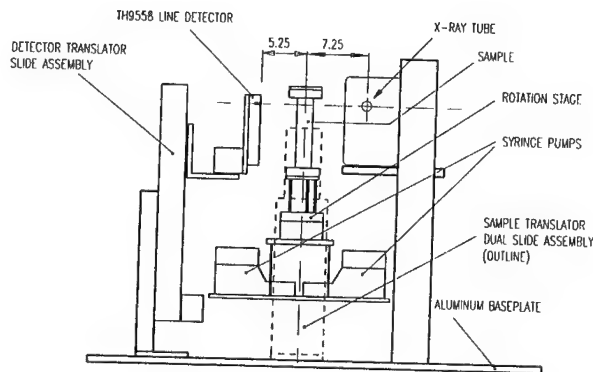
Figure 1: Layout (elevation) of x-ray imaging apparatus. Sample-to-source and sample-to-detector distances are in inches.

explicitly demonstrated by Sprunt, *et al.* [5]. In our work, we overcome this problem using an array of electrodes to determine both resistance and saturation gradients. In general, saturation gradients occur because of the presence of viscous and gravitational pressure gradients. These are characterized by the capillary number Ca and the Bond number Bo. In a packing of glass beads with diameter D_b, we have $Ca \equiv \Delta P_{\mathrm{vis}}/\Delta P_{\mathrm{cap}} \approx D_b^2\, \upsilon\, \eta\, /\, \gamma\, k$ and $Bo \equiv \Delta P_g/\Delta P_{\mathrm{cap}} \approx D_b^2 g \Delta \rho\, /\, \gamma$, where υ is the Darcy velocity, η the viscosity, γ the surface tension, k the permeability, g the gravitational acceleration and $\Delta \rho$ the density difference between the two fluids. ΔP_{vis}, ΔP_{cap} and ΔP_g are the pressure drop across a bead diameter due to viscous flow, surface tension and gravity, respectively. In our experiments, the flow velocity υ is sufficiently low such that $Bo \gg Ca$.

EXPERIMENTAL METHOD

Since gravity is the dominant cause for saturation gradients in practice, we built an x-ray imaging system designed to scan a sample vertically. This is in contrast to other studies which usually employ a reconfigured medical machine designed to scan a patient lying horizontally [5]. This system is illustrated in Figure 1; a detailed description is given elsewhere [6, 7]. Briefly, the sample is a cylindrical column filled with glass beads. It is mounted on a rotation stage atop a dual dovetail slide assembly which moves the sample vertically (z-direction). A 90 MHz Pentium PC controls stepper motors which drive rotation and translation stages. This allows us to to perform radiography and CT scans at different z positions.

The detector is a 1024-element linear diode array (Thomson TH9558) that spans 230 mm. Sensitive areas of each element (Gd_2O_2S phosphor-coated Si diode) are 0.225 mm wide by 0.6 mm high. The intensity dynamic range is 12 bits (4096 gray levels). Mounted on its own dovetail slide, the detector can also be translated vertically and tilted to align the imaging plane. It integrates x-ray flux over 100 ms; typically, we average data over 30 acquisitions to keep fluctuations from counting statistics to within $2-3\,\%$. At the sample position, the effective spatial resolution is 0.13 mm $\times$ 0.3 mm (H$\times$V), comparable to the bead sizes used.

Except during the initial alignment of the instrument, the detector remains stationary during our measurements. For radiography, the sample is scanned vertically, but not rotated. The brine saturation profile $S_w(z)$ (where z is measured from the top of the column along its axis) is calculated
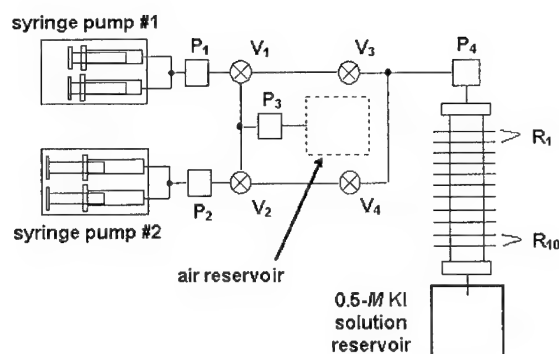
Figure 2: Schematic of fluid drive system. Drainage (imbibition) occurs when air is infused into (withdrawn from) top of column. Resistances are measured between successive electrodes.

by interpolating the measured intensities between those for air-saturated ($S_w = 0$) and brine-saturated ($S_w = 1$) columns. CT data are acquired by fixing the z-position of the sample and rotating it through $360°$ in $0.75°$ steps (480 view angles). The 90 MHz Pentium PC can reconstruct a 640×640-pixel cross-sectional image in 5.4 minutes using a standard filtered backprojection algorithm (fan beam, flat detector) [8].

X rays are generated by a fixed-tube microfocus (0.3 mm) source. An 0.25-mm thick brass foil is used to filter out the low-energy photons, raising the average beam energy and narrowing the spectral distribution. The x-ray tube's power supply is controlled by computer. A section of the detector is used to monitor the beam intensity away from the sample. This enables the computer to perform feedback control of tube current. We typically operate at 80 kVp and a beam current close to 1 mA. This setting is chosen based on tube and detector specifications, and the sample's attenuation characteristics.

Our porous media consist of unconsolidated glass beads (microspheres) with diameters $100 < D_b < 500\,\mu$m, sorted into five narrow size ranges. Close-packed into a hollow acrylic cylinder 200 mm long and 44 mm in diameter, they form a medium with porosity $\phi \sim 0.39$ and permeabilities k in the range $14 - 360$ darcies. The sample is initially saturated by 0.5-M potassium iodide (KI) solution by quickly (~ 8 ml/min) drawing about 140 ml of the solution into the column. KI is used to increase the x-ray contrast between brine and air. Subsequent drainage and imbibition runs were performed with flow rates of either 0.4 or 1.2 ml/min, corresponding to Darcy velocities v of (4.4 or 13) $\times 10^{-4}$ cm/s. Taking the viscosity to be $\eta = 1$ cP, $\gamma = 72$ dyn/cm and $\Delta\rho = 1$ g/cm^3, we find that for D_b between 100 and 500 μm, Ca is in the range of $(4.3 - 13) \times 10^{-5}$. In contrast, the Bond number Bo is in the range $(1.4 - 35) \times 10^{-3} \gg Ca$. Thus, gravity is the dominant cause for saturation gradients in our experiment.

Figure 2 is a schematic diagram of the fluid drive system. It consists of two stepper motor-driven syringe pumps, two-way and three-way solenoid valves, four pressure transducers, sample column and reservoirs. The largest syringes accommodated by the pumps can deliver or withdraw volumes up to 100 ml. Since the samples' fluid capacity is ~ 140 ml, we require two pumps; valves and pressure sensors are used to maintain a constant flow during the course of the experiment. A computer program ensures that pressure fluctuations due to pump switching are minimal. Note that, in Figure 1, the pumps (and fluid reservoir) are mounted on the sample translator to move

373
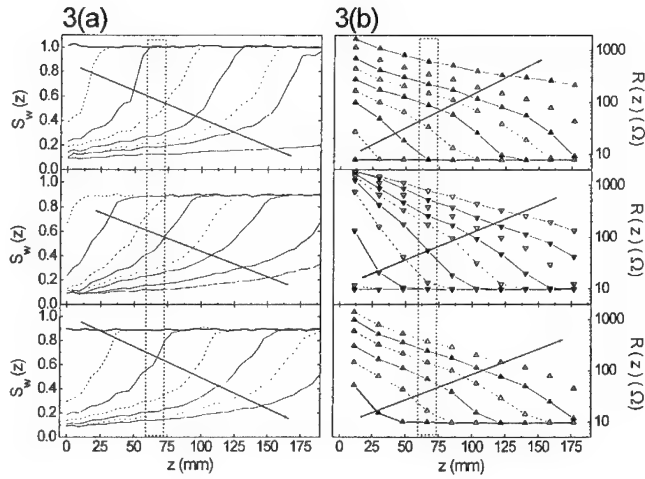
Figure 3: (a) Saturation profiles $S_w(z)$ for full drainage (top), full reimbibition (middle), and a second full drainage (bottom). (b) Resistance profiles $R(z)$ for same fluid flow sequence. Arrows indicate time sequence; dotted lines show section for which $R(S_w)$ is plotted in Figure 4.

vertically with the sample. This avoids changes in hydrostatic pressure across the sample when it is scanned vertically. A 20 MHz 386SX PC controls both fluid delivery system and a 4-wire ac resistance bridge which makes the resistance measurements. The current electrodes are perforated copper disks located in the top and bottom caps of the sample column. Eleven voltage electrodes (1.6-mm diameter brass rods) are implanted in the column every 2 cm so that the resistances of ten sample sections are measured. The ac bridge operates at 15.9 Hz with a small current ($\lesssim$ 1 mA). Radiography data is taken at 4.6-mm intervals so that there are four S_w measurements in each sample section.

Figure 3(a) shows plots of saturation profiles measured at 10-minute intervals during 0.4 ml/min flow through a $210 - 297\,\mu$m glass bead pack ($Ca \approx 4.3 \times 10^{-5}$, $Bo \approx 8.5 \times 10^{-3}$). After preparing the sample in the initial state with $S_w = 1$, we perform a full drainage, full reimbibition, and a second full drainage. Note that, after the first drainage, S_w reached an irreducible saturation $S_{\mathrm{irr}} \sim 0.10$. S_{irr} is bead-size dependent: it is higher for smaller D_b due to larger surface area and stronger capillary forces. When the column is refilled, S_w does not exceed 0.90, so there is an irreducible air saturation as well.

Figure 3(b) plots the resistance profiles $R(z)$ measured while the radiography profiles in Fig. 3(a) were measured. The arrows indicate the time sequence, since resistance increases as saturation decreases (drainage), and vice versa (imbibition). When the column is fully refilled, the smallest resistances attained ($10\,\Omega$) are larger than those measured at the outset ($7.8\,\Omega$), corresponding to the difference between full saturation with and without an irreducible air saturation. We note that for the same electrode arrangement, we measured the resistance of the brine R_w to be about $2.7\,\Omega$. Since $R_o \approx 7.8\,\Omega$ when $S_w = 1$ in the bead pack, the formation factor is $F = R_w/R_o \approx 3.0$, as expected for dense random sphere packs. Moreover, we verified that these resistances are close to values calculated for a parallel-plate electrode configuration, *i.e.*, the voltage electrodes do not distort the electric field significantly.
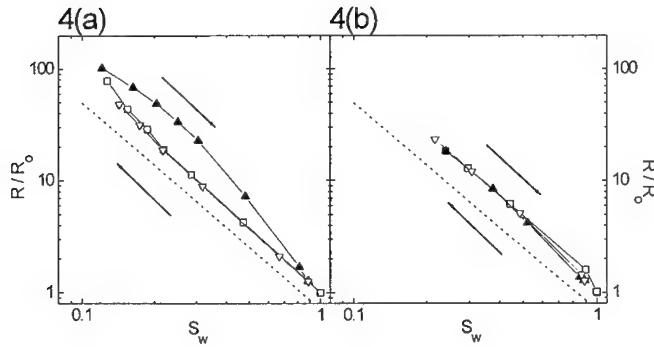
Figure 4: (a) Hysteresis loop $R(S_w)$ when threshold $S^* \approx 0.2$ is crossed; $R_o \approx 7.8\,\Omega$ for section shown betwen dotted lines in Figure 3. (b) $R(S_w)$ when S^* is not crossed. In both plots, points $\square$ are on the first drainage branch, $\blacktriangle$ are on the reimbibition branch, and $\triangledown$ are on the second drainage branch. The dashed line shows the Archie relation for $n \approx 1.85$, offset for clarity.

RESULTS AND DISCUSSION

For each of the ten sections of the column, we match up the resistance R with the saturation S_w measured at the same time. R is normalized to the initial value R_o, while the four S_w measurements for each section are averaged. Figures 4(a) and (b) show how R/R_o varies with S_w for the fourth section from the top of the column. Except for sections at the very top and bottom of the column where end effects are important, the $R(S_w)$ dependence is reproduced well in each section and upon repetition of the experiment. The difference between Fig. 4(a) and (b) is that the former shows a hysteresis loop when S_w was decreased to about 0.1 during the first drainage while the latter shows no significant hysteresis when S_w was kept above 0.2. Moreover, for $S_w > 0.2$, the data is well approximated by Eq. (1) with an exponent $n \approx 2.0$ during drainage. A clear departure occurs at $S_w \approx 0.2$. Upon reimbibition after reaching S_{irr}, only the few data points with $S_w > 0.3$ can be approximated by Eq. (1) with $n \approx 2.8$. These findings hold for all bead sizes $(100 - 500\,\mu\text{m})$ and flow rates $(0.4, 1.2\text{ ml/min})$ in our experiment.

The physics behind the behavior shown in Fig. 4 is not obvious, but it is interesting to note that the departure from the Archie relation and the onset of hysteresis both occur at a saturation $S_w = S^* \approx 0.2$. Since drainage is known to be well described by invasion percolation, we might speculate that S^* is the percolation threshold of the wetting (brine) phase. If the flow direction is reversed when the brine phase is still fully connected, perhaps the water 'remembers' which pores to reoccupy. To shed light on this, we carried out CT imaging using a sample column without electrodes. This is necessary because the sensing leads and electrodes interfere with sample rotation. Figure 5 shows two cross-sectional images of a slice with $S_w \approx 0.42$. The bead size, flow rate, and slice position match those for Fig. 4. The flow was stopped during the CT scans. The image on the left was obtained during the first drainage, showing the brine phase to be highly correlated. The image on the right was obtained after reaching S_{irr} then reimbibing brine back to $S_w \approx 0.42$; here, the brine phase appears to be uncorrelated. They correspond to the two branches of the loop in Fig. 4(a) and show clearly why R is smaller for the drainage branch. To fully understand the details of the hysteresis and test the hypothesis that S^* is related to percolation, more extensive
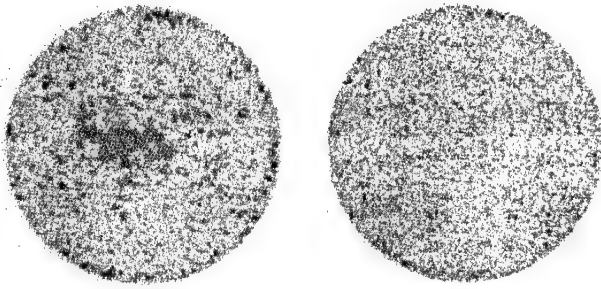
Figure 5: CT images of column cross section for slice at $z = 60$ mm, $S_w \approx 0.42$ before (left) and after (right) S^* is crossed during drainage. Darker regions have higher S_w.

imaging in the region near S^* is necessary; such efforts are presently ongoing. Meanwhile, it is safe to conclude that our experiment has shown that Archie's second relation holds only if S_w does not fall below S^* during the flow history, the cause of which awaits further investigation.

ACKNOWLEDGMENTS

REFERENCES

1. G. Archie, *AIME Trans.* **146**, 54 (1942).
2. F. A. L. Dullien, *Porous Media: Fluid Transport and Pore Structure* (Academic Press, New York, 1992).
3. P-z. Wong, *MRS Bull.* **19**, 32 (1994).
4. H. F. Dunlap, H. L. Bilhartz, E. Schuler, and C. R. Bailey, *Trans. Am. Inst. Min. Eng.* **186**, 259 (1949).
5. E. S. Sprunt, K. P. Desai, M. E. Coles, R. M. Davis, and E. L. Muegge, *Soc. Pet. Eng.* 21433 (1991).
6. R. Farrell, "Principles and construction of a small-scale X-ray computerized tomography and digital radiography system," M. S. Thesis, University of Massachusetts (1993).
7. E. H. Kawamoto, J. Wang, R. Farrell, and P-z. Wong, preprint.
8. R. H. Huesman, G. T. Gullberg, W. L. Greenberg, and T. F. Budinger, "Users Manual: Donner Algorithms for Reconstruction Tomography," U. S. Department of Energy PUB-214 (1977).

SCANNING PROBE MICROSCOPE STUDY OF MIXED CHAIN-LENGTH PHASE-SEGREGATED LANGMUIR-BLODGETT MONOLAYERS

D.D. KOLESKE, W.R. BARGER, G.U.LEE, R.J. COLTON
Chemistry Division, Code 6177, Naval Research Laboratory, Washington, DC 20375-5342

ABSTRACT

Using a scanning probe microscope, the influence of adhesion on measured film height of mixed-chain-length fatty acid Langmuir-Blodgett monolayers was investigated. A 1:1 mixture of $CH_3[CH_2]_{22}COOH$ and $CH_3[CH_2]_{14}COOH$, was deposited in which the long chain-length acid, C_{24}, was segregated from the short chain-length acid, C_{16}. Two experiments were performed, contact scanning and force curve mapping. From both experiments, the film height difference measured between the C_{16} and C_{24} regions was larger than expected. Adhesion of the tip was 20% larger over the C_{16} acid regions. Using a compressional modulus derived from film pressure vs. area isotherms of the pure components, the adhesion difference and apparent film height difference over the two regions can be understood.

INTRODUCTION

Both adhesion and friction depend strongly on the chemical and structural properties of contacting surfaces. Recently, using scanning probe microscopy (SPM), several groups have investigated chemical aspects of adhesion between the cantilever tip and chemically patterned surfaces. The magnitude of the lateral cantilever twist (friction) [1,2] or pull-off force (adhesion) [3,4] has been correlated to specific combinations of chemical end groups. However, general application of SPM techniques to identify chemical unknowns on surfaces is complicated by the structural properties of the film (i.e., thermodynamic phase) and the interaction of the tip with the surface (i.e., contact area, surface/tip compliance).

Several authors have reported that the measured film height for some L-B monolayers is less than the fatty acid chain length [5-7]. Recently, Schaper et al. [6] found the C_{16} acid to be 1.6 nm high using SPM vs. 2.3 nm high using x-ray diffraction.

In this paper, we demonstrate that the film height measured using SPM depends partly on the compressional modulus, E, of the film. The surface compressional modulus of the film on water derived from the film pressure (π) vs. area per molecule (A) isotherm is defined as $E = -A(\delta\pi/\delta A)$. The computed moduli can be used to qualitatively explain adhesion differences and differences in film height between the regions of mixed films with different chain lengths. The results discussed here are particularly important when considering the use of mixed chain length LB films as step height standards to calibrate the SPM, or understanding the image contrast and chemical functionality of organic, polymeric or biological materials.

EXPERIMENTAL

A KSV 5000 Langmuir-Blodgett system was used to deposit monolayers on freshly cleaved muscovite mica. A 0.912 mM solution of a 1:1 mixture of $CH_3[CH_2]_{22}COOH$ and $CH_3[CH_2]_{14}COOH$ in benzene was spread on triply distilled water. Films were compressed at a rate of 1 mN/m per minute. All films were deposited at a constant surface pressure of 30 mN/m at 25 °C. After deposition, the surface was uniformly methyl terminated and hydrophobic.

Our SPM, based on the optical lever method, has been described elsewhere [8]. It was designed for low thermal drift and ease of calibration. The normal bending and lateral twisting of cantilever are measured using a 4-quadrant photodetector. The plane of the sample is never oriented perfectly normal to the axis of motion of the cantilever tip, so the tip twists slightly in the lateral direction on approaching and contacting the surface, and the laser is deflected laterally. The 4-quadrant detector permits separation of the normal and lateral signals. A unique feature of the force curve measuring algorithm is that the maximum applied force between the tip and surface is controlled. Force vs. distance curves can be measured at many locations on the surface to simultaneously map the surface topography, pull-off force (adhesion), and lateral twisting of the cantilever (friction).

Oxide sharpened silicon oxynitride cantilevers with a nominal tip radius of 20 nm and normal spring constants of 0.016 N/m were used. The cantilever resonant frequency was measured and the normal force constant scaled following Ref. 8. Over time the tip adsorbed some of the deposited LB film resulting in reduction of the pull-off force. Once coated, these tips typically produced stable bi-modal pull-off force distributions. Probe tips silanized using octadecyltrichlorosilane produced results similar to tips coated with the LB film.

RESULTS

The π vs. A isotherms for the pure C_{16} and C_{24} acids are shown in Figure 1. There is an abrupt change in the slope of the π vs. A isotherms for both acids near 19.5 Å^2/molecule denoting a change in the film phase from the more "liquidlike" L_2 phase to the more "solidlike" LS or S phase using the Harkins-Stenhagen notation [9]. In these regions, the isotherms are well-represented by two straight lines from which E can be computed. The π vs. A isotherm for the 1:1 mixture (not shown) is similar to the isotherm for the C_{16} acid but has a gradual change of slope.
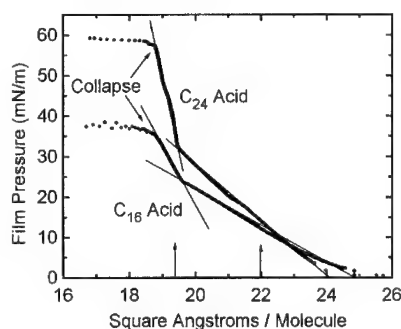
Figure 1. Π vs. A isotherm for pure C_{16} and C_{24} monolayers. The compressional modulus of each film was calculated from the slope of the straight lines. Arrows along the x-axis denote the two areas for which the modulus was calculated.

Figure 2. Topographical contact scan over a 2 μm x 2 μm region of a 1:1 mixed C_{16} and C_{24} acid film. Light areas correspond to C_{24} regions while dark areas correspond to C_{16} regions. Measured film height difference is $\sim$ 2 nm.

A 2 μm x 2 μm scan of the mixed LB film is shown in Figure 2 measured at an applied load of approximately 2 nN. The surface topography has two discrete levels resulting from the segregation

of the mixed fatty acids. The higher (lighter) levels correspond to C_{24} regions and the lower (darker) levels correspond to C_{16} regions. Fitting the two height levels with Gaussian distribution curves, a height difference of 2.0 ± 0.5 nm is measured which is approximately twice the 1.01 nm [10] chain length difference between the C_{16} and C_{24} fatty acids. Others have also found an increased value. Calculating the height difference between C_{16} and C_{24} acids from the SPM data of Schaper *et al.* [6], gives 1.7 ± 0.2 nm.

Adhesion to the LB film was measured directly by the force to pull the tip off the surface. The force between the tip and surface was measured as a function of the z-piezo position as shown in Figure 3. The surface was moved toward the cantilever tip to make contact (point A) and then moved farther to apply a controlled maximum force (point B), and then withdrawn until the tip and surface separated (point C). At each of the points A, B, and C the z-piezo position, normal cantilever deflection, and lateral cantilever deflection were recorded. From an array of force curves measured over the surface, maps of the topography, adhesion, and lateral force were constructed. For brevity, lateral force data are not treated in this paper.
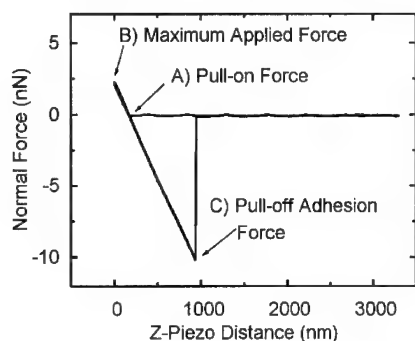
Figure 3. Force curve measured over the C_{16} acid region. Z-piezo position, normal cantilever deflection, and lateral cantilever deflection were recorded at each of the points A, B, and C.

Topography and adhesion are shown in Figure 4 for a 256 x 256 array of force curves measured over 2 hours. The topography map (Figure 4, left) was constructed from the z-piezo position at the maximum applied force of 2.6 nN. As in the contact scan (Fig. 2), a height difference of 2 nm was also measured between two distinct height levels.
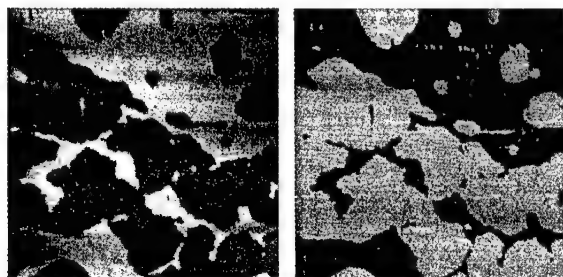
Figure 4. Maps shows the topography (a) and adhesion (b) for a 256 x 256 force curve array.

The adhesion map (Figure 4, right) was constructed from pull-off force data. The pull-off force was determined from the difference between the cantilever deflection measured at point C in Figure 3 and the undeflected cantilever position when the tip is well separated from the surface. Two discrete adhesion levels were observed with the pull-off force over the C_{16} regions being 20% larger. The pull-off force for over 86,000 force curves was analyzed in Figure 5. Two Gaussian distribution curves were used to fit the two discrete adhesion levels at 8.9 ± 1.1 nN (C_{24} region) and 10.8 ± 1.0 nN (C_{16} region) with a third Gaussian used to fit the

intermediate adhesion level between these two regions. Increased adhesion over the C_{16} regions supports the observation that the tip penetrates more deeply into the C_{16} regions of the LB film.
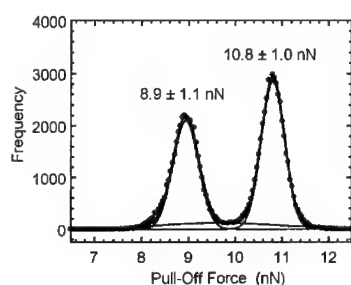
Figure 5. Histogram of the pull-off force from 86,000 force curves. The heavy line is the sum of three Gaussians used to fit the data.

DISCUSSION

During both contact scanning and force curve mapping a film height difference of 2.0 nm was measured, and there was a 20% increased adhesion of the tip to the C_{16} region. However, the difference in the chain length between C_{16} and C_{24} is only 1.01 nm[10]. Both the remaining 0.99 nm of the measured height difference and the increased adhesion can be explained by considering how the surface film responds during contact scanning or force curve mapping.

The moduli for the pure C_{16} and pure C_{24} acid films were calculated using the π vs. A curves shown in Figure 1 and are listed in Table 1 along with data for the mixed film. In Figure 1, the straight lines are fits to the L_2 phase from 19.6-25 Å^2/molecule and LS phase from 18.6-19.6 Å^2/molecule. The slope of the straight line ($\delta\pi/\delta A$) multiplied by the area/molecule gives E at that area/molecule. Note in Table 1 that for both the L_2 and LS phases, the pure C_{24} film has the highest computed modulus, the pure C_{16} film has the next highest, and the mixed C_{24} and C_{16} film has the lowest. As the films are compressed, E increases by a factor of 2.5-4 during the L_2 to LS phase transition. The C_{24} film also has the highest collapse pressure listed in Table 1.

Table 1. Fatty Acid Monolayer Film Properties

	C-24	C-16	1:1 C-16:C-24
$\delta\pi/\delta A$ in high π region	-34.1	-14.6	-12.2
$\delta\pi/\delta A$ in low π region	-6.88	-4.78	-3.34
E^a @ 19.4 Å^2/molecule	630±40	260±50	236±50
E^a @ 22 Å^2/molecule	150±10	100±10	73±10
Å^2/molecule at 30 mN/m	19.73	19.18	19.35
Collapse Pressure (mN/m)	57	36	37

[a] $E = -A(\delta\pi/\delta A)$; units = mN/m. Compression rate: 1 mN/m per min. Slopes of the π vs. A isotherm ($\delta\pi/\delta A$), E value, and collapse pressures all indicate that the longer chain acid is more resistant to compression.

Interaction between the SPM tip and the two regions of the LB film is schematically shown in Figure 6. When the tip contacts the film, the film yields and is thinned locally under the tip. The force that thins the film is opposed by intermolecular cohesive forces between the fatty acid chains. The collapse pressure of the LB film (Table 1) is a measure of this intermolecular cohesiveness

[11]. In addition to being thinned, the film will also be compressed in the surface plane near the contact perimeter and may be partially lifted from the mica surface. The amount that the film is compressed depends on balancing the force applied by the tip with the repulsive electronic overlap forces of the fatty acid chains. Upon withdrawal of the tip, the film spreads back over the high energy mica surface [12]. In Figure 6 the region of the tip in contact with the LB film during loading is indicated by shading. Note that the contact region is larger for the C_{16} film than for the C_{24} film.
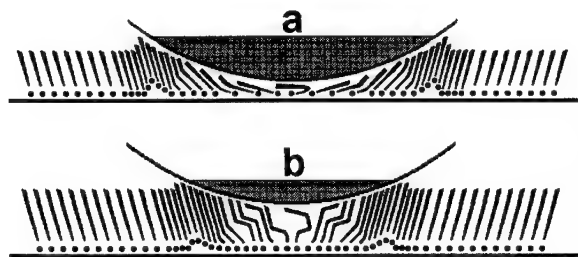
Figure 6. Schematic representation of the compression of the LB film by the SPM tip over the C-16 region (a) and the C-24 region (b). The shaded area of the tip indicates the contact region.

To explain the difference in adhesion levels, we first examine the contact mechanics relationships governing the tip-surface interaction. From Hertz, we know that the contact radius, a, is dependent on the modulus of the materials, i.e.,

$$a^3 = 3PR/4K \qquad (1)$$

where P is the applied load, R is the tip radius, and K is the reduced modulus given (for the case where only the substrate is deformable) by $1/K = (1-v^2)/E$ where v is Poisson's ratio and E is Young's modulus. For an elastic surface and rigid tip, the contact area increases under an applied load, but on reducing the load to zero the contact area also goes to zero unless there is adhesion between the tip and substrate. Adhesive forces act as an additional load so that even at zero applied load there is a finite force and contact area at separation. For a spherical tip and flat surface, JKR theory [13] predicts that the pull-off or adhesive force, F_a is

$$F_a = -1.5\pi W_{12}R \qquad (2)$$

where W_{12} is the work of adhesion. $W_{12} = \gamma_1 + \gamma_2 - \gamma_{12}$ where γ_1 and γ_2 are the surface energy of the tip and substrate and γ_{12} is the interfacial surface energy. The work of adhesion can be approximated by $2\sqrt{\gamma_1\gamma_2}$ when only dispersion forces are considered. From Hertzian contact mechanics we also know the geometrical relationship $R = a^2/\delta$ where a is defined above and δ is the surface deformation.

From our experimental measurements, the ratio of the pull-off forces is $F_{a16}/F_{a24} = 1.2$, which suggests a change in either W_{12} or R over the two different regions. For the elastic models described above, R and the resulting contact area at separation should be constant. Therefore, the only way for F_a to change is for there to be a corresponding change in surface energy over the two regions. For example, Berger et al. [14] have measured a difference in adhesion between crystalline

solid and amorphous liquid phases of a monolayer formed from the single compound, dimyristoyl phosphatidylethanolamine (DMPE). They correlate the adhesive force with differences in surface energy between CH_2 groups along the hydrocarbon chain and CH_3 end groups. While the phases of the DMPE film are vastly different, we did not expect this same result for the mixed fatty acid film. In the mixed acid film, both domains have the same molecular orientation, packing density, and CH_3 group surface termination, and therefore they should have the same surface energy as measured by contact angle. However the two domains do differ substantially in their compressional modulus; the shorter chain having the smaller modulus (see Table 1). As a result, these films respond differently to an applied load. For a given load, the shorter chain length film deforms more than the longer chain length film, giving rise to a measured step height difference of 2 nm. As the film is deformed underneath the tip, the tip-surface interaction changes, exposing the tip to other functional groups buried within the film or to the substrate itself. The area of maximum deformation is likely to occur directly under the tip where the contact pressures are highest, which may even exceed the yield strength of the thin film resulting in plastic or viscoelastic deformation. Any plastic or viscoelastic deformation of the LB film will invalidate the elastic models discussed here and may cause the adhesive force to depend directly or indirectly on parameters such as the LB compressional modulus and the contact area. (For example, it has been previously demonstrated that for a 20 nm tip radius, inelastic behavior can begin for applied loads as small as 7 nN, resulting in an increased contact radius and increased pull-off force relative to elastic models [15].) Figure 6 schematically indicates that the force with which the solid film resists deformation can be related to the compressional modulus of the film because the molecules must be displaced laterally, becoming compressed in the region surrounding the perimeter of the contact area. The dependence of SPM image contrast on adhesive and frictional forces and their relationship to the mechanical properties of the film can be observed by examining the pull-off force as a function of fatty acid chain length. This effect is presently under investigation in our laboratory.

CONCLUSIONS

We have shown that variations in the compliance of surface films can directly affect pull-off (and lateral) force measurements by SPM leading to image contrast in both the adhesion and frictional force images and maps of the surface. This mechanical contrast mechanism has two important ramifications for SPM imaging of soft, heterogeneously compliant materials. First, as demonstrated by this study of mixed chain-length LB films, SPM cannot directly measure the actual height or height differences of films without taking into account compliance differences. Secondly, when interpreting adhesion or frictional force images or maps, one must now consider both mechanical and chemical effects giving rise to the observed contrast. This consideration alone has far reaching consequences in our endeavor to develop a chemical force microscope.

REFERENCES

1. T. Nakagawa, K. Ogawa, and T. Kurumizawa, J. Vac. Sci. Technol. **B 12**, 2215 (1994).
2. C.D. Frisbie, L.F. Rozsnyai, A. Noy, M.S. Wrighton, C.M. Lieber, Science **265**, 2071 (1994).

3. T. Nakagawa, K. Ogawa, T. Kurumizawa, and S. Ozaki, Jpn. J. Appl. Phys. **32**, L294 (1993).

4. R.C. Thomas, P. Tangyunyong, J.E. Houston, T.A. Michalske, and R.M. Crooks, J. Phys. Chem. **98**, 4493 (1994).

5. L.F. Chi, M. Anders, H. Fuchs, R.R. Johnston, H. Ringsdorf, Science **259**, 213 (1993).

6. A. Schaper. L. Wolthaus, D. Mobius and T. M. Jovin, Langmuir **9**, 2178 (1993).

7. M. Salmeron, G. Neubauer, A. Folch. M. Tomitori, D.F. Ogletree, and P. Sautet, Langmuir **9**, 3600 (1993).

8. D.D. Koleske, G. U Lee, B.I. Gans, K.P. Lee, D.P. DiLella, K.J. Wahl, W.R. Barger, L.J. Whitman, and R.J. Colton, Rev. Sci. Instrum. **66**, 4566 (1995).

9. I.R. Peterson, V. Brzezinski, R.M. Kenn, R. Steitz, Langmuir **8**, 2995 (1992).

10. M. Rösch, in Nonionic Surfactants, edited by M.J. Schick, (Marcel Dekker Inc, New York, 1969), p.753. For every pair of carbons, the chain length is increased by 0.252 nm.

11. G.L. Gaines, Jr., Insoluble Monolayers at Liquid-Gas Interfaces, (Interscience Publishers, New York, 1966), p. 144.

12. There is very little damage to LB films for applied loads < 5 nN, see X.-D. Xiao, G.-Y Liu, D.H. Charych, and M. Salmeron, Langmuir **11**, 1600 (1995).

13. J.N. Israelachvili, Intermolecular and Surface Forces, 2nd edition (Academic Press, New York, 1992).

14. C. E. H. Berger, K. O. van der Werf, R. P. H. Kooyman, B. G. de Grooth, and J. Greve, Langmuir **11**, 4188 (1995).

15. T. P. Weihs, Z. Nawaz, S. P. Jarvis and J. B. Pethica, Appl. Phys. Lett. **59**, 3536 (1991).

AUTHOR INDEX

385

SUBJECT INDEX